Bayesian modelling of seismic scattering and intrinsic attenuation in the lithosphere

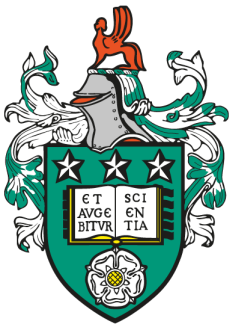

Itahisa Nesoya González Álvarez

Submitted in accordance with the requirements for the degree of
Doctor of Philosophy

The University of Leeds
School of Earth and Environment

May 2022

The candidate confirms that the work submitted is their own and that appropriate credit has been given where reference has been made to the work of others.

Acknowledgements

It feels surreal to be writing this section. For some reason, it always felt that the moment of finishing my PhD was so far ahead in time and now that I'm here, it feels it was only yesterday that I started it. Thinking of these past few years brings so many moments and, especially, so many people to mind, that I probably cannot make them all justice, but I'll try as best as I can.

Someone told me once that, for a PhD, having the right supervisors was much more important than choosing the right project. I know first hand how true this statement is, because I have had the privilege to always work with great supervisors and know what big of a difference they make. My PhD project has ended up being completely different to what I thought I'd do. It's been hard, and long, and often frustrating, but also fun and full of excitement, and I know I wouldn't have been able to get to its end hadn't it been for my supervisors. Sebastian Rost and Andy Nowacki, have been extraordinarily approachable and supportive, and have guided me through my PhD, teaching me so much, not just academically but also as a person. You have shown me that, even if things don't work, or don't go according to plan, there is still something of value to get out of them. Sebastian Rost in particular has been a constant reminder that there is life outside work and that I should always prioritise my physical and mental health, which I am very grateful for. I also want to mention my AWE Blacknest supervisor, Neil Selby. It was great to have the opportunity to work there with you and meet and learn from all the fantastic people there. I would also like to thank past supervisors, who have contributed to making me the scientist I am today. Antonio Eff-Darwich Peña, for introducing me to research and outreach and for his endless enthusiasm and curiosity. It's been, and continues to be, a pleasure to learn from and work with you. Javier Almendros González, for challenging and guiding me in my first steps as a researcher, and also for helping me achieve my dreams of working on active volcanoes and Antarctica. These experiences have not only made me a better scientist but a better person, and I will be forever grateful for that.

It is very true that science doesn't happen in a vacuum, and I also feel very lucky to have been part of IGT and work and interact with so many brilliant colleagues. All the coffee breaks, IGT seminars and research group meetings have not only been welcome

distractions from everyday research stress and problems but also great ways to learn about a multitude of fascinating topics. Many thanks in particular to the SeisMatters group members and organisation team, past and present. I have truly enjoyed our meetings and learnt so much from all of you. To Locko Neuberg, for offering me the chance to join the Lanzarote field trips and take part in your outreach events. These are, without a question, some of the best and most memorable moments of my PhD. To Roger Clark, for an extremely long and fun chat about all things scattering and attenuation that helped me see my research from a completely different point of view. I wish we could have had more of those.

My friends have also played a huge role in getting me through this PhD. My Leeds friends, Rachel, Thirze, Maeve, Edna and Jamie. You have been inspirations and mentors, colleagues and friends, and have helped me in more ways than I can describe here. You have made a huge difference for me and I wouldn't have made it without all of you. My Tenerife friends, my chosen family, Yaiza, Carmen, Gabry, José Ángel, Juanjo, MariaJo, Laura and Juanmi. Thank you for helping me stay grounded, remind me of the things that really matter and also let me occasionally rant my frustrations out. Despite the distance, each and every one of you have played a role in getting me this far and I am grateful for that. Especial mention to Marja, always cheering on me from the distance, encouraging me to pursue my dreams and trying to convince me that I am better and stronger than I myself think I am. You are a huge inspiration and incredible role model, and I am convinced I would not be here today if I had not met you. I am incredibly lucky to have all of you in my life.

Many, many thanks to my family, who have always supported me as best as they can and always been interested in my progress and wellbeing. To my grandma, who wouldn't have understood what I am doing or why, but would have been immensely proud of me. Her tireless work, as well as my parents', have opened new opportunities for our family, which I am truly grateful for.

Last, but not least, I want to thank Gonzalo for his endless support and love, for all the silliness and laughs, for our incredible adventures, and, especially, for always believing in me even more than I do in myself. You are and have always been an inspiration and made me want to be better, be curious and take up challenges. I definitely would not be here if it wasn't for you, and I am very much looking forward to discovering what new adventures and challenges await ahead of us.

And, finally, thanks to past me, who (mostly) managed to overcome the fear, shame and anger of years of abuse and struggle to pursue her childhood dream of becoming a scientist and do research. You made it.

Abstract

Heterogeneities present within the structure of our planet cause seismic waves to attenuate, especially when they are on the order of the seismic wavelength. Cracks, fluids, and patches of different temperature or composition are only a few examples of such inhomogeneities, all of which can produce complex wavefield fluctuations in time and amplitude and affect the signals recorded at the surface. Seismic source and velocity inversions, the discrimination and yield of a chemical or nuclear explosion, or peak ground velocity and acceleration are only a few examples of calculations directly derived from seismic data which require accurate amplitude measurements. However, while seismic amplitudes are particularly affected by scattering and absorption, many of the models used for these and other estimations are laterally homogeneous or smoothly varying, potentially biasing the results obtained from them.

In this thesis, I combine both single- and multi-layer energy flux models (EFMs) with a Bayesian inference algorithm to rigorously and probabilistically characterise the small-scale heterogeneity and attenuation structure of the lithosphere beneath seismic stations and arrays. The single-layer energy flux model, or EFM, characterizes the energy losses to the ballistic arrivals by means of the intrinsic, scattering and diffusion quality factors. I then use these values to compare the strength of these different attenuation mechanisms and their effects on the recorded signals. I implemented two main versions of the multi-layer EFM. The first of these, called here the Depth Dependent Energy Flux Model (EFMD), uses the intrinsic quality factor obtained from the EFM and a new Bayesian inversion algorithm to compute synthetic coda envelopes. By comparing synthetic and data envelopes, I can then obtain the scattering parameters (correlation length (a) and RMS velocity fluctuations (ε)) in each layer of the model. The second, expanded, version of the EFMD, called the E-EFMD, does not rely on the EFM and can simultaneously invert for both the scattering and intrinsic attenuation (intrinsic quality factor at 1 Hz (Q_{i0}) and its frequency dependence coefficient (α)) parameters in each layer of the model. Both the EFMD and E-EFMD use the Metropolis-Hastings algorithm to sample the likelihood space and obtain posterior probability distributions for each parameter and layer in the model.

My thorough testing of these methods reveals the specific effect each of these pa-

rameters has on the seismic codas, with initial coda amplitudes being more affected by the scattering parameters and decay rates controlled mostly by intrinsic attenuation. Independent calculation of these parameters in multi-layer models using the EFMD or E-EFMD remains challenging due to complex and strong trade-offs between them and to solutions being extremely non-unique in most cases. This issue is accentuated by an apparent bias of the E-EFMD towards extreme values of the intrinsic quality factor at 1 Hz. Overall, my results highlight the importance and usefulness of the Bayesian inference framework in this kind of study, since it provides detailed information about the uncertainty and uniqueness of the solutions. I applied these approaches to large, high quality, datasets of teleseismic events recorded by the Pilbara (PSA), Alice Springs (ASAR), Warramunga (WRA), Eielson (ILAR), Lajitas (TXAR), Pinedale (PDAR), Yellowknife (YKA) and Boshof (BOSA) seismic arrays or stations. For PSA, ASAR and WRA, my EFM and EFMD results suggest scattering is the main driver of attenuation, with the crust beneath them presenting different heterogeneity strengths and the lithospheric mantle being mostly homogeneous. Data inversions of ILAR, PDAR, TXAR, YKA and BOSA data using the EFMD and E-EFMD point to the algorithm being unable to fit the data in many cases, likely because of the assumed power law frequency dependence for Q_i not being good enough to explain the complex coda behaviours shown in their datasets but also due to the aforementioned bias of the algorithm towards extreme values of some parameters, which is also observed in PSA, ASAR and WRA E-EFMD data inversions. Relating these inversion results to the physical structure beneath the stations is, therefore, not possible. In general, my results suggest that parameter trade-offs and solution non-uniqueness in the E-EFMD are too extreme to allow for successful simultaneous recovery of all the parameters, while the combination of the EFM and EFMD can yield stable and reliable results for 1- and 2-layer models and also allow us to compare between different attenuation mechanisms.

Contents

List of Figures

List of Tables

Chapter 1

Introduction

The Earth is heterogeneous on a variety of scales, ranging from the grain scale to scales of hundreds of kilometers. Heterogeneities such as changes in composition or temperature, cracks, the presence of gas bubbles or fluids are evident in data and results from geo-disciplines with as varying sensitivity to different scales as geochemistry, petrology or seismology, and at depths ranging from the surface to the inner core (e.g. Wu and Aki, 1988; Vernik and Nur, 1992; Romanowicz and Durek, 2000; Cormier and Li, 2002; Sato et al., 2012; Kennett and Furumura, 2016; Rost et al., 2021). In a laterally homogeneous medium, direct seismic waves can be reflected or refracted at layer boundaries, but most of the energy they carry reaches the free surface, and the recording instruments on it, within a short time interval (Fig. 1.1). In contrast, when seismic waves propagate through a heterogeneous medium (Fig. 1.2), only a fraction of the energy of the initial wavefront reaches the free surface in the same time window as the ballistic arrival (Fig. 1.1). Since recorded amplitudes of seismic waves are directly related to the energy they carry, this reduction in the direct wave energy results in lower recorded amplitudes (Fig. 1.1, also e.g. Toksöz et al., 1979). Part of this "lost" energy is scattered at the inhomogeneities in the medium and can either reach the free surface at later times or be backscattered into lower layers (Fig. 1.2). The energy that gradually reaches the free surface at later times forms a tail that trails the ballistic arrivals called the seismic coda (Fig. 1.1). Aki (1969) showed that the power spectra of these coda waves for a given station are independent of epicentral distance and earthquake magnitude. They proposed that seismic codas were caused by backscattered energy from discrete heterogeneities randomly distributed beneath the stations. The presence and shape of the coda strongly depends on the heterogeneity structure and, therefore, can be related to the geology beneath the station. Later studies (e.g. Aki and Chouet, 1975; Rautian and Khalturin, 1978; Aki, 1980b; Sato et al., 2012) showed that the stable decay in coda wave amplitude was also independent of epicentral distance and source mechanism, and that other attenuation mechanisms failed to

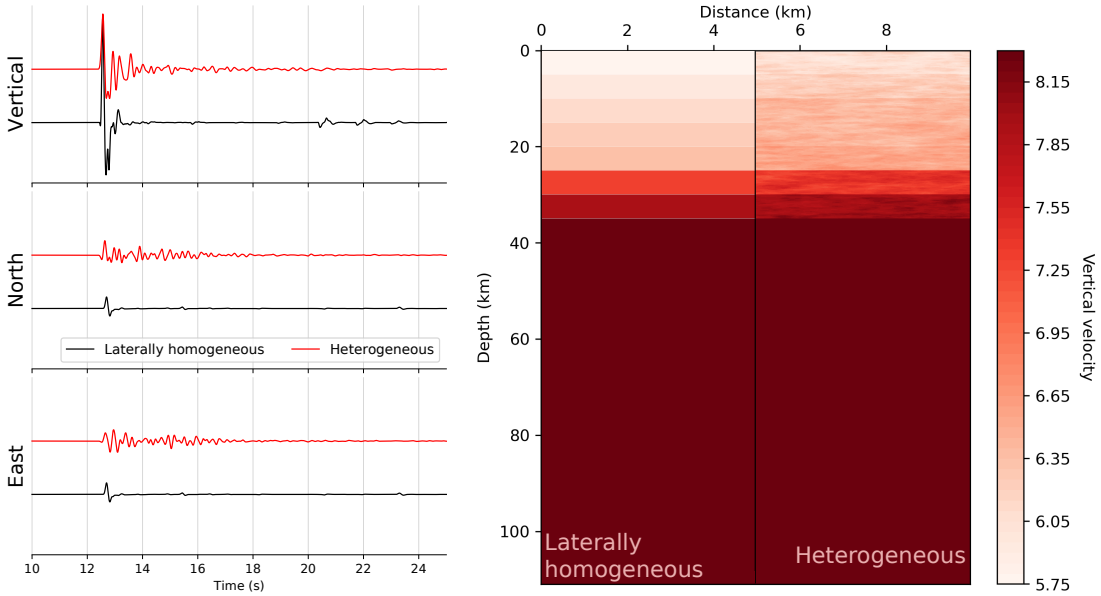

Figure 1.1: Comparison of synthetic traces obtained using OpenSWPC (Maeda et al., 2017) for a laterally homogeneous model (black lines, velocity model on the left) and those for the same model with added crustal random heterogeneities (red lines, model on the right). These inhomogeneities are characterized by their average spatial distribution, controlled by the correlation length a, and the velocity fluctuations with respect to the background medium, ε. In this example, these parameters follow an exponential autocorrelation function, with $a = a_x = a_y = a_z = 0.5$ km (x and y representing the horizontal directions and z the vertical), and $\varepsilon = 0.5$ km.

reproduce the observed signals, thus fully supporting the scattering hypothesis. Several scattering regimes can be identified based on key parameters such as the wavenumber (k), the correlation length (a), the RMS velocity fluctuations of the heterogeneity (ε) or combinations of these. As an example, the normalised wavenumber (ka) is commonly used to define scattering as quasi-homogeneous ($ka < 0.01$), Rayleigh type ($ka \ll 1$), Mie or large-angle ($ka \approx 1$) or small-angle ($ka \gg 1$) (e.g. Wu and Aki, 1988). The length and amplitude of the coda is, therefore, directly related to the small-scale heterogeneity structure in the areas surrounding either the seismic source, the receiver or both (e.g. Sato et al., 2012; Napolitano et al., 2020; Aki, 1969; Aki, 1980b), as well as its average spatial distribution and strength. It is not, however, the only source of seismic attenuation. Within the Earth, both elastic and inelastic processes take place. In the former, the energy of the wavefield is conserved, as in the case of scattering, while in the latter, the seismic energy is not conserved (e.g. Müller et al., 2010; Sato et al., 2012). Absorption, also called intrinsic or anelastic attenuation, is caused by anelastic processes such as the conversion of seismic energy into heat due to friction, or the movement of fluids within cracks and pores in the structure (e.g. Müller et al., 2010; Tisato et al., 2015; Sun et al., 2015). These phenomena result in an exponential decrease in the recorded amplitudes of direct waves as a function of time (e.g. Sato et al., 2012; Carcolé and Sato, 2010; Müller et al., 2010). Although seismic codas

are most frequently related to scattering, at certain lapse times and for specific frequency bands, they can also carry information about absorption (e.g. Aki, 1980a; Aki and Chouet, 1975; Aki, 1980b; Rautian and Khalturin, 1978; Wegler, 2003; Sketsiou et al., 2020; De Siena et al., 2014). As with seismic scattering, the occurrence and intensity of intrinsic attenuation is also closely related to the heterogeneity structure of the Earth (e.g. Romanowicz and Durek, 2000; Tisato et al., 2015; Sun et al., 2015), changes in rheology (e.g. Romanowicz and Durek, 2000; Stachnik et al., 2004) and the local tectonic and volcanic history/activity, so that recent or more intense tectonic or volcanic activity is associated with stronger scattering and intrinsic attenuation (e.g. Romanowicz and Durek, 2000; Sketsiou et al., 2021; Rost et al., 2021; Borleanu et al., 2017; Napolitano et al., 2020). Finally, the recorded amplitudes of seismic waves are also affected by the geometric spread of the wavefront, by which the energy density at any point of the wavefront will gradually decrease with increasing travel time/distance as it is spread over a larger surface area (e.g. Sato et al., 2012; Fehler et al., 1992; Xia et al., 2020; Müller et al., 2010; Kennett and Phạm, 2018). As opposed to scattering and intrinsic attenuation, this phenomenon is mostly independent of the properties of the medium the seismic waves travel through. The addition of the effects of these three attenuation mechanisms (scattering, anelasticity and geometric spreading) provides a measure of the total attenuation experienced by the seismic wavefield as it propagates through the structure of the Earth (e.g. Sato et al., 2012; Toksöz et al., 1979; Müller et al., 2010).

Many seismological Earth models are laterally homogeneous or smoothly varying, with a lack of small-scale heterogeneity (e.g. Helmberger, 1968; Dziewonski and Anderson, 1981; Kennett and Engdahl, 1991; Randall and Owens, 1994). Estimations inferred from seismic data often rely on amplitude measurements (e.g. Selby et al., 2012; McLaughlin and Jih, 1988; Zhang and Wen, 2013), which, as stated above, are affected by both elastic and anelastic processes that take place along the entire ray path. The use of smooth, simplified models of the Earth, not only limits our understanding of high-frequency seismic wave propagation but can potentially bias any calculations derived from seismic amplitudes. In tectonic settings, studies have suggested a dependence of intrinsic attenuation on strain rates (e.g. Eberhart-Phillips et al., 2014) and shown that having accurate characterizations of the scattering and absorption structures beneath and around fault systems can help us better understand their dynamics and improve our seismic hazard assessments (e.g. Sketsiou et al., 2021; Rost et al., 2021; Napolitano et al., 2020; Borleanu et al., 2017). For volcanoes, where scattering and attenuation can be very strong and significantly affect seismic signals, the spatial mapping of scattering and intrinsic attenuation parameters have been used to image their plumbing systems and magma pathways (e.g. Prudencio et al., 2017; De Siena et al., 2014; Wegler, 2003), which in turn can also help us refine our volcanic

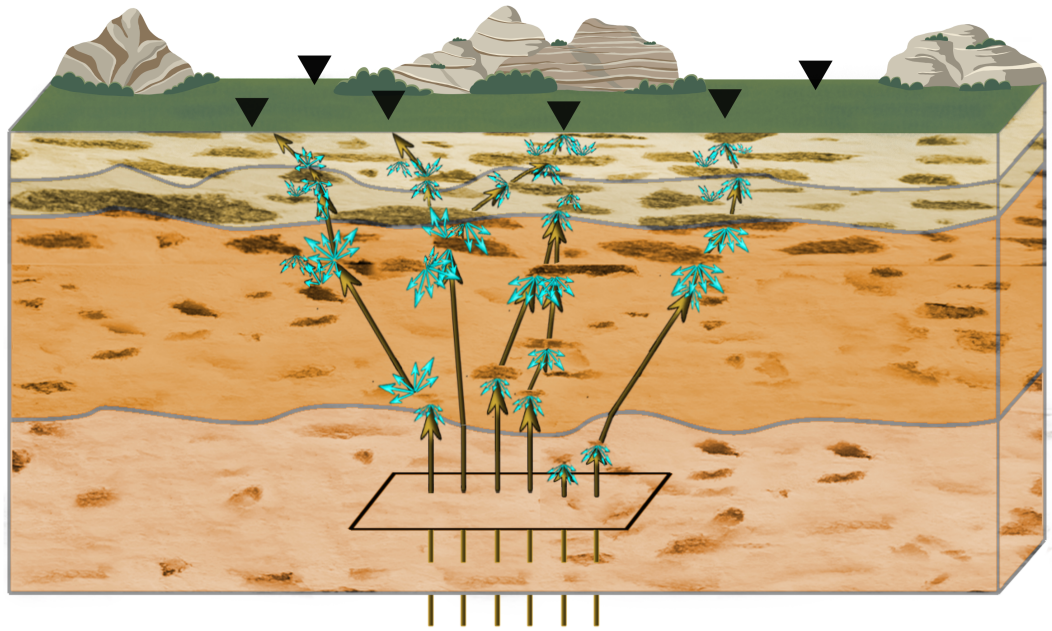

Figure 1.2: Simplified representation of the scattering and intrinsic attenuation processes as seismic waves propagate through a heterogeneous layer. A plane wavefront, represented by the vertical arrows at the bottom of the model, enters the structure, where it encounters discontinuities and heterogeneities that deviate the ray paths from a straight line path (scattered trajectories are represented by blue arrows) and cause the energy to reach the surface at later times and/or be backscattered into the lower layers again.

hazard estimates. The study of scattering and attenuation is also key for nuclear explosion monitoring purposes, since event discrimination and magnitude-yield estimations are obtained, directly or indirectly, from recorded seismic amplitudes and need to be corrected for path effects using attenuation models and/or calibration using historical datasets (e.g. Selby et al., 2012; Zhang and Wen, 2013; McLaughlin and Jih, 1988; Douglas, 2013). Seismic hazard estimations would also benefit from improved scattering and attenuation characterizations, since these affect peak ground velocity and acceleration estimations (e.g. Eulenfeld and Wegler, 2016). These are only some examples that show the importance of understanding and accurately characterizing the heterogeneity and attenuation structures, as well as their effects on recorded wavefields.

Methods to study scattering and attenuation within the Earth vary depending on the type and scale of the heterogeneity. Many seismological studies use deterministic methods to characterize the structure of the Earth (e.g. Christensen and Mooney, 1995; Zelt and Barton, 1998) or to find, locate and characterize individual scatterers (e.g. Etgen et al., 2009; Thorbecke et al., 2017; Neut et al., 2015). (e.g. Thorbecke et al., 2017; Neut et al., 2015)(e.g. Etgen et al., 2009). These techniques tend to have limited spatial resolution due to the wavelength of the studied waves and do not always take into account small-scale heterogeneities (on the order of magnitude of the

wavelength or smaller), therefore failing to explain or reproduce the complex coda waves we see in seismograms. A different approach that partially overcomes these issues uses a stochastic description of the heterogeneity (e.g. Korn, 1990; Korn, 1997; Ritter et al., 1998; Hock et al., 2004; Margerin, 2005). This kind of approach (e.g. Frankel and Wennerberg, 1987; Korn, 1990; Fehler et al., 1992; Shapiro and Kneib, 1993; Hock et al., 2004; Margerin, 2005; Sato and Emoto, 2018) provides a statistical description of the structure and determines the integrated effect of heterogeneity on propagating seismic waves, so the characteristics and locations of individual scatterers are not relevant. Studies show the crust and lithospheric heterogeneity are statistically complex (e.g. Kennett and Furumura, 2016) and the necessity of heterogeneous Earth models that are capable of explaining not only the main waveforms but also coda waves (e.g. Aki, 1973; Flatté and Wu, 1988; Langston, 1989). Single-scattering perturbation theory (e.g. Aki and Chouet, 1975; Sato, 1977; Sato, 1984) was one of the first methods designed for this purpose. Here, scattering is a weak process and limited to a single scattering event along the path. Coda waves are considered the superposition of single scattered waves generated at randomly distributed heterogeneities within the Earth. It often makes use of the Born approximation (e.g. Sato et al., 2012), a first-order perturbation condition which does not take into account the energy loss due to scattering. As a result, within this model, energy is not conserved in the scattering process (e.g. Aki and Chouet, 1975; Sato et al., 2012). In this model and at low frequencies, the quality factor of coda waves, Q_c, includes both the effects of scattering and anelastic attenuation. At the other end of the heterogeneity strength spectrum is the stochastic diffusion model (Aki and Chouet, 1975). In this framework, scattering is strong and can occur multiple times along the ray path, thus resulting in codas being mainly composed of multiply scattered waves. All the seismic energy is scattered through diffusion, and Q_c includes only energy losses due to anelasticity. These two approximations are at the core of many, widely used, techniques.

In recent years, Radiative Transfer Theory (RTT) has become one of the most frequently used methods to either separately or jointly characterize the effects of scattering and intrinsic attenuation on propagating seismic waves. This stochastic technique was initially developed for light propagation (Chandrasekhar, 1950) and it was first applied to seismology in the 1980s (e.g. Wu, 1985; Gusev and Abubakirov, 1987) but has been significantly improved and expanded (e.g. Margerin et al., 1998; Przybilla and Korn, 2008; Nakahara and Yoshimoto, 2011; Sanborn et al., 2017; Sato and Emoto, 2017; Sato and Emoto, 2018; Hirose et al., 2019; Margerin et al., 2019) since then. In particular, the development and improvement of Monte Carlo simulations (e.g. Hoshiba, 1991) and analytical approaches to solve the radiative transfer equations have made it possible to apply RTT to a wide variety of tectonic and geological settings (e.g. Gaebler et al., 2015b; Gaebler et al., 2015a; Margerin, 2003; Hirose et al., 2019; Wegler, 2003;

Prudencio et al., 2015; Nardoni et al., 2021; Fielitz and Wegler, 2015; Carcolé and Sato, 2010). RTT is not, by any means, the only statistical method currently used to study seismic scattering and/or absorption. Other methods to analyse coda energy and study lithospheric heterogeneity have been proposed and are also frequently used, such as Multiple Lapse Time Window Analysis (MLTWA, e.g. Hoshiba, 1991; Fehler et al., 1992), the coda normalization method (Aki, 1980a; Sketsiou et al., 2021; De Siena et al., 2014), the teleseismic fluctuation wavefield method (TFWM, e.g. Shapiro and Kneib, 1993; Ritter et al., 1998; Ma and Huang, 2020), peak-delay time measurements (e.g. Borleanu et al., 2017; Napolitano et al., 2020), energy flux models (e.g. Frankel and Wennerberg, 1987; Langston, 1989; Korn, 1990; Korn, 1997) or coda wave interferometry (e.g. Snieder, 2006), among others. From the computational point of view, a number of codes implementing RTT and other methods of stochastic wave propagation in random media have been developed and made publicly available in recent years (e.g. Eulenfeld and Wegler, 2016; Sanborn et al., 2017; Maeda et al., 2017), and the combination of Machine Learning algorithms with RTT or other stochastic methods (e.g. Belochitski and Krasnopolsky, 2021) offers a very promising path into the future of scattering and attenuation studies. However, while these methods are able to characterize the heterogeneity structure of the Earth, they all use approximations, are computationally expensive, or both, which highlights the need for improvements both within the theoretical and computational frameworks if we want to advance and better our models of the small-scale structure of the Earth.

In this thesis, I use single-layer and depth-dependent Energy Flux Models (EFM and EFMD respectively, Korn, 1990; Korn, 1997) to study and compare scattering and intrinsic attenuation in the lithosphere. In Chapters 2 and 3, I describe and test my implementation of these methods based on their description in the literature, as well as my Bayesian inference algorithm, and apply them to large, high quality datasets from three seismic arrays in Australia (Pilbara Seismic Array (PSA), Alice Springs Array (ASAR) and Warramunga (WRA)). Then, in Chapter 4, I expand my initial implementation of the EFMD to allow for the joint Bayesian inversion of scattering and intrinsic attenuation parameters. After thoroughly testing this new algorithm both by means of synthetic tests and real data inversions, in Chapter 5, I apply it to datasets from five seismic arrays or stations part of the International Monitoring System (IMS). My results show complex trade offs between the scattering and/or intrinsic attenuation parameters, which highlight the importance and usefulness of Bayesian inference in this context, since this approach provides detailed information about the posterior probability distributions and the parameter space. The EFM/EFMD combination yields stable and reliable results for one- and two-layer models, while their expansion to invert also for the absorption parameters suggest the trade-offs between the parameters are too extreme to be accurately resolved.

Chapter 2

Methods

The Energy Flux Model, or EFM (Frankel and Wennerberg, 1987), is a technique initially developed as an alternative to the single-scattering theory (e.g. Chernov and Silverman, 1960; Aki, 1980b; Sato, 1984) for the statistical characterization of the small-scale heterogeneity of the crust. The original formulation of the EFM, developed by Frankel and Wennerberg (1987), was designed to model seismic S wave codas from local earthquakes using a phenomenological approach based on the energy conservation law. By considering the balance of energy between the direct wavefront propagating through a scattering medium and the coda, Frankel and Wennerberg (1987) derived equations that predict coda levels and decays for any random media without explaining the scattering processes that are the origin of coda waves. As opposed to the single-scattering theory (e.g. Chernov and Silverman, 1960; Aki, 1980b; Sato, 1984), the EFM implicitly included multiple scattering, was applicable to both weak and strong scattering and allowed one to obtain independent estimates of the intrinsic (Q_i) and scattering (Q_s) quality factors. Frankel and Wennerberg (1987) tested their approach both on synthetic data obtained from 2D acoustic finite difference simulations and real data from two M$\sim$3 earthquakes from southern California. They found that the EFM could explain the coda decays and levels observed both in synthetic and recorded waveforms and proposed it as an improvement over the single-scattering theory which was commonly used at the time to analyse codas from local earthquakes.

Korn (1988) was one of the first studies to apply the EFM. However, instead of using it to analyse codas from spherical or cylindrical wavefronts spreading from a point source nearby and travelling approximately horizontally through a heterogeneous medium, Korn (1988) changed the formulation of the method to use it on plane wavefronts reaching a model formed by a heterogeneous layer above a homogeneous half-space from below and travelling upwards to the free surface. This new geometry made the updated EFM applicable to P wave codas from deep teleseismic events and suitable

for the study of the near-receiver, small-scale heterogeneity structure. Korn (1988) used this new implementation of the EFM to analyse P codas from 54 events from the Flores, Timor and Banda Sea region recorded at the Warramunga Array in central Australia.

Korn (1990) added diffusion attenuation to the EFM, to take into account the energy that is constantly scattered back from the inhomogeneous layer into the half-space. The implementation by Korn (1988) did not include diffusion in its formulation, thus forcing the scattered energy to stay within the scattering layer at all times and causing an overestimation of the intrinsic attenuation. Langston (1989) also extended the EFM from Frankel and Wennerberg (1987) to apply it to teleseismic P codas and include diffusion, but his version of the method only allowed the energy to leave the heterogeneous layer once the direct wave left it on its way down after total reflection at the free surface, while diffusion was permitted at any time in Korn (1990). This method does not take into account any phase conversions or reflections at interfaces other than the free surface, and assumes no strong lateral velocity changes are present beneath the seismic stations. When the technique is applied to full arrays, it is assumed that the same velocity and heterogeneity structure is present beneath all the stations. My implementation of the EFM, detailed in this section and applied in Chapter 3, is based on the modified Energy Flux Model developed by Korn (1990). All mentions of the EFM from here on will refer to this version of the method and any references to other implementations will be clearly indicated.

Building on the EFM, Korn (1997) expanded the formulation from Korn (1990), which included intrinsic, diffusion and scattering attenuation, to take into account variations in the small-scale heterogeneity structure with depth. From here on, and to avoid confusion with the EFM, I will refer to the depth-dependent Energy Flux Model from Korn (1997) as the EFMD.

In the past, the EFM and EFMD have been used both independently (e.g. Korn, 1993; Rothert and Ritter, 2000), together (Hock and Korn, 2000), or in combination with a third technique, called the Teleseismic Fluctuation Wavefield Method (TFWM, e.g. Ritter et al., 1998). This method is designed to statistically study the heterogeneity structure beneath seismic arrays (e.g. Ritter et al., 1998; Rothert and Ritter, 2000; Ritter and Rothert, 2000) and is based on the separation of the recorded P wavefields into a coherent or mean wavefield, which is observed at all stations, and an incoherent or fluctuating wavefield, which varies from one station to another. Overall, these techniques have been applied to a variety of tectonic and geologic scenarios, such as central Australia (Korn, 1990), the circumpacific area (Korn, 1993), central Europe (e.g. Ritter et al., 1998; Rothert and Ritter, 2000) or the Sichuan Basin, China (Li, 2010), among others. In this chapter, I focus on the single layer modified Energy Flux Model (EFM, Korn, 1990) and the depth dependent Energy Flux Model (EFMD, Korn, 1997) on Sections 2.1.1 and 2.1.2, but I also describe and test the Teleseismic Fluctuation

Wavefield Method in Section 2.2. This work is partially based on work published as González Álvarez et al. (2021).

2.1 Energy Flux Models

2.1.1 The modified Energy Flux Model (EFM)

When a plane wavefront travels through a heterogeneous unlayered medium, part of the energy propagates with the ballistic wavefront, while part forms the forward scattered coda energy that arrives later at the surface and some energy scatters back into the half-space. Total energy E_{tot} within the scattering layer is conserved in this process and it can be written in terms of angular frequency, ω, and time, t, as

$$E_{tot}(\omega,t) = E_d(\omega,t) + E_c(\omega,t) + E_{diff}(\omega,t) + E_i(\omega,t), \tag{2.1}$$

with E_d being the energy density of the direct wave, E_c the energy density that is transferred from the direct wave into the coda (forward scattered), E_{diff} the energy density that is leaked or diffused (backscattered) from the heterogeneous layer back into the half-space and E_i the anelastic or intrinsic energy losses due to dissipation into heat. At time $t = 0$, the wavefront enters the scattering layer from below, so $E_{tot}(\omega,0) = E_d(\omega,0) = E_0$ and $E_c(\omega,0) = E_{diff}(\omega,0) = E_i(\omega,0) = 0$. Direct wave energy losses due to scattering and anelasticity, controlled by quality factors Q_s and Q_i respectively, occur continuously while the ballistic wave is inside the inhomogeneous layer but stop at $t = 2t_1$ (t_1 being the one-way travel time through the layer), when it enters the half-space after total reflection at the free surface. Intrinsic attenuation also happens within the homogeneous half-space and is measured by Q_i', but it does not affect the coda and is not addressed by the EFM. Diffusion of energy out of the scattering layer and into the half-space can continue after $2t_1$ and is controlled by the diffusion quality factor Q_{diff}. Based on this, the energy balance within the inhomogeneous layer can be described with a system of differential equations (Korn, 1990; Korn, 1993):

$$\frac{d}{dt}\begin{pmatrix} E_d \\ E_c \\ E_{diff} \end{pmatrix} = \begin{pmatrix} -\omega(\frac{H(2t_1-t)}{Q_s} + \frac{1}{Q_i}) & 0 & 0 \\ \omega\frac{H(2t_1-t)}{Q_s} & -\omega(\frac{1}{Q_{diff}} + \frac{1}{Q_i}) & 0 \\ 0 & \frac{\omega}{Q_{diff}} & \frac{-\omega}{Q_i'} \end{pmatrix}\begin{pmatrix} E_d \\ E_c \\ E_{diff} \end{pmatrix}, \tag{2.2}$$

where H is the Heaviside step function or unit step function. From Eq. 2.2, the coda energy density E_c for times $t > t_1$ (after the direct wave reaches the free surface) can be defined as

$$E_c(\omega,t) = \frac{2E_0}{1 - Q_s/Q_{diff}} \sinh[\omega t_1 (Q_s^{-1} - {Q_{diff}}^{-1})] \cdot \\ e^{[-\omega t_1 (Q_i^{-1} + Q_s^{-1})]} e^{[-\omega t (Q_i^{-1} + {Q_{diff}}^{-1})]} . \tag{2.3}$$

The initial energy, E_0, can be calculated from the direct wave energy (E_D) measured at the free surface at $t = t_1$ as

$$E_0(\omega) = E_d(t_1)\ e^{-\omega t_1 (Q_s^{-1} + Q_i^{-1})} \quad . \tag{2.4}$$

The energy densities in Eqs. 2.2 and 2.3 cannot be directly estimated from data, but are related to the power spectral density, $P(\omega, t)$, which can be measured from the squared envelopes of filtered velocity seismograms (see Frankel and Wennerberg (1987), Korn (1990) or Langston (1989) for details), through:

$$E(\omega, t) = \frac{1}{c} \int P(\omega, t)\, dV \quad , \tag{2.5}$$

with c being a scaling factor and V the whole volume occupied by E.

For the coda, if we assume that coda energy within the heterogeneous layer is approximately homogeneously distributed in space, and that d represents the thickness of the scattering layer, the relationship between the coda energy density and the coda-power spectral density can be written as:

$$E_c = \frac{d\ \delta F}{c} P_c \quad . \tag{2.6}$$

This assumption, also supported by energy transport theory (e.g. Sato, 1995), is based on the independence of coda amplitudes with respect to hypocentral distance (e.g. Aki, 1980a), and backed up by results from numerical modelling (e.g. Frankel and Wennerberg, 1987; Korn, 1990). Further assumptions in the EFM are that the velocity of the scattered energy through the heterogeneous layer is the same as the P-wave and that energy propagates isotropically.

For the direct wave, if we define the average velocity of the scattering layer and the horizontal area increment as v and δF respectively, we can write $V = d\delta F = v t_1 \delta F$, and Eq. 2.5 becomes

$$E_d(\omega, 0) = \frac{1}{c} \iiint P_d\, dV = \frac{v \delta F}{c} \int_0^{\delta t} P_d(\omega, t)\, dt = \frac{v \delta F}{c} I_d \quad , \tag{2.7}$$

in which the integral I_d is calculated over the time window of the direct wave arrival, as estimated from the data based on the duration of the large amplitudes in the power spectral density plots.

Combining Eqs. 2.3, 2.4, 2.6 and 2.7, we can calculate the coda-power spectral density $P_c(\omega, t)$ as a function of the intrinsic, diffusion and scattering quality factors,

as well as the one-way travel time through the scattering layer:

$$P_c(\omega,t) = \frac{2I_d}{t_1\,(1-Q_s/Q_{diff})}\sinh[\omega t_1\left(Q_s^{-1}-{Q_{diff}}^{-1}\right)]e^{-\omega t\left(Q_i^{-1}+{Q_{diff}}^{-1}\right)} \tag{2.8}$$

Taking the logarithm of the theoretical coda-power spectral density shown in Eq. 2.8 for a fixed frequency converts the exponential decay shown in Eq. 2.8 into a linear function, from which we can define the coda decay rate, a_1, and the coda amplitude at zero time (t_0 being defined by the direct wave entering the heterogeneous layer), a_0 (Korn, 1990; Korn, 1993), as

$$\log_{10} P_c(\omega,t) = \log_{10}\ a_0 - a_1 t \tag{2.9}$$

with

$$a_1(\omega) = \omega \log_{10} e\left[Q_i^{-1}+{Q_{diff}}^{-1}\right] \tag{2.10}$$

and

$$a_0(\omega) = \log_{10}\left(\frac{2I_d}{t_1\,(1-Q_s/Q_{diff})}\sinh\left[\omega t_1\left(Q_s^{-1}-{Q_{diff}}^{-1}\right)\right]\right). \tag{2.11}$$

Calculating a_0 and a_1 at different frequencies using a linear least squares fit of Eq. 2.9 for a fixed frequency ω allows us to separately calculate Q_i, Q_s and Q_{diff}. For the scattering quality factor, Korn (1990) discussed the dependence of a_0 on Q_s and Q_{diff} for different scenarios and concluded that Q_s can always be estimated from a_0 without precise knowledge of Q_{diff}. In particular, if the scattering and diffusion quality factors are on the same order of magnitude, the hyperbolic sine in Eq. 2.11 approximately takes the value of its argument, which leads to

$$Q_s(\omega) \approx 2I_D\omega 10^{-a_0} \quad . \tag{2.12}$$

We can then use the relationship between Q_s^{-1}, the correlation length (a) and the RMS velocity fluctuations (ε) of the heterogeneity structure for different types of autocorrelation functions (ACFs) to determine the type of ACF that fits the data best. For isotropic exponential media, Fang and Müller (1996) obtained:

$$Q_s^{-1}(\omega) = \varepsilon^2\frac{28.73(a\omega/v)^3}{1+16.77(a\omega/v)^2+2.40(a\omega/v)^4} \quad , \tag{2.13}$$

where v is the mean P velocity of the random medium. Since the EFM does not allow any layering, a and ε represent an approximation to the average spatial distribution and strength of the heterogeneity of a hypothetical single scattering layer beneath the array or station.

The intrinsic and diffusion quality factors are obtained from the coda decay rate,

a_1, based on their different frequency dependence. Assuming that the relative energy loss of the coda per unit time does not depend on frequency, we can write:

$$Q_{diff}(\omega) = \frac{Q_{d0}\omega}{2\pi} \quad , \tag{2.14}$$

with Q_{d0} being the intrinsic quality factor value at 1 Hz. Equation A7 from Korn (1990), obtained using basic assumptions about the propagation of the wavefield in and out of the scattering layer in 3D media, defines the relationship between Q_{diff} and the one-way travel time through the scattering layer, t_1, as $Q_{diff} = 4\omega t_1$. This expression makes it possible to estimate the thickness of the layer, d, as long as a background velocity can be defined. However, this thickness is only a rough approximation to the real value and will not be used in my applications of the EFM.

For the intrinsic quality factor, the frequency dependence is described by

$$Q_i(\omega) = Q_{i0}\left(\frac{\omega}{2\pi}\right)^{\alpha} \tag{2.15}$$

where α is the exponent controlling the power law frequency dependence of Q_i (Korn, 1990, Eq. 17). Laboratory measurements of α have shown that it probably remains below 1 for most of the frequency range considered in most seismological studies (Korn, 1990, and references therein). Replacing these expressions for $Q_i(\omega)$ and $Q_{diff}(\omega)$ in Eq. 2.10, we obtain

$$a_1(\omega) = -2\pi[Q_{d0}^{-1} + Q_{i0}^{-1}(\omega/2\pi)^{1-\alpha}]\log_{10} e, \tag{2.16}$$

which, for a fixed α, allows us to calculate the intrinsic and diffusion quality factors values at 1 Hz, Q_{i0} and/or Q_{d0}, by measuring the coda decay rate at different frequencies and using a least squares inversion of Eq. 2.16. My attempts at obtaining α as a third free parameter in the inversion revealed a very complicated trade-off with Q_{i0} and Q_{d0}, with high values of α corresponding to negative values of Q_{i0} and/or Q_{d0}. Therefore, I limited α to the range of 0.0 - 0.6, in steps of 0.1, and chose the value that minimised the misfit to the data. Both my results and those of Korn (1990) show that α has a strong effect on Q_i but only weakly affects Q_{diff}. The impossibility to fully invert for α makes it difficult to accurately calculate Q_i within the EFM, but has a minor effect in the determination of Q_{diff} (Korn, 1990).

Finally, we calculated the combined quality factor, Q_{comb}, as the combination of the scattering, intrinsic and diffusion quality factors:

$$\frac{1}{Q_{comb}} = \frac{1}{Q_{diff}} + \frac{1}{Q_i} + \frac{1}{Q_s} \tag{2.17}$$

Please note that Q_{comb}, as opposed to other quality factors, is not related to the

energy decay of the wavefield nor is it applied to any specific part of the seismogram. Its only intent is to summarise the total coda attenuation and make it easier to compare my results from different arrays or stations.

2.1.2 The Depth-Dependent Energy Flux Model

In the EFMD, a plane wavefront enters a stack of N heterogeneous layers from below. Each layer j has its own characteristic transit time δt_j and scattering parameters a_j and ε_j (Fig. 2.1). The stack of layers is symmetric with respect to the free surface, at the center of the stack, to take into account the reflection of the wavefront.

For a given angular frequency ω_c, the normalised coda energy envelope of a velocity seismogram at the free surface is computed from the squared amplitude envelope $A^2(\omega_c;t)$ and is related to the energy balance within the different layers in the model through

$$\sqrt{\frac{A^2(\omega_c;t)}{I_d}} = \sqrt{\frac{2E_{C_N}(\omega_c;t)}{t_N E_D(\omega_c;t_N)}} \quad , \tag{2.18}$$

with I_d defined as in Eq. 2.7, $E_{C_N}(\omega_c;t)$ being the spectral coda energy density of the layer containing the free surface, t_N the traveltime from the bottom of the stack of layers to the free surface and $E_D(\omega_c;t)$ the energy density of the direct wave measured at the free surface. This normalization procedure ensures that the stacking of the envelopes from events with different magnitudes is not affected by differences in the amplitude scale of the original seismograms. Q_s and Q_i control the decay of the direct

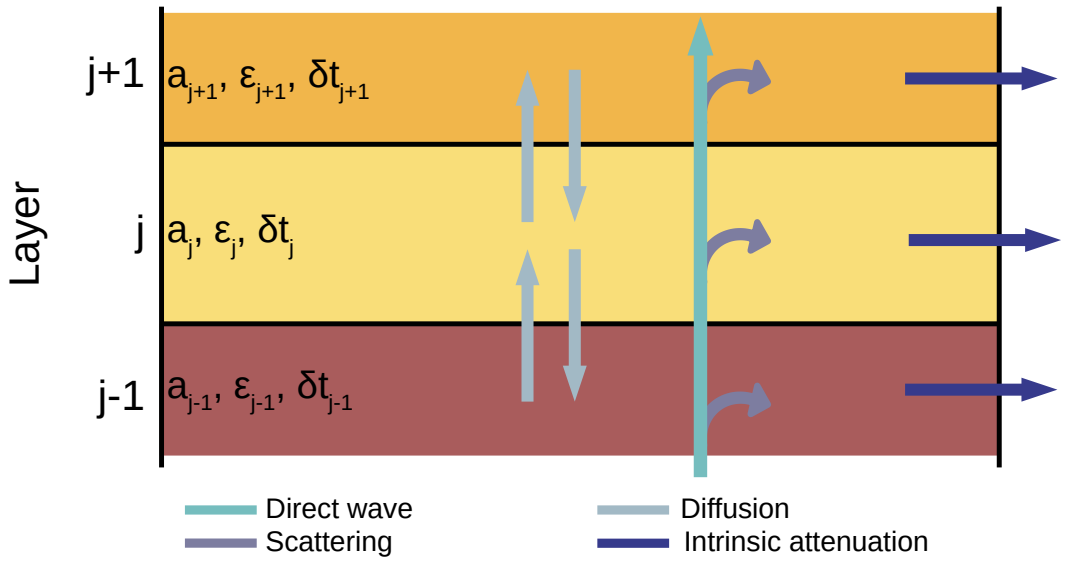

Figure 2.1: Total energy balance for layer j, according to the EFMD. (After Korn, 1997).

wave energy over time due to scattering and intrinsic attenuation via

$$E_D(\omega; t_j) = E_D(\omega_c; t_{j-1}) e^{-\omega(t_j - t_{j-1})(Q_{s_j}^{-1} + Q_{i_j}^{-1})} \quad , \tag{2.19}$$

where t_j represents the one-way travel time through each layer. As in the EFM, at time $t = 0$ the incident wavefront reaches the bottom of the model vertically from below and $E_d(\omega, 0) = E_0$. The EFM assumption of homogeneous scattered energy density within the volume behind the wavefront is now applied to each layer in the model (Korn, 1997), but differences between layers are allowed. Assumptions regarding isotropic energy spread and scattered energy velocity (see Section 2.1.1) are also applied to the EFMD. The energy balance within layer j ($j = 1, ..., N$) is represented by

$$\begin{aligned} \frac{dE_{C_j}}{dt} = & -\frac{1}{4\delta t_j} E_{C_j}(t)\, H(t - t_j) \\ & - \frac{1}{4\delta t_j} E_{C_j}(t)\, H(t - t_{j-1}) \\ & + \frac{1}{4\delta t_{j-1}} E_{C_{j-1}}(t)\, H(t - t_{j-1}) \\ & + \frac{1}{4\delta t_{j+1}} E_{C_{j+1}}(t)\, H(t - t_j) \\ & - \frac{\omega}{Q_{i_j}} E_{C_j}(t)\, H(t - t_{j-1}) \\ & + \frac{\omega}{Q_{s_j}} E_D(t)\, H(t - t_{j-1})\, H(t_j - t) \end{aligned} \quad , \tag{2.20}$$

where H is the Heaviside function. The first two terms of Eq. 2.20 describe the energy flux from layer j to the layers above and below, while the next two terms describe the opposite flux from the neighbouring layers into layer j. The last two terms represent the anelastic or intrinsic energy loss and the direct wave energy input into the layer.

In practice, for a given model $\mathbf{m}$, comprising a single value of a and ε for each layer in the stack, Q_s is calculated from the structural parameters a_j and ε_j using the analytical approximation for isotropic exponential media defined in Eq. 2.13. Q_i is obtained from the EFM and assumed to take the same values within each layer of the model. With these values, E_D can be calculated for each time sample using Eq. 2.19, starting from the energy value measured at the free surface. Then, the system of linear differential equations in Eq. 2.20 is solved for the layer containing the free surface and data and synthetic coda envelopes are calculated for each frequency band using the left and right hand sides of Eq. 2.18 respectively. These envelopes can now be used in an inversion to obtain the scattering parameters for each layer in the model.

2.1.3 Bayesian approach to the Depth-Dependent Energy Flux Model

Previous studies using the EFMD (Korn, 1997; Hock and Korn, 2000; Hock et al., 2004) obtained the correlation length and RMS velocity fluctuation values for each layer in the model by systematically calculating the synthetic envelopes for a series of predetermined lithospheric models. The parameter space can be efficiently and meticulously explored using this kind of grid search, but it is impractical and does not easily allow the inclusion of prior information.

For my study, I decided to take a different approach and use Bayesian inference (e.g. Tarantola, 2005) to obtain the scattering parameter values for each layer in the model. In this type of inversion, the aim is not to obtain a single, best fitting model, but to test a large number of models with parameters drawn from a prior probability distribution $p(\mathbf{m})$ (or prior) defined by previous knowledge on them. Different sampling algorithms exist that allow us to probe the posterior probability distribution and obtain the probability of each test model of explaining the observed data, thus providing detailed information about uncertainties and trade-offs in the determination of the different parameters.

Bayesian inference theory

The likelihood associated with model $\mathbf{m}$, $p(\mathbf{d}|\mathbf{m})$, is the probability of observing my data, $\mathbf{d}$, given the model parameters in $\mathbf{m}$. Within the Bayesian EFMD framework, this data is defined as the set of normalised coda envelopes (obtained by means of Eq. 2.18) for all events and stations in the dataset (see Section 2.1.4) and each of the frequency bands of interest (Table 2.3). The variance-covariance matrix of the data, $\mathbf{C}$, is built as a diagonal matrix, with elements representing the variance of each time sample of the data envelopes. In this context, I used the Mahalanobis distance $\Phi(\mathbf{m})$ (Mahalanobis, 1936) between $\mathbf{d}$ and the synthetic envelopes ,$g(\mathbf{m})$, to calculate the fit to my data:

$$\Phi(\mathbf{m}) = (g(\mathbf{m}) - \mathbf{d})^T \mathbf{C}^{-1} (g(\mathbf{m}) - \mathbf{d}), \tag{2.21}$$

which I then applied to the calculation of the likelihood of model $\mathbf{m}$:

$$p(\mathbf{d}|\mathbf{m}) = \frac{1}{\sqrt{(2\pi)^n |\mathbf{C}|}} \exp\left(\frac{-\Phi(\mathbf{m})}{2}\right) \tag{2.22}$$

Bayes' theorem (Bayes, 1763) allows us to calculate the corresponding sample of the posterior probability distribution (or posterior), that is, the probability density associated with model $\mathbf{m}$, or $p(\mathbf{m}|\mathbf{d})$:

$$p(\mathbf{m}|\mathbf{d}) \propto p(\mathbf{d}|\mathbf{m}) p(\mathbf{m}) \tag{2.23}$$

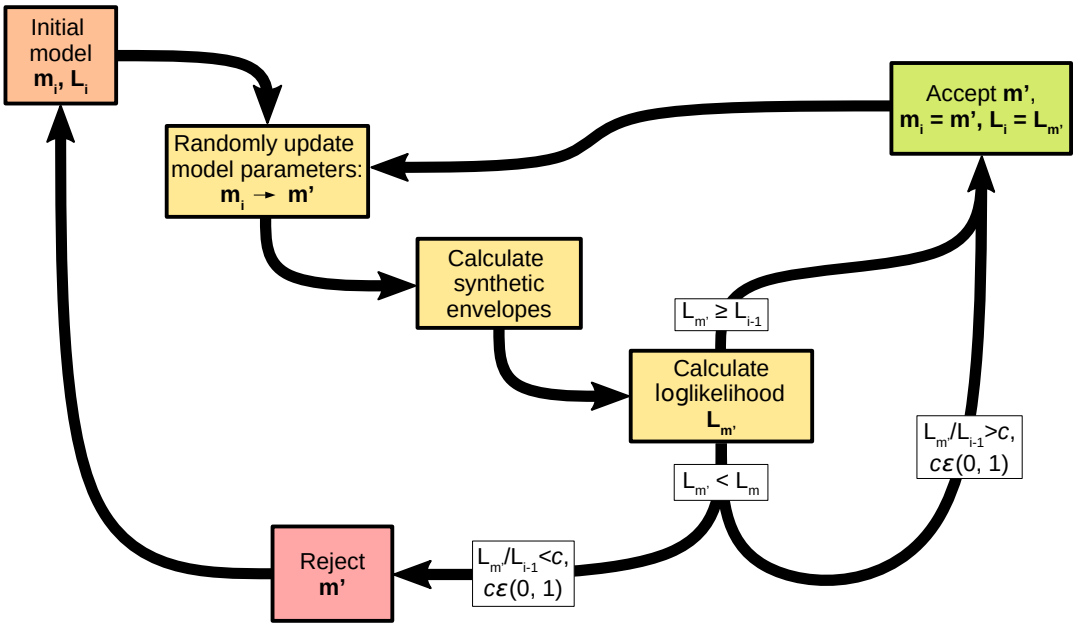

Figure 2.2: Graphic representation of the Metropolis-Hastings algorithm (Metropolis and Ulam, 1949; Metropolis et al., 1953; Hastings, 1970) which is the base of the Markov Chain Monte Carlo (MCMC) algorithm. m and L represent a model, consisting on a correlation length and velocity fluctuation value for each layer in the model, and its *loglikelihood*, respectively. c is a random number between 0 and 1. See text for more details.

In my case, I use a uniform prior. I create an initial model by selecting a random value for the correlation length and velocity fluctuations in all layers in the (a_{min}, a_{max}) or $(\varepsilon_{min}, \varepsilon_{max})$ intervals, with $a_{min} = 0.2\lambda_{min}$ [m], $a_{max} = 2\lambda_{max}$ [m] (λ_{min} and λ_{max} being the minimum and maximum wavelengths in the layer, depending on signal frequency and background velocity), $\varepsilon_{min} = 4.5 \cdot 10^{-3}$ % and $\varepsilon_{max} = 10$ %. These maximum and minimum values were chosen considering the relevant range for detectable scattering while being geologically feasible (e.g Korn, 1993; Hock et al., 2004).

I then applied the Metropolis-Hastings algorithm (graphically represented in Fig. 2.2; Metropolis and Ulam, 1949; Metropolis et al., 1953; Hastings, 1970) to sample the posterior probability distribution and generate my ensemble of solution models. This way, at every time step, this Markov Chain Monte Carlo (MCMC) algorithm generates a new model $\mathbf{m}'$ by randomly choosing one of the parameters in the previous model ($\mathbf{m}$) and updating its value by adding a random number in the $(-\delta a, \delta a)$ or $(-\delta\varepsilon, \delta\varepsilon)$ interval, with δa and $\delta\varepsilon$ being the step size for correlation length and RMS velocity fluctuations respectively. In case the new value of the parameter exceeds the boundaries defined by (a_{min}, a_{max}) or $(\varepsilon_{min}, \varepsilon_{max})$, the distance Δ to the boundary is calculated and the new parameter value is forced to bounce back into the valid parameter range by the same distance Δ. The algorithm then takes model $\mathbf{m}'$ and uses Eqs. 2.20 and 2.18 to obtain the corresponding synthetic envelopes. In order to decide whether to accept or reject the new model, the algorithm uses the posterior

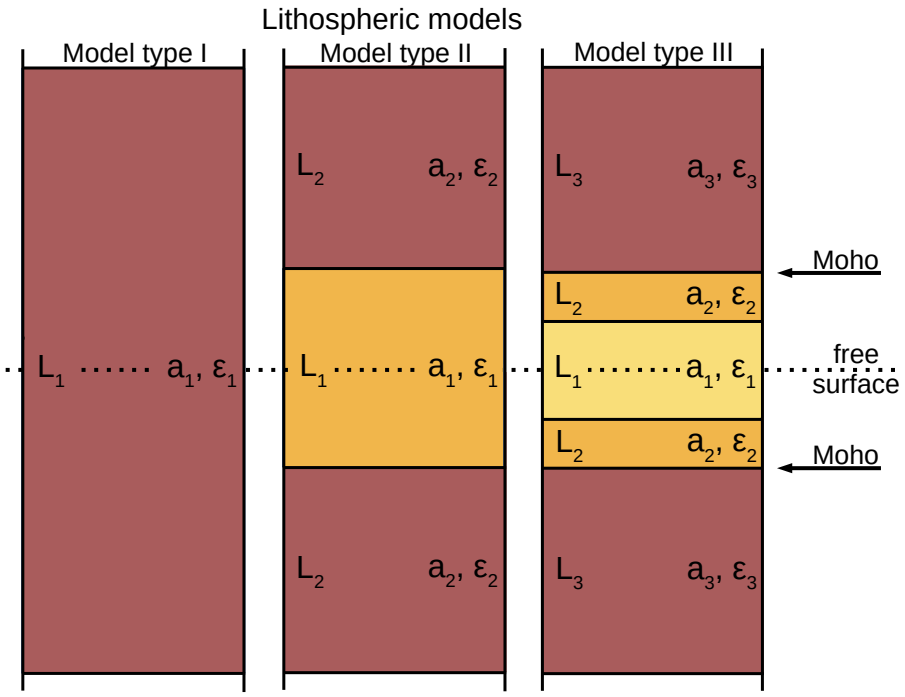

Figure 2.3: 1-layer, 2-layer and 3-layer lithospheric models used to test my implementation of the Bayesian EFMD analysis. Model 1 from Table 2.1 corresponds to model type I here, models 2, 3 and 4 to model type II and model 5 has the same layering as model type III. The free surface is at the center of the middle layer of each one of these models to account for the total reflection of the wavefront at the surface.

probability exponent (Eq. 2.22), $\Phi(\mathbf{m})/2$, called here the *loglikelihood*, L, associated with model $\mathbf{m}$, as an estimator of the likelihood and the goodness of the fit to the data. Thus, if $L(\mathbf{m})/L(\mathbf{m}') \geq 1$, $\mathbf{m}'$ will be accepted. If $L(\mathbf{m})/L(\mathbf{m}') < 1$, however, it will only be accepted if $\exp(L(\mathbf{m}) - L(\mathbf{m}')) \geq q$, q being a random number between 0 and 1. This algorithm ensures that parameter values closer to the true value have high likelihoods and are accepted more often than values further from the true value. The acceptance rate (AR) represents the percentage of times new parameter values were accepted through the Markov chain. There are several criteria defining what the value of the AR should be, most of them making assumptions about the properties of the target distributions (e.g. Brooks et al., 2011). In my case, since I do not have any a priori information about the posterior distributions, I aimed at AR values between 30–60 %. Finally I calculate the 5- to 95- percentile range (PR) for each parameter in each layer in the model from my ensemble of accepted models.

For more detailed descriptions of Bayesian inference and MCMC, see Tarantola (2005) or Brooks et al. (2011).

Synthetic tests

Previous studies have tested the validity of both the EFM and EFMD: Frankel and Wennerberg (1987) and Korn (1990) used a 2–D acoustic finite difference code to check the validity of their respective versions of the EFM; Korn (1997) and Hock et al. (2004) tested their approaches by obtaining synthetic seismograms from a fully elastic 2–D finite difference method and comparing them with synthetic envelopes obtained from the EFMD. More testing of the forward method is, therefore, not necessary. Here, I tested my Bayesian inversion code with five different synthetic datasets, corresponding to lithospheric models with varying number of layers and parameter values (Fig. 2.3). Synthetic envelopes for these five models were calculated using the EFMD algorithm, as described in Section 2.1.2. Parameter values for each one are shown in Table 2.1, together with a summary of my synthetic tests results. In all of them, I used Pilbara Seismic Array (PSA, Section 3.1) as a reference array and obtained its velocity model and Moho depth from the Australian Seismological Reference Model (AuSREM, Kennett and Salmon, 2012; Kennett et al., 2013; Salmon et al., 2013a) and AusMoho model (Kennett et al., 2011) respectively, although my results should be applicable to any array or seismic station. Based on the lower bound of the lithosphere-asthenosphere boundary (LAB) for this array (Yoshizawa and Kennett, 2015; Kennett, 2015), I set the bottom depth of all models to 200 km. Frequency bands used are listed in Table 2.3.

Figures 2.4 to 2.8 illustrate the results from my synthetic tests for Models 1 to 5 (Table 2.1). In order to test the convergence of my algorithm, I ran three independent Markov chains for each model, with a total of 3 million iterations (parameter combinations tested) for the single layer model, 9 million for the 2-layer models, and 15 million for the 3-layer model. For each chain, I discarded the models corresponding to the burn-in phase, during which the algorithm is not efficiently sampling the posterior probability distribution and models are still affected by the random initialization of the Markov chain. In order to define the point at which the algorithm reached convergence and the burn-in phase ended, I first calculated the mean loglikelihood value in the second half of the chain (during which the algorithm is stable) and then subtracted 5% off that value. I consider the algorithm has converged the first time it accepts a model with loglikelihood L equal or higher than this value. My threshold was defined based on the observation, in test runs of the EFMD, that L generally remained stable after reaching the defined threshold for the first time. L provides an estimation of the goodness-of-fit of the synthetic data to my real data and takes negative values, meaning fits improve as L gets closer to zero (Eq. 2.22). In terms of parameter values, I consider that a narrow 5–95 percentile range (PR) points to clearly determined values of the structural parameters, while wide 5–95 PRs would suggest multiple parameter values are equally likely and good at fitting my data.

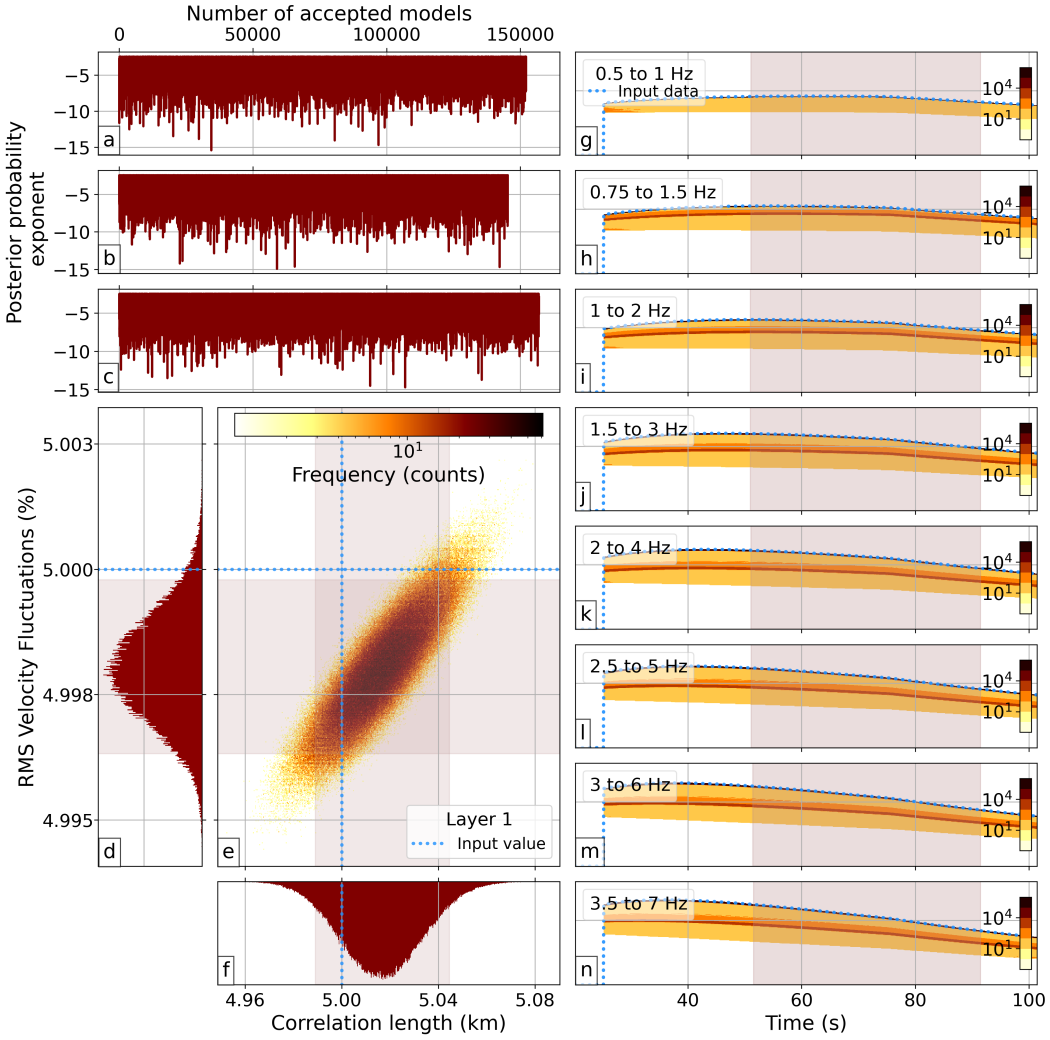

Figure 2.4: Summary of the results obtained from my EFMD algorithm for synthetic model 1 from Table 2.1 from three separate chains, adding up to a total of 3 million iterations (parameter combinations tested). Panels a–c show the loglikelihood (or posterior probability exponent) for each accepted model in the chain, once the burn-in phase was removed. Panels d–f contain the posterior PDFs of the structural parameters, as well as the joint PDF. Dotted blue lines in these plots represent the input parameter values and the shaded area corresponds to the 5–95 percentile range (PR). Panels g–n on the right show 2D histograms of the synthetic envelopes for all accepted models and frequency bands, with color bars indicating the number of models that produced a data sample within each bin. Vertical scale is the same in all plots. The shaded area here indicates the time window used for the fitting and blue dotted lines are the input data.

For Model 1, with a single layer encompassing the entire lithosphere, all three chains reached stability and converged within 10000 iterations. Panels d–f in Fig. 2.4 show my posterior probability density functions (PDFs) for each parameter, as well as the joint PDF. In both cases, the distributions are approximately Gaussian and symmetric, with the 5–95 PR being ~ 0.06 km and $\sim 0.01\%$ wide for the correlation length and RMS velocity fluctuations respectively (Table 2.1), which indicated that the range of suitable values of the parameters is very well defined. The algorithm slightly overestimates the correlation length and underestimates the RMS velocity fluctuations, with the input

value of the parameter being included in the 5–95 PR for the latter but not for the former (Table 2.1, Fig. 2.4). However, the difference between the central value of the PDFs and the true value of the parameter is $< 0.4\%$ for both the correlation length and the RMs velocity fluctuations. Graphs on the right hand side of Fig. 2.4 (panels g–n) show histograms of the synthetic envelopes for my ensemble of accepted models for all frequency bands. It is convenient to note that the synthetic envelopes obtained from the EFMD do not include the impulsive primary arrival and aim only at reproducing coda amplitudes and decay rates within the time window of interest. The sharp increase in amplitude observed here at ∼25 s corresponds to the one way travel time through the lithosphere, at which the direct wave is totally reflected at the free surface. Coda energy within the top layer of the model (the one used to compute the synthetic envelopes) continues to increase after this moment due to scattering from the direct wave into the layer, but will start to decay once the direct wavefront leaves the layer. This is generally observed as a sharp peak or a maximum in the synthetic envelopes (e.g. Figs. 2.5–2.8). For single layer models, the large thickness of the scattering layer makes this variation in energy much more subtle, even if it continues to present the same behaviour observed in the rest of the synthetic tests. It is also possible to observe that, as frequency increases, both envelope amplitudes and width of the ensemble of synthetic envelopes increase too. However, in all cases, the highest density of envelopes, indicated by a dark brown color, is found along a very narrow region that matches the input data envelopes, not only in the time window used for the fit (shadowed area in the plots), but also outside of it.

Model 2 contains two layers, representing the crust and lithospheric mantle. My three chains converged in less than 120000 iterations and remained stable for the rest of the inversion, as shown in panels a–c in Fig. 2.5. Panels d–i in this figure summarise my results. In this case, the PDFs for the parameters in both layers are narrow (the

Table 2.1: Summary of the synthetic model layering and my synthetic tests results. For each model, I include the 5–95 percentile range (PR) and the acceptance rate (AR) for each parameter, as well as the maximum loglikelihood (L) found during the inversion. Bottom depth of all models is 200 km, after the LAB depth estimated by Yoshizawa and Kennett (2015) or Kennett and Saygin (2015). Crustal thickness for model types II and III is 32 km, as defined in the AusMoho model (e.g. Kennett et al., 2011) for PSA.

Model	Number of layers	Layer number	Input model a (km)	Input model ε (%)	Correlation length (a) 5 – 95 PR (km)	Correlation length (a) AR (%)	RMS velocity fluctuations (ε) 5 – 95 PR (%)	RMS velocity fluctuations (ε) AR (%)	Maximum L
1	1	1	5.0	5.0	4.99 – 5.05	23	4.99 – 5.00	8	-2.5
2	2	1	2.0	5.0	1.7 – 2.4	12	4.8 – 5.3	47	-0.02
		2	3.0	4.0	2.8 – 3.4		3.9 – 4.1		
3	2	1	1.0	7.0	1.00 – 1.01	51	6.95 – 7.02	47	-0.03
		2	6.0	1.0	7 – 32		1.0 – 1.8		
4	2	1	6.0	1.0	6 – 25	50	1.0 – 1.8	51	-1.3
		2	1.0	7.0	0.998 – 1.002		6.998 – 7.003		
5	3	1	1.0	4.0	1 – 23	52	0.1 – 4.7	31	-0.02
		2	2.0	3.0	1 – 21		0.6 – 6.1		
		3	4.0	2.0	3 – 30		1.8 – 3.3		

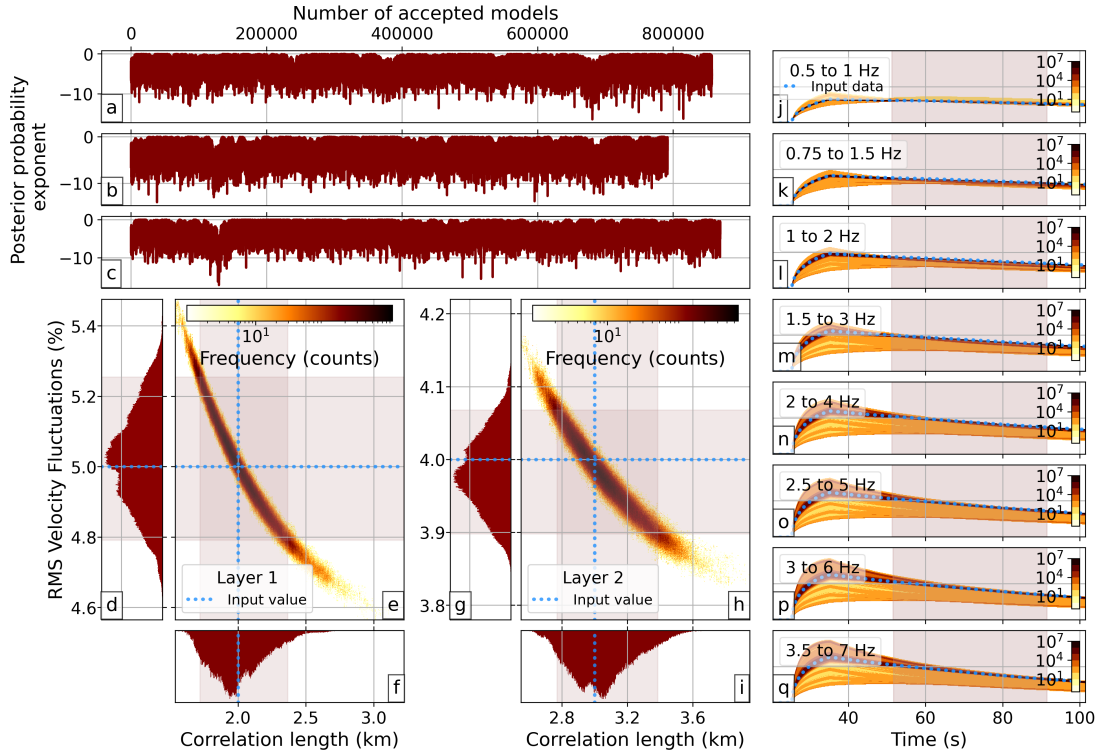

Figure 2.5: As Fig. 2.4 but for synthetic model 2 from Table 2.1 (2-layer model).

5–95 PR is < 0.7 km wide at most for a and $< 0.5\%$ for ε) and approximately centered around the input values, even if they are not Gaussian and show some local maxima. The true values of the parameters lie within the 5–95 PR in all cases, near the center of the joint PDFs, and the maximum difference between the input values and the absolute maxima of the PDFs is 2%. Panels j–q in Fig. 2.5 indicate fits to the synthetic data are good, since they show again that the largest concentration of synthetic envelopes for all frequencies coincides with the input data envelopes.

Models 3 and 4 have the same interface structure as model 2 (Table 2.1) and investigate high contrast situations in which a strong heterogeneity layer is above or below a layer containing weak heterogeneities, respectively. Figs. 2.6 and 2.7 summarise my results. In both cases, the chains reached stability within 11000 iterations. Posterior PDFs for the strongly scattering layer are approximately Gaussian and narrow for both models 3 and 4, with maxima that deviate from the input parameter values by 0.4% at most (Table 2.1). The weakly scattering layer, however, is poorly resolved for both models. The posterior PDFs for this layer are very similar in both cases and clearly non-Gaussian. They show multiple maxima that do not correspond to the input parameter values, which widens the 5–95 PR, especially for a. The RMS velocity fluctuation values seem to be constrained to the range from 0.5–1.9 % for both models, while the shape of the PDFs suggests any value of the correlation length would be equally acceptable, even if large values (> 5 km) are favoured. The stability of the chains, shown

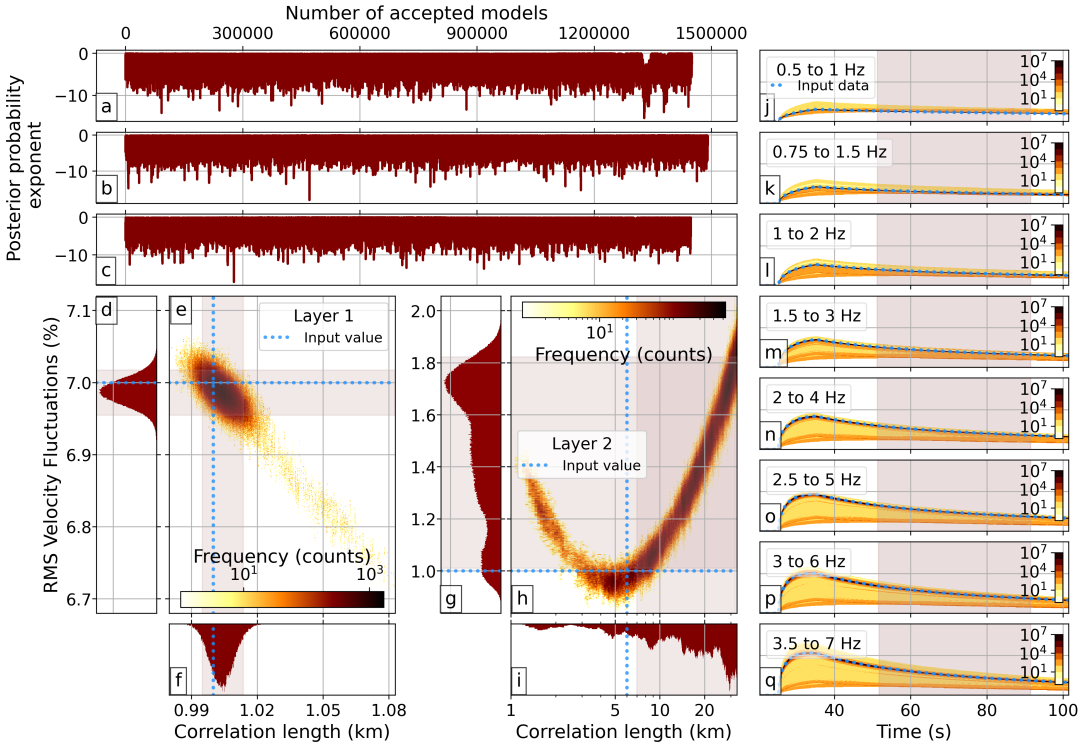

Figure 2.6: As Fig. 2.4 but for synthetic model 3 from Table 2.1 (2-layer model).

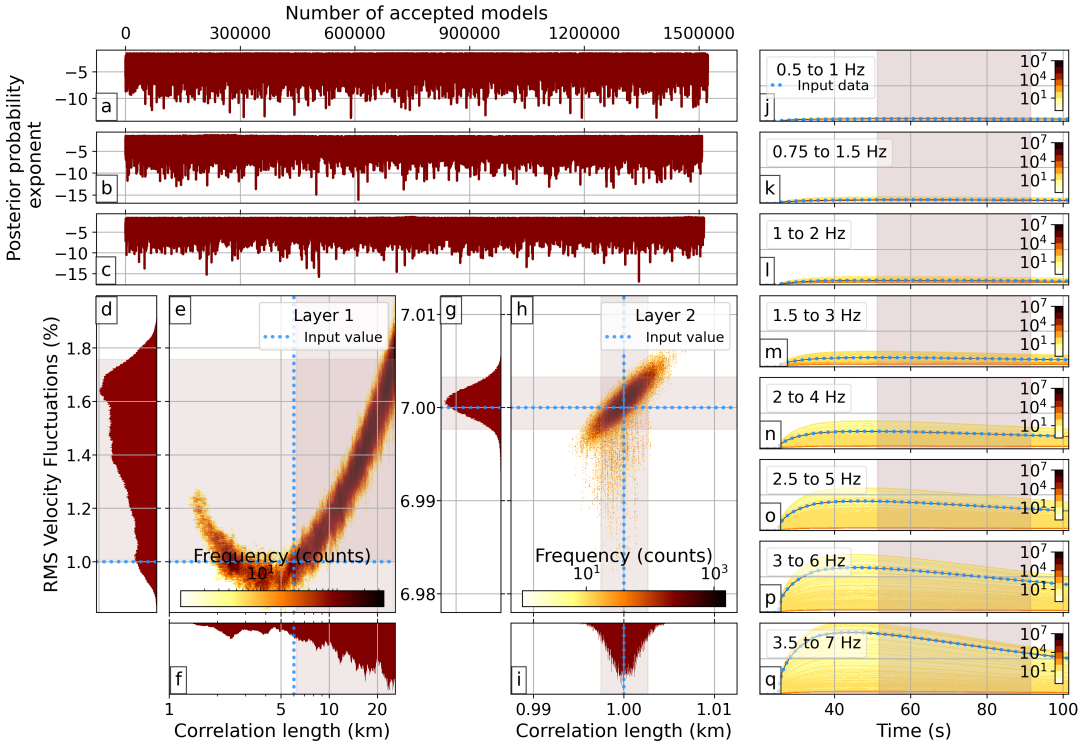

Figure 2.7: As Fig. 2.4 but for synthetic model 4 from Table 2.1 (2-layer model).

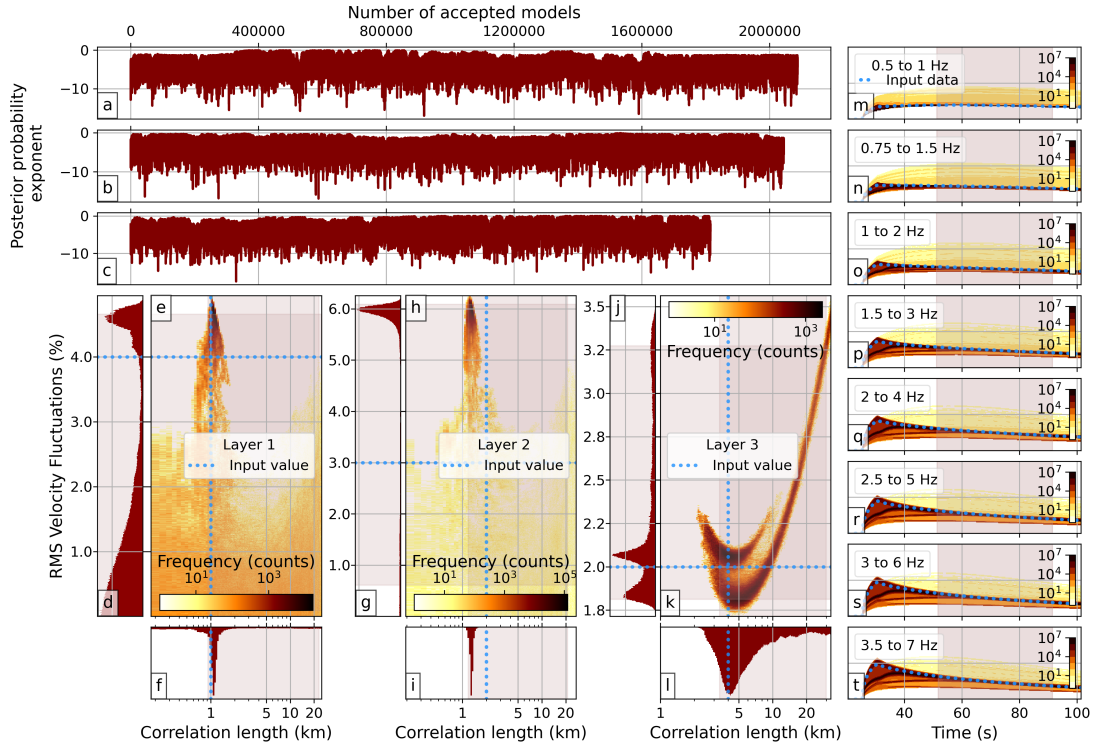

Figure 2.8: As Fig. 2.4 but for synthetic model 5 from Table 2.1 (3-layer model).

in panels a–c in Figs. 2.6 and 2.7, together with the ensemble of synthetic envelopes on panels j–q, indicate that all these models provide similarly good fits to the data and have similar loglikelihoods. This observation points to solutions being highly non-unique, and to the scattering parameters of the weakly heterogeneous layer not being easily recoverable for these high contrast cases.

Finally, model 5 contains three layers, with boundaries corresponding to upper and lower crust and lithospheric mantle. My results are shown in Figs.
2.8 and Table 2.1. Chains converged in less than 130000 iterations. In all cases, PDFs are clearly non-Gaussian (panels d-l on Fig. 2.8) and have complex shapes, which widens the 5–95 PR and increases the range of suitable values of the parameters. The correlation length PDFs show clearly defined maxima near the true values of the parameter in all layers (the maximum distance between the maximum and the input parameter value being 0.35%). RMS velocity fluctuations PDFs are more complex and neither of them show clear maxima near the input parameter values. Figure 2.9 contains the marginal PDFs for all parameters in all layers, as well as the PDF for each individual parameter. It shows a strong trade-off between parameter values in different layers of the model, especially the two crustal layers, and allows me to identify two independent families of parameters that separately fit my data within my posterior PDFs. Subindices Li (i being the layer number) are used here to refer to parameter values in each layer of the model. Starting on panel 3–1 on Fig. 2.9, I observe how all accepted models cor-

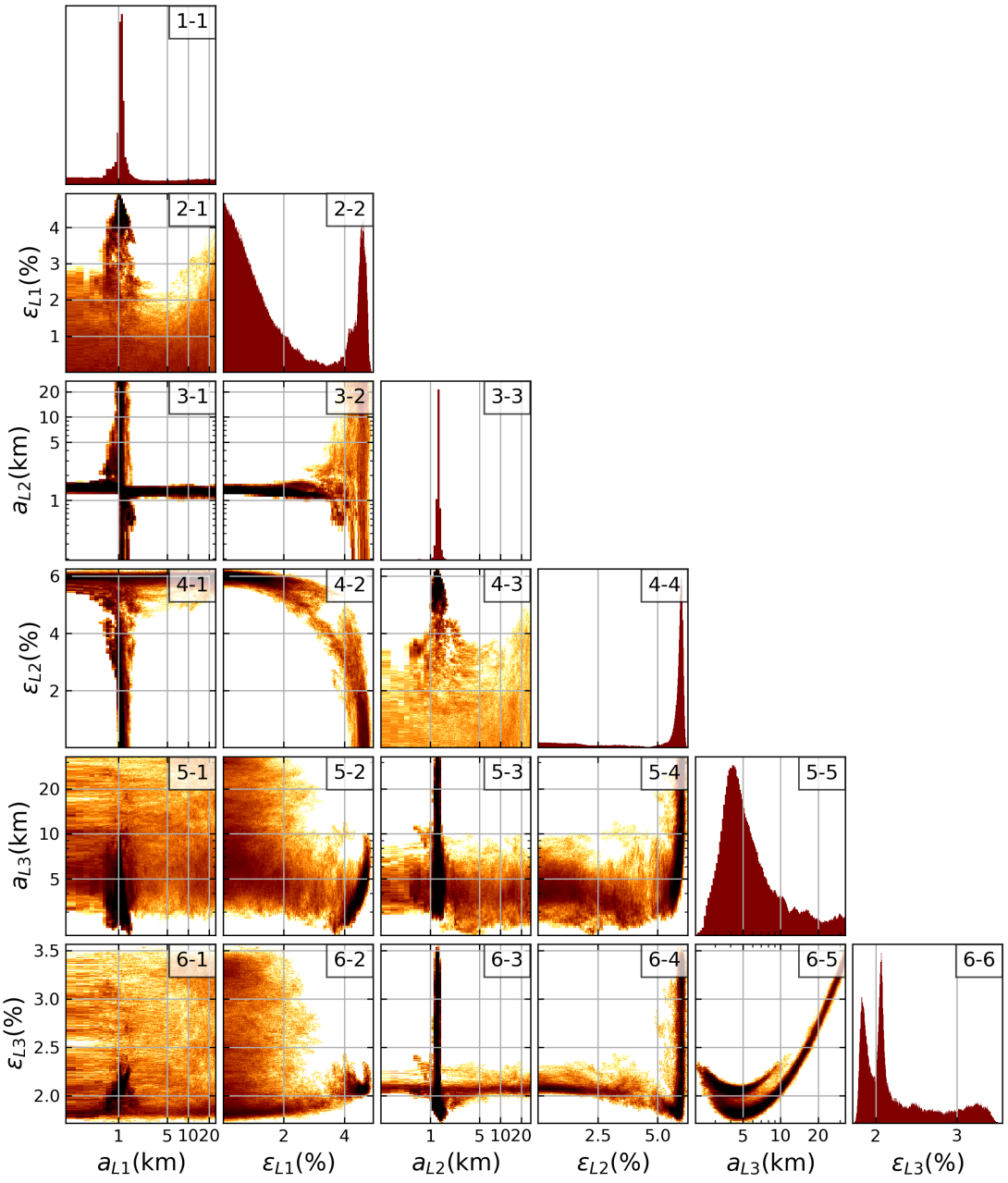

Figure 2.9: Joint PDFs for all parameters and layers in synthetic model 5 from Table 2.1. Plots in the diagonal of the figure contain the individual PDF for the different scattering parameters.

responding to $a_{L1} \sim 1$ km (the sharp peak on panel 1–1) have a_{L2} values either lower than 1 km or higher than 2 km, which would correspond to the tails of the a_{L2} PDF on panel 3–3. Panel 3–2 compares ε_{L1} and a_{L2} and I can see how all models with a_{L2} in the ranges mentioned before have $\varepsilon_{L1} > 3.5\%$. Similarly, panels 4–1, 5–2 and 5–3 show that these values of a_{L1}, a_{L2} and ε_{L1} correspond to $\varepsilon_{L2} <\sim 5\%$, $\varepsilon_{L3} \sim 2.1\%$ (the second, sharp, peak on the PDF on panel 6–6) and $2 < a_{L3} < 10$ km (the wide peak on the PDF on panel 5–5). Interestingly, the first peak and the side tail on the ε_{L3} PDF

Table 2.2: Summary of the two independent and equally likely families of parameters extracted from Fig. 2.9 for synthetic model 5 from Table 2.1.

	a_{L1} (km)	ε_{L1} (%)	a_{L2} (km)	ε_{L2} (%)	a_{L3} (km)	ε_{L3} (%)
Input model	1.0	4.0	2.0	3.0	4.0	2.0
Parameter family 1	~ 1	$> 3.5\%$	< 1 & > 2	< 5	2–10	~ 2.1
Parameter family 2	<0.6 & >1.1	< 3.5	∼1.2	∼6	3–30	∼1.6–3.7

(panel 6–6) correspond to the same parameter family, as do the tail and the base of the peak on the a_{L3} PDF (panel 5–5). Following the same reasoning detailed above, I extracted the other family of parameters, which is summarised in Table 2.2. This interaction between the parameters is caused by two main factors: first, the energy balance the EFMD is based on (Eq. 2.20) is strongly dependent on the layering of the model, since the maximum energy that can be present within a layer at any time depends on its thickness (i.e. energy leaks out of thinner layers faster); second, correlation length values have a much smaller effect on coda amplitudes, compared with RMS velocity fluctuations, so the algorithm uses ε to compensate the excess or lack of energy within a layer and match data coda amplitudes. Since panels m–t on Fig. 2.8 do not show two clearly different sets of envelopes in my ensemble of synthetic envelopes, and given that the loglikelihood values remained stable throughout the three independent chains I ran for this example, I conclude that both sets of parameters I obtained from my inversion provide equally good fits to the data, even if neither of them match my input parameter values.

2.1.4 Data selection and processing for the EFM/EFMD analysis

The modelling of the seismic coda carried out by both the EFM and EFMD requires the data used in the analysis to have minimum near-source scattering and no secondary arrivals in the time window of interest. These conditions guarantee that the observed coda is generated by near-receiver, small-scale heterogeneities, and limit the range of seismic events that can be used with these methods. To ensure the data meet these requirements, I select events with epicentral distances between 30 and 80 degrees from the array centres, source depths greater than 200 km and magnitudes from 5 to 7 for the analysis. These conditions ensure vertical or nearly vertical incidence angles and prevent near-source scattering and unwanted deep seismic phases from appearing in the time window of interest.

Before using these data in the EFM or EFMD, I preprocess and quality control the raw data. For this purpose, I first convert the waveforms to SAC format and remove the instrument response from each seismic trace to obtain ground velocity values. All the required information about the station and the event is included in the headers of each SAC file in this step, and horizontal component traces are rotated from north and

east to radial and transverse directions respectively.

After this initial preprocessing, I calculate the signal-to-noise ratio (SNR) for each trace and frequency band (Table 2.3) dividing the peak-to-peak amplitude values in two separate time windows: for noise, I use a 20 s long window, starting $\sim$ 25 s before the theoretical P-wave arrival (as estimated from PREM (Dziewonski and Anderson, 1981)), while for the signal I choose a time window starting 1 second before the theoretical first arrival and ending 40 s later. I only include in the study those traces with signal-to-noise ratio equal to or higher than 5. For arrays of 3-component stations, I only use events with 5 or more good quality traces, while for single seismic stations or arrays of mostly 1-component stations, I use every available, good quality, 3-component trace. As an additional precautionary measure, data for each array/station, event and frequency band is also manually inspected to ensure that there are no secondary arrivals or events within the time window of interest for the EFM/EFMD. Figure 2.10 contains a comparison of two events with SNR$>$ 5 with and without the presence of secondary arrivals within the time window of the EFM/EFMD analysis. Events such as the one shown in panel b in this figure are excluded from the analysis.

The eight different one octave-wide frequency bands we used in my analysis for both methods are shown in Table 2.3.

EFM/EFMD processing

The processing steps described in the section above prepare my data for the EFM/EFMD analysis. Prior to the application of these methods, I need to obtain a P-wave velocity model of the lithosphere beneath each seismic array or station, as well as the Moho and LAB depths, which can be obtained from local or global models and/or previous studies on the area of study. For each array, I can then proceed to calculate the coda envelopes as described in Sections 2.1.1 and 2.1.2 for each frequency band (Table 2.3) and calculate the quality factors and scattering coefficients as follows:

(i) Computation of 3-component envelopes for each frequency band, station and event, by taking the square root of the sum of the squared envelopes for all components. All traces are aligned to the P-wave arrival for each event using the frequency-wavenumber analysis (e.g. Rost and Thomas, 2002) and then trimmed

Table 2.3: List of all frequency bands used for the EFM/EFMD analysis. All traces were filtered using fourth order Butterworth bandpass filters with a zero phase shift and corner frequencies as defined below.

Frequency band	A	B	C	D	E	F	G	H
Minimum frequency (Hz)	0.5	0.75	1	1.5	2	2.5	3	3.5
Maximum frequency (Hz)	1.0	1.5	2	3	4	5	6	7

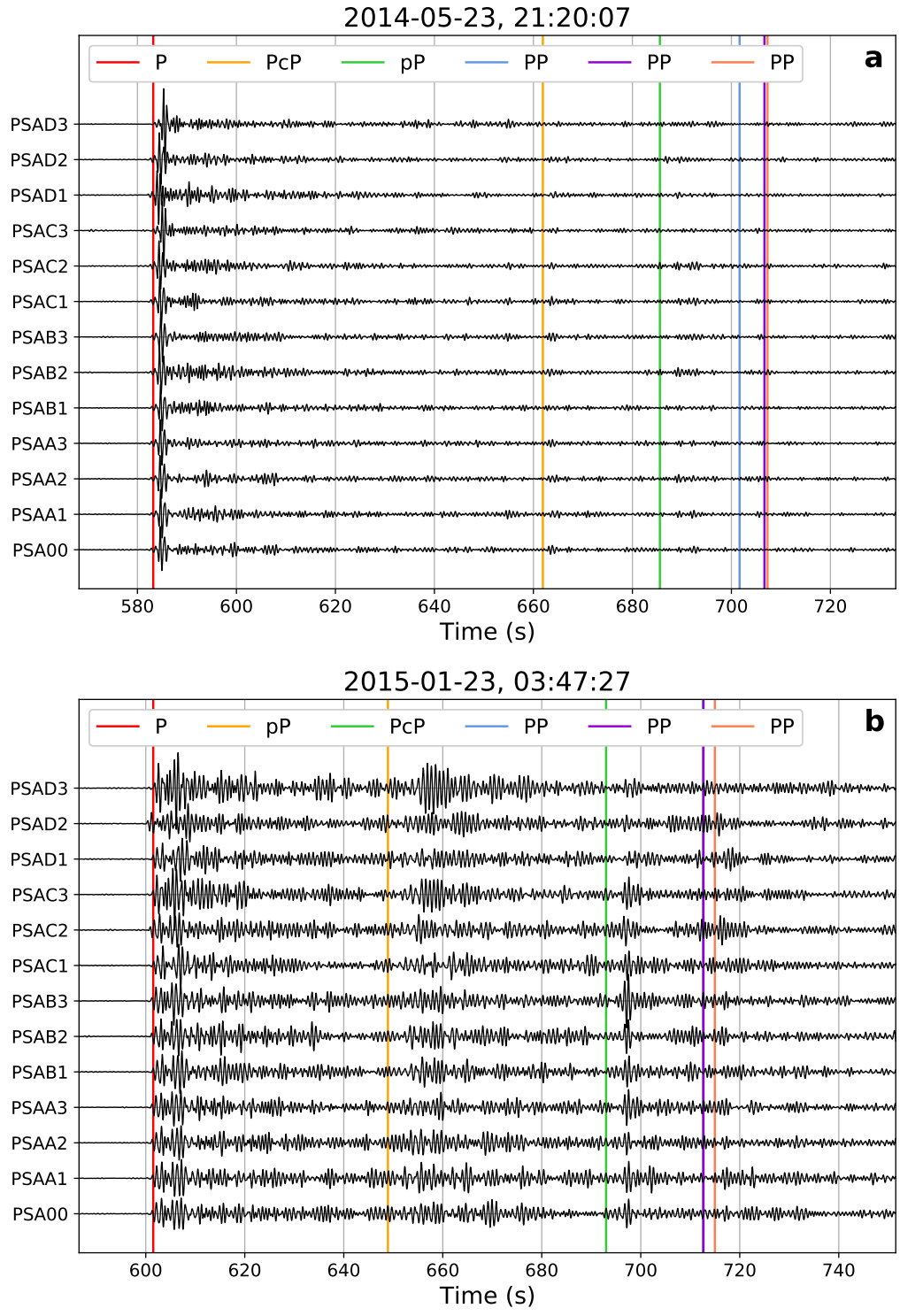

Figure 2.10: Comparison between two events recorded by the Pilbara Seismic Array (PSA). Event a, from March 23^{rd}, 2014, took place 47.4 degrees away from the array, 565 km below the surface and had a moment magnitude of 5.7. Event b, with a magnitude of 6.8, happened on January 23^{rd} 2015, at a distance of 46.2 degrees from the center of the array and 224 km deep. Traces for both events have a SNR$>$ 5. However, event b shows secondary arrivals within the time window of interest for the EFM/EFMD analysis and could not, therefore, be used.

to the time window going from t_N seconds before to at least $3t_N$ seconds after the theoretical P wave arrival (t_N being the travel time through the lithosphere). For the EFMD, these are then stacked by event, normalised using Eq. 2.18 and stacked by frequency band, while for the EFM unnormalised envelopes for all events are also stacked by event and frequency band. The variance of both normalised and unnormalised envelopes is calculated sample by sample from all individual event stacked envelopes and used as the uncertainty of the data.

(ii) Estimation of Q_s, Q_i, Q_{diff}, a and ε for a single scattering layer using the EFM.

(iii) Bayesian inversion for the structural parameters of each layer in each model type from Fig. 2.3 by applying the envelope modelling technique from the EFMD, as described in Section 2.1.2, and using the Q_i values obtained from the single layer EFM (Section 2.1.1). In order to speed this process up, the data are resampled to a common sampling rate of 15 Hz before applying the EFMD algorithm.

Comparison of 1-component and 3-component data

Hock et al. (2004) pointed out that the EFMD generally overestimates the RMS velocity fluctuations by up to 3% when using only vertical-component data and that a mix of 1-component (vertical) and 3-component data produced unstable results, both of them caused by the difference in coda amplitudes between 1-component and 3-component data. However, 3-component data are not always available. To address this issue, I tried calculating a correction factor to approximate vertical 1-component to 3-component coda levels. I tested different approaches to obtain this correction factor, all of them based on the ratio between every available 3-component unnormalised coda envelope $A(t;\omega_c)$ or normalised envelope (left hand side on Eq. 2.18) and its 1-component (vertical) counterpart. Since all of its stations are 3-component, the Pilbara Seismic Array (PSA, Section 3.1) is an ideal array for these tests. Figure 2.11 shows the 3-component to 1-component ratios for both the normalised and unnormalised coda envelopes for all frequency bands listed on Table 2.3. These ratios were calculated sample-by-sample for each event in the PSA dataset (Table 3.1). I used the mean of the ratios as a multiplicative correction factor (Fig. 2.12) for each frequency band that I proceeded to apply to the 1-component traces to try to obtain an approximation to 3-component data.

I found that these ratios vary significantly from event to event and frequency band to frequency band, even after using a large dataset to calculate them, and are generally higher for unnormalised envelopes than for the normalised ones (Figs. 2.11 and 2.12). The corrected 1-component envelopes did not in general fully match the 3-component coda amplitudes for all frequency bands using this approach (Fig. 2.12). Both the EFM and EFMD are highly sensitive to variations in coda amplitudes, so small differences

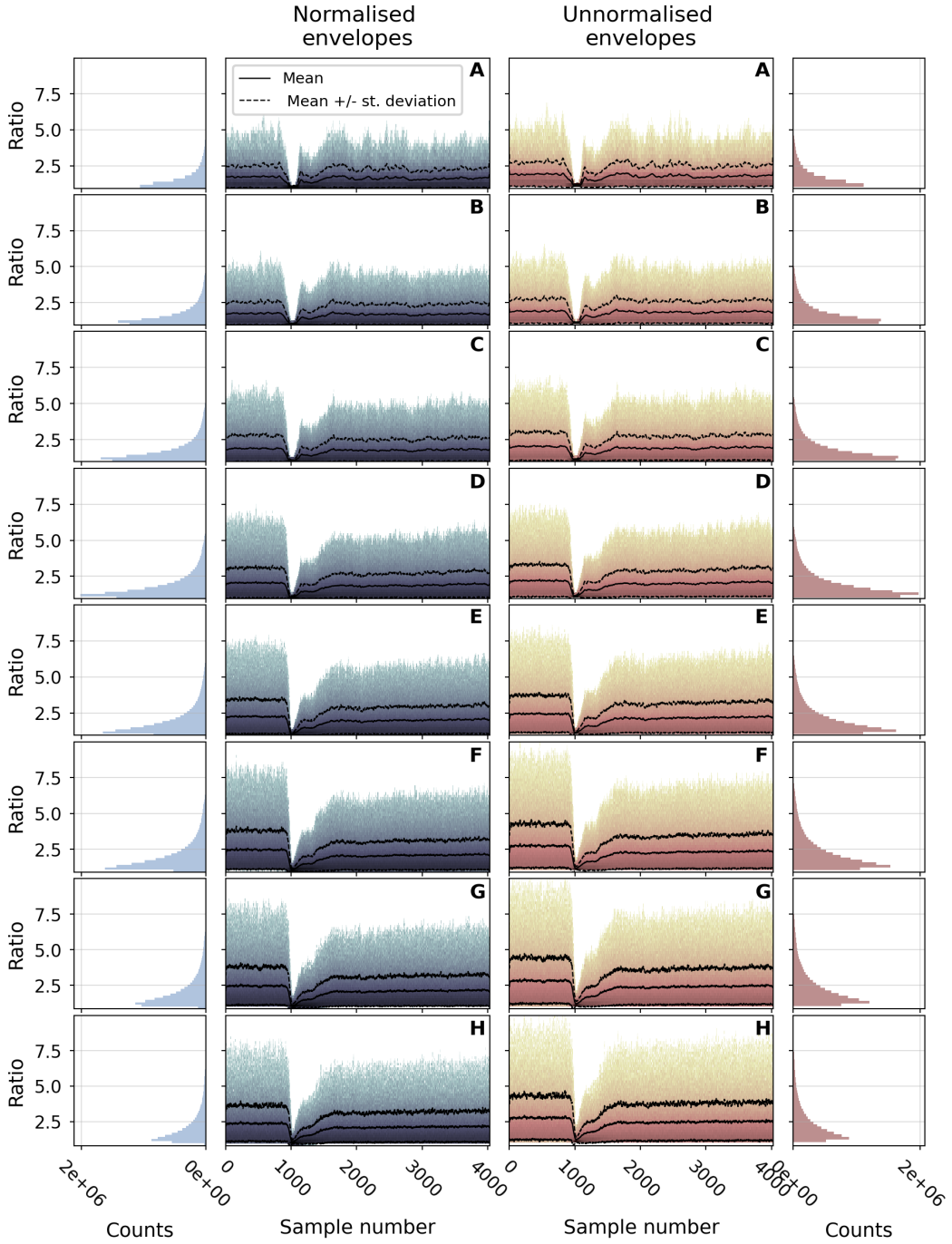

Figure 2.11: Sample-by-sample ratios of the 3-component normalised and unnormalised envelopes for all events in the PSA dataset (Table 3.1) and their 1-component counterparts for all frequency bands listed on Table 2.3 (bold capital letters in the panels).

between the corrected 1- and 3-component envelopes result in large differences in quality factor and scattering parameter values. I tested the "corrected" 1-component data in my EFM-EFMD algorithm and compared the results for the lithospheric models on Table 3.3 with those from my 3-component data for PSA. Quality factors obtained

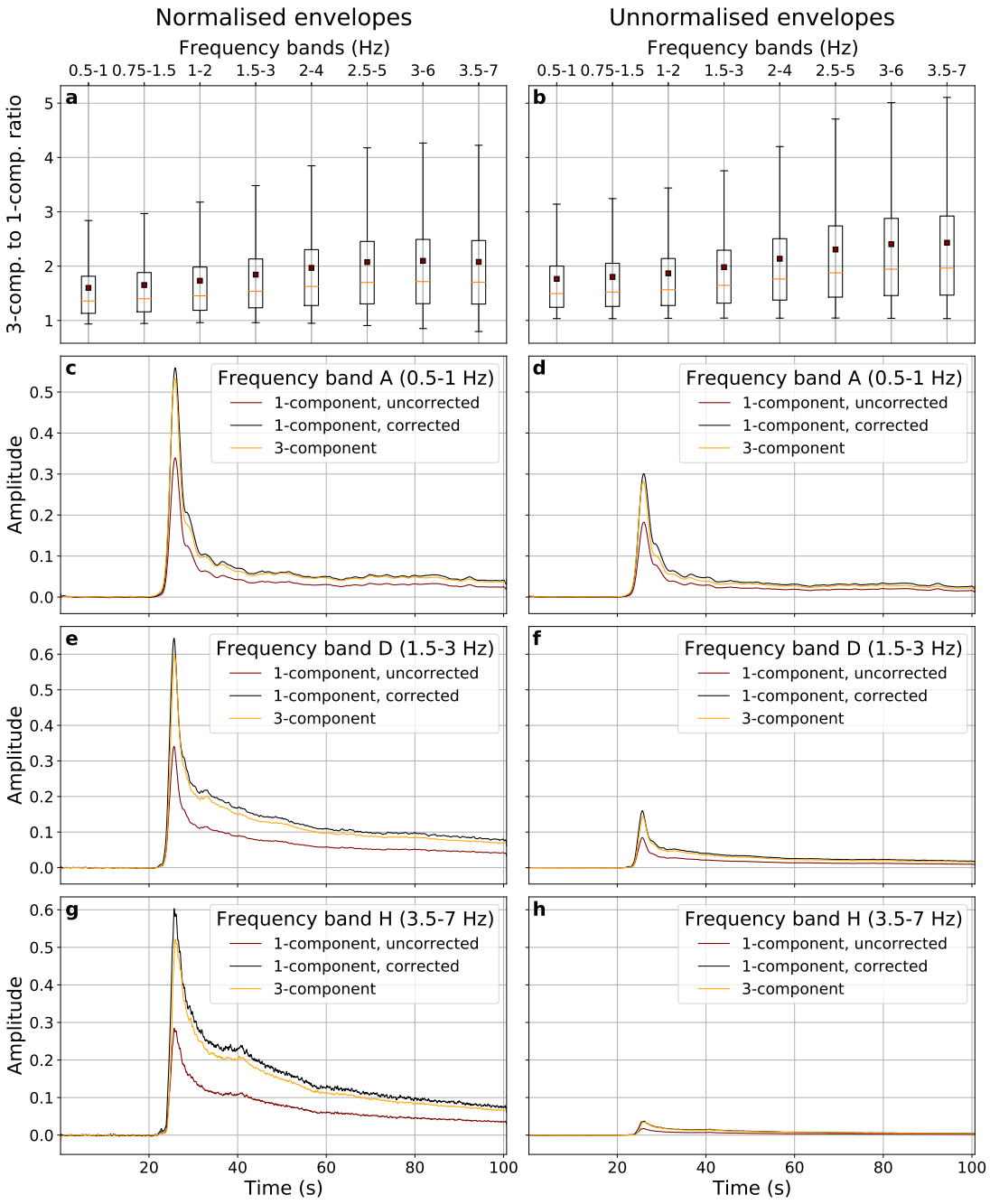

Figure 2.12: Panels a and b contain boxplots of the 3-component to 1-component ratios shown in Fig. 2.11, both for normalised and unnormalised envelopes and all frequency bands. Outliers have been removed from these plots. Panels c to h contain the stacked uncorrected 1-component, corrected 1-component and 3-component normalised and unnormalised envelopes for frequency bands A, D and H from Table 2.3.

from the EFM varied significantly (e.g. $Q_{i\,0\,1comp} \approx 600$ vs. $Q_{i\,0\,3comp} \approx 2000$, or $Q_{diff\,0\,1comp} \approx 4000$ vs. $Q_{diff\,0\,3comp} \approx 500$) and the distribution of the heterogeneity shown in posterior PDFs did not follow similar patterns. Therefore, I concluded that this approximation to 3-component data from 1-component data did not yield satisfac-

tory results and did not use it for any application of the EFM/EFMD analysis, which was restricted to data from 3-component stations.

2.1.5 Limitations and assumptions

A possible source of error in EFM/EFMD inversion is the prescribed thickness of the layers in my models. The EFM does not allow any layering in the structure and the thickness of the scattering layer is not clearly constrained. The EFMD is sensitive to changes in the bottom depth of the different layers, especially for the shallowest layer, as this affects the diffusion out of them. A priori information on Moho and lithosphere-asthenosphere boundary (LAB) depths can be used to help design the lithospheric models, but uncertainty in these reported depths always exists. Lateral velocity variations in the structuree are also not included within the EFM/EFMD framework, since they can only take 1-D velocity models. This is usually not a problem when working with individual seismic stations, especially considering the steep incidence angles required for the method, but might become an issue when working with large aperture arrays and should be taken into account. Array apertures also have an effect on their sensitivity to different frequencies, with larger arrays being more sensitive to lower frequencies. The selection of the frequency bands to be used in the analysis should therefore be adjusted to each specific case.

Other limitations of my approach are the assumptions for the determination of the different quality factors in the EFM and the fact that neither the EFM nor the EFMD take into account phase conversions and reflections at interfaces other than the free surface. Equation 15b from Korn (1990), which I use in this study, is based on the assumption that Q_s and Q_{diff} are of the same order of magnitude, even if that is not necessarily always the case (Fig. 3.8). The intrinsic quality factor (Q_i) value used in the EFMD was determined by the EFM, with a limitation to a single scattering layer and a poorly constrained frequency dependence of Q_i, since α could not be fully inverted for in the EFM (Section 2.1.1). Therefore, all layers in my EFMD models in Chapters 2 and 3 have the same Q_i and frequency dependence as obtained in the EFM, as opposed to the more complex inversions for Q_i in Chapters 4 and 5 of this thesis. The heterogeneity anisotropy observed by Kennett and Furumura (2016) and Kennett et al. (2017) could be included in future approaches of Bayesian inversion for heterogeneity structure but given the range of acceptable models I find and the trade-offs inherent in inverting for scattering parameters I have demonstrated, it is unlikely anisotropy in scattering could be well resolved with this kind of approach.

2.1.6 Conclusions

Overall, results from the synthetic tests in Section 2.1.3 show that my Bayesian algorithm is capable of successfully fitting my data and retrieving the input parameter

values for 1-layer and 2-layer models. For 3-layer models, however, the method provides good fits to the data but fails to obtain the correct parameter values due to the inherent trade-offs in scattering studies. For real data inversions, since scattering parameters values are not known beforehand, results from a 3-layer model would not be reliable. My observations illustrate the usefulness of the Bayesian approach I take in this study. It provides detailed information about the parameter space in the region of the local likelihood maximum and indicates whether a single set of parameters that fits the data exists or a range of models can equally match the data. Any estimation of scattering parameters in a maximum-likelihood or best-fitting framework would therefore have led to erroneous conclusions about the physical parameters in these systems, which I have avoided. The joint PDFs highlight the complicated relationships and trade-offs between the model parameters in the different settings explored here, which had not been observed in previous studies using the EFMD. I do not observe systematic overestimation of a in the EFMD, as reported by Hock et al. (2004). This observation might be related to the limited number of models tested in grid search approaches and the observed trade-offs between parameters.

Energy flux models are simple, heuristic and phenomenological models based on the conservation of energy and the geometrical spread of the wavefront as it travels through a model. However, they are versatile, and apt to the study of small-scale heterogeneity on Earth and other planets or moons: they can be applied both to seismic arrays or single seismic stations, do not rely on local or regional seismicity, since they use teleseismic data, and do not require the strength of the heterogeneity to be limited to a specific range. Finally, the computational efficiency of the EFMD means it can be combined with Bayesian inference algorithms to explore wide and complex parameter spaces. The posterior PDFs obtained from my inversion algorithm provide detailed information about the trade-offs and uncertainties in the determination of the structural parameters and allow us to determine whether a single set of scattering parameters can successfully explain the data or whether solutions are not unique. All of these characteristics show that the Bayesian approach to the Energy Flux Model I use in my study is an effective tool to quantify heterogeneities in the lithosphere and can contribute to our understanding of heterogeneity distribution in the Earth.

2.2 The Teleseismic Fluctuation Wavefield Method

The Teleseismic Fluctuation Wavefield Method (TFWM) is a technique designed to statistically study the heterogeneity structure beneath seismic arrays (e.g. Ritter et al., 1998; Rothert and Ritter, 2000; Ritter and Rothert, 2000). It is based on the separation of the recorded P wavefields, comprising the P wave arrival and the coda immediately following, into a coherent or mean wavefield, which is observed at all stations, and an incoherent or fluctuating wavefield, which varies from one station to another. The ratio

between the intensities of these two wavefields can be related to material properties of the scattering medium such as the correlation length of the heterogeneity (a), the RMS velocity fluctuations (ε) and background velocity (v) or the thickness of the scattering layer (L). The TFWM is an adaptation to the teleseismic case of the theory by Shapiro and Kneib (1993) and Shapiro et al. (1996).

Several studies have used the TFWM in the past. Ritter et al. (1998) applied it to characterize the lithospheric structure beneath a temporary seismic network deployed in the French Massif Central. This network was part of a tomographic experiment and was operative for six months. It recorded 140 teleseismic events during this period, but only 6 of them fulfilled the requirements of the TFWM and could be used in the analysis. Rothert and Ritter (2000) applied it to a dataset of 17 teleseismic events from the Hindu Kush region recorded by the Gräfenberg array in southeast Germany. Ritter and Rothert (2000) used common teleseismic events simultaneously recorded by a temporary network and the permanent Auvergne network, both in the Massif Central (the former was also used by Ritter et al. (1997)), and the Gräfenberg array to analyse and directly compare the heterogeneity structure in these areas. These studies found increased seismic scattering in the Massif Central, up to 2–3 times stronger than in the Frankonian Jura, where the Gräfenberg array is located. These differences were attributed to differences in geologic and tectonic history between these regions, and especially to the presence of solidified magmatic intrusions in the Massif Central. An attempt to use the TFWM to characterize the lithospheric heterogeneity structure beneath small-aperture arrays was done by Shen and Ritter (2010) and Shen et al. (2010). However, synthetic tests carried out by Li (2011) proved that the inhomogeneities are heavily underestimated when applying the TFWM to recordings from seismic arrays with apertures smaller than the maximum wavelength and the correlation length. This is likely caused by heterogeneities the size or larger than the array aperture generating scattered waves that appear to be coherent at different stations. More recently, Ma and Huang (2020) combined the TFWM with the Monte Carlo seismic phonon algorithm developed by Shearer and Earle (2004). They applied this approach to a dataset of 188 events recorded by two large seismic networks in the northern Tien Shan region. They tested four different thicknesses for the scattering layer and RMS velocity fluctuation values ranging from 1% to 9%. To resolve the trade-off between a and ε, they compared their data with synthetic seismograms obtained using the Monte Carlo method for a range of models. Their results show strong heterogeneities beneath these seismic networks, which they attribute to isolated melt pockets caused by the upwelling of hot mantle materials. Fan et al. (2020) also applied the TFWM to a large seismic network, located in the Longmenshan fault zone and the adjacent regions of the Songpan-Ganzi fold belt and the Yangtze Blocks. They analysed the teleseismic P wavefield of 13 events and related the strong scattering parameters they obtained from their analysis

to the intense tectonic activity and lithospheric flow within these regions.

Of particular interest here is the different approach taken by Hock et al. (2004), which combined the TFWM with the EFM/EFMD analysis (Section 2.1). They compared both methods with 2-D numerical wave propagation simulations and reported reliable results from the TFWM as long as the product $a\varepsilon^2$ remained below ~ 0.01 km (a being the correlation length and ε the RMS velocity fluctuations of the heterogeneities). For the EFM, their results suggest a severe and systematic overestimation of a. To take advantage of the strengths of the EFM/EFMD and the TFWM while avoiding their shortcomings, Hock et al. (2004) combined them so that they could obtain the type of autocorrelation function (ACF), thickness of the scattering layer and RMS velocity fluctuation values from either the EFM or EFMD and use these results within the TFWM to finally obtain the correlation length values. They applied their technique to recordings from the Gräfenberg array in Germany, the Auvergne network in France and three temporary networks across Europe, with stations deployed in France, Sweden, Denmark, Belgium, Luxembourg, Germany and the Netherlands. The good results obtained with this combined approach to the EFM/EFMD and TFWM methods make it an interesting option to tackle some of the weaknesses of the energy flux models.

The following sections summarise the theoretical background of the TFWM and some of the tests I carried out using the large dataset of teleseismic events recorded by the Pilbara Seismic Array (PSA) described in Section 3.1.

2.2.1 Theory

The TFWM is based on the mathematical formulation of wave theory by Shapiro and Kneib (1993) and Shapiro et al. (1996) for plane body waves propagating in 2-D or 3-D acoustic media with constant density and background velocity and random velocity fluctuations. The adaptation to the teleseismic case, which I follow here, was developed by Ritter et al. (1998).

In this framework, the total P wavefield recorded at site $\mathbf{r}(x, y, z)$ and time t after propagation through the heterogeneous layer, $u_t(\mathbf{r}, t)$, is the combination of an attenuated coherent or mean wavefield, $\langle u(\mathbf{r}, t)\rangle$ (angular brackets represent spatial or statistical averaging), and a fluctuating or incoherent one, $u_f(\mathbf{r}, t)$, so that

$$u_t(\mathbf{r}, t) = \langle u(\mathbf{r}, t)\rangle + u_f(\mathbf{r}, t) \quad . \tag{2.24}$$

Assuming anelastic attenuation and backscattering (diffusion out of the heterogeneous layer) are negligible, the only attenuation affecting the coherent wavefront is caused by the flux of energy into the scattered or fluctuating wavefield and the total

intensity I_t of the wavefield remains constant within the volume of interest. If we define the intensities of the total, coherent and incoherent wavefields as $I_t = |u_t(\mathbf{r},t)|^2$, $I_c = |\langle u(\mathbf{r},t)\rangle|^2$ and $I_f = |u_f(\mathbf{r},t)|^2$ respectively, then $I_t = I_c + I_f$ (e.g. Shapiro and Kneib, 1993; Shapiro et al., 1996; Ritter et al., 1998). The ratio between I_f and I_c provides an estimation of the strength of the wavefield fluctuations:

$$\langle \xi^2 \rangle = \frac{|u_f(\mathbf{r},t)|^2}{|\langle u(\mathbf{r},t)\rangle|^2} = \frac{I_f}{I_c} = \frac{I_t - I_c}{I_c} = \frac{I_t}{I_c} - 1 \tag{2.25}$$

Based on this expression, we can now define the regions of weak and strong wavefield fluctuations regimes (Shapiro and Kneib, 1993; Shapiro et al., 1996; Ritter et al., 1998). In the weak fluctuations regime, defined by $\langle \xi^2 \rangle \ll 1$, the coherent wavefield in the denominator dominates over the fluctuating one. Similarly, the strong fluctuations regime, in which the incoherent wavefield predominates, is characterised by $\langle \xi^2 \rangle \gg 1$.

In this context, and under the assumptions stated above, $I_t/I_c \approx e^{2\alpha L}$ (Shapiro and Kneib, 1993; Ritter et al., 1998), where L is the thickness of the scattering layer and α the scattering coefficient of the coherent wavefield. If the isotropic correlation length of the heterogeneities, a, is on the order or larger than the wavelength ($ka \geq 1$, k being the wavenumber), and the velocity contrasts are weak ($ak\varepsilon^2 \ll 1$ and $\langle \xi^2 \rangle \ll 1$), then for an exponential autocorrelation function $\alpha = \varepsilon^2 k^2 a$ (Ritter et al., 1998). From Eq. 2.25, we now have:

$$\langle \xi^2 \rangle = e^{2\alpha L} = e^{2\varepsilon^2 k^2 a L} - 1 = e^{8\pi^2 \varepsilon^2 f^2 a L / v^2} - 1 \tag{2.26}$$

where f and v represent the frequency and background velocity of the random medium respectively. This equation allows us to characterize the heterogeneity structure beneath the seismic array by calculating the product $a\varepsilon^2$. L and v need to be obtained from previous seismic or geologic studies of the area of interest. In particular, by taking the natural logarithm of Eq. 2.26, we can express the frequency dependence of $\langle \xi^2 \rangle$ as:

$$\ln(\langle \xi^2 \rangle + 1) = \frac{8\pi^2 \varepsilon^2 a L}{v^2} f^2 = \gamma f^2 \tag{2.27}$$

The coefficient γ can now be calculated within the weak fluctuations regime from a parabolic least-squares fit of $\ln(\langle \xi^2 \rangle + 1)$ in the frequency domain. In practice, most studies (e.g. Ritter et al., 1998; Rothert and Ritter, 2000; Ritter and Rothert, 2000) using the TFWM determine the frequency at which the transition between the weak and strong fluctuation regimes takes place, and at which the parabolic fit of $\ln(\langle \xi^2 \rangle + 1)$ must end, f_{max}, from the $\ln(\langle \xi^2 \rangle)$ curves, since the shift takes place at $\ln(\langle \xi^2 \rangle) \approx 0$. Shapiro et al. (1996) established a more flexible threshold by pointing out the transition happens where $\langle \xi^2 \rangle = \mathcal{O}(1)$, while Ma and Huang (2020) chose to define the transition frequency as the frequency at which $\langle \xi^2 + 1 \rangle$ saturates. Fan et al. (2020), on the other

hand, kept the definition of the transition frequency used by Ritter et al. (1998), Rothert and Ritter (2000) or Ritter and Rothert (2000) but introduced a cutoff frequency which determines where the parabolic fit of $\langle \xi^2 + 1 \rangle$ should stop. Finally, Hock et al. (2004) did not set any specific threshold for the transition frequency but calculated the fits up to a range of different limits. They compared the average of γ for the two lowest and two highest frequencies and lowered f_{max} until the average for the two highest frequencies was at least 80% that for the two lowest. Once f_{max} is obtained, if L and v are known, then we can determine $a\varepsilon^2$ from this estimation of γ. The TFWM is unable to further separate the heterogeneity parameters a and ε. Previous studies, such as Ritter et al. (1998), Rothert and Ritter (2000) or Ritter and Rothert (2000), have used estimates of ε from previous seismic studies to solve this unavoidable trade-off, while Hock et al. (2004) combined it with the EFM (see Section 2.2).

2.2.2 Data selection and processing

This method assumes plane seismic waves travelling vertically, or approximately vertically, towards the free surface, on which seismic stations are deployed. The TFWM focuses on the P wavefield, which includes the direct P wave arrival and the scattered coda waves immediately behind it. Care has to be taken to avoid the presence of secondary arrivals or depth phases within this time window, thus making teleseismic events with 30–80 degrees source distances, source depths larger than 200 km and magnitudes 5–7 the ideal type of data to apply the TFWM to, similarly to the EFM/EFMD analysis.

Data processing steps prior to the TFWM are similar to those described in Section 2.1.4. First, I remove the instrument response from all raw SAC waveforms and add relevant station and event information to file headers for later use. To quality control the data, I calculate the peak-to-peak amplitudes within a noise time window and the P wave time window for each unfiltered, vertical component trace. The noise time window starts 25 s before the theoretical P wave arrival (estimated using PREM (Dziewonski and Anderson, 1981)) and lasts for 20 s, while the P wave one begins 1 s before this time and ends 40 s later. I then calculate the signal-to-noise ratio (SNR) by dividing these peak-to-peak amplitudes. Only events with 5 or more traces with $SNR \geq 5$ are used in the TFWM analysis. Fig. 2.13 shows an example of a good quality event for array PSA (Section 3.1).

As opposed to the EFM or EFMD, the TFWM does not require 3-component data. The first step in the TFWM analysis is to normalize all vertical-component traces for a given event and array. Then, traces are aligned using slowness and backazimuth measurements obtained from the frequency-wave number analysis (e.g. Rost and Thomas, 2002) and trimmed to the time window of interest. Seismic traces in Fig. 2.13 have been processed following these steps. Previous studies using the TFWM defined the

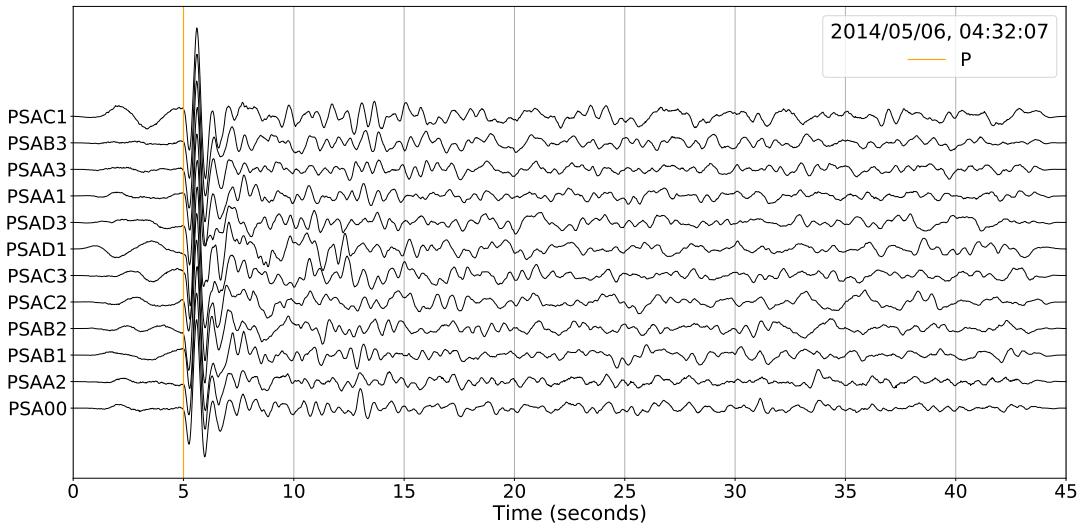

Figure 2.13: Teleseismic M5.4 event recorded by PSA stations (Section 2.1.4). Traces are normalized, aligned using the frequency-wave number analysis (e.g. Rost and Thomas, 2002) and trimmed to the TFWM time window, which extends from 5 seconds before the theoretical P wave arrival, as estimated from PREM (Dziewonski and Anderson, 1981) and marked here with an orange line, to 40 seconds after. No other phases appear within this time window for this event.

time window of interest differently (e.g. Ritter et al. (1998) analysed recordings from 4 s before to 17 s after P wave arrival, while Rothert and Ritter (2000) used waveforms from 5 s before to 40 s after P wave arrival), without any specific criteria seemingly being followed for this purpose across different studies. In my study, I applied the TFWM to 45 s long traces, extending from 5 seconds before the theoretical P wave arrival (obtained from PREM (Dziewonski and Anderson, 1981)), to 40 s later, and I manually checked the recordings for each event to ensure that no secondary arrivals could be found within the time window of interest before proceeding with the rest of the TFWM analysis.

The mean or coherent wavefield is calculated by stacking (averaging) all traces recorded by an array for a specific event, once they have been processed as described above. This procedure accentuates phases that are recorded at all stations within the array. For teleseismic data from the range of distances studied here, these coherent phases originate at the source and along the common ray path seismic waves follow on their way to the receivers. Random scattered waves generated by heterogeneities immediately beneath the stations, where ray paths separate, do not form part of this wavefield. They make up the fluctuating or incoherent wavefield, which is determined for each station by subtracting the mean wavefield from each individual recording. Figure 2.14 shows the coherent and incoherent wavefields for the same event shown in Fig. 2.13.

Intensities I_c and I_f are calculated as the squared amplitude spectra of the mean

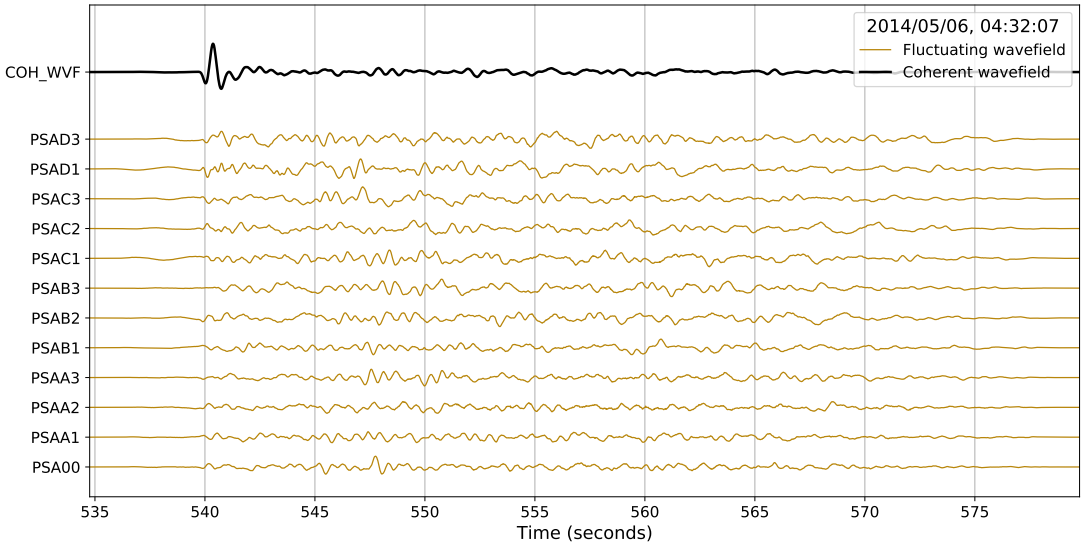

Figure 2.14: Coherent or mean wavefield for the M5.4 event shown on Fig. 2.13 (black line) and fluctuating or incoherent wavefield recorded at each PSA station (Section 2.1.4). Scale is the same for all traces.

wavefield and the average of all individual fluctuating wavefields. These intensities allow us to determine $\langle \xi^2 \rangle$ (Eq. 2.25), from which we can now obtain the product $a\varepsilon^2$ via the parabolic fit shown on Eq. 2.27. The coefficient γ is calculated separately for each event and also for the average of all the $\langle \xi^2 \rangle$ curves. The maximum and minimum γ values from the individual events, γ_{min} and γ_{max}, are used to constrain the uncertainty in the estimation of this parameter, while the value obtained from the stacked $\langle \xi^2 \rangle$ is taken as its mean value, γ_{mean}. Finally, a range of suitable ε, together with v and L values, are used to determine the correlation length from γ.

2.2.3 TFWM tests and results

I used the dataset described in Section 3.1 for the Pilbara Seismic Array, in Australia, to test the TFWM. The quality control process described above was applied to unfiltered, vertical-component traces, and a total of 102 events with 5 or more good quality traces were included in the analysis. This dataset is much larger than those used in previous studies using the TFWM (e.g. Ritter et al. (1998) used 6 events, Rothert and Ritter (2000) 17, Ritter and Rothert (2000) 13, or Hock et al. (2004) only 3 for some of their regions of interest), which helps ensure a thorough sampling of the heterogeneity structure beneath the arrays.

For each array and event, I separated the coherent and fluctuating wavefields, as described in Section 2.2.2, and calculated $\langle \xi^2 \rangle$ by taking the ratio between their intensities. Calculating f_{max}, the frequency at which the incoherent wavefield begins to dominate over the mean field, is not at all obvious and needs to be carefully done, since

the TFWM cannot be applied within the strong fluctuation regime. I tested and compared the results obtained from different approaches used in previous studies. For the first, and most common one, used by Ritter et al. (1998) and called "Ritter" in Table 2.4, I calculated f_{max} as the frequency at which $\ln(\langle\xi^2\rangle)$ becomes positive. Shapiro et al. (1996) stated the transition from the weak to the strong fluctuation regimes takes place when the ratio $\langle\xi^2\rangle = \mathcal{O}(1)$. Considering that the coherent wavefield rarely has energy beyond 5 Hz, I tested different threshold values ranging from 1 to 9 and defined f_{max} as the first time the ratio becomes equal or higher than these values. Setting $\langle\xi^2\rangle = 1$ as the condition to calculate f_{max} often yielded transition frequencies below 2 Hz and failed to provide good fits to the $\ln(\langle\xi^2\rangle + 1)$ curves. Threshold values above 2, however, often extended the parabolic fit beyond 5 Hz and, therefore, into the strong fluctuations regime, where the TFWM is not applicable anymore. For this reason, I set the final threshold value to 2, which produces maximum f_{max} values only up to 5.4 Hz. Results obtained using this method are labelled "Shapiro" in Table 2.4. Finally, I tested the approach used by Hock et al. (2004) (labelled "Hock" in my results table) by calculating the parabolic fits of $\ln(\langle\xi^2\rangle + 1)$ up to frequencies from 2 to 5.5 Hz, in steps of 0.25 Hz. If the average parabolic fit coefficient, γ, from the two highest

Table 2.4: Summary of the TFWM results for PSA, ASAR and WRA. The saturation or transition frequency f_{max} was calculated for each event and for the stack of all the $\langle\xi^2\rangle$ curves using three different approaches, described in Ritter et al. (1998), Shapiro et al. (1996) and Hock et al. (2004) respectively. Minimum and maximum values of f_{max} and γ are obtained from the individual events using each approach, while mean values correspond to the transition frequency for the stacked $\langle\xi^2\rangle$. Results from the TFWM analysis obtained using all three approaches are shown together here for comparison. Different RMS velocity fluctuations values, scattering layer thicknesses and velocities were used to estimate the correlation length both in the crust and the entire lithosphere.

Array	Layer	Method	f_{max} (Hz)	γ (Hz^{-2})	Correlation length (km) $\varepsilon = 1\%$	$\varepsilon = 3\%$	$\varepsilon = 5\%$	$\varepsilon = 7\%$	$\varepsilon = 9\%$
PSA	Crust $L/v^2 = 0.8$ (s^2/km)	Ritter	1.5	0.01	0.022	0.007	0.005	0.003	0.002
			3.0	0.07	0.108	0.036	0.022	0.015	0.012
			4.2	0.24	0.39	0.13	0.08	0.06	0.04
		Shapiro	1.5	0.02	0.028	0.009	0.006	0.004	0.003
			3.3	0.06	0.091	0.030	0.018	0.013	0.010
			5.4	0.19	0.31	0.10	0.06	0.04	0.03
		Hock	2.1	0.02	0.040	0.013	0.008	0.006	0.004
			5.3	0.07	0.120	0.040	0.024	0.017	0.013
			5.1	0.19	0.31	0.10	0.06	0.04	0.03
	Lithosphere $L/v^2 = 3.2$ (s^2/km)	Ritter (1998)	1.5	0.01	0.0054	0.0018	0.0011	0.0008	0.0006
			3.0	0.07	0.026	0.009	0.005	0.004	0.003
			4.2	0.24	0.096	0.032	0.019	0.014	0.011
		Shapiro	1.5	0.02	0.0068	0.0023	0.0014	0.0010	0.0008
			3.3	0.06	0.022	0.007	0.004	0.003	0.002
			5.4	0.19	0.075	0.025	0.015	0.011	0.008
		Hock	2.1	0.02	0.0097	0.0032	0.0019	0.0014	0.0011
			5.3	0.07	0.029	0.010	0.006	0.004	0.003
			5.1	0.19	0.075	0.025	0.015	0.011	0.008

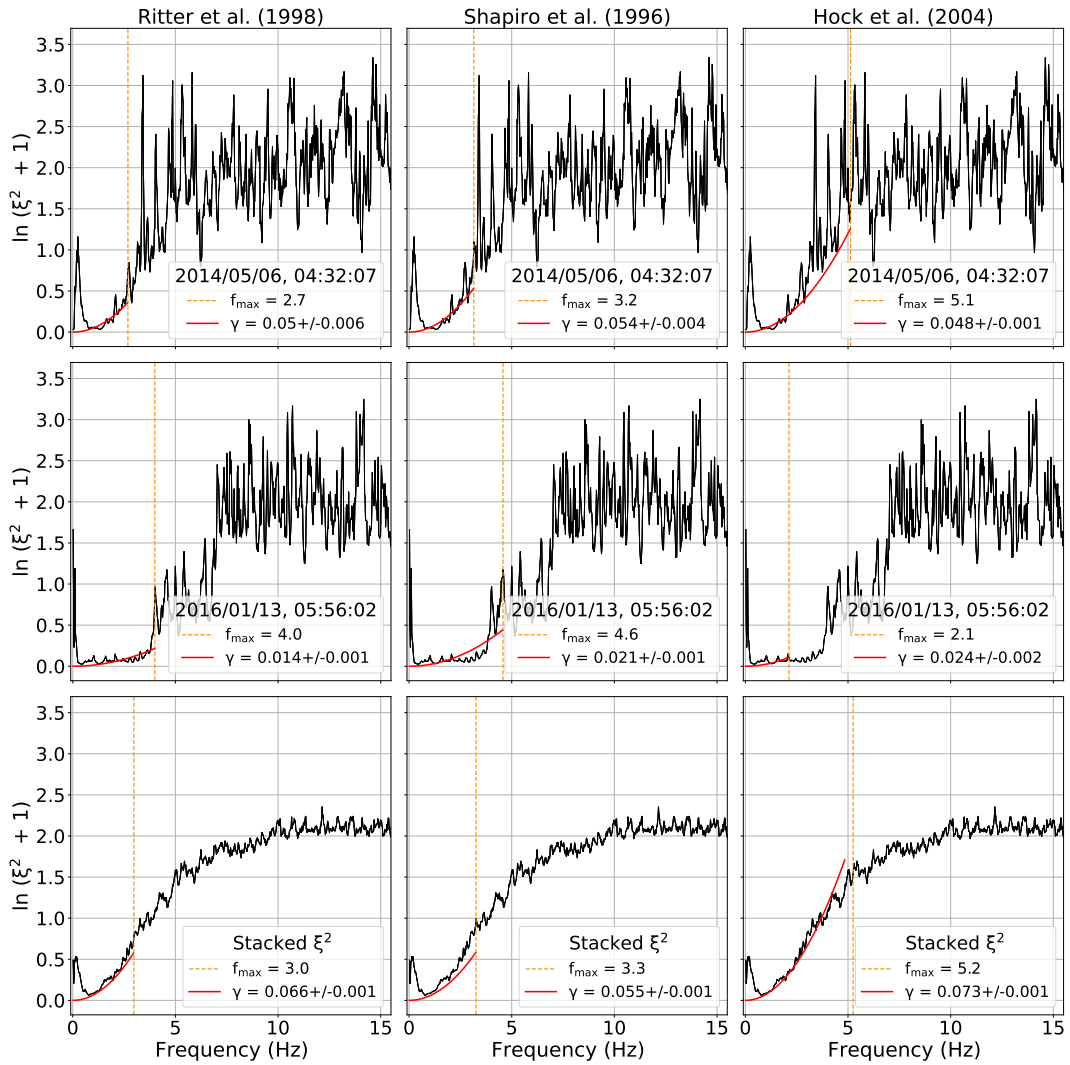

Figure 2.15: $\ln(\langle\xi^2\rangle + 1)$ curves for the M5.4 event shown on Figs. 2.13 and 2.14 (top row), a M5.9 event (middle row) and the stack of all ratios $\langle\xi^2\rangle$ curves. Transition frequency f_{max} values for each of the three different methods tested here are shown with orange dashed lines and their values indicated in the legends. Red lines represent the parabolic least-squares fits curves. The obtained γ in each case is included in the legend of each panel.

frequencies was lower than 80% of the value for the two lowest, then the highest frequency was discarded and the process repeated until this condition was satisfied. Table 2.4 contains the results obtained from the TFWM analysis using these three different approaches. Minimum and maximum f_{max} and γ are obtained from the results from individual events (top and bottom rows of results for each method, respectively), while mean values (central row) correspond to the stack of all individual $\langle\xi^2\rangle$ curves.

Figure 2.15 contains the $\ln(\langle\xi^2\rangle + 1)$ curves for the 2014 event shown in Fig. 2.13, as well as a M5.9 event recorded by PSA stations in 2016 and the stack for all events. In all cases, the curves saturate at $\ln(\langle\xi^2\rangle + 1) + \sim 2$, but the frequency at which that happens varies. A sharp peak at low frequencies can be observed in all three cases. It

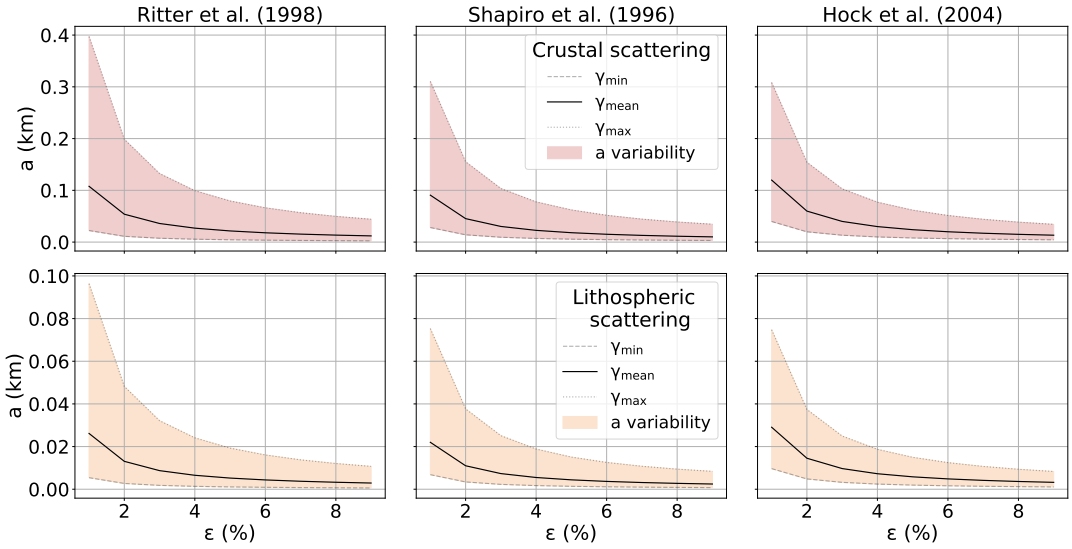

Figure 2.16: Correlation length values obtained for both crustal and lithospheric scattering and the range of tested values of the RMS velocity fluctuations, using all three different approaches to f_{max} calculation tested here.

is caused by low frequency noise, especially in the time window prior to the P wave arrival, increasing the ratio between the fluctuating and coherent wavefields. This peak is not easily removed from the $\ln(\langle\xi^2\rangle + 1)$ curves, since it varies in amplitude between events and sometimes extends up to ∼1 Hz, while for other events it is barely noticeable. A potential solution to this issue, which Ma and Huang (2020) or Fan et al. (2020) apply to certain extent, would be filtering the original seismograms prior to the TFWM analysis or manually inspecting the $\langle\xi^2 + 1\rangle$ curves for every single event in the dataset and removing those which do show this peak at low frequencies. Red lines in Fig. 2.15 represent the parabolic fits required in the TFWM to obtain γ and the heterogeneity parameters, a and ε. They extend up to the f_{max} value calculated for each one of the methods described above. The parabolic trend of $\ln(\langle\xi^2\rangle + 1)$ is more obvious for the 2014 event than for the 2016 one or the stack for all events. This results in very small differences in γ values between the three methods, even if the transition frequency does vary from 2.7 to 5.1 Hz. For the 2016 event, the $\ln(\langle\xi^2\rangle + 1)$ is almost constant from ∼0.5–4 and 4–7 Hz, before reaching its saturation value of ∼2 at ∼7 Hz. f_{max} and γ values range in this case from 2.1–4.6 and 0.014–0.024 respectively. The stacked $\ln(\langle\xi^2\rangle + 1)$ curve grows smoothly and continuously up to ∼10 Hz, when it reaches its saturation value. Transition frequencies vary from 3.0–5.3 Hz here, which translates into larger differences between obtained γ values.

Finally I calculated the product $a\varepsilon^2$ using the obtained γ values, as well as Moho and lithospheric thicknesses and P wave velocities obtained from previous studies for this array (Kennett and Salmon, 2012; Kennett et al., 2011; Yoshizawa and Kennett, 2015). The TFWM does not have the power to resolve these two parameters independently, so

previous studies have either used ε values previously obtained in their areas of interest or a range of suitable or realistic values. The only exception here is the approach taken by Fan et al. (2020), who used f_{max} and the average P wave velocity within the scattering layer to obtain the corresponding correlation length value from $v = af_{max}$. They then obtained RMS velocity fluctuations using these values together with the $a\varepsilon^2$ factors obtained from γ. In my case, I chose to determine the correlation length values for RMS fluctuations varying from 1–9 %, in steps of 2%, in an approach similar to Ritter et al. (1998), Rothert and Ritter (2000) or Ma and Huang (2020). Results from this calculation are shown in Table 2.4 and represented in Fig. 2.16. My γ values are generally much lower than those obtained by previous studies, in which they varied from 0.25–0.84 Hz^{-2} (Ritter et al., 1998), 0.11–0.23 Hz^{-2} (Rothert and Ritter, 2000) or 0.16–0.67 Hz^{-2} (Ma and Huang, 2020), or had averages ranging from 0.11–0.84 Hz^{-2} (Ritter and Rothert, 2000), 0.16–0.39 Hz^{-2} (Hock et al., 2004) or 0.97–1.50 Hz^{-2} (Fan et al., 2020). This difference could be related to differences in the heterogeneity structure beneath these different study areas, but also to my dataset being larger and less manually curated than those in past studies. Looking at parabolic fit figures in these studies (Fig. 2.17), it is not always clear whether their parabolic functions included a second parameter and took the $\gamma f^2 + b$ form (as opposed to the γf^2 form stated in the theory), since they do not always seem to cross the origin at (0,0) (Fig. 2.17). I did try this approach but found the fits to the data were usually worse which can even result into negative correlation length values, possibly because of the effect of the noise related peak at low frequencies. The frequency at which the parabolic fit starts also seems to be manually selected and varies for different events or stacks in many of these studies (Fig. 2.17), probably to avoid the peak at low frequencies. In my case, forcing the parabolic fit to start at f=0 Hz inevitably results in flatter curves and lower γ values. Starting the fits right after the low frequency peak while adding a second parameter (which would be equivalent to subtracting the lowest value in $\ln(\langle\xi^2\rangle + 1)$, in a water level removal fashion) can probably greatly improve the fits to the data and increase the obtained γ values, but are hardly practical for large datasets like the one used in this study. Correlation lengths obtained from these γ and the range of tested ε values are generally higher for the crustal scattering case than for the lithospheric one, but in both cases they are much lower than those obtained in previous studies and range from a few meters to a maximum of ∼400 m. These results are not realistic, especially considering that, with a minimum P wave velocity of ∼6.4 km/s (average velocity in the crust, according to the AuSREM model (Kennett and Salmon, 2012)) and a maximum frequency of 5.5 Hz, the minimum wavelength the array would be sensitive to is ∼1.2 km. The TFWM requires heterogeneities to be on the order of, or larger, than the wavelength. This means this technique is, by definition, not sensitive to scatterers of the scale lengths my results suggest, which deems them not just unrealistic but also unreliable.

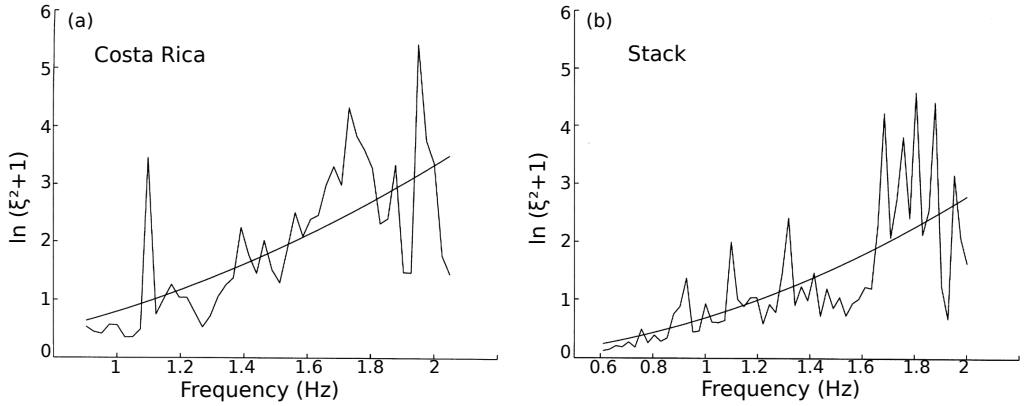

Figure 2.17: Parabolic fits carried out by Ritter et al. (1998) according to the TFWM for an event with epicenter in Costa Rica (a) and the stack of all events included in their dataset (b), as recorded by seismic stations located in the French Massif Central. Modified from Ritter et al. (1998).

2.2.4 Conclusions

The Teleseismic Fluctuation Wavefield Method, or TFWM, has both been used independently (e.g. Ritter et al., 1998; Rothert and Ritter, 2000; Shen and Ritter, 2010) and in combination with the Energy Flux Model (Hock et al., 2004) or a Monte Carlo seismic phonon algorithm (Ma and Huang, 2020). While the TFWM on its own is not capable of independently recovering the heterogeneity parameters of the crust or lithosphere, its association with these other methods appeared to be capable of circumventing their individual disadvantages to obtain a more robust solution.

However, my tests have revealed a number of issues with the TFWM, which are accentuated when working with a large dataset. It is sensitive to the transition frequency (f_{max}) between the weak and strong fluctuation regimes, and at which the parabolic fit of $\ln(\langle\xi^2\rangle + 1)$ needs to end. I calculated f_{max} using three different approaches used in past studies, which yielded different results, not just for individual events but also for the stack of all events. Accurately calculating f_{max} remains the biggest challenge when working with the TFWM, but my tests have also shown that, for results to be reliable, the frequency at which the parabolic fits start also needs to be manually and carefully selected for each event, and that a second parameter may be required within the fitting function.

In addition to this, the TFWM only allows a single heterogeneous layer within the structure and is only applicable for weak heterogeneities and seismic arrays. Further limitations are anelasticity and backscattering not being taken into account within the theoretical framework of the method, which inherently makes TFWM less accurate and realistic than other methods that do take these phenomena into account. For all these reasons, I decided not to use the TFWM to characterize the heterogeneity structure, either on its own or in combination with the EFM/EFMD analysis.

Chapter 3

Characterization of seismic scattering and attenuation beneath two Australian cratons

Major tectonic processes have an effect not only on the large-scale lithospheric structure of the continents, but also on the small-scale heterogeneity, especially along the margins of tectonic blocks. Understanding the distribution and characteristics of the small-scale heterogeneity of the lithosphere helps us improve our earthquake monitoring efforts through better understanding of the effects of the inhomogeneity on the recorded wavefield while also providing a link to the tectonic history of the lithosphere seismic waves travel through. In this context, past studies have shown that the small-scale heterogeneity of the lithosphere, which strongly affects seismic attenuation and scattering, tends to be stronger in areas which have undergone more tectonic reworking, while these propagation effects are much weaker in less tectonically active regions (e.g. Cormier, 1982; Korn, 1993; Sipkin and Revenaugh, 1994; Domínguez and Rebollar, 1997).

The continent of Australia is an interesting research area both for lithospheric structure and tectonic history studies, since it has not always been the isolated giant that we know today. The main tectonic blocks that form current Australia first merged within the Nuna supercontinent. Very large supercontinents, comprising all, or nearly all, of the continental blocks on the planet have developed at least three times in Earth's history (e.g. Rogers and Santosh, 2003; Zhao et al., 2004). The earliest of such supercontinents, called Nuna/Columbia, formed at ∼2100–1800 Ma and started breaking apart ∼200–600 Ma later, after a subduction-related accretion period (e.g. Rogers and Santosh, 2002; Rogers and Santosh, 2003; Zhao et al., 2004; Betts et al., 2016). Despite the uncertainties in determining the exact configuration of Nuna (e.g.

Rogers and Santosh, 2002; Zhao et al., 2004; Pisarevsky et al., 2014), paleomagnetic, tectonic, geochemical and geochronology data support its existence (e.g. Karlstrom et al., 2001; Zhao et al., 2004; Evans and Mitchell, 2011; Condie et al., 2011; Pisarevsky et al., 2014). It was during the amalgamation of this supercontinent that the Western, Northern and Southern Australian Cratons first joined, even if their present-day configuration was not reached until ∼650 Ma, after a series of rotations, accretionary processes and continent-continent collisions separated by lithospheric extension periods (e.g. Betts et al., 2002; Pisarevsky et al., 2014; Betts et al., 2016). Most of present-day tectonic activity in Australia takes place along the large subduction zones along its northern and eastern margins, thus making it difficult to study its structure using seismic waves from local or regional earthquakes while turning it into an ideal candidate for methods that rely on teleseismic data.

In order to resolve and compare potential variations of small-scale structure with tectonic history and large-scale structure, I applied the single-layer Energy Flux Model (EFM, Korn, 1990) and multi-layer Energy Flux Model (EFMD, Korn, 1997) described in Chapter 2 to large datasets from three medium aperture arrays located on different tectonic terranes. Warramunga (WRA) and Alice Springs (ASAR) seismic arrays are part of the International Monitoring System (IMS), a worldwide network created to ensure compliance with the ban on nuclear tests as part of the Comprehensive Test Ban Treaty. The arrays are located on the Proterozoic North Australian Craton (NAC), with ASAR being located on its southern margin, next to the Amadeus Basin. The Pilbara Seismic Array (PSA), designed for research purposes (Kennett et al., 2015), is located on the Archaean West Australian Craton (WAC). All three arrays are part of the Australian National Seismic Network, operated by Geoscience Australia.

This work is published as González Álvarez et al. (2021) and this chapter is partially based on that article. My EFM results for PSA show that quality factors take higher values for this array than for ASAR or WRA, thus pointing to the small-scale structure beneath PSA being less attenuating and heterogeneous than below the other arrays. Scattering and total attenuation are similarly strong for the NAC arrays, while intrinsic and diffusion attenuation are stronger for ASAR than for WRA or PSA. My EFMD results show the lithospheric mantle is less heterogeneous than the crust for all three arrays, an observation which may be linked to the cratonic nature and the longevity of the lithosphere beneath them (Wang et al., 2014). The scattering parameters (correlation length and RMS velocity fluctuations) are lower for PSA than for ASAR and WRA, pointing to weaker and smaller scale heterogeneity being present beneath PSA. These differences and similarities in the lithospheric small-scale structure beneath the arrays agree with variations in the tectonic histories of these regions, as well as results from previous studies using different data analysis techniques (e.g. Kennett and Furumura, 2016; Kennett et al., 2017).

3.1 Data selection and processing

Data selection and processing for this study follows the processes described in Section 2.1.4. I used used the FDSN Client tool from Obspy (Beyreuther et al., 2010) to obtain event metadata directly from IRIS Data Management Services (DMS) and build a catalog with all events occurring between January 1, 2012, and December 31, 2018, with 30 – 80 degrees epicentral distance to the array centers, source depths greater than 200 km and magnitudes from 5 to 7 (Section 2.1.4).

I collected waveforms and station metadata from PSA stations from IRIS DMS, while for WRA and ASAR I acquired waveforms and station metadata directly from

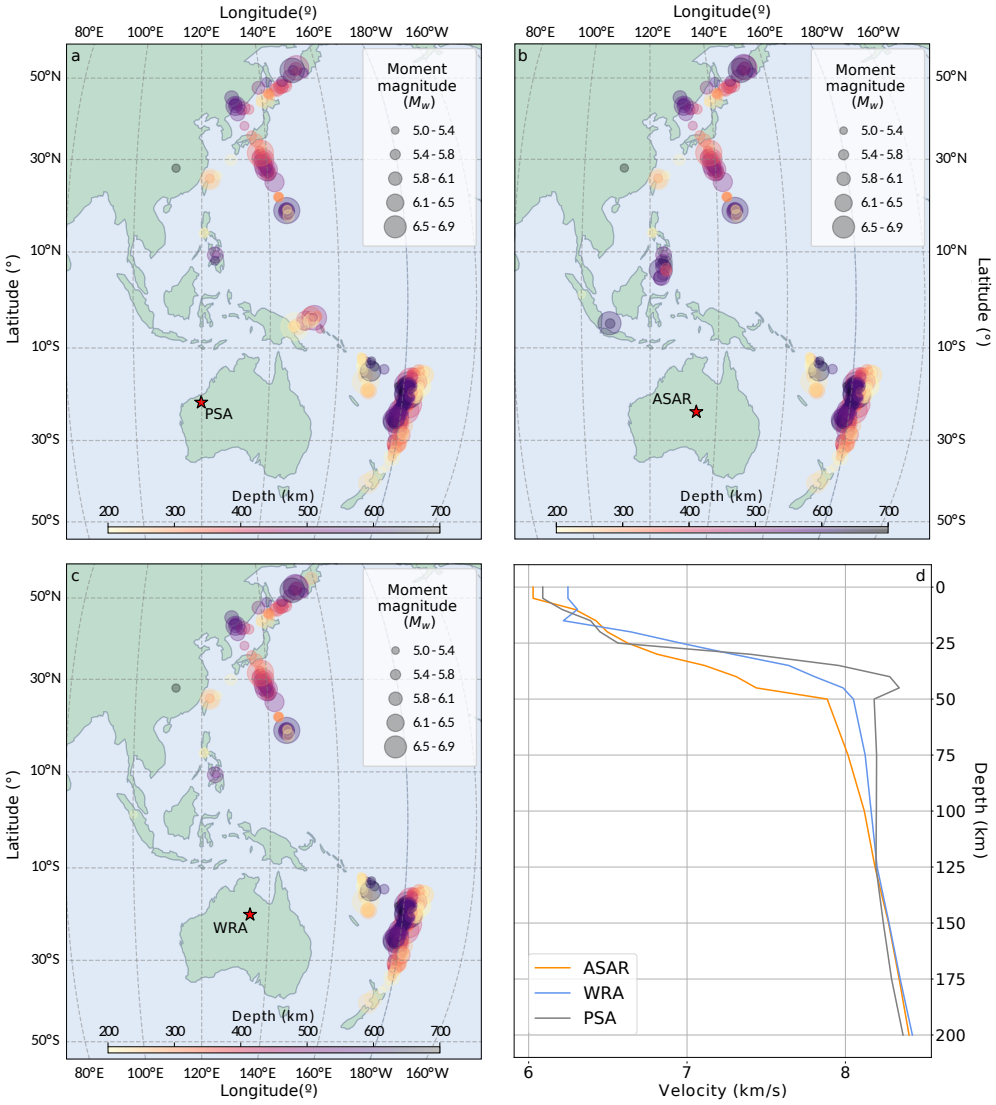

Figure 3.1: Events locations for PSA, ASAR and WRA datasets used for this study (a, b, c) and velocity models for the arrays obtained from the Australian Seismological Reference Earth Model (AuSREM; Kennett and Salmon, 2012; Salmon et al., 2013a; Kennett et al., 2013) (d).

Table 3.1: Number of events and good quality (SNR > 5) traces for each array and frequency band.

		Number of events per frequency band							
		0.5–1 Hz	0.75–1.5 Hz	1–2 Hz	1.5–3 Hz	2–4 Hz	2.5–5 Hz	3–6 Hz	3.5–7 Hz
PSA	Events	86	161	213	276	343	268	212	158
	Traces	973	1899	2489	3226	3179	2965	2282	1641
WRA	Events	292	355	385	407	413	410	412	406
	Traces	709	843	916	977	983	984	980	965
ASAR	Events	309	375	440	429	405	397	386	374
	Traces								

the IMS. The EFM/EFMD analysis requires 3-component seismic data (Section 2.1.4), which means the number of seismic stations included in these datasets varies from array to array. For PSA, all its stations are 3-component, while only 3 and 1 are for WRA and ASAR, respectively. Table 3.1 contains the number of good quality events (as defined in Section 2.1.4) recorded by PSA, WRA and ASAR stations used in this study for the frequency bands listed on Table 2.3. Panels a, b and c on Fig. 3.1 show the epicentres, magnitudes and depths of all events included in this study for each array.

I obtained the required P-wave background velocity model of the lithosphere for each array from the Australian Seismological Reference Model (AuSREM; Kennett and Salmon, 2012; Salmon et al., 2013a; Kennett et al., 2013). These velocity structures are shown in Fig. 3.1 d.

3.1.1 Dataset size analysis

A characteristic of past studies using the EFM or EFMD is the small number of seismic events used in the analysis: Hock and Korn (2000) and Hock et al. (2004) used only 3 events, recorded by stations from three temporary seismic networks in Europe; Korn (1990) analysed data from 11 events from the Flores, Timor and Banda Sea region recorded by WRA stations; Korn (1993) included 188 seismograms from 9 stations in the circumpacific area, with most stations recording 10–24 events and a maximum of 62 events recorded by a single station; Li (2010) does not specify how many events were used in their analysis.

Considering that the EFM and EFMD are stochastic methods, I decided to study the effect of the size of the dataset on coda amplitudes stability and smoothness, as well as on the results obtained from these methods. To test this, I used the dataset of normalised coda envelopes calculated for WRA for the EFMD as described in Sections 2.1.2 and 2.1.4. Given that the only difference between normalized and unnormalized coda envelopes is a scaling factor, I believe the dataset size would have a similar effect on both EFM and EFMD results. To evaluate such an effect, I stacked all available normalised envelopes for each frequency band (Table 3.1) and used the result as a proxy of the"true envelope". For each frequency band, I randomly selected 250 groups

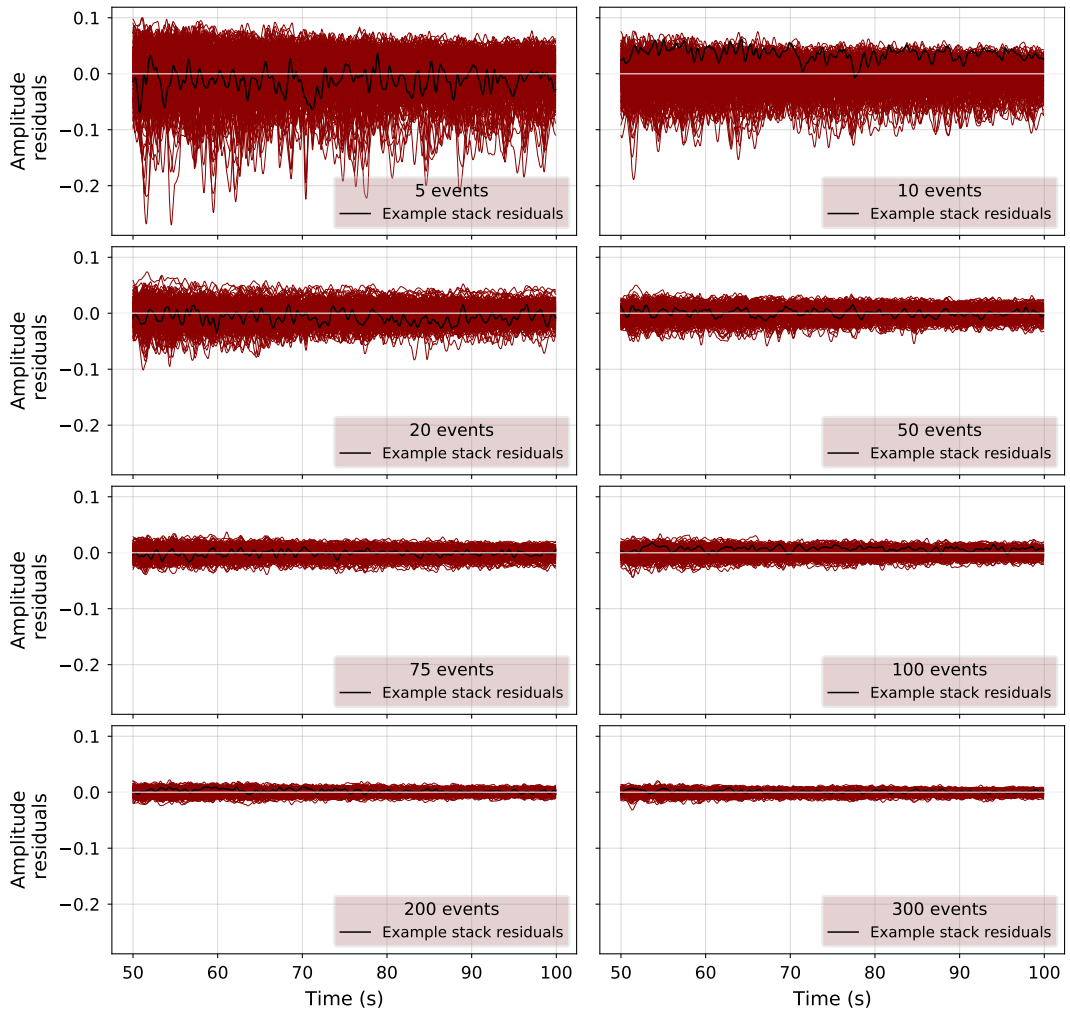

Figure 3.2: Amplitude residuals obtained by subtracting each of the 250 realizations of stacks of N events from the stack of the full dataset (407 events, Table 3.1) available for frequency band D (1.5 – 3 Hz, Table 2.3). Black lines highlight the residuals for a randomly chosen stack.

of N events and calculated the mean and standard deviation of the envelopes, with N ranging from 2 to 200 in steps of 1 event. Figure 3.2 contains the residuals obtained from subtracting each realization of stacks of 5, 10, 20, 50, 75, 100, 200 and 300 events from the full stack (the "true envelope") for frequency band D (Table 2.3). Residuals for the other frequency bands can be found in Appendix A.1. Up to 50 events, the variation of the residuals rapidly diminishes as the number of events used to compute the stacks increases. For stacks of more events, residuals continue decreasing but become more stable.

To further illustrate the potential effect of the dataset size on the EFM/EFMD results and establish an optimum or recommended dataset size, I ran the first step of the EFM analysis (the linear fit of the coda) on these data to obtain the coda decay rate (a_1) and coda intercept (a_0) values for each N value. Fig. 3.3 contains a statistical

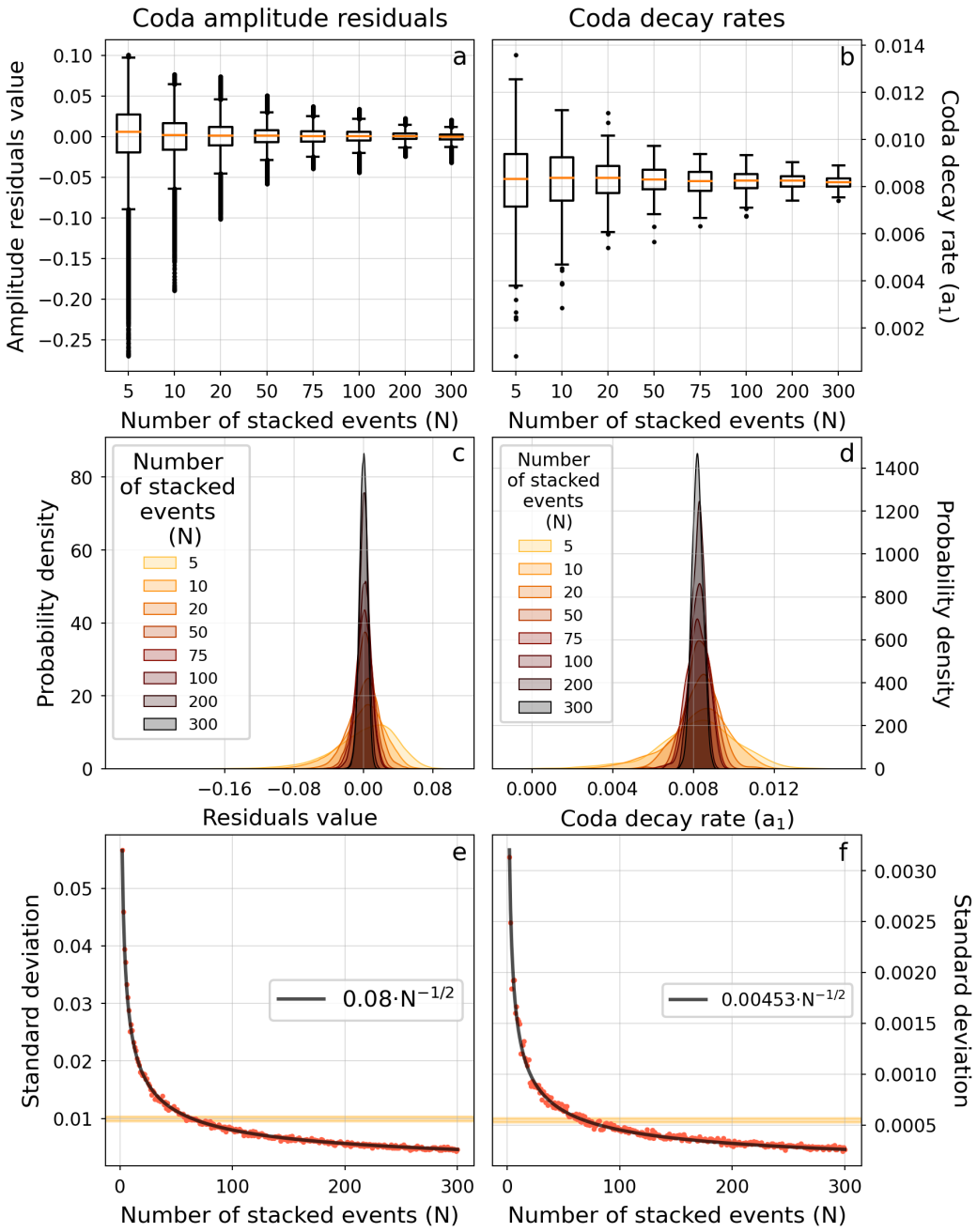

Figure 3.3: Statistical analysis of the residuals shown in Fig. 3.2 and coda decay rates (a_1) obtained from the first step of the EFM analysis for frequency band D (Table 2.3). a and b) Boxplots of the values for stacks of 5, 10, 20, 50, 75, 100, 200 and 300 events; c and d) probability density functions; e and f) standard deviation value for all tested N values. Orange lines in panels a and b represent the median of the residuals for each value of N. Boxes mark the interquartile range (IQR), while upper and lower whiskers extend from both ends of the box to 1.5 · IQR above and below the box respectively. Residuals or coda decay rates values outside this range are considered outliers. Black lines on panels e and f represent the expected decay of the standard deviation, according to the Central Limit Theorem. The orange shaded areas on the same panels mark the standard deviation value for $N = 60$–80, which we suggest as the minimum number of events necessary to ensure coda and coefficients stability.

analysis of the coda decay rate (a_1) values obtained from this analysis for frequency band D (1.5 – 3 Hz, Table 2.3). Results for the other frequency bands and coda intercept (a_0) values are consistent with those included here and shown on Appendix A.1. Fig. 3.3 shows that the interquartile range (IQR) and the probability density functions (PDFs) of the residuals become narrower as the number of events used in each stack increases. The median remains relatively constant, regardless of the number of events used in the stacks, but the standard deviation decreases rapidly as N increases, up to ∼60–80 events for the residuals and ∼80–100 events for a_1. Beyond that threshold, marked by red dashed lines on Fig. 3.3 e, f, the standard deviation decreases more slowly but does not become constant, following the $cN^{-1/2}$ (c =const) decay predicted by the Central Limit Theorem. This "convergence" is also illustrated on Fig. 3.3 a–d, in the form of IQRs on panels a and b stabilizing or the narrowing of the PDFs on panels c and d becoming negligible for stacks of more than 50 events.

The EFM and EFMD analysis are based on the fitting of coda amplitudes to different functions. Therefore, stable codas are essential to ensure results from these techniques are reliable and accurate. Based on the standard deviation of the coda decay rates shown on Fig. 3.3 f, I suggest an optimum dataset size of at least 60 – 80 events, since these are the parameters required for the EFM/EFMD analysis. Smaller datasets, such as the ones used by Korn (1990), Hock and Korn (2000) or Hock et al. (2004), cannot provide stable codas that guarantee the reliability of the coefficients, while larger datasets would offer little improvement and increase processing time in the first steps of the analysis. For this study, however, I decided to take advantage of the full datasets for PSA, ASAR and WRA (Table 3.1), since higher computing costs were not a concern and some, if minor, improvement could still be gained from using more events.

3.2 Tectonic Setting

ASAR and WRA are located on the North Australian Craton (NAC), one of the Proterozoic cratons in the Precambrian westernmost two-thirds of the Australian continent (e.g. Myers, 1990; Simons et al., 1999; Cawood and Korsch, 2008; Wellman, 1998) (Fig. 3.4). The NAC consists of late Archaean to Proterozoic cratonic blocks overlaid by Proterozoic and Phanerozoic orogenic belts and basins. PSA is located on Archaean lithosphere part of the West Australian Craton (WAC), which includes both the Pilbara and Yilgarn Archaean cratons, as well as some Proterozoic orogens and basins (Cawood and Korsch, 2008) (Fig. 3.4). Present day tectonic activity in Australia is concentrated along the active plate boundaries in the north and east, with continental regions presenting only moderate seismicity (Fichtner et al., 2009).

Previous studies have investigated crust and lithospheric thicknesses and structure

around the three arrays studied here. Thick crust ($L_c > 40$ km) with a wide and smooth Moho transition has generally been found in the Proterozoic shields of Central Australia while the Archaean regions of western Australia have thinner crust ($L_c < 40$ km) and sharper crust-mantle transitions (e.g. Clitheroe et al., 2000; Sippl, 2016; Salmon et al., 2013b; Kennett et al., 2011; Kennett and Saygin, 2015). This difference in crustal thickness between Archaean and Proterozoic regions seems not to fit the trend of crustal thickness increasing with age suggested for Australia (e.g. Clitheroe et al., 2000). It has been attributed to post Archaean tectonic activity underplating material at the base of the crust in these regions, as opposed to the Archaean cratons being located at passive margins and, therefore, not being affected by more recent tectonics (e.g. Drummond and Collins, 1986).

Sippl (2016) and Kennett and Sippl (2018) imaged a series of Moho offsets along a north-south profile in the NAC. One of these offsets is associated with the Redbank Shear Zone, which separates the Aileron Province and the location of ASAR from the Amadeus Basin, just south of the array (e.g Goleby et al., 1989; Korsch et al., 1998; Sippl, 2016). The profile used in Sippl (2016) and Kennett and Sippl (2018) is located roughly 50 km west of ASAR and shows an offset of up to 20 km coinciding with ASAR latitude, even though they show constant Moho depths beneath the array. An east-west gravity anomaly has been found at the location of this Moho offset (Sippl, 2016, Fig. 1) and attributed to denser lithosphere at the base of the crust caused by the overthrusting of the Aileron crustal block during the Alice Springs Orogeny 400-350 Ma ago (Goleby et al., 1989; Aitken, 2009; Aitken et al., 2009; Sippl, 2016). Another offset imaged by Sippl (2016) and Kennett and Sippl (2018), further north, shows a north-south decrease in Moho depth of about 10 km just south from WRA, which has been associated with a Proterozoic suture zone. Corbishley (1970) also found evidence of a layered and dipping structure below WRA. Gravimetric data do not show any anomalies here (Sippl, 2016), which has been attributed to a layer of sediments near the surface, isostatically compensating the mass excess at depth.

Several studies have addressed the thickness of the lithosphere in the Australian continent. Some suggest similarly deep interfaces across all Precambrian cratonic regions in Australia ($L_l \approx 200$ km) (e.g. Debayle and Kennett, 2000). More recent studies use a lithosphere-asthenosphere transition zone (LAT), defined as a mechanical or thermal boundary layer related to changes in rheology, as opposed to a simple interface at the bottom of the lithosphere (e.g. Kennett and Sippl, 2018; Yoshizawa and Kennett, 2015). Specifically, Kennett and Sippl (2018) place the upper and lower bounds of the LAT at 140 and 170 km depth respectively for ASAR, and at 120 and 160 km for WRA, while Yoshizawa and Kennett (2015) place them at 100 and 200 km depth for PSA. Some studies have also found evidence for mid-lithospheric discontinuities below both ASAR and WRA, at 90 and 91 km respectively, which have been interpreted as

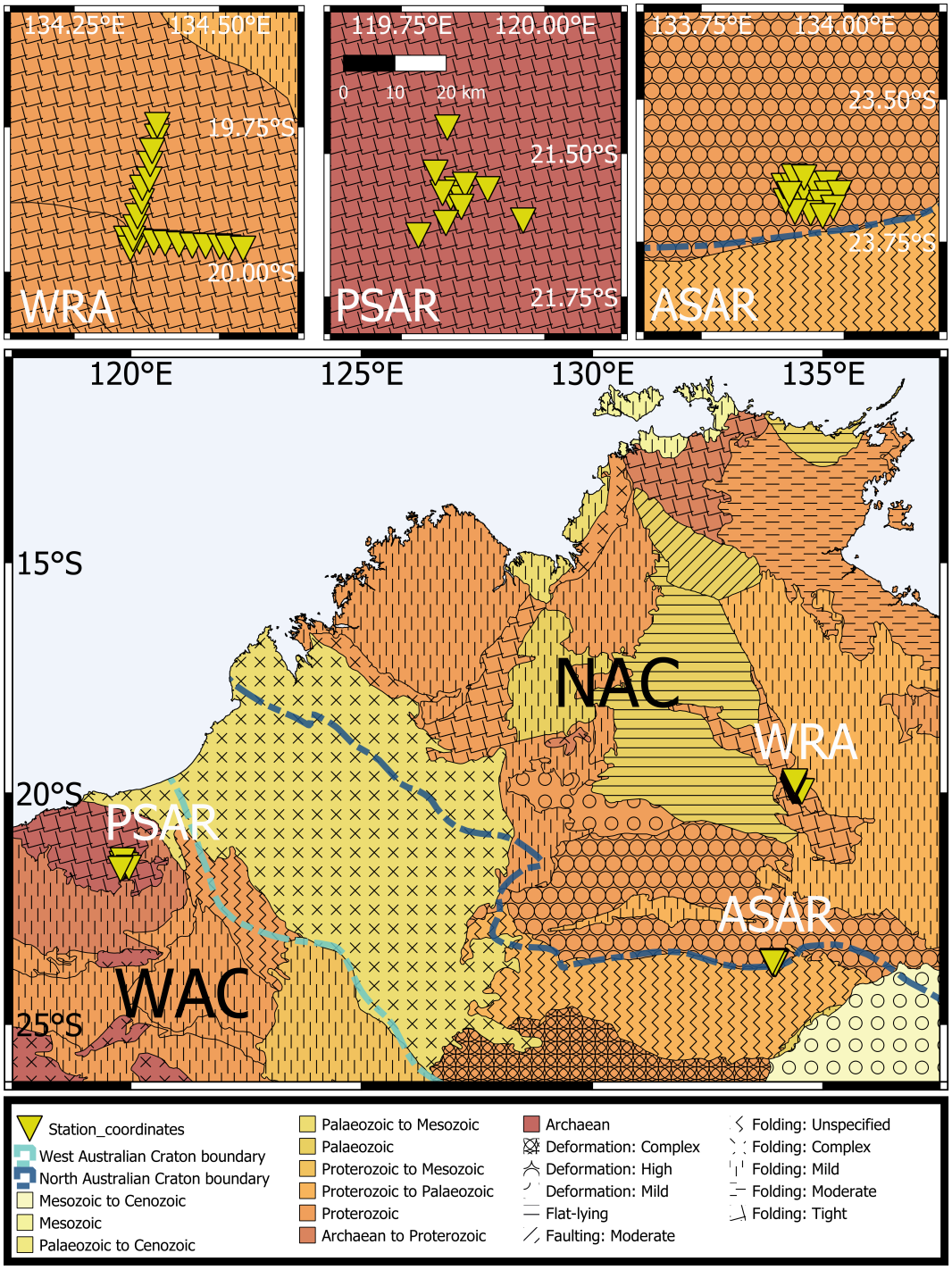

Figure 3.4: Simplified geological map of northwestern Australia and location of the three seismic arrays used in this study (Alice Springs Array (ASAR), Warramunga Array (WRA) and Pilbara Seismic Array (PSA)). Blue dashed lines represent the boundary of the West Australian Craton (WAC, light blue line) and the North Australian Craton (NAC, dark blue line). PSA and WRA are located on Archaean and Proterozoic basement respectively, inside the cratons, while ASAR is situated at the southern boundary of the NAC. Panels on the right show the station configuration of the arrays, with the same scale bar shown for PSA being applicable to all three maps. Geological structure based on Blake and Kilgour (1998) and Raymond et al. (2018).

vertical variations in mantle composition, grain size or fabric, for example a low velocity melt cumulate layer (Ford et al., 2010) and as a former mantle detachment zone associated with the Alice Springs orogeny (Kennett and Sippl, 2018).

3.3 Results and discussion

I applied the single-layer EFM to the dataset summarised on Table 3.1 to obtain the intrinsic, diffusion and scattering quality factors that characterize the lithospheric structure beneath ASAR, PSA and WRA. Then, as described in Section 2.1.4, I characterized the heterogeneity structure beneath the arrays by applying the EFMD analysis to the same dataset. Detailed data selection and processing steps can be found in Sections 2.1.4 and 3.1.

3.3.1 EFM results

I calculated the coda decay rate, a_1, and its value at zero time, a_0, for all frequency bands and arrays as stated in Section 2.1.1. I applied the linear least-squares fit of the squared stacked envelopes at the free surface (Fig. 3.5) to a time window starting t_N seconds after the theoretical P wave arrival (t_N being the one-way traveltime through the lithosphere, listed for each array on Table 3.2), since the EFM is only applicable after the direct wave has left the scattering layer (Korn, 1990; Hock and Korn, 2000). The length of this time window varied from 42.5 to 48 s for all arrays and frequency bands, with variations depending on differences in P wave velocities based on the AuSREM model (Kennett and Salmon, 2012; Salmon et al., 2013a; Kennett et al., 2013; Salmon et al., 2013b) (Table 3.2).

A least-squares fit using Eq. 2.16 then allowed me to calculate the quality factors for diffusion and anelasticity at 1 Hz from a_1 (Fig. 3.6). For all arrays, the coda decay rate for the lowest frequency band did not follow the trend defined by the other frequency bands. Including it in the least squares fit produced inconsistent results, and it was excluded from the analysis (Fig. 3.6). A possible explanation for this observation are the lack of smoothness in the amplitude of the coda envelopes for this frequency band (top left panel in Fig. 3.5), possibly caused by noise or phase conversions or reflections at large scale heterogeneities, which made the linear fits of the coda less robust and increased the uncertainty in the determination of a_1. The intrinsic quality factor at 1 Hz derived from this calculation, Q_{i0}, takes similar, frequency independent ($\alpha = 0$), values of ~ 2000 for WRA and PSA. For ASAR, my best fits to the coda decay rate (Eq. 2.2) correspond to $\alpha = 0.2$ (Fig. 3.6) and $Q_{i0} \sim 1000$. Diffusion quality factor (Q_{diff}) values at 1 Hz are similar for ASAR and WRA (~ 400), and higher for PSA (~ 500). Since this quality factor does not depend on α (Eq. 2.14), this translates into Q_{diff} following the same trend for all arrays but being higher for PSA than for WRA

and ASAR.

Figure 3.7 shows measured scattering quality factor (Q_s) values, obtained from Eq. 2.3, together with the theoretical least-squares regression curves derived by Fang and Müller (1996) for the relationship between the structural parameters, a and ε, and Q_s for an exponential isotropic ACF. As explained in Section 2.1.1, these parameters represent a first approximation to the average spatial distribution and strength of the heterogeneity of a single scattering layer beneath the arrays. Correlation length values are similar for the three arrays, varying from 0.9 – 1.1 km. Heterogeneities appear to be weaker beneath PSA than ASAR or WRA, with ε varying from $\sim 3.0\%$ for PSA to $\sim$4.5% and $\sim$4.7% for WRA and ASAR respectively.

Figure 3.8 shows the frequency dependence of the different quality factors obtained from the EFM. The combined quality factor (Section 2.1.2, Eq. 2.17), Q_{comb}, follows a similar trend to Q_s, with both of them taking their highest and lowest values for PSA and ASAR respectively. For WRA and ASAR, maximum Q_s and Q_{comb} values are found in the 0.5–1 Hz and 0.75–1.5 Hz bands respectively, and the minimum in the 1.5–3 Hz frequency band. The frequency dependence of Q_s and Q_{comb} above 2 Hz is similar for both arrays. This indicates that the dominating scale length of the heterogeneity is likely in the range of 3–5 km for these arrays when I consider a single scattering layer. For PSA, however, Q_s decreases for frequencies below 1.5 Hz and then remains approximately constant, which could be indicative of different scale lengths of the heterogeneity being equally present in the structure. For this array, Q_{comb} increases slowly over the frequency range covered here.

In general, diffusion is the strongest attenuation mechanism (lowest Q) at low frequencies, with scattering dominating at higher frequencies. For WRA, this transition happens at 0.75 Hz, while for ASAR and PSA, the change takes place at 1.125 Hz. Anelasticity remains the weakest attenuation mechanism (highest Q) at low frequencies, up to 4.5 Hz for WRA and PSA and 3.75 Hz for ASAR. Above that frequency, Q_{diff} becomes dominant. These results agree with the observations by Korn (1990), who obtained $Q_i > 1000$ and $Q_{diff} \sim 300 - 400$ at 1 Hz for WRA, even if his results showed that Q_i remained larger than Q_{diff} up to 10 Hz. My Q_{comb} results suggest that, even if Q_s, Q_i and Q_{diff} are lower at most frequencies for ASAR than for the other two

Table 3.2: Summary of the main results obtained from the EFM for all arrays: intrinsic (Q_{i0}) and diffusion (Q_{d0}) quality factors values at 1 Hz, intrinsic quality factor frequency dependence coefficient (α), correlation length (a) and RMS velocity fluctuations (ε).

Array	v_P (km/s)	t_N (s)	Q_{i0}	Q_{d0}	α	a (km)	ε (%)
PSA	7.9	25.2	2100 ± 200	500 ± 40	0.0	0.9 ± 0.1	2.9 ± 0.1
WRA	7.9	25.3	2100 ± 100	400 ± 20	0.0	1.1 ± 0.1	4.5 ± 0.1
ASAR	7.8	25.6	1000 ± 100	400 ± 40	0.2	0.9 ± 0.2	4.7 ± 0.2

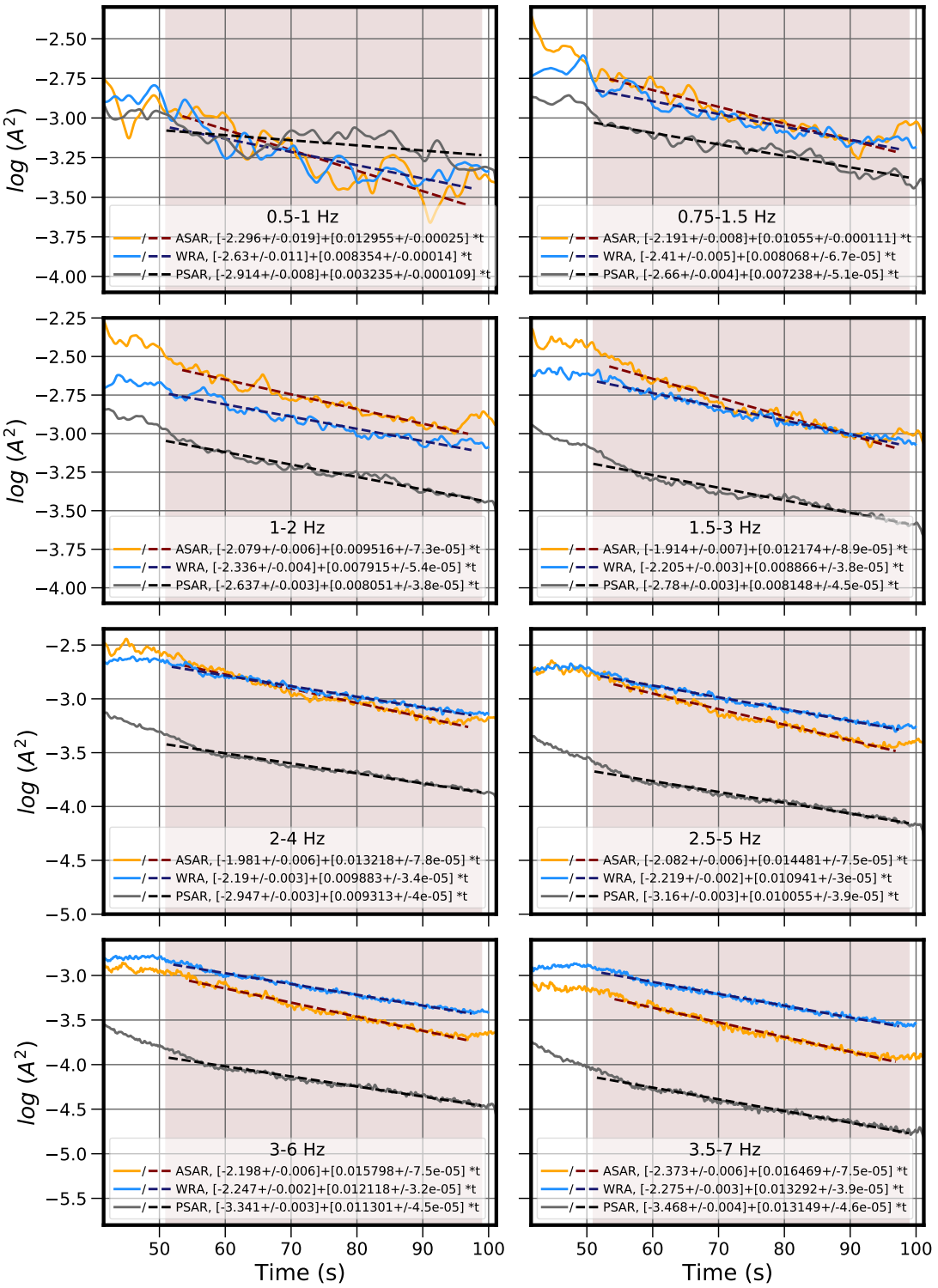

Figure 3.5: Linear fit of the logarithm of the squared normalised coda envelopes for all arrays, as described in Section 2.1.1. The shaded area represents the maximum time window used for the fits. Lighter solid lines represent my data envelopes. Darker, dashed lines show the linear fits whose equations are shown in the legend.

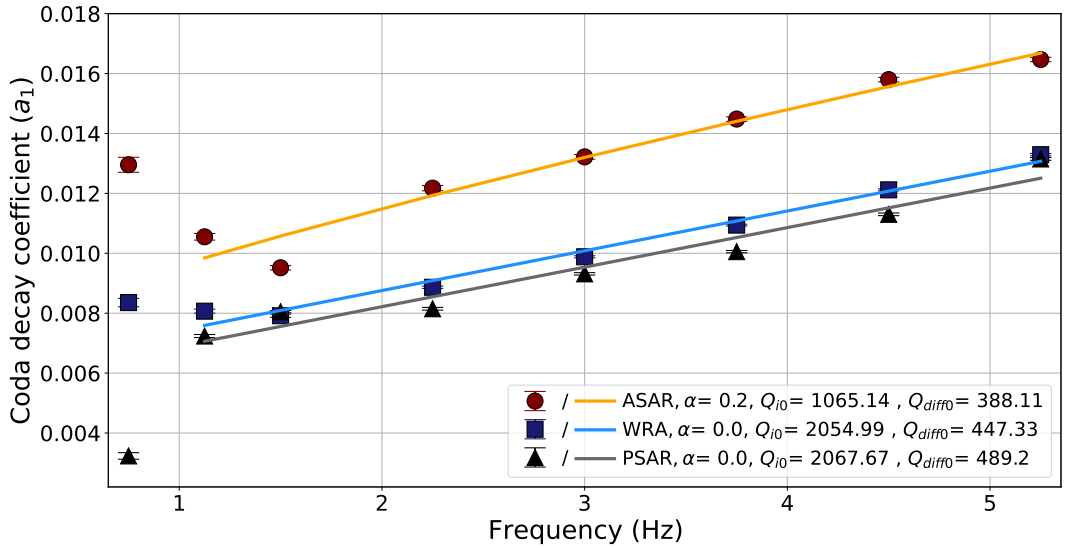

Figure 3.6: Coda decay coefficient (a_1) vs. frequency for all arrays. Solid lines represent the regression curves defined by Eq. 18 from Korn (1990). The legend contains my obtained values of the intrinsic and diffusion quality factors at 1 Hz, as well as the indicative estimation of the thickness of the scattering layer.

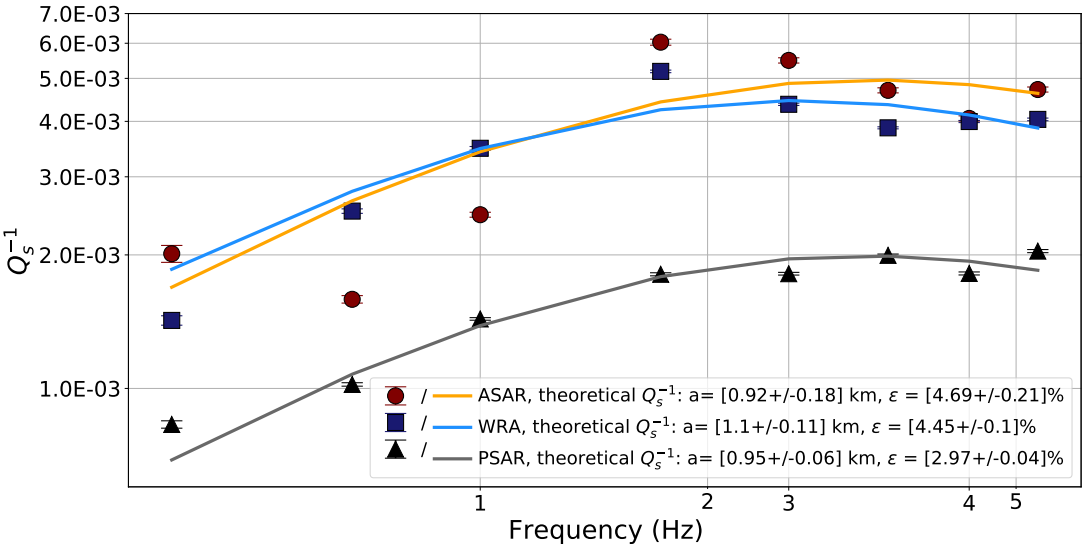

Figure 3.7: Scattering quality factor, Qs, vs. the theoretical curve derived by Fang and Müller (1996). The legend contains my estimation of the correlation length and RMS velocity fluctuations for a single scattering layer.

arrays, total attenuation strength is similar for ASAR and WRA. These lower Q_{comb} values could be related to the location of these arrays on the NAC, younger in origin than the WAC (Section 3.2). The location of ASAR, on the southern edge of the NAC, in an area widely affected by the accretionary processes that took place during the assembly of the Australian continent, as well as major events like the Petermann and

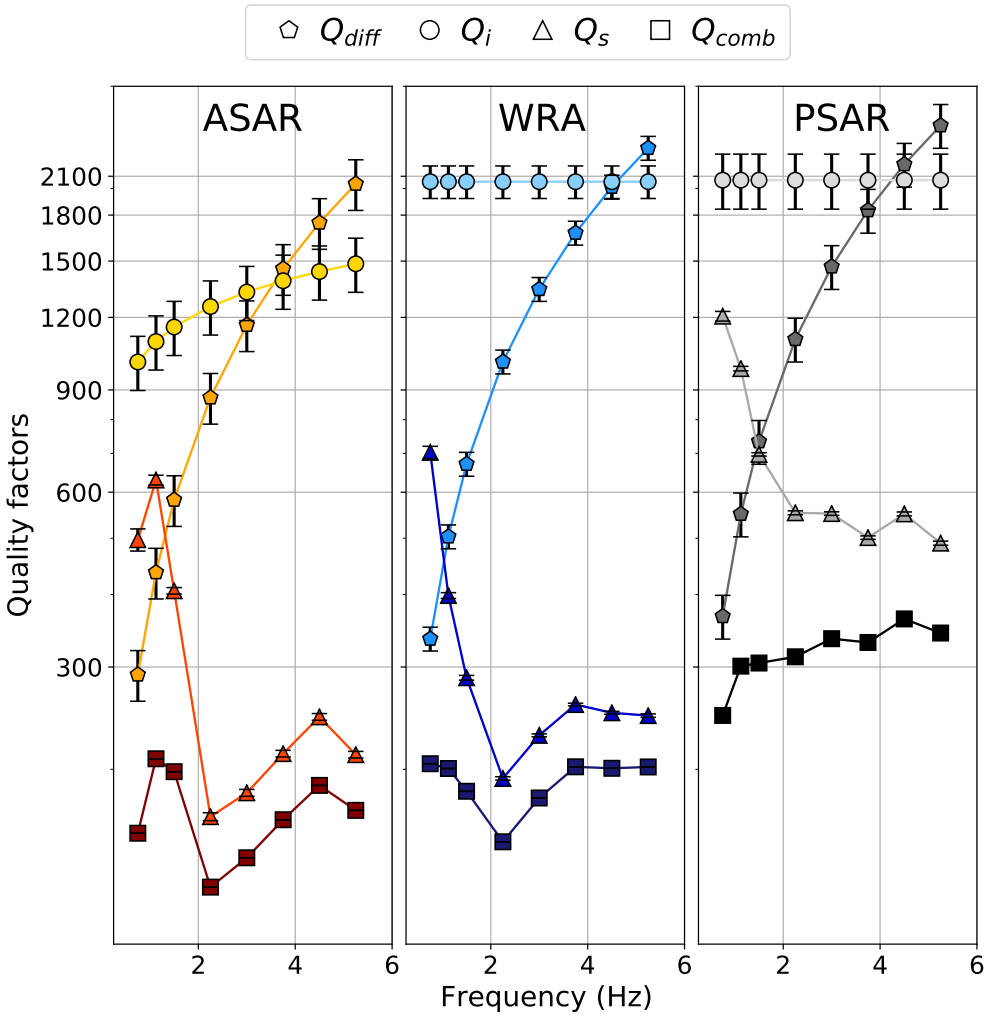

Figure 3.8: Frequency dependence of the intrinsic (Q_i), the diffusion (Q_{diff}), scattering (Q_s) and total (Q_{comb}) quality factors for all arrays.

Alice Springs orogens (Section 3.2), could explain the lower values of the different quality factors obtained for this array. For PSA, the generally high quality factors values I obtained could be related to the location of the array on a tectonically quiet Archaean craton (Section 3.2). Previous studies (e.g. Cormier, 1982; Korn, 1993; Sipkin and Revenaugh, 1994; Domínguez and Rebollar, 1997) have also found lower Q values in regions with quiet tectonic histories, an observation that matches my results from the EFM for all three arrays.

3.3.2 EFMD results

I use lithospheric model types I and II (1-layer and 2-layer respectively), shown in Fig. 2.3, in my inversion of the data for all three arrays. All models are 200 km thick and, for 2-layer models, the top layer represents the crust and extends down to the Moho

depth obtained from the AusMoho model (Kennett et al., 2011). Q_i values necessary to calculate the synthetic envelopes from Eq. 2.18 are determined by the EFM and are assumed to be constant throughout the lithosphere. As with my synthetic tests, I ran three parallel Markov chains for each array and model type, with 1 million or 3 million iterations for models with 1 and 2 layers respectively. The burn-in phase, defined as described in section 2.1.3, was removed from all chains. Table 3.3 summarises my results.

Inversion of PSA data with model type I, revealed this model produces very large amplitude codas that barely decay over time (Fig. 3.9). All chains were stable and converged within 14000 iterations, but the maximum loglikelihood reached during the inversion ($< -10^6$, panels a–c on Fig. 3.9), indicated fits to the data are very poor, which is also obvious from the comparison of the ensemble of synthetic envelopes with the data (panels g–n on Fig. 3.9). The posterior PDFs suggest a nearly homogeneous lithosphere, with $\varepsilon \sim 0\%$ and $a > 20$ km. This is likely due to the large thickness of the layer (200 km) greatly reducing diffusion out of it and, therefore, energy levels in the heterogeneous layer remaining high at all times, regardless of the magnitude of the scattering parameters. I also tested model type I on ASAR data, since coda levels for this array are higher (Fig. 3.10). Despite the higher coda amplitudes, model type I also fails to fit my data for this array, with the maximum loglikelihood reached being on the order of −10000. ASAR coda amplitudes are similar to WRA, indicating similar behaviour. Therefore, this model was not tested for WRA. It is convenient to note that, as stated in Section 2.1.4, the datasets used in these inversions were carefully curated to ensure that no deep or secondary arrivals were present in the seismograms between the direct P-wave arrival and the end of the time window of interest. This means that the small amplitude peak between the direct wave and the start of the EFMD time window in Figs. 3.9, 3.10, or 3.14 is probably not caused by such an arrival. Considering the size of the datasets analysed here, conversions and reflections

Table 3.3: Summary of my EFMD results for all arrays and model types. Bottom depth of all models is 200 km, after the LAB depth estimated by Yoshizawa and Kennett (2015) or Kennett and Saygin (2015) (see Section 3.2) . Crustal thickness for model type II is 32 km for PSA and 46 km for ASAR and WRA, as defined in the AusMoho model (e.g. Kennett et al., 2011).

Array	Model type	Frequency bands	Layer number	Correlation length (a) 5–95 PR (km)	Correlation length (a) AR (%)	RMS velocity fluctuations (ε) 5–95 PR (%)	RMS velocity fluctuations (ε) AR (%)	Maximum L
PSA	I	A-H	1	23 – 32	48	< 0.01	47	$< -14 \times 10^6$
	II	A-H	1	0.5 – 25	75	< 0.01	47	< -450000
			2	0.5 – 32		< 0.01		
	II	D-H	1	0.5 – 0.8	59	2.3 – 2.5	44	−7.1
			2	4 – 32		0.1 – 1.8		
ASAR	I	A-H	1	2 – 30	93	0.01 – 0.07	44	−10500
	II	D-H	1	0.2 – 1.4	59	2.4 – 3.0	50	−2.2
			2	3 – 32		0.1 – 3.7		
WRA	II	D-H	1	0.7 – 1.5	60	3.1 – 3.9	53	−0.7
			2	3 – 32		0.2 – 5.0		

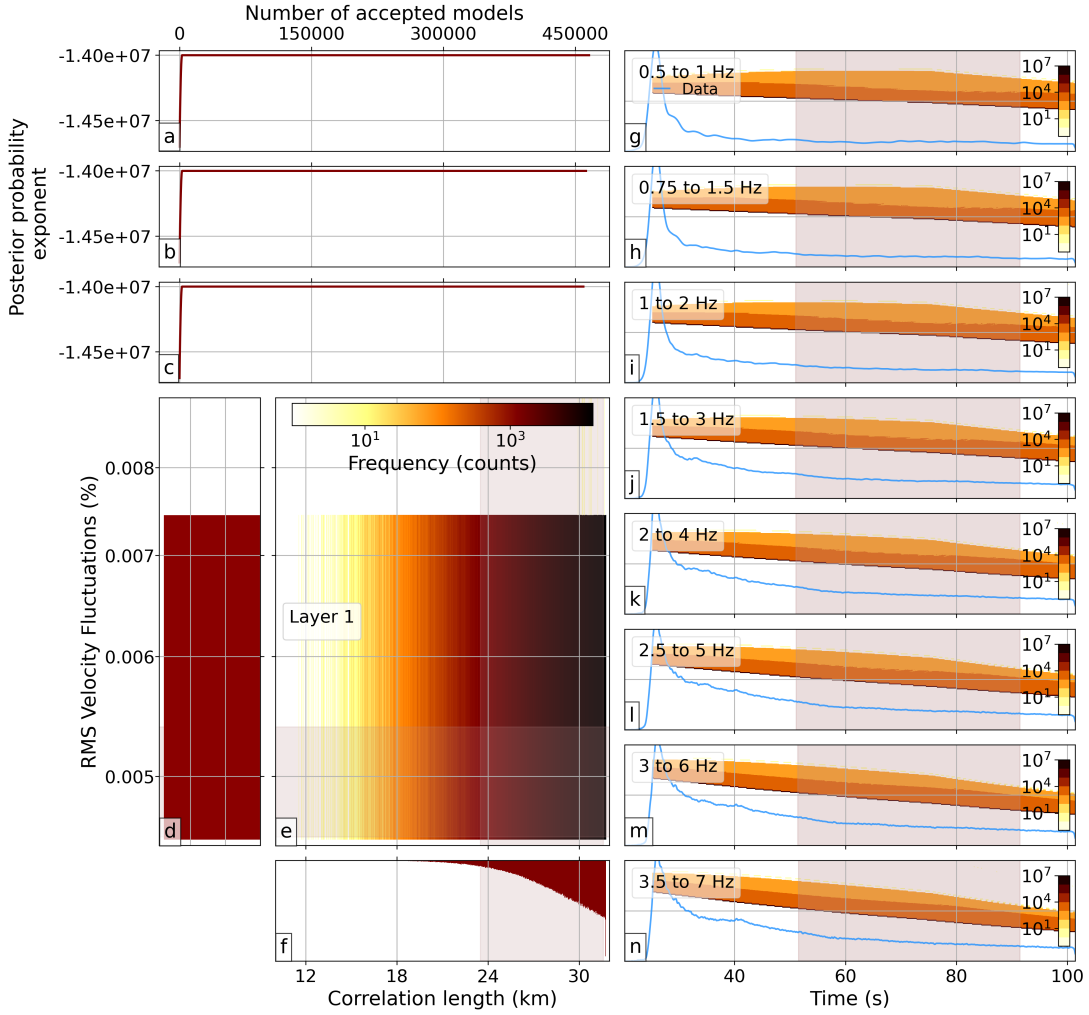

Figure 3.9: EFMD results for PSA and model type I. Panel content is as in Fig. 2.4.

(especially P-S conversions) at heterogeneities and boundaries near the receivers are the most likely cause for these peaks. These phenomena are not taken into account within the EFMD framework, but given their low amplitude and their presence well outside the time window used for the analylsis, their overall effect on the obtained results is likely small.

Model type II inversions for all three arrays showed much better fits for frequency bands D-H (central frequencies above 2.25 Hz, Table 2.3) than for A-C (below 1.125 Hz, example for PSA in Fig. 3.11). However, loglikelihood values are still very low ($< -4 \times 10^5$), Table 3.3), which indicates poor fits to the data and, therefore, unreliable parameter estimations, even if there is a substantial improvement with respect to model type I. My EFM results show scattering only becomes the dominant attenuation mechanism above 1.5 Hz for PSA (Fig. 3.8). This, together with coda amplitudes shown on panels j–q in Fig. 3.11 being barely above the noise level in the time window of interest for the lowest frequency bands, suggests these codas are affected by large-

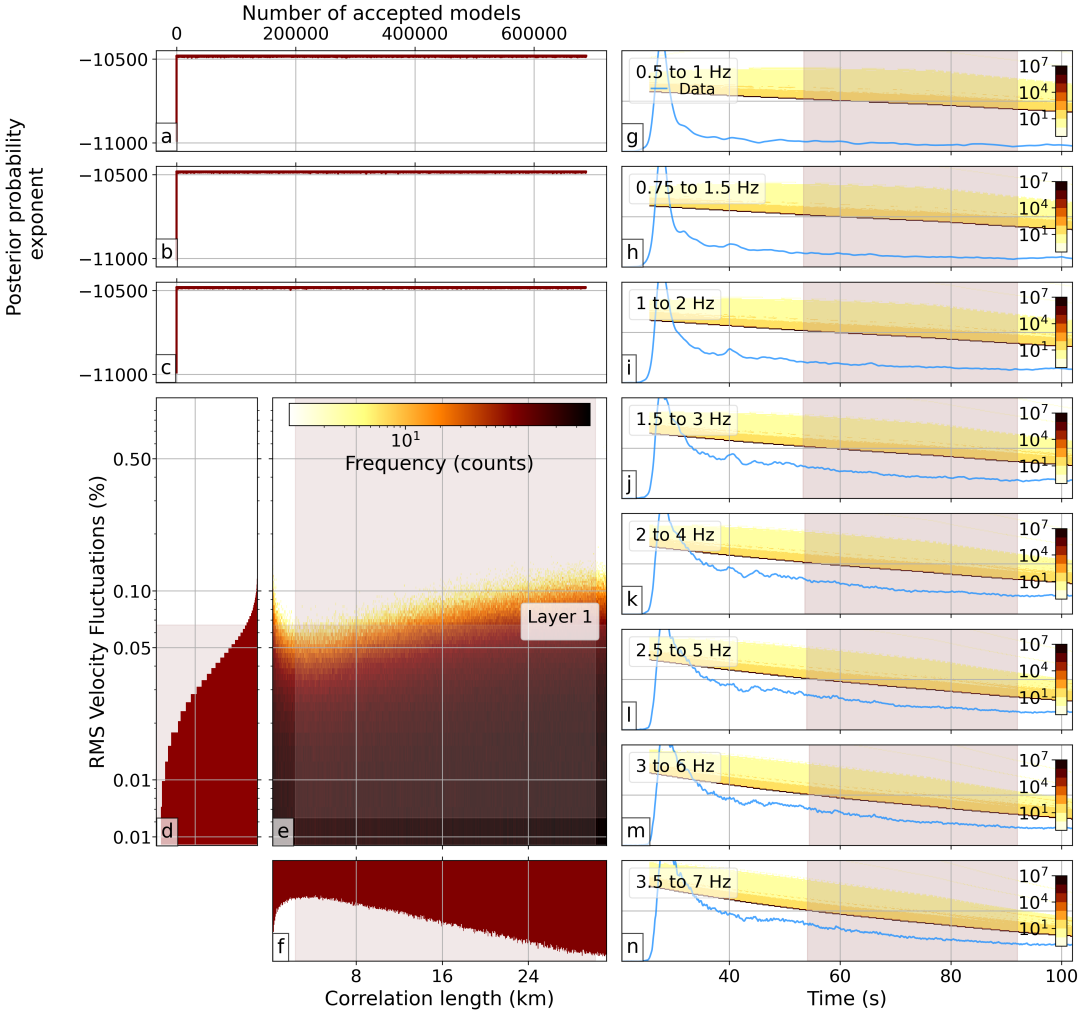

Figure 3.10: EFMD results for ASAR and model type I.

scale heterogeneities and might not be composed only of energy scattered at small-scale structure. Therefore, the EFMD may not be able to fit my coda envelopes for frequencies below this threshold. To test this, I ran my EFMD inversion code for frequency bands D to H (Table 2.3) alone. By comparing my results for PSA in Fig. 3.11 and Fig. 3.12, I observe considerable improvement in the fits to the data, also evidenced by much higher loglikelihood values (< -10). Given these new observations, I remove frequency bands A to C (0.5–1 Hz, 0.75–1.5 Hz and 1–2 Hz, Table 2.3) from future inversions of the data for all arrays.

Figures 3.12, 3.13 and 3.14 summarise my results for all three arrays and model type II. The Markov chains converged within 10000, 7000 and 4000 iterations for PSA, ASAR and WRA, respectively. The scattering structure beneath the arrays shows varying amounts of heterogeneity in the crust and a relatively homogeneous lithospheric mantle. The posterior PDFs for both parameters in the top layer in all cases are roughly Gaussian and narrow (Table 3.3). Maxima for the correlation length PDFs for PSA,

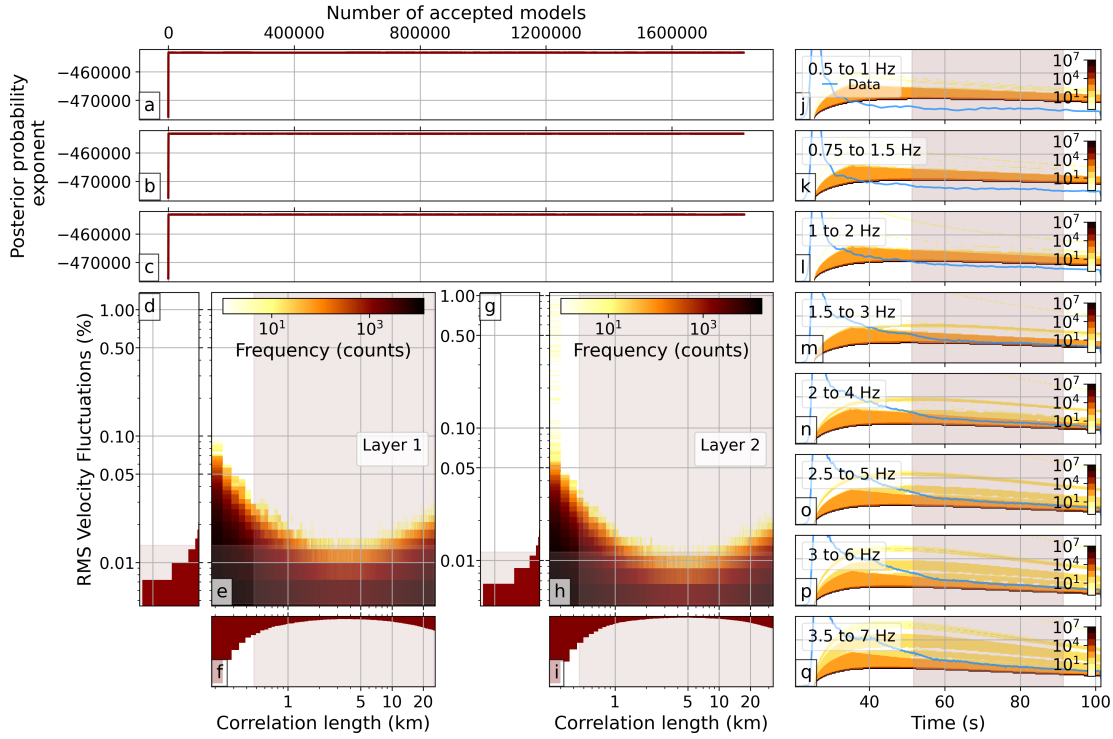

Figure 3.11: EFMD results for PSA and model type II (2-layer) using all eight frequency bands listed on Table 2.3.

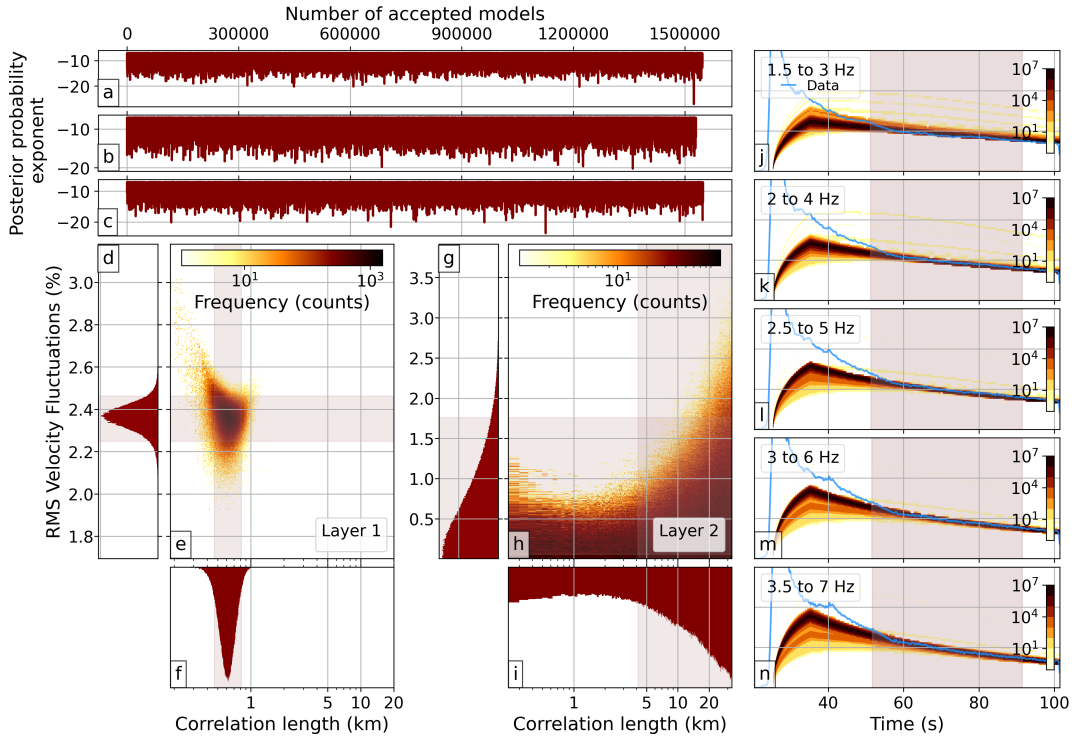

Figure 3.12: Results from model type II (2-layer) and PSA using only the five highest frequency bands from Table 2.3.

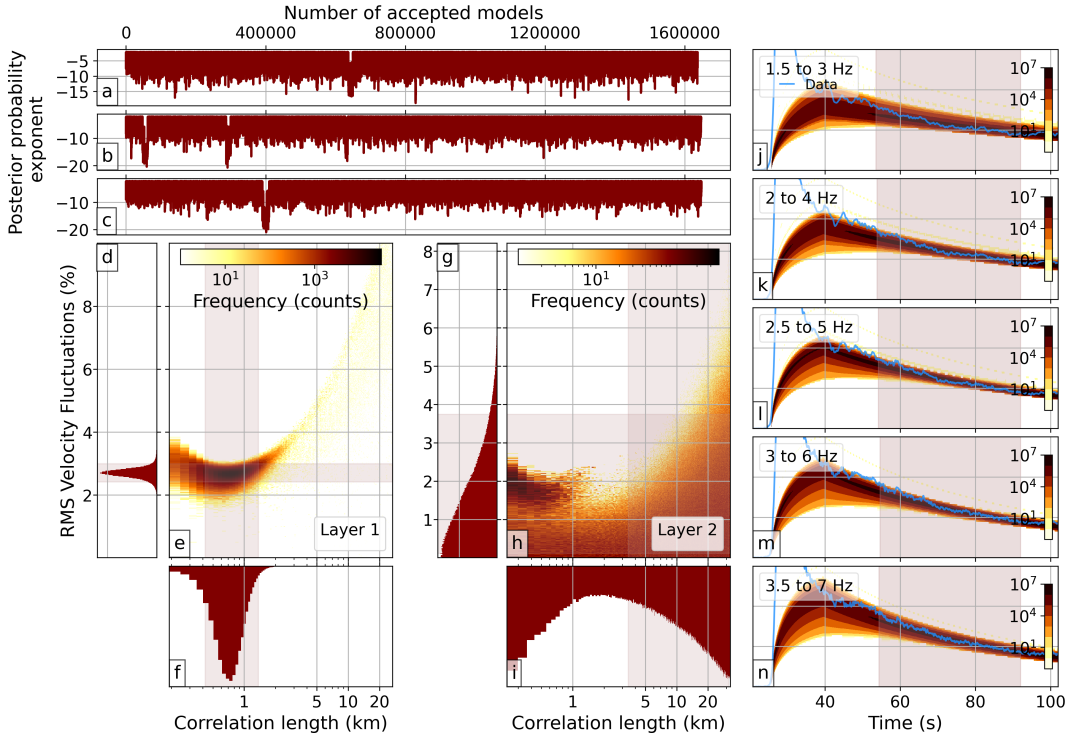

Figure 3.13: As Fig. 3.12 but for ASAR.

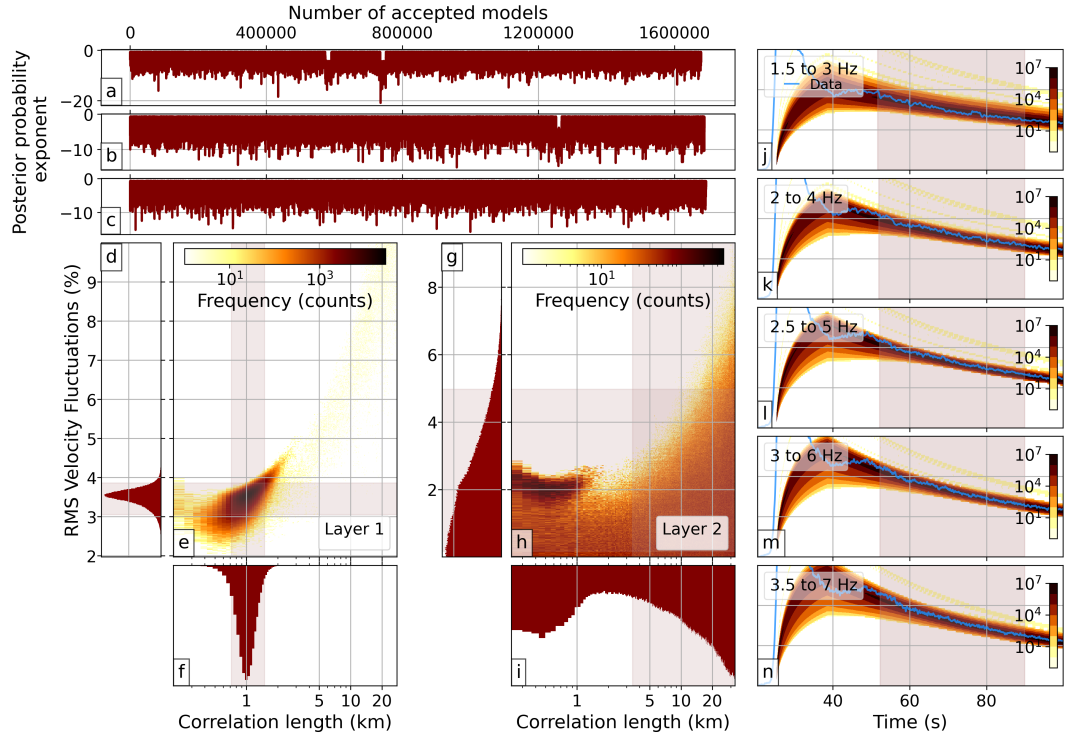

Figure 3.14: As Fig. 3.12 but for WRA.

ASAR and WRA are at 0.6, 0.7 and 1 km, while RMS velocity fluctuations posteriors peak at 2.4%, 2.7% and 3.6% respectively. PDFs for layer 2, on the other hand, show no clear maxima and also have similar shapes for all arrays. For PSA, ε only takes values below $\sim$ 3%, while for WRA and ASAR, the PDF extends up to $\sim$8 % and $\sim$6 % respectively. In all cases, the majority of the accepted models have $\varepsilon < 1\%$. The correlation length PDF, on the other hand, extends throughout the entire parameter space, not allowing us to constrain scale length values. For PSA and WRA, large values of a (> 5 km) are favoured, while small correlation lengths (< 1 km) seem to work better for ASAR. Loglikelihood values are high (> -10) for all arrays, which suggests fits to the data are generally good. The shape of the PDFs for the bottom layer makes my solutions non-unique and similar to my results for synthetic model 4, which had strong scattering in the crust and a fairly homogenous lithospheric mantle. This would mean scattering takes place mostly in the crust for all three arrays, with very weak or no scattering at all in the lithospheric mantle.

These results agree with observations from previous studies. Kennett (2015) studied P-wave reflectivity in the lithosphere and asthenosphere in Australia. Their results point to strong lithospheric heterogeneity being present beneath stations in the Proterozoic NAC and they suggest correlation lengths of at most a few kilometres and $\sim$ 2% velocity fluctuations in the crust. For the lithospheric mantle, they propose much larger correlation lengths (10-20 km) and $\varepsilon < 1\%$. Kennett and Furumura (2016) and Kennett et al. (2017) also addressed the presence and interaction of multi-scale lithospheric heterogeneity in the Australian continent. In their simulations, they combined large scale heterogeneities with stochastic media and fine scale structure. Their results indicate a wide range of heterogeneity spatial scales are present and interact within the lithosphere. Their models contain four different layers for the fine scale structure, two in the crust and two in the lithospheric mantle, and different horizontal (a_H) and vertical (a_V) correlation lengths. Their scattering parameters suggest a mildly heterogeneous asthenospheric mantle ($a_H = 10$ km, $a_V = 10$ km, $\varepsilon = 0.5\%$) and an increase in the strength of the heterogeneity in the lithosphere-asthenosphere transition zone ($a_H = 5$ km, $a_V = 1$ km, $\varepsilon = 1$ %). The crust is generally more heterogeneous in these models, with $a_H = 2.6$ km, $a_V = 0.4$ km for both crustal layers and RMS velocity fluctuations of 0.5% and 1.5% for the upper and lower crust respectively. At resolvable scales, these values are consistent with my results from the EFMD (Table 3.3).

3.4 Conclusions

For three Australian seismic arrays, I applied the single layer modified Energy Flux Model (EFM) and depth dependent Energy Flux Model (EFMD) to a large dataset which includes events from a wide range of magnitudes, distances and azimuths. This ensures I am thoroughly sampling the structure of the lithosphere beneath the arrays

and reduces azimuthal and lateral bias. My EFM results highlight similarities and differences in the behaviour of the quality factors (intrinsic (Q_i), diffusion (Q_{diff}), scattering (Q_s) and combined (Q_{comb})) for the three arrays studied here and, therefore, the attenuation structure beneath them. Generally, Q_i and Q_{diff} are lower at all frequencies for ASAR than for the other two arrays, which would indicate that attenuation caused by these two mechanisms would be strongest for ASAR. However, the scattering and combined quality factors take similar values for ASAR and WRA, making their heterogeneity and overall attenuation structure comparable but different to PSA. These results are consistent with the tectonic histories and settings of the regions the arrays are located on. WRA and ASAR lie on the Proterozoic North Australian Craton (NAC), but while WRA is situated near its center, ASAR is on its southern border, a margin with more complex and recent tectonic history than the interior of the craton, which correlates with the generally lower quality factor values I observe for ASAR. The EFMD confirms some of these similarities and differences. My results suggest the crust is more heterogeneous than the lithospheric mantle for all arrays, which could be related to the cratonic nature of the lithosphere in these areas. Correlation lengths in the crust vary from ∼0.2–1.5 km and RMS velocity fluctuations take values in the 2–4 % range. The scattering structure of the lithospheric mantle, on the other hand, is more complex. Solutions for this layer are not unique, with both low (< 2 km) and high (> 5 km) correlation lengths being equally probable. Low velocity fluctuation values are favoured in the inversion results for all arrays, but the posterior PDFs for ASAR and WRA extend up to ∼6% and ∼7% respectively and only to $\sim 3\%$ for PSA, thus supporting our hypothesis that the similarities and differences in the heterogeneity structure beneath these arrays are caused by their different locations on the cratons and the different tectonic histories of these areas. These results agree with previous studies and our current knowledge about the tectonic histories of these regions. This means that, despite the theoretical limitations of the methods discussed in Section 2, the addition of a large enough dataset and a Bayesian inversion algorithm to these methods substantially contributes to improving the reliability of the small-scale characterization obtained from them.

This study is also an example of the versatility of energy flux methods. I have shown that these techniques can be used for seismic arrays or groups of stations (PSA, WRA) and single seismic stations (the single available 3-component station at ASAR). Regions with limited local and regional seismicity, such as my study areas in northern and western Australia, can be investigated using energy flux methods, since they rely on teleseismic data. Finally, the lack of constraints on the strength of the heterogeneity makes this approach applicable to both strong and weak scattering regimes and apt to the study of small-scale heterogeneity on Earth and other planets.

Chapter 4

The Extended Depth-Dependent Energy Flux Model

Chapters 2 and 3 contain an extensive description of both the single-layer and multi-layer Energy Flux Models (EFM and EFMD respectively), as well as their capabilities to resolve the heterogeneity structure beneath a seismic station or array and compare between different attenuation mechanisms. My implementation of these methods makes the EFM completely independent, while the EFMD relies on the EFM to obtain the intrinsic quality factor, Q_i, and its frequency dependence, required for the inversion of either real or synthetic data. Previous studies using the EFMD have worked around this issue by not including intrinsic attenuation within the EFMD. Korn (1997) included anelasticity within the theoretical framework of the EFMD but decided to omit it from his tests to focus on the differences in coda shapes caused by different scattering parameters. Hock and Korn (2000) and Hock et al. (2004) obtained Q_i for some of their regions of study from the EFM but did not take intrinsic attenuation into account in their implementation of the EFMD.

This necessity of separately obtaining Q_i, either from the EFM or from other approaches reported in the literature, is one of the biggest shortcomings of the EFMD. The EFM is, in itself, a useful, quick and easy tool to quantify the heterogeneity structure and its results can either be used on their own or serve as a basis for more advanced methods. However, its inherent limitation to a single scattering layer with unspecified thickness reduces the accuracy of the EFMD results. For this reason, I decided to remove the dependence of the EFMD on the EFM by expanding the Bayesian inference algorithm described in Chapter 2 to make it capable of independently determining the intrinsic quality factor and its frequency dependence for each layer in the model. To my knowledge, none of the previous studies applying the EFMD have ever attempted to independently obtain the Q_i, either in a depth-dependent or independent fashion,

using this technique. Additionally, I optimized the algorithm and improved its overall performance by adding internal adaptive step size and continuation algorithms, which allow me to benchmark the Markov chains and prevent me from having to manually select the step sizes of the parameters. This improved, or extended, EFMD algorithm, called here the E-EFMD, is generally on the order of 10 times faster than the original EFMD, and allows us to directly obtain the scattering (a, ε) and intrinsic attenuation (Q_{i0}, α) parameters from the inversion, thus making it possible to compare these two attenuation mechanisms layer by layer. Such an algorithm would remove the dependence of the EFMD on previous studies on the area of interest or alternative methods to obtain Q_i and lead to a complete and consistent determination of the attenuation beneath a seismic station or array.

In this chapter, I describe the expansion to my previous Bayesian inversion algorithm and provide the results from a series of synthetic tests designed to assess its capability to successfully recover the input values of both scattering parameters, as well as the intrinsic quality factor and its power law exponent. In addition to this, I use the E-EFMD to characterize the heterogeneity structure beneath PSA, ASAR and WRA, the three Australian seismic arrays studied in Chapter 3, and compare the results obtained from the two algorithms.

4.1 The Extended Depth-Dependent Energy Flux Model (E-EFMD)

Intrinsic or anelastic attenuation, also known as absorption, is one of the two main causes of attenuation of seismic waves. The other one, scattering, as discussed in previous chapters, is produced by heterogeneities redistributing the energy of the wavefield, leading to a reduction of the direct wave amplitudes and the excitation of coda waves. In contrast, intrinsic attenuation is caused by the conversion of seismic energy into heat and has often been related to the presence of cracks and fluids within the medium the wavefield is propagating through (e.g. Picotti et al., 2010; Sketsiou et al., 2021). As a result of this seismic energy loss, both the direct and coda waves amplitudes decrease. In Chapters 2 and 3, I discussed a third attenuation mechanism, diffusion, which is explicitly included within the EFM formulation (Section 2.1.1) in order to ensure the conservation of energy in the system. Total seismic attenuation can be calculated then as the combination of scattering and absorption through their respective quality factors or their inverses, also called dissipation factors:

$$Q_T^{-1} = Q_i^{-1} + Q_s^{-1} \qquad , \tag{4.1}$$

where Q_T^{-1}, Q_i^{-1} and Q_s^{-1} represent the inverse of the total attenuation, intrinsic and scattering quality factors. In the case of scattering, it is widely accepted that Q_s varies

with frequency, and a number of relationships have been proposed over the years for different kinds of media (e.g. Sato et al., 2012; Fang and Müller, 1996). For intrinsic attenuation, this dependence is not so clear. For decades, there has been considerable debate about the frequency dependence (or lack of) of Q_i, possibly triggered by differences in frequency ranges of interest, part of the seismic wavefield being used and overall purpose of the study. Frequencies used in lab-based, rock-physics experiments can often reach hundreds or even thousands of Hz (e.g. Tisato et al., 2015), well above local or even teleseismic frequencies (0.01–10 Hz), and these are themselves much higher than those required for normal modes analysis ($f < 0.01$ Hz) (e.g. Romanowicz, 1995; Durek and Ekström, 1996). The response of seismic waves to medium properties depends largely on their wavelength and, therefore, their frequency, thus making it difficult to compare attenuation structures obtained from these different studies. Additional challenges in translating laboratory results to observations in the Earth are their limitations to accurately reproduce realistic rheological conditions or comparable source-receiver distances. Still, some form of frequency dependence is widely accepted nowadays (e.g. Aki, 1980a; Romanowicz, 1995; Sams et al., 1997; Korn, 1997; Sato et al., 2012; Eulenfeld and Wegler, 2016) , with a power law often being used to describe its behaviour (e.g. Korn, 1990; Sato et al., 2012; Sketsiou et al., 2021).

The Depth-Dependent Energy Flux Model (EFMD), described in Section 2.1.2, has the ability to calculate not only the heterogeneity parameters of the structure (correlation length a and RMS velocity fluctuations ε), but also the intrinsic (Q_i) and scattering (Q_s) quality factors for each layer within the model. Q_s values for each layer and frequency band are always calculated within the EFMD for each tested model, but previous implementations of the method have either neglected anelasticity altogether (Korn, 1997; Hock and Korn, 2000; Hock et al., 2004) or, in the case of my own version, used a constant value for all layers. The E-EFMD goes a step further by including the intrinsic quality factor at 1 Hz, either as Q_{i0} or its inverse, Q_{i0}^{-1}, and the exponent controlling its power law frequency dependence, α (Eq. 4.2), as free parameters that can be obtained from the Bayesian inference algorithm. Here, a given model $\mathbf{m}$ includes a single value of a, ε and Q_{i0} for each layer, as well as α, which is constant for all layers (Fig. 4.1). Intrinsic Q values for all frequency bands are then calculated using:

$$Q_i(\omega) = Q_{i0}\ f_c^{\alpha} \quad , \tag{4.2}$$

where f_c is the central frequency for each frequency band of interest. Thus, for a 2-layer model, $\mathbf{m}$ would contain a total of 7 free parameters, as opposed to the 4 included in my previous implementation of the EFMD. The relationship stated in Eq. 4.2 is equivalent to the one on Eq. 2.15, used by Korn (1990). I should note that, while the E-EFMD is, in theory, capable of independently resolving Q_i values for different frequency bands, without the need to define a specific frequency dependence, in practice this

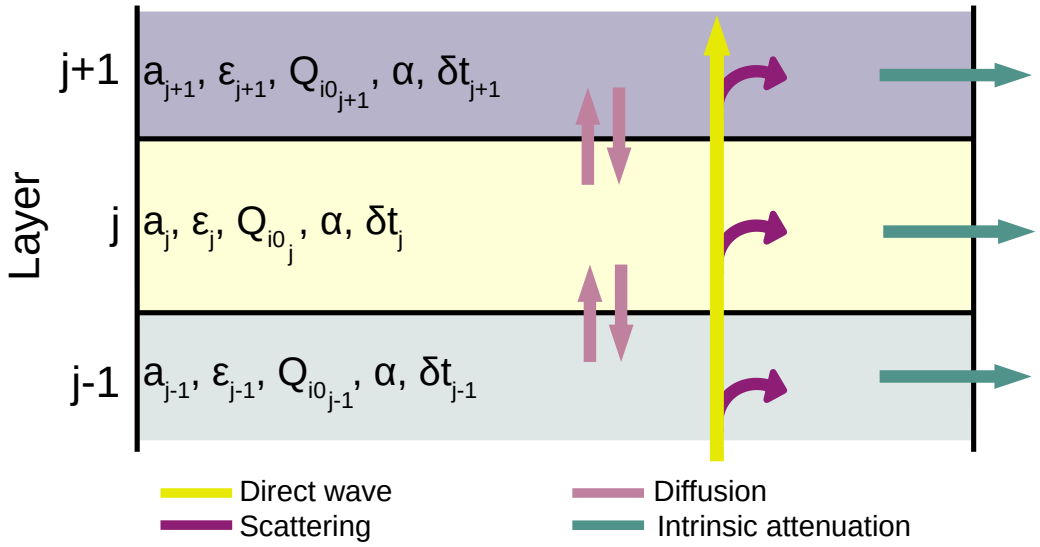

Figure 4.1: Total energy balance and parameter dependence within the E-EFMD. After Korn (1997).

problem is severely underconstrained and requires extremely long chains before reaching convergence (see Section 4.1.2). As before, parameters are only allowed to vary within a limited range of reasonable values, chosen to represent realistic heterogeneity values but also to produce detectable scattering or intrinsic attenuation. Correlation lengths and RMS velocity fluctuations range from $0.2\lambda_{min}$–$2\lambda_{max}$ (λ being the wavelength in the layer and calculated from the central frequency and the mean P wave velocity) and ε from $4.5 \cdot 10^{-3}$–10% respectively. The prior probability distributions for Q_{i0} and α are also uniform and range from 10–2000 ($5 \cdot 10^{-4} < Q_{i0}^{-1} < 0.1$) and 0–1 respectively. For Q_{i0}, these limits were chosen by considering a range of realistic values of the quality factor in the lithosphere, while still having a perceivable effect on coda amplitudes. For its power exponent, my prior distribution takes constant values from 0–1, based on Korn (1990, and references therein), which stated that α probably takes values within this range for most of the seismic frequency band.

I create the initial model by randomly selecting a value of each parameter within their prior probability distributions. From these parameters, the direct wave energy and the energy balance for each layer and frequency band can be calculated with Eqs. 2.19 and 2.20 respectively, before computing the synthetic envelopes for the layer containing the free surface using Eq. 2.18. These envelopes can be compared with the data by means of the loglikelihood, L (Eq. 2.22). The Metropolis-Hastings algorithm (Metropolis and Ulam, 1949; Metropolis et al., 1953; Hastings, 1970) then guides the random walk and helps sampling the posterior probability distribution. In each iteration, the MCMC algorithm randomly chooses a parameter for one of the layers in the model and updates its value by adding a random number in the range $(-\delta a, \delta a)$,

$(-\delta\varepsilon, \delta\varepsilon)$, $(-\delta Q_i, \delta Q_i)$ or $(-\delta\alpha, \delta\alpha)$, with δa, $\delta\varepsilon$, δQ_i and $\delta\alpha$ being the step size for the correlation length, RMS velocity fluctuations, intrinsic quality factor and α respectively. These step sizes do not remain constant throughout the inversion, as opposed to the approach taken in Section 2.1.3. Step size values are a key element of the design for an efficient random walk and need to be carefully chosen. When they are too small, the algorithm moves very slowly through the parameter space and tends to accept most updated models, which increases the acceptance rate (AR) for the parameter. If step sizes are too large, the algorithm moves too fast between regions of the parameter space, which increases the probability of rejection for the updated model and decreases the AR. As detailed in Section 2.1.3, there are several criteria that define the optimum value of the AR, but since most of them make assumptions about the properties of the posterior probability distribution (e.g. Brooks et al., 2011), I opted for the more flexible AR range of 30–50% stated by Tarantola (2005) as generally reasonably efficient. This way, when the AR for a given parameter goes below 30% or exceeds 50%, the algorithm increases or decreases its step size accordingly so that the AR remains within this interval at all times.

A final addition to my initial implementation of the Bayesian EFMD is the possibility of starting a new MCMC from where a previous chain ended to allow the use of HPC with restricted execution times. The E-EFMD inverts for three more parameters than the EFMD, which increases the number of required steps for the chain before convergence is reached. It is therefore useful to be able to split very long chains into multiple, smaller segments which help reduce memory requirements while keeping the algorithm fast enough to test many millions of parameter combinations.

4.1.1 E-EFMD sensitivity

The EFMD and E-EFMD are based on fitting either synthetic or real data coda amplitudes and decays within a specified time window and frequency band. As explained in Sections 2.1.3 and 4.1, they do so by testing different parameter combinations obtained by randomly sampling the parameter space and estimating how likely each set of parameters is to produce the observed coda envelopes. However, solutions are often not unique, as shown by the results of my EFMD synthetic tests in Section 2.1.3, and as the number of parameters to be recovered from the inversion increases, it is essential to study and understand the effect of each individual parameter on the coda. This knowledge can offer some insight into the algorithm's ability to accurately recover parameter values, as well as help interpret both synthetic and real data inversion results.

For this purpose, I created and computed the synthetic envelopes for 28 synthetic datasets in which six of the free-varying parameters of the E-EFMD remain constant and only one is allowed to change (Figure 4.2). Model layering and velocities are the same I used in my EFMD and E-EFMD synthetic tests (Sections 2.1.3 and 4.1.2

respectively). For each varying parameter with the exception of α, I created two main groups of datasets: in the first, the parameter values remain constant in the lithospheric mantle and vary within the crust, while in the second it is the crustal parameters that are left unchanged (left and right column panels in Fig. 4.2 respectively). Analyzing the synthetic envelopes for each frequency band of interest and all parameter combinations, grouped by varying parameter, allows me to compare coda amplitudes and decays and, therefore, estimate the sensitivity of my E-EFMD algorithm to each individual parameter. Figure 4.2 contains the synthetic envelopes for frequency band D (1.5–3 Hz, Table 2.3) and all 28 different synthetic datasets. Similar figures for the other frequency bands in Table 2.3 can be found in Appendix A.2.

At first sight, the plots in Fig. 4.2 allow us to determine which parameters control each part of the synthetic envelopes. Those corresponding to models with varying scattering parameters (panels A–1 to B–2) all have different starting amplitudes but comparable decay rates, while coda amplitudes for models with varying attenuation parameters (panels C–1 to D–1) decay at different speeds, even if they all had similar initial values. As explained above, seismic scattering reduces the amplitudes of direct waves by displacing energy to later portions of the seismogram. The amount of energy that is redistributed from the coherent arrivals to the coda waves depends on the strength of the heterogeneity present in the structure. In terms of the synthetic envelopes obtained from the E-EFMD, this means that initial coda amplitudes are mainly determined by the scattering parameters, and particularly by ε, as shown in panels B–1 and B–2 in Fig. 4.2. Correlation lengths play a role in these initial coda amplitudes and have a small effect on decay rates as well, but it is much smaller than that of the other parameters (panels A–1 and A–2). Intrinsic attenuation, on the other hand, entails a real energy loss, since seismic energy is converted into heat as the wavefield propagates through the structure. This results in coda decay rates being primarily controlled by Q_{i0} and α. As shown in panels C–1, C–2 and D–1 in Fig. 4.2, a model layer with strong attenuation (low Q_i/high Q_i^{-1}) means that a significant portion of the energy that propagates through it does not effectively reach the layer above it or the free surface, causing a fast reduction in coda amplitudes. The power law exponent, α, also has an effect on coda decay rates, though much smaller than that of Q_{i0} (panel D–1). Plots A–2 to C–2 in Fig. 4.2 suggest that parameters for the bottom layer of the model have a bigger effect both on coda amplitudes and decay rates. However, this could be an artifact of the different layer thicknesses (layer 1 of the model is 32 km thick, as opposed to the 168 km of layer 2) and should not be over-interpreted.

Regarding E-EFMD sensitivity, it is obvious from Fig. 4.2 that even small variations of some of these parameters can lead to large changes in coda amplitude, decay rate, or both, while others have much smaller effects on the synthetic envelopes. Panel D–1, for example, illustrates how an increase of 0.25 in α produces synthetic envelopes with

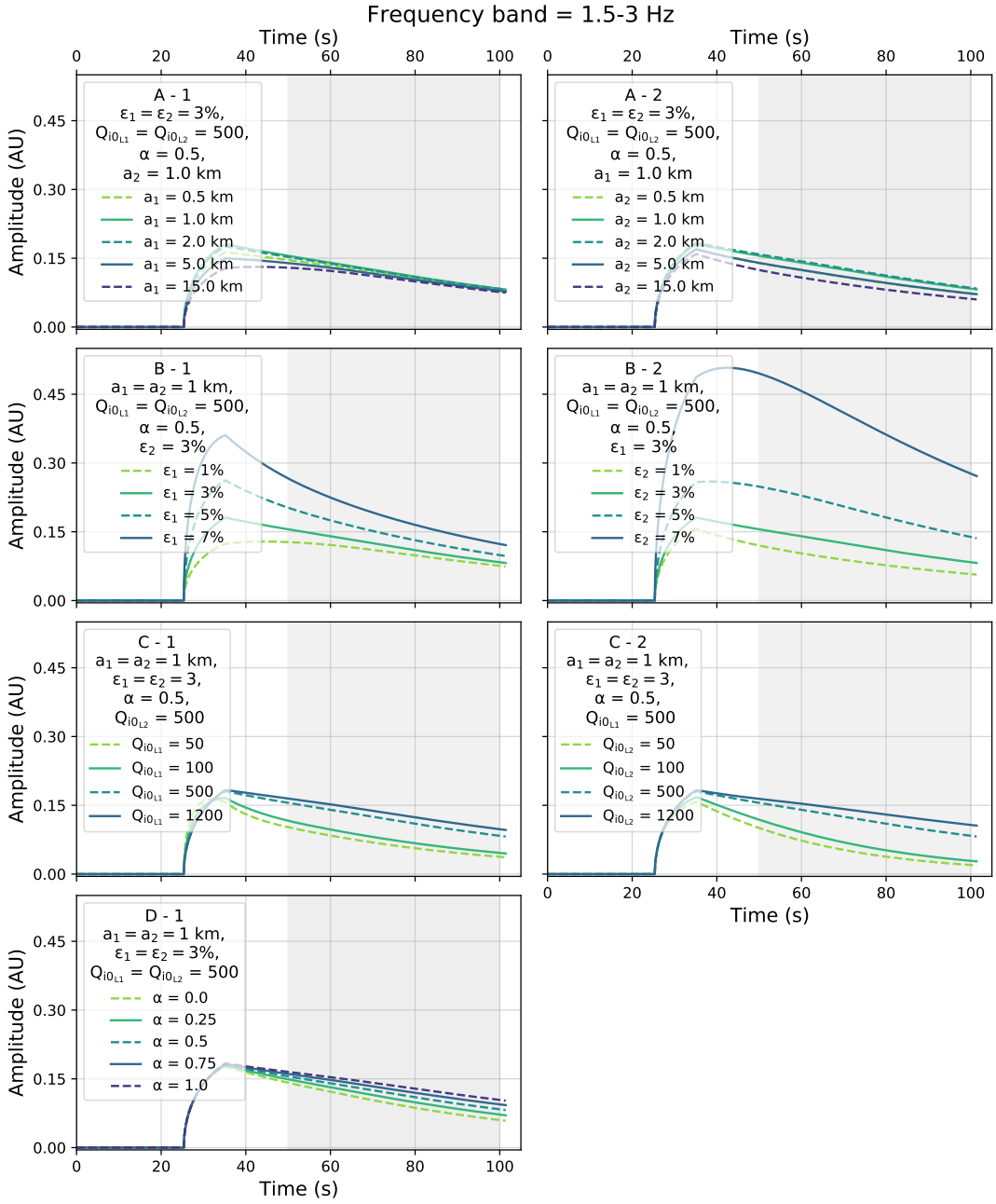

Figure 4.2: Synthetic envelopes for frequency band D (Table 2.3) and a collection of 28 synthetic datasets in which one of the seven parameters the E-EFMD inverts for is allowed to vary, while the rest remains constant. Envelopes in panels A–1 and A–2 correspond to datasets with varying correlation length in the crust and lithospheric mantle, respectively, and constant ε, Q_{i0}^{-1} and α. Panels B–1/B–2, C–1/C–2 and D–1 contain coda envelopes for synthetic datasets with varying RMS velocity fluctuations, inverse intrinsic Q at 1 Hz and coda power respectively. Scale in both axes is the same for all plots.

slightly, but clearly, higher coda amplitudes. Changes in ε or Q_{i0}^{-1} in either layer of the model (panels B–1/B–2 and C–1/C–2 respectively) produce alterations in initial coda amplitudes and decay rate, with these changes being especially pronounced for variations in the velocity fluctuations within the lithospheric mantle. Panels A–1 and

A–2, on the other hand, show that even large variations in the correlation length structure, including sharp contrasts between crustal and lithospheric values, lead to very small differences in coda amplitudes or decay rates for all frequency bands (Figs. 4.2 and A15–A21), with several envelopes partially or completely overlapping within the time window of interest for the E-EFMD. These tests suggest synthetic envelopes, and therefore the EFMD and E-EFMD algorithms, should be more sensitive to variations in ε and Q_{i0}^{-1} than they are to α or a and, therefore, more capable of accurately recovering their values from an inversion. However, the fact that initial coda amplitudes are not included within the time window used for the E-EFMD (or the EFMD) analysis will inevitably result in a reduction in the weight of ε in the inversions and, as discussed in Section 4.1.2, contribute to the highly complex interactions and strong trade offs between the parameters. The combination of these factors is likely the main cause of the extremely non-unique E-EFMD solutions observed in Sections 4.1.2, 4.2 or 5.2 and the fact that Q_{i0}^{-1} is generally worse recovered than all the other parameters. It is also reasonable to conclude that at least part of the non-uniqueness observed in the results of my EFMD synthetic tests and real data inversions in sections 2.1.3 and 3.3, evidenced by very wide correlation length PDFs and uniform loglikelihoods, could have been caused by the wide variety of correlation length configurations that result in similar codas within the time window of interest, as well as the reduced weight of the RMS velocity fluctuations caused by initial coda amplitudes not being part of the time window of interest in the analysis. This behaviour could also be behind the generalised overestimation of a by the EFM/EFMD observed by Hock et al. (2004). This lack of uniqueness in EFMD solutions could not only continue to exist in the E-EFMD, but also become more acute due to the increased number of parameters. For this reason, I recommend thoroughly testing the ability of the E-EFMD to accurately recover all seven parameter values for a wide variety of configurations, as has been done in the following section.

4.1.2 Synthetic tests

I created 22 different synthetic datasets which represent a wide range of lithospheric attenuation scenarios (Table 4.1) to test both the ability of the E-EFMD code to accurately recover any input parameter values and fit the data at all frequency bands, as well as its sensitivity to variations in either Q_{i0} or α. In terms of model layering, results from my EFMD synthetic tests (Section 2.1.3) of 3-layer models show that the code provides good fits to the synthetic data but fails to successfully retrieve the input parameter values. Because of this, I decided to only test 1- and 2-layer models for the E-EFMD. I did not include any variations in correlation length and RMS velocity fluctuations in these new datasets, since those were already analysed in my EFMD synthetic tests in Section 2.1.3. In particular, for 2-layer models, I kept correlation length and RMS velocity fluctuation values constant and equal to the values used for

the EFMD synthetic test 2 (Table 2.1). My results from that test show that the original EFMD algorithm is capable of accurately recovering all of these parameter values for fixed Q_{i0} and α. Scattering parameters for the single-layer models tested here are the same I used for the crustal layer in the 2-layer models (Tables 2.1 and 4.1). Finally, and to further test the algorithm and assess its performance for varying numbers of parameters, I also developed two alternative versions of the inversion code in which either Q_{i0} is allowed to vary freely, without any specific frequency dependence being imposed (therefore inverting for a total of 20 parameters), or α is fixed and only Q_{i0} for each layer is recovered (6 inversion parameters).

Table 4.1 contains the layering and inversion results for each of these synthetic tests. I used the Pilbara Seismic Array (PSA) as my reference array again and obtained its velocity model and Moho depth from the AuSREM (Kennett and Salmon, 2012; Kennett et al., 2013; Salmon et al., 2013b) and AusMoho models (Kennett et al., 2011) respectively. The LAB depth is kept at 200 km, based on previous studies in the area (Yoshizawa and Kennett, 2015; Kennett and Saygin, 2015). For each of the synthetic models in Table 4.1, I ran and combined the results from three independent Markov chains, each 10 million iterations long. The final results for each test were obtained by taking only 1 in every 100 accepted models in each chain. This common practice in Bayesian inference (Zhang et al., 2020; Bodin et al., 2012; Bodin et al., 2014) not only improves the manageability of the results, but also helps avoiding bias or correlation between consecutive samples in the chain. Figures 4.3, 4.6, 4.7 and 4.8, are shown here as examples, with the rest being placed in Appendix A.3 to avoid repetition. These figures are analogous to EFMD results figures in Chapters 2 and 3, and contain a summary of my results for each of these individual synthetic tests. This joint representation of all parameters and chains allows me to estimate whether all the accepted models are equally likely to produce the observed coda envelopes, while also comparing the obtained PDFs for each parameter with their input values and the data envelopes for each frequency band with the ensemble of envelopes from all accepted models. Please note that both Table 4.1 and these summary plots show the inverse quality factor, Q_{i0}^{-1}, common in attenuation studies, instead of Q_{i0}. This change places obtained Q_{i0}^{-1} values within a narrower range in which low parameter values represent weaker attenuation and viceversa, and any potential bias associated with high Q_{i0} variations (which have little to no physical effect on synthetic envelopes) is reduced, therefore helping assess the performance of the E-EFMD algorithm and interpret the inversion results.

Synthetic datasets 1–4 in Table 4.1 correspond to single-layer synthetic datasets. The frequency dependence coefficient of Q_i, α, is constant for all these datasets and equal to 0.5. For the intrinsic quality factor, I chose and tested four different values, which I categorise as "extremely low" (Q_{i0}=50, Q_{i0}^{-1}=0.02), "low" (Q_{i0}=100,

Table 4.1: Summary of the layering, parameter values and results of the inversion for synthetic models 1 to 22 used to test the validity of the E-EFMD. Models 1–4 correspond to single-layer models, while 5–22 all have 2 layers. Models 5–10 have constant Q_{i0} and α throughout the lithosphere, while models 11–22 present varying degrees of contrast between crustal and lithospheric mantle attenuation. An alternative version of the E-EFMD code, which does not solve for α, was also tested with synthetic datasets 9 and 17. Results from these inversions are also included here and marked with a * symbol.

Model	Layer	Input model				Corr. length (a)		RMS vel. flucts. (ε)		Inv. int. Q at 1 Hz (Q_{i0}^{-1})		Freq. power of Q_i (α)		Maximum
number	number	a (km)	ε (%)	Q_{i0}^{-1}	α	5 – 95 PR (km)	AR (%)	5 – 95 PR (%)	AR (%)	5 – 95 PR	AR (%)	5 – 95 PR	AR (%)	L
1	1	2.0	5.0	0.05	0.5	1.99-2.01	40.6	4.98–4.99	39.4	0.0199–0.020	42.3	0.49–0.51	42.8	-0.01
2	1	2.0	5.0	0.01	0.5	1.99–2.01	40.2	4.99–5.0	37.9	0.0099–0.010	39.8	0.49–0.50	38.6	-0.01
3	1	2.0	5.0	0.005	0.5	1.99–2.01	40.4	4.99–5.0	40.0	0.00199-0.0020	41.8	0.49–0.51	39.2	-0.01
4	1	2.0	5.0	0.001	0.5	1.99–2.0	38.6	4.99–5.0	37.8	0.00083–0.00084	39.8	0.49–0.52	40.4	-0.01
5	1	2.0	5.0	0.02	0.5	2 – 25	41.9	1 – 9	41.0	0.0117 – 0.0692	39.6	0.36 – 0.63	39.6	-0.06
	2	3.0	4.0			3 – 30		0.5 – 8		0.0169 – 0.0929				
6	1	2.0	5.0	0.01	0.0	2 – 18	40.0	4.3 – 7.0	39.3	0.0067 – 0.0130	39.3	0.003 – 0.1	40.8	-0.06
	2	3.0	4.0			2 – 9		3.4 – 4.9		0.009 – 0.012				
7	1	2.0	5.0	0.01	0.5	1 – 14	40.0	4.3 – 5.8	40.9	0.0035 – 0.018	38.7	0.05 – 0.5	39.3	-0.02
	2	3.0	4.0			2 – 30		2.6 – 6.6		0.0085 – 0.0271				
8	1	2.0	5.0	0.002	0.0	1.6 – 3.1	39.7	4.5 – 5.3	40.6	0.0016 – 0.0033	38.2	0.001 – 0.04	40.5	-0.06
	2	3.0	4.0			2.6 – 3.5		3.9 – 4.4		0.0016 – 0.0023				
9	1	2.0	5.0	0.002	0.5	2 – 22	40.3	4.3 – 7.0	40.0	0.0007 – 0.0075	40.9	0.26 – 0.52	39.3	-0.10
	2	3.0	4.0			2.4 – 3.4		3.8 – 5.3		0.0008 – 0.0027				
9*	1	2.0	5.0	0.002	0.5*	2 – 24	41.8	4.7 – 7.6	35.0	0.0013 – 0.0056	38.7	–	–	-0.05
	2	3.0	4.0			2.6 – 3.4		3.8 – 5.0		0.0012 – 0.0023				
10	1	2.0	5.0	$0.0008\overline{3}$	0.5	2 – 12	39.6	4.6 – 5.8	38.8	0.0005 – 0.0017	40.0	0.38 – 0.58	41.2	-0.03
	2	3.0	4.0			2.4 – 3.3		3.9 – 4.8		0.0005 – 0.001				
11	1	2.0	5.0	0.02	0.5	1.8 – 3.8	40.2	4.0 – 4.4	40.7	0.0044 – 0.0077	40.0	0.18 – 0.52	41.2	-0.05
	2	3.0	4.0	0.01		1 – 32		0.1 – 6.0		0.0152 – 0.0633				
12	1	2.0	5.0	0.01	0.5	1–25	40.3	0.3–6.5	41.0	0.0085–0.0437	37.7	0.39–0.63	39.2	-0.06
	2	3.0	4.0	0.02		3–28		5.2–6.8		0.0118 – 0.0278				
13	1	2.0	5.0	0.02	0.5	2 – 22	40.7	4.0 – 7.7	40.5	0.0009 – 0.0251	40.3	0.46 – 0.76	39.5	-0.09
	2	3.0	4.0	0.002		2 – 30		0.1 – 4.4		0.0019 – 0.0061				
14	1	2.0	5.0	0.002	0.5	2 – 19	40.7	2.8 – 6.9	39.0	0.0013 – 0.0234	40.1	0.26 – 0.79	40.6	-0.13
	2	3.0	4.0	0.02		2 – 28		1.3 – 6.3		0.0058 – 0.0293				
15	1	2.0	5.0	0.02	0.5	2–23	41.3	4..1–7.4	41.2	0.0129–0.0282	41.6	0.46–0.69	39.5	-0.08
	2	3.0	4.0	$0.0008\overline{3}$		2.1–3.5		3.8–4.5		0.0006–0.0012				
16	1	2.0	5.0	$0.0008\overline{3}$	0.5	2–22	40.2	1.3–5.9	40.4	0.0007–0.0287	39.6	0.45–0.85	40.3	-0.07
	2	3.0	4.0	0.02		2–26		1.7–6.3		0.0045–0.0220				
17	1	2.0	5.0	0.01	0.5	1.9 – 3.0	38.5	4.4 – 5.0	40.4	0.0006 – 0.0075	38.5	0.39 – 0.62	39.2	-0.07
	2	3.0	4.0	0.002		1.7 – 4.9		1.5 – 3.7		0.0023 – 0.0052				
17*	1	2.0	5.0	0.01	0.5*	2.0 – 2.7	40.4	4.4 – 4.8	39.9	0.0006 – 0.0016	40.1	–	–	-1.13
	2	3.0	4.0	0.002		2 – 24		1.5 – 2.8		0.0042 – 0.0052				
18	1	2.0	5.0	0.002	0.5	1.6 – 2.9	40.3	4.3 – 5.4	38.1	0.0008 – 0.0049	39.0	0.13 – 0.63	40.3	-0.06
	2	3.0	4.0	0.01		2.0 – 3.9		3.6 – 5.1		0.0067 – 0.0145				
19	1	2.0	5.0	0.01	0.5	1.9–5.0	39.7	4.4–5.2	38.6	0.0005–0.0124	39.9	0.41–0.73	40.2	-0.09
	2	3.0	4.0	$0.0008\overline{3}$		2.0–4.3		1.7–4.4		0.0007–0.0031				
20	1	2.0	5.0	$0.0008\overline{3}$	0.5	1.7–2.5	39.7	4.8–5.4	41.0	0.0006–0.0106	41.9	0.38–0.71	40.2	-0.06
	2	3.0	4.0	0.01		2.2–4.3		3.4–4.3		0.0039–0.0109				
21	1	2.0	5.0	0.002	0.5	2 – 14	40.4	4.4 – 6.2	40.0	0.0006 – 0.0035	38.3	0.34 – 0.54	41.4	-0.14
	2	3.0	4.0	$0.0008\overline{3}$		2.4 – 3.4		3.7 – 4.8		0.0005 – 0.0013				
22	1	2.0	5.0	$0.0008\overline{3}$	0.5	1.7 – 2.9	40.7	4.6 – 5.3	40.7	0.0005 – 0.0045	42.6	0.42 – 0.56	40.4	-0.07
	2	3.0	4.0	0.002		2.4 – 3.5		3.8 – 4.3		0.0008 – 0.0022				

Q_{i0}^{-1}=0.01), "medium" (Q_{i0}=500, Q_{i0}^{-1}=0.002) or "high" (Q_{i0}=1200, $Q_{i0}^{-1} = 8.\overline{3}\cdot 10^{-4}$), and would correspond to extremely strong, strong, medium or weak attenuation, respectively. Figure 4.3, shown here, and Figs. A22, A23 and A24, in Appendix A.3, contain the results from these inversions. In all of them, posterior PDFs for all parameters are approximately gaussian, narrow and very close to input parameter values. This, together with the good fits to the data shown in panels h–o in these figures, and the very high loglikelihood values reached during the inversions ($L \sim -0.01$ in all cases), point to parameter recovery and E-EFMD performance being excellent for 1-layer models.

For 2-layer models, synthetic datasets 5–10 represent the simplest intrinsic attenuation configuration, with the quality factor at 1 Hz taking the same values I used for the single-layer models. In addition to this, datasets 6–7 and 8–9 test the ability of

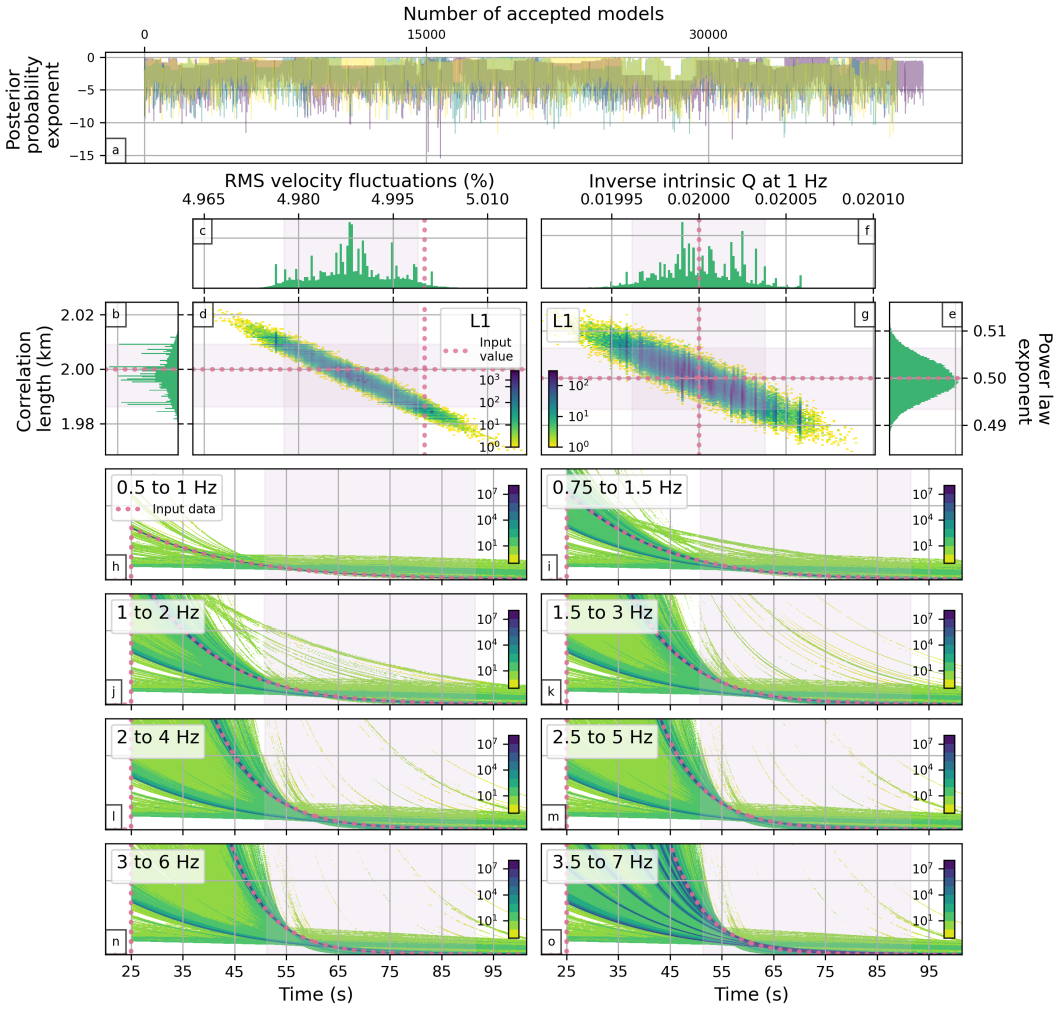

Figure 4.3: Summary of the results for the synthetic test number 1 (Table 4.1), representing a single-layer model of the lithosphere in which intrinsic attenuation is extremely strong and frequency dependent ($Q_{i0}^{-1} = 0.02$, $\alpha = 0.5$). Panel a contains the posterior probability exponent, or loglikelihood (L), for all accepted models in each of the three chains I combined to produce the full set of results. Panels b–c and e–f show the posterior PDFs for each of the parameters obtained from the E-EFMD inversion for this model (correlation length (a), RMS velocity fluctuations (ε), inverse intrinsic quality factor at 1 Hz (Q_{i0}) and power law exponent (α)), while panels d and g present the joint PDFs for the scattering and intrinsic attenuation parameters respectively. Dotted lines in plots b–e point to input parameter values, while shaded areas represent the 5–95 percentile range for each of them. Finally, panels h–o show the input data envelopes for each frequency band (dotted lines) together with the ensemble of envelopes obtained from all accepted models during the inversion (represented by the colormap in the background). Shaded areas in these plots highlight the time window used for the fit to the coda.

the algorithm to resolve different values of α for a fixed Q_{i0} value. To explore more complex lithospheric attenuation and scattering settings, datasets 11–22 have different values of the intrinsic quality factor at 1 Hz in each layer of the model and have been designed to represent lithospheric structures with varying degrees of contrast in intrinsic attenuation. Models 11, 12, 17 and 18 would represent a low contrast setting, in which Q_{i0} varies from extremely low to low or low to medium and viceversa. Medium

contrasts, meaning Q_{i0} goes from extremely low to medium or medium to high are illustrated by models 13, 14, 21 and 22. Finally, models 15, 16, 19 and 20 describe high contrast situations, with Q_{i0} varying from extremely low to high or low to high. The power law exponent for the intrinsic quality factor, α, remains constant throughout the lithosphere and equal to 0.5 in all these datasets but is allowed to vary during the inversion and obtained as an independent parameter, as opposed to synthetic tests 9* and 17*, which tested the alternative implementation of the E-EFMD inversion algorithm for fixed α. Synthetic envelopes for all frequencies and datasets detailed here were calculated using the E-EFMD algorithm.

Due to the large number of parameter combinations I evaluate here, especially for 2-layer models, I created a score system both for each individual parameter and synthetic test, to make it easier to compare results from different tests and summarise my overall results. This system, graphically represented in Fig. 4.4, assigns a score (S) between 0 and 3 to each 2-layer model test's parameter recovery results, as well as to its overall performance, based on three criteria.

For each parameter:

1. If the input value (IV) of the parameter lies within the 5–95 percentile range (PR) of the probability density function (PDF), then both the individual parameter score and the overall score are increased by 1 point. Otherwise, no points are added to either score.

2. If the mode (M) of the PDF for each parameter is located within the interval defined by (0.8·IV–1.2·IV), 1 point is added to the parameter and global scores. If this condition is not met, but M can be found inside the (0.6·IV–0.8·IV) or (1.2·IV–1.4·IV) intervals, 0.5 is added to the scores. For modes further from the input values, neither score is increased.

3. For each parameter, if the 5–95 PR is narrower than 30% of its total permitted range (interval from minimum to maximum allowed values), the parameter score and the global score are both increased by 1. If the width of the 5–95 PR is between 30–50% of the total permitted range, then the scores are increased by 0.5. Wider 5–95 PRs do not get any points added.

The only exception to these criteria corresponds to the two synthetic tests for which $\alpha = 0.0$ (tests 6 and 8 on Table 4.1). The input parameter value matches its minimum allowed value, which prevents it from being included within the 5–95 PR and always results in a score of 0 from the first criterion. At the same time, the intervals defined in the second criterion to establish the difference between the mode and the input value of the parameter will always be equal to 0 in this case, the score then failing to reflect the algorithm's ability to recover this parameter. Therefore, and to prevent the bias, these

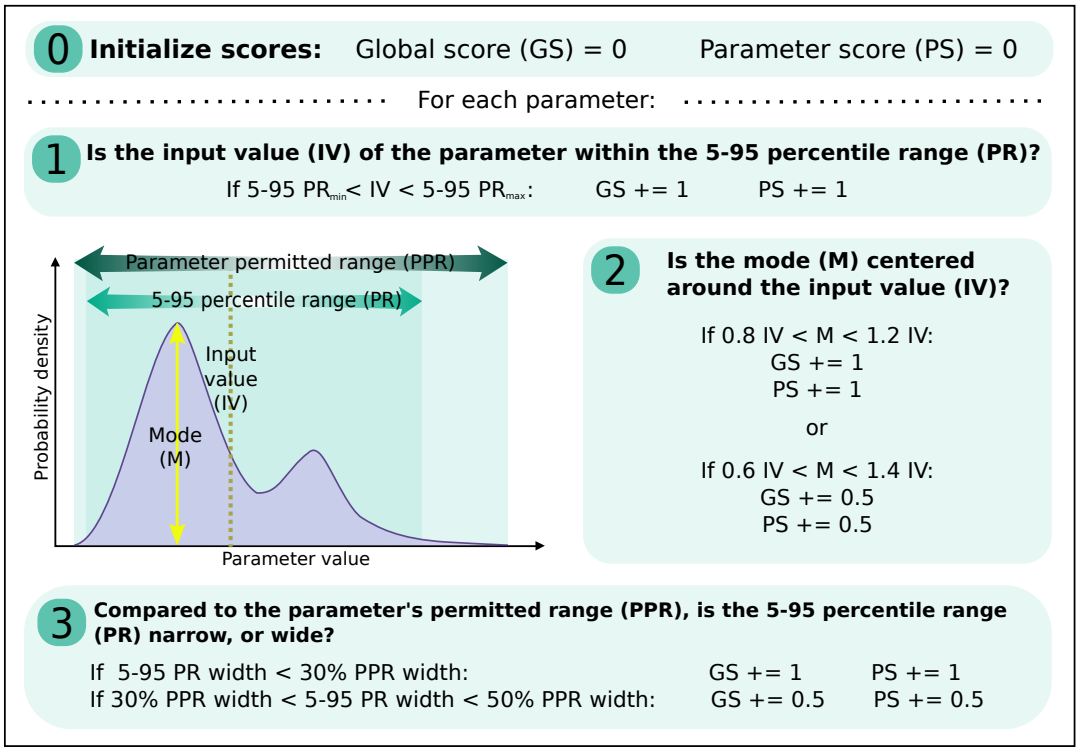

Figure 4.4: Graphic representation of the score system I designed to be able to compare the ability of the E-EFMD algorithm to accurate recover the input parameter values used in all 18 synthetic tests for 2-layer models. x symbols are used to indicate cases in which α was fixed and, therefore, not recovered from the inversion. See text for more details.

criteria were adjusted for all tests with $\alpha = 0.0$. The correction for the first criterion is based on the comparison between the mode, obtained from the PDF, and the input value. If they are close enough, this will always result in their exclusion from the 5–95 PR. To avoid this artifact in S, I compare the mode with a very low value (0.01, 1/100 of the total permitted range for the parameter). If the mode is lower than this number, then 1 is added both to the parameter and the global score, with no points added to either of them for higher mode values. The mode is also the key for the second criterion amendment: if it is lower than 0.2 (i.e., it can be found within the lowest 20% of the total permitted range), 1 point is added to the parameter and global S; if it is higher than 0.2 but lower than 0.4, scores are increased only by 0.5; no points are added for higher modes.

This score system ensures we will obtain a minimum of 0 and a maximum of 3 points for each individual parameter and synthetic test. Global scores for each test go up to 21, but are normalized to the 0–3 range so they can be compared with parameter scores. Parameter scores lower or equal than 1 are indicative of poor parameter recovery, with the 5–95 PR not including the input parameter value, its mode being at least 20% off that value and/or its width at least larger than 30% or the total permitted range. Global S in this range represent poor overall performance of the algorithm (the majority of the

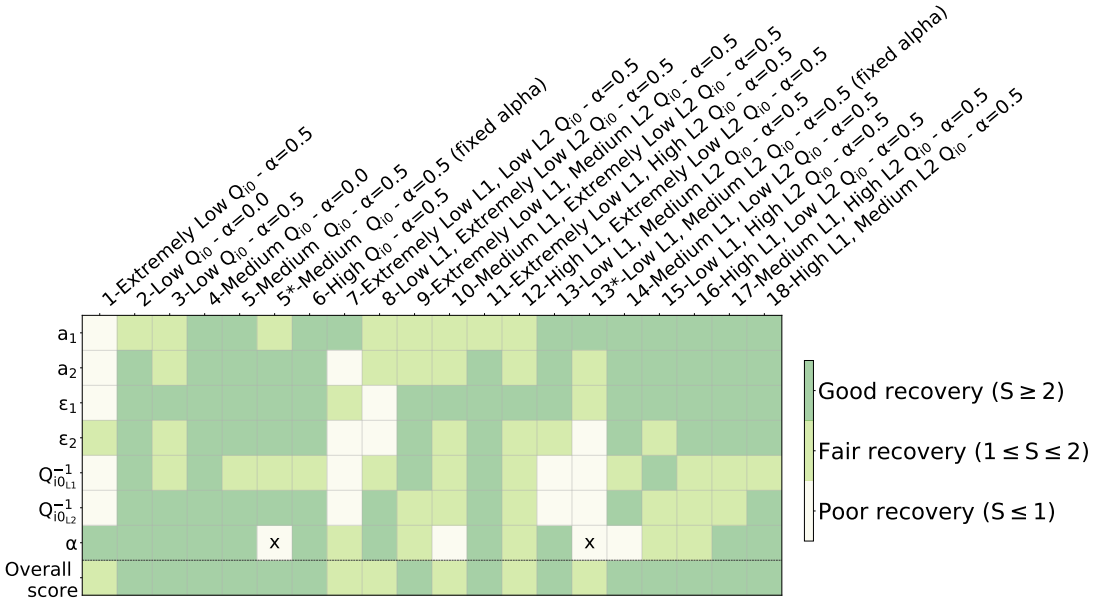

Figure 4.5: Graphic representation of the global and parameter scores obtained by the E-EFMD algorithm for each of the 2-layer model synthetic tests summarised in Table 4.1. Labels along the x axis indicate synthetic test numbers, as stated in Table 4.1, as well as a summary of the intrinsic attenuation parameters values in each layer of the model (with extremely low, low, medium and high Q_{i0} values each corresponding to 50, 100, 500 and 1200). L1 and L2 are used here to refer to layers 1 and 2 of the lithospheric models, respectively. x symbols are used here to highlight tests for which α was fixed and, therefore, not obtained from the E-EFMD inversion.

parameters have a score below 1) for that synthetic test. Scores larger than 1 but lower or equal to 2 are labelled as fair recovery/performance, since at least one of the three criteria was fully met for most parameters. Finally, $S > 2$ point to good parameter recovery and overall performance for the current synthetic test. Figure 4.5 contains a graphic representation of S for all parameters and synthetic tests I carried out to investigate the parameter recovery capabilities and assess the overall performance of the E-EFMD algorithm. The top seven rows in this figure refer to individual parameters I invert for in the E-EFMD, allowing me to evaluate the general performance of the algorithm to recover them, while columns give us the parameter score for each synthetic test and its global score in the bottom row.

Based on the global scores on Fig. 4.5, the overall performance of the E-EFMD for 2-layer models is satisfactory. Recovery of individual parameters varies widely, both between different tests and for each model layer within a test. Scores for ε_1 are higher than 2 for 16 synthetic tests and only below or equal to 1 in 2 of them, making it the best recovered parameter. By contrast, $Q_{i0_{L1}}^{-1}$ is well ($S > 2$) and poorly ($S \leq 1$) recovered for 5 and 4 synthetic tests, respectively, which represents the lowest overall score for a parameter. In terms of global scores, 14 of my 2-layer model synthetic tests (out of 20, if we include tests 9* and 17*) have $S > 2$, meaning good recovery of most parameters. An example of a well resolved case is illustrated in Fig. 4.6, with all seven parameters

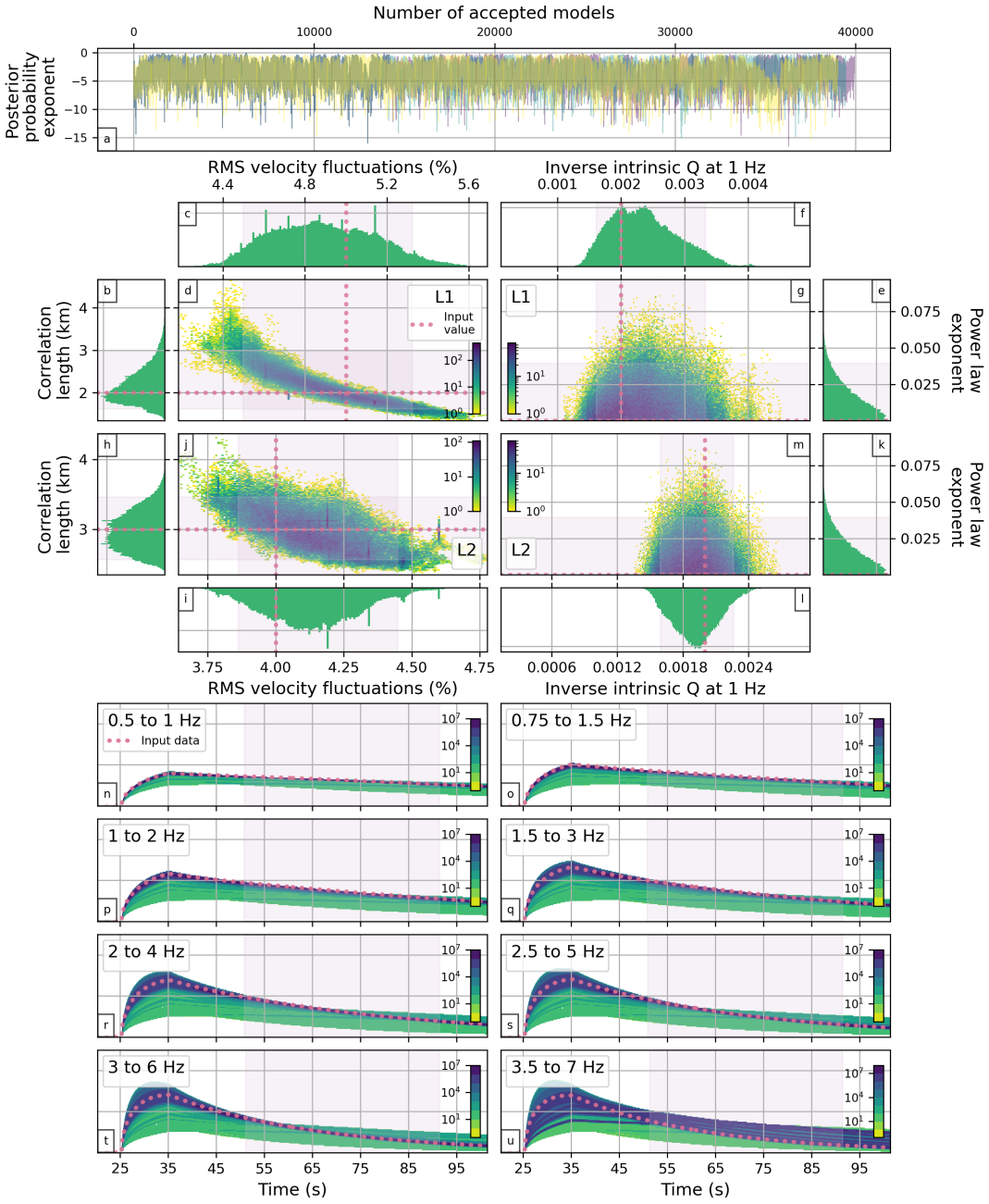

Figure 4.6: Summary of my results for synthetic test number 8 (Table 4.1), which represents a lithosphere with constant medium intrinsic attenuation ($Q_{i0}^{-1} = 0.002$) without any frequency dependence ($\alpha = 0$). Panel content is as in Fig. 4.3, with the addition of panels h–k for parameters in the lithospheric mantle.

being accurately recovered from the inversion for this test (number 8, Table 4.1). The remaining 6 tests obtained scores between 1 and 2, placing them in the "fair recovery" range. Out of these 6 cases, 5 had extremely strong intrinsic attenuation in at least one layer of the model (e.g., Q_{i0}^{-1}=0.02) and 3 of them had either strong (e.g., Q_{i0}^{-1}=0.01) or extremely strong attenuation in both layers, which results in very low coda amplitudes.

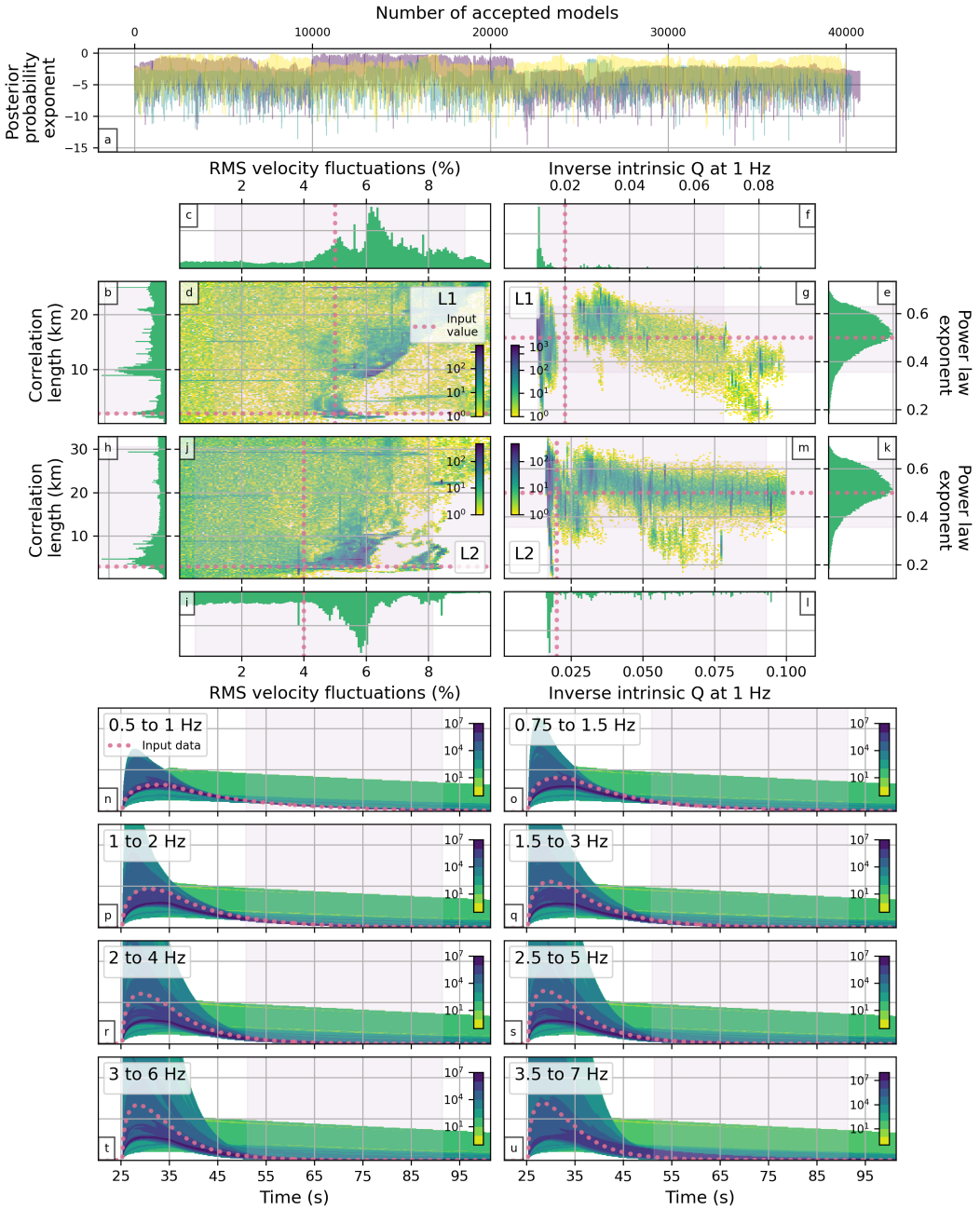

Figure 4.7: As Fig. 4.6 but for synthetic test number 5 from Table 4.1. Results for this test show an overall good fit to the synthetic envelopes but poor parameter recovery.

Synthetic tests 5 and 11 (from now on, ST5 and ST11, respectively; Table 4.1, and Figs. 4.7 and 4.8) clearly illustrate this phenomenon. These tests are generally poorly resolved, with only one parameter getting $S > 2$ both for ST5 and ST11, and 1 and 2 having $1 \leq S \leq 2$ for each test respectively (Fig. 4.5). In both cases, $Q^{-1}_{i0_{L1}}$=0.02, but while this value remained constant throughout the lithosphere for ST5, $Q^{-1}_{i0_{L2}}$=0.01 for ST11 (Table 4.1). As a result of this strong or extremely strong attenuation, coda amplitudes are barely above zero for at least 1/3 of the time window used for the fit

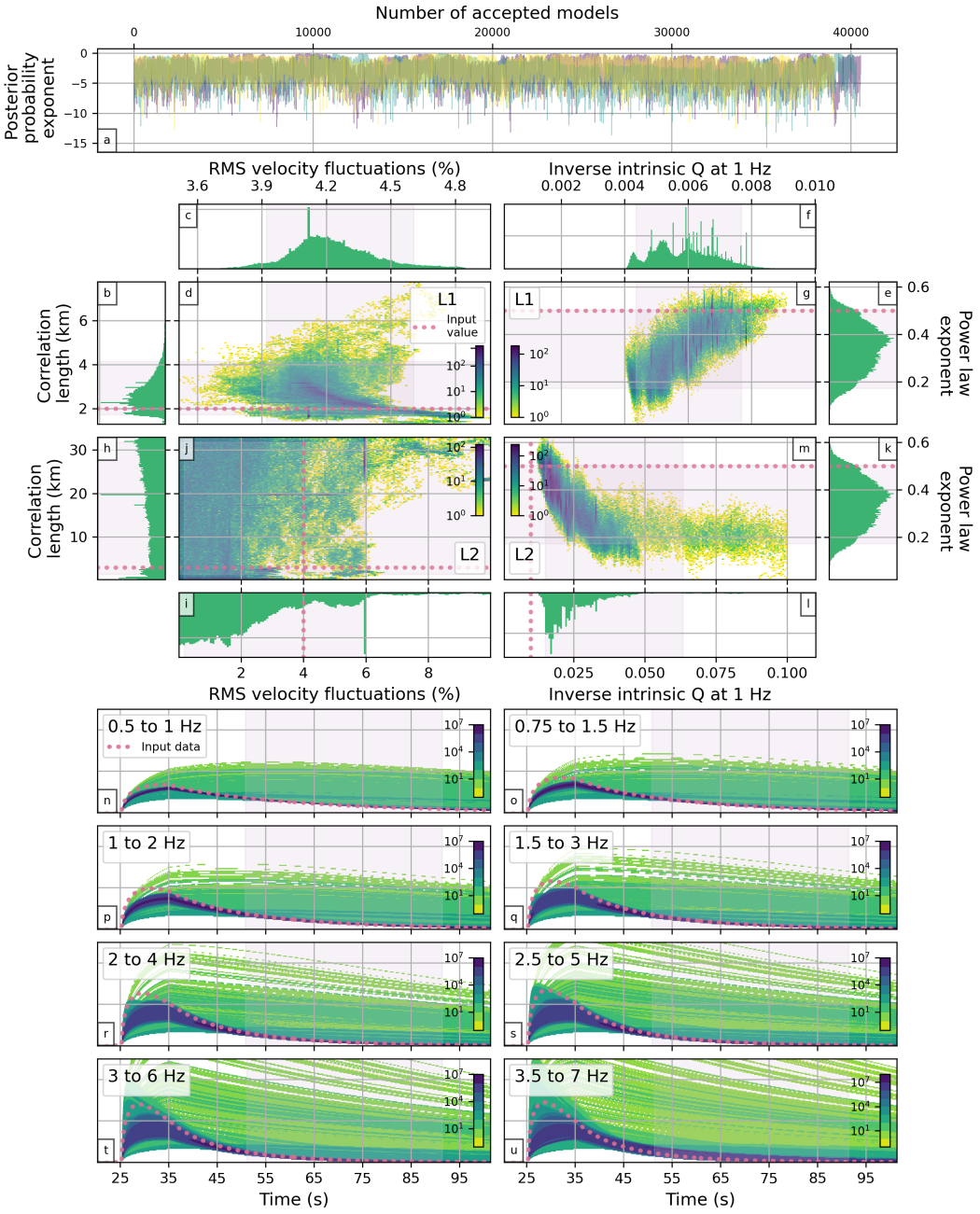

Figure 4.8: As Fig. 4.6 but for synthetic test number 11 from Table 4.1. Similarly to test number 5, shown in Fig. 4.7, fits to the synthetic envelopes are good for all frequency bands, but the input parameter values are poorly recovered.

and all frequency bands (panels n–u in Figs. 4.3 and A26). Posterior PDFs for Q_{i0}^{-1} in both layers have complex shapes, with multiple maxima, and are constrained to the $0.01 < Q_{i0}^{-1} < 0.1$ interval, which defines the strong to extremely strong attenuation range (panels f and l). PDFs for the power law exponent are approximately gaussian and narrow for ST5 and ST11 (panels e or k), but those for the scattering parameters (panels b–c and h–i) in both tests show long tails and broad 5–95 PRs (Table 4.1)

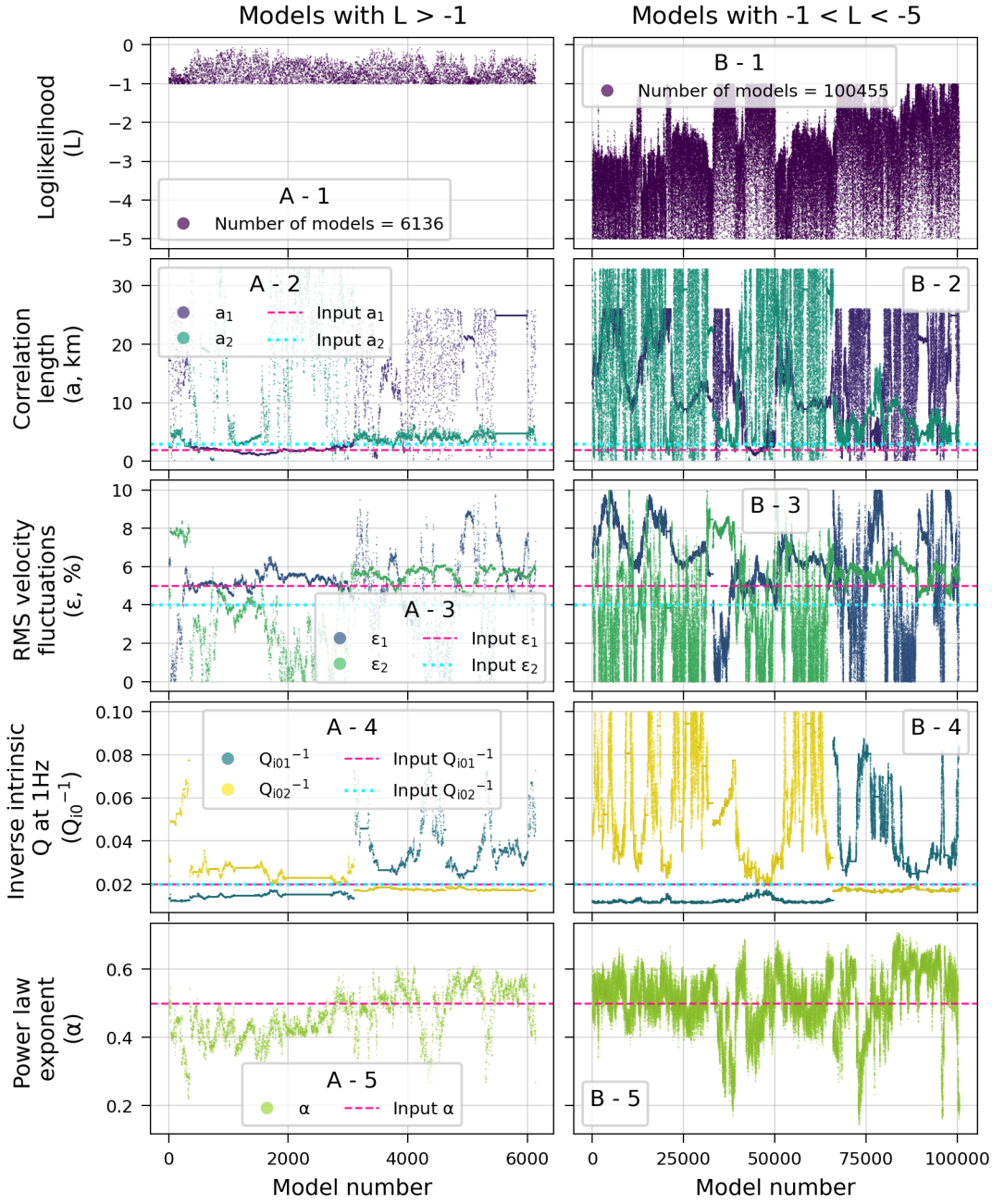

Figure 4.9: Samples of the E-EFMD results for synthetic test 5 from Table 4.1. Panels A1–A5 contain the loglikelihood (L), correlation length (a), RMS velocity fluctuation (ε), inverse intrinsic quality factor at 1 Hz (Q_{i0}^{-1}) and power law exponent (α) for all models with $L > -1$, as well as the input parameter values in each case. Panels B1–B5 have the same content, but for models with $-1 > L > -5$.

for at least one of the layers in the model. These wider distributions indicate strong variability and a reduced effect of these parameters on coda amplitudes, which greatly increases the difficulty to determine their true value.

To investigate variations in parameter combinations as fits to the synthetic data

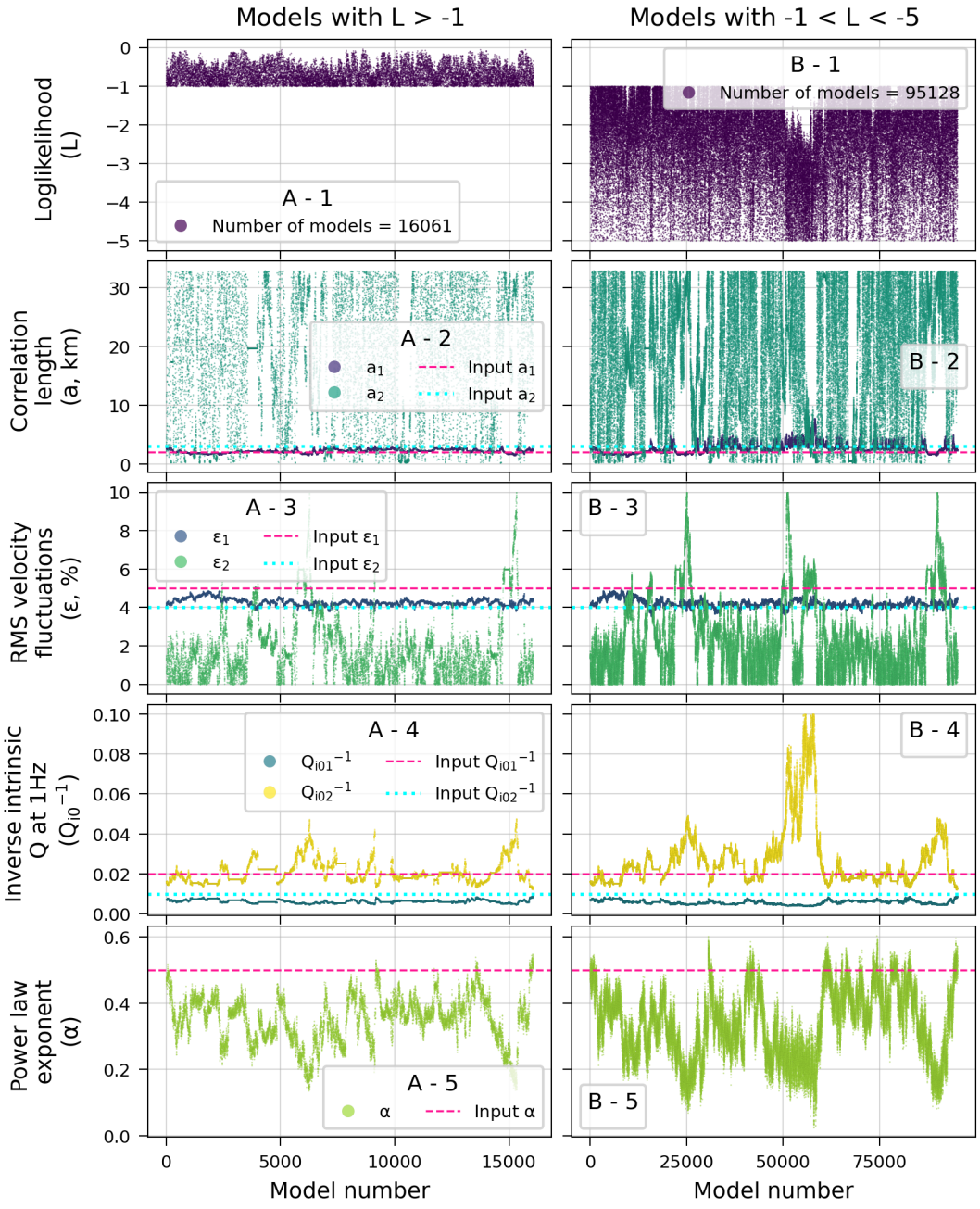

Figure 4.10: Same as Fig. 4.9 but for synthetic model 11 from Table 4.1.

improve, I decided to sample the obtained PDFs and extract two groups of models based on their loglikelihoods (L). The first group (G1) includes all models with $L > -1$, that is, the models that have the highest likelihoods and are, therefore, more likely to produce the input synthetic envelopes (panels A1–A5 in Fig. 4.9). The second group (G2) comprises models with $-1 > L > -5$ which represents slightly worse fits to the data (panels B1–B5 in Fig. 4.9). Figures 4.9 and 4.10 present loglikelihood and parameter value variations within these two groups of models and compares them with

their input values (similar figures for the remaining synthetic tests can be found in Appendix A.3). For ST5, Fig. 4.9 highlights the presence of two distinct sets of solutions or preferred parameter combinations (also visible in Fig. 4.7, especially panel g, and Fig. A42), characterized by having either relatively constant $Q_{i0_{L1}}^{-1} < 0.02$ and widely varying $Q_{i0_{L2}}^{-1} > 0.02$ or vice versa. These two sets of solutions are clearly observed both within the G1 and G2 groups, indicating that they can produce equally good fits to the data. For the first set, $Q_{i0_{L1}}^{-1}$ is the only parameter that remains stable, with the rest of the parameters taking values throughout most of their permitted range. Within the second of these sets, most models have fairly stable $\varepsilon_2 \sim 5 - 6\%$, $a_2 \sim 3 - 10$ km and $0.3 < \alpha < 0.7$ (a combination that does not match the input values), while the rest of parameters present much more variability. These sets of solutions suggest that, as we increase $Q_{i0_{L2}}^{-1}$ towards its higher limit (0.1) and coda amplitudes decrease, the effect of all the other parameters on coda shapes is greatly reduced, and, therefore, the importance of their actual value. A $Q_{i0_{L2}}^{-1} \leq 0.02$ appears to be low enough for the effect of the rest of the parameters to be required again to match the observed amplitudes. The high $Q_{i0_{L1}}^{-1}$ values observed in the second set of solutions also appear to have an important effect on the relevance of the values of the scattering parameters, although only in layer 1 of the model. Samples for ST11, shown in Fig. 4.10, show that, in this case, the algorithm converged to a single set of solutions. Input Q_{i0}^{-1} values for this test are 0.02 and 0.01 for layers 1 and 2 of the model, respectively, but recovered values show almost the opposite configuration, with fairly stable $Q_{i0_{L1}}^{-1} \sim 0.01$ and widely varying $Q_{i0_{L2}}^{-1} > 0.01$. Correlation lengths and RMS velocity fluctuations in layer 1 remain approximately constant throughout the entire inversion, with a_1 approximately matching its input value, while parameters for layer 2 present strong variations. Values of α were lower than its input value for most of the inversion, although with wide variability. This increased stability and variability of the scattering parameters in layers 1 and 2 of the model, respectively, appear to be related to the behaviour of $Q_{i0_{L1}}^{-1}$ and $Q_{i0_{L2}}^{-1}$, and clearly highlight a trade off between them. As results for ST5 showed, high $Q_{i0_{L2}}^{-1}$ values are enough, on their own, to match low coda amplitudes present in the input envelopes. While it is possible for the algorithm to obtain them by using different combinations of the scattering and attenuation parameters, all three Markov chains I ran for ST11 converged to the same solution, showing that the algorithm favours forcing $Q_{i0_{L2}}^{-1}$ to take higher values to achieve the required coda amplitudes over more complex parameter combinations.

The examination of Figs. 4.12 or 4.13, which contain the marginal PDFs for all parameters and layers, as well as the PDF for each individual parameter, provides more insight into the behaviour of the Bayesian E-EFMD algorithm (similar figures for the remaining synthetic tests can be found in Appendix A.3). At first sight, they suggest the presence of two main groups of synthetic tests, based on the interactions or trade

offs between the parameters shown in the marginals. The first group, of which synthetic test 9 (ST9 from now on, Fig. 4.12) is an example of, is characterized by strong interactions between the intrinsic attenuation quality factor in both layers of the model (panel 6–5) and, to some extent, between $Q_{i0_{L1}}^{-1}$, $Q_{i0_{L2}}^{-1}$ and ε_2 (panels 5–4 and 6–4), while also presenting very weak interactions between the scattering parameters in both layers. PDFs for $Q_{i0_{L1}}^{-1}$, $Q_{i0_{L2}}^{-1}$ and ε_2 (panels 4–4, 5–5 and 6–6 respectively) show two clear peaks and a correspondence between lower values of $Q_{i0_{L1}}^{-1}$ and ε_2 and higher values of $Q_{i0_{L2}}^{-1}$. These relationships between the parameters are also obvious in the high loglikelihood samples for this test (Fig. A62). Parameter values for the highest loglikelihod models confirm that these two peaks in the PDFs define two independent sets of parameters. The observed variability in the scattering parameters, especially in layer 1, is associated to changes in $Q_{i0_{L1}}^{-1}$ or $Q_{i0_{L2}}^{-1}$ and follows patterns similar to those observed for ST5 and ST11. Marginals for synthetic tests in the second group, represented here by synthetic test 7 (ST7, Fig. 4.13), appear to be more complex and suggest very strong trade offs between the scattering parameters (panels 2–1, 3–1, 3–2, 4–1, 4–2 and 4–3) in both layers and weaker interactions with the attenuation parameters. However, a closer look at the parameter values for the models with highest L (Fig. 4.11) shows these results greatly resemble those for ST5. Despite the PDFs for the parameters not being as evidently bimodal for this case as they are for ST5, two independent sets of solutions can clearly be identified in Fig. 4.11. Set 1, characterized by $Q_{i0_{L1}}^{-1} < 0.01$ and $Q_{i0_{L2}}^{-1} > 0.01$, presents strong variability for the scattering parameters in layer 2 of the model and relatively stable values for those in layer 1. The second set is almost the opposite, with lower $Q_{i0_{L2}}^{-1}$ and higher, unstable $Q_{i0_{L1}}^{-1}$, which in turn causes fluctuations of the scattering parameters in layer 1. The combined observation of the marginals and models samples for the rest of the synthetic tests show that the patterns described here for ST9 and ST7 are not isolated occurrences. In every single case, the trade offs between the scattering parameters observed for tests belonging to this second group, can be explained by the algorithm's convergence to two sets of solutions and/or variations in the intrinsic quality factor.

These observations provide strong evidence about the non-uniqueness of the solutions within the E-EFMD, as well as the complex relationships and trade-offs between the parameters. To help demonstrate this phenomenon even further, I carefully selected and calculated the synthetic envelopes for eight parameter combinations that represent different scattering and attenuation scenarios. Figure 4.14 shows the envelopes for these models, grouped into three sets. Panel A contains the envelopes for four of these models, all of them with strong to extremely strong intrinsic attenuation ($0.00\overline{6} \leq Q_{i0}^{-1} \leq 0.02$) in the crust and/or lithospheric mantle. Crustal scattering for the first and last models in these panels could be described as medium to strong, while for the remaining two models it is very weak. The lithospheric mantle also has

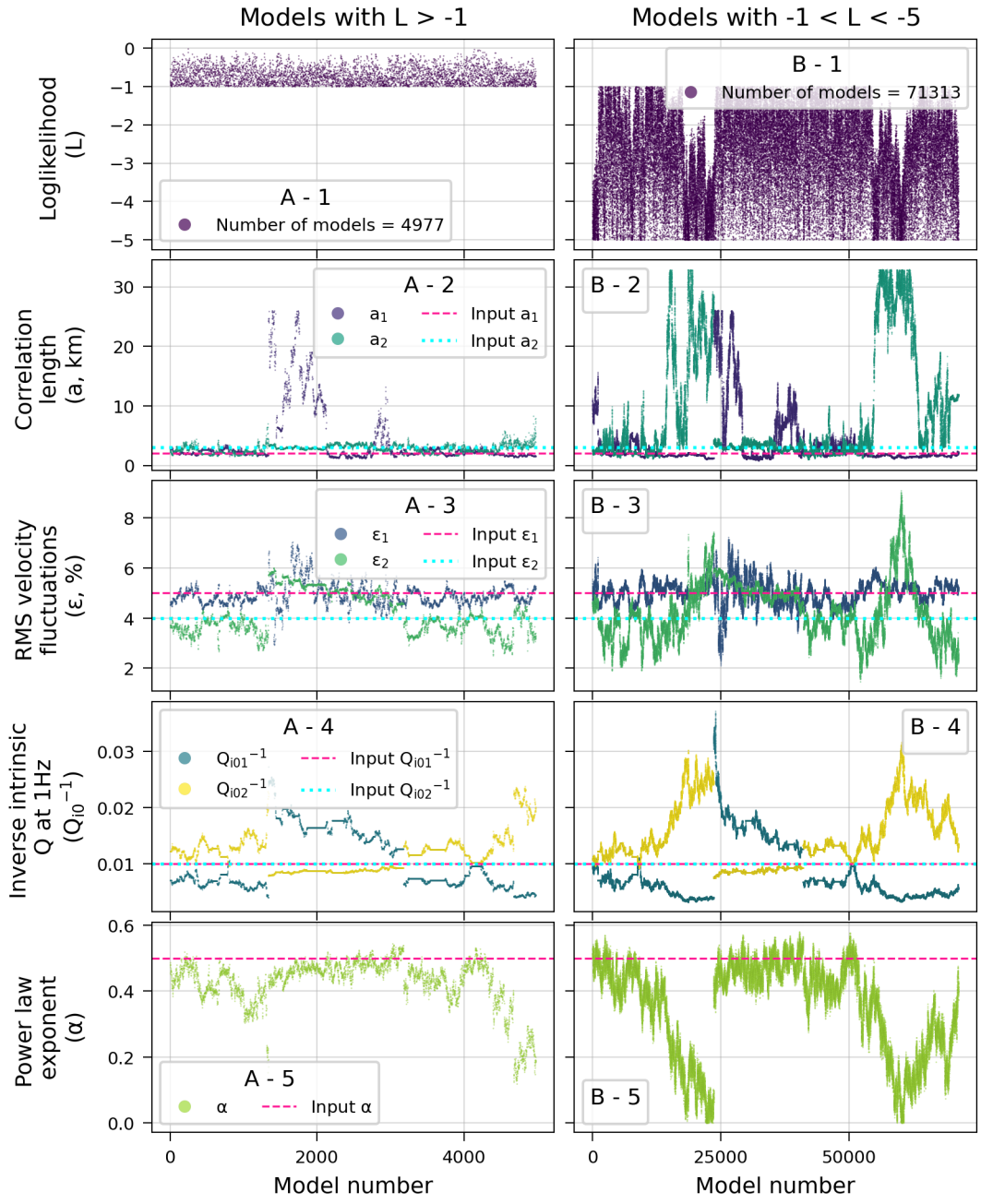

Figure 4.11: Same as Fig. 4.9 but for synthetic model 7 from Table 4.1.

varying degrees of heterogeneity in these models, with this layer being relatively homogeneous for the first and third models and moderately to strongly scattering in the rest. All of these parameter combinations, however, produce coda envelopes that are essentially identical within the time window used for the fit by the E-EFMD Bayesian inversion algorithm, which means that it would not be able to differentiate between these very distinct scenarios. This coincidence in both coda amplitudes and decay rates is not exclusive to the specific frequency band represented here, and figures for

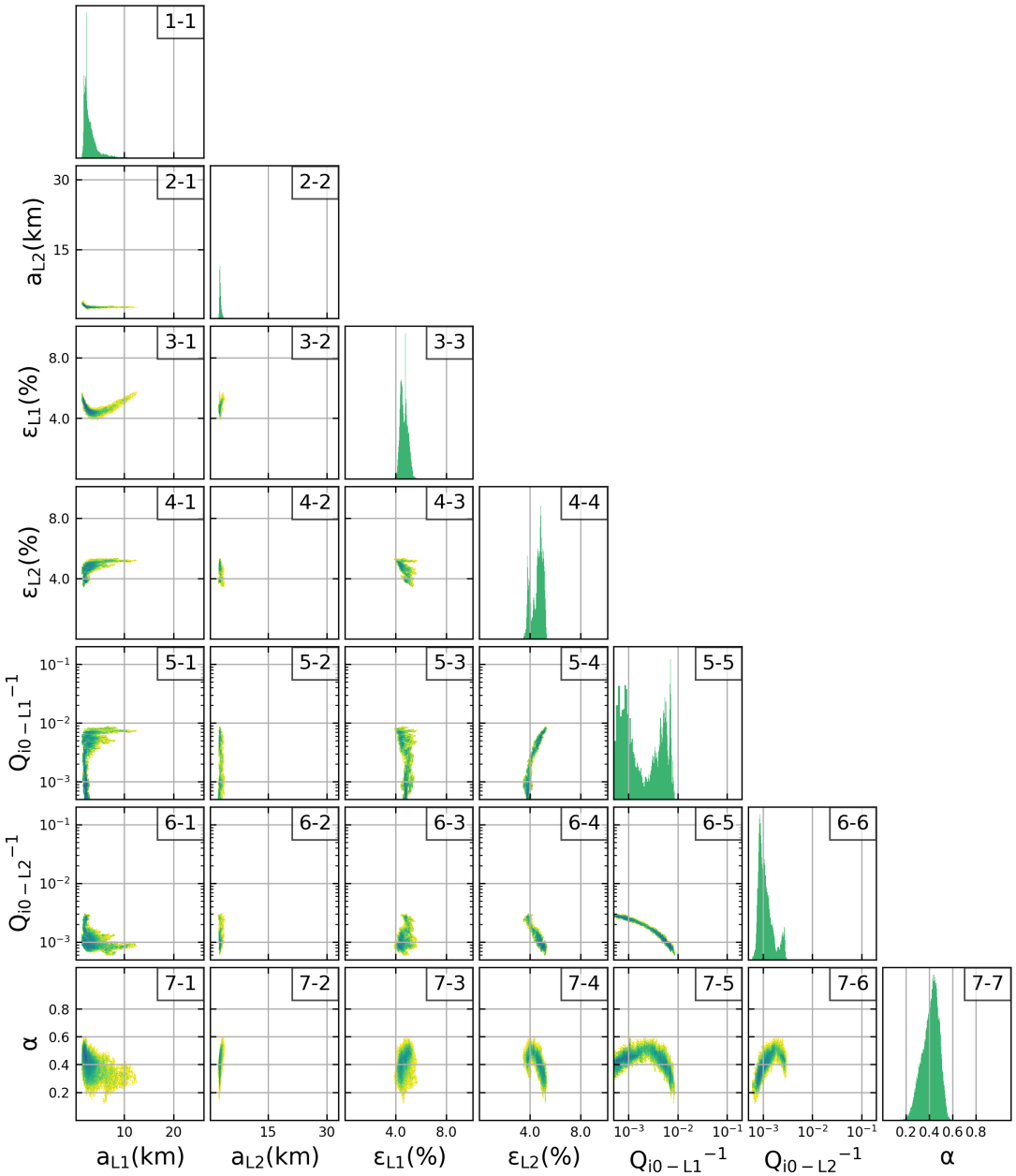

Figure 4.12: Obtained joint PDFs for all parameters and layers in synthetic model 9 from Table 4.1. Plots in the diagonal of the figure contain the individual PDF for the individual scattering and intrinsic attenuation parameters parameters.

the same datasets and the rest of the bands contained in Table 2.3 can be found in Appendix A.3. Panels B and C in Fig. 4.14 show two additional sets of models which also produce matching coda envelopes. The first parameter set in panel B represents a weakly heterogeneous and moderately attenuating lithospheric mantle beneath a much more heterogeneous but less attenuating crust. The parameter values for the second model in this plot describe almost the opposite situation: here, a weakly scattering but very strongly attenuating crust lies above a moderately heterogeneous and attenuating

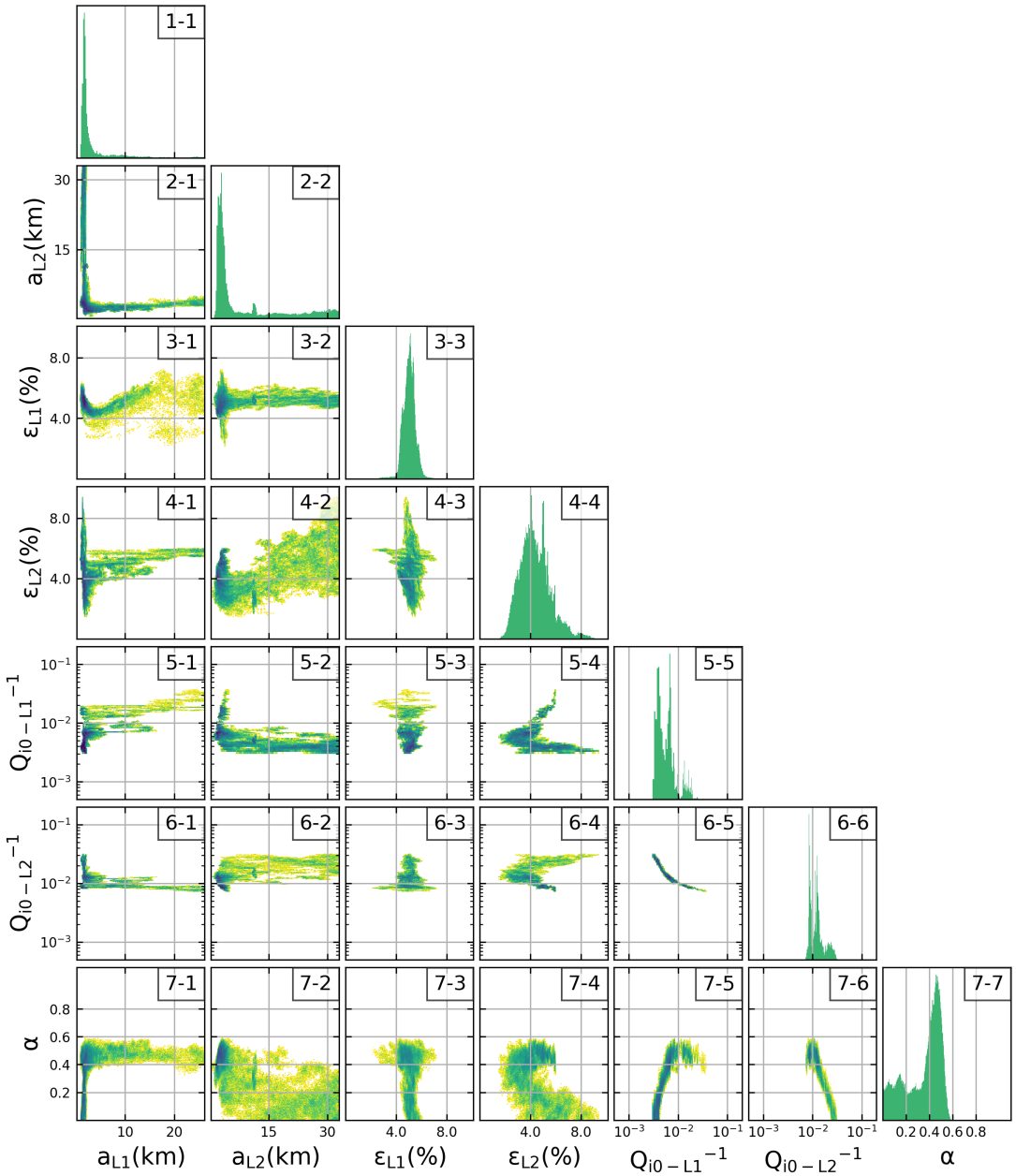

Figure 4.13: As Fig. 4.12 but for synthetic test 7 from Table 4.1.

lithospheric mantle. Finally, models in panels C have identical scattering structures and high contrasts in intrinsic attenuation between both layers in the model. These four combinations of parameters correspond to radically different scenarios, but result in nearly indistinguishable codas within the time window of interest.

The results in this section, as well as those in Appendix A.3, show that, even if the performance of the Bayesian E-EFMD algorithm is generally good in terms of the score system illustrated by Figs. 4.4 and 4.5, great care has to be taken when interpreting the obtained results. The "interchangeability" of $Q_{i0_{L1}}^{-1}$ and $Q_{i0_{L2}}^{-1}$, defined as an exchange in

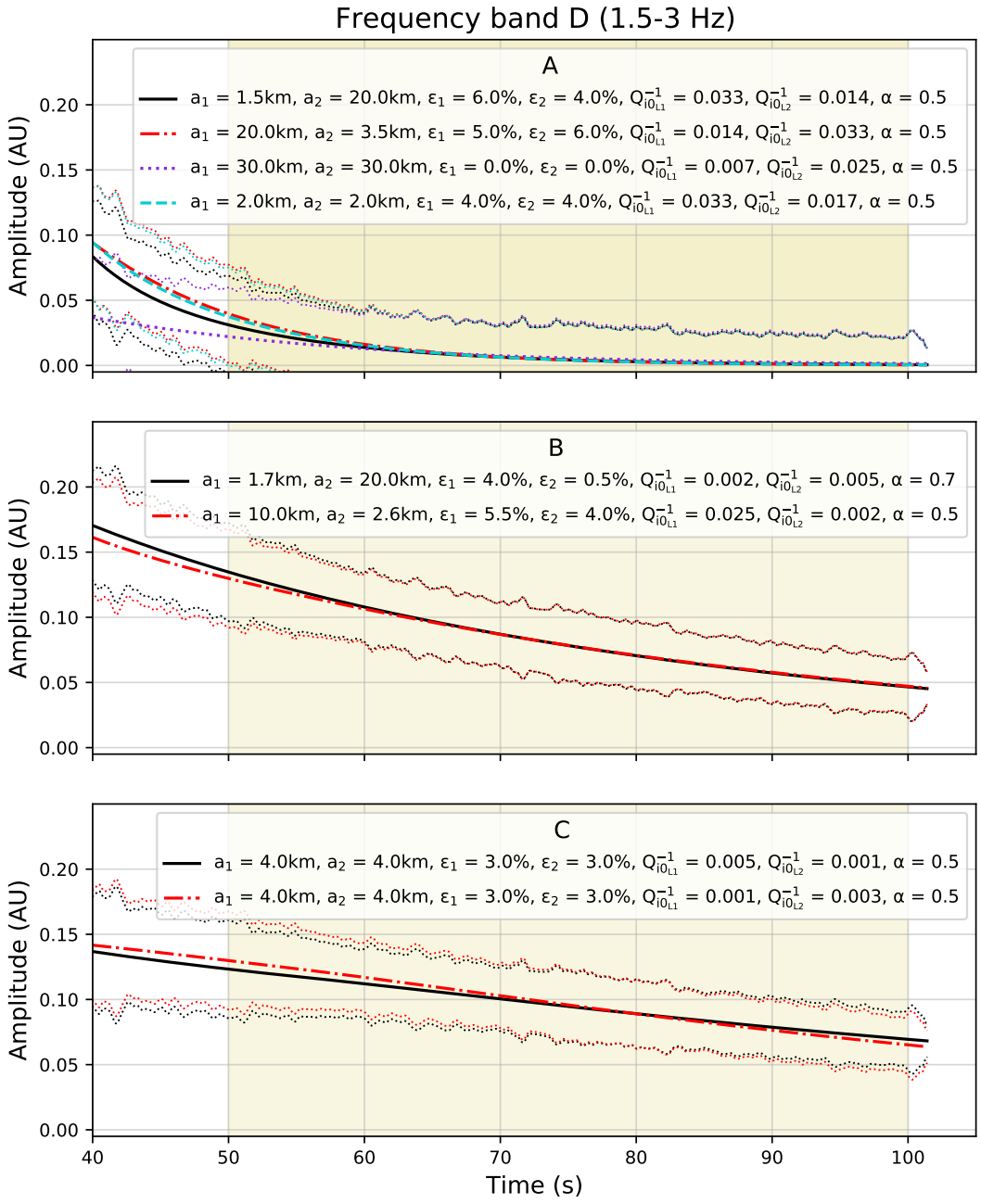

Figure 4.14: Synthetic envelopes for frequency band D (Table 2.3) and eight synthetic datasets that represent a variety of scattering and intrinsic attenuation scenarios. Models in panel A all have strong to extremely strong intrinsic attenuation ($0.00\overline{6} \leq Q_{i0}^{-1} \leq 0.02$) in the crust and/or lithospheric mantle and varying scattering strengths within each layer. Datasets in panel B represent models with strong contrasts in scattering between the two layers and weaker variations in anelasticity. Envelopes in panel C result from models with the same heterogeneity structure and sharp contrasts in intrinsic attenuation between the model layers. Shaded areas in all plots represent the time window used for the fit in the E-EFMD, and dotted lines the uncertainty associated to each synthetic envelope used in the inversion algorithm.

their values having little to no effect on the produced synthetic codas, and observed in ST5 and ST11, is present in 13 other synthetic tests (see Figs. A60–A76) and is the main

cause of the poor parameter recovery for Q_{i0}^{-1}. The convergence to two independent sets of solutions observed for ST5 or ST7 is not unique either, and is also caused by the interactions between $Q_{i0_{L1}}^{-1}$ and $Q_{i0_{L2}}^{-1}$ and appears to be independent of the strength of the contrast in anelastic attenuation between the layers of the model. On 13 occasions, the algorithm found two different combinations of parameters that were equally capable of reproducing the input data envelopes (e.g. Figs. A68, A72, A75, A76). Test results which do not show either of these behaviours (e.g. models 8 or 16 from Table 4.1, Figs. A61 and A69) have generally higher scores both for $Q_{i0_{L1}}^{-1}$ and $Q_{i0_{L2}}^{-1}$. However, the algorithm's convergence to a single set of solutions does not necessarily guarantee accurate parameter recoveries either, especially for low coda amplitudes, as shown for ST11. Finally, reducing the number of parameters to 6 by forcing α to remain constant throughout the E-EFMD inversion, as tested for models 9* and 17* from Table 4.1, does not seem to improve the overall performance of the algorithm (Fig. 4.5). This could be related to the role of this parameter in helping control coda decay rates (Section 4.1.1) and its interactions with Q_{i0}^{-1}. A potential solution to this E-EFMD behaviour, that could also reduce the uncertainty in parameter recovery, would be including additional information into the prior probability distributions for the parameters, especially Q_i.

Free frequency dependence of the intrinsic quality factor

In addition to the synthetic tests described in Section 4.1.2, I tried a version of the E-EFMD code which includes the intrinsic quality factor for each layer and frequency band as a free parameter that can be obtained from the Bayesian inference algorithm. In this code, for each layer, a given model $\mathbf{m}$ includes a single value of a and ε, as well as a Q_i value for each frequency band. Instead of forcing Q_i values to follow a specific frequency dependence, I designed the algorithm so they could vary freely and independently within the same uniform prior probability distribution used in the synthetic tests above ($10 < Q_i < 2000$, $5 \cdot 10^{-4} < Q_{i0}^{-1} < 0.1$). Priors for the correlation length and RMS velocity fluctuation are also uniform and the same used in my initial implementation of the EFMD and the synthetic tests of the E-EFMD ($0.2\lambda_{min} < a < 2\lambda_{max}$, $4.5 \cdot 10^{-3} < \varepsilon < 10\%$). Thus, for a 2-layer model and the eight frequency bands described in Table 2.3, $\mathbf{m}$ would contain a total of 20 free parameters, as opposed to the 4 included in my initial implementation of the EFMD, or 7 used in the final version of the E-EFMD described in the section above. The initialization of the random walk and updating of the model at each step are as described in Section 4.1.

I tested the capacity of this version of the E-EFMD code to accurately recover all of the input parameter values and fit the data at all frequency bands by creating a synthetic dataset which represents a simple scenario in which the intrinsic quality factor takes the same value throughout the lithosphere and for all frequency bands. Correlation length and RMS velocity fluctuations values are the same used in previous

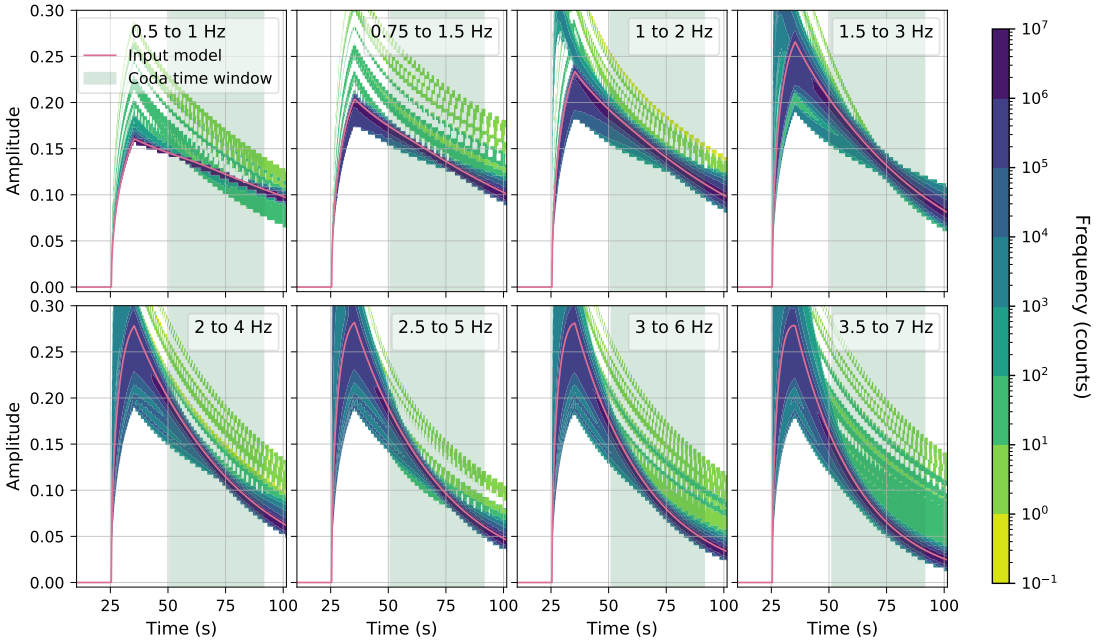

Figure 4.15: Results from a synthetic test for the version of the E-EFMD with free Q_i frequency variation. Black lines represent the synthetic envelopes corresponding to the input model for all frequency bands from Table 2.3, while shaded areas represent the time window used for the fit and loglikelihood calculation. Contours represent the histograms of all synthetic envelopes within the ensemble obtained from all accepted models for all frequency bands, such as darker areas represent a higher density of envelopes.

EFMD and E-EFMD synthetic tests (Tables 2.1 and 4.1). I used PSA as a reference array in terms of velocity model and interface depths for this test as well. As stated above, the number of parameters in this version of the E-EFMD is five times higher than for my initial implementation of the Bayesian EFMD. To take this fact into account, and to ensure the algorithm had enough time to properly sample the parameter space, I decided to run a 15 million iterations long chain for this first test, divided into three 5 million iterations long segments for manageability. Table 4.2, and Figs. 4.16 and 4.15 summarise the layering, input parameter values and results obtained from this synthetic test.

This version of the E-EFMD does not appear to be capable of accurately recovering any of the input parameter values. Histograms for correlation length, RMS velocity fluctuations and Q_i^{-1} at each frequency band for both layers in the model are shown in Fig. 4.16. None of the histograms are gaussian, and many have complex shapes with either multiple or no prominent peaks at all. All input parameter values are within their respective 5–95 percentile ranges (PRs). However, the significance of this result is greatly diminished by the fact that these 5–95 PRs are extremely wide in most cases and that input values do not match a peak in the histograms in most cases. Despite the poor input parameter recovery, fits to the synthetic envelopes (Fig. 4.15) are very good within the time window used for the fit, as evidenced by the high loglikelihood values

reached during the inversion (Table 4.2). This observation points to solutions to this problem being extremely non-unique due to the very complex relationships between the parameter, thus making it potentially impossible to solve using the free-varying intrinsic quality factor approach followed here. For all these reasons, I decided not to continue testing this version of the E-EFMD.

4.2 Application to the Australian arrays

As a final test of the E-EFMD algorithm, I compare the results I obtained for the 2-layer lithospheric model with my initial version of the EFMD for the three Australian arrays (PSA, ASAR and WRA) shown in Chapter 3 and those obtained using this new, expanded algorithm. The results I obtained for these arrays using the Bayesian EFMD (Chapter 3) show that the EFMD is not suited to fit real data envelopes for frequency bands A–C (Table 2.3) for these arrays. For this reason, I focus on bands D–H from Table 2.3 in the E-EFMD inversions, in which I also used the same datasets, data processing, background velocity model and Moho and LAB depths described in Sections 3.1 and 3.2 for each array.

Each inversion consisted of three parallel, 10 million iterations long, Markov chains. Their results were resampled as described in Section 4.1.2 and combined into a single ensemble of models. The E-EFMD algorithm used in these inversions is identical to the one used for the synthetic tests in Section 4.1.2 except in the width of the prior distribution for the intrinsic quality factor at 1 Hz. In those tests, this uniform prior ranges from 10–2000. However, the results from the single-layer EFM results suggest $Q_{i0} \sim 2100$ for PSA and WRA. Therefore, and to prevent any bias on the results and

Table 4.2: Summary of the layering, parameter values and results of the inversion for a synthetic model used to test the validity of the free Q_i frequency variation version of the E-EFMD. I include 5–95 percentile ranges (PRs) and acceptance rates (ARs) for each scattering parameter (correlation length and RMS velocity fluctuations), as well as those for the intrinsic quality factor at 1 Hz (Q_{i0}) at each frequency band.

Layer	Input model			Corr. length (a)		RMS vel. fluct. (ε)		Int. quality factor (Q_i)		Maximum
number	a (km)	ε (%)	Q_i	5 – 95 PR (km)	AR (%)	5 – 95 PR (%)	AR (%)	5 – 95 PR (%)	AR (%)	L
1	2.0	5.0	0.002	2–5	42	4.0–4.6	39	0.001–0.005	35	-0.83
								0.0005–0.0025	40	
								0.0005–0.003	39	
								0.0006–0.03	44	
								0.0005–0.005	40	
								0.0006–0.025	39	
								0.0005–0.01	38	
								0.0006–0.01	45	
2	3.0	4.0	0.002	2–8	42	4.6–5.4	39	$0.00\overline{1}$–0.0025	35	
								0.0014–$0.00\overline{3}$	40	
								0.001–$0.00\overline{3}$	39	
								0.0008–$0.00\overline{3}$	44	
								0.0013–0.005	40	
								0.0013–0.005	39	
								0.0014–0.005	38	
								0.0014–0.005	45	

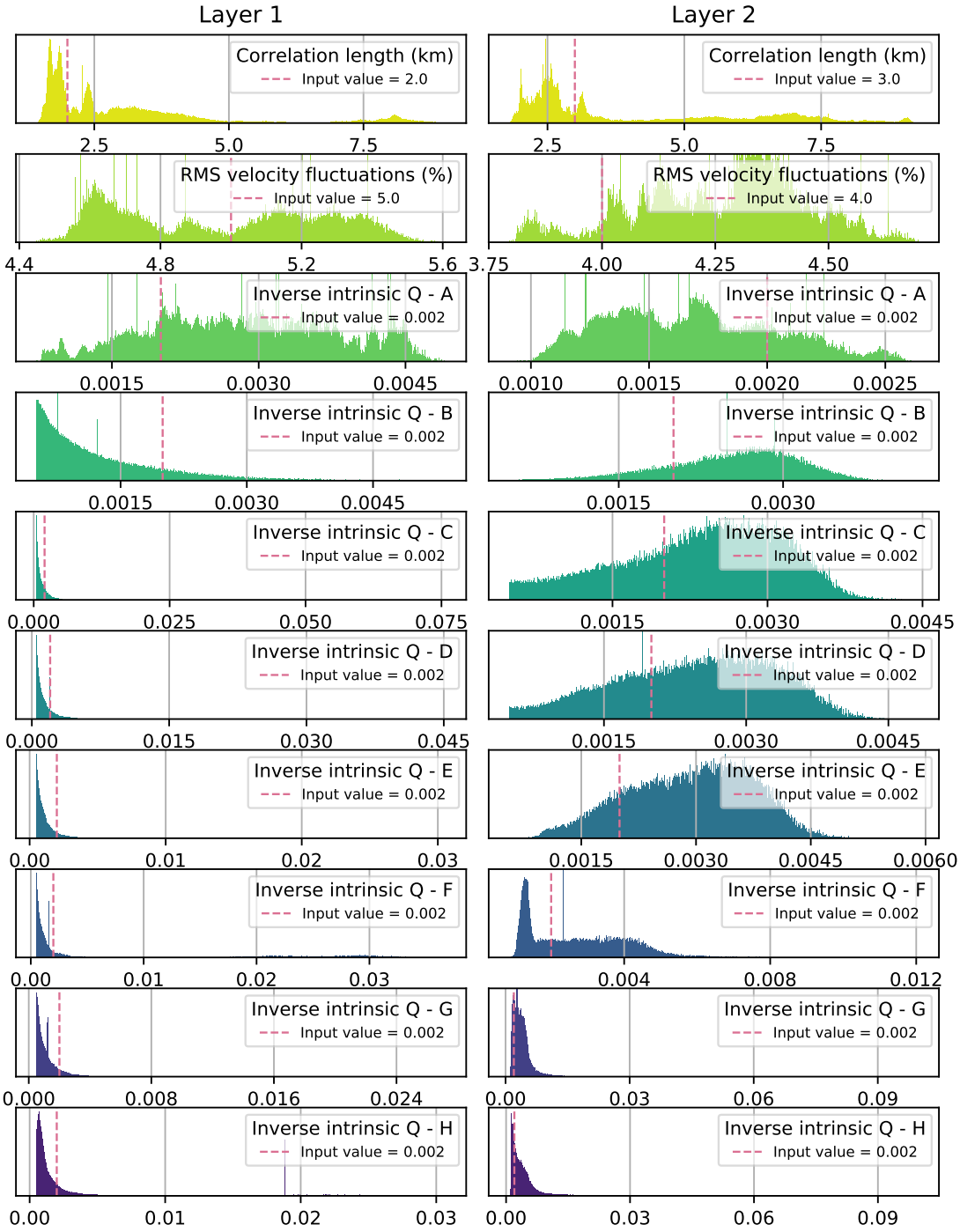

Figure 4.16: Results from a synthetic test for the version of the E-EFMD with free Q_i frequency variation. Histograms for the two scattering parameters (a and ε, rows (a) and (b) respectively) and the instrinsic quality factor for all eight frequency bands from Table 2.3 (rows (d)–(j)). Left and right columns represent results for layers 1 and 2 of the model respectively. Black dashed lines and shaded areas represent the input parameter values and 5–95 percentile range (PR) respectively.

ensure all suitable values are included within the Q_{i0} prior, I widened it to include values up to 3000 ($Q_{i0}^{-1} \sim 0.00033$). Table 4.3 and Figures 4.17 to 4.20 summarise the

results from these inversions.

In the crust, the posterior PDFs for both scattering parameters and all three arrays show clear peaks, even if for ASAR and WRA they also present significant tails on both sides of the maximum (panels b–d in Figs. 4.18 and 4.19). These tails result in the widening of 5–95 PRs for these arrays. For the correlation length, they range from $\sim$ 1–24 km and $\sim$ 1–21 km for ASAR and WRA, in contrast with the much narrower PDF for PSA, which extends from 0.6–2.5 km (Table 4.3). Correlation length modes in this layer are approximately 0.8 for PSA and ASAR, and 1.2 km for WRA. RMS velocity fluctuations PDFs are also much wider for ASAR and WRA than for PSA, spanning $\sim$82 and $\sim$65 % of the permitted range for these arrays, as opposed to only $\sim$15% for PSA. Modes suggest the strongest and weakest crustal velocity fluctuations correspond to WRA ($\sim$3.7%) and PSA ($\sim$2.5%) respectively (Figs. 4.19 and 4.17). PDFs for the inverse intrinsic Q at 1 Hz in the crust for ASAR and WRA also show some similarities (panels f and g in Figs. 4.18 and 4.19). Both of them have a clear but very narrow maximum at very low values ($\sim$0.02) and long tails that extend throughout most of the entire permitted range ($4 \cdot 10^{-4} \leq Q_{i0}^{-1} \leq 0.1$). For PSA, the Q_{i0}^{-1} PDF in this layer (panel f in Fig. 4.17) shows a similarly clear and narrow maximum at $\sim$0.004 and a short, low amplitude tail similar to that obtained for WRA. 5–95 PRs for $Q_{i0_{L1}}^{-1}$ are narrow for PSA and WRA ($\sim$5% and $\sim$ 17% of the permitted range for this parameter, respectively) and wider for ASAR ($\sim$ 39%) (Table 4.3). The uncertainty in the determination of Q_{i0}^{-1} appears to be more accentuated for WRA and ASAR than for PSA, for which the PDF maximum is much sharper compared to the width of the tail (Fig. 4.18). PDFs for the power law exponent, α, clearly favour higher values for ASAR and WRA, with modes being $\sim$0.98 in both cases, while for PSA there is a wide but distinct maximum at $\sim$0.32 (panels e and g in Figs. 4.17, 4.18 and 4.19). 5–95 PRs for this parameter are wide for all three arrays as well, with the ones for PSA and ASAR, ranging from 0.11–0.91 and 0.18–0.98 ($\sim$80% of the permitted range for α)

Table 4.3: Summary of the results of the inversions of the data from the Australian arrays (PSA, ASAR and WRA) described in Chapter 3.

Array name	Layer number	Corr. length (a)		RMS vel. fluct. (ε)		Inv. int. Q at 1 Hz (Q_{i0}^{-1})		Freq. power of Q_i (α)		Maximum L
		5 – 95 PR (km)	AR (%)	5 – 95 PR (%)	AR (%)	5 – 95 PR	AR (%)	5 – 95 PR	AR (%)	
PSA	1	0.6–2.5	38.5	2.3–3.9	38.5	0.0005–0.005	40.9	0.07–0.91	39.6	-6.4
	2	3–32		0.1–3.0		0.0004–0.0016				
PSA	1	0.7–1.4	39.3	2.3–3.1	36.4	0.0006–0.0026	41.4	–	–	-6.9
Fixed α	2	3–32		0.1–2.8		0.0005–0.0014				
ASAR	1	1–24	39.9	1.4–9.6	39.2	0.0004–0.0396	40.0	0.16–0.98	38.3	-0.95
	2	2–31		0.3–9.4		0.0004–0.0222				
ASAR	1	1–24	39.8	1.0–9.4	38.5	0.0005–0.0254	41.3	–	–	0.94
Fixed α	2	1–31		0.4–9.6		0.0005–0.0092				
WRA	1	1–21	37.5	2.7–9.2	40.7	0.0004–0.0182	38.6	0.09–0.97	40.0	-0.61
	2	1–32		0.2–8.1		0.0004–0.0046				
WRA	1	1–22	39.5	2.3–8.3	41.0	0.0005–0.0056	37.9	–	–	-0.81
Fixed α	2	1–32		0.2–6.8		0.0005–0.003				

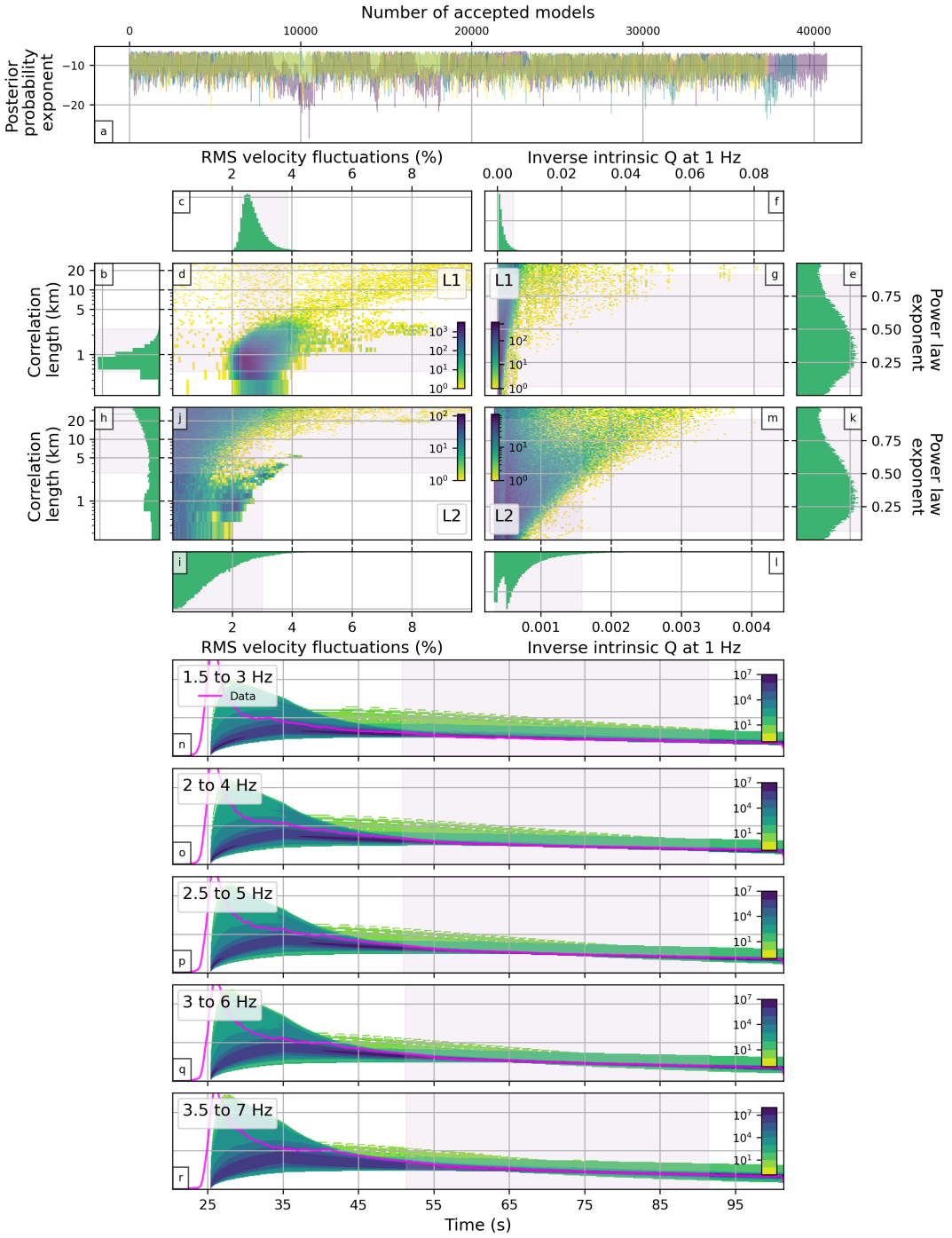

Figure 4.17: Summary of the results obtained from the E-EFMD algorithm for PSA. Panels content is as in Fig. 4.3 , with the addition of panels h–k for parameters in the lithospheric mantle.

respectively, being narrower than for WRA (∼84% of the allowed range). Since this parameter was not allowed to take different values for each layer, these values apply to both the crust and lithospheric mantle.

Scattering parameters PDFs in the lithospheric mantle for ASAR and WRA (panels

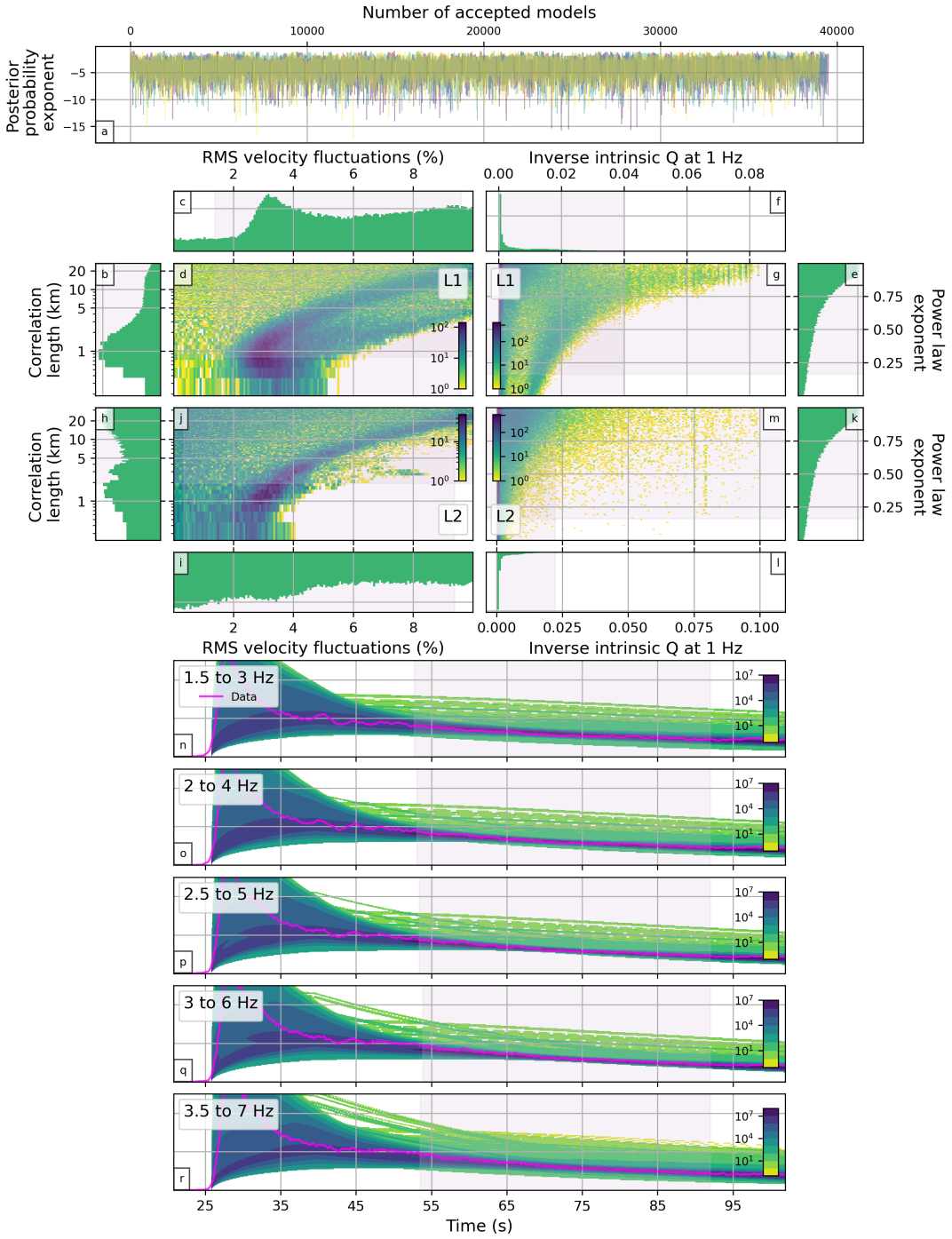

Figure 4.18: Same as Fig. 4.17 but for ASAR.

h–j in Figs. 4.18 and 4.19) also share many features. Correlation lengths for these arrays show both a wide maximum at ∼1.5 km (ASAR) and ∼1.4 km (WRA), but also a high amplitude tail or secondary maximum towards higher values (> 15 km), even if this characteristic is more pronounced for ASAR than it is for WRA. For PSA, there is a clear preference for high (> 10 km) a values in this layer (panels h–j in

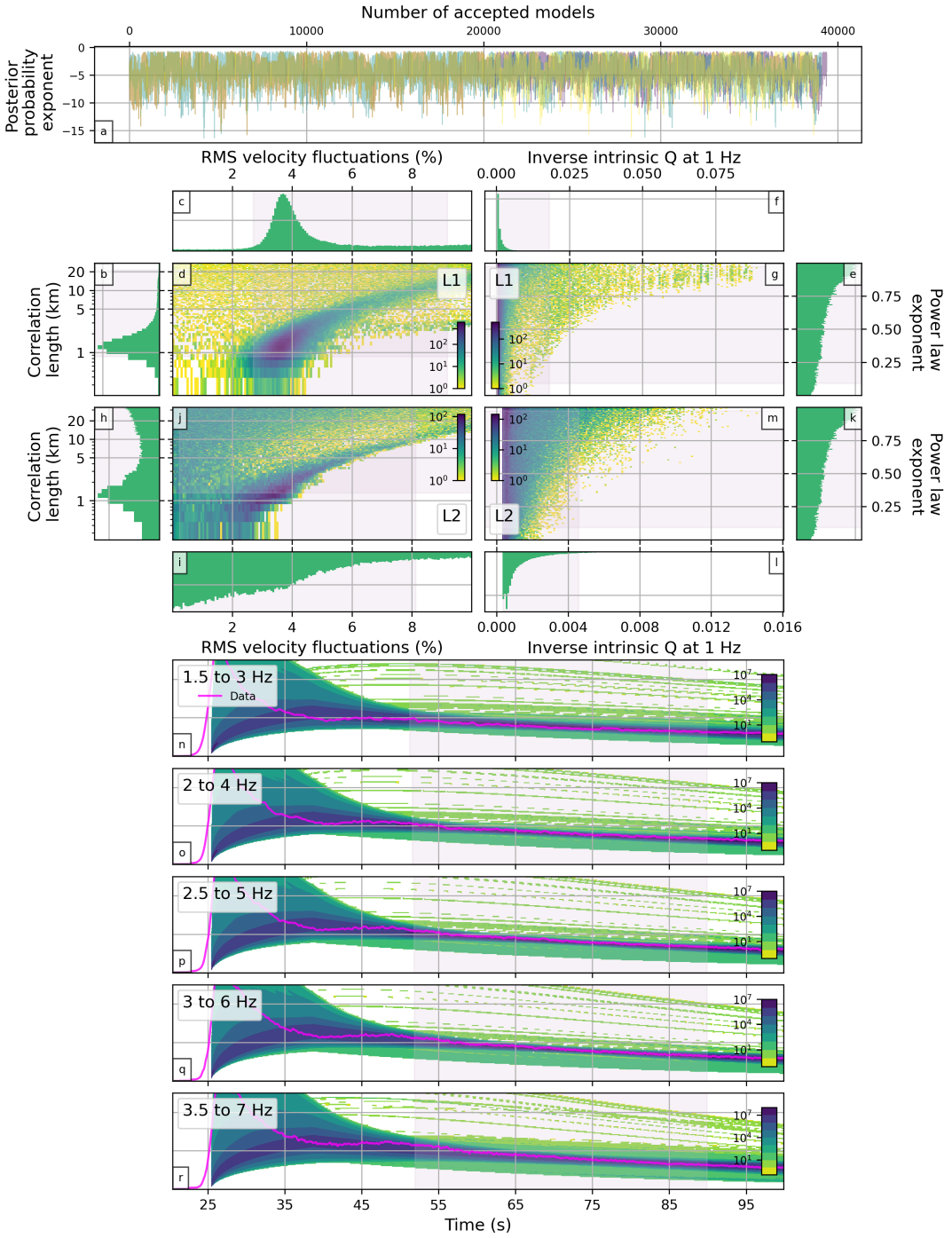

Figure 4.19: Same as Fig. 4.17 but for WRA.

Fig. 4.17). Correlation length 5–95 PRs are similarly broad for all three arrays, with widths ranging from 29–30 km (Table 4.3). RMS velocity fluctuations PDFs for ASAR and WRA suggest medium to low values ($< 5\%$) are slightly favoured (Figs. 4.18 and 4.19). However, the largest density of models occurs around a secondary maximum at $\sim$4% both for ASAR and WRA, which corresponds to the broad maxima observed at

a ∼1 km. For PSA (Fig. 4.17), this secondary maximum is absent from the velocity fluctuations, whose PDF shows a very distinct preference for very low (< 3%) values. 5–95 PRs for this parameter are much narrower for PSA than they are for ASAR or WRA, with values ranging from 0.1–3.0 %, 0.3–9.4 % and 0.2–8.1 % respectively. These PDFs point to scattering parameters for this layer being largely unconstrained for all three arrays. Q_{i0}^{-1} PDFs are similar for all arrays in this layer again (panel l or m in Figs. 4.17, 4.18 and 4.19). For ASAR, it contains a sharp and clear maximum at ∼0.01, followed by a low amplitude tail that extends up to ∼ 0.0004 (Fig. 4.18). For WRA, the PDF shows a preference for low or extremely low values of the parameter, but suggests any value below 0.004 would be equally likely to produce the observed codas (Fig. 4.19). In the case of PSA, the algorithm also favours low and extremely low values ($Q_{i0_{L2}}^{-1} < 0.0015$, Fig. 4.17). The PDF shows two, similarly high, narrow peaks for values <∼ 0.0005. 5–95 PRs are narrow for all three arrays, spanning from $4{\cdot}10^{-4}$–$2{\cdot}10^{-3}$, $4{\cdot}10^{-4}$–0.02 and $4{\cdot}10^{-4}$–$5{\cdot}10^{-3}$ for PSA, ASAR and WRA respectively (Table 4.3).

The results described above are analogous to my EFMD results (Section 3.3) and suggest that the scattering and intrinsic attenuation structures beneath ASAR and WRA are similar to each other and different to that for PSA. PDFs for crustal Q_{i0} and α for these arrays (Table 4.3) show similar patterns for these arrays which would be indicative of strong intrinsic attenuation in this layer and a linear frequency dependence of Q_i. Correlation length and RMS velocity fluctuations PDFs (Table 4.3) point to heterogeneities beneath ASAR being similar than those below WRA, since the overall effect of lower correlation lengths for ASAR may be compensated by higher ε values for WRA. The crust beneath PSA appear to be less heterogeneous and attenuating than its ASAR or WRA counterparts, while there is still significant scattering and attenuation taking place within the layer. The lithospheric mantle, on the other hand, seems to be mostly homogeneous and non-attenuating, as evidenced by extremely low velocity fluctuations and high correlation lengths and intrinsic Q at 1 Hz values (Table 4.3). The broad width of the 5–95 PRs for most parameters and all arrays is indicative of non-unique solutions and complex trade-offs between the parameters. Reducing the number of parameters in the inversion to six by inverting the data with my alternative implementation of the E-EFMD for fixed α does not help reduce the non-uniqueness of the parameters. Figures A84, A85 and A86, in Appendix A.4, as well as Table 4.3, show that, as observed in Section 4.1.2, removing this parameter from the inversion has very limited effects on the results for the scattering parameters or the intrinsic quality factor.

These results are in good agreement with the EFM/EFMD structure (Tables 3.2 and 3.3), which suggested ASAR and PSA had the most and least scattering and attenuating structures respectively, as well as with the tectonic history and setting for

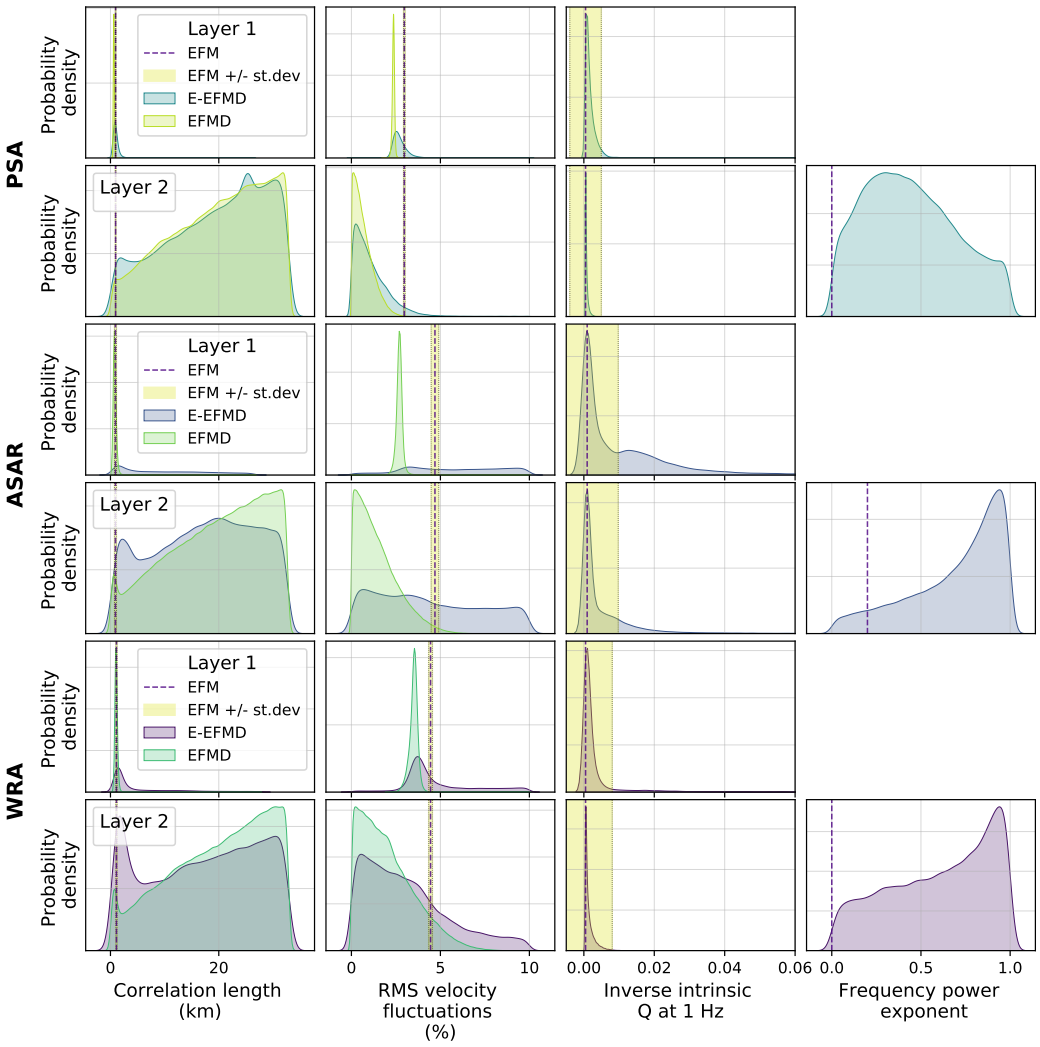

Figure 4.20: Comparison of the posterior PDFs obtained from the E-EFMD and EFMD algorithms for the three Australian arrays analysed here (PSA, ASAR and WRA). Please note that no negative values of the intrinsic quality factor were allowed in the inversion. The apparent negative values shown in this figure are a result of the smoothing applied to rough distribution edges by the plotting function.

these arrays (Sections 3.2 and 3.3.2). Figure 4.20 compares the PDFs obtained for a and ε from the EFMD and E-EFMD, as well as the numerical results from the EFM for all three arrays. For Q_{i0}^{-1} and α, the figure contains the PDFs obtained from the E-EFMD, as well as the results for the single-layer considered in the EFM. In the crust, the correlation length PDFs from the EFMD and all three arrays show a very sharp peak which corresponds to the EFM value for this parameter (0.9 km for PSA and ASAR and 1.1 km for WRA, Table 3.2). The E-EFMD PDFs also present clear maxima around this value of the parameter. In the lithospheric mantle, the shapes of the a PDFs from the EFMD and E-EFMD have similar widths and amplitudes, with matching, though broader, maxima at approximately the EFM value for ASAR and WRA. The agreement between the EFMD and E-EFMD PDFs for the RMS velocity

fluctuations, in both layers of the model, is also very good. E-EFMD PDFs for this parameter and all arrays are wider than those from the EFMD, but in all cases they have clear maxima roughly centered around the same values. In this case, the concordance with EFM results is not as good, with values from this method being higher than the modes from both methods for all arrays. In the case of the inverse intrinsic quality factor at 1 Hz and the frequency power for Q_i, I can only compare the PDFs from the E-EFMD with the EFM estimation for a single layer. The agreement between these results is worse for α than for the other parameters, probably because of the difficulty in obtaining it as an independent parameter from the EFM inversion (Section 2.1.1). EFMD and E-EFMD results for Q_{i0}^{-1}, however, appear to be in good agreement for all arrays and model layers.

However, if I take samples of the posterior PDFs obtained from the E-EFMD for these arrays, as I did for my E-EFMD synthetic tests, it is clear that these results show the same strong trade offs shown in my synthetic tests (Section 4.1.2), especially for ASAR and WRA. Figures 4.21, 4.22 and 4.23 are analogous to Figs. 4.9 or 4.10, and contain the loglikelihoods and parameter values for the highest likelihood models obtained from the inversion for each array. For ASAR, this figure shows very strong variability of the scattering parameters in both layers, which is also clear in panels d and j in Fig. 4.18. For PSA and WRA, this effect is more obvious for the bottom layer of the model (Figs. 4.17 and 4.21), even if it is also present in the crust for both arrays. For PSA and WRA, $Q_{i0_{L1}}^{-1}$ presents more variability than $Q_{i0_{L2}}^{-1}$ (panels A–4 and B–4, Figs. 4.21 and 4.23), but while for PSA its values tend to mostly remain below 0.01 (which I defined as "low" Q_{i0} in the previous section), for WRA it takes values which extend up to 0.1. For ASAR, both $Q_{i0_{L1}}^{-1}$ and $Q_{i0_{L2}}^{-1}$ take values throughout the entire parameter space and are often found within the extremely strong attenuation range ($0.02 < Q_{i0}^{-1} < 0.1$, panels A–4 and B–4 of Fig. 4.22). Physically, these parameter combinations would indicate that the crust and lithospheric mantle beneath ASAR would both be extremely attenuating and only weakly heterogeneous. Crustal scattering beneath WRA and PSA would be stronger than for ASAR, but the lithospheres beneath PSA would be less attenuating than that under WRA. My thorough analysis of the E-EFMD sensitivity (Section 4.1.1), as well as my synthetic tests (Section 4.1.2), allow me to relate these extreme variations in the scattering parameters to the behaviour of the intrinsic quality factor, instead of interpreting them as the effect of the physical structure beneath the arrays on the recorded wavefields. Therefore, and despite the good agreement between my EFMD and E-EFMD results for PSA, ASAR and WRA, any interpretations derived from these results should be cautiously done.

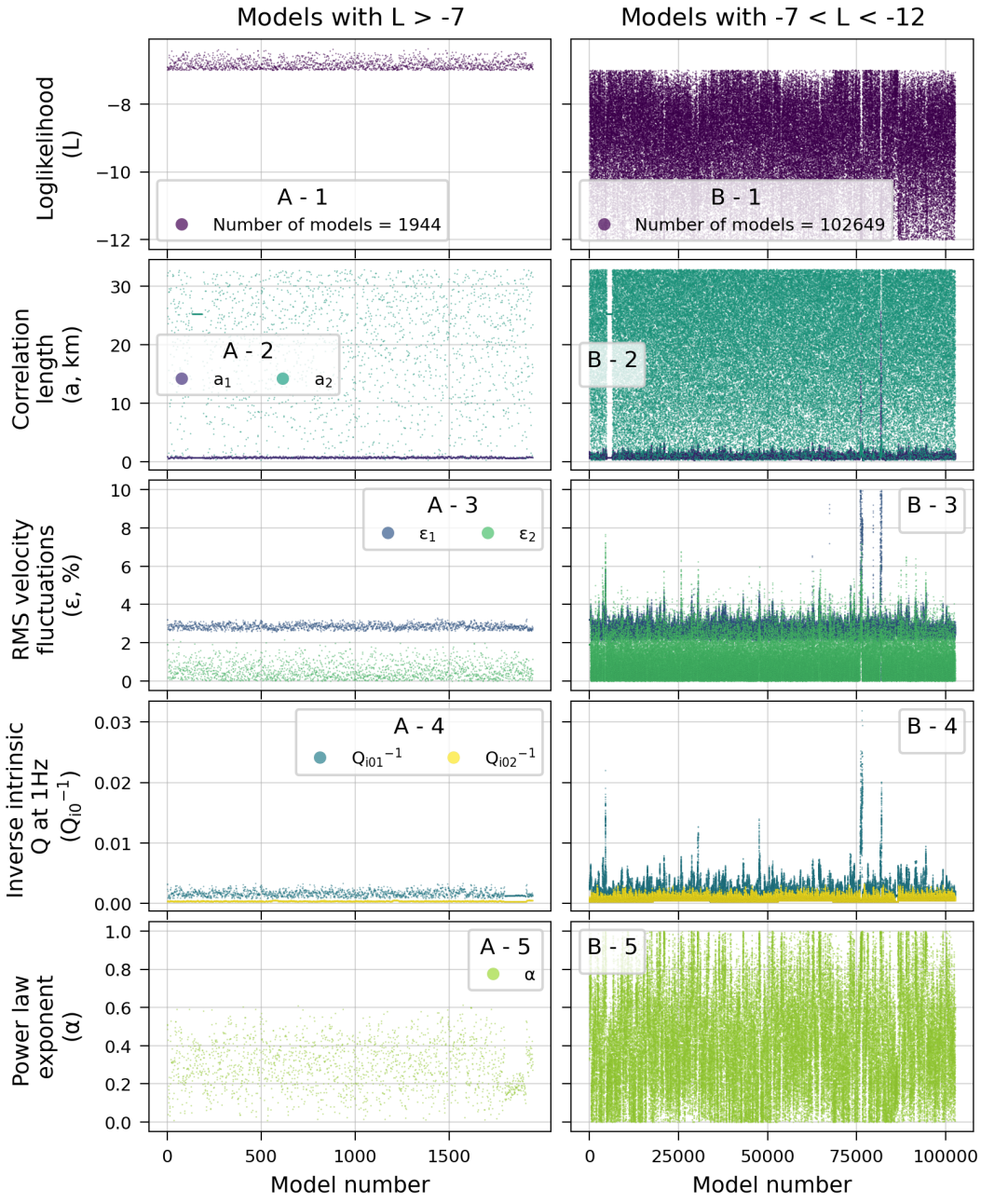

Figure 4.21: Samples of the E-EFMD results for PSA shown in Fig. 4.17. Panels A1–A5 contain the loglikelihood (L), correlation length (a), RMS velocity fluctuation (ε), inverse intrinsic quality factor at 1 Hz (Q_{i0}^{-1} and power law exponent (α) for all models with $L > -1$, as well as the input parameter values in each case. Panels B1–B5 have the same content, but for models with $-1 > L > -5$. Loglikelihood thresholds for each column were adjusted to the maximum value present in the ensemble of accepted models, so this figure could be compared with those obtained for my synthetic tests in Section 4.1.2.

4.3 Conclusions

The E-EFMD results I present in this chapter illustrate, in great detail, the behaviour of the algorithm both within synthetic tests and real data inversions. My tests in Section

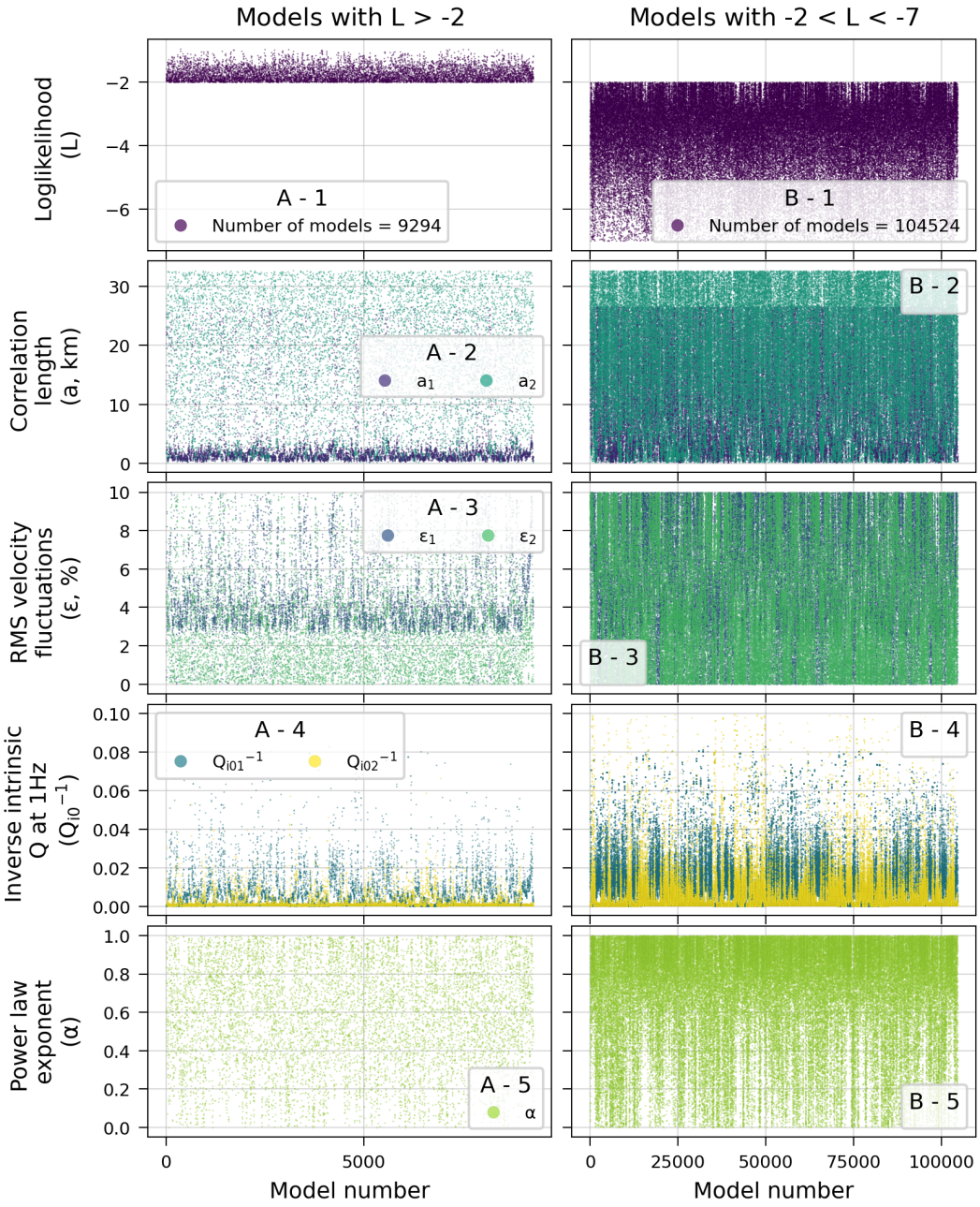

Figure 4.22: Same as Fig. 4.21, but for ASAR.

4.1.2 demonstrate that the non-uniqueness of the solutions already observed for the EFMD in Section 2.1.3 is increased in the E-EFMD, not necessarily because of the larger number of free parameters, but mostly due to the complex trade-offs between them. For most of the synthetic tests I carried out in Section 4.1.2, the algorithm converged to two independent sets of solutions, many of those showing a great degree of interchangeability between $Q_{i0_{L1}}^{-1}$ and $Q_{i0_{L2}}^{-1}$ and wide variability of the scattering parameters and α. However, cases for which the algorithm found a single, preferred

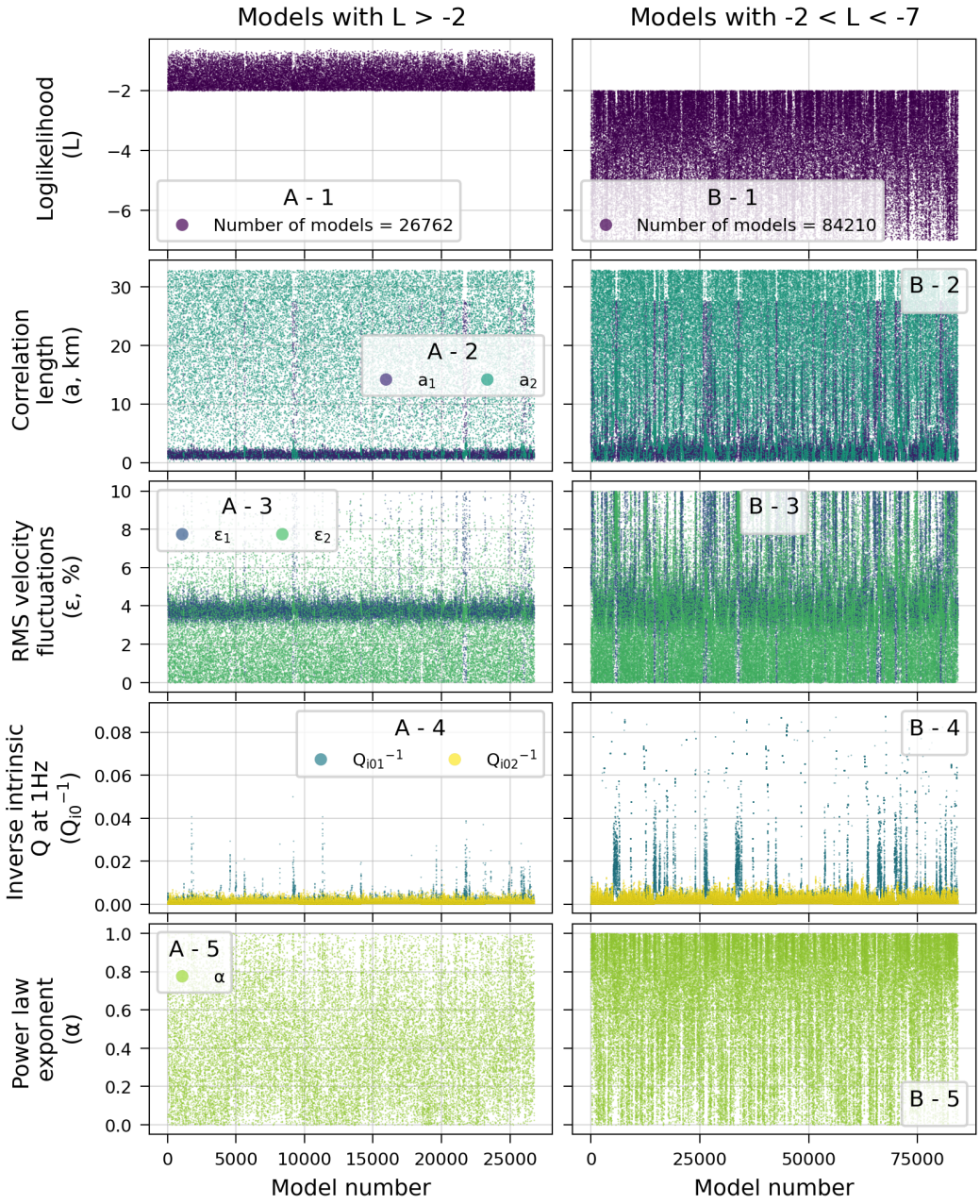

Figure 4.23: Same as Fig. 4.21, but for WRA.

combination of parameters, also often showed the wide 5–95 PRs that tend to appear with non-unique solutions. My sensitivity analysis (Section 4.1.1) clearly show the effect of each parameter on the calculated synthetic envelopes, with ε and a mainly regulating initial coda amplitudes and Q_{i0}^{-1} and α controlling the decay rate. This separation in the effect of the parameters is the main cause of the lack of uniqueness in the E-EFMD solutions and the poor recovery scores obtained for some of them (Fig. 4.5), since it controls the complex parameter interactions observed in my synthetic tests results. The performance of the E-EFMD algorithm was generally worse (e.g. got lower

parameter and global S) for cases with strong or extremely strong intrinsic attenuation ($Q_{i0}^{-1} \geq 0.01$) in any model layer. These parameter combinations usually result in lower coda amplitudes and a clear dominance of the intrinsic quality factor in the inversion results that also affects the accurate recovery of the rest of the parameters. However, as pointed out in Section 4.1.1, the large difference in thickness between the model layers used in all my synthetic tests could be partly behind some of these behaviours. My inversion results for some IMS stations in Chapter 5 show that 1- or 2-layer models for lithospheres less than 70 km thick with crusts up to 4 times thicker than the lithospheric mantle beneath them do present the same wide posterior PDFs and non-uniqueness than the results in this chapter. Further testing of the E-EFMD should, therefore, thoroughly investigate the effect of the model layering on the obtained results, so it could be determined whether the extreme non-uniqueness and interchangeability of $Q_{i0_{L1}}^{-1}$ and $Q_{i0_{L2}}^{-1}$ are common issues within the E-EFMD framework or artifacts caused by the (predetermined) layering of the models. Potentially interesting experiments to help reduce the non-uniqueness of the solutions could be adding prior information about the parameters from other studies (instead of assuming uniform prior distributions), including S-wave codas in the datasets or trying to estimate ε, within an uncertainty range, from the initial coda amplitudes using the EFM and then running the standard inversion shown here for the rest of the parameters. Considering the trade-offs between Q_{i0}^{-1} and ε observed in this chapter, such modifications of the E-EFMD could potentially help avoiding the convergence to more than one combination of parameters.

E-EFMD results for the Australian arrays, shown in Section 4.2, show the same parameter variability and lack of uniqueness, especially for ASAR and WRA. The clear association between this increased uncertainty and fluctuations in Q_{i0}^{-1} makes unique interpretations of the physical scattering and attenuation structure beneath the stations difficult. However, since the model layering for PSA, ASAR and WRA is similar to each other and to the one used in my synthetic tests, it is possible that these results are also affected by the difference in layer thicknesses mentioned before. More testing in this regard is again recommended, but in the meantime, it is reasonable to expect the issues reported here to arise again in future data inversions, especially when working with low coda amplitudes.

In summary, the results I present here reveal the usefulness of the added information about the attenuation parameters provided by the E-EFMD. The frequency dependence of Q_{i0} is generally poorly understood, as are its variation with depth or interaction and trade-offs with the scattering parameters, all of which the E-EFMD brings some insight into. These results also demonstrate that any attempts at characterizing seismic scattering and attenuation should always be done in a Bayesian fashion, with Section 4.1.2 confirming that any non-Bayesian approach to this problem will necessarily lead to incomplete solutions at best, and utterly inaccurate at worst. In recent years, studies

such as Cormier and Sanborn (2019), Prieto et al. (2009), Del Pezzo et al. (2016), Ogiso (2019) or Takeuchi (2016) , have addressed the challenge of separating the effects of intrinsic and scattering attenuation and simultaneously estimating the parameters that characterize them, as well as the trade-offs between them. In most cases, these studies have focused on the S-wave codas from local and regional earthquakes, but similar, strong, frequency-dependent trade-offs can also be expected for the scattering and attenuation of teleseismic P-waves. The results shown in this thesis show the ability of Bayesian inference to provide great insight into these complex relationships between parameters.

My figures sampling the posterior PDFs for all synthetic tests (e.g. Figs. 4.9 and 4.10) show that highest likelihood or best fitting models do not always match the input parameter values, despite achieving excellent fits to the synthetic envelopes. In addition to this, Fig. 4.14 further proves that P-wave codas can be achieved through a wide variety of parameter combinations, by showing that models that represent radically different scattering and attenuation settings can produce identical coda envelopes, which the E-EFMD algorithm will not be able to differentiate. Most inversions using grid search approaches use them to obtain a single, best fitting, parameter combination to match the observed data. However, the detailed information about the parameter space, trade offs, uncertainty and uniqueness of the solutions that my Bayesian inference results contain highlight that it is not possible to ensure that a maximum likelihood model would be truly and uniquely representative of the heterogeneity and attenuation structure beneath the seismic station or array.

Chapter 5

Lithospheric scattering and intrinsic attenuation beneath International Monitoring System stations

On 16 July 1945, the first-ever nuclear bomb was detonated at the Alamogordo Test Range, New Mexico. In the following decades, over 2000 atmospheric, underground and underwater nuclear tests were conducted worldwide (Fig. 5.1), in a race to develop increasingly more powerful weapons. As a consequence, vast amounts of radioactive materials were dispersed into the atmosphere and deposited all around the globe (e.g. Maceira et al., 2017). These increased radioactivity levels posed a danger to human lives and health and the environment (e.g. Upton, 1962), while the growing tensions of the arms race threatened political stability and peace. In 1962 alone, 175 nuclear weapons were detonated, most of them in the atmosphere (Fig. 5.1), which lead to the highest global level of environmental radioactivity ever being measured the following year (e.g. Maceira et al., 2017). In 1963, the opening for signature of the Partial or Limited Test-Ban Treaty (PTBT/LTBT) meant nuclear explosions in the atmosphere, underwater and in space were banned. This change helped reduce the amount of radioactivity present in the environment (e.g. Maceira et al., 2017), but did not prevent further underground testing (Fig. 5.1). This purpose was only achieved in September 1996 with the Comprehensive Test-Ban Treaty (CTBT, 1996), after decades of negotiations. The text of the CTBT establishes that "(...)the most effective way to achieve an end to nuclear testing is through the conclusion of a universal and internationally and effectively verifiable comprehensive nuclear test-ban treaty (...)" (CTBT, 1996). As per this treaty, signatory countries agree to refrain from causing or encouraging nuclear

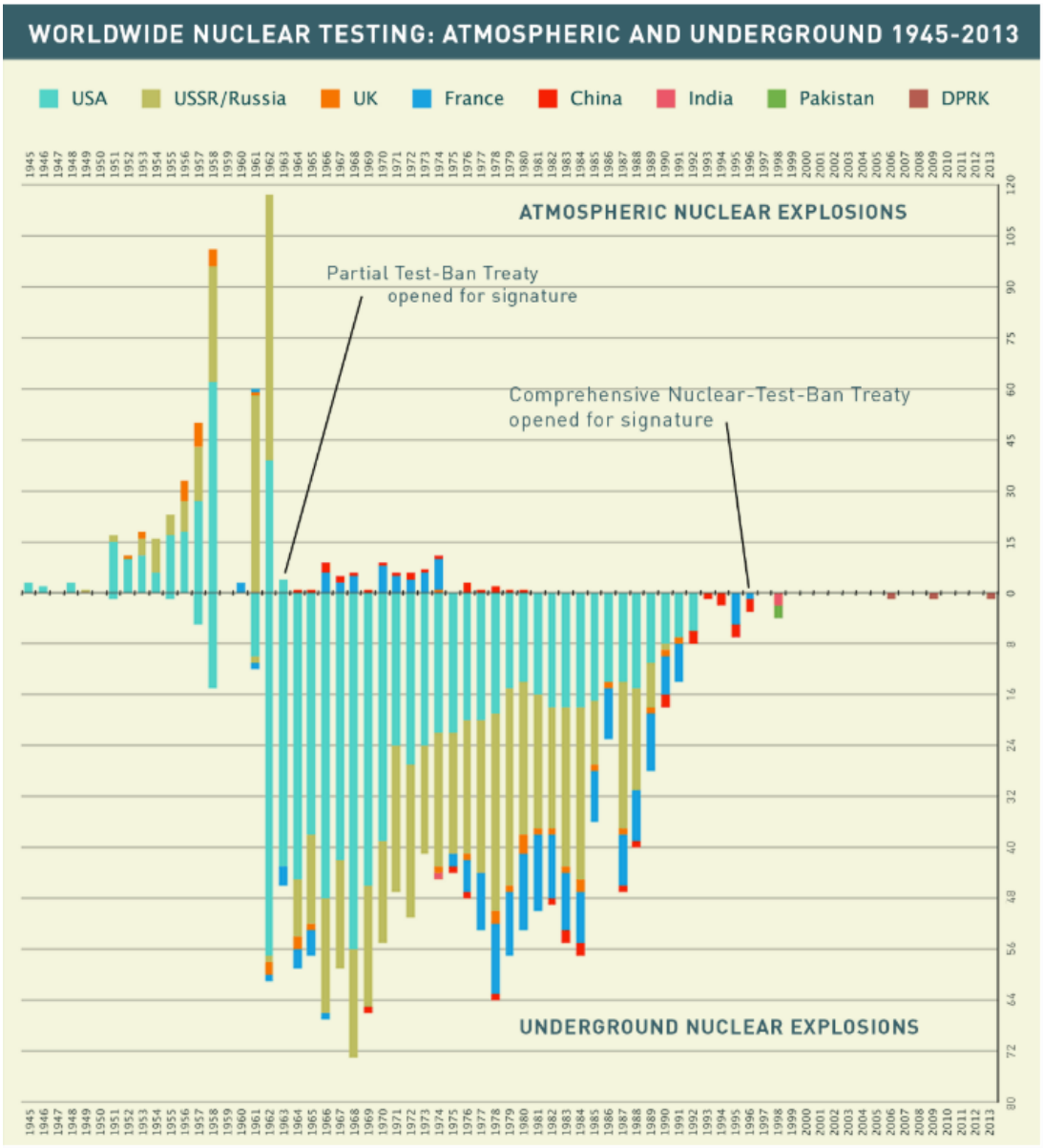

Figure 5.1: Number of atmospheric and underground nuclear explosions carried out in the 1945-2013 period, together with the dates the Partial Test-Ban and Comprehensive Nuclear-Test-Ban Treaties opened for signature (from ctbto.org)

explosions and to not to carry out nuclear tests of any kind anywhere on Earth, thus effectively contributing to putting an end to nuclear testing. As of March 2022, 185 countries have signed the CTBT, 172 of which have also ratified it (ctbto.org), but the treaty cannot enter into force until all of the countries that initially participated in its elaboration sign and ratify it. Eight of these countries (which include India, China, Israel and the United States of America) have yet to sign and/or ratify the CTBT, but in the meantime, signatory countries have adopted a *de facto* moratorium on nuclear testing, with only 10 nuclear tests having been carried out since 1996 (Fig. 5.1). Currently, the Comprehensive Nuclear-Test-Ban Treaty Organisation (CTBTO),

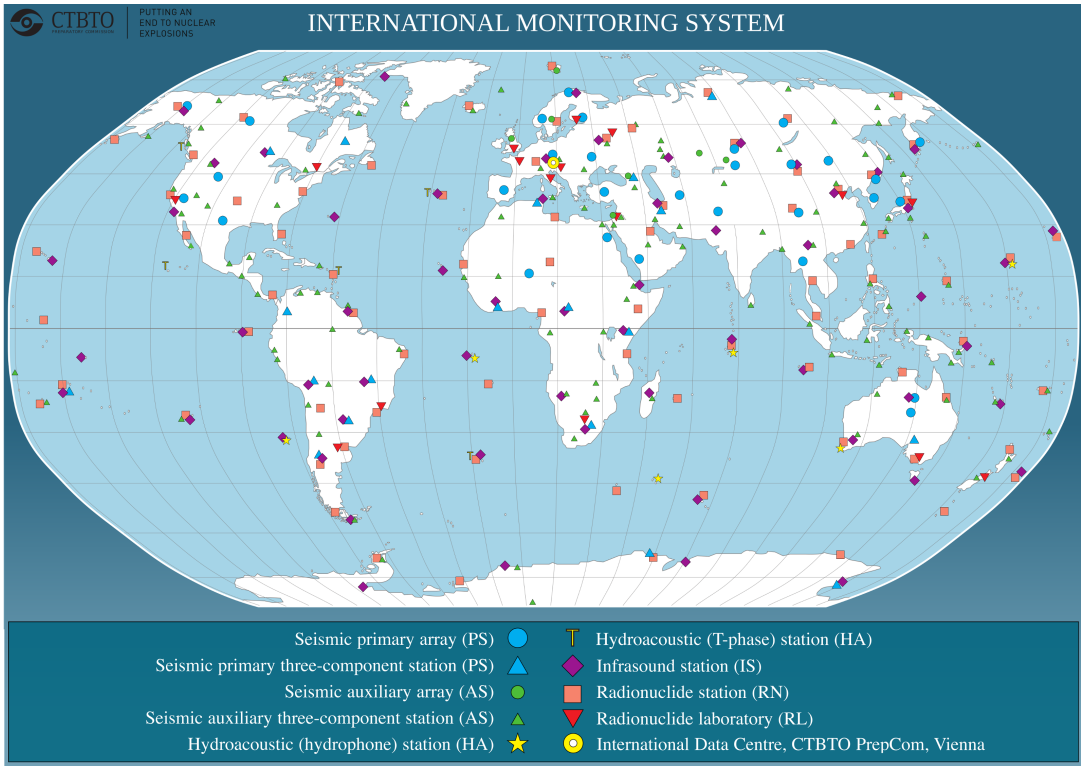

Figure 5.2: Map of the International Monitoring System (IMS), which includes primary and auxiliary seismic arrays and stations, as well as hydroacoustic, infrasound and radionuclide stations. The International Data Center is also marked on the map, as well as radionuclide laboratories. (Modified from ctbto.org)

based in Vienna, is in charge of the promotion of the Treaty and the building of its verification regime.

The International Monitoring System (IMS) is a worldwide instrument network built by the CTBTO to ensure compliance with the CTBT (Fig. 5.2). Four core technologies and 321 monitoring stations within this network help ensure that no nuclear test or explosion goes unnoticed (e.g. Maceira et al., 2017; Kalinowski and Mialle, 2021). The seismic, infrasound and hydroacoustic instruments of the IMS can detect and identify explosive atmospheric, underground or underwater events, even at large distances (e.g. Koper et al., 2001; Heyburn et al., 2020; Pilger et al., 2021; Zhang and Wen, 2013). However, these waveform-based techniques cannot discriminate whether the origin of an explosion is chemical or nuclear, and radionuclide sensors and laboratories are normally required for confirmation. The continuous data recorded at all the IMS monitoring stations is automatically sent to the International Data Center (IDC) in Vienna, where most of the analysis is carried out (e.g. Maceira et al., 2017; Kalinowski and Mialle, 2021). In recent years, the IMS has successfully detected the six underground nuclear tests carried out by the Democratic People's Republic of Korea in the 2006–2017 period (e.g. Zhang and Wen, 2013; Carluccio et al., 2014; De Meutter et al., 2018; Myers et al., 2018; Gibbons et al., 2018). In addition to this, IMS data has also been widely

used outside the nuclear monitoring community, with applications ranging from Earth structure investigations (e.g. Rost et al., 2006; Liu et al., 2019; Jerkins et al., 2020; González Álvarez et al., 2021) to the study of drifting icebergs (Evers et al., 2013), submarine volcanism (Metz et al., 2018), tracking whales (Le Bras et al., 2016) or investigate accidental explosions (Savage and Helmberger, 2001; Heyburn et al., 2020; Pilger et al., 2021).

The solid Earth is monitored by the IMS using 50 primary and 120 auxiliary seismic stations deployed all around the world (Fig. 5.2), such as the Alice Springs (ASAR) and Warramunga (WRA) seismic arrays, described in Chapter 3. These seismic stations are key tools for the detection, discrimination and characterization of underground explosions, since hydroacoustic and infrasound sensors may not record them as clearly. Once a potential explosive event has been detected by IMS seismic stations, discrimination between different event types at teleseismic distances is usually done by taking the m_b: M_S ratio, where m_b and M_S are the network-averaged body-wave and surface-wave magnitudes respectively (e.g. Selby et al., 2012). Another calculation of critical importance within the nuclear monitoring community is that of explosion yield, which is usually obtained from either body-wave or surface-waves magnitudes (e.g. Douglas, 2013; Maceira et al., 2017; Zhao et al., 2017). The computation of these magnitudes require accurate amplitude measurements (e.g. Douglas, 2013; Stein and Wysession, 2005), while also taking into account that signal amplitudes are affected by path effects like scattering or intrinsic attenuation. These effects are implicitly accounted for in the empirical formulas used for magnitude and/or yield calculations (e.g. Peacock et al., 2017; Maceira et al., 2017; Douglas, 2013), and inverse filter approaches are also sometimes used to correct signals from intrinsic attenuation (e.g. Douglas, 2013). Having accurate characterizations of the attenuation structure immediately beneath the stations, as well as its effects on the recorded signals, is therefore essential.

In this chapter, I apply the approach described in Chapter 4 to the characterization of the lithospheric scattering and attenuation structures beneath seismic stations part of four primary seismic arrays (Eielson (ILAR), Lajitas (TXAR), Pinedale (PDAR), Yellowknife (YKA)) and a primary seismic station (Boshof (BOSA)) of the International Monitoring System.

5.1 Data

With the aim of analysing the scattering and attenuation structure in as wide a variety of regions and tectonic settings as possible, I used the FDSN Client tool from Obspy (Beyreuther et al., 2010) and the IRIS DMS to explore event catalogues for over twenty primary and secondary IMS seismic arrays and stations (Boshof (BOSA), Brasilia (BDFB), Borovoye (BVAR), Chiang Mai (CMAR), Villa Florida (CPUP)),

Eskdalemuir (EKA), Geress (GERES), Eielson (ILAR), Kilima Mbogo (KMBO), Kurchatov (KURK), La Paz (LPAZ), Matsushiro (MJAR), Makanchi (MKAR), Nevada (NVAR), Pinedale (PDAR), Paso Flores (PLCA), Songino (SONM), Torodi (TORD), Lajitas (TXAR), Ussuriysk (USRK) and Yellowknife (YKA)).

Data selection and processing for this chapter is analogous to the one described in Chapter 2 and applied in Chapters 3 and 4 (Section 2.1.4). For each array or station of interest, I built a catalogue of deep events (source depths greater than 200 km) with moment magnitudes between 5–7 and 30 – 80 degrees epicentral distances to the array centers or stations. To maximise the number of available events included in these catalogues, their start dates vary between arrays or stations and include all available earthquakes from then until the end of 2020. Arrays or stations for which 3-component data were not available through the FDSN Client tool from Obspy (Beyreuther et al., 2010) or the IRIS DMS, had less than 60 suitable events in their catalogue (See Section 3.1.1) with a signal-to-noise ratio above 5 at least for three of the D–H frequency bands from Table 2.3 or had missing, wrong or incomplete instrument response information, were excluded from the analysis. These specifications resulted in many stations not being suitable for the analysis, either because of their short operating time or the lack of suitable events in the right distance range and/or problems with the instrument response information. Table 5.1 contains the number of good quality events (as defined in Section 2.1.4) used in this study for ILAR, PDAR, TXAR, YKA and BOSA and the frequency bands listed on Table 2.3, as well as the time period of their event catalogues. Panel a in Fig. 5.3 shows the epicenters, magnitudes and depths of all events for each array included in this study, as well as their LITHO1.0 P-wave background velocity models (Pasyanos et al., 2014) and Moho and lithosphere-asthenosphere boundaries in panel b.

Table 5.1: Number of events with good quality (SNR > 5) traces for each array/station and frequency band and start and end of the seismic catalogue built for each one of them. Arrays for which the number of events and traces coincide had only one available 3-component station.

		Number of events per frequency band								Catalogue	
		0.5–1 Hz	0.75–1.5 Hz	1–2 Hz	1.5–3 Hz	2–4 Hz	2.5–5 Hz	3–6 Hz	3.5–7 Hz	Start date	End date
ILAR	Events	96	121	122	123	117	106	93	83	2012	2020
	Traces										
PDAR	Events	120	110	100	124	118	113	96	85	1990	2020
	Traces										
TXAR	Events	11	33	68	72	79	68	62	54	1990	2020
	Traces	17	57	122	129	141	119	103	83		
YKA	Events	81	103	117	146	154	149	119	91	1990	2020
	Traces	113	140	161	198	223	211	151	125		
BOSA	Events	17	22	27	46	67	67	62	53	1995	2020
	Traces										

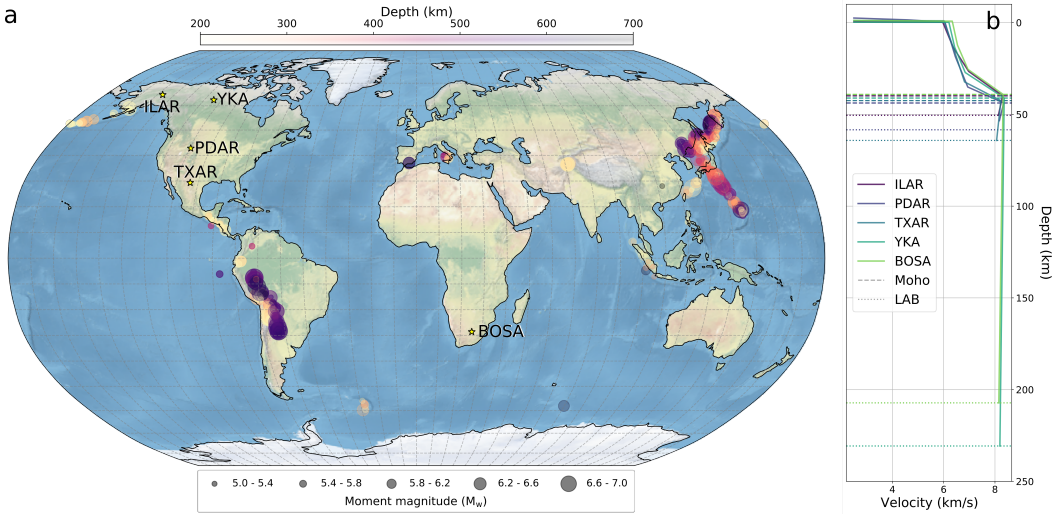

Figure 5.3: (a) Catalogue of seismic events included in this study for all IMS stations with available 3-component data and 60 or more good quality events for at least three of the D–H frequency bands from Table 2.3. Marker colors represent event depths, while sizes indicate their magnitudes. (b) LITHO 1.0 P-wave velocity model for each of the stations (solid lines), as well as their Moho and LAB depths (dashed and dotted lines, respectively), also obtained from the LITHO 1.0 model (Pasyanos et al., 2014).

5.2 Results and discussion

5.2.1 Extended Depth-Dependent Energy Flux Model results

I applied the E-EFMD approach described in Chapter 4 to the datasets described in Section 5.1 for ILAR, PDAR, TXAR, YKA and BOSA. I ran inversions using both 1- and 2-layer models, as well as the E-EFMD version for fixed frequency dependence coefficient (α). In all cases, I initially ran 3 parallel Markov chains per inversion, each 10 million iterations long. In some cases I considered the maximum loglikelihood (L) reached at the ends of these chains was too low ($L < -100$) and continued them for another 10 million iterations to increase the chances of getting out of local maxima and improve fits to the data. However, L values remained stable, without any significant increases, so I decided not to continue them any further and chose not to extend chains for similar tested models either, such as the two 1-layer models I tested for PDAR (Table 5.2). As described in Section 4.1.2, results from the 3 Markov chains were thinned by taking only 1 in every 100 accepted models and combined into a single, final ensemble of models. In all cases, I used only frequency bands D–H from Table 2.3, since my previous inversions using the EFM/EFMD and E-EFMD show that it is probably not possible to simultaneously fit all of them, at least with this kind of approach. Table 5.2 summarises my results.

In Chapter 3, I inverted the data for ASAR and PSA using the EFM/EFMD approach and a 1-layer model. In both cases, my results showed that the large thickness of the layer (200 km) prevents diffusion out of it, therefore generating codas with very

large amplitudes that failed to fit the data (Section 3.3). However, given the different tectonic settings and lithospheric structures of the IMS stations studied in this chapter (Section 5.1), I decided to attempt to invert the normalised coda envelopes datasets for those stations with thinner lithospheres (PDAR, ILAR and TXAR, Fig. 5.3) using the E-EFMD and a 1-layer model. Figure 5.4 and Figures A87 and A88, placed in Appendix A.5 to avoid repetition, summarise the results from these inversions. All three sets of results show that, while fits are improved, compared to those for the AU arrays in Figs. 3.10 and 3.9, synthetic codas produced by this model are still too high and simple to successfully fit the input data. PDFs for the scattering parameters, shown in panels b–d in these figures, suggest a non-scattering lithosphere, with more likely correlation lengths above 20 km and RMS velocity fluctuations close to 0%. Still, initial coda amplitudes produced by these models are still too high to match those observed in my data envelopes. PDFs for the intrinsic attenuation parameters are narrow and Gaussian, or approximately Gaussian in all cases, but the coda decay rates they produce still fail to match those of the data. These poor fits lead to the maximum loglikelihoods reached in these inversions being all very low ($L < -200$ for ILAR and $L < -10^4$ for PDAR and TXAR, Table 5.2), which means the scattering and attenuation parameters obtained from them are not at all reliable. As a final test of the 1-layer model, I decided to check whether a model that includes only the crust was capable of improving the fits to the data. Such a model would make diffusion out of the layer easier, thus reducing the amount of energy present within it and generating lower coda amplitudes. Figure A89 contains the results for this case and PDAR. Synthetic coda levels obtained for this crustal model are only barely lower than for the lithospheric case, which results in a slightly higher maximum L of $\sim -15 \cdot 10^3$, as opposed to $\sim -16 \cdot 10^3$). Posterior PDFs for all parameters remain largely unchanged, but the poor fits still deem them unreliable and I decided not to test the 1-layer model for the remaining stations studied here.

The results of my E-EFMD inversions for all stations and the 2-layer model are summarised in Figures 5.5, 5.6, 5.7, 5.8 and 5.9. Except for ILAR (Fig. 5.5), fits to the data are generally poor, as evidenced by the extremely low loglikelihood ($L < 10^3$) values obtained for the rest of the arrays (Table 5.2). As discussed below, this is likely related to the E-EFMD algorithm not being capable of simultaneously fit the input envelopes for all frequency bands, and to complex coda behaviours. All five inversions yield nearly identical results for the scattering parameters in both layers of the model, despite large differences in the lithospheric structure and tectonic history of the regions the stations are located on. Correlation lengths vary widely (the 5–95 PRs start at 3–4 km and extend up to 25 km or higher, Table 5.2), but there is a clear preference for values above 10 km throughout the lithosphere. PDFs for the RMS velocity fluctuations vary more in width from one station to another, and between

Table 5.2: Summary of the results of the E-EFMD inversions of the data from ILAR, PDAR, TXAR, YKA and BOSA using 1- or 2-layer models. I tested both the implementation that includes α as a free parameter and the alternative version with fixed α. 234. For PDAR, I also tested two different 1-layer models, one for which the layer encompasses the entire lithosphere, and another that only takes the crust into account (marked with a * below). For information on the layering of the models, see Figure 5.3.

Array or station	Freq. bands	Iterations per chain	Layer number	Corr. length (a)		RMS vel. flucts. (ε)		Inv. int. Q at 1 Hz (Q_{i0}^{-1})		Freq. power of Q_i (α)		Maximum L
				5 – 95 PR (km)	AR (%)	5 – 95 PR (%)	AR (%)	5 – 95 PR	AR (%)	5 – 95 PR	AR (%)	
ILAR	D–H	$2 \cdot 10^6$	1	3–27	81.6	0.0–0.8	38.2	0.0035–0.0050	38.4	0.63–0.83	39.6	-230
	D–H	10^6	1 2	3–26 4–32	62.7	0.1–3.0 0.3–8.7	40.2	0.0005–0.0009 0.0218–0.0437	40.9	0.22–0.46	40.5	-8.4
	D–H	10^6	1 2	4–26 5–32	63.7	0.1–2.6 0.3–9.0	34.8	0.0006–0.0012 0.0240–0.0495	41.5	0.5*	–	-10.3
TXAR	D–H	$2 \cdot 10^6$	1	4–28	81.2	0.0–0.1	39.6	0.0015–0.0017	38.8	0.04–0.11	38.9	$-97{\cdot}10^3$
	D–H	$2 \cdot 10^6$	1 2	3–26 4–32	81.2	0.0–0.1 0.0–0.3	41.1	$5.0 \cdot 10^{-4}$–$5.005 \cdot 10^{-4}$ 0.0918–0.0921	36.8	0.99–1.0	37.1	$-26{\cdot}10^3$
	D–H	10^6	1 2	3–26 4–32	81.2	0.0–0.1 0.0–0.3	43.7	$5.0 \cdot 10^{-4}$–$5.002 \cdot 10^{-4}$ 0.0309–0.0310	39.3	0.5*	–	$-30{\cdot}10^3$
	C–E	10^6	1 2	4–26 6–32	63.4	0.09–3 0.3–8	36.5	0.0005–0.0008 0.0018–0.0059	38.3	0.003–0.1	36.2	-24.0
	F–H	10^6	1 2	3–26 4–32	81.2	0.001–0.05 0.01–0.2	38.0	$5.0 \cdot 10^{-4}$–$5.003 \cdot 10^{-4}$ 0.0918–0.09199	41.3	1.0–1.0	41.1	$-43 \cdot 10^3$
	D–F	10^6	1 2	4–26 6–32	63.5	0.05–1.8 0.3–8	37.5	0.0005–0.0006 0.0049–0.0079	36.1	0.001–0.07	40.0	-52
	G–H	10^6	1 2	3–26 4–32	81.2	0.001–0.05 0.005–0.2	39.0	$5.0 \cdot 10^{-4}$–$5.003 \cdot 10^{-4}$ 0.0919–0.0921	41.9	1.0–1.0	42.4	$-64 \cdot 10^3$
PDAR	D–H	$2 \cdot 10^6$	1	4–26	81.2	0.0–0.2	40.5	0.0091–0.0108	41.2	0.9–1.0	39.9	$-16{\cdot}10^3$
	D–H	10^6	1*	3–25	81.3	0.0–0.2	39.3	0.0069–0.0092	38.3	0.82–0.99	43.1	$-15{\cdot}10^3$
	D–H	$2 \cdot 10^6$	1 2	3–25 4–32	80.7	0.0–0.1 0.0–1.0	38.3	$5.0 \cdot 10^{-4}$–$5.02 \cdot 10^{-4}$ 0.0995–0.1	40.5	0.21–0.22	38.5	$-4{\cdot}10^3$
YKA	D–H	$2 \cdot 10^6$	1 2	3–26 4–32	81.9	0.0–0.1 0.0–0.1	40.3	0.0021–0.0023 0.00059–0.00063	39.8	0.14–0.20	42.3	$-14{\cdot}10^3$
BOSA	D–H	$2 \cdot 10^6$	1 2	4–26 4–32	80.7	0.02–0.8 0.01–0.3	40.8	0.0075–0.0080 $5 \cdot 10^{-4}$–$5.2 \cdot 10^{-4}$	40.6	0.50–0.53	39.1	-10^3

different layers of the model. Distributions for this parameter in the crust are generally narrower than those for the lithospheric mantle, but in all cases the algorithm tends to favour values close to 0%, indicating that scattering beneath these stations is generally very weak. PDFs for the intrinsic attenuation parameters are more variable. For ILAR, they are approximately gaussian for α and $Q_{i0_{L2}}$. In all cases, they present clear, single, maxima centered around $\sim 5 \cdot 10^{-4}$ and ~ 30 for Q_{i0} in layers 1 and 2 of the model respectively, and ~ 0.34 for α, which point to intrinsic attenuation being weak in the crust and extremely strong in the lithospheric mantle. For PDAR, TXAR, YKA and BOSA, these PDFs are much narrower, almost spike-like for TXAR and PDAR and approximately gaussian for YKA and BOSA. In all cases, these PDFs show long but extremely low amplitude tails, such as those in panels e–g and k–m in Figs. 5.6 or 5.7. As for ILAR, results for PDAR and TXAR also point to weak and extremely strong intrinsic attenuation in the crust and lithospheric mantle respectively. Crustal attenuation beneath YKA and BOSA appears to be medium for the former and low for the latter, and weak in the lithospheric mantle in both cases.

As mentioned above, fits to the data envelopes are poor for all stations but ILAR. Panels n–r in Figs. 5.6, 5.7, 5.8 and 5.9 show that, while the algorithm appears to be capable of successfully fitting the data envelopes for some frequency bands, doing so for

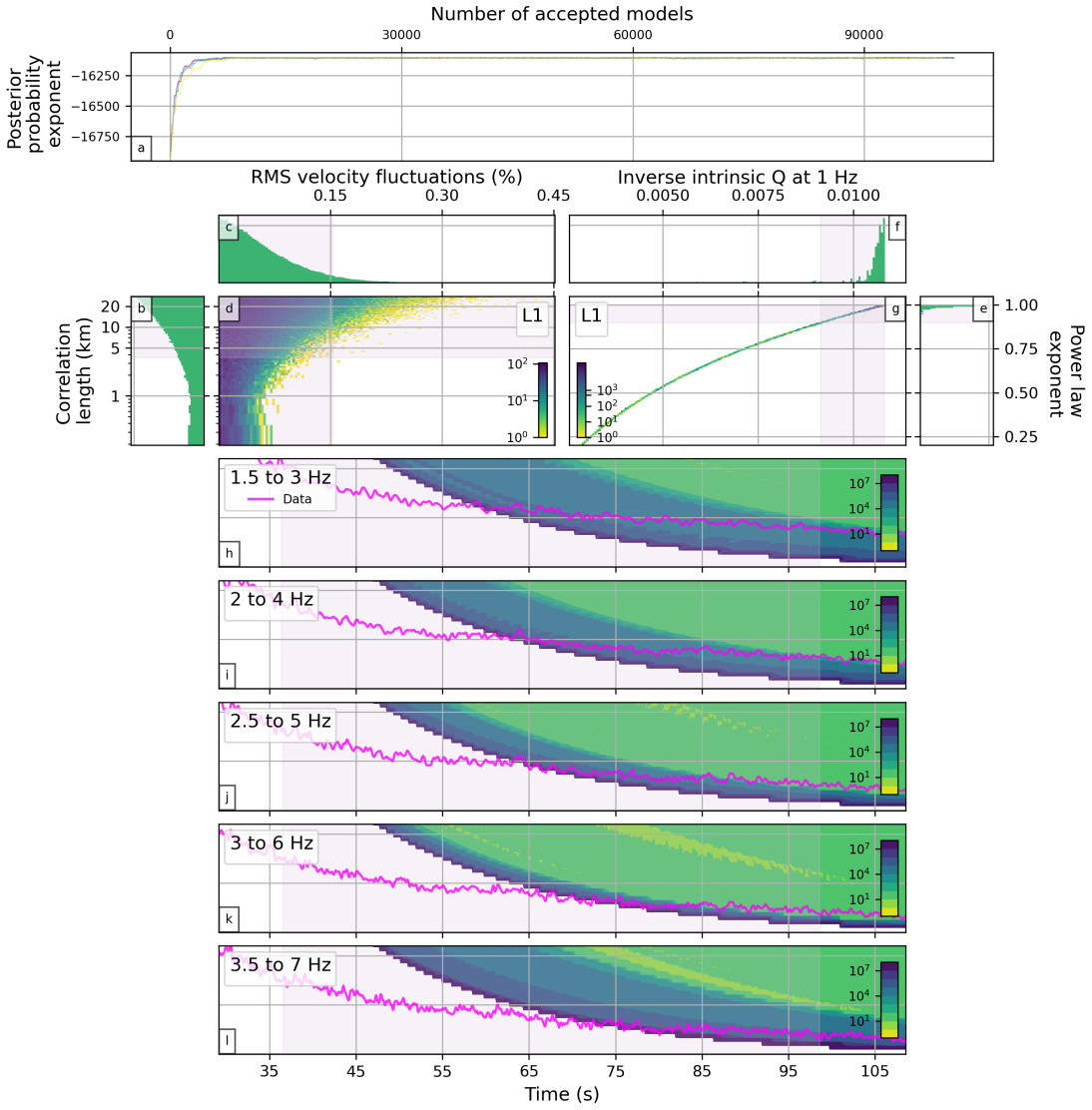

Figure 5.4: Summary of the results obtained from the E-EFMD algorithm for PDAR and a 1-layer model that encompasses the entire lithosphere. Panels content is as in Fig. 4.3.

all five bands simultaneously remains a challenge with these datasets. In particular, for TXAR, panels n–r in Fig. 5.7 suggest that the E-EFMD algorithm might be capable of fitting frequency bands G–H (Table 2.3) while failing to do so for frequency bands D–F. To test whether such a division of the frequency bands into smaller groups could help improve the inversion results for this station, I decided to run individual inversions for frequency bands D–F, G–H, C–E and F–H. Instead of the full inversion, I ran a single MCMC for each case, the results of which are represented in Figs. A90, A91, A92 and A93, in Appendix A.5, and included in Table 5.2. Loglikelihoods from these inversions indicate that fitting frequency bands C–E or D–F alone significantly improves the results, compared to the full E-EFMD inversion results for TXAR shown in Fig. 5.7. Inversions of frequency band groups F–H and G–H, on the other hand, yield

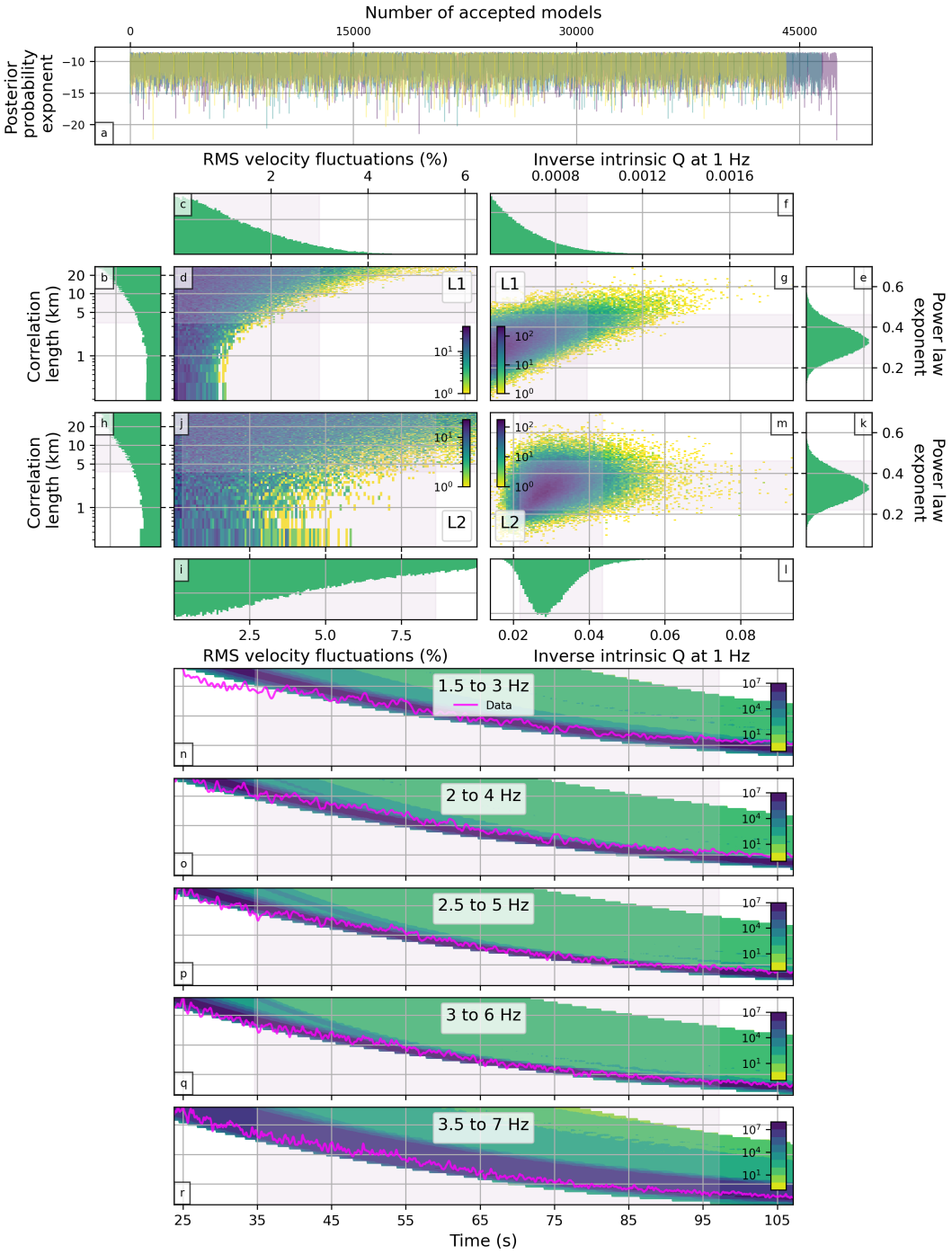

Figure 5.5: Summary of the results obtained from the E-EFMD algorithm for ILAR and a 2-layer model, with layers 1 and 2 representing the crust and lithospheric mantle, respectively. Panel content is as in Fig. A24.

much lower L values ($L < -10^4$, as opposed to $L > -60$ for bands C–E and D–F), suggesting a much worse performance of the algorithm for these cases. PDFs for the scattering parameters are all similar to each other and to those obtained for the rest of the inversions shown in Figs. 5.5–5.9. Distributions for the attenuation parameters

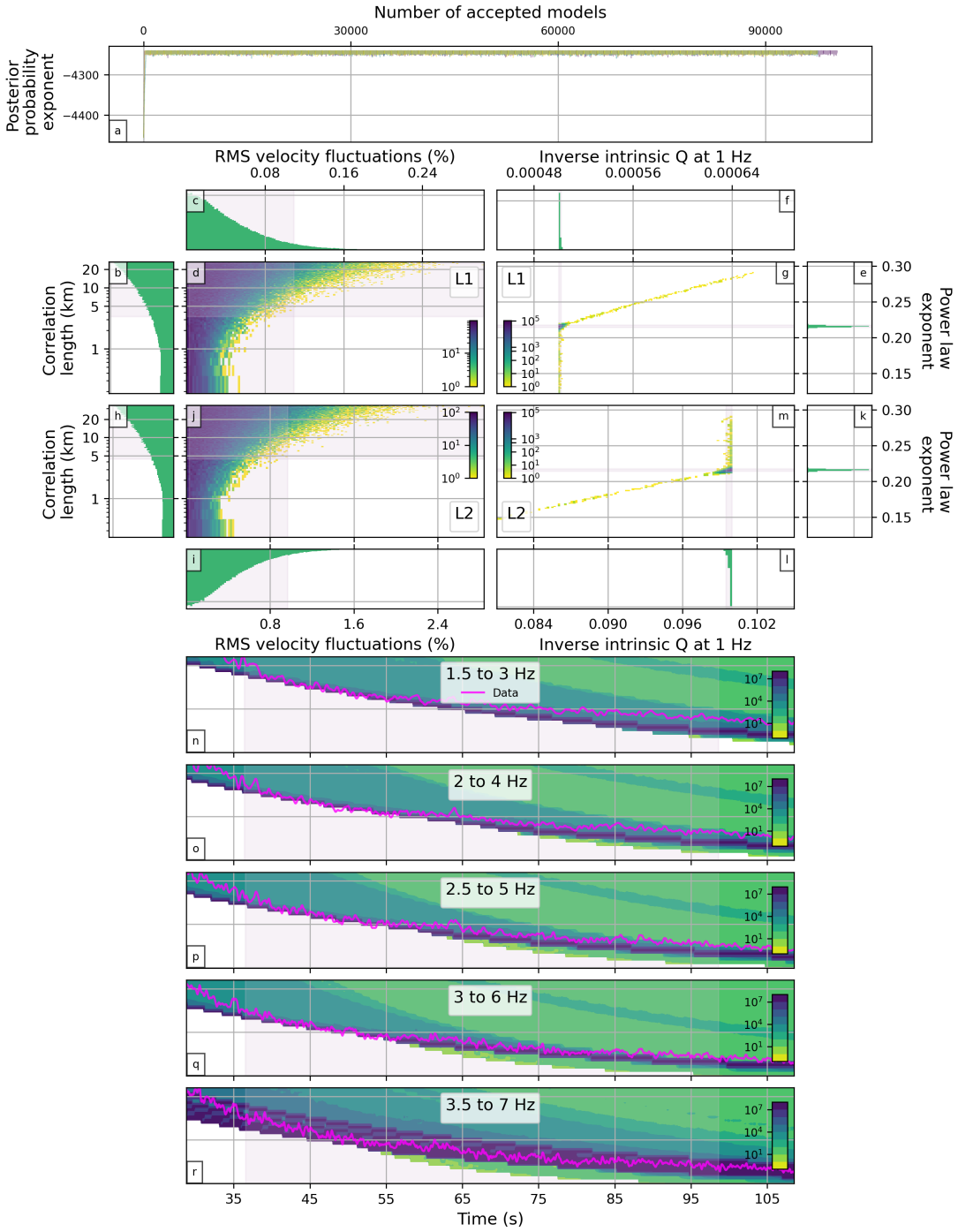

Figure 5.6: As Fig. 5.5 but for PDAR.

are more variable, with those for inversions of the C–D and D–F groups being more gaussian, while those for groups F–H and G–H are much narrower, almost spike-like, with long but low tails for α in layer 2 of the model.

Despite the E-EFMD incorporating the adaptive step size algorithm described in Section 4.1, all of the inversions shown in Table 5.2 have very high acceptance rates

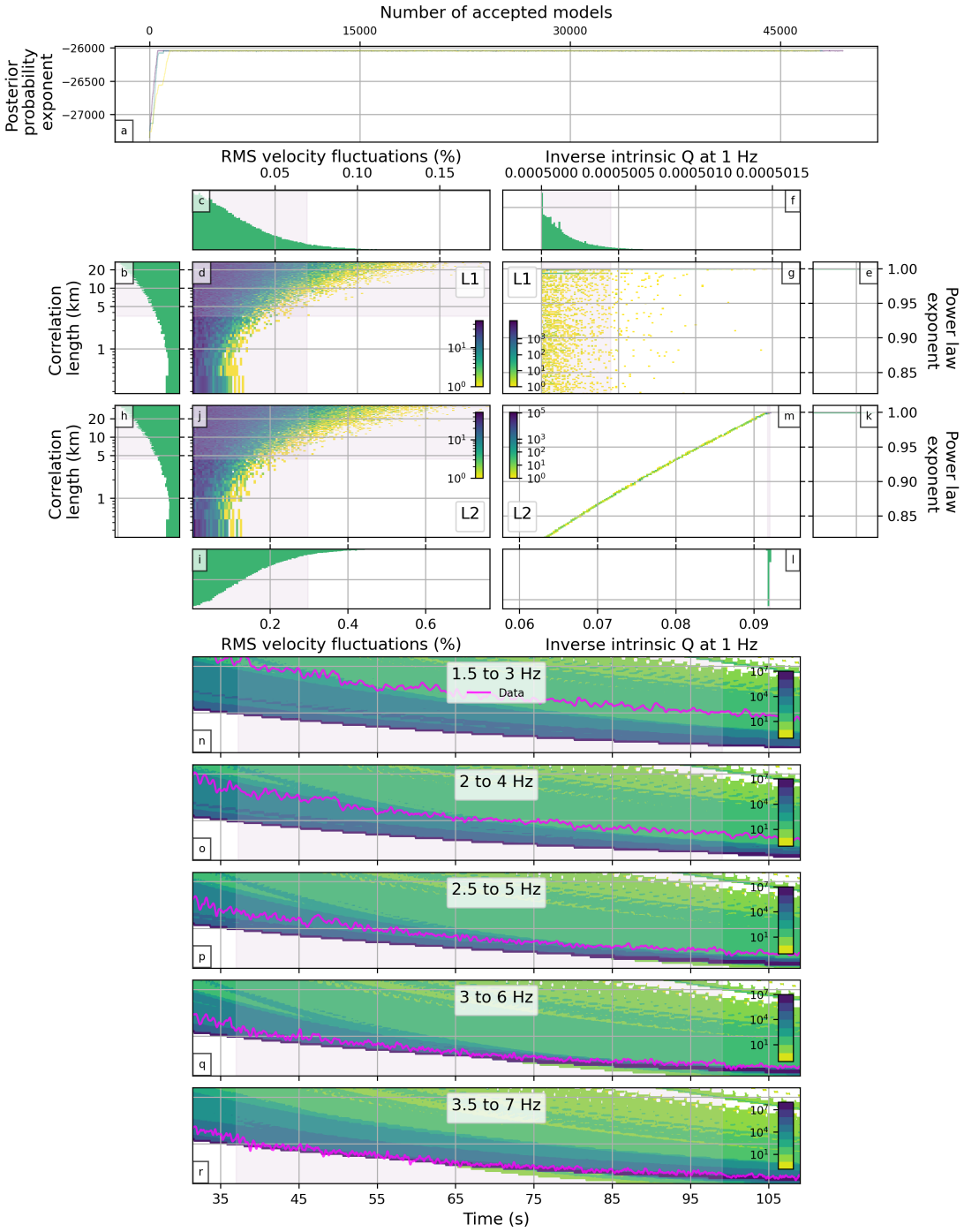

Figure 5.7: As Fig. 5.5 but for TXAR.

for the correlation length (up to $\sim$ 82%). This result is caused by the small effect this parameter has on the synthetic envelopes and the inability of the E-EFMD to simultaneously fit the data for all frequency bands for these arrays. A high acceptance rate will cause the step size for the parameter to increase, but large step sizes may results in the parameter value being outside the allowed range (defined by a_{min}–a_{max}

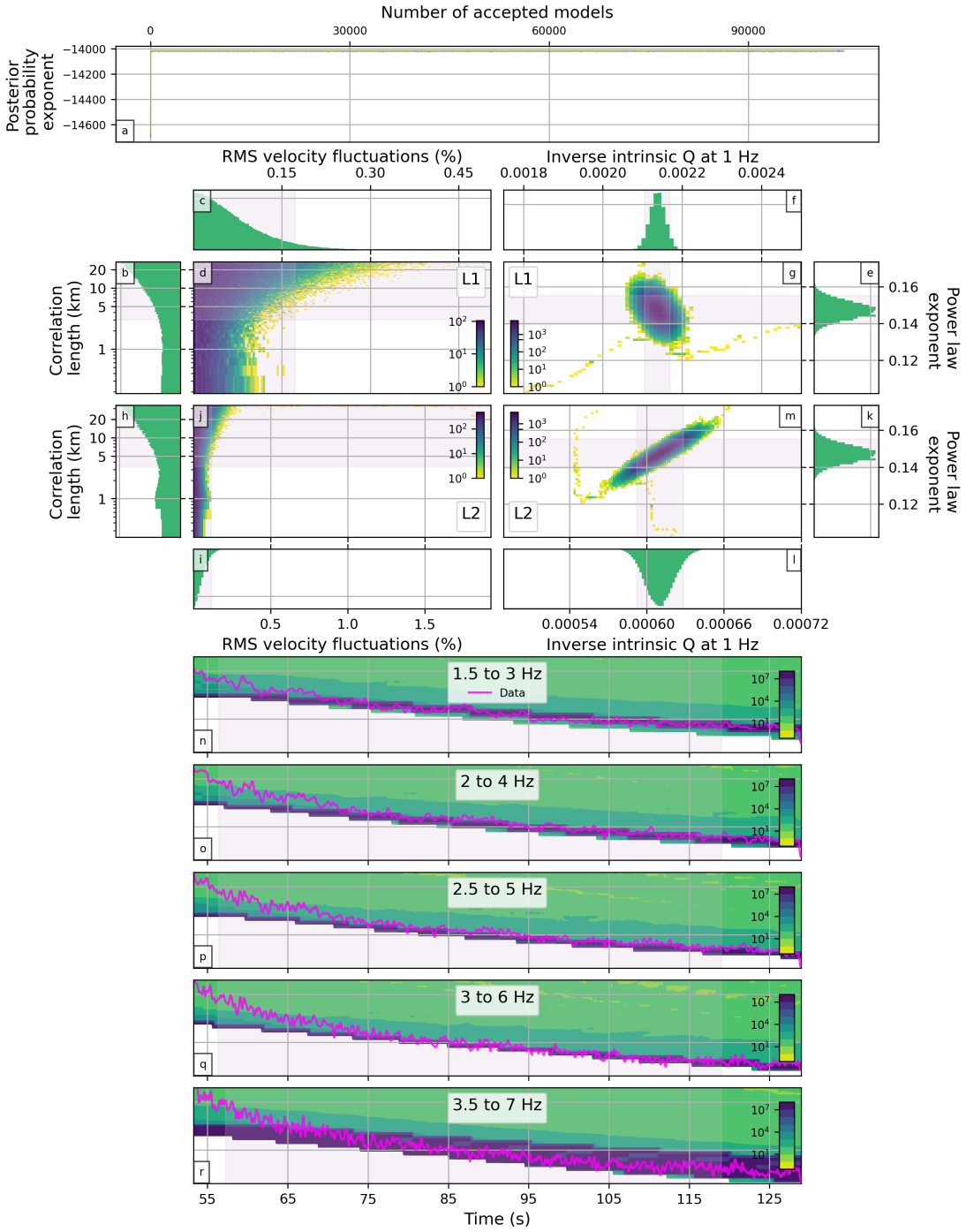

Figure 5.8: As Fig. 5.5 but for YKA.

in this case). The E-EFMD fixes this issue the same way the EFMD does, by forcing it to bounce back within the limits of the prior distribution (Section 2.1.3). However, the algorithm continued to accept almost all proposed updates of the correlation length, regardless of its value (panels b and h in Figs. 5.5, 5.6, 5.7, 5.8 or 5.9), which likely resulted in these increased acceptance rates.

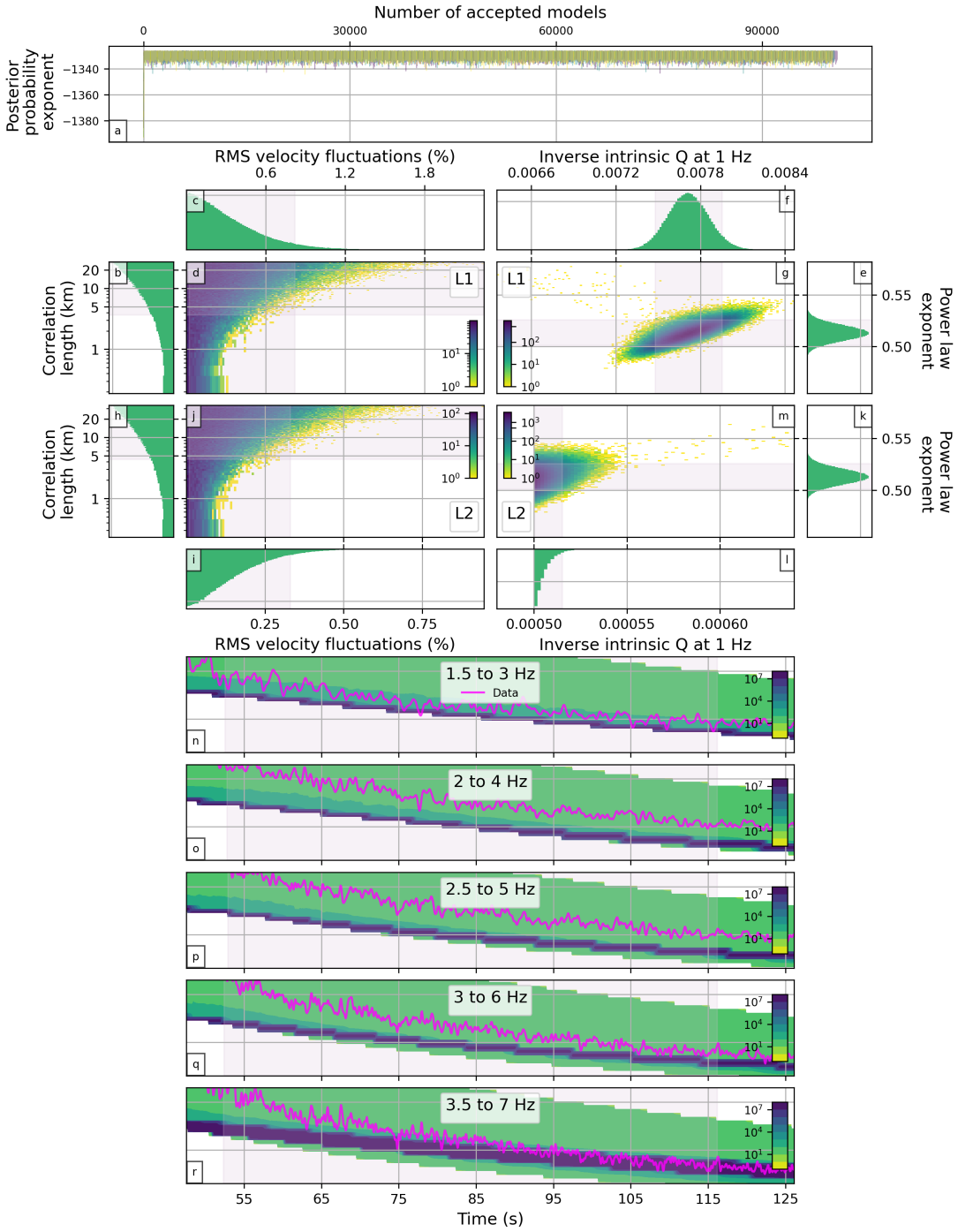

Figure 5.9: As Fig. 5.5 but for BOSA.

In an attempt to improve the poor fits to the data, I inverted the data for ILAR and TXAR again using my alternative implementation of the E-EFMD in which the frequency dependence coefficient of Q_{i0}, α, is fixed. Results from these inversions are shown in Figures A94 and A95, and also included in Table 5.2. The removal of one parameter from the inversion not only did not improve the results, compared to the full

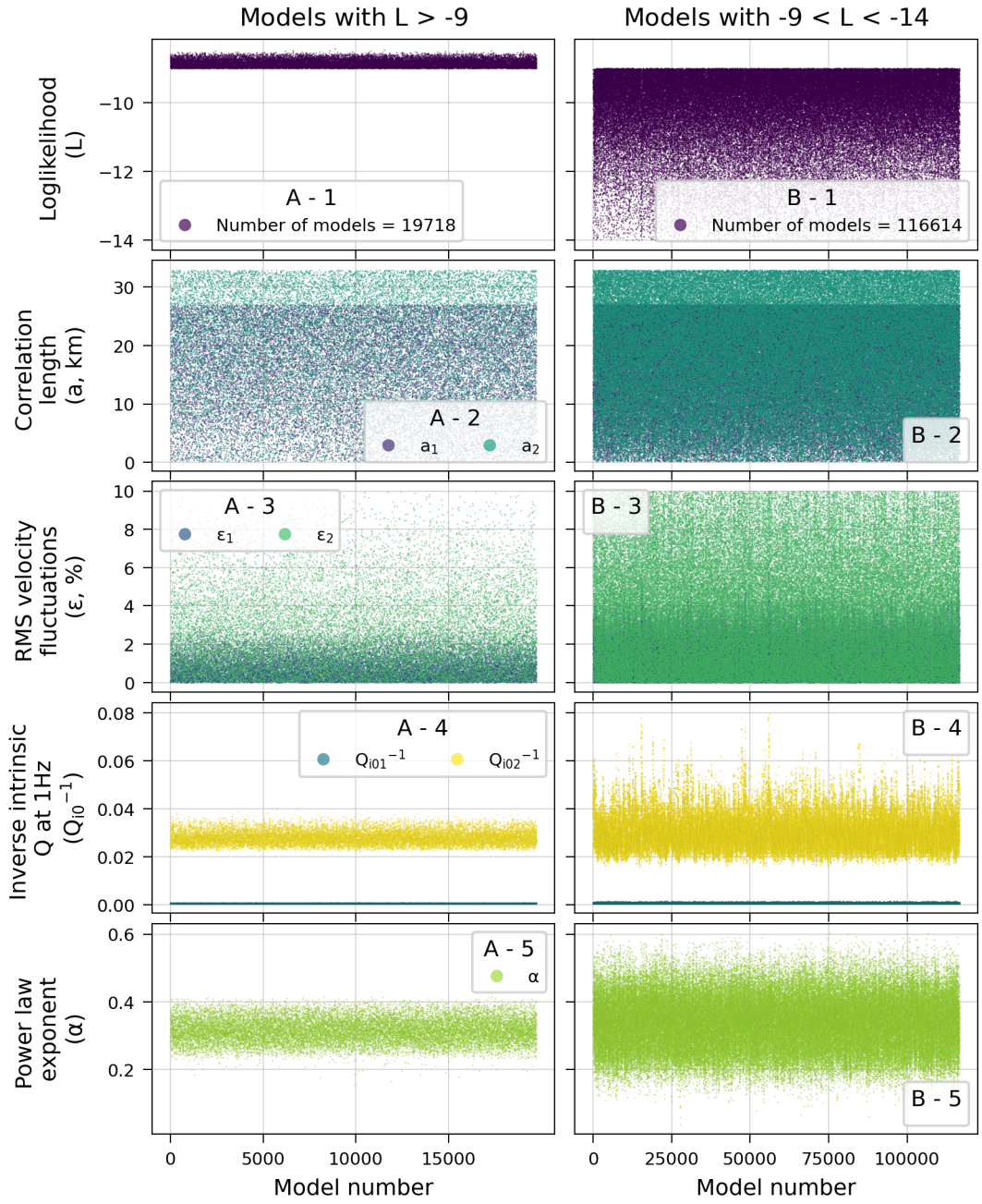

Figure 5.10: Samples of the highest loglikelihood models extracted from the E-EFMD results for ILAR shown in Fig. 5.5. Panel content is as in Fig. 4.21.

E-EFMD inversion, it made fits to the data slightly worse (maximum L reached during the inversion decreased) in both cases. PDFs for the attenuation parameters show a slight increase in Q_{i0} in layer 1 for ILAR and a decrease in layer 2 for TXAR, with the other layers of the models showing distributions very similar to those on panels l and f of Figs. A94 and A95 respectively. Posterior PDFs for the scattering parameters do not significantly change for either layer or station. Given the minor effect of removing

α from the inversion on the results for ILAR and TXAR, I decided not to use this approach for any of the remaining IMS stations.

Sampling the posterior PDFs for models with the highest loglikelihoods shows that the behaviour of the algorithm in the inversions of the data from these IMS stations is similar to that observed for my synthetic tests and data inversions for PSA, ASAR and WRA in Chapter 4. Figure 5.10, and figures A96–A99, in Appendix A.5, contain the loglikelihood and parameter values for the models that produce the best fits to the data in each case. For the stations on thinner lithospheres (ILAR, PDAR and TXAR, Fig. 5.3), values of the intrinsic quality factor at 1 Hz are very high ($Q_{i0} > 0.02$, well within the extremely strong intrinsic attenuation regime) in the lithospheric mantle, while those for the crust tend to 0. Q_{i0}^{-1} values for YKA and BOSA are lower ($Q_{i0} < 0.008$) in the crust than those for the rest of the stations and similarly low in the lithospheric mantle. As discussed in Sections 4.1.2 and 4.2, these extreme values of the intrinsic quality factor at 1 Hz generally result in increased variability of the scattering parameters, which is obvious in panels A/B–2 and A/B–3 in Figs. 5.10, A96, A97, A98 and A99. This means that, even for ILAR, for which fits to the data are reasonably good, associating the parameter values obtained from these inversions to the physical structure beneath the stations is probably impossible. The results for ILAR, TXAR and PDAR also show that the layering of the model, discussed in 4.2, is likely a minor contributor to the non-uniqueness of the solutions and the bias of the E-EFMD towards extreme Q_{i0} values.

Despite the similarities in the behaviour of the E-EFMD algorithm both for the Australian and IMS arrays/stations, the results from these inversions also highlight intriguing differences in its ability to simultaneously fit the data envelopes for all frequency bands. To investigate this observation, in Figure 5.11 I represent the data envelopes for all arrays/stations and frequency bands. Figure 5.11 shows that coda amplitude variations with frequency change greatly between different arrays/stations. For the Australian arrays, for frequency bands A–E (Table 2.3), coda amplitudes increase with frequency while keeping relatively constant decay rates. Envelope variations for the higher frequency bands (F–H) are very small though, with only a slight decrease in amplitude towards the end of the time window of interest for the E-EFMD analysis (shaded area in plots in Fig. 5.11), which points to marginally faster decay rates. For PDAR, variations in amplitude are small and similar for all frequency bands, but coda levels clearly decrease with increasing frequency. Codas for ILAR, YKA, TXAR and BOSA show a much more complex behaviour, with amplitudes initially increasing with frequency to then decrease again. Decay rates also appear to vary more for these stations than for the rest and to follow different patterns. For TXAR, for example, envelopes for frequency band A (Table 2.3) have amplitudes and decay rates resembling those for frequency bands F–H, even if their initial amplitudes vary, while frequency

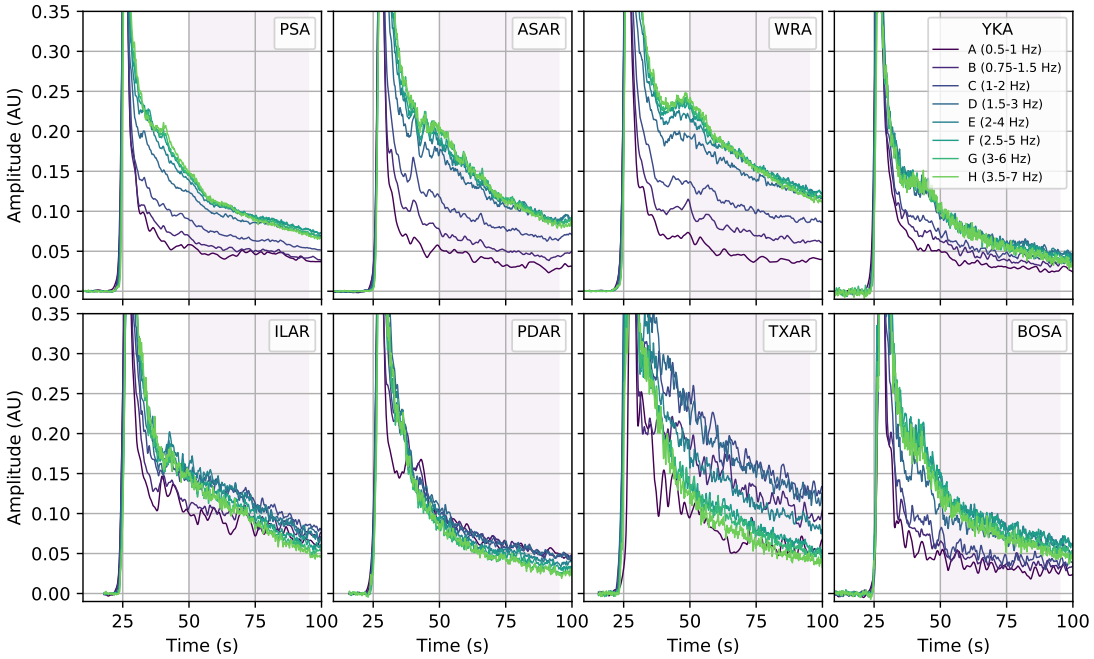

Figure 5.11: Coda variation with frequency in the data envelopes for all arrays/stations studied in this thesis (PSA, ASAR, WRA, ILAR, PDAR, TXAR, YKA and BOSA) and all frequency bands from Table 2.3.

bands B and E, on one hand, and C and D, on the other, show codas similar to each other. For ILAR, however, initial coda amplitudes rise with frequency for the lowest frequency bands before stabilising for the highest, while decay rates become steeper as frequency increases, thus decreasing coda amplitudes within the time window of interest for the E-EFMD analysis. YKA and BOSA show similar increase and stabilisation of initial coda amplitudes to ILAR, but decay rates appear to initially become slower, for frequency bands A–D/E, to then increase again for bands D/E–H.

The data envelopes in Fig. 5.11 clearly point to significant differences in the small-scale structure beneath these arrays and stations. Envelopes for YKA and PDAR have generally much lower amplitudes at all frequencies than the rest of arrays/stations, while those for WRA and TXAR are much higher than the rest, especially at high frequencies. Since codas are caused by scattering (e.g. Aki, 1969), and coda levels are related to stronger contrasts at heterogeneities (as I show in Section 4.1.1), these disparities are clear indicators of differences in scattering strength beneath the stations. The variations in amplitude and decay rate with frequency discussed above also point to the local structure, since intrinsic attenuation strength, directly related to coda decay rates, is affected by the presence, amount and characteristics of cracks and fluids beneath the stations (e.g. Müller et al., 2010; Tisato et al., 2015; Sun et al., 2015; Picotti et al., 2010; Sketsiou et al., 2021). Decay rate changes, in particular, point to the frequency dependence of the intrinsic quality factor. Here, I chose a power law

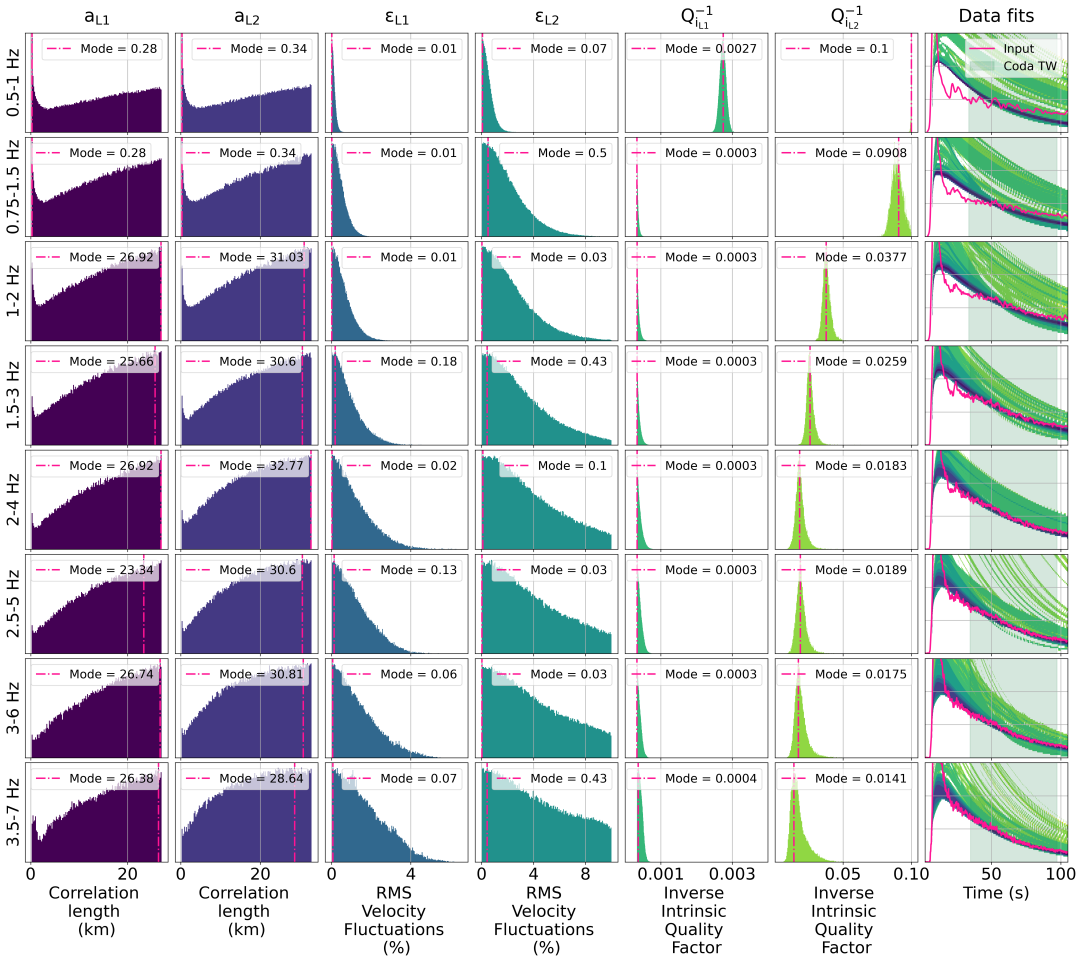

Figure 5.12: Results from the E-EFMD single frequency inversions for ILAR. Panels in each row contain the posterior PDFs for each parameter in the 2-layer model, as well as the fits to the data envelope for each of the frequency bands in Table 2.3. Modes for each parameter have been included in the legends for further reference.

of the form $Q_i = Q_{i0} f^{\alpha}$ for my implementation of the E-EFMD, a relationship that has often been used in other attenuation studies (e.g. Korn, 1990; Sato et al., 2012; Sketsiou et al., 2021). For an α in the 0–1 range (see Section 2.1.1), such an equation implies that Q_i will either remain constant or increase with frequency, which in turn leads to decay rates becoming slower as frequency grows. However, as shown in Fig. 5.11, that is not always the case, which points to a power law frequency dependence of Q_i not being accurate or complex enough in general.

As a preliminary test of this hypothesis, I developed another version of the E-EFMD code, similar to the one described in Section 4.1.2, in which the frequency dependence of Q_i is not predetermined, but with the ability to run the inversion for a single frequency band. For each frequency band from Table 2.3 and each of the Australian arrays studied in Chapters 3 and 4, and each of the IMS stations in this chapter, I ran three parallel Markov Chains, each 2 million iterations long, which I then combined into a single set

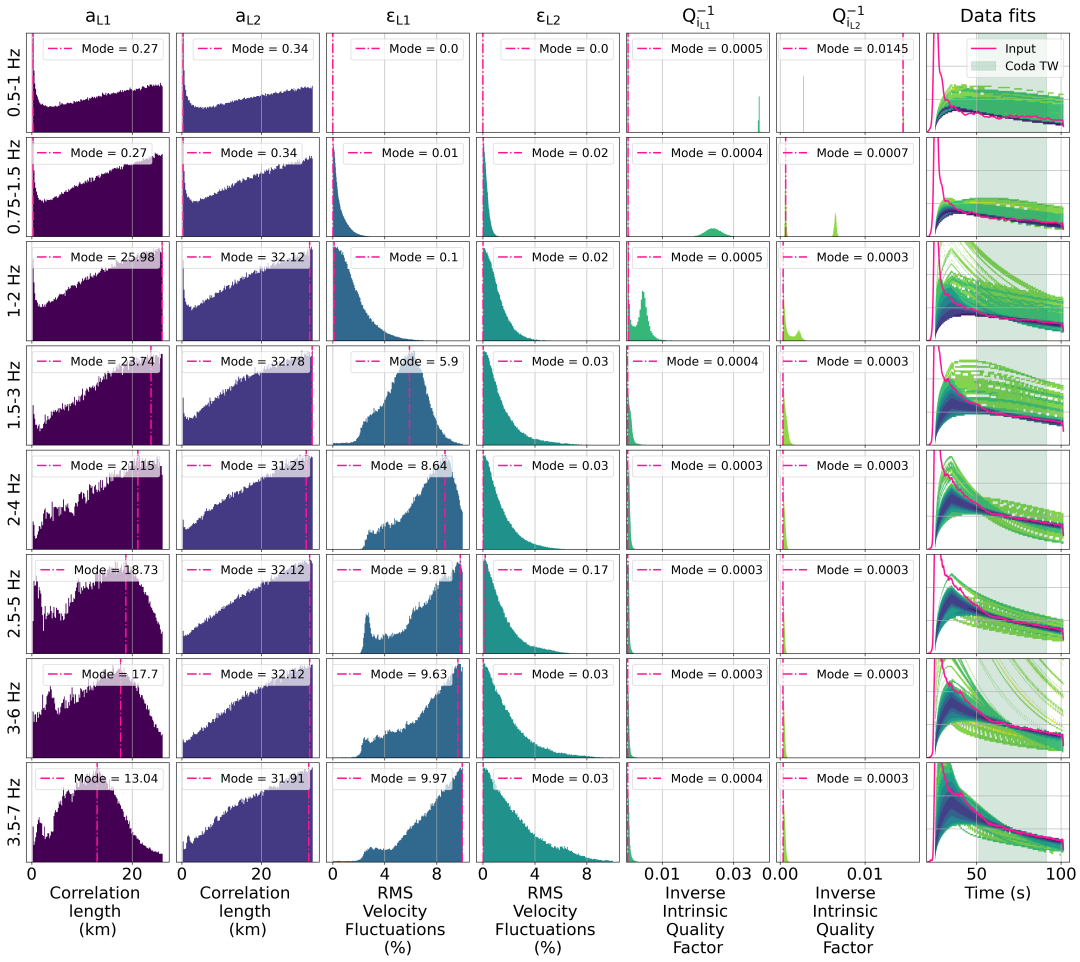

Figure 5.13: As Fig. 5.12 but for PSA.

of results. Models in this version of the E-EFMD consist of the correlation length, RMS velocity fluctuations and intrinsic quality factor for each layer of the model, thus making a total of 6 parameters per frequency band. Results from this inversion for ILAR and PSA are shown in Figs. 5.12 and 5.13, while similar figures for the rest of the arrays can be found in Appendix A.6. For all arrays, posterior PDFs for the correlation length in both layers of the model are very wide, with those for the lowest frequency bands showing a sharp peak at low values ($a < 1km$) that gradually disappears as frequency increases. PDFs for ε and Q_i show much more variability, both in the shape of the distributions and its evolution with frequency, with some parameters remaining largely constant (ε_{L1} for ILAR, in Fig. 5.12, and ${Q_{i_{L1}}}^{-1}$ for PSA, in Fig. 5.13, are such examples) while others do change with frequency (like ${Q_{i_{L2}}}^{-1}$ for ILAR or ε_{L1} for PSA, Figs. 5.12 and 5.13). Common patterns in the frequency dependence of these parameters are not obvious from these results, but it is generally clear that a simple power law is probably not representative of the attenuation structure. Fits to the data in these results are not always good (such as frequency bands A and B for ILAR

and TXAR, Figs. 5.12 and A103) and loglikelihoods for some cases are extremely low ($L < -1000$). This seems to be a consequence of the bias of the E-EFMD algorithm towards the attenuation parameters, as evidenced by the broad posterior PDFs for a and ε and narrow or extremely narrow distributions for $Q_{i_{L1}}$ and $Q_{i_{L2}}$ (Figs. 5.12 and 5.13). In general, this new approach appears to be capable of helping avoid the issues created by forcing a single set of scattering parameters to fit the data at all frequencies and would allow us to determine how the intrinsic quality factor varies with frequency in each of these structures. Additionally, since we can also obtain the frequency dependence of a and ε, we could also determine the type of ACF that best fits the data, instead of assuming an exponential ACF. However, it is still unclear whether it will be fully capable of allowing us to estimate the frequency dependence of Q_i and relate the parameter values to the physical structure beneath the arrays and stations and further work in this direction is recommended.

The data and results presented in this section clearly highlight the complex behaviour of both the scattering and intrinsic attenuation parameters with frequency for these datasets, with a single set of parameters probably not being capable of representing the heterogeneity structure beneath the stations. For the scattering parameters, the frequency dependence of a and ε is usually tied to the autocorrelation function (ACF) of the medium (e.g. Fang and Müller, 1996). The E-EFMD assumes an exponential autocorrelation function, but other studies suggest a von Kármán distribution may be a more accurate representation of random media (e.g. Sato and Emoto, 2017; Sato and Emoto, 2018; Fielitz and Wegler, 2015). For the intrinsic quality factor, alternative models to the power law I use in my initial implementation of the E-EFMD have been proposed, such as those by Anderson and Given (1982) or Lekić et al. (2009), but more research into this topic is still needed to fully determine how the intrinsic quality factor varies with frequency. Finally, amplitude fluctuations similar to those shown in Fig. 5.11 can also be caused, or accentuated, by other structure related phenomena, such as the amplification of some frequencies at shallow sediment layers and/or contributions to scattering by near-receiver topography (e.g. Lee et al., 2009a; Lee et al., 2009b).

5.2.2 Depth-Dependent Energy Flux Model results

The E-EFMD results shown in Section 5.2.1 do not provide reliable estimations of the scattering and intrinsic attenuation parameters (a, ε, Q_{i0} and α) for the IMS arrays studied in this chapter. For this reason, I decided to implement my adaptive step size and continuation algorithms (see Section 4.1 for details) into my original EFMD algorithm and apply it to the IMS arrays datasets previously analysed with the E-EFMD method. The resulting EFMD version is ∼10–15 times faster than my initial implementation and can be run on HPC clusters, but is otherwise identical to the algorithm described in Chapter 2. The EFM method applied here is the same described

and applied in Chapters 2 and 3.

EFM results

As detailed in Chapters 2 and 3, coda decay rates (a_1) and values at zero time (a_0) for each frequency band are obtained in the EFM by fitting coda amplitudes for each one using a linear least-squares algorithm (Figs. A106–A110). From the decay rate values, intrinsic and diffusion quality factors at 1 Hz (Q_{i0} and Q_{d0}, respectively) can be obtained using Eq. 2.16, with their values at other frequencies being defined by equations 2.15 and 2.14 respectively. The scattering quality factors are calculated from a_0 using Eq. 2.12, and these values can then be used to obtain a first estimation of a and ε using Eq. 2.13. Finally, the combined quality factor Q_{comb} was calculated from Eq. 2.17. A summary of my EFM results for the IMS arrays studied in this chapter can be found in Table 5.4 and Fig. 5.14.

According to the ranges defined and used throughout chapters 4 and 5, intrinsic attenuation appears to be weak ($Q_{i0} \geq 1000$) and frequency independent ($\alpha = 0.0$) for PDAR, TXAR and BOSA. Seismic waves recorded at ILAR and BOSA experience medium, frequency dependent, intrinsic attenuation ($Q_{i0} \sim 400 - 500, \alpha = 0.4$, Table 5.3). Diffusion is medium-strong (Q_{d0} ∼200–700) beneath PDAR, TXAR and BOSA, and weak ($Q_{d0} \sim 1400$) under ILAR and YKA (Table 5.3). The scattering parameters (a and ε) take similar values for BOSA and YKA (400 and 700 m, respectively, for the correlation length, and 3.0% and 3.9% for the velocity fluctuations), but there is more variability for the rest of the arrays, with a being similar for ILAR and TXAR (2.9 and 3 km), but are much higher for PDAR (> 10 km) (Table 5.3), and the RMS velocity fluctuation ranging from 3.8–6.4% (Table 5.3). Scattering appears to be the dominating attenuation mechanism at most frequencies for ILAR and TXAR, while for YKA and BOSA it only becomes the main driver of attenuation above 2 Hz. For PDAR, Q_s is similarly strong to anelasticity throughout most of the frequency range of interest and only takes lower values above 3.8 Hz. The lowest Q_s values obtained from the EFM inversion, which would correspond to the strongest heterogeneity, are measured for TXAR in the 1–2 Hz range, where this parameter presents a sharp minimum that is

Table 5.3: Summary of the main results obtained from the EFM for the IMS arrays: intrinsic (Q_{i0}) and diffusion (Q_{d0}) quality factors values at 1 Hz, intrinsic quality factor frequency dependence coefficient (α), correlation length (a) and RMS velocity fluctuations (ϵ).

Array	v_P (km/s)	t_N (s)	Q_{i0}	Q_{d0}	α	a (km)	ε (%)
ILAR	7.1	7.1	400 ± 20	1400 ± 400	0.4	2.9 ± 0.3	3.8 ± 0.1
PDAR	6.8	8.5	1200 ± 80	200 ± 10	0.0	13.2 ± 10.0	6.4 ± 3.0
TXAR	7.1	9.0	1300 ± 100	300 ± 20	0.0	3.0 ± 2.0	5.7 ± 1.0
YKA	8.0	28.9	500 ± 50	1700 ± 1000	0.4	0.7 ± 0.2	3.0 ± 0.2
BOSA	7.9	26.1	1100 ± 60	700 ± 90	0.0	0.4 ± 0.1	3.9 ± 0.7

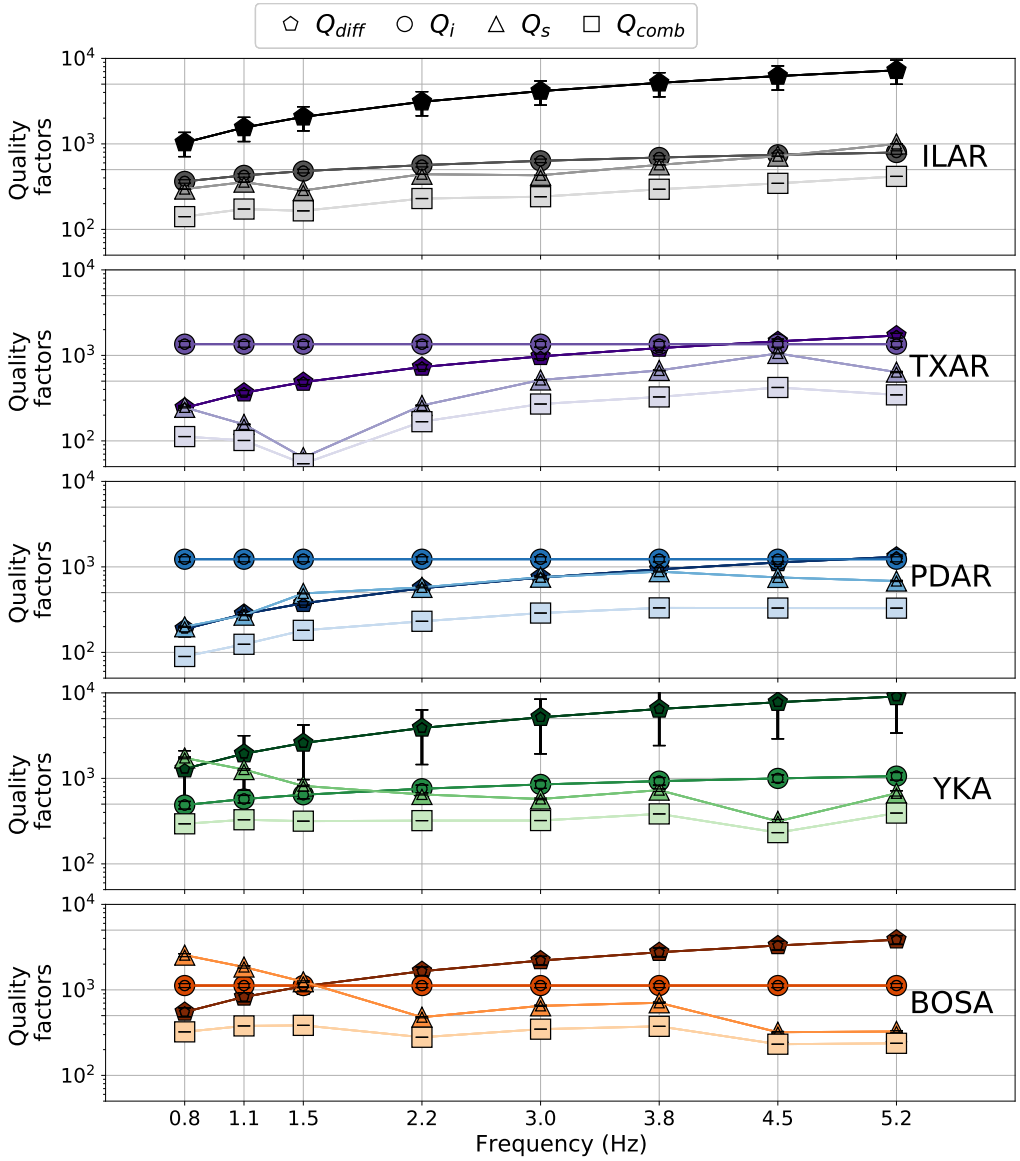

Figure 5.14: Frequency dependence of the intrinsic (Q_i), diffusion (Q_{diff}), scattering (Q_s) and total (Q_{comb}) quality factors for the five IMS arrays analysed in this chapter.

not observed for any of the other arrays. For YKA and BOSA, Q_s takes higher values at low frequencies and decreases as frequency increases, while for the rest of the arrays this quality factor slowly rises with frequency. Finally, the combined quality factor (Fig. 5.14) suggests overall attenuation is stronger beneath ILAR, TXAR and PDAR for frequencies below 4 Hz, and for BOSA above those frequencies, even if differences between arrays become smaller as frequency increases.

The trends and behaviours of the quality factors and scattering parameter values presented in Table 5.3 and Fig. 5.14 do not appear to immediately correlate with lithospheric type or thickness, nor with mean P-wave velocities. YKA, BOSA and

Table 5.4: Summary of the results of the EFMD inversions of the data from ILAR, PDAR, TXAR, YKA and BOSA using 1- or 2-layer models. For information on the layering of the models, see Figure 5.3.

Array or station	Freq. bands	Iterations per chain	Layer number	Corr. length (a) 5 – 95 PR (km)	Corr. length (a) AR (%)	RMS vel. flucts. (ε) 5 – 95 PR	RMS vel. flucts. (ε) AR (%)	Inv. int. Q at 1 Hz (Q_{i0}^{-1})	Maximum loglikelihoood
ILAR	A–H	10^6	1	2–27	87.2	0.01–0.2	41.3	400±20	-2500
	D–H	10^6	1	4–27	81.8	0.01–0.5	39.1	400±20	-260
	D–H	10^6	1 2	2–26 3–32	81.4	0.1–1.7 0.2–4.8	36.8	400±20	-50
TXAR	D–H	10^6	1	3–27	81.6	0.0–0.001	38.4	1600±300	$< -1 \cdot 10^8$
	D–H	10^6	1 2	3–25 4–31	68.3	0.0–0.001 0–0.002	41.0	1600±300	$< -3 \cdot 10^7$
PDAR	D–H	10^6	1	4–26	80.9	0.0–0.005	36.8	1200±70	$< -4 \cdot 10^6$
	D–H	10^6	1 2	3–25 4–32	80.8	0.0–0.005 0.0–0.01	42.4	1200±70	$< -3 \cdot 10^6$
YKA	D–H	10^6	1 2	3–26 4–32	81.4	0.0–0.001 0.0–0.01	37.9	1500±100	$< -10^5$
BOSA	D–H	10^6	1 2	3–26 0.26–0.38	41.2	0.01–0.3 1.11–1.26	39.3	1100±60	$< -3 \cdot 10^3$

PDAR are all installed on cratons (which tend to be less tectonically active), but their lithospheric thickness varies. For PDAR, the LAB is located at relatively shallow depths ($\sim$ 60 km, Fig. 5.3), while the ones beneath YKA and BOSA are much deeper (sim200 km). ILAR and TXAR both, on the other hand, sit above thinner lithosphere ($\leq$65 km) outside cratons. There appears to be some similarities in the scattering parameter values for YKA–BOSA and ILAR–TXAR, but they fail to appear when we compare the values of the different quality factors. In general, these results are suggestive of important variations in the strength and characteristics of scattering and intrinsic attenuation in the lithospheres beneath the arrays that do not appear to correlate with their general tectonic setting in an obvious manner.

EFMD results

I applied my new implementation of the EFMD algorithm to the datasets described in Section 5.1 for ILAR, PDAR, TXAR, YKA and BOSA. I inverted the data using 1- and 2-layer models. In all cases, their bottom depth is equivalent to the LAB, while for 2-layer models the interface between the two layers represents the Moho (Fig. 5.3). For each array and model tested, I ran three parallel Markov chains per inversion, each 10 million iterations long. I then combined them into a single ensemble of models and parameters, after applying the thinning approach described in Section 4.1.2. A summary of the results from these inversions can be found in Table 5.4.

My results for PSA and ASAR in Section 3.3.2 show that the 1-layer EFMD for arrays above thick lithospheres generally produces high amplitude codas that fail to fit the data. As discussed in Section 3.3.2, this is likely caused by the large thickness of the scattering layer (twice the thickness of the lithosphere) effectively preventing diffusion out of it and helping keep high energy levels within the layer at all times. For this reason, I decided not to attempt inverting the data from YKA or BOSA using this

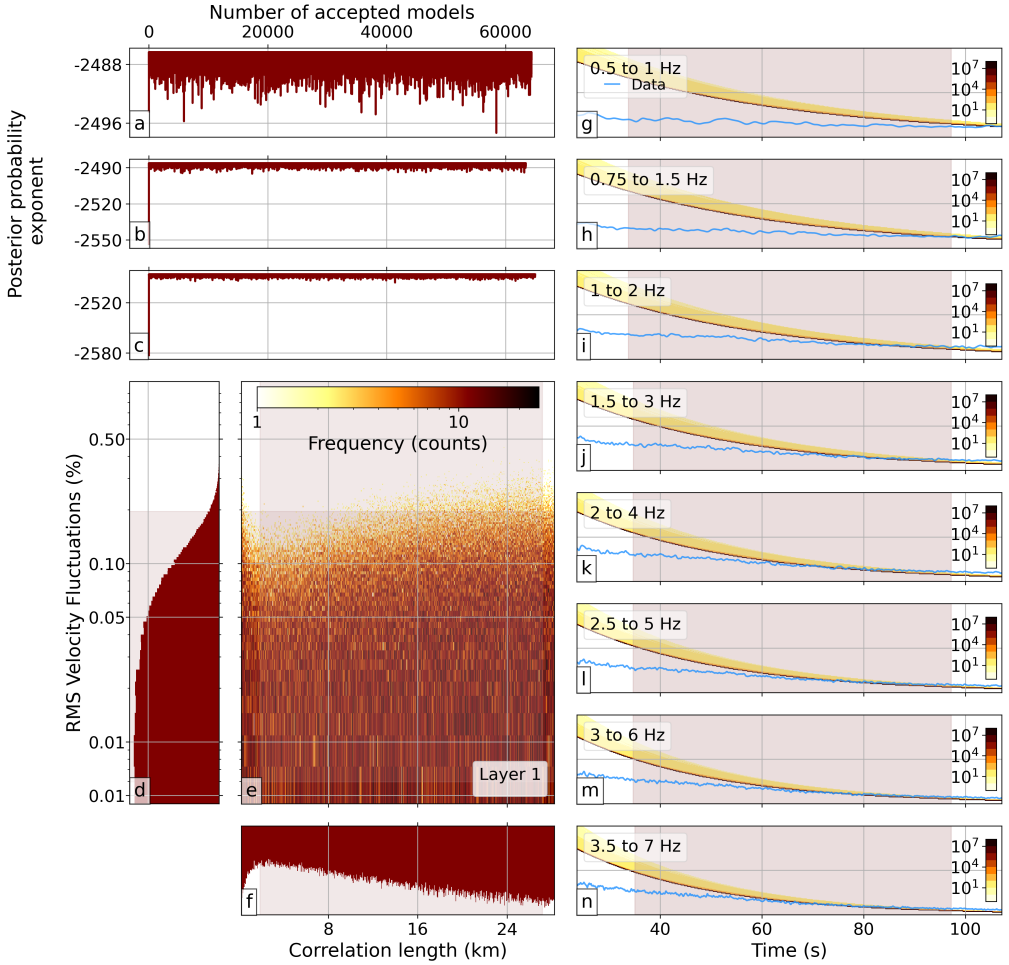

Figure 5.15: Summary of the results obtained from the EFMD algorithm for ILAR and a 1-layer model that encompasses the entire lithosphere. Panel content is as in Fig. 3.9.

new approach of the EFMD, since the lithospheres beneath them extend down to ∼200 km depth, similar to the Australian arrays studied in Chapter 3. For ILAR, I initially ran the inversion using all frequency bands from Table 2.3. Loglikelihood (L) values are much higher than they were for ASAR or PSA ($L \sim -2500$ for ILAR (Table 5.4), as opposed to $< -1.4 \cdot 10^7$ for PSA and ~ -10500 for ASAR (Table 3.3)), but these values are still indicative of poor fits to the data. Panels g–n in Fig. 5.15 shows that the obtained synthetic envelopes only seem to fit the second part of the coda, with synthetic coda amplitudes at the beginning of the time window of interest being much higher than the data ones, especially at low frequencies. RMS velocity fluctuations obtained from the inversion are extremely low (5–95 PR only extends up to 0.2%). Since ε is the main controller of initial coda amplitudes (Section 4.1.1, these results clearly point to the 1-layer EFMD also not being capable of fitting the data from arrays on thinner lithospheres. For all these reasons, I decided not to use this model to invert the data from any of the other arrays.

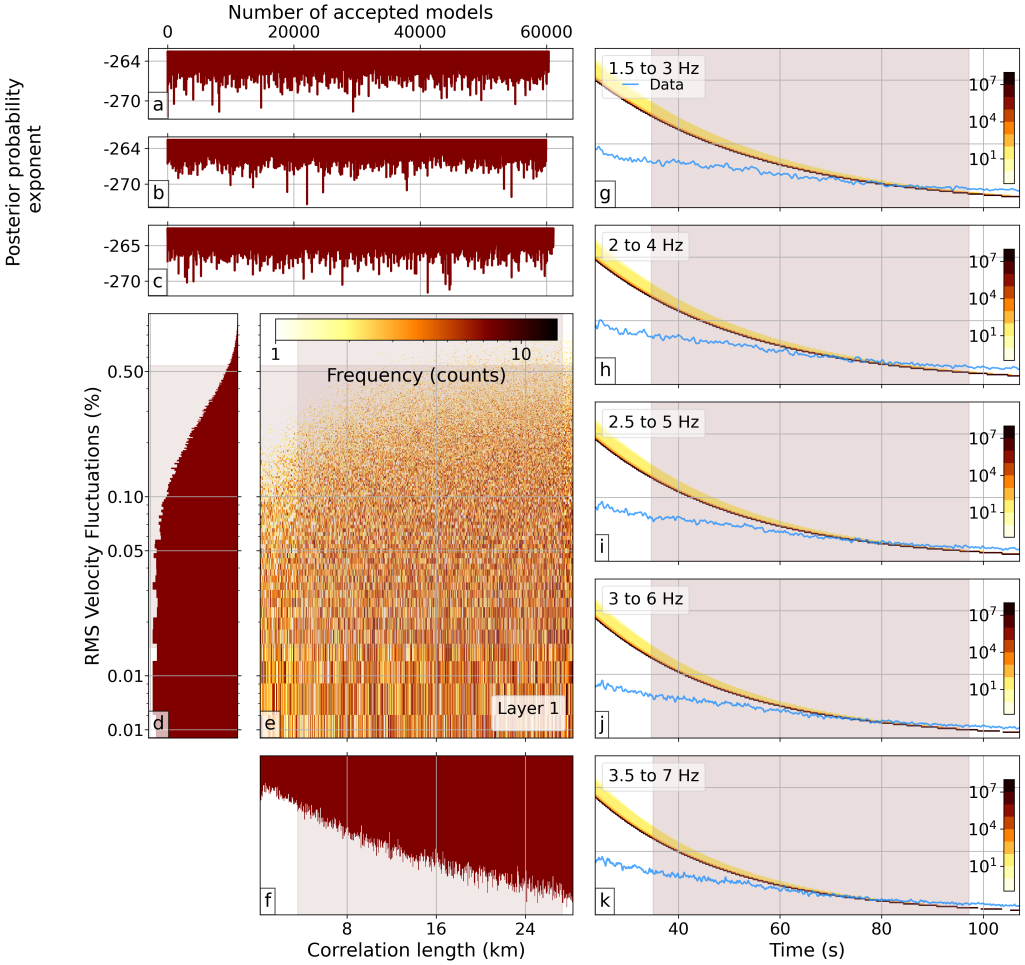

Figure 5.16: Same as Fig. 5.15 but including only frequency bands D–H from Table 2.3 in the analysis. Panel content is as in Fig. 3.12.

Using only frequency bands D–H from Table 2.3 in the EFMD inversion of ILAR data with a 1-layer model produced much better fits to the data, as evidenced by loglikelihood values in the 260–270 range (Table 5.4, Fig. 5.16). However, initial coda amplitudes are still too high to match the data envelopes, despite obtained RMS values being extremely low ($\varepsilon < 0.5\%$, Table 5.4). I also inverted the data from TXAR and PDAR using this configuration, but fits to the data for these arrays are much worse than for ILAR, with maximum loglikelihoods reached during these inversions being on the order of $< -10^8$ and $< -10^6$ respectively (Table 5.4). Results from these inversions are summarised in Figs. A112 and A111. Despite the increase in loglikelihood values for ILAR, these results continue to point to 1-layer models generally being too simple to successfully explain the input data, regardless of the thickness of the lithospheric model considered.

Similarly, results for the 2-layer model and ILAR show an increase in the maximum loglikelihood reached during the inversion ($L \sim -50$, Table 5.4), compared to the 1-

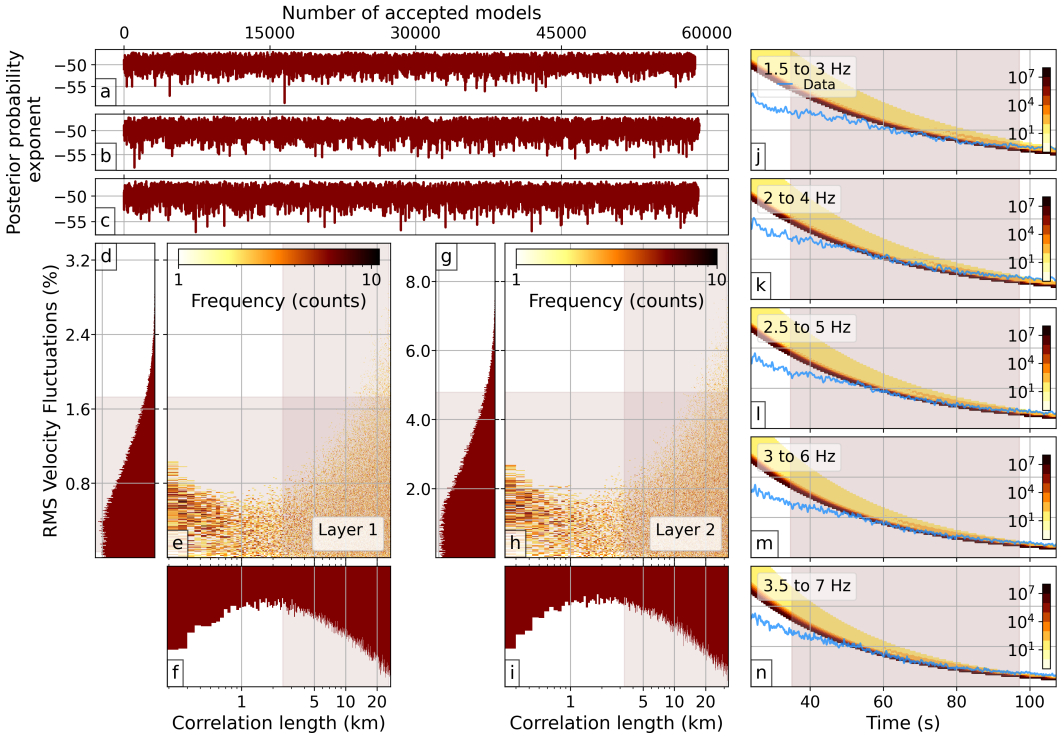

Figure 5.17: Same as Fig. 5.16 but for a 2-layer model that represents the crust and lithospheric mantle. Panel content is as in Fig. 3.12.

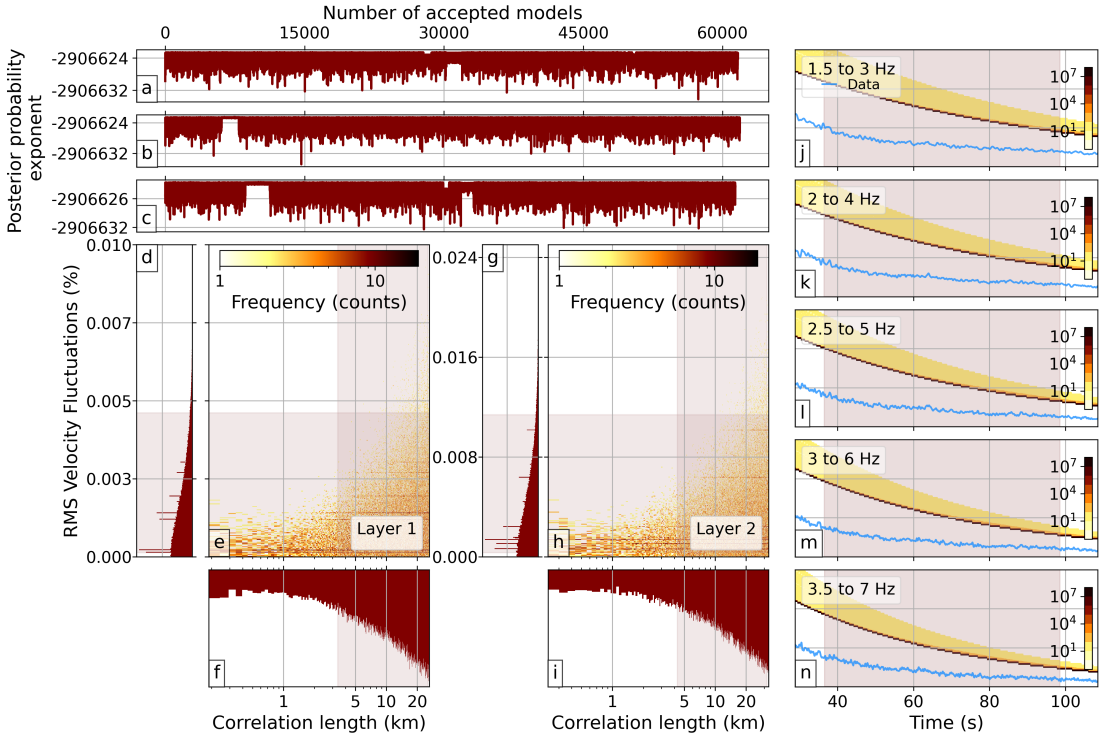

Figure 5.18: Same as Fig. 5.16 but for PDAR.

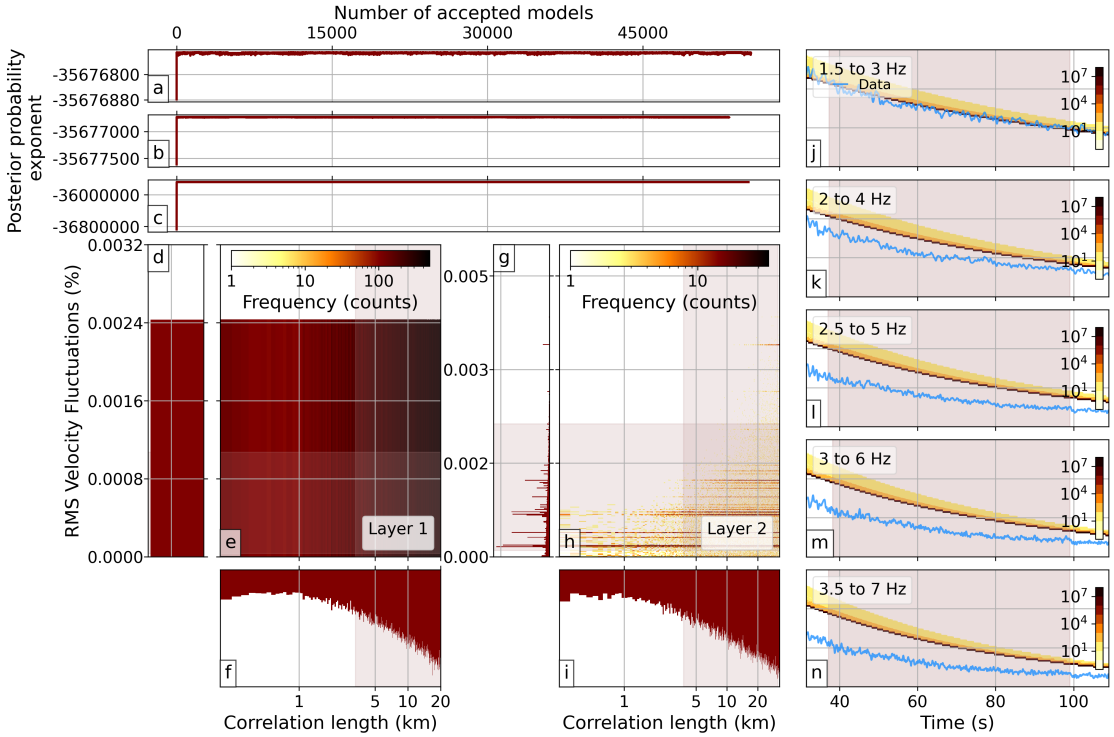

Figure 5.19: Same as Fig. 5.16 but for TXAR.

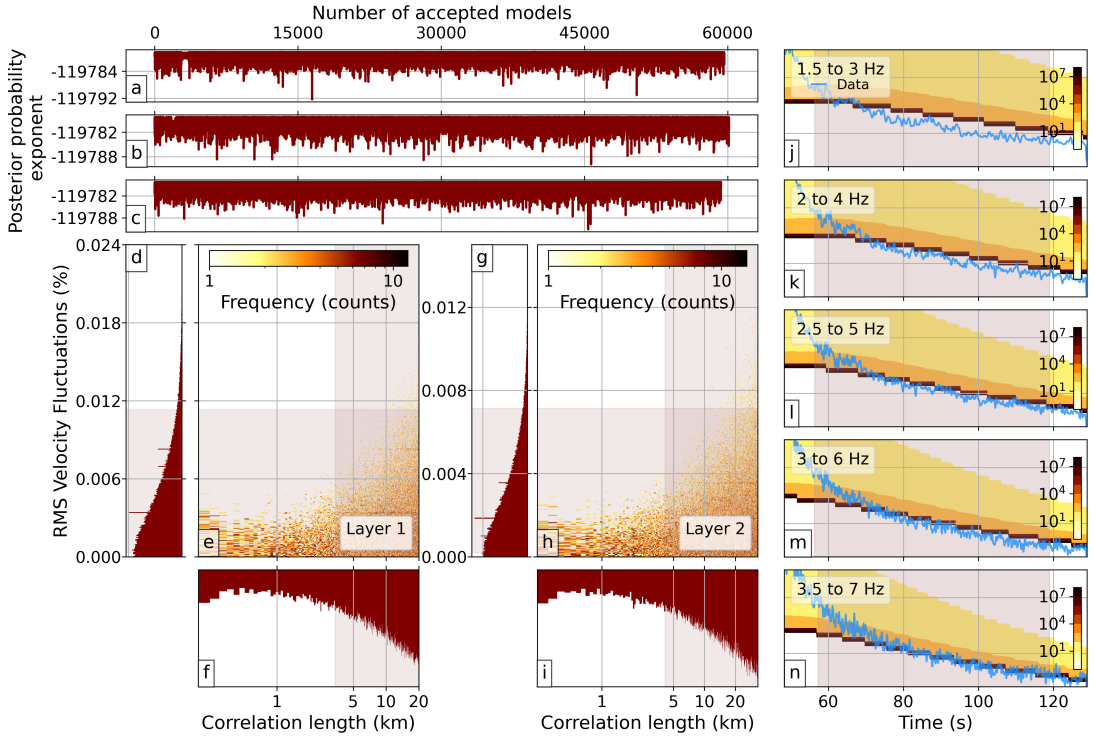

Figure 5.20: Same as Fig. 5.16 but for YKA.

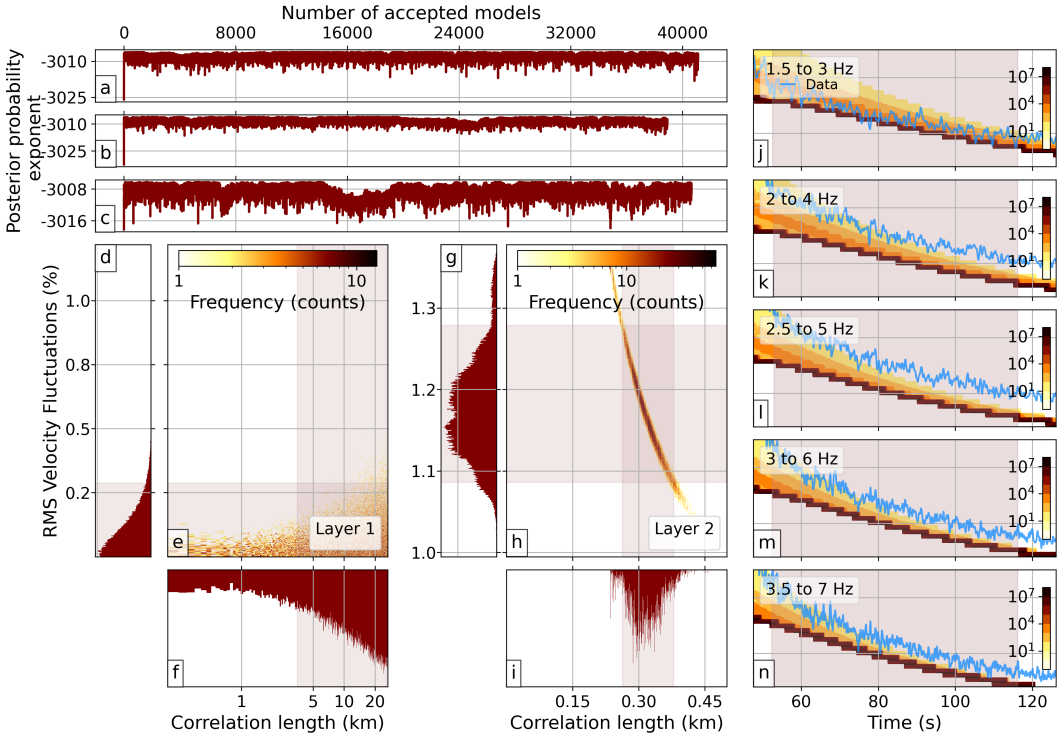

Figure 5.21: Same as Fig. 5.16 but for BOSA.

layer models. For the rest of the arrays,however, loglikelihoods remained extremely low ($L < -10^5$, Table 5.4). Panels j–n in Figs. 5.17–5.21 show that the ensembles of synthetic envelopes miss the data envelopes either partially or completely throughout the time window used for the fits. For ILAR (Fig. 5.17), the portion of the initial coda that the synthetic envelopes fail to match is shorter than for 1-layer models, but the EFMD algorithm is still uncapable of fully fitting the data envelopes, especially at low frequencies. 5–95 PRs for the RMS velocity fluctuations are wider in this case than they were for the 1-layer model, ranging from 0.1–1.7% in the crust and 0.2–4.8% in the lithospheric mantle. The algorithm still shows a marked preference for ε values below 0.8% in the crust and 2% in the mantle, but these appear to be still to high for synthetic initial coda amplitudes to match the input data. Correlation lengths take values throughout the entire allowed range in both layers, but their 5–95 PRs show the algorithm favours values above 2–3 km. For PDAR, the EFMD completely fails to fit the data at all frequency bands (panels j–n in Fig. 5.18), with maximum loglikelihoods for this case being $\sim 3 \cdot 10^6$. RMS velocity fluctuations take extremely low ($\varepsilon < 0.01\%$) values in both layers of the model. These results suggest the EFMD is not suitable for the inversion of data from this array, which generally shows much lower coda amplitudes at all frequency bands than data from the other arrays, as well as little variation in coda amplitudes with frequency (Fig. 5.11). In the case of TXAR, the EFMD algorithm seems capable of fitting the data for frequency band D (1.5–3 Hz,

Table 2.3), but not the rest of the bands included in the analysis (panels j–n in Fig. 5.19), an observation that is evidenced by the very low L values reached during the inversion ($< -3 \cdot 10^7$, Table 5.4). For frequency bands E–H, the ensemble of synthetic envelopes has higher amplitudes than the input data throughout the time window used for the fit. ε values for this case are also very low ($< 0.002\%$) in both layers of the model, but initial synthetic coda amplitudes continue to be too high to match the data envelopes. Fits for the YKA data are better than for PDAR or TXAR, but worse than for ILAR, with maximum likelihoods in this case being on the order of -10^5 (Table 5.4). While synthetic envelopes get much closer to the input codas in this case (panels j–n in Fig. 5.20), their amplitudes continue to be higher than data ones for most of the time window of interest, especially for frequency bands D–G. Fits for frequency band H, however, are much better than for the rest, matching the input envelopes throughout most of the EFMD time window. RMS velocity fluctuation values are very low in both layers ($\varepsilon < 0.01\%$), but in this case synthetic initial coda amplitudes are generally lower than those shown in the input data. Finally, results for BOSA again point to low or extremely low ε and high a values in the crust, but in this case parameters appear to take very well constrained values in the lithospheric mantle. The 5–95 PRs of the parameters in the bottom layer of the model are extremely narrow (0.12 km and 0.15%, respectively, Table 5.4) and centered around 0.29 km for a and 1.16% for ε. Despite this difference with respect to inversions for the other arrays, the maximum loglikelihood found during the inversion continued to be very low ($< -10^3$, Table 5.4) because of synthetic coda envelopes having lower amplitudes than the data ones for most of the frequency bands.

The results shown in Figs. 5.17–5.21 suggested the EFMD algorithm is not capable of simultaneously fitting neither all the frequency bands from Table 2.3 nor a selection of the five highest bands. However, they also show that it could be capable of individually fitting some of them, especially for some of the arrays. For this reason, I decided to develop the EFMD equivalent of the single-frequency inversion code tested for the E-EFMD in Section 5.2.1. For these inversions, I ran 3 parallel Markov chains for each array, each 2 million iterations long. I thinned the resulting chains by taking one in ten samples and combined them into a single set of results, similarly to the processing of the EFMD or E-EFMD results. Figures 5.22 and 5.23, shown here, as well as A113, A114 and A115, placed in Appendix A.7 (Section A.7.2) to avoid repetition, summarise these results. Panels on the right column of these plots show the data envelopes together with the ensemble of synthetic envelopes built during the inversions. These plots continue to show a lot of variability in the ability of the algorithm to successfully fit the data. For ILAR or YKA (Figs. 5.22 and A115, respectively), for example, fits tend to improve as frequency increases, even if synthetic envelopes still fail to match the initial parts of the coda. For TXAR or BOSA (Figs. A114 and 5.23), the algorithm can only fit the

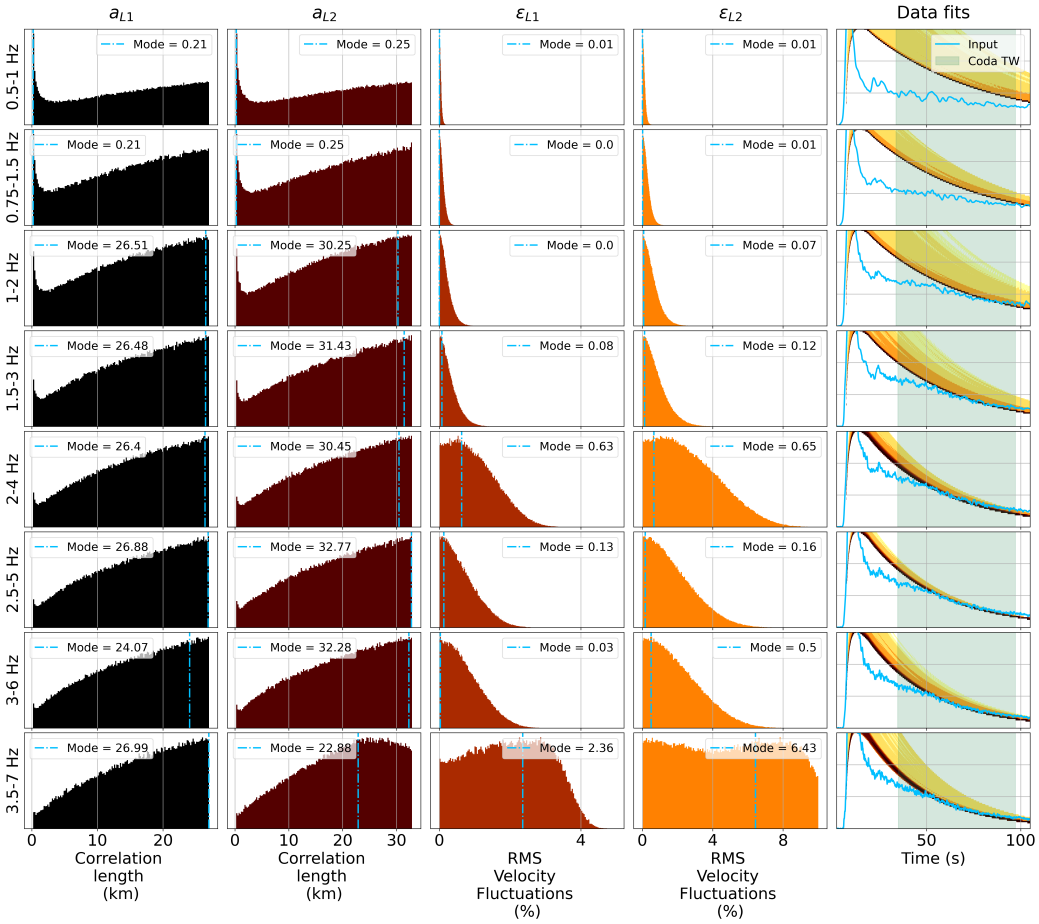

Figure 5.22: Results from the EFMD single frequency inversions for ILAR. Panels in each row contain the posterior PDFs for each parameter in the 2-layer model, as well as the fits to the data envelope for each of the frequency bands in Table 2.3. Modes for each parameter have been included in the legends for further reference.

data at some frequencies (C–D for TXAR, D–G for BOSA, Table 2.3). Finally, in the case of PDAR (Fig. A113), the EFMD appears to be incapable of fitting the data at any frequency band.

Most of the multi-frequency and single-frequency inversion results presented in this section point to very high correlation lengths (> 10 km), as well as low or extremely low RMS velocity fluctuations values ($< 1\%$) in both layers of the model for all arrays. These results are probably caused by the EFMD trying to match the low initial coda amplitudes of the input data by lowering ε, which in turn reduces the effect correlation lengths have on the synthetic coda envelopes. This is also the most likely cause of the high acceptance rates shown for a in Table 5.4. This behaviour of the algorithm, which can be considered a sort of bias towards low ε values, and similar to the one that the E-EFMD exhibits towards low Q_{i0} values, greatly reduces the reliability of these results and prevents further interpretation of the obtained parameter values. In Chapter 3, the higher amplitudes and comparable frequency behaviour of the data from the Australian

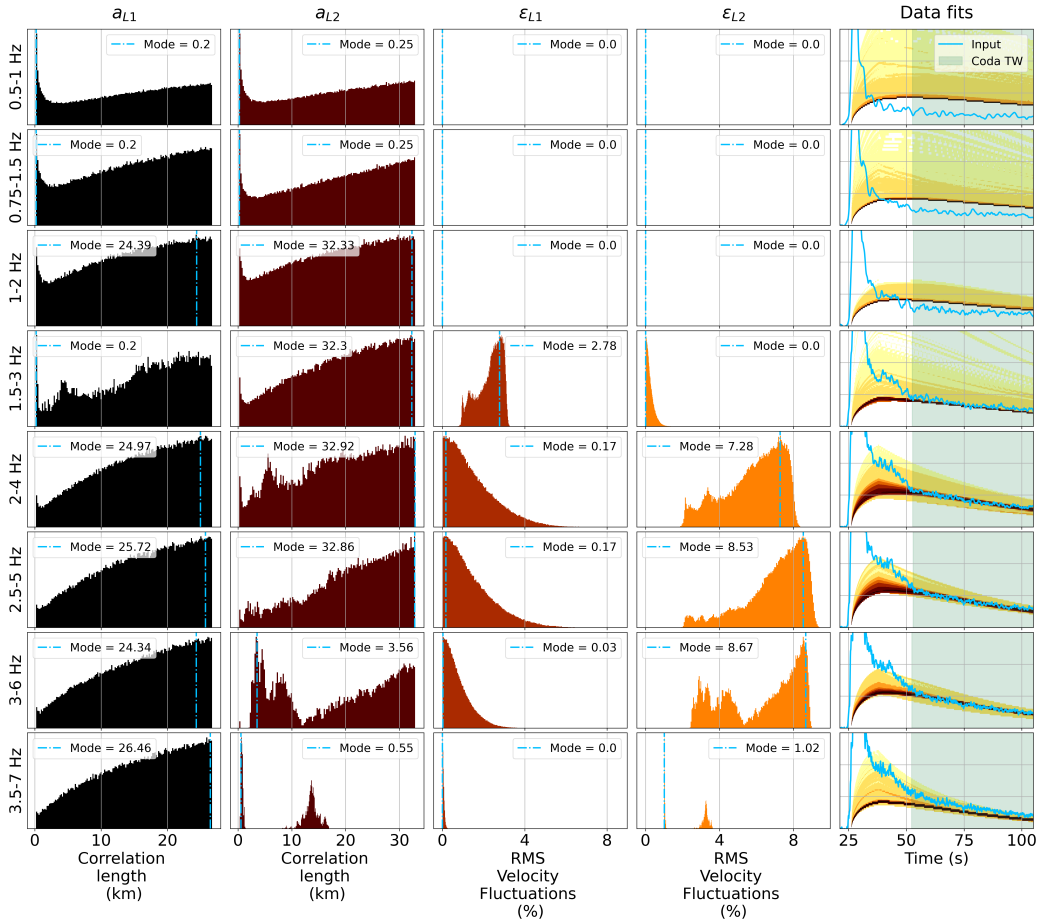

Figure 5.23: As Fig. 5.12 but for BOSA.

arrays prevented me from observing this effect. However, as shown in Fig. 5.11, the coda envelopes from the IMS arrays present much more complex and large variations of amplitude with frequency, thus adding more difficulty to their inversion and favouring the apparition of extreme behaviours of the algorithm.

In summary, the results presented in this chapter show that my E-EFMD and EFMD algorithms, while capable of producing good fits to the input data in some cases, can be heavily biased towards extreme values of some of the parameters. As discussed in Chapter 4, the origin of this behaviour is the clearly differentiated effect of each parameter on the obtained synthetic envelopes. Few, if any, conclusions can be drawn from the inversion results, and it is not possible to relate parameter values to the physical structure beneath the stations. Complex variations in coda amplitudes and decay rates add an extra challenge to the E-EFMD and EFMD inversions of datasets from areas with varying tectonic and geological contexts. Given the limitations and simplicity of the method, it is not clear whether it is at all suited to simultaneously resolve the depth dependence of the scattering and intrinsic attenuation parameters, as well as the frequency dependence of Q_i.

5.3 Conclusions

In this chapter, I initially apply the E-EFMD algorithm described and applied in Chapter 4 to new, large, high quality datasets of teleseismic events recorded at five stations part of the International Monitoring System, ILAR, PDAR, TXAR, YKA and BOSA. In addition to the standard E-EFMD, which inverts for the scattering and intrinsic attenuation parameters for each layer of 1- or 2-layer models, I also inverted the data for some stations using alternative implementations in which the frequency dependence coefficient of Q_i, α, is fixed, or inversions are carried out for each individual frequency band. The results from these inversions suggest that neither a lithospheric nor a crustal 1-layer model are complex enough to reproduce the observed coda envelopes. 2-layer models greatly improve the fits to the data for these IMS datasets, but these are still generally worse at all frequency bands than those for the Australian arrays presented in Section 4.2. This can be at least partly explained by the observation that, while data envelopes for PSA, ASAR and WRA have similar variations of coda amplitude and decay rate with frequency, those for the IMS stations are much more complex and change from one station to another (Fig. 5.11). These disparities are directly related to changes in the small-scale structure beneath the stations and point to the power law frequency dependence of Q_i assumed in my E-EFMD implementation and many attenuation studies possibly not being complex enough to explain them. As mentioned above, in this chapter I tested a new approach that allows me to independently invert the data for each frequency band without assuming any specific frequency dependence of Q_i. However, fits to the input data in these inversions are not always good and the parameter results show the same wide variability and bias towards extreme values of the attenuation parameters than my previous E-EFMD implementations.

Posterior PDFs from the E-EFMD inversions of the IMS stations data in this chapter also show the same extreme non-uniqueness and trade-offs present in the results for my synthetic tests and data inversions in Chapter 4, thus highlighting again the suitability of Bayesian inference for this kind of study. Posterior PDFs for the scattering and intrinsic attenuation parameters allowed me here to confirm that this behaviour is a consequence of the bias of the E-EFMD towards extreme values of Q_{i0}, which is itself caused by the very specific effect each parameter has on the computed synthetic envelopes (Section 4.1.1). These results strongly suggest that, whenever trying to simultaneously characterise seismic scattering and attenuation, either with an Energy Flux Model or a different technique, it is highly advisable to carry out detailed sensitivity analyses similar to the one in Section 4.1.1 in order to detect and potentially prevent bias in the obtained parameter values.

I also inverted the datasets for the IMS arrays studied in this chapter using an improved version of my initial implementation of the EFMD. This new version of the

code, faster and more efficient, confirmed my previous observation of 1-layer models not being complex enough to explain the data. Results for 2-layer models continued to present poor fits to the data in general. This observation is likely caused by the inability of the algorithm to match the low initial coda amplitudes present in the data, which in turn results in an effective bias towards low or extremely low values of ε. The apparent ability of the algorithm to fit some specific frequency bands in these inversions led me to invert the data using the single-frequency approach also applied to the E-EFMD in Section 5.2.1. These inversions continued to show the same tendency towards low ε values in most cases, even if the algorithm managed to accurately fit the data in more cases than for the multi-frequency inversions. As with my E-EFMD results, the EFMD bias towards low values of the RMS velocity fluctuations observed in the IMS arrays inversions prevents me from interpreting the obtained parameter values, or relating them to the physical structure beneath the arrays.

The data inversions in this chapter also explore the role of variations in the layering of the models on the obtained E-EFMD and EFMD results, which was suggested as a potential source for the non-uniqueness of the results in Chapter 4. While the lithospheric structures beneath YKA and BOSA are similar to those for the Australian arrays, with Moho and LAB depths being ~ 40 and ~ 200 km, those for ILAR, TXAR and PDAR have similar crustal thicknesses to YKA and BOSA but LABs less than 70 km deep (Fig. 5.3), thus resulting in very thin (10–20 km) bottom layers in their models. Still, inversion results for these arrays show the same non-uniqueness in the solutions and strong trade-offs between the scattering and intrinsic attenuation parameters (Figs. 5.5–5.9, 5.10 and A96–A99). Layer thicknesses in the lithospheric models for ILAR, TXAR and PDAR are almost the opposite to those for the Australian arrays, YKA and BOSA, with crusts up to 4 times thickner than the lithospheric mantle beneath them. Both the EFMD and E-EFMD are highly sensitive to variations in the model layering, but the fact that such different settings can produce such similar results from both of them suggests the trade-offs and effects of the different parameters to coda amplitudes are likely more important contributors to the non-uniqueness of the solutions. Still, it would be advisable to continue testing the algorithm for models with varying layer thicknesses, so this hypothesis could be confirmed.

Finally, my results show that, regardless of the origin of the lack of uniqueness in the solutions, relating the obtained parameter values to the physical small-scale structure beneath any of these stations remains not only difficult, but even potentially impossible. As discussed in Chapter 4, adding more prior information about the parameters and/or jointly inverting for P- and S-wave codas could help avoid extreme values of the parameters, thus potentially reducing the width of the obtained posterior PDFs and ameliorating the trade-offs between the parameters.

Chapter 6

Conclusions

Seismic scattering and absorption greatly affect the signals recorded by seismic instruments. Many disciplines obtain measurements from seismic amplitudes, either directly or indirectly, like seismic hazard estimates (e.g. Somerville, 2000; Jarahi, 2016; Malagnini et al., 2007) or magnitude-yield calculations in nuclear or chemical explosion monitoring (e.g. Selby et al., 2012; Zhang and Wen, 2013; Pilger et al., 2021). Therefore, it is essential to have an accurate and realistic characterization of the small-scale scattering and attenuation structures and the effects they have on recorded signals. Additionally, knowledge about these mechanisms can help us improve our understanding of the structure and dynamics of our planet, from the deep Earth to volcanoes and faults (e.g. De Siena et al., 2014; Napolitano et al., 2020; Sketsiou et al., 2021; Carcolé and Sato, 2010; Cormier and Li, 2002). For this purpose, in this thesis I applied Energy Flux Models to the study of scattering and intrinsic attenuation in the lithosphere. These simple but versatile techniques aim at characterizing the small-scale heterogeneity and attenuation structure of the lithosphere beneath seismic arrays or stations. Based on the conservation of energy and geometric spread as the seismic wavefront propagates through the model, Energy Flux Models implicitly include multiple scattering and are applicable to both weak and strong scattering regimes. Details on the theoretical background, implementation and testing of these methods, together with my Bayesian inference algorithm, as well as their application to real datasets, have been thoroughly described and discussed in the individual chapters. The present chapter summarises and draws conclusions over the entirety of the thesis.

In Chapter 2, I combined the single-layer Energy Flux Model (EFM, Korn, 1990), the depth-dependent Energy Flux Model (EFMD, Korn, 1997) and my own, new, Bayesian inference algorithm. From the EFM (Section 2.1.1), I obtain a first estimation of the intrinsic, scattering and diffusion quality factors, which I then use to compare the strength and effect of these different attenuation mechanisms on the recorded seis-

mograms. This method does not permit any layering in the structure, so these quality factors represent the average within a scattering layer of unspecified thickness. The EFMD (Section 2.1.2) allows multi-layer models, and I tested 1-, 2- and 3-layer models (Section 2.1.3), with these layers representing either the whole lithosphere (1-layer models), the crust and lithospheric mantle (2-layer models), or the upper and lower crust and lithospheric mantle (3-layer models). Adaptive variations in the thickness of these layers are not included in the EFMD Bayesian algorithm, since they modify the energy balance within the model and can greatly affect the results of the inversion. The intrinsic quality factor (Q_{i0}) and frequency dependence coefficient (α) obtained from the EFM are used to characterize the absorption structure in the EFMD models and assumed to take the same value throughout the entire lithosphere, since my initial implementation of this method does not allow for their independent calculation. The results from my EFMD synthetic tests (Section 2.1.3) show the ability of this approach to accurately recover the input parameter values for 1- and 2-layer models (correlation length, a, and RMS velocity fluctuations, ε, for each layer of the model). Fits to the synthetic data for the 3-layer model were excellent, but the EFMD inversion algorithm was not capable of accurately recovering the input parameter values and pointed to two independent families of parameters being equally capable of reproducing the input synthetic codas. These results highlight the presence of strong and complex trade-offs between the scattering parameters, as well as non-unique solutions (Section 2.1.3).

With the aim of testing the ability of the EFM/EFMD approach described above to resolve small differences in the scattering and attenuation structures and relate them to local tectonic histories, I applied it to large, high-quality datasets of teleseismic events recorded at the Pilbara (PSA), Alice Springs (ASAR) and Warramunga (WRA) seismic arrays in Chapter 3. PSA is located on the Archaean West Australian Craton (WAC), a tectonic block that has been located at passive margins without being affected by much tectonic activity throughout most of its history (e.g. Drummond and Collins, 1986) (Section 3.2). ASAR and WRA are located on the Proterozoic North Australian Craton (NAC) (e.g. Cawood and Korsch, 2008), with WRA being near the center of the craton in a tectonically quiet area, and ASAR lying on its southern edge (Fig. 3.4), in an area affected by more recent and intense tectonic activity (e.g. Aitken et al., 2009; Aitken, 2009) (Section 3.2). 3.3 From the EFM, I obtained lower ($Q_{i0} = 1000$), frequency dependent, values of the intrinsic quality factor for ASAR, while for PSA and WRA Q_i appears not to vary with frequency and takes higher values ($Q_i = 2100$, Table 3.2). The scattering, diffusion and combined quality factors, as well as the first estimation of the scattering parameters, take similar values for ASAR and WRA ($Q_{d0} = 400$ in both cases, and a and ε are 0.9 and 1.1 km, and 4.7 % and 4.5 % for ASAR and WRA respectively), while taking generally higher values for PSA (Table 3.2, Fig. 3.8), pointing to scattering and diffusion being weaker beneath this array

than under the others. My EFMD results provide more details about the heterogeneity structure and clearly point to the crust beneath the arrays being more heterogeneous than the lithospheric mantle (Section 3.3). Crustal correlation lengths take values in the 0.5–0.8, 0.2–1.4 and 0.7–1.5 km range for PSA, ASAR and WRA respectively, while in the lithospheric mantle they vary from 3–4 km to 32 km in all cases (Table 3.2). RMS velocity fluctuations in the crust and lithospheric mantle range from 2.3–2.5 % and 0.1–1.8 % for PSA, 2.4–3.0 % and 0.1–3.7 % for ASAR and 3.1–3.9 % and 0.5–5.0 % for WRA (Table 3.2). These inversions further highlight the non-uniqueness of the solutions observed in my synthetic tests in Section 2.1.3. All these values agree with previous studies in these regions and suggest the scattering structures under ASAR and WRA are similar to each other and different to PSA, a result that positively correlates with the tectonic histories of these areas and also matches previous scattering studies in the area (e.g. Kennett, 2015; Kennett and Furumura, 2016; Kennett et al., 2017).

To help overcome some of these limitations, in Chapter 4 I extended the EFMD Bayesian inference algorithm to include the value of Q_i at 1 Hz (Q_{i0}) and its frequency dependence coefficient (α) as free parameters, in addition to the correlation length (a) and RMS velocity fluctuations (ε). This new code, the E-EFMD, is therefore completely independent from the EFM and aims to overcome the limitation of the homogeneous Q_i structure assumed in my previous implementation of the method. To my knowledge, this is the first attempt at trying to simultaneously characterize the depth-dependent scattering and absorption structures of the lithosphere using a depth-dependent Energy Flux Model. My comprehensive testing of this new approach in Chapter 4 revealed very strong trade-offs between the same parameter in different layers of the model, but also between different parameters and layers. Of particular interest are the interactions between the intrinsic quality factors in the different layers of the model, which appear to be almost interchangeable and have a strong effect on the inversion results (Sections 4.1.2 and 4.3). These interactions lead to extremely non-unique inversion solutions, with parameter combinations representative of very different scattering and attenuation scenarios being capable of producing identical synthetic envelopes within the time window used for the analysis at all frequency bands (Sections 4.1.1 and 4.1.2). This inability to accurately retrieve the input parameter values means that, despite the algorithm achieving good fits to the data at all frequency bands, results from these inversions might not entirely represent the structure beneath the station.

To further test the E-EFMD, in Chapters 4 and 5, I applied it to the same datasets from PSA, ASAR and WRA I used in Chapter 3, but also to five new, analogous datasets of events recorded at arrays or stations part of the International Monitoring System (IMS). Results from these data inversions show the same extreme trade-offs and lack of unique solutions as my E-EFMD synthetic tests in Section 4.1.2, preventing

me from drawing any final conclusions for many of these stations. The comparison of my EFM, EFMD and E-EFMD results for the Australian arrays shows relatively good agreement between them (Section 4.2), but uncertainties (represented by wider, less Gaussian, posterior PDFs) are larger for the E-EFMD and most of the variability of the parameters can be attributed to the behaviour of the algorithm itself, instead of the physical structure beneath the arrays. These results are, therefore, less reliable than those from the EFMD, shown in Section 3.3. Inversion results for the IMS stations in Chapter 5 show a similar algorithm behaviour, with the addition of very poor fits to the input data in most cases. For some of them, the E-EFMD appears to be capable of fitting some of the frequency bands, but a simultaneous fit of bands D–H from Table 2.3 was only possible for ILAR. EFMD inversion results for the IMS arrays also failed to produce reliable, or interpretable, results that could be used to characterize the heterogeneity structure of the lithosphere beneath them. In this case, the algorithm shows a marked bias towards low or extremely low values of the RMS velocity fluctuations that reduce the effect of correlation lengths in the obtained synthetic envelopes. The most likely cause for this behaviour is the low initial coda amplitudes present in the data for most of the arrays (Fig. 5.11). In general, the results I present here illustrate that relating either the E-EFMD or EFMD results to the scattering and attenuation structure of the lithosphere beneath any of these arrays/stations, or the tectonic history of the regions they are located on, is extremely challenging, and few clear conclusions can be drawn from them.

The synthetic tests and real data inversions I carried out provide a thorough insight into the characteristics and behaviour of both single-layer and depth-dependent Energy Flux Models when combined with a Bayesian inference algorithm. My results suggest full inversions for the scattering and attenuation parameters within each layer of the model, such as the ones done by the E-EFMD, fail to yield reliable results. Inverting only for the scattering parameters, using the EFM/EFMD combination, decreases the magnitude of the trade-offs between the parameters and helps, therefore, reducing the non-uniqueness in the parameter inversions. These results are mainly caused by the simplicity of the EFMD algorithm and the different effect each parameter has on the computed synthetic envelopes. Equation 2.20 defines the energy balance within each layer of the model in the EFMD and E-EFMD in terms of the one-way travel times through the layers and the scattering and absorption quality factors. My sensitivity tests (Section 4.1.1) show that each parameter has a very specific effect on the synthetic envelopes, with the scattering and attenuation parameters being related to the initial coda amplitudes and the decay rate, respectively. In general, the effect of even small variations in Q_{i0} on the synthetic codas was much greater than for the other parameters, which results in the E-EFMD algorithm being biased towards Q_{i0}, an effect that is also observed, though at a smaller scale, for ε variations in the EFMD. This, together with

the extreme non-uniqueness inherent to the EFMD/E-EFMD, also shown in Sections 2.1.3, 4.1.2, 4.2 or 5.2, greatly reduces the importance of the remaining parameters in the inversion, as well as the reliability of the results.

There are some approaches that could be taken to overcome the issues discussed here, both with the EFM/EFMD and the E-EFMD algorithms. For cases in which we are more interested in resolving the absorption structure than the scattering one, an alternative implementation of the EFM/EFMD in which the scattering parameters are obtained from the EFM, in a 1D approximation, while the EFMD inverts for the absorption could help invert for Q_{i0} and α without the problems shown in E-EFMD results. However, the limitation of the EFM to a single, unconstrained, layer would remain. Combining the EFMD with other methods, such as the coda normalization method (e.g. Aki, 1980a; Yoshimoto et al., 1993) or peak-delay measurements (e.g. Takahashi et al., 2009), to invert for either the scattering or absorption parameters, instead of using the EFM, could also help resolve some of the complex trade-offs and reduce the uncertainty in the inversion results while circumventing the disadvantages of the EFM. Adding more constraints to the problem, by simultaneously fitting both P- and S-wave codas could also help improve the results and reduce the non-uniqueness of the solutions.

My results also highlight the importance of carrying out the inversion in a probabilistic sense using Bayesian inference, a conclusion from this study that is probably valid beyond Energy Flux Models and applies to any method aimed at characterizing the small-scale structure of the Earth. As discussed above, the sensitivity analysis I carried out in Section 4.1.1 clearly shows the effect of each parameter on the obtained coda envelopes, and proves that essentially identical amplitudes can be obtained from parameter combinations representative of very different scattering and attenuation scenarios. Such a complex behaviour in a system requires, by necessity, either to be combined with a Bayesian inference algorithm, such as the one I use here, or a comprehensive sampling of the entire parameter space, so a clearer representation of the misfit and posterior PDF can be obtained. The Bayesian framework I incorporated into the EFMD and expanded in the E-EFMD could also provide some assistance in eliminating part of the non-uniqueness of the solutions shown in my results. Throughout this thesis, I have always assumed no prior knowledge on the values of the parameters. However, it would be possible to obtain information about some of the parameters from previous studies, either in the areas of interest or comparable locations, and add those to the algorithm in the form of non-uniform prior distributions, thus effectively narrowing down the range of suitable parameter combinations and focusing the inversion towards more realistic values.

In summary, in this thesis I characterize the small-scale heterogeneity and attenuation structure of the lithosphere beneath seismic arrays and stations by using Energy

Flux Models. The main advantage of these techniques is their computational efficiency, which allowed me to combine them with a Bayesian inference algorithm and test millions of parameter combinations in a fast manner. Results from this algorithm provide comprehensive information about the parameter space, as well as the uncertainty and trade-offs in the determination of the parameters. My synthetic tests suggest we can either resolve the scattering or the absorption parameters in 1- or 2-layer models, but challenges in inverting for both remain. Still, and despite their simplicity, real data inversions using my EFM/EFMD approach have proven to yield reasonable results in agreement with similar past studies. The EFM/EFMD approach can still be considered, therefore, as a useful and computationally efficient tool that can either be used on their own or as a first step in the application of other, more computationally expensive, methods.

Bibliography

Aitken, A. (2009). "The architecture, kinematics, and lithospheric processes of a compressional intraplate orogen occurring under Gondwana assembly: The Petermann orogeny, central Australia". *Lithosphere* 1 (6), 343–357.

Aitken, A. R. A., P. G. Betts, R. F. Weinberg, and D. Gray (2009). "Constrained potential field modeling of the crustal architecture of the Musgrave Province in central Australia: Evidence for lithospheric strengthening due to crust-mantle boundary uplift". *Journal of Geophysical Research* 114 (B12), B12405.

Aki, K. (1969). "Analysis of the seismic coda of local earthquakes as scattered waves". *Journal of Geophysical Research* 74 (2), 615–631.

Aki, K. (1973). "Scattering of P waves under the Montana Lasa". *Journal of Geophysical Research* 78 (8), 1334–1346.

Aki, K. (1980a). "Attenuation of shear-waves in the lithosphere for frequencies from 0.05 to 25 Hz". *Physics of the Earth and Planetary Interiors* 21 (1), 50–60.

Aki, K. (1980b). "Scattering and attenuation of shear waves in the lithosphere". *Journal of Geophysical Research: Solid Earth* 85 (B11), 6496–6504.

Aki, K. and B. Chouet (1975). "Origin of coda waves: Source, attenuation, and scattering effects". *Journal of Geophysical Research* 80 (23), 3322–3342.

Anderson, D. L. and J. W. Given (1982). *Absorption Band Q Model for the Earth.* Tech. rep. B5, 3893–3904.

Bayes, T. (1763). "LII. An essay towards solving a problem in the doctrine of chances. By the late Rev. Mr. Bayes, F. R. S. communicated by Mr. Price, in a letter to John Canton, A. M. F. R. S". *Philosophical Transactions of the Royal Society of London* 53, 370–418.

Belochitski, A. and V. Krasnopolsky (2021). "Robustness of neural network emulations of radiative transfer parameterizations in a state-of-the-art general circulation model". *Geoscientific Model Development* 14 (12), 7425–7437.

Betts, P. G., R. J. Armit, J. Stewart, A. R. A. Aitken, L. Ailleres, P. Donchak, L. Hutton, I. Withnall, and D. Giles (2016). "Australia and Nuna". *Geological Society, London, Special Publications* 424 (1), 47–81.

Betts, P. G., D. Giles, G. S. Lister, and L. R. Frick (2002). "Evolution of the Australian lithosphere". *Australian Journal of Earth Sciences* 49 (4), 661–695.

Beyreuther, M., R. Barsch, L. Krischer, T. Megies, Y. Behr, and J. Wassermann (2010). "ObsPy: A Python Toolbox for Seismology". *Seismological Research Letters* 81 (3), 530–533.

Blake, D. and B. Kilgour (1998). "Geological Regions of Australia 1:5,000,000 Scale [Dataset]". *Geoscience Australia, Canberra. Available at: http://pid.geoscience.gov.au/dataset/ga/32366.*

Bodin, T., M. Sambridge, H. Tkalčić, P. Arroucau, K. Gallagher, and N. Rawlinson (2012). "Transdimensional inversion of receiver functions and surface wave dispersion". *Journal of Geophysical Research: Solid Earth* 117 (B2), n/a–n/a.

Bodin, T., H. Yuan, and B. Romanowicz (2014). "Inversion of receiver functions without deconvolution—application to the Indian craton". *Geophysical Journal International* 196 (2), 1025–1033.

Borleanu, F., L. De Siena, C. Thomas, M. Popa, and M. Radulian (2017). "Seismic scattering and absorption mapping from intermediate-depth earthquakes reveals complex tectonic interactions acting in the Vrancea region and surroundings (Romania)". *Tectonophysics* 706-707, 129–142.

Brooks, S., A. German, G. Jones, and X.-L. Meng, eds. (2011). *Handbook of Markov chain Monte Carlo*. CRC Press, 619.

Carcolé, E. and H. Sato (2010). "Spatial distribution of scattering loss and intrinsic absorption of short-period S waves in the lithosphere of Japan on the basis of the Multiple Lapse Time Window Analysis of Hi-net data". *Geophysical Journal International* 180 (1), 268–290.

Carluccio, R., A. Giuntini, V. Materni, S. Chiappini, C. Bignami, A. Caracciolo, A. Pignatelli, S. Stramondo, R. Console, M. Chiappini, F. D'Ajello Caracciolo, A. Pignatelli, S. Stramondo, R. Console, and M. Chiappini (2014). "A Multidisciplinary Study of the DPRK Nuclear Tests". *Pure and Applied Geophysics* 171 (3-5), 341–359.

Cawood, P. and R. Korsch (2008). "Assembling Australia: Proterozoic building of a continent". *Precambrian Research* 166 (1-4), 1–35.

Chandrasekhar, S. (1950). *Radiative Transfer*. Oxford: Clarendon Press, 408.

Chernov, L. A. and R. A. Silverman (1960). *Wave Propagation in a Random Medium*. New York: McGraw-Hill.

Christensen, N. I. and W. D. Mooney (1995). "Seismic velocity structure and composition of the continental crust: A global view". *Journal of Geophysical Research: Solid Earth* 100 (B6), 9761–9788.

Clitheroe, G., O. Gudmundsson, and B. L. N. Kennett (2000). "The crustal thickness of Australia". *Journal of Geophysical Research: Solid Earth* 105 (B6), 13697–13713.

Condie, K. C., M. E. Bickford, R. C. Aster, E. Belousova, and D. W. Scholl (2011). "Episodic zircon ages, Hf isotopic composition, and the preservation rate of continental crust". *Bulletin of the Geological Society of America* 123 (5), 951–957.

Corbishley, D. J. (1970). "Structure under Seismic Arrays". *Geophysical Journal International* 21 (5), 415–425.

Cormier, V. F. and X. Li (2002). "Frequency-dependent seismic attenuation in the inner core 2. A scattering and fabric interpretation". *Journal of Geophysical Research: Solid Earth* 107 (B12), 14–1.

Cormier, V. F. (1982). "The effect of attenuation on seismic body waves". *Bulletin of the Seismological Society of America* 72 (6), S169–S200.

Cormier, V. F. and C. J. Sanborn (2019). "Trade-Offs in Parameters Describing Crustal Heterogeneity and Intrinsic Attenuation from Radiative Transport Modeling of High-Frequency Regional Seismograms". *Bulletin of the Seismological Society of America* 109 (1), 312–321.

CTBT (1996). *Comprehensive Nuclear-Test-Ban Treaty*. Tech. rep. New York: United Nations General Assembly.

De Meutter, P., J. Camps, A. Delcloo, and P. Termonia (2018). "Source localisation and its uncertainty quantification after the third DPRK nuclear test". *Scientific Reports 2018 8:1* 8 (1), 1–11.

De Siena, L., C. Thomas, G. P. Waite, S. C. Moran, and S. Klemme (2014). "Attenuation and scattering tomography of the deep plumbing system of Mount St. Helens". *Journal of Geophysical Research: Solid Earth* 119 (11), 8223–8238.

Debayle, E. and B. L. N. Kennett (2000). "The Australian continental upper mantle: Structure and deformation inferred from surface waves". *Journal of Geophysical Research: Solid Earth* 105 (B11), 25423–25450.

Del Pezzo, E., J. Ibañez, J. Prudencio, F. Bianco, and L. De Siena (2016). "Absorption and scattering 2-D volcano images from numerically calculated space-weighting functions". *Geophysical Journal International* 206 (2), 742–756.

Domínguez, T. and C. J. Rebollar (1997). "Regional variations of seismic attenuation from coda and L g waves in northern Baja California". *Journal of Geophysical Research: Solid Earth* 102 (B7), 15259–15268.

Douglas, A. (2013). *Forensic Seismology and Nuclear Test Bans*. First. Cambridge: Cambridge University Press, 72–120.

Drummond, B. and C. Collins (1986). "Seismic evidence for underplating of the lower continental crust of Australia". *Earth and Planetary Science Letters* 79 (3-4), 361–372.

Durek, J. J. and G. Ekström (1996). "A Radial Model of Anelasticity Consistent with Long-Period Surface-Wave Attenuation". *Bulletin of the Seismological Society of America* 86 (1A), 144–158.

Dziewonski, A. M. and D. L. Anderson (1981). "Preliminary reference Earth model". *Physics of the Earth and Planetary Interiors* 25 (4), 297–356.

Eberhart-Phillips, D., S. Bannister, and S. Ellis (2014). "Imaging P and S attenuation in the termination region of the Hikurangi subduction zone, New Zealand". *Geophysical Journal International* 198 (1), 516–536.

Etgen, J., S. H. Gray, and Y. Zhang (2009). "An overview of depth imaging in exploration geophysics". *Geophysics* 74 (6), WCA5–WCA17.

Eulenfeld, T. and U. Wegler (2016). "Measurement of intrinsic and scattering attenuation of shear waves in two sedimentary basins and comparison to crystalline sites in Germany". *Geophysical Journal International* 205 (2), 744–757.

Evans, D. A. and R. N. Mitchell (2011). "Assembly and breakup of the core of Paleoproterozoic-Mesoproterozoic supercontinent Nuna". *Geology* 39 (5), 443–446.

Evers, L. G., D. N. Green, N. W. Young, and M. Snellen (2013). "Remote hydroacoustic sensing of large icebergs in the southern Indian Ocean: Implications for iceberg monitoring". *Geophysical Research Letters* 40 (17), 4694–4699.

Fan, X.-P. P., Y.-C. C. He, C.-J. J. Yang, and J.-F. F. Wang (2020). "Evaluation of crustal inhomogeneity parameters in the southern Longmenshan fault zone and adjacent regions". *Journal of Seismology* 24 (6), 1175–1188.

Fang, Y. and G. Müller (1996). "Attenuation Operators and Complex Wave Velocities for Scattering in Random Media". *Pure and Applied Geophysics* 148 (1), 269–285.

Fehler, M., M. Hoshiba, H. Sato, and K. Obara (1992). "Separation of scattering and intrinsic attenuation for the Kanto-Tokai region, Japan, using measurements of S -wave energy versus hypocentral distance". *Geophysical Journal International* 108 (3), 787–800.

Fichtner, A., B. L. Kennett, H. Igel, and H. P. Bunge (2009). "Full seismic waveform tomography for upper-mantle structure in the Australasian region using adjoint methods". *Geophysical Journal International* 179 (3), 1703–1725.

Fielitz, D. and U. Wegler (2015). "Intrinsic and scattering attenuation as derived from fluid induced microseismicity at the German Continental Deep Drilling site". *Geophysical Journal International* 201 (3), 1346–1361.

Flatté, S. M. and R.-S. Wu (1988). "Small-scale structure in the lithosphere and asthenosphere deduced from arrival time and amplitude fluctuations at NORSAR". *Journal of Geophysical Research* 93 (B6), 6601.

Ford, H. A., K. M. Fischer, D. L. Abt, C. A. Rychert, and L. T. Elkins-Tanton (2010). "The lithosphere–asthenosphere boundary and cratonic lithospheric layering beneath Australia from Sp wave imaging". *Earth and Planetary Science Letters* 300 (3-4), 299–310.

Frankel, A. and L. Wennerberg (1987). "Energy-Flux Model of Seismic Coda: Separation of Scattering and Intrinsic Attenuation". *Bulletin of the Seismological Society of America* 77 (4), 1223–1251.

Gaebler, P. J., T. Eulenfeld, and U. Wegler (2015a). "Seismic scattering and absorption parameters in the W-Bohemia/Vogtland region from elastic and acoustic radiative transfer theory". *Geophysical Journal International* 203 (3), 1471–1481.

Gaebler, P. J., C. Sens-Schönfelder, and M. Korn (2015b). "The influence of crustal scattering on translational and rotational motions in regional and teleseismic coda waves". *Geophysical Journal International* 201 (1), 355–371.

Gibbons, S. J., T. Kværna, S. P. Näsholm, and S. Mykkeltveit (2018). "Probing the DPRK Nuclear Test Site down to Low-Seismic Magnitude". *Seismological Research Letters* 89 (6), 2034–2041.

Goleby, B. R., R. D. Shaw, C. Wright, B. L. N. Kennett, and K. Lambeck (1989). "Geophysical evidence for 'thick-skinned' crustal deformation in central Australia". *Nature* 337 (6205), 325–330.

González Álvarez, I. N., S. Rost, A. Nowacki, and N. D. Selby (2021). "Small-scale lithospheric heterogeneity characterization using Bayesian inference and energy flux models". *Geophysical Journal International* 227 (3), 1682–1699.

Gusev, A. A. and I. R. Abubakirov (1987). "Monte-Carlo simulation of record envelope of a near earthquake". *Physics of the Earth and Planetary Interiors* 49 (1-2), 30–36.

Hastings, W. K. (1970). "Monte Carlo sampling methods using Markov chains and their applications". *Biometrika* 57 (1), 97–109.

Helmberger, D. V. (1968). "The crust-mantle transition in the Bering sea". *Bulletin of the Seismological Society of America* 58 (1), 179–214.

Heyburn, R., D. Bowers, and D. N. Green (2020). "Seismic and hydroacoustic observations from recent underwater events in the South Atlantic Ocean". *Geophysical Journal International* 223 (1), 289–300.

Hirose, T., H. Nakahara, and T. Nishimura (2019). "A Passive Estimation Method of Scattering and Intrinsic Absorption Parameters From Envelopes of Seismic Ambient Noise Cross-Correlation Functions". *Geophysical Research Letters* 46 (7), 3634–3642.

Hock, S., M. Korn, J. R. R. Ritter, and E. Rothert (2004). "Mapping random lithospheric heterogeneities in northern and central Europe". *Geophysical Journal International* 157 (1), 251–264.

Hock, S. and M. Korn (2000). "Random heterogeneity of the lithosphere across the Trans-European Suture Zone". *Geophysical Journal International* 141 (1), 57–70.

Hoshiba, M. (1991). "Simulation of multiple-scattered coda wave excitation based on the energy conservation law". *Physics of the Earth and Planetary Interiors* 67 (1-2), 123–136.

Jarahi, H. (2016). "Probabilistic Seismic Hazard Deaggregation for Karaj City (Iran)". *American Journal of Engineering and Applied Sciences* 9 (3), 520–529.

Jerkins, A. E., H. A. Shiddiqi, T. Kværna, S. J. Gibbons, J. Schweitzer, L. Ottemöller, and H. Bungum (2020). "The 30 June 2017 North Sea Earthquake: Location, char-

acteristics, and context". *Bulletin of the Seismological Society of America* 110 (2), 937–952.

Kalinowski, M. B. and P. Mialle (2021). "Introduction to the Topical Issue on Nuclear Explosion Monitoring and Verification: Scientific and Technological Advances". *Pure and Applied Geophysics* 178 (7), 2397–2401.

Karlstrom, K. E., S. S. Harlan, M. L. Williams, J. McLelland, and J. W. Geissman (2001). *Long-lived (1.8-1.0 Ga) convergent orogen in southern Laurentia, its extensions to Australia and Baltica, and implications for refining Rodinia.* Tech. rep., 5–30.

Kennett, B. L. N. and E. R. Engdahl (1991). "Traveltimes for global earthquake location and phase identification". *Geophysical Journal International* 105 (2), 429–465.

Kennett, B. L. N., A. Fichtner, S. Fishwick, and K. Yoshizawa (2013). "Australian Seismological Reference Model (AuSREM): mantle component". *Geophysical Journal International* 192 (2), 871–887.

Kennett, B. L. N. and T. Furumura (2016). "Multiscale seismic heterogeneity in the continental lithosphere". *Geochemistry, Geophysics, Geosystems* 17 (3), 791–809.

Kennett, B. L. N. and M. Salmon (2012). "AuSREM: Australian Seismological Reference Model". *Australian Journal of Earth Sciences* 59 (8), 1091–1103.

Kennett, B. L. N., M. Salmon, E. Saygin, and A. W. Group (2011). "AusMoho: the variation of Moho depth in Australia". *Geophysical Journal International* 187 (2), 946–958.

Kennett, B. L. N., J. Stipčević, and A. Gorbatov (2015). "Spiral-Arm Seismic Arrays". *Bulletin of the Seismological Society of America* 105 (4), 2109–2116.

Kennett, B. L., K. Yoshizawa, and T. Furumura (2017). "Interactions of multi-scale heterogeneity in the lithosphere: Australia". *Tectonophysics* 717, 193–213.

Kennett, B. (2015). "Lithosphere–asthenosphere P-wave reflectivity across Australia". *Earth and Planetary Science Letters* 431, 225–235.

Kennett, B. and T.-S. Phạm (2018). "Evolution of the correlation wavefield extracted from seismic event coda". *Physics of the Earth and Planetary Interiors* 282 (May), 100–109.

Kennett, B. and E. Saygin (2015). "The nature of the Moho in Australia from reflection profiling: A review". *GeoResJ* 5, 74–91.

Kennett, B. and C. Sippl (2018). "Lithospheric discontinuities in Central Australia". *Tectonophysics* 744 (June), 10–22.

Koper, K. D., T. C. Wallace, S. R. Taylor, and H. E. Hartse (2001). "Forensic seismology and the sinking of the Kursk". *Eos, Transactions American Geophysical Union* 82 (4), 37–37.

Korn, M. (1988). "P-wave coda analysis of short-period array data and the scattering and absorptive properties of the lithosphere". *Geophysical Journal* 93 (3), 437–449.

Korn, M. (1990). "A modified energy flux model for lithospheric scattering of teleseismic body waves". *Geophysical Journal International* 102 (1), 165–175.

Korn, M. (1993). "Determination of Site-Dependent Scattering Q From P -Wave Coda Analysis With an Energy-Flux Model". *Geophysical Journal International* 113 (1), 54–72.

Korn, M. (1997). "Modelling the teleseismic P coda envelope: depth dependent scattering and deterministic structure". *Physics of the Earth and Planetary Interiors* 104 (1-3), 23–36.

Korsch, R., B. Goleby, J. Leven, and B. Drummond (1998). "Crustal architecture of central Australia based on deep seismic reflection profiling". *Tectonophysics* 288 (1-4), 57–69.

Langston, C. A. (1989). "Scattering of teleseismic body waves under Pasadena, California". *Journal of Geophysical Research* 94 (B2), 1935.

Le Bras, R. J., H. Kuzma, V. Sucic, and G. Bokelmann (2016). "Observations and Bayesian location methodology of transient acoustic signals (likely blue whales) in the Indian Ocean, using a hydrophone triplet". *The Journal of the Acoustical Society of America* 139 (5), 2656.

Lee, S. J., Y. C. Chan, D. Komatitsch, B. S. Huang, and J. Tromp (2009a). "Effects of realistic surface topography on seismic ground motion in the Yangminshan region of Taiwan based upon the spectral-element method and LiDAR DTM". *Bulletin of the Seismological Society of America* 99 (2 A), 681–693.

Lee, S. J., D. Komatitsch, B. S. Huang, and J. Tromp (2009b). "Effects of topography on seismic-wave propagation: An example from Northern Taiwan". *Bulletin of the Seismological Society of America* 99 (1), 314–325.

Lekić, V., J. Matas, M. Panning, and B. Romanowicz (2009). "Measurement and implications of frequency dependence of attenuation". *Earth and Planetary Science Letters* 282 (1-4), 285–293.

Li, L. (2010). "Strongly frequency-dependent intrinsic and scattering Q for the western margin of the Sichuan basin, China, as revealed by a phenomenological model". *Pure and Applied Geophysics* 167 (12), 1577–1578.

Li, L. (2011). "Comment on "Small-scale heterogeneities below the Lanzhou CTBTO seismic array, from seismic wave field fluctuations" by Shen and Ritter". *Journal of Seismology* 15 (1), 165–170.

Liu, T., S. L. Klemperer, G. Ferragut, and C. Yu (2019). "Post-critical SsPmp and its applications to Virtual Deep Seismic Sounding (VDSS) – 2: 1-D imaging of the crust/mantle and joint constraints with receiver functions". *Geophysical Journal International* 219 (2), 1334–1347.

Ma, X. and Z. Huang (2020). "Small-scale scattering heterogeneities beneath the northern Tien Shan from the teleseismic P wavefield". *Earth, Planets and Space* 72 (13).

Maceira, M., P. S. Blom, J. K. MacCarthy, O. E. Marcillo, G. G. Euler, M. L. Begnaud, S. R. Ford, M. E. Pasyanos, G. J. Orris, M. P. Foxe, S. J. Arrowsmith, B. J. Merchant, and M. E. Slinkard (2017). *Trends in Nuclear Explosion Monitoring Research & Development - A Physics Perspective*. Tech. rep. Los Alamos, NM (United States): Los Alamos National Laboratory (LANL), 170.

Maeda, T., S. Takemura, and T. Furumura (2017). "OpenSWPC: an open-source integrated parallel simulation code for modeling seismic wave propagation in 3D heterogeneous viscoelastic media". *Earth, Planets and Space* 69 (1), 102.

Mahalanobis, P. C. (1936). *On the generalized distance in statistics*. National Institute of Science of India.

Malagnini, L., K. Mayeda, R. Uhrhammer, A. Akinci, and R. B. Herrmann (2007). "A Regional Ground-Motion Excitation/Attenuation Model for the San Francisco Region". *Bulletin of the Seismological Society of America* 97 (3), 843–862.

Margerin, L. (2003). "Multiple scattering of high-frequency seismic waves in the deep Earth: PKP precursor analysis and inversion for mantle granularity". *Journal of Geophysical Research* 108 (B11), 2514.

Margerin, L. (2005). "Introduction To Radiative Transfer Theory". *Geophysical Monograph-American Geophysical Union* 157, 1–47.

Margerin, L., A. Bajaras, and M. Campillo (2019). "A scalar radiative transfer model including the coupling between surface and body waves". *Geophysical Journal International* 219 (2), 1092–1108.

Margerin, L., M. Campillo, and B. Van Tiggelen (1998). "Radiative transfer and diffusion of waves in a layered medium: new insight into coda Q". *Geophysical Journal International* 134 (2), 596–612.

McLaughlin, K. L. and R. .-. Jih (1988). "Scattering from near-source topography: Teleseismic observations and numerical simulations". *Bulletin of the Seismological Society of America* 78 (4), 1399–1414.

Metropolis, N., A. W. Rosenbluth, M. N. Rosenbluth, A. H. Teller, and E. Teller (1953). "Equation of State Calculations by Fast Computing Machines". *The Journal of Chemical Physics* 21 (6), 1087–1092.

Metropolis, N. and S. Ulam (1949). "The Monte Carlo Method". *Journal of the American Statistical Association* 44 (247), 335–341.

Metz, D., A. B. Watts, I. Grevemeyer, and M. Rodgers (2018). "Tracking Submarine Volcanic Activity at Monowai: Constraints From Long-Range Hydroacoustic Measurements". *Journal of Geophysical Research: Solid Earth* 123 (9), 7877–7895.

Müller, T. M., B. Gurevich, and M. Lebedev (2010). "Seismic wave attenuation and dispersion resulting from wave-induced flow in porous rocks — A review". *Geophysics* 75 (5), 147–75.

Myers, J. S. (1990). "Precambrian tectonic evolution of part of Gondwana, southwestern Australia". *Geology* 18 (6), 537.

Myers, S. C., S. R. Ford, R. J. Mellors, S. Baker, and G. Ichinose (2018). "Absolute Locations of the North Korean Nuclear Tests Based on Differential Seismic Arrival Times and InSAR". *Seismological Research Letters* 89 (6), 2049–2058.

Nakahara, H. and K. Yoshimoto (2011). "Radiative transfer of elastic waves in two-dimensional isotropic scattering media: Semi-analytical approach for isotropic source radiation". *Earth, Planets and Space* 63 (6), 459–468.

Napolitano, F., L. De Siena, A. Gervasi, I. Guerra, R. Scarpa, and M. La Rocca (2020). "Scattering and absorption imaging of a highly fractured fluid-filled seismogenetic volume in a region of slow deformation". *Geoscience Frontiers* 11 (3), 989–998.

Nardoni, C., L. De Siena, F. Cammarano, F. Magrini, and E. Mattei (2021). "Modelling regional-scale attenuation across Italy and the Tyrrhenian Sea". *Physics of the Earth and Planetary Interiors* 318, 106764.

Neut, J. van der, K. Wapenaar, J. Thorbecke, E. Slob, and I. Vasconcelos (2015). "An illustration of adaptive Marchenko imaging". *The Leading Edge* 34 (7), 818–822.

Ogiso, M. (2019). "A method for mapping intrinsic attenuation factors and scattering coefficients of s waves in 3-D space and its application in southwestern Japan". *Geophysical Journal International* 216 (2), 948–957.

Pasyanos, M. E., T. G. Masters, G. Laske, and Z. Ma (2014). "LITHO1.0: An updated crust and lithospheric model of the Earth". *Journal of Geophysical Research: Solid Earth* 119 (3), 2153–2173.

Peacock, S., A. Douglas, and D. Bowers (2017). "Joint maximum-likelihood magnitudes of presumed underground nuclear test explosions". *Geophysical Journal International* 210 (2), 621–644.

Picotti, S., J. M. Carcione, J. G. Rubino, J. E. Santos, and F. Cavallini (2010). "A viscoelastic representation of wave attenuation in porous media". *Computers and Geosciences* 36 (1), 44–53.

Pilger, C., P. Gaebler, P. Hupe, A. C. Kalia, F. M. Schneider, A. Steinberg, H. Sudhaus, and L. Ceranna (2021). "Yield estimation of the 2020 Beirut explosion using open access waveform and remote sensing data". *Scientific Reports 2021 11:1* 11 (1), 1–14.

Pisarevsky, S. A., S.-Å. Elming, L. J. Pesonen, and Z.-X. Li (2014). "Mesoproterozoic paleogeography: Supercontinent and beyond". *Precambrian Research* 244, 207–225.

Prieto, G. A., J. F. Lawrence, and G. C. Beroza (2009). "Anelastic Earth structure from the coherency of the ambient seismic field". *Journal of Geophysical Research* 114 (B7), B07303.

Prudencio, J., J. M. Ibáñez, E. Del Pezzo, J. Martí, A. García-Yeguas, and L. De Siena (2015). "3D Attenuation Tomography of the Volcanic Island of Tenerife (Canary Islands)". *Surveys in Geophysics* 36 (5), 693–716.

Prudencio, J., Y. Aoki, M. Takeo, J. M. Ibáñez, E. Del Pezzo, and W. Song (2017). "Separation of scattering and intrinsic attenuation at Asama volcano (Japan): Evi-

dence of high volcanic structural contrasts". *Journal of Volcanology and Geothermal Research* 333-334, 96–103.

Przybilla, J. and M. Korn (2008). "Monte Carlo simulation of radiative energy transfer in continuous elastic random media-three-component envelopes and numerical validation". *Geophysical Journal International* 173 (2), 566–576.

Randall, G. E. and T. J. Owens (1994). "Array analysis of the large-aperture array of the 1988–89 PASSCAL Basin and Range Passive-Source Seismic Experiment". *Geophysical Journal International* 116 (3), 618–636.

Rautian, T. G. and V. I. Khalturin (1978). "The use of the coda for determination of the earthquake source spectrum". *Bulletin of the Seismological Society of America* 68 (4), 923–948.

Raymond, O., J. Totterdell, M. Woods, and A. Stewart (2018). "Australian Geological Provinces 2018.01 edition". *Geoscience Australia, Canberra. Available at: http://pid.geoscience.gov.au/dataset/ga/116823.*

Ritter, J. R. and E. Rothert (2000). "Variations of the lithospheric seismic scattering strength below the Massif Central, France and the Frankonian Jura, SE Germany". *Tectonophysics* 328 (3-4), 297–305.

Ritter, J. R. R., S. A. Shapiro, and B. Schechinger (1998). "Scattering parameters of the lithosphere below the Massif Central, France, from teleseismic wavefield records". *Geophysical Journal International* 134 (1), 187–198.

Ritter, J. R., P. Martin Mai, G. Stoll, and K. Fuchs (1997). "Scattering of teleseismic waves in the lower crust observations in the Massif Central, France". *Physics of the Earth and Planetary Interiors* 104 (1-3), 127–146.

Rogers, J. J. and M. Santosh (2002). "Configuration of Columbia, a Mesoproterozoic Supercontinent". *Gondwana Research* 5 (1), 5–22.

Rogers, J. J. and M. Santosh (2003). "Supercontinents in earth history". *Gondwana Research* 6 (3), 357–368.

Romanowicz, B. (1995). "A global tomographic model of shear attenuation in the upper mantle". *Journal of Geophysical Research* 100 (B7), 375–387.

Romanowicz, B. and J. J. Durek (2000). "Seismological constraints on attenuation in the Earth: A review". *Washington DC American Geophysical Union Geophysical Monograph Series*. Vol. 117, 161–179.

Rost, S., G. A. Houseman, A. W. Frederiksen, D. G. Cornwell, M. Kahraman, S. Altuncu Poyraz, U. M. Teoman, D. A. Thompson, N. Türkelli, L. Gülen, M. Utkucu, and T. J. Wright (2021). "Structure of the northwestern North Anatolian Fault Zone imaged via teleseismic scattering tomography". *Geophysical Journal International* 227 (2), 922–940.

Rost, S., E. J. Garnero, and Q. Wiliams (2006). "Fine-scale ultralow-velocity zone structure from high-frequency seismic array data". *Journal of Geophysical Research: Solid Earth* 111 (B9).

Rost, S. and C. Thomas (2002). "Array seismology: Methods and applications". *Reviews of Geophysics* 40 (3), 1008.

Rothert, E. and J. R. R. Ritter (2000). "Small-scale heterogeneities below the Gräfenberg array, Germany from seismic wavefield fluctuations of Hindu Kush events". *Geophysical Journal International* 140 (1), 175–184.

Salmon, M., B. L. N. Kennett, and E. Saygin (2013a). "Australian Seismological Reference Model (AuSREM): crustal component". *Geophysical Journal International* 192 (1), 190–206.

Salmon, M., B. Kennett, T. Stern, and A. Aitken (2013b). "The Moho in Australia and New Zealand". *Tectonophysics* 609, 288–298.

Sams, M. S., J. P. Neep, M. H. Worthington, and M. S. King (1997). "The measurement of velocity dispersion and frequency-dependent intrinsic attenuation in sedimentary rocks". *Geophysics* 62 (5), 1456–1464.

Sanborn, C. J., V. F. Cormier, and M. Fitzpatrick (2017). "Combined effects of deterministic and statistical structure on high-frequency regional seismograms". *Geophysical Journal International* 210 (2), 1143–1159.

Sato, H. (1977). "Energy propagation including scattering effects single isotropic scattering approximation." *Journal of Physics of the Earth* 25 (1), 27–41.

Sato, H. (1984). "Attenuation and envelope formation of three-component seismograms of small local earthquakes in randomly inhomogeneous lithosphere". *Journal of Geophysical Research: Solid Earth* 89 (B2), 1221–1241.

Sato, H. (1995). "Formulation of the multiple non-isotropic scattering process in 3-D space on the basis of energy transport theory". *Geophysical Journal International* 121 (2), 523–531.

Sato, H. and K. Emoto (2017). "Synthesis of a scalar wavelet intensity propagating through von Kármán-type random media: joint use of the radiative transfer equation with the Born approximation and the Markov approximation". *Geophysical Journal International* 211 (1), 512–527.

Sato, H. and K. Emoto (2018). "Synthesis of a Scalar Wavelet Intensity Propagating Through von Kármán-type Random Media: Radiative Transfer Theory Using the Born and Phase-Screen Approximations". *Geophysical Journal International*, 909–923.

Sato, H., M. C. Fehler, and T. Maeda (2012). *Seismic Wave Propagation and Scattering in the Heterogeneous Earth : Second Edition*. Springer Science & Business Media.

Savage, B. and D. V. Helmberger (2001). "Kursk Explosion". *Bulletin of the Seismological Society of America* 91 (4), 753–759.

Selby, N. D., P. D. Marshall, and D. Bowers (2012). "mb:Ms Event Screening Revisited". *Bulletin of the Seismological Society of America* 102 (1), 88–97.

Shapiro, S. A. and G. Kneib (1993). "Seismic Attenuation By Scattering: Theory and Numerical Results". *Geophysical Journal International* 114 (2), 373–391.

Shapiro, S. A., R. Schwarz, and N. Gold (1996). "The effect of random isotropic inhomogeneities on the phase velocity of seismic waves". *Geophysical Journal International* 127 (3), 783–794.

Shearer, P. M. and P. S. Earle (2004). "The global short-period wavefield modelled with a Monte Carlo seismic phonon method". *Geophysical Journal International* 158 (3), 1103–1117.

Shen, X. and J. R. R. Ritter (2010). "Small-scale heterogeneities below the Lanzhou CTBTO seismic array, from seismic wave field fluctuations". *Journal of Seismology* 14 (3), 481–493.

Shen, X.-Z., C.-Z. Zhang, C. Zheng, and C.-Y. Hao (2010). "Study on the small-scale heterogeneities below the Hailaer CTBTO seismic array". *Chinese Journal of Geophysics* 53 (5), 1158–1166.

Simons, F. J., A. Zielhuis, and R. D. der Hilst (1999). "The deep structure of the Australian continent inferred from surface wave tomography". *Lithos* 48, 17–43.

Sipkin, S. A. and J. Revenaugh (1994). "Regional variation of attenuation and travel time in China from analysis of multple- ScS phases". *Journal of Geophysical Research: Solid Earth* 99 (B2), 2687–2699.

Sippl, C. (2016). "Moho geometry along a north-south passive seismic transect through Central Australia". *Tectonophysics* 676, 56–69.

Sketsiou, P., L. De Siena, S. Gabrielli, and F. Napolitano (2021). "3-D attenuation image of fluid storage and tectonic interactions across the Pollino fault network". *Geophysical Journal International* 226 (1), 536–547.

Sketsiou, P., F. Napolitano, A. Zenonos, and L. De Siena (2020). "New insights into seismic absorption imaging". *Physics of the Earth and Planetary Interiors* 298, 106337.

Snieder, R. (2006). "The Theory of Coda Wave Interferometry". *Pure and Applied Geophysics* 163 (2-3), 455–473.

Somerville, P. (2000). "Seismic hazard evaluation". *Bulletin of the New Zealand Society for Earthquake Engineering* 33 (3), 371–386.

Stachnik, J. C., G. A. Abers, and D. H. Christensen (2004). "Seismic attenuation and mantle wedge temperatures in the Alaska subduction zone". *Journal of Geophysical Research: Solid Earth* 109 (10), 10304.

Stein, S. and M. Wysession (2005). *An Introduction to Seismology, Earthquakes, and Earth Structure (Google eBook)*, 512.

Sun, W., J. Ba, T. M. Müller, J. M. Carcione, and H. Cao (2015). "Comparison of P -wave attenuation models of wave-induced flow". *Geophysical Prospecting* 63 (2), 378–390.

Takahashi, T., H. Sato, T. Nishimura, and K. Obara (2009). "Tomographic inversion of the peak delay times to reveal random velocity fluctuations in the lithosphere:

Method and application to northeastern Japan". *Geophysical Journal International* 178 (3), 1437–1455.

Takeuchi, N. (2016). "Differential Monte Carlo method for computing seismogram envelopes and their partial derivatives". *Journal of Geophysical Research: Solid Earth* 121 (5), 3428–3444.

Tarantola, A. (2005). *Inverse problem theory and methods for model parameter estimation*. Vol. 89. Siam.

Thorbecke, J., E. Slob, J. Brackenhoff, J. van der Neut, and K. Wapenaar (2017). "Implementation of the Marchenko method". *Geophysics* 82 (6), WB29–WB45.

Tisato, N., B. Quintal, S. Chapman, Y. Podladchikov, and J.-P. Burg (2015). "Bubbles attenuate elastic waves at seismic frequencies: First experimental evidence". *Geophysical Research Letters* 42 (10), 3880–3887.

Toksöz, M. N., D. H. Johnston, and A. Timur (1979). "Attenuation of seismic waves in dry and saturated rocks: I. Laboratory measurements". *Geophysics* 44 (4), 681–690.

Upton, A. C. (1962). "Comments on report of the United Nations Scientific Committee on the Effects of Atomic Radiation." *Cancer research* 22 (10), 1139–41.

Vernik, L. and A. Nur (1992). "Ultrasonic velocity and anisotropy of hydrocarbon source rocks". *GEOPHYSICS* 57 (5), 727–735.

Wang, H., J. van Hunen, D. G. Pearson, and M. B. Allen (2014). "Craton stability and longevity: The roles of composition-dependent rheology and buoyancy". *Earth and Planetary Science Letters* 391, 224–233.

Wegler, U. (2003). "Analysis of multiple scattering at Vesuvius volcano, Italy, using data of the TomoVes active seismic experiment". *Journal of Volcanology and Geothermal Research* 128 (1-3), 45–63.

Wellman, P. (1998). "Mapping of geophysical domains in the Australian continental crust using gravity and magnetic anomalies". *Structure and evolution of the Australian continent*. Washington, D.C: AGU: American Geophysical Union, 59–71.

Wu, R.-S. (1985). "Multiple scattering and energy transfer of seismic waves – separation of scattering effect from intrinsic attenuation – I. Theoretical modelling". *Geophysical Journal International* 82 (1), 57–80.

Wu, R.-S. and K. Aki (1988). "Introduction: Seismic wave scattering in three-dimensionally heterogeneous earth". *Pure and Applied Geophysics PAGEOPH* 128 (1-2), 1–6.

Xia, H., X. Song, R. Weaver, and J. Li (2020). "Amplitude and decay of long-period coda of great earthquakes". *Physics of the Earth and Planetary Interiors* 306, 106538.

Yoshimoto, K., H. Sato, and M. Ohtake (1993). "Frequency-Dependent Attenuation of P and S Waves In the Kanto Area, Japan, Based On the Coda-Normalization Method". *Geophysical Journal International* 114 (1), 165–174.

Yoshizawa, K. and B. L. N. Kennett (2015). "The lithosphere-asthenosphere transition and radial anisotropy beneath the Australian continent". *Geophysical Research Letters* 42 (10), 3839–3846.

Zelt, C. A. and P. J. Barton (1998). "Three-dimensional seismic refraction tomography: A comparison of two methods applied to data from the Faeroe Basin". *Journal of Geophysical Research: Solid Earth* 103 (B4), 7187–7210.

Zhang, M. and L. Wen (2013). "High-precision location and yield of North Korea's 2013 nuclear test". *Geophysical Research Letters* 40 (12), 2941–2946.

Zhang, X., C. Roy, A. Curtis, A. Nowacki, and B. Baptie (2020). "Imaging the subsurface using induced seismicity and ambient noise: 3-D tomographic Monte Carlo joint inversion of earthquake body wave traveltimes and surface wave dispersion". *Geophysical Journal International* 222 (3), 1639–1655.

Zhao, G., M. Sun, S. A. Wilde, and S. Li (2004). "A Paleo-Mesoproterozoic supercontinent: assembly, growth and breakup". *Earth-Science Reviews* 67, 91–123.

Zhao, L. F., X. B. Xie, W. M. Wang, N. Fan, X. Zhao, and Z. X. Yao (2017). "The 9 September 2016 North Korean Underground Nuclear Test". *Bulletin of the Seismological Society of America* 107 (6), 3044–3051.

Appendices

A.1 Dataset size analysis complementary results

Figures in this section complement those showed in Section 3.1.1, which analyses the effect of the size of the dataset on coda amplitudes and results obtained from the EFMD inversion. Figures A1 to A7 contain the amplitude residuals for all frequency bands listed on Table 2.3, except from frequency band B, which was already included in Section 3.1.1. Similarly, Figs. A8 to A14 contain the statistical analysis of the coda amplitude residuals shown in Figs. A1 to A7, as well as the decay rates obtained from the EFM (Section 2.1.1).

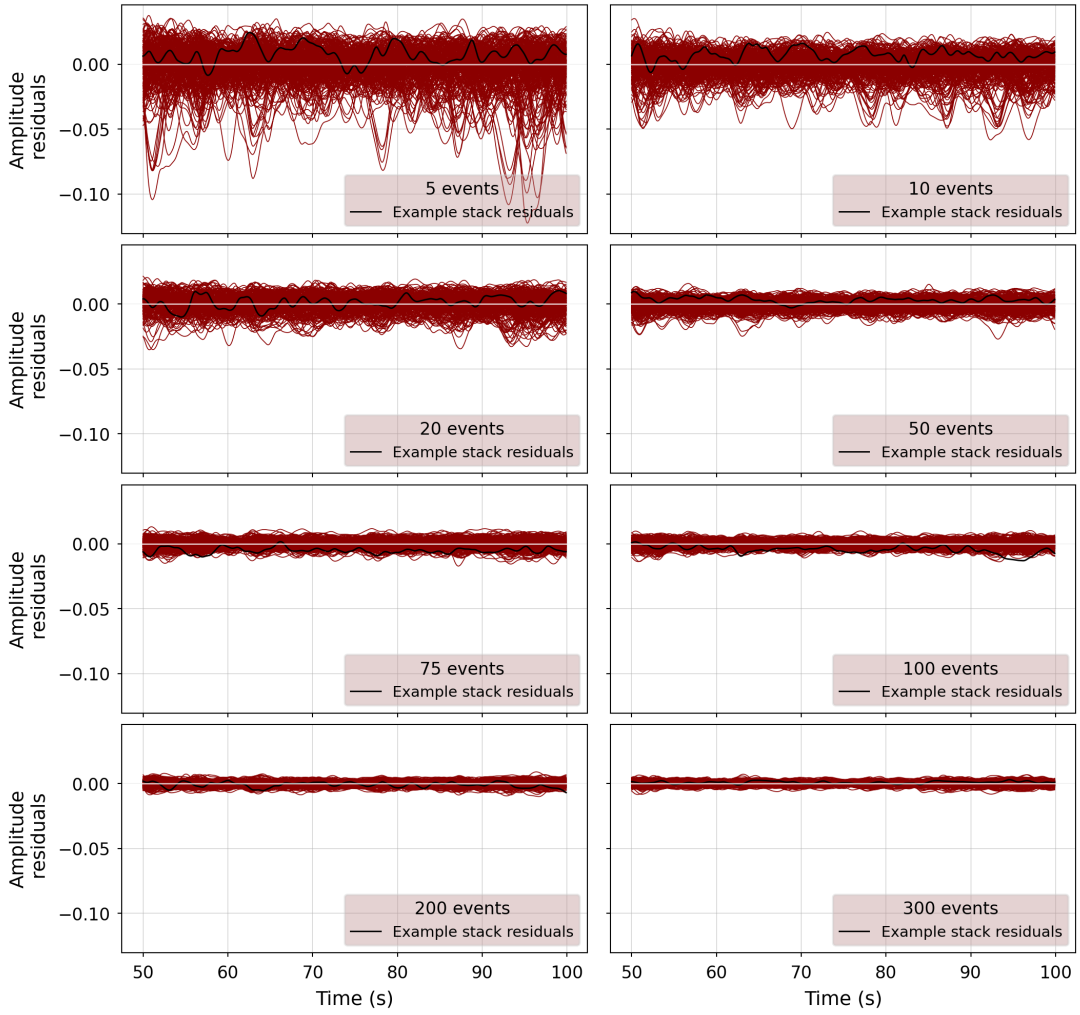

Figure A1: Amplitude residuals obtained by subtracting each of the 250 realizations of stacks of N events from the stack of the full dataset (407 events, Table 3.1) available for frequency band A (0.5 – 1 Hz, Table 2.3). Black lines highlight the residuals for a randomly chosen stack.

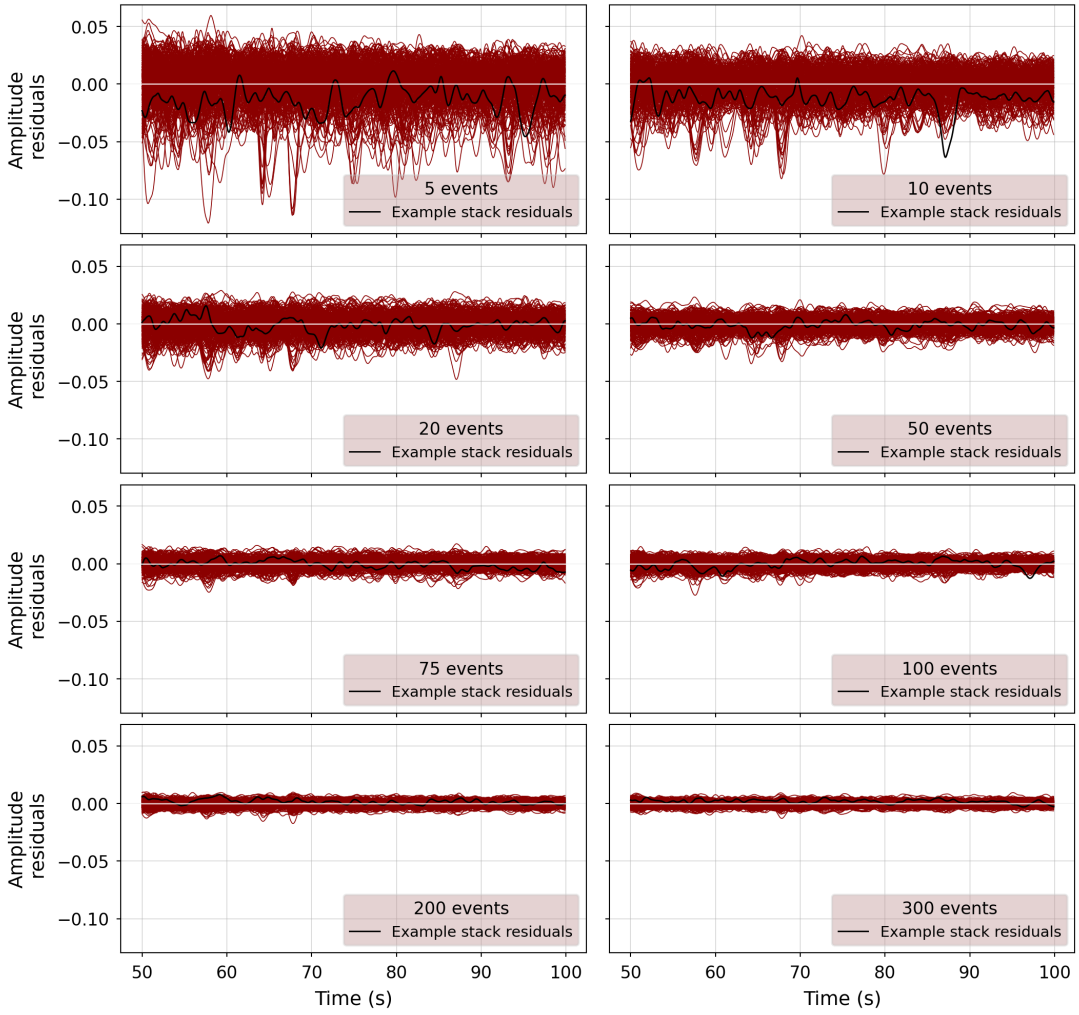

Figure A2: As Fig. A1, but for frequency band B (0.75 – 1.5 Hz, Table 2.3).

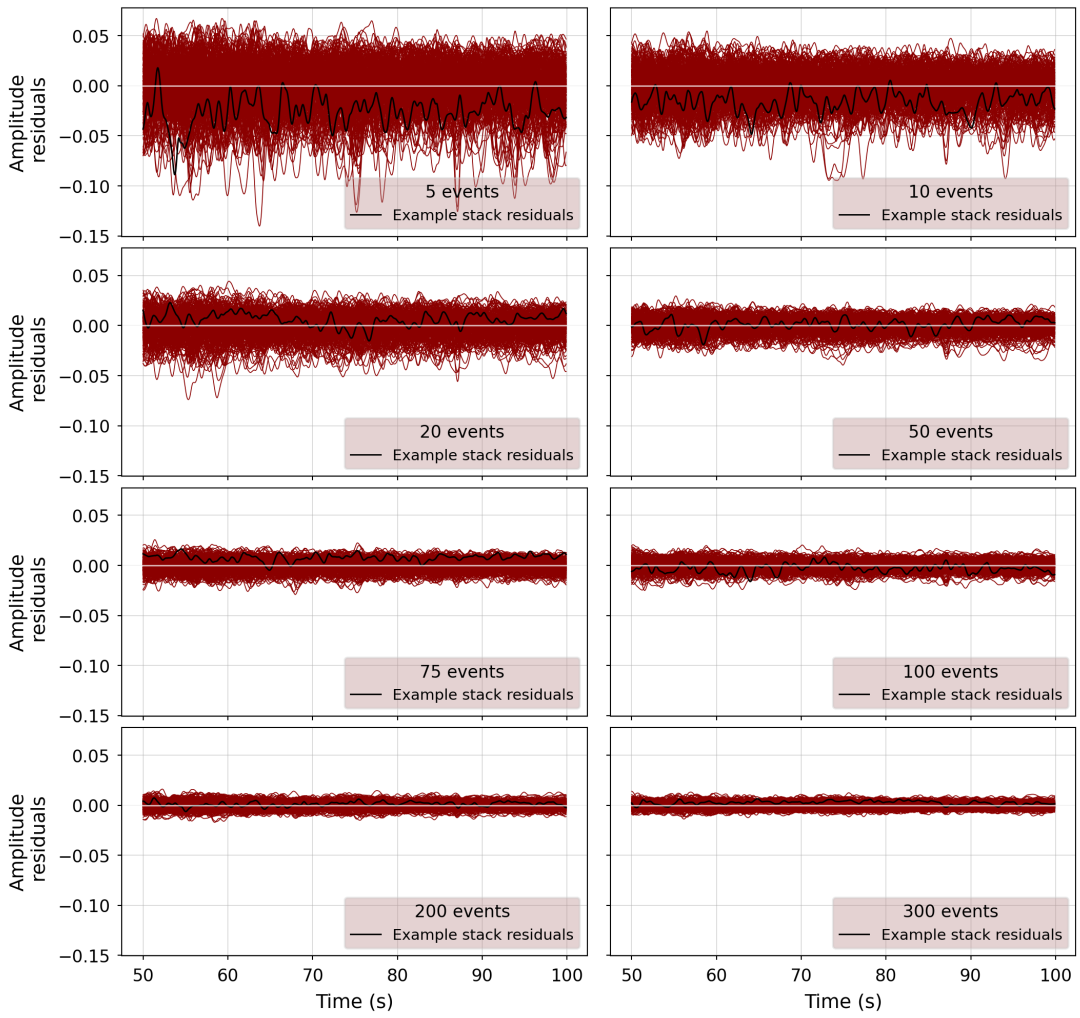

Figure A3: As Fig. A1, but for frequency band C (1 – 2 Hz, Table 2.3).

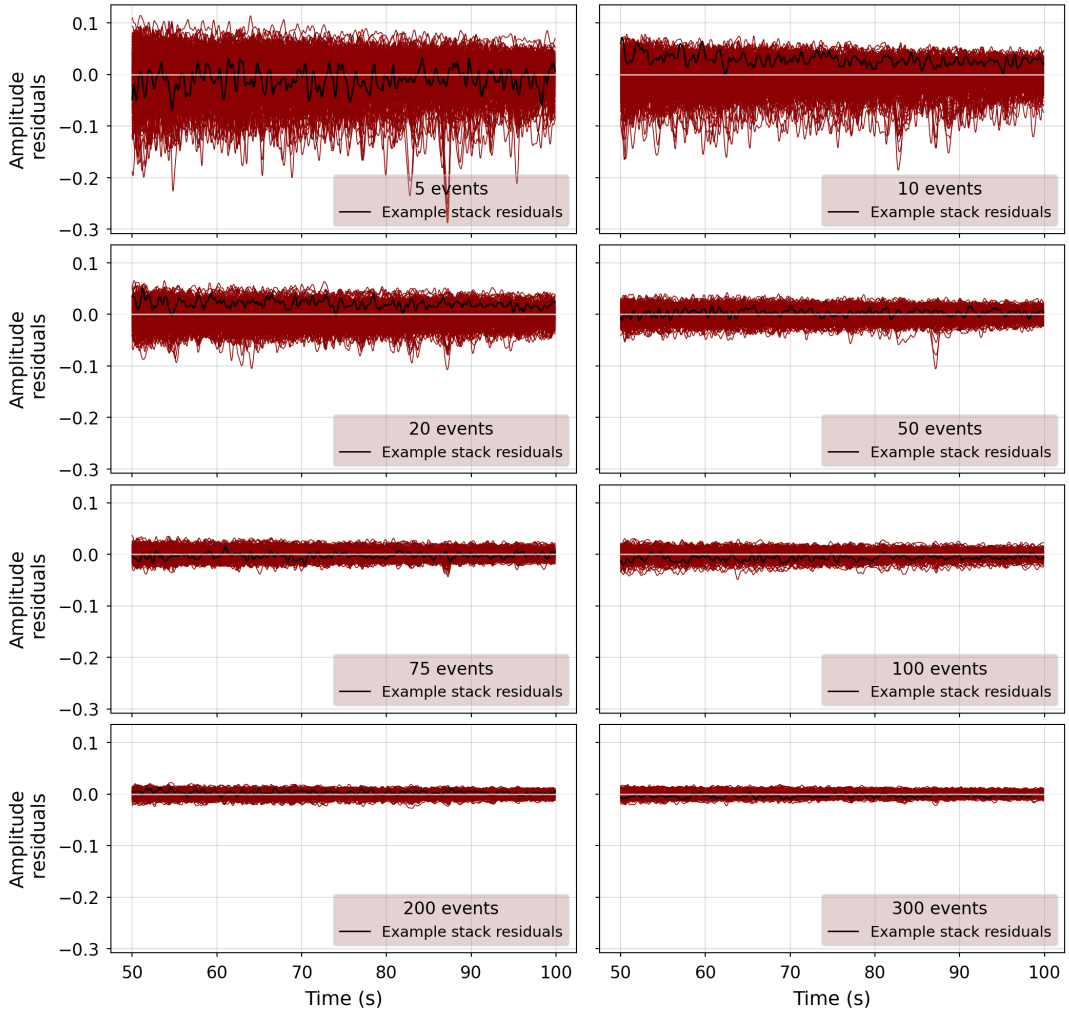

Figure A4: As Fig. A1, but for frequency band E (2 – 4 Hz, Table 2.3).

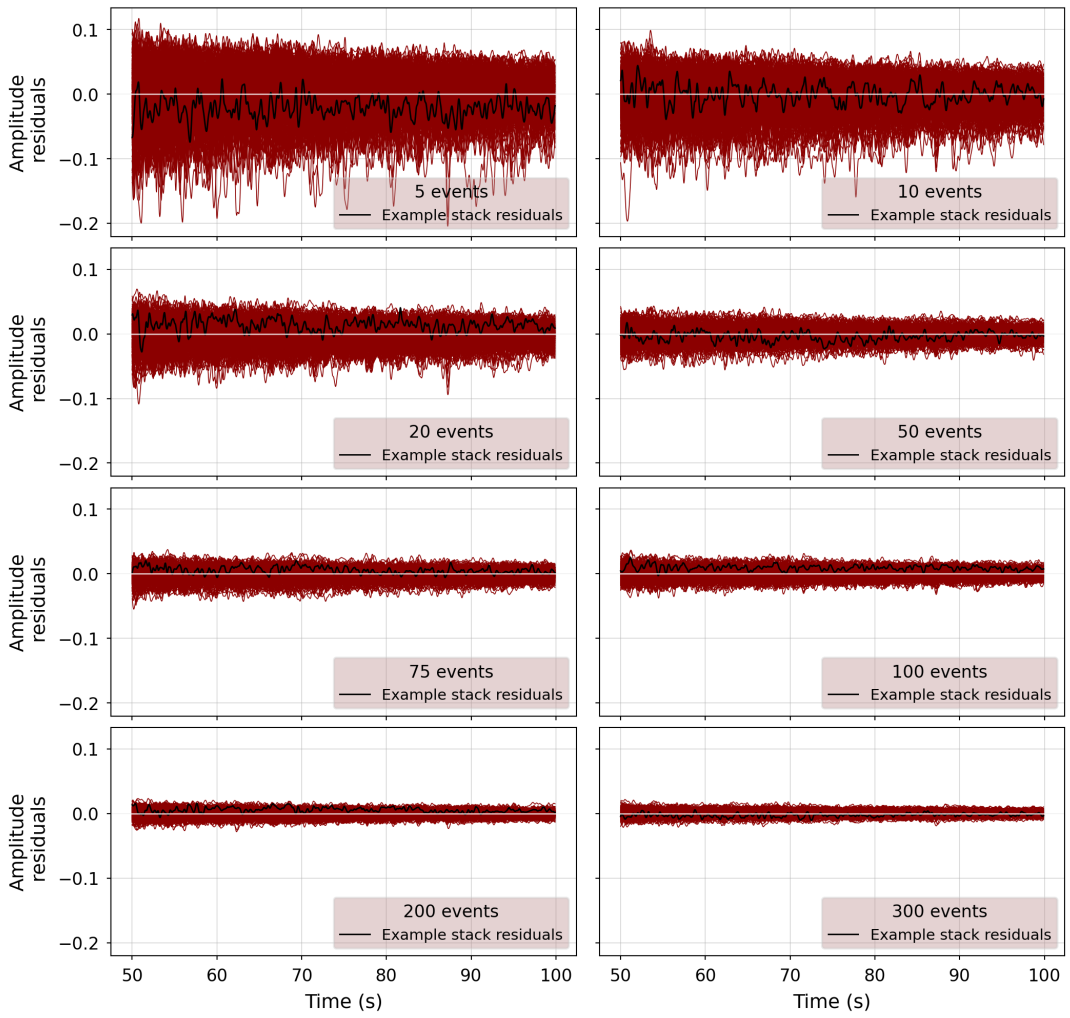

Figure A5: As Fig. A1, but for frequency band F (2.5 – 5 Hz, Table 2.3).

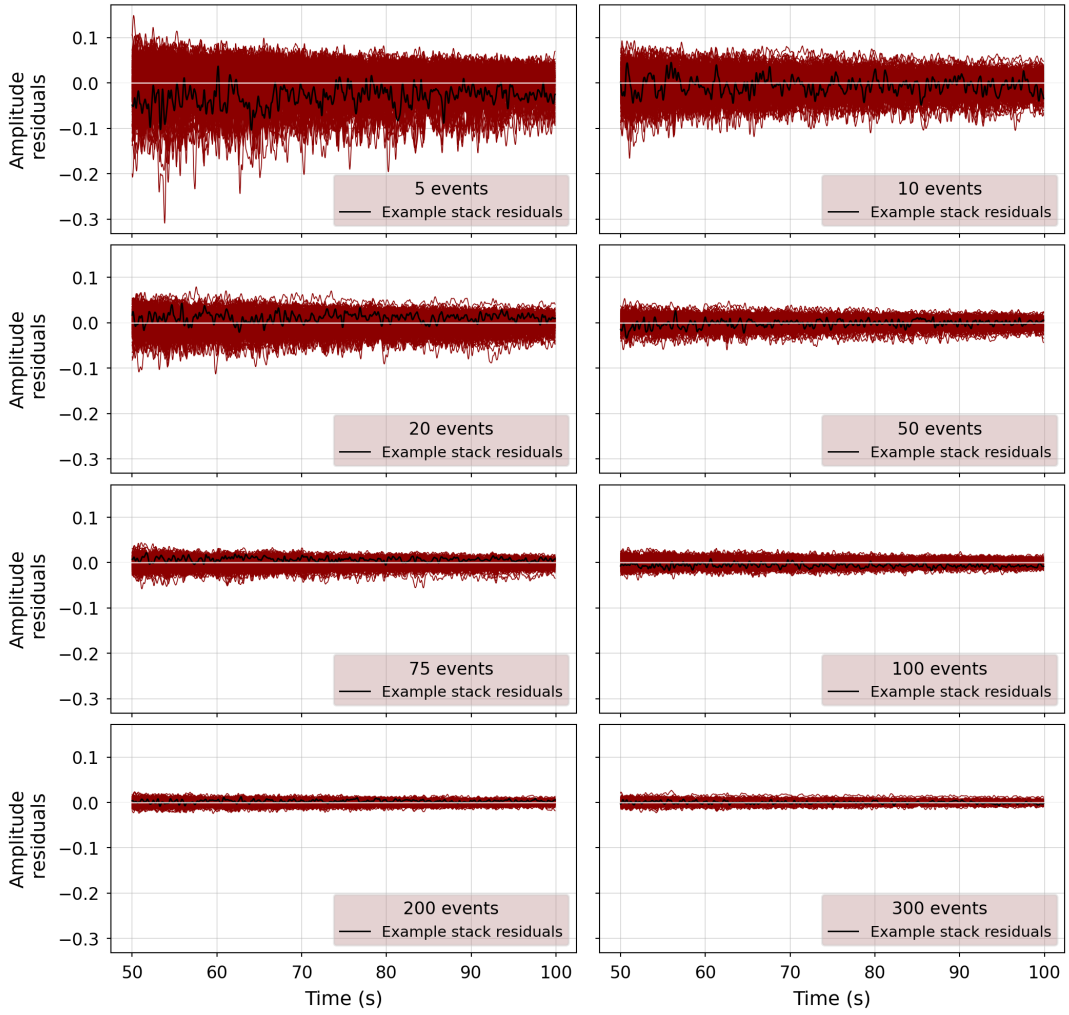

Figure A6: As Fig. A1, but for frequency band G (3 – 6 Hz, Table 2.3).

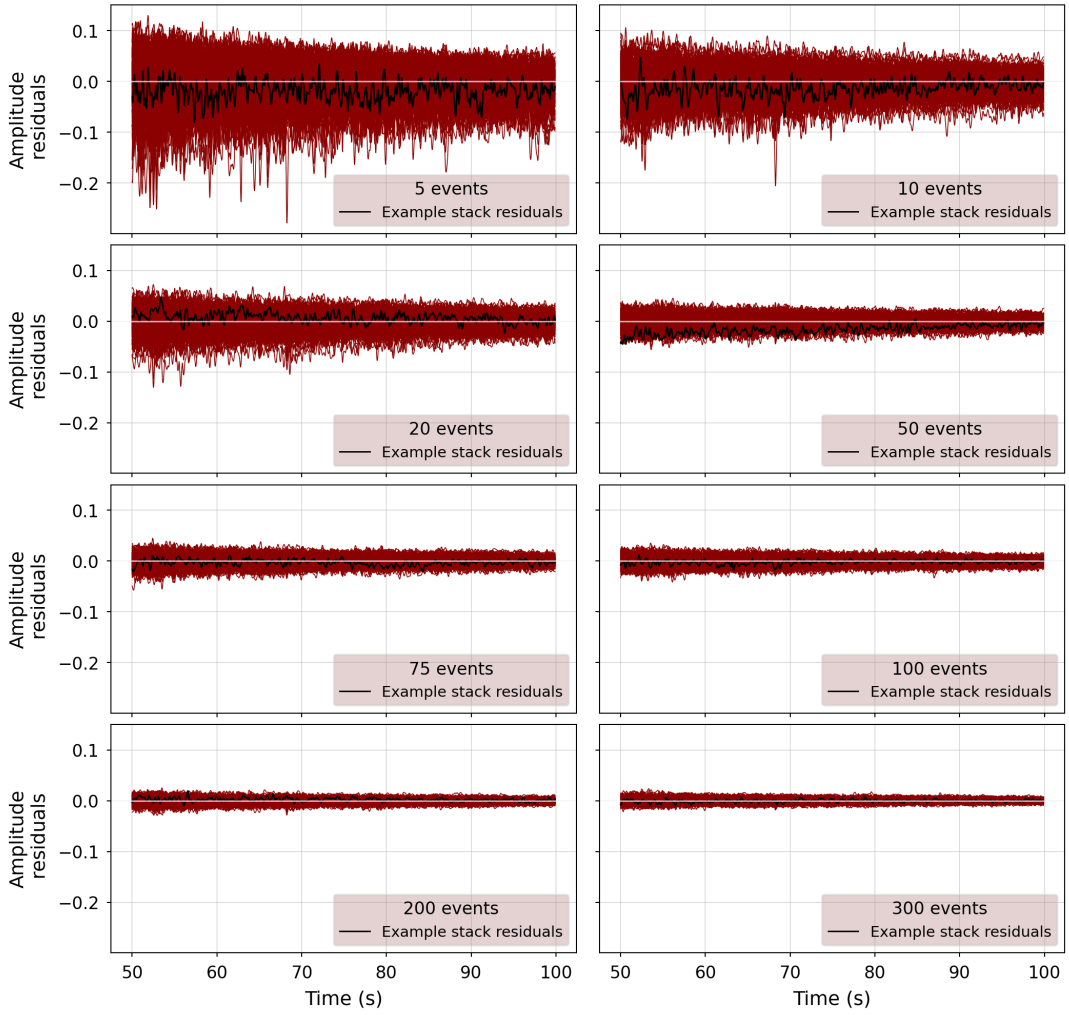

Figure A7: As Fig. A1, but for frequency band H (3.5 – 7 Hz, Table 2.3).

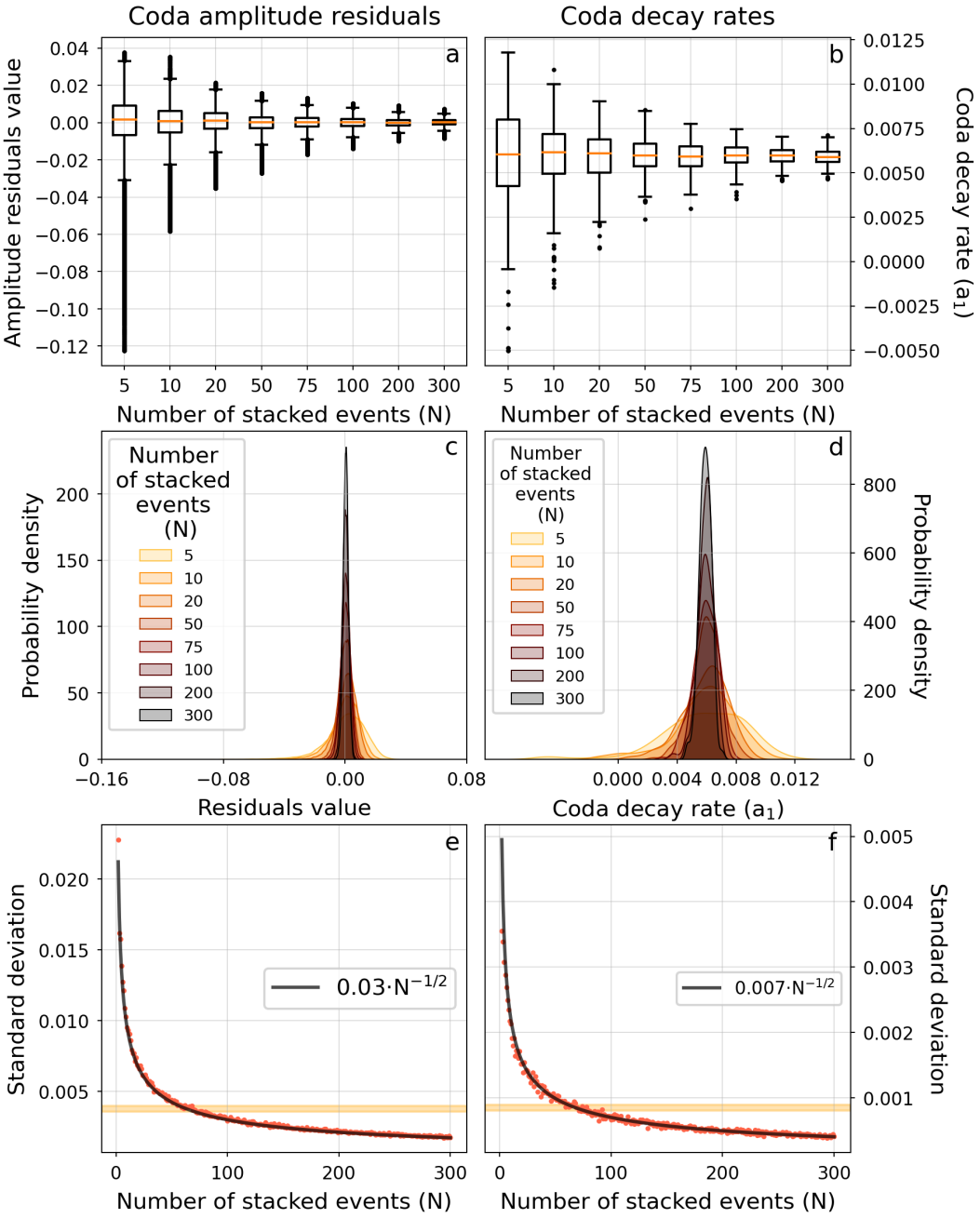

Figure A8: Statistical analysis of the amplitude residuals shown in Fig. A1 and coda decay rates (a_1) obtained from the first step of the EFM analysis for frequency band A (Table 2.3). a and b) Boxplots of the values for stacks of 5, 10, 20, 50, 75, 100, 200 and 300 events; c and d) probability density functions; e and f) standard deviation value for all tested N values. Orange lines in panels a and b represent the median of the residuals for each value of N. Boxes mark the interquartile range (IQR), while upper and lower whiskers extend from both ends of the box to 1.5 · IQR above and below the box respectively. Residuals or coda decay rates values outside this range are considered outliers. Black lines on panels e and f represent the expected decay of the standard deviation, according to the Central Limit Theorem. The orange shaded areas on the same panels mark the standard deviation value for $N = 60$–80, which we suggest as the minimum number of events necessary to ensure coda and coefficients stability.

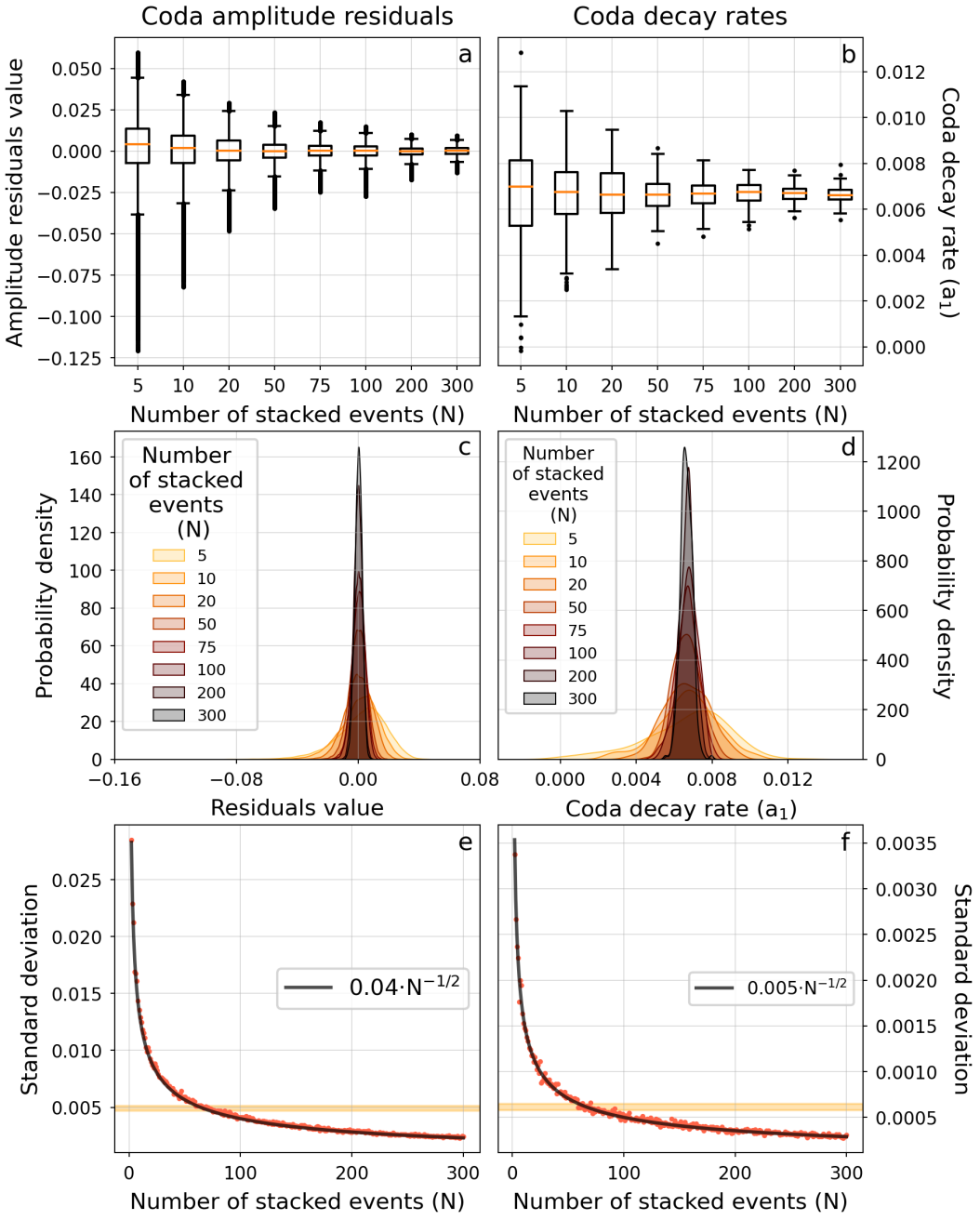

Figure A9: Same as Fig. A1 but for frequency band B (Table 2.3).

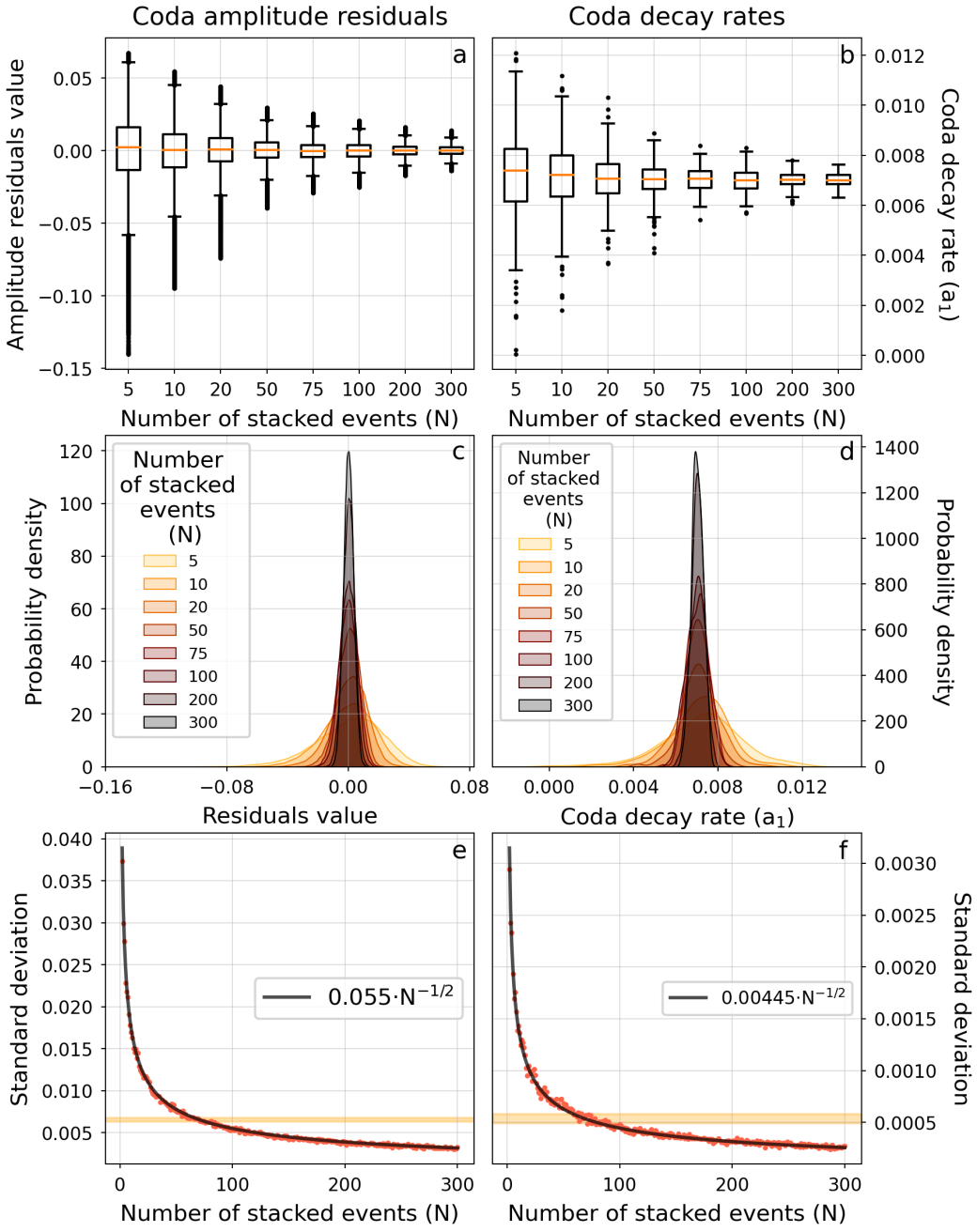

Figure A10: Same as Fig. A1 but for frequency band C (Table 2.3).

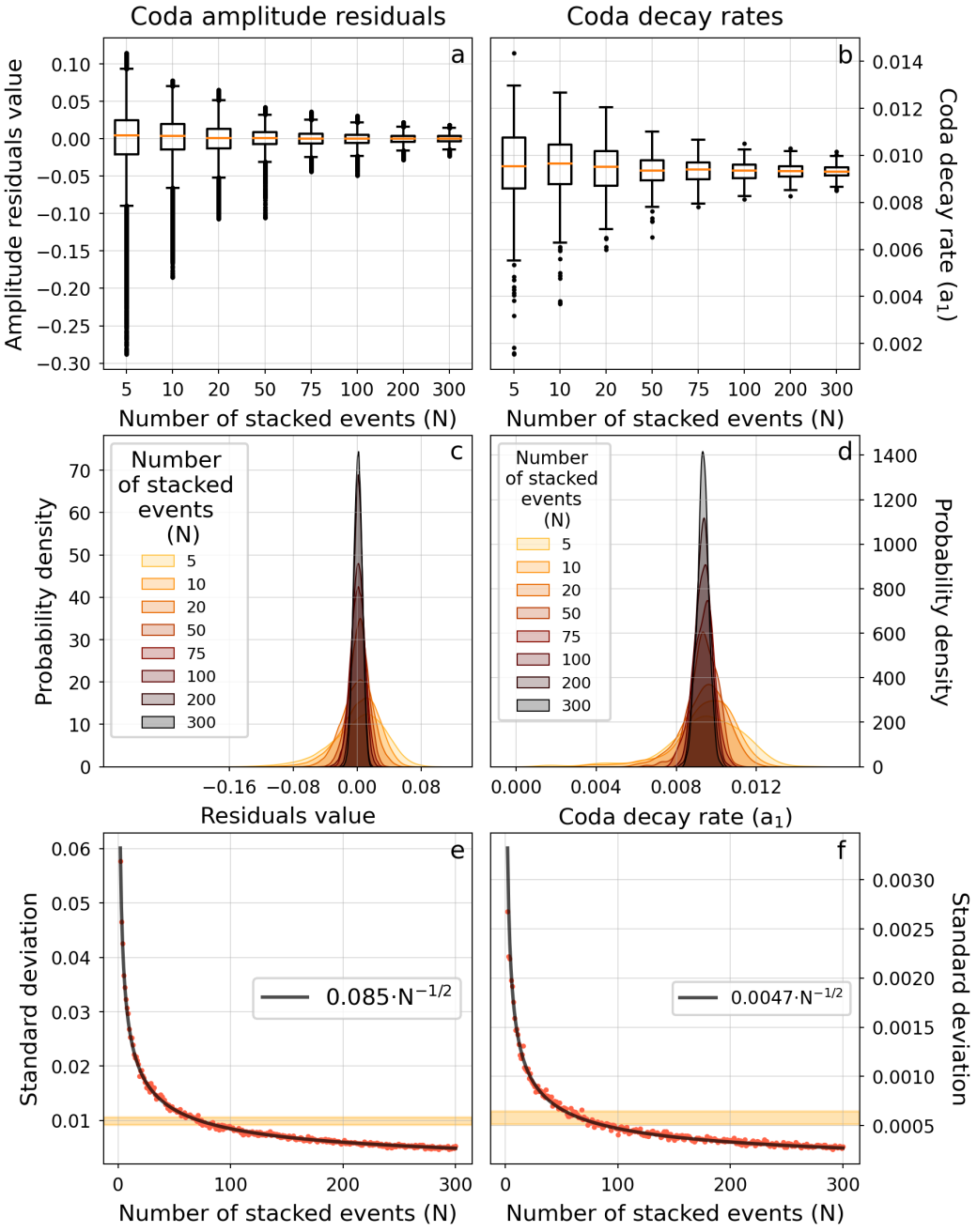

Figure A11: Same as Fig. A1 but for frequency band E (Table 2.3).

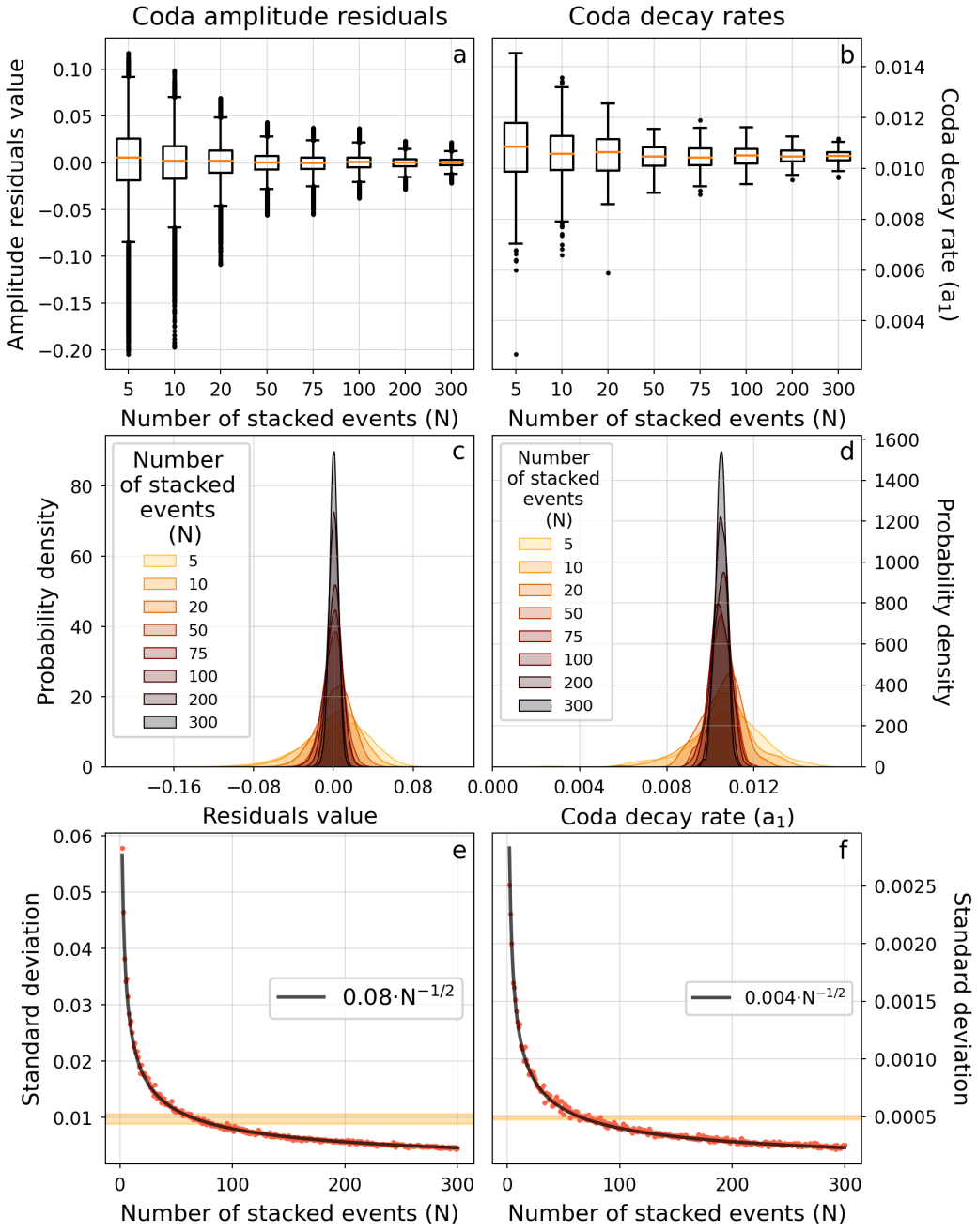

Figure A12: Same as Fig. A1 but for frequency band F (Table 2.3).

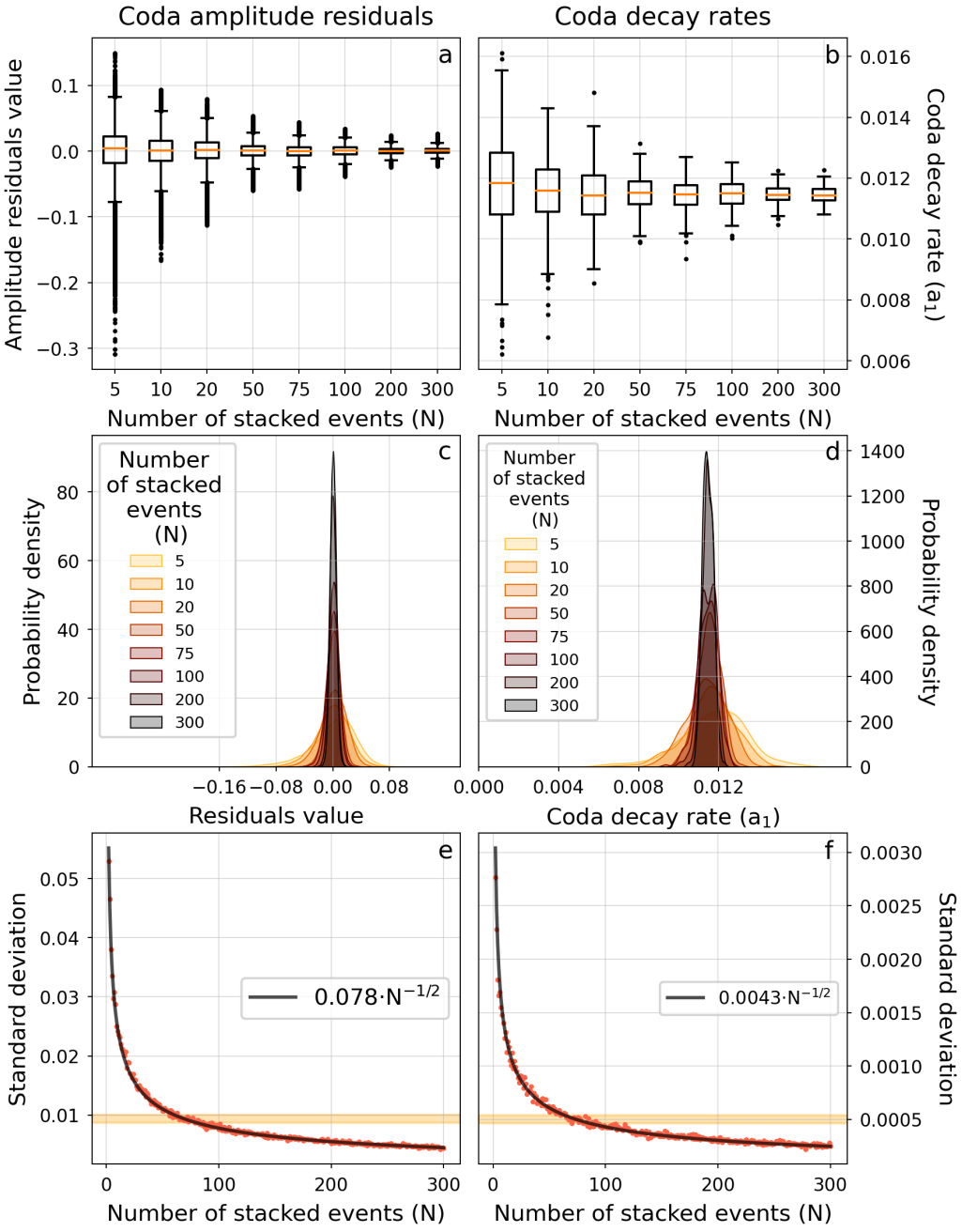

Figure A13: Same as Fig. A1 but for frequency band G (Table 2.3).

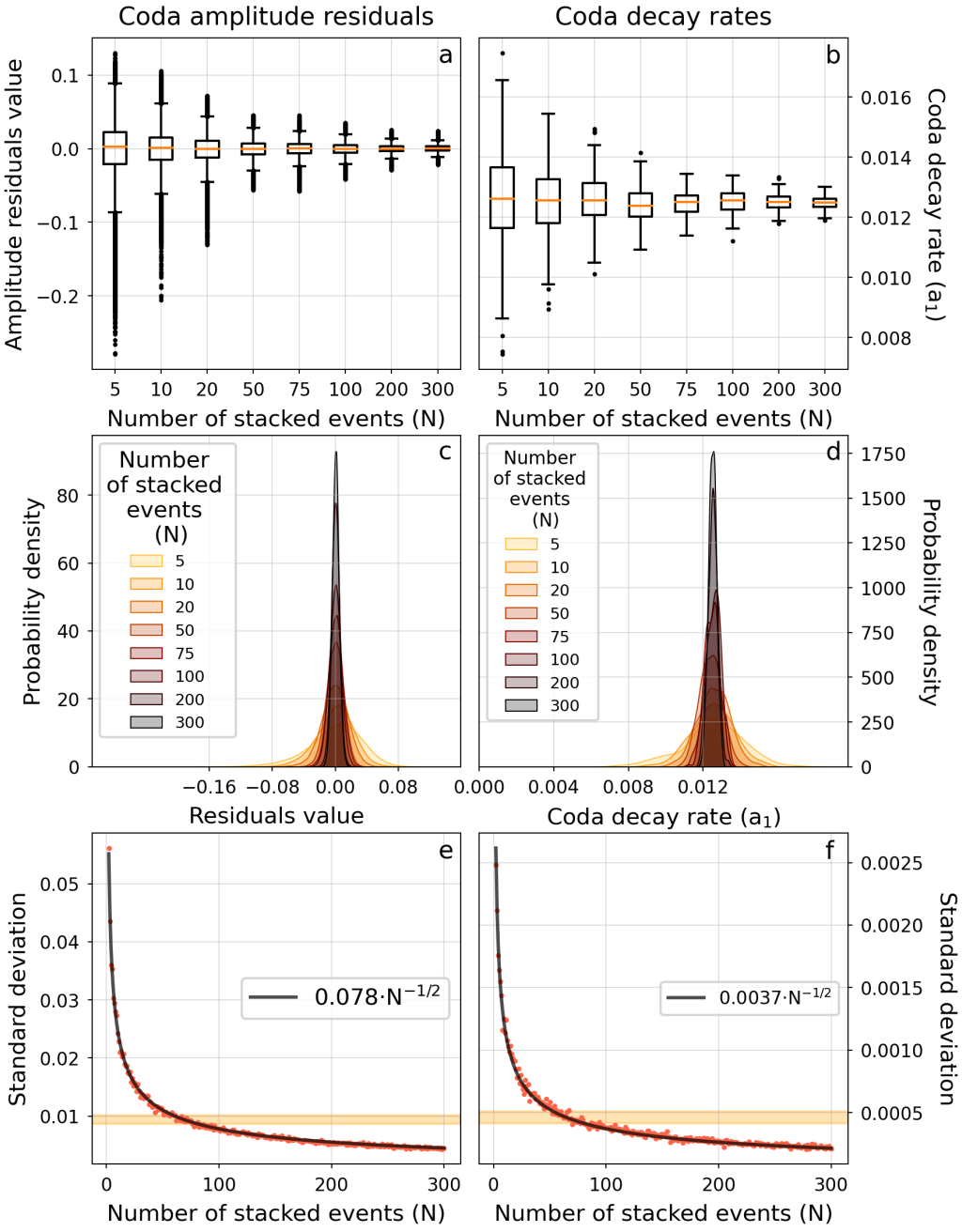

Figure A14: Same as Fig. A1 but for frequency band H (Table 2.3).

A.2 E-EFMD sensitivity test complementary results

Section 4.1.1 analyses the sensitivity of the E-EFMD to each of the parameters obtained from the Bayesian inversion. Figure 4.2 shows the synthetic envelopes for frequency band D (Table 2.3) and a collection of datasets designed so that only one of the seven parameters is allowed to vary. Figures in this section are analogous to Fig. 4.2 but for the remaining frequency bands in Table 2.3.

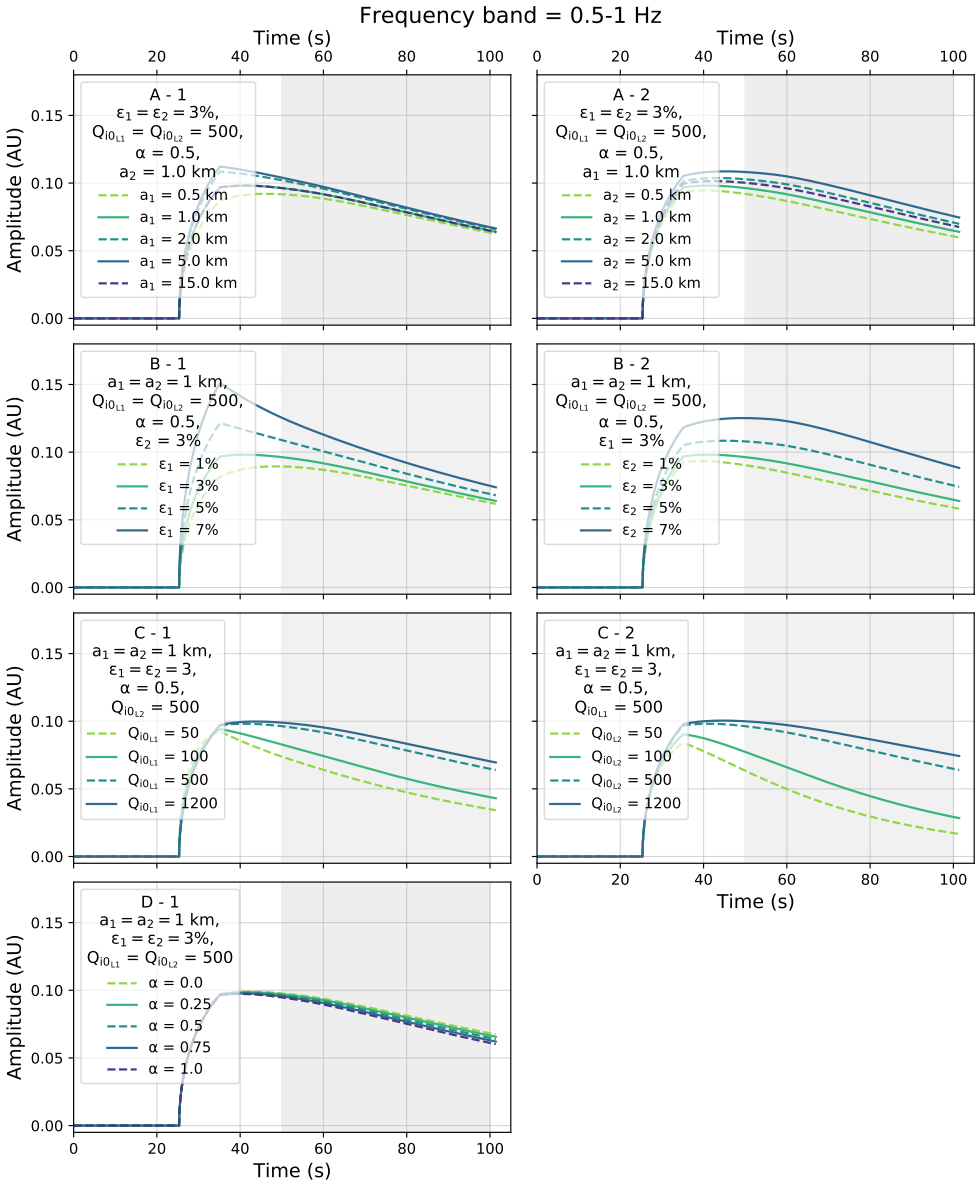

Figure A15: Synthetic envelopes for frequency band A (Table 2.3 and a collection of synthetic datasets in which one of the seven parameters the E-EFMD inverts for is allowed to vary, while the rest remains constant. Panels in the bottom row contain the same synthetic envelopes than panels A–1 to D–1, but I zoomed into the time window ranging from 60–70 s so I could observe differences in coda levels and decay rates in more detail. All plots within each row have the same scale in both axes.

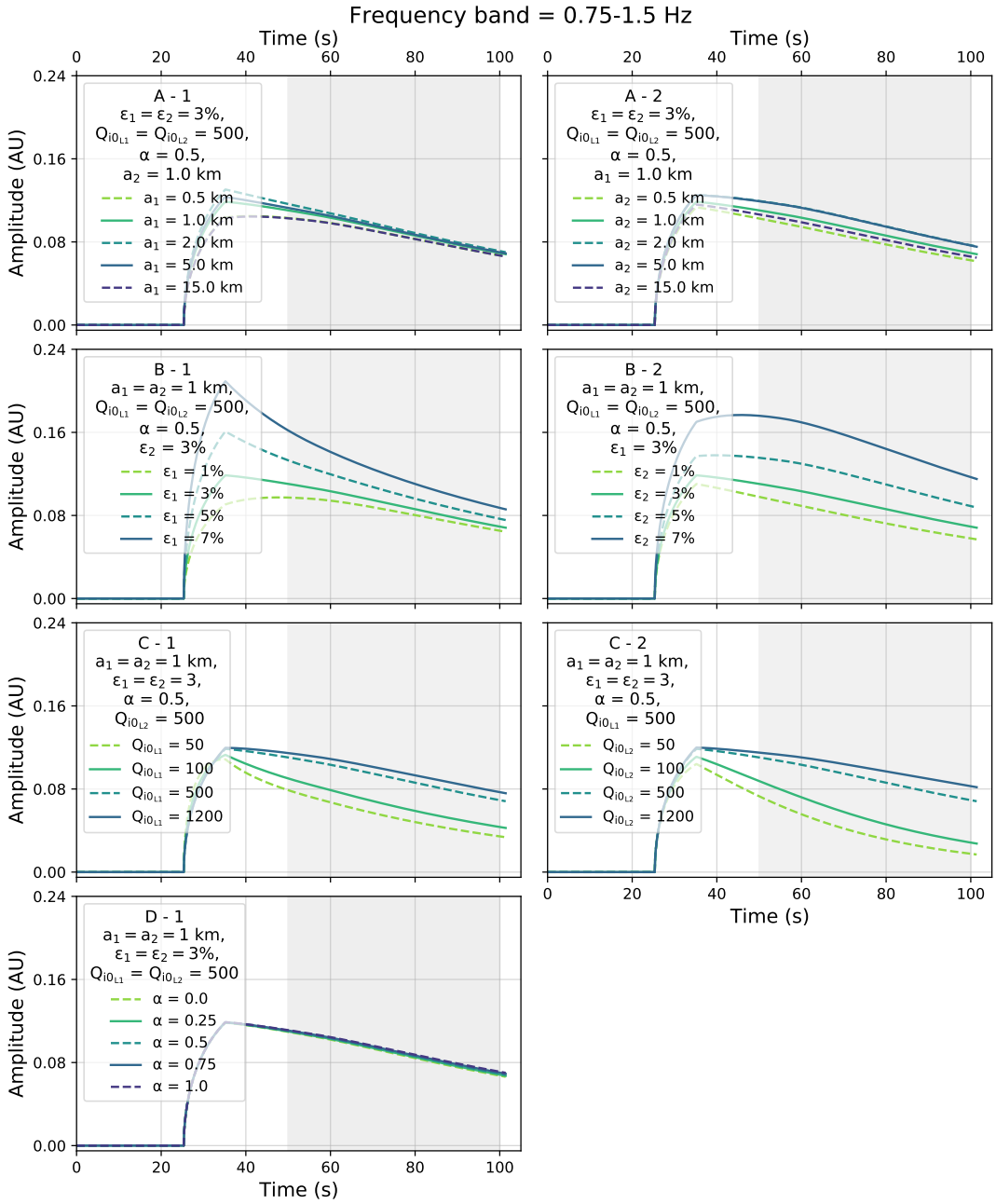

Figure A16: As Fig. A15 but for frequency band B from Table 2.3.

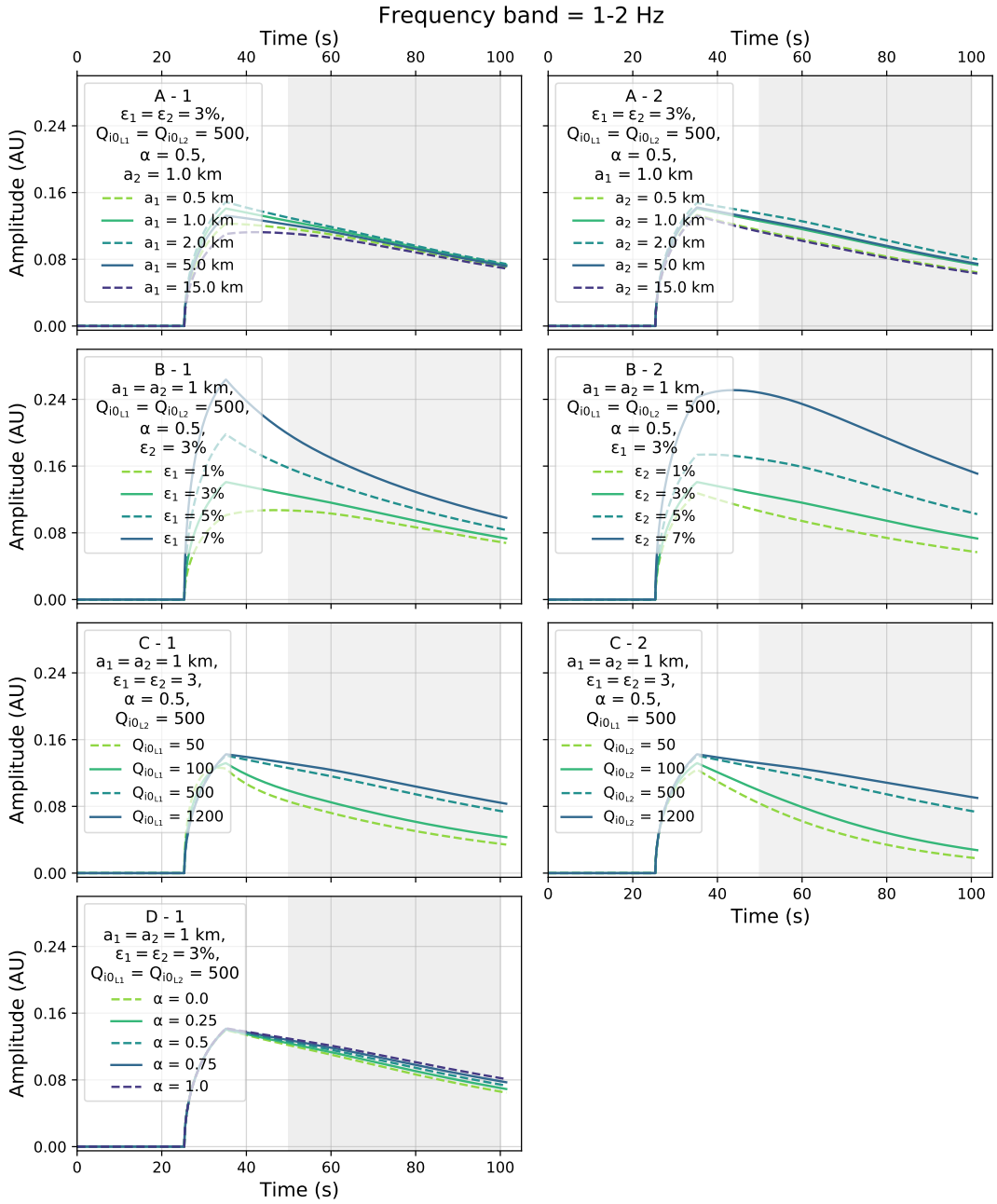

Figure A17: As Fig. A15 but for frequency band C from Table 2.3.

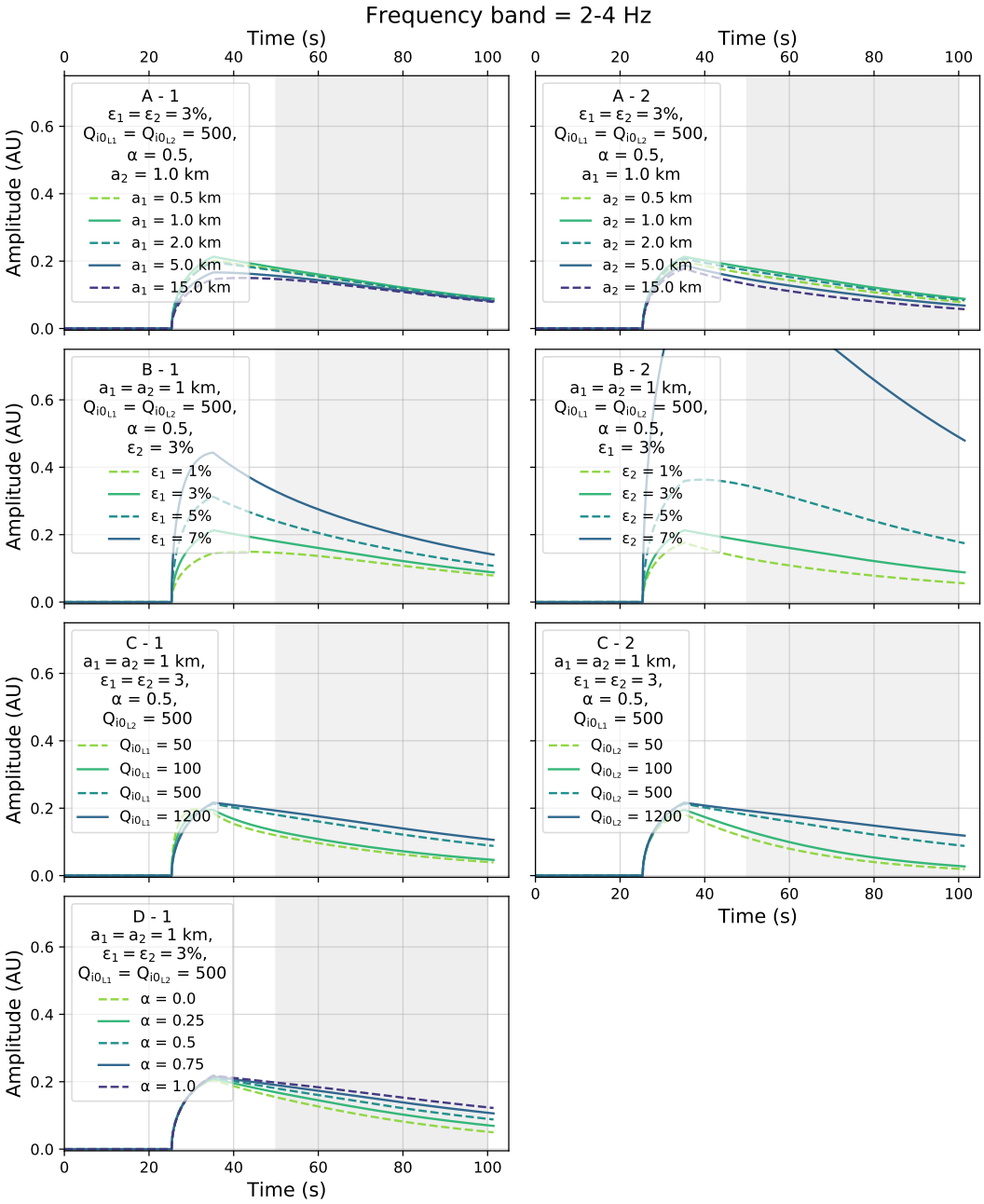

Figure A18: As Fig. A15 but for frequency band E from Table 2.3.

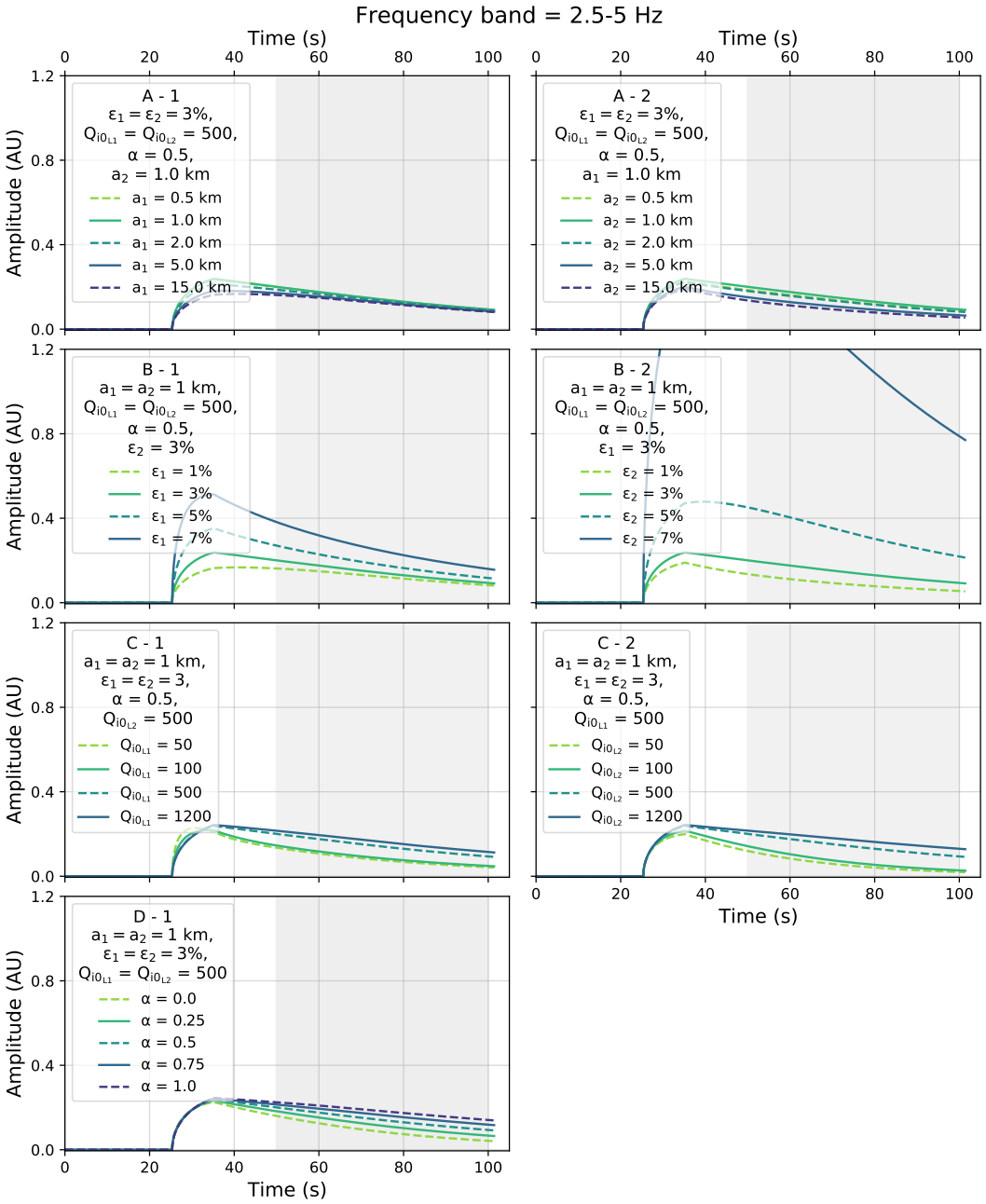

Figure A19: As Fig. A15 but for frequency band F from Table 2.3.

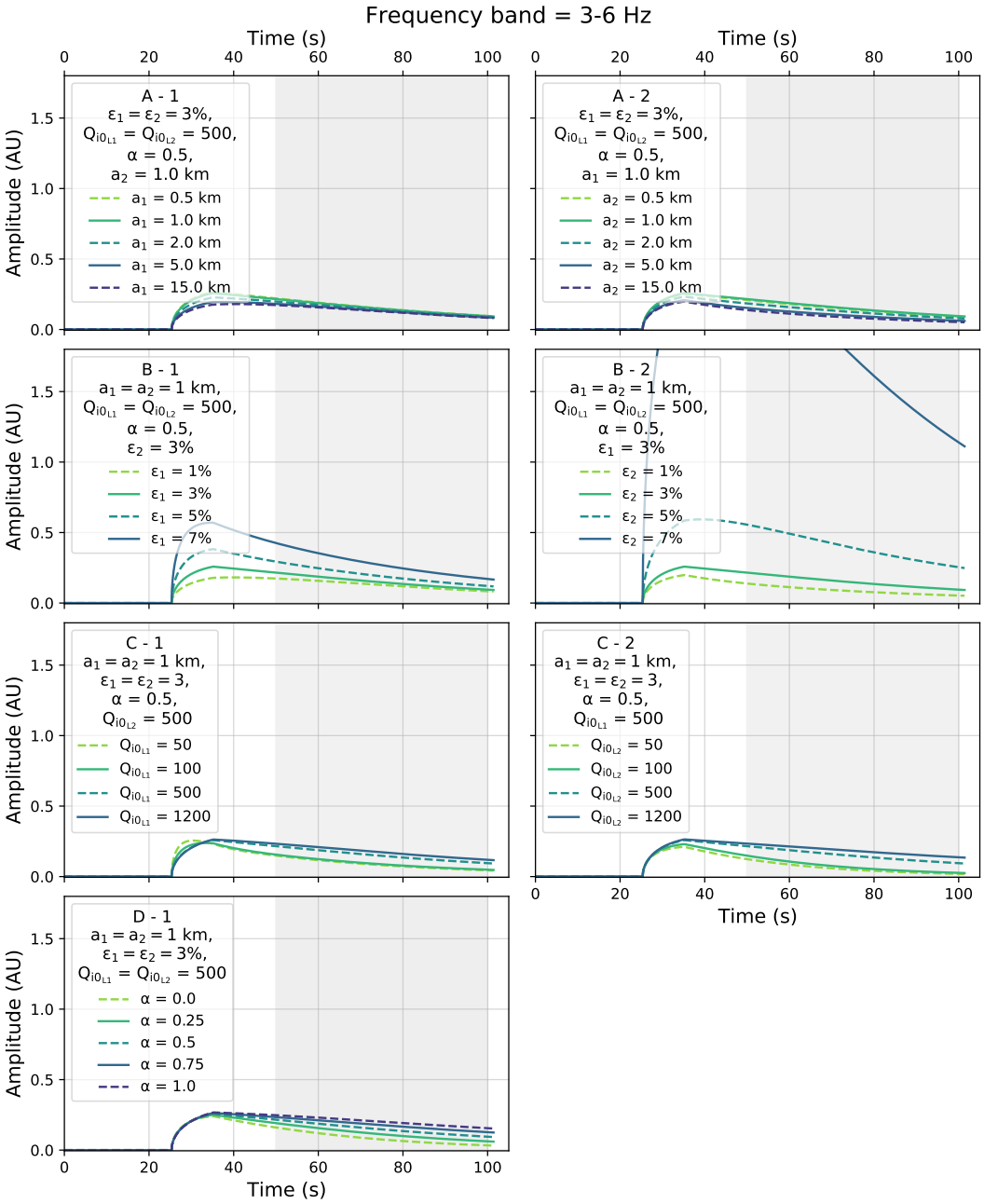

Figure A20: As Fig. A15 but for frequency band G from Table 2.3.

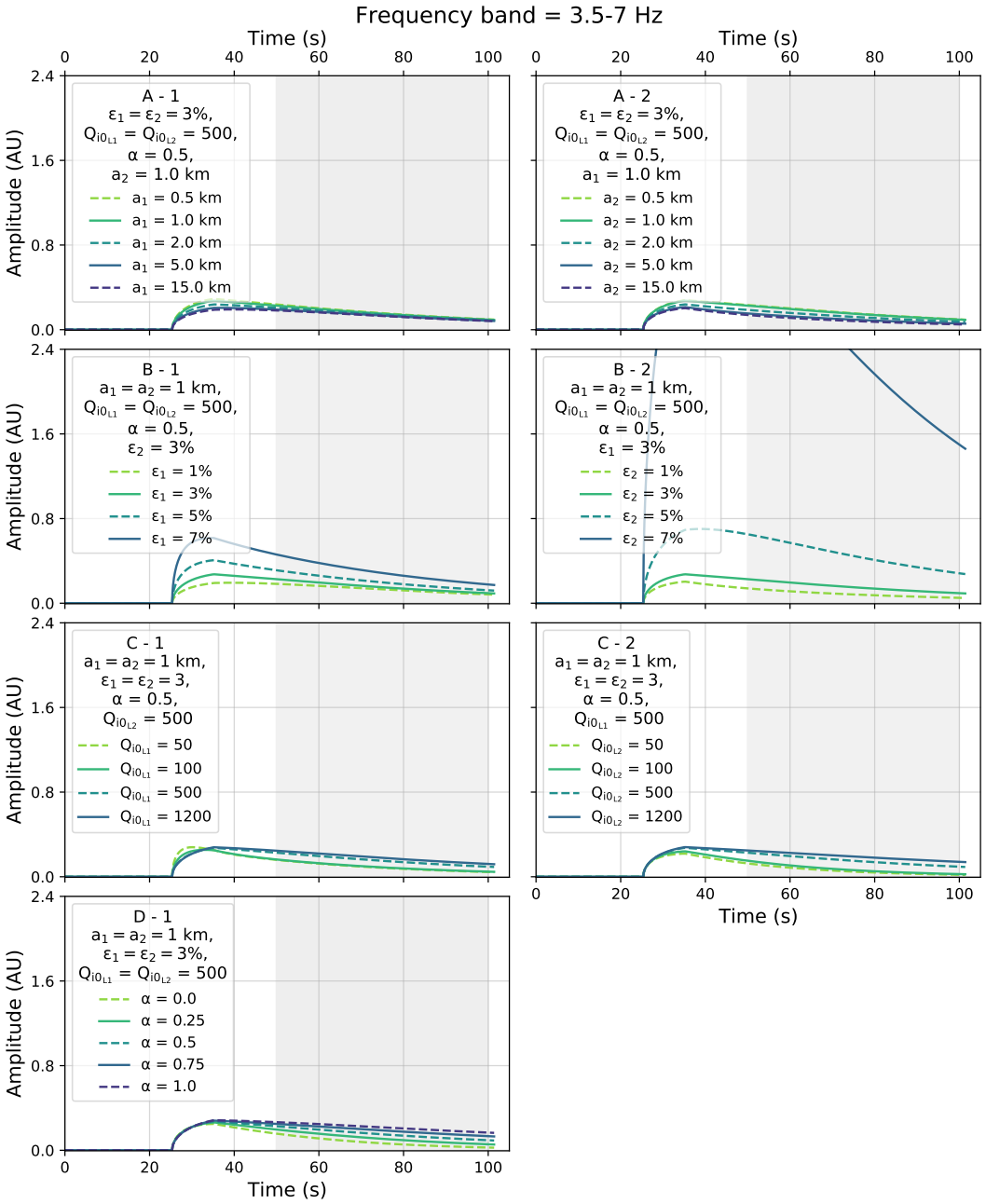

Figure A21: As Fig. A15 but for frequency band H from Table 2.3.

A.3 E-EFMD synthetic tests complementary results

A.3.1 Synthetic tests results summaries

Table 4.1 summarises the layering, input parameter value and inversion results for all of the synthetic tests I carried out to test the ability of the E-EFMD to accurately recover the input model in a wide variety of intrinsic attenuation settings. Figures in this section, similarly to Figs. 4.3, 4.6, 4.7 and 4.8, graphically summarise the results of the E-EFMD Bayesian inversion for the rest of the synthetic tests in Table 4.1.

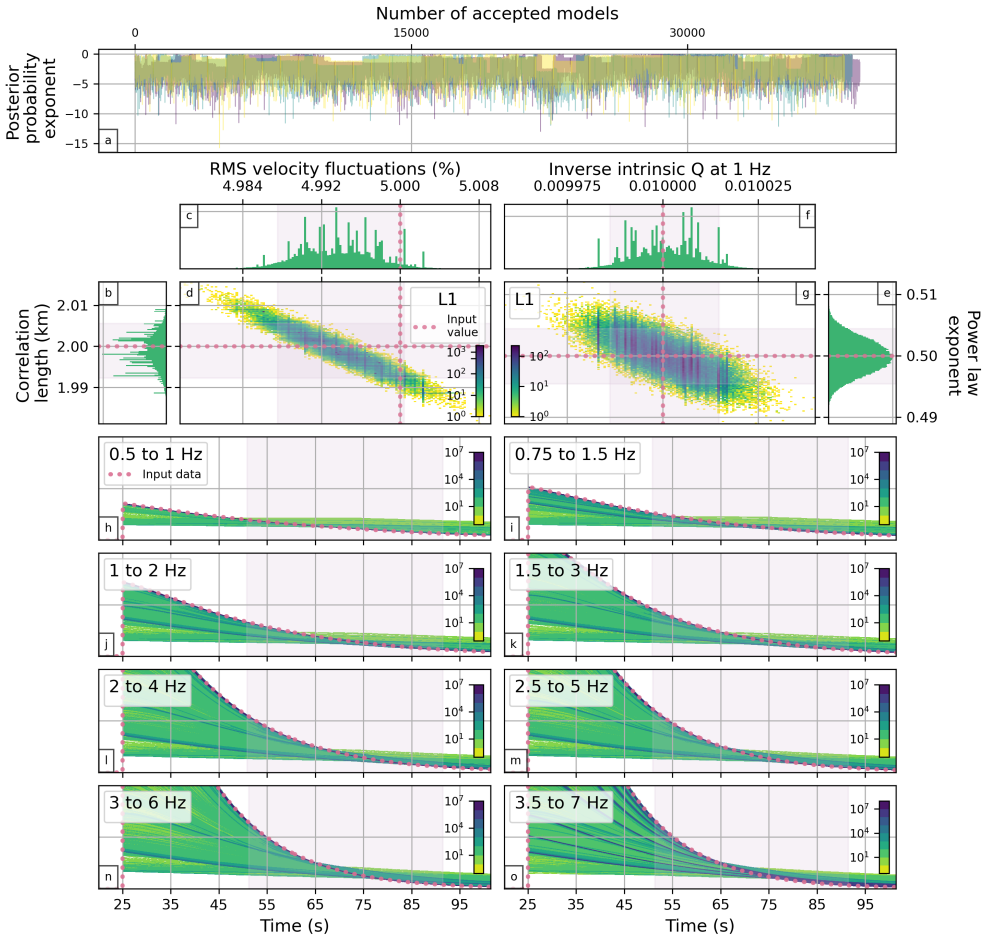

Figure A22: Summary of the results for the synthetic test number 2 (Table 4.1), representing a single-layer model of the lithosphere in which intrinsic attenuation is strong and frequency dependent ($Q_{i0}^{-1} = 0.01$, $\alpha = 0.5$). Panel a contains the posterior probability exponent, or loglikelihood (L), for all accepted models in each of the three chains I combined to produce the full set of results. Panels b–c and e–f show the posterior PDFs for each of the parameters obtained from the E-EFMD inversion for this model (correlation length (a), RMS velocity fluctuations (ε), inverse intrinsic quality factor at 1 Hz (Q_{i0}) and power law exponent (α)), while panels d and g present the joint PDFs for the scattering and intrinsic attenuation parameters respectively. Dotted lines in plots b–e point to input parameter values, while shaded areas represent the 5–95 percentile range for each of them. Finally, panels h–o show the input data envelopes for each frequency band (dotted lines) together with the ensemble of envelopes obtained from all accepted models during the inversion (represented by the colormap in the background). Shaded areas in these plots highlight the time window used for the fit to the coda.

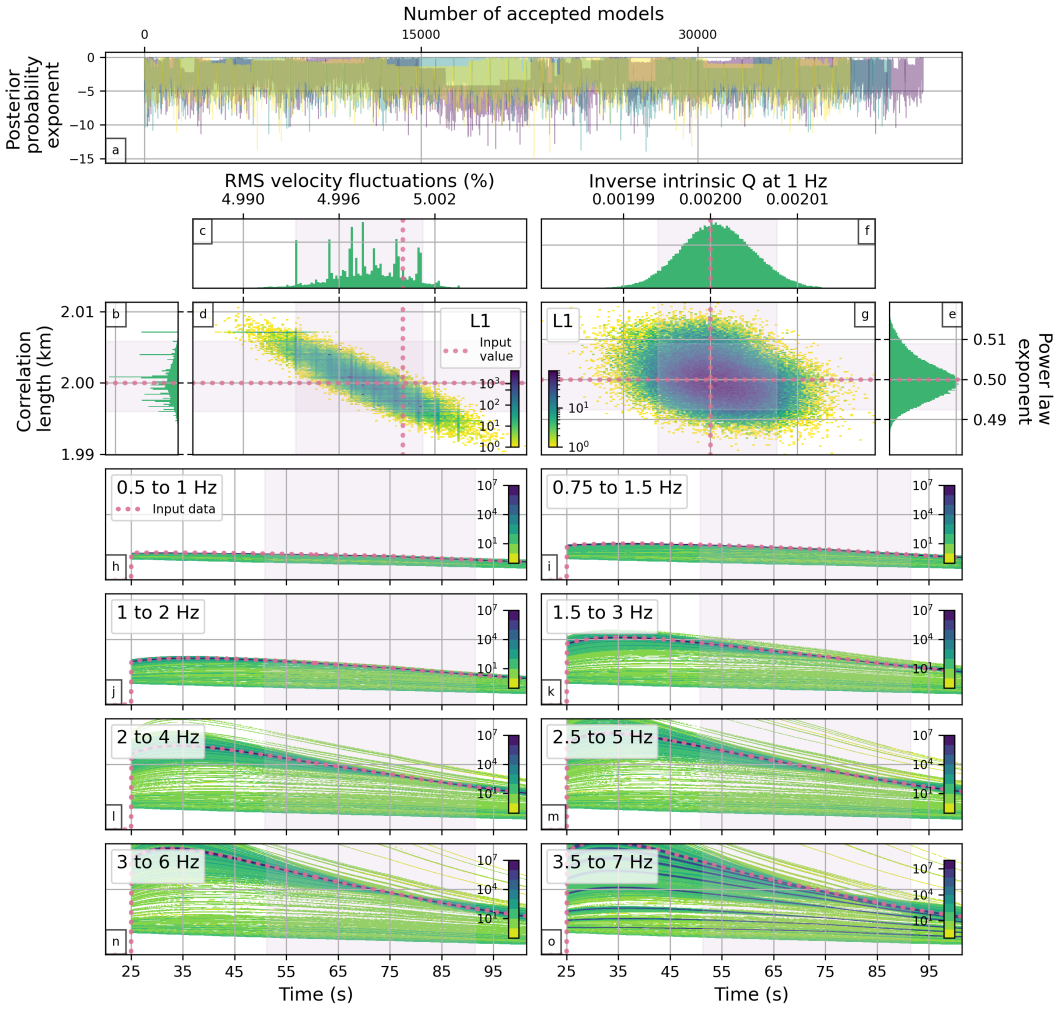

Figure A23: As Fig. A22 but for synthetic test 3 from Table 4.1.

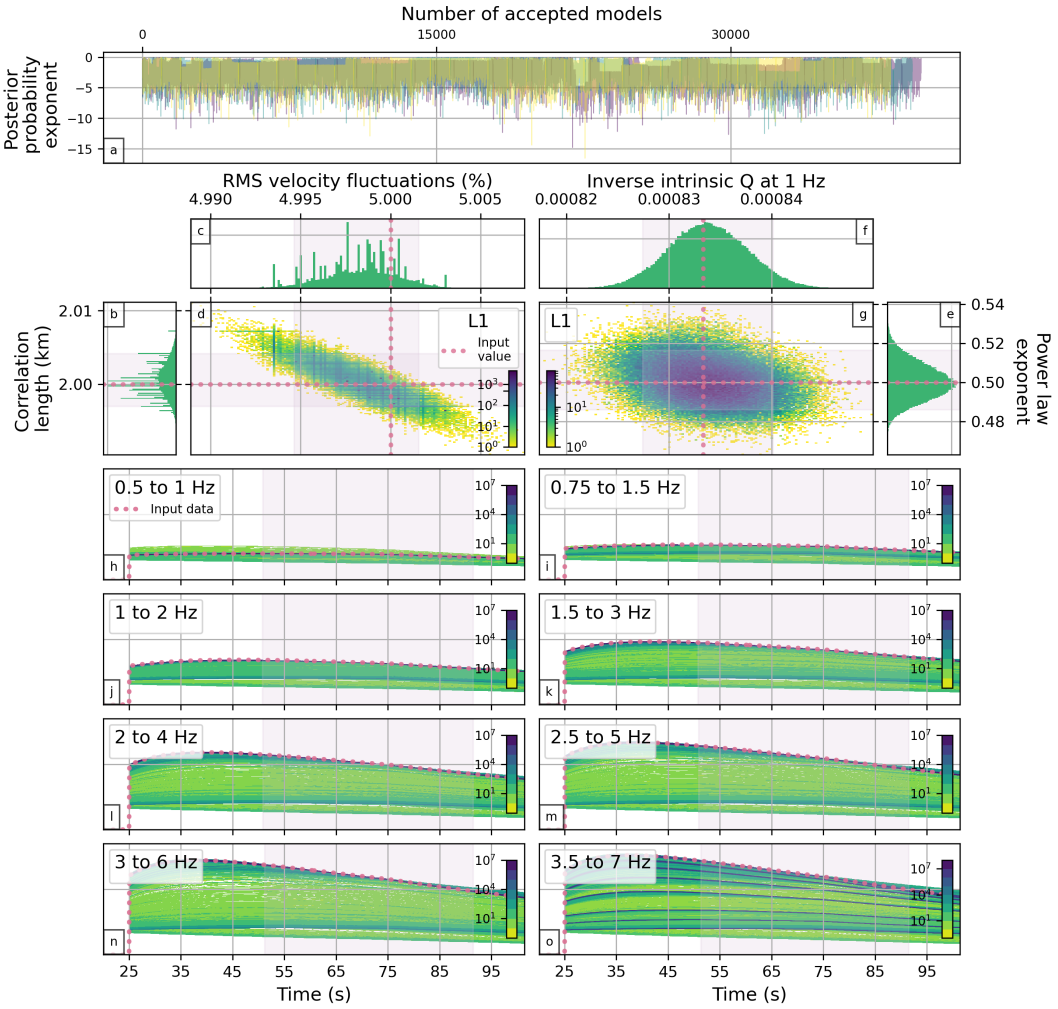

Figure A24: As Fig. A22 but for synthetic test 4 from Table 4.1.

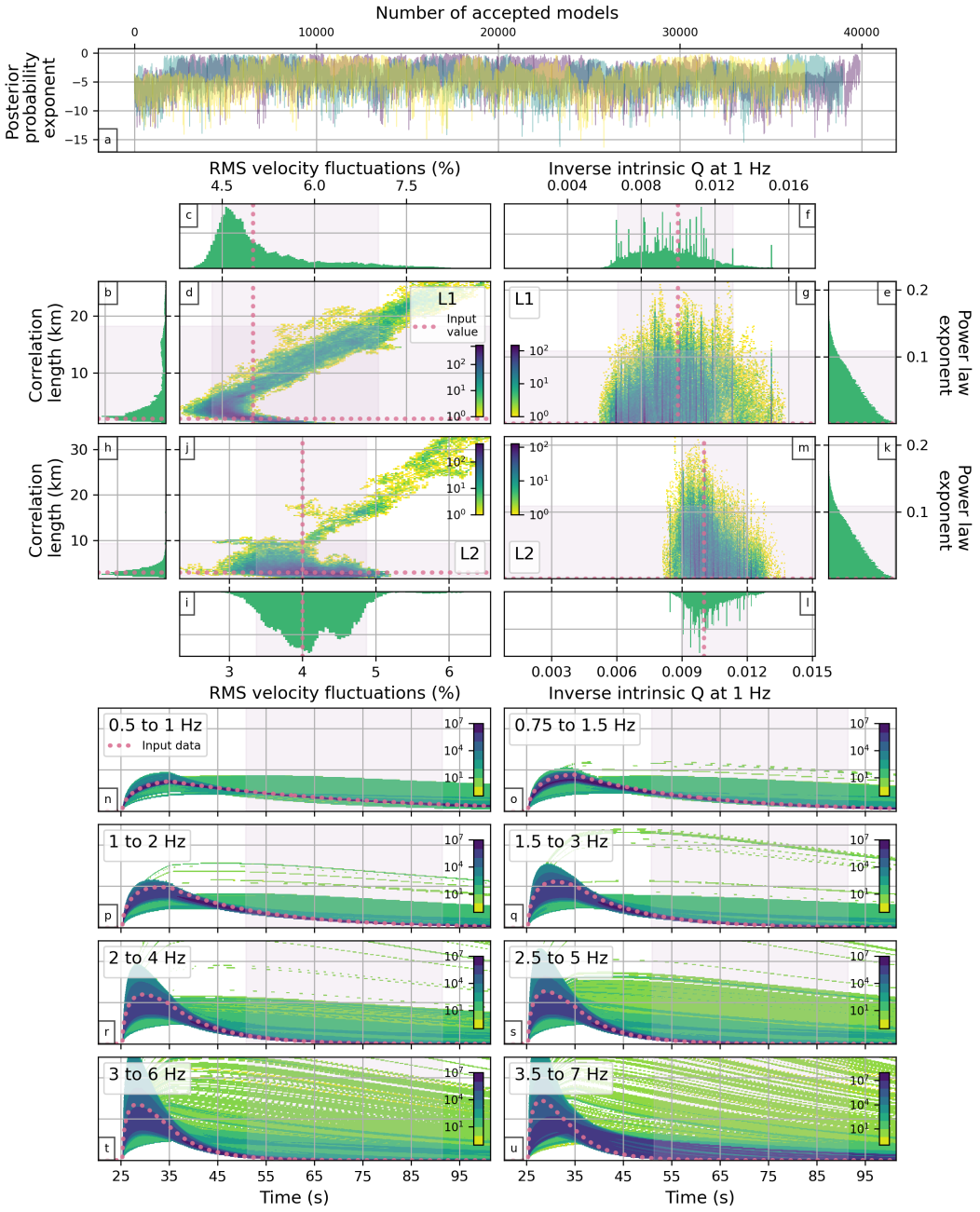

Figure A25: Summary of the results for the synthetic test number 6 (Table 4.1), representing a lithosphere with constant intrinsic attenuation ($Q_{i0}^{-1} = 0.01$) without any frequency dependence ($\alpha = 0$). Panel content is as in Fig. 4.3, with the addition of panels h–k for parameters in the lithospheric mantle.

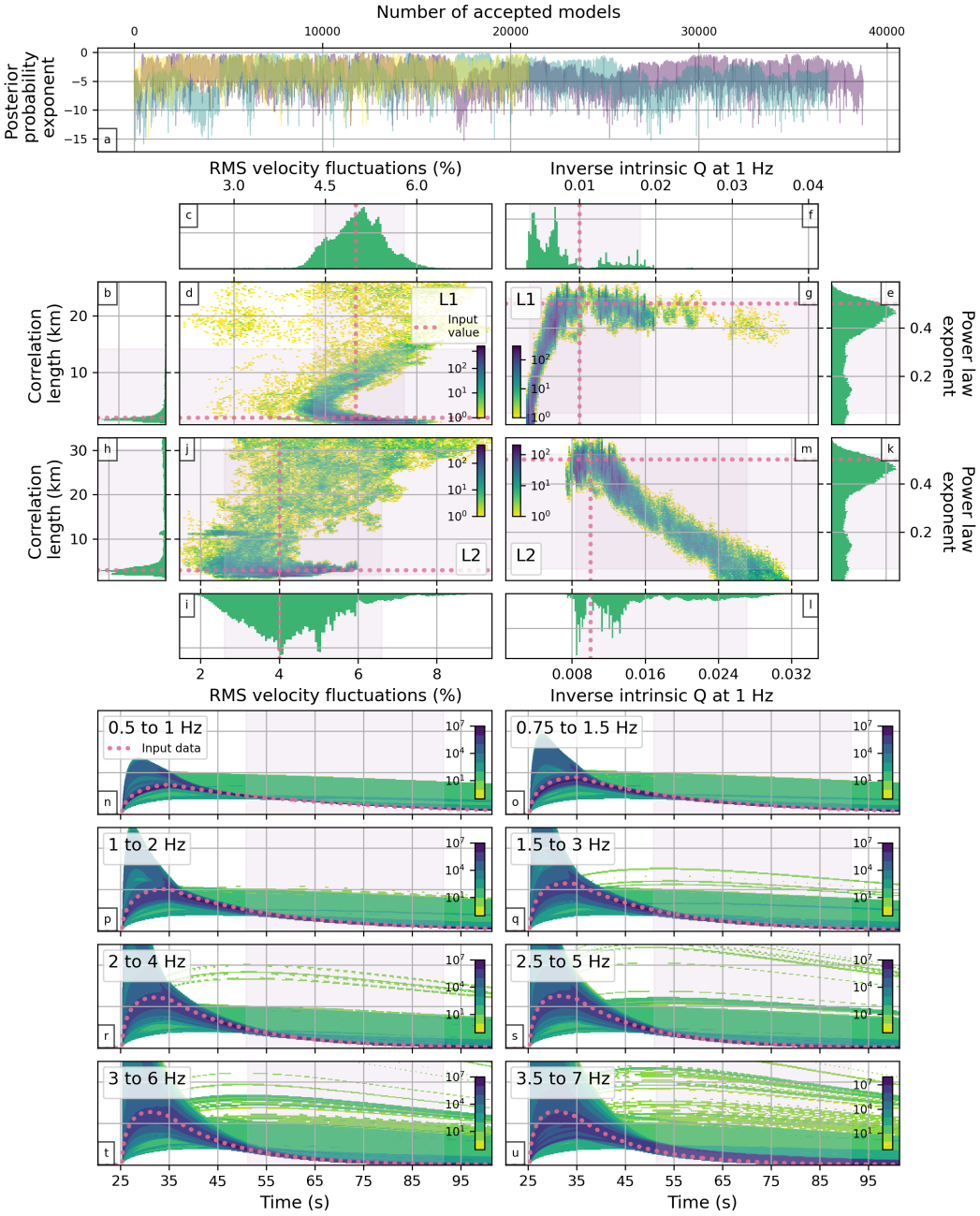

Figure A26: As Fig. A25, but for synthetic test 7 from Table 4.1.

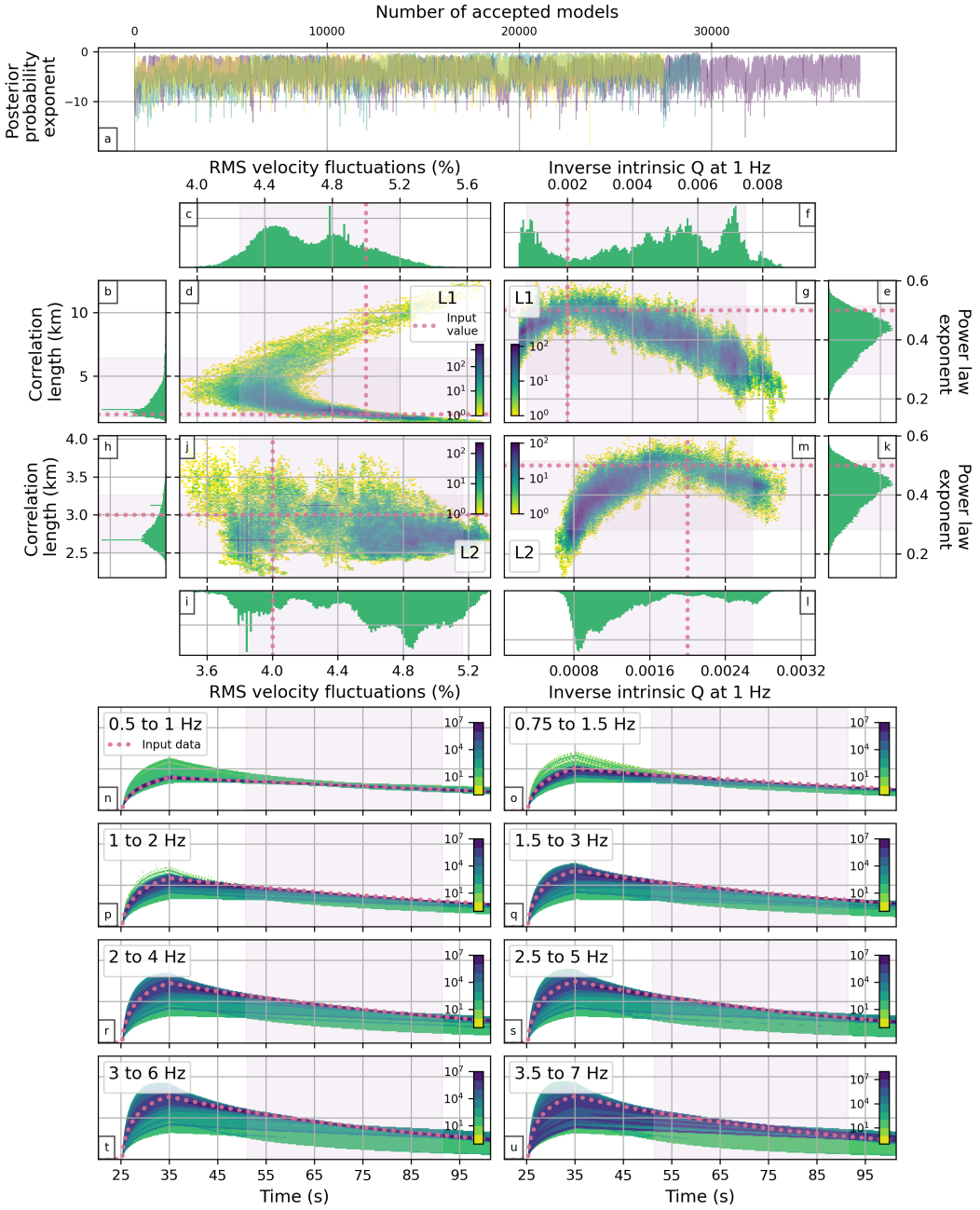

Figure A27: As Fig. A25, but for synthetic test 9 from Table 4.1.

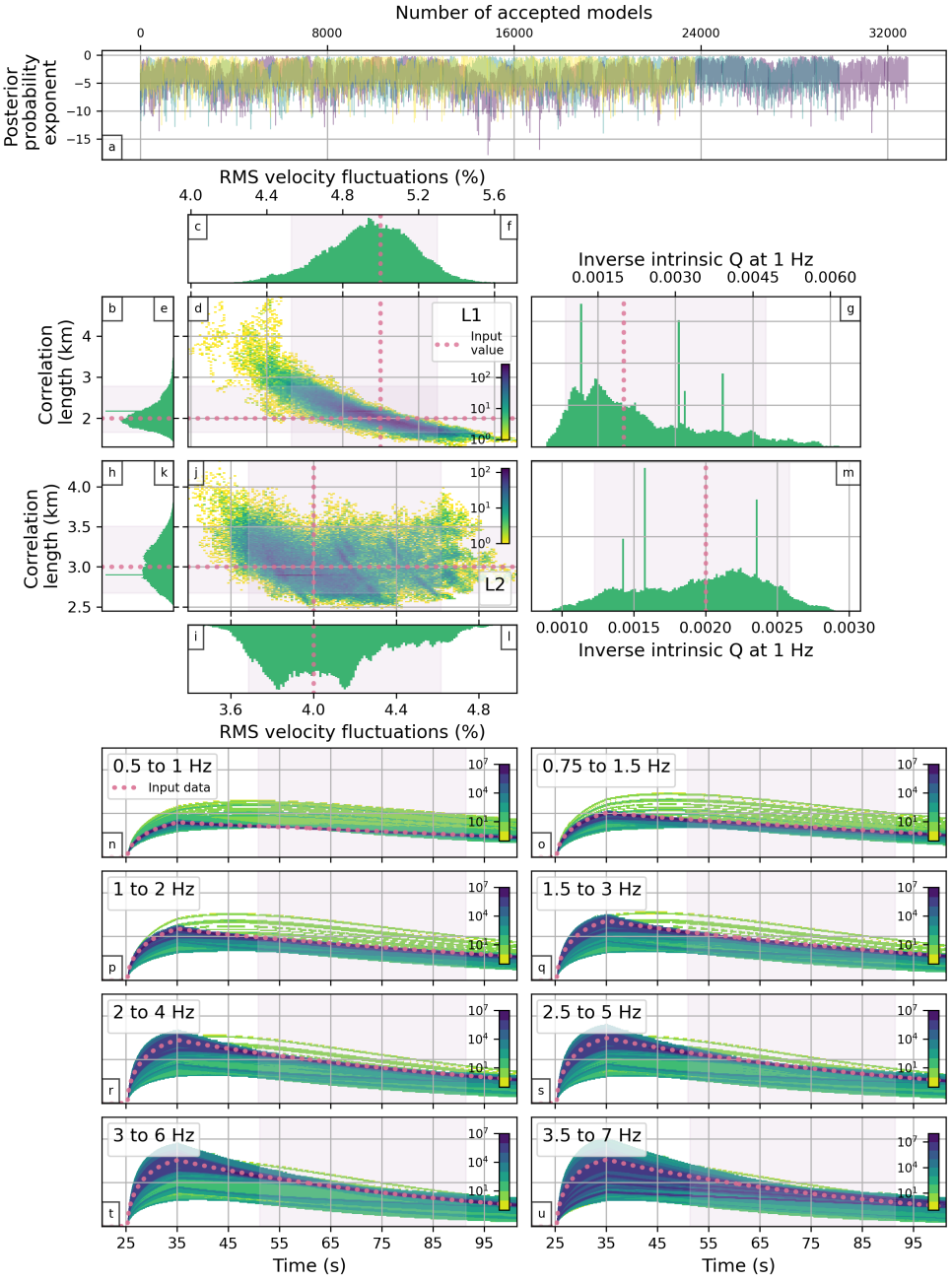

Figure A28: As Fig. A25, but for synthetic test 9* from Table 4.1, in which α is not inverted for but fixed at 0.5.

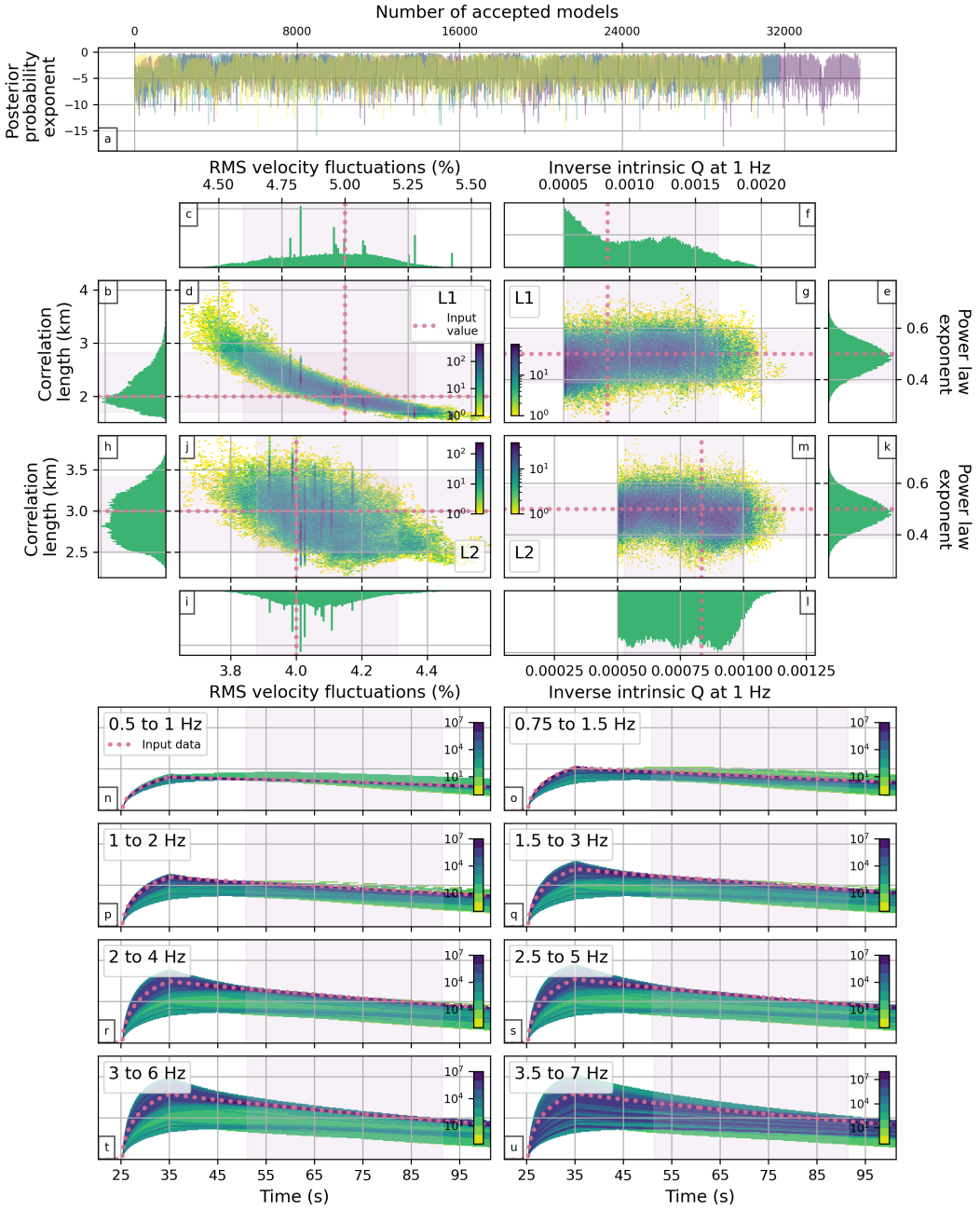

Figure A29: As Fig. A25, but for synthetic test 10 from Table 4.1.

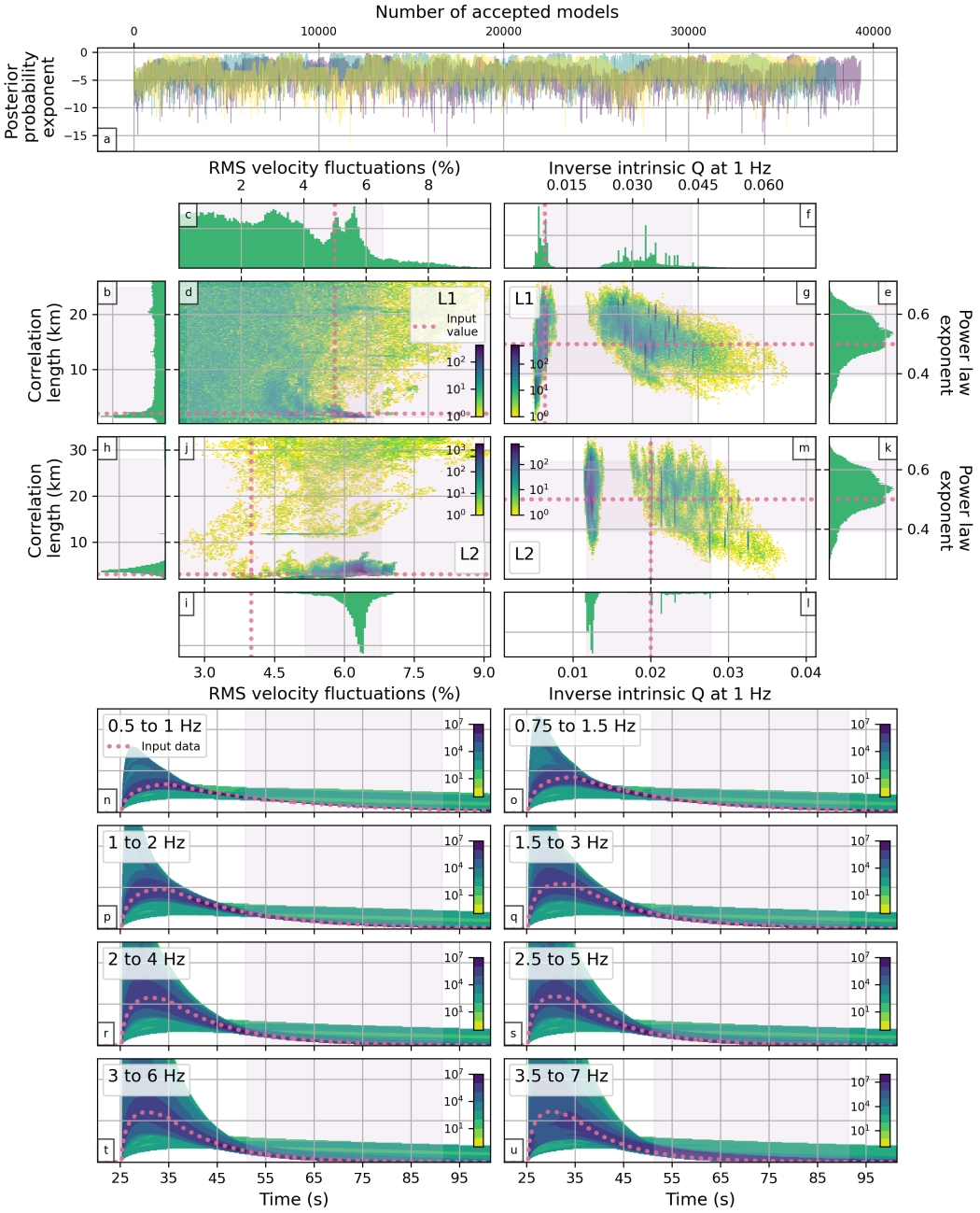

Figure A30: As Fig. A25, but for synthetic test 12 from Table 4.1.

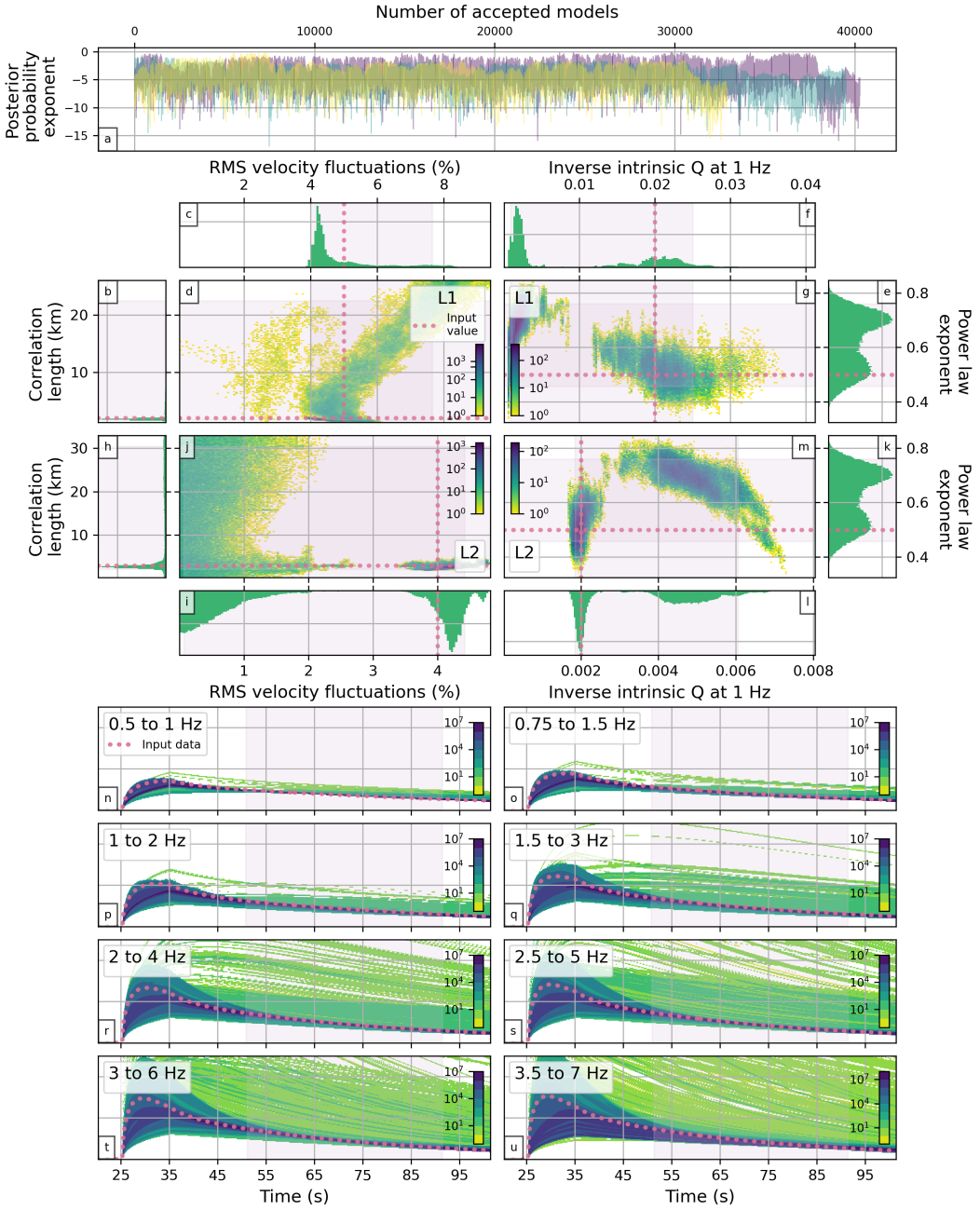

Figure A31: As Fig. A25, but for synthetic test 13 from Table 4.1.

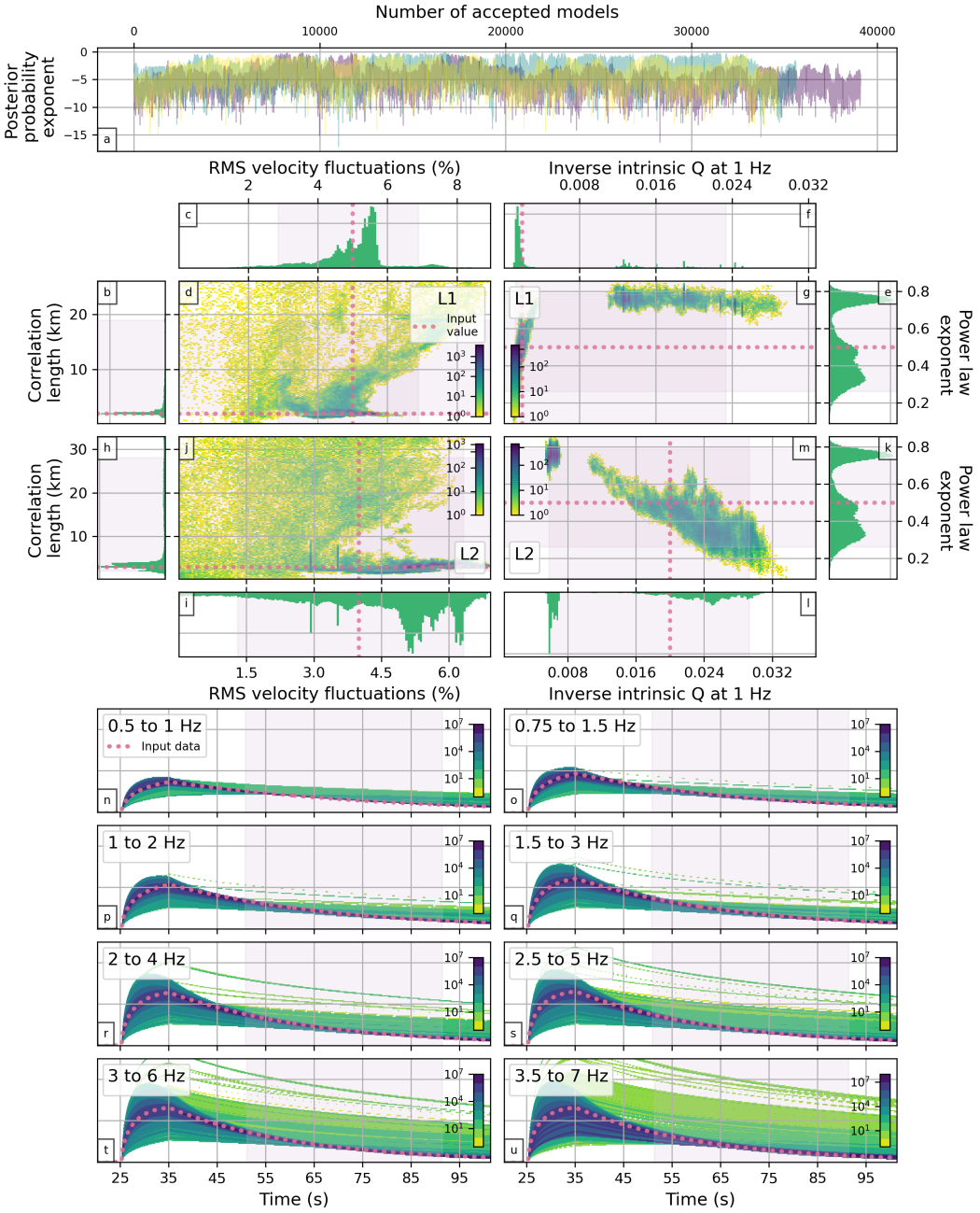

Figure A32: As Fig. A25, but for synthetic test 14 from Table 4.1.

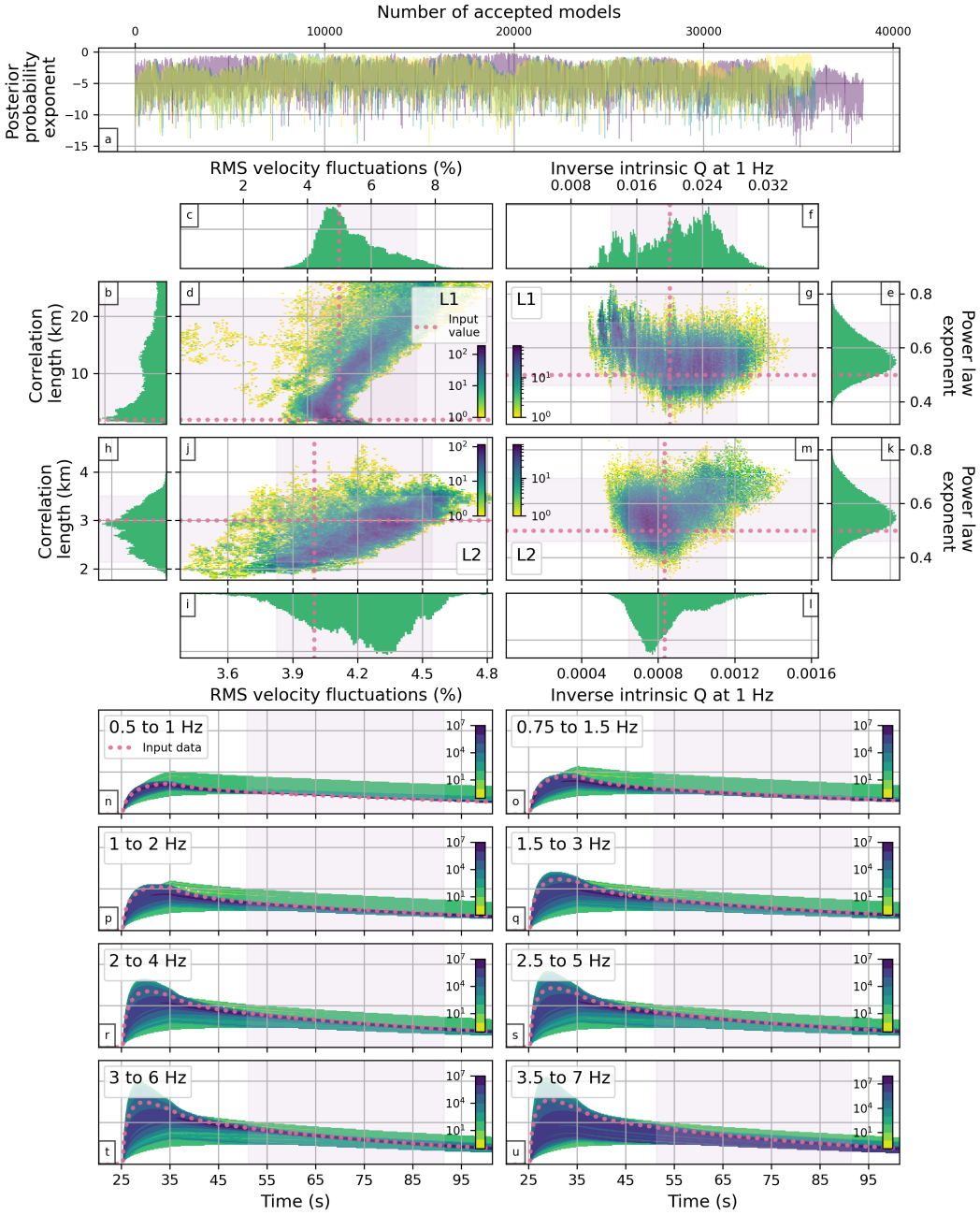

Figure A33: As Fig. A25, but for synthetic test 15 from Table 4.1.

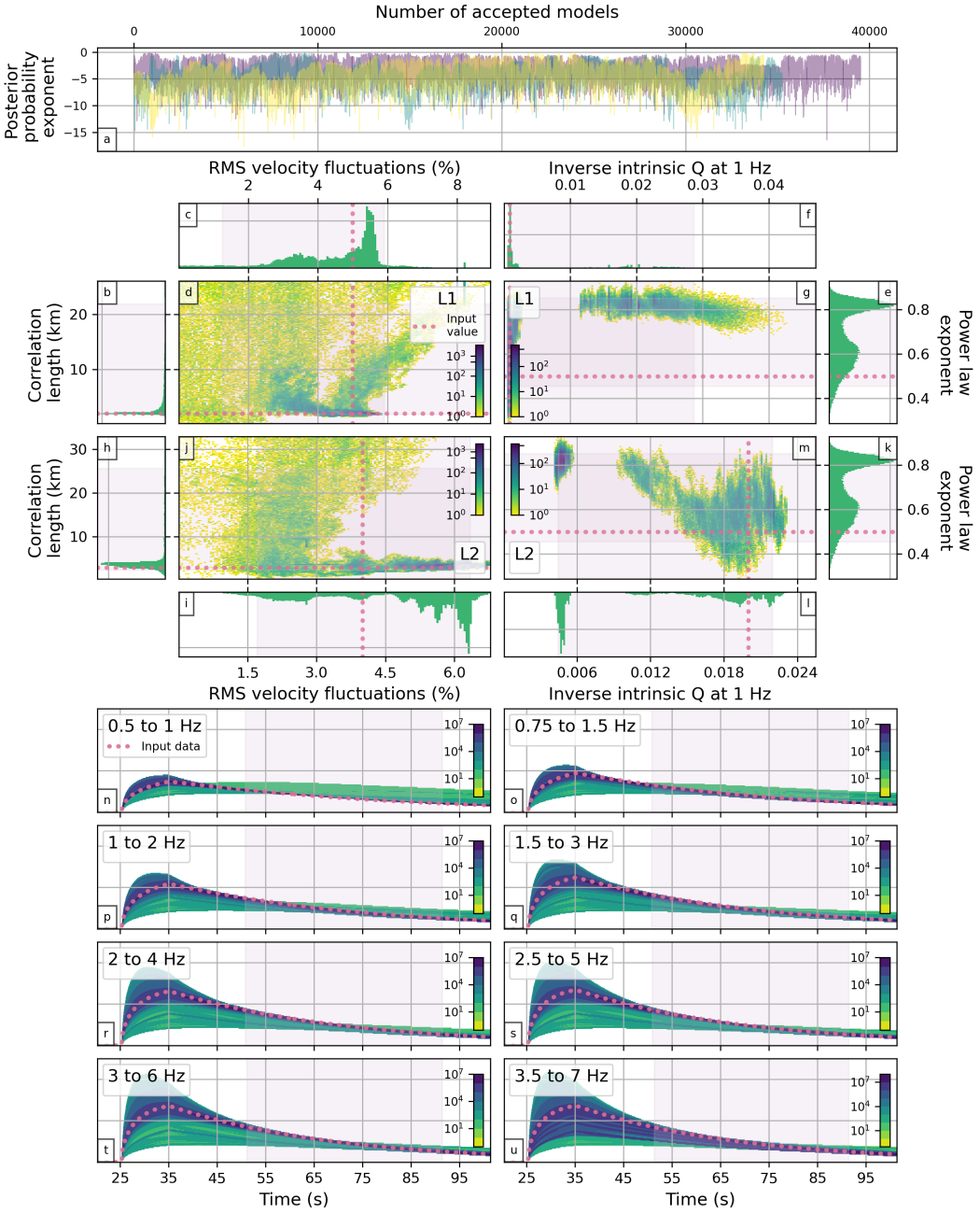

Figure A34: As Fig. A25, but for synthetic test 16 from Table 4.1.

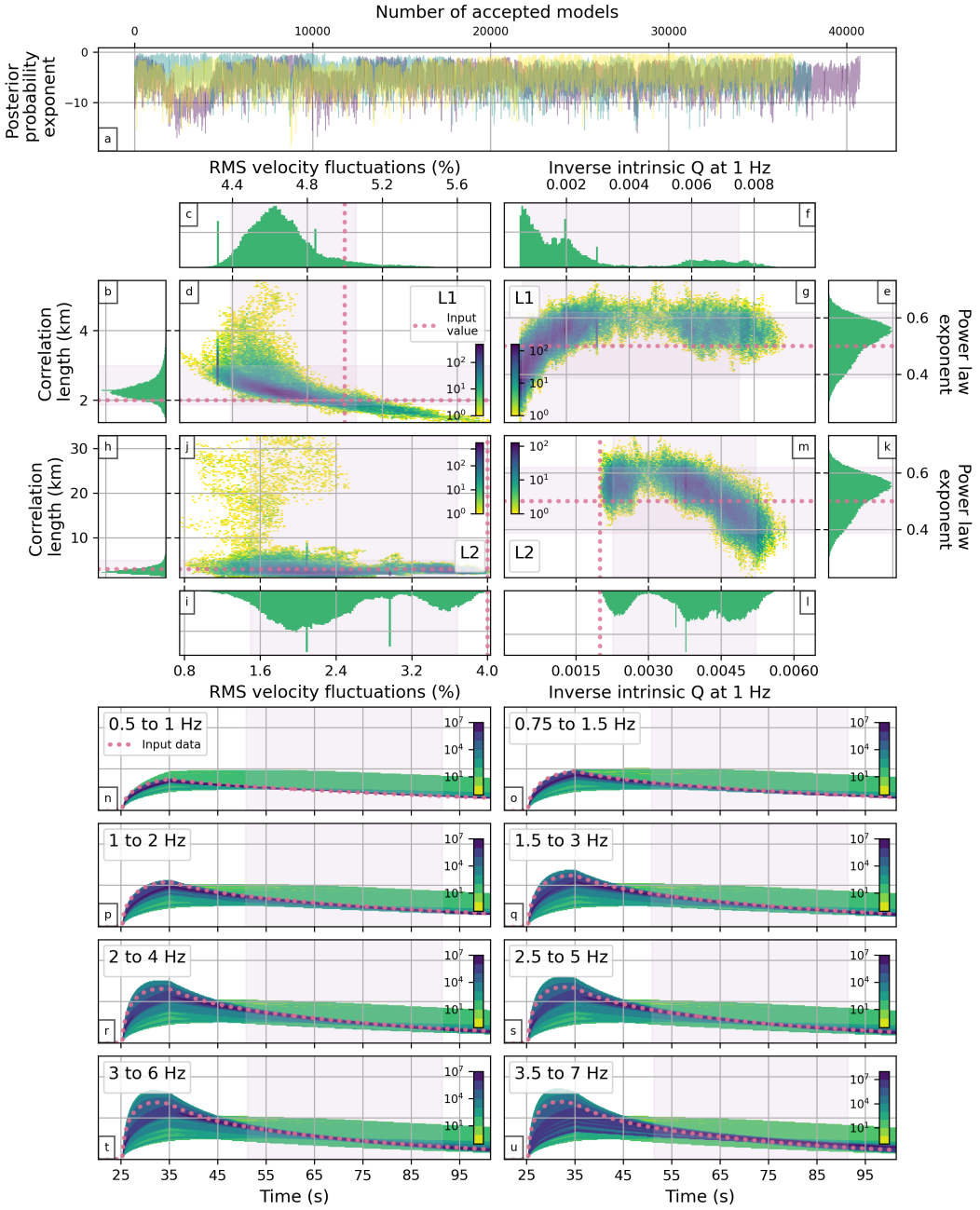

Figure A35: As Fig. A25, but for synthetic test 17 from Table 4.1.

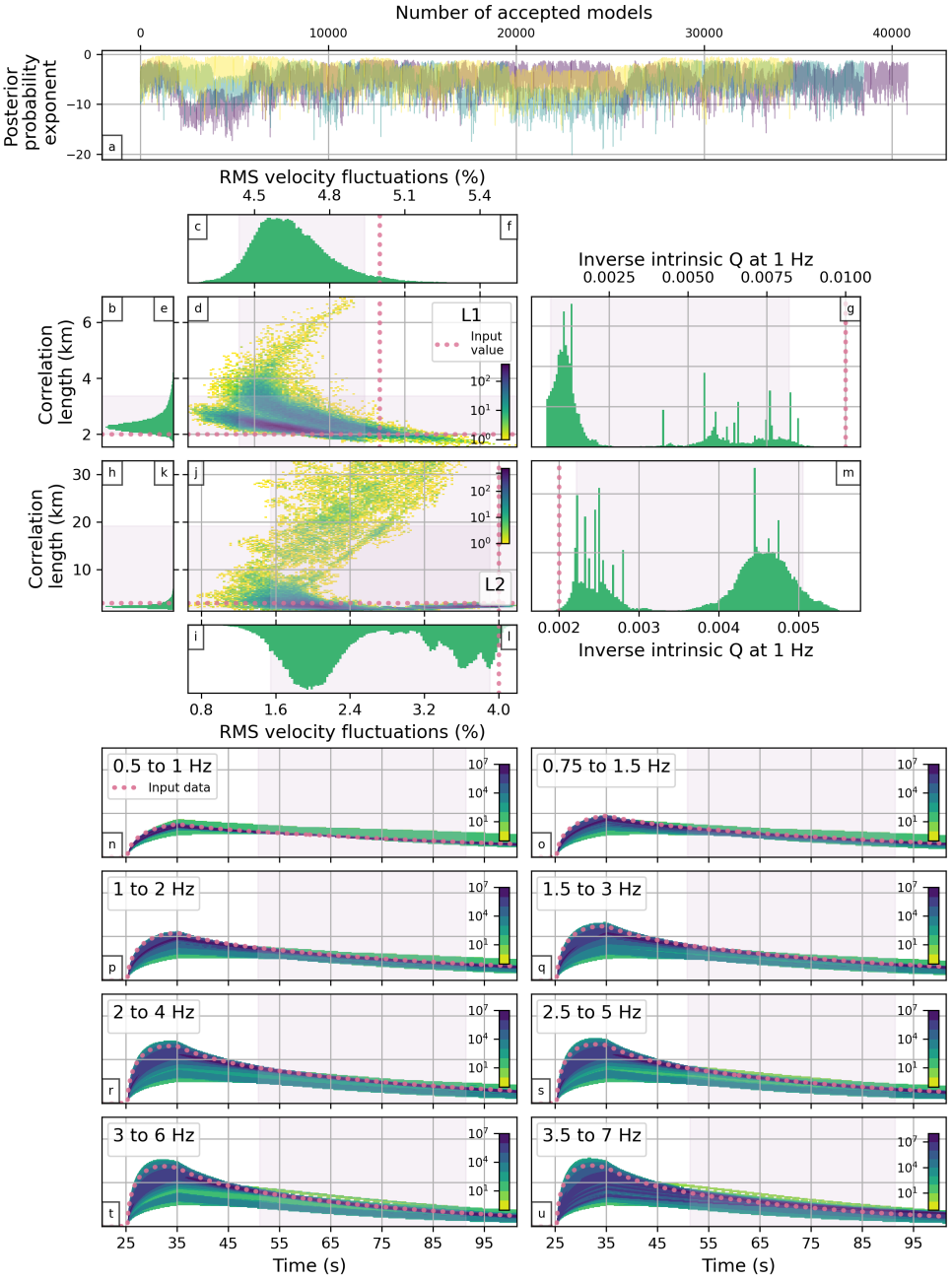

Figure A36: As Fig. A25, but for synthetic test 17* from Table 4.1.

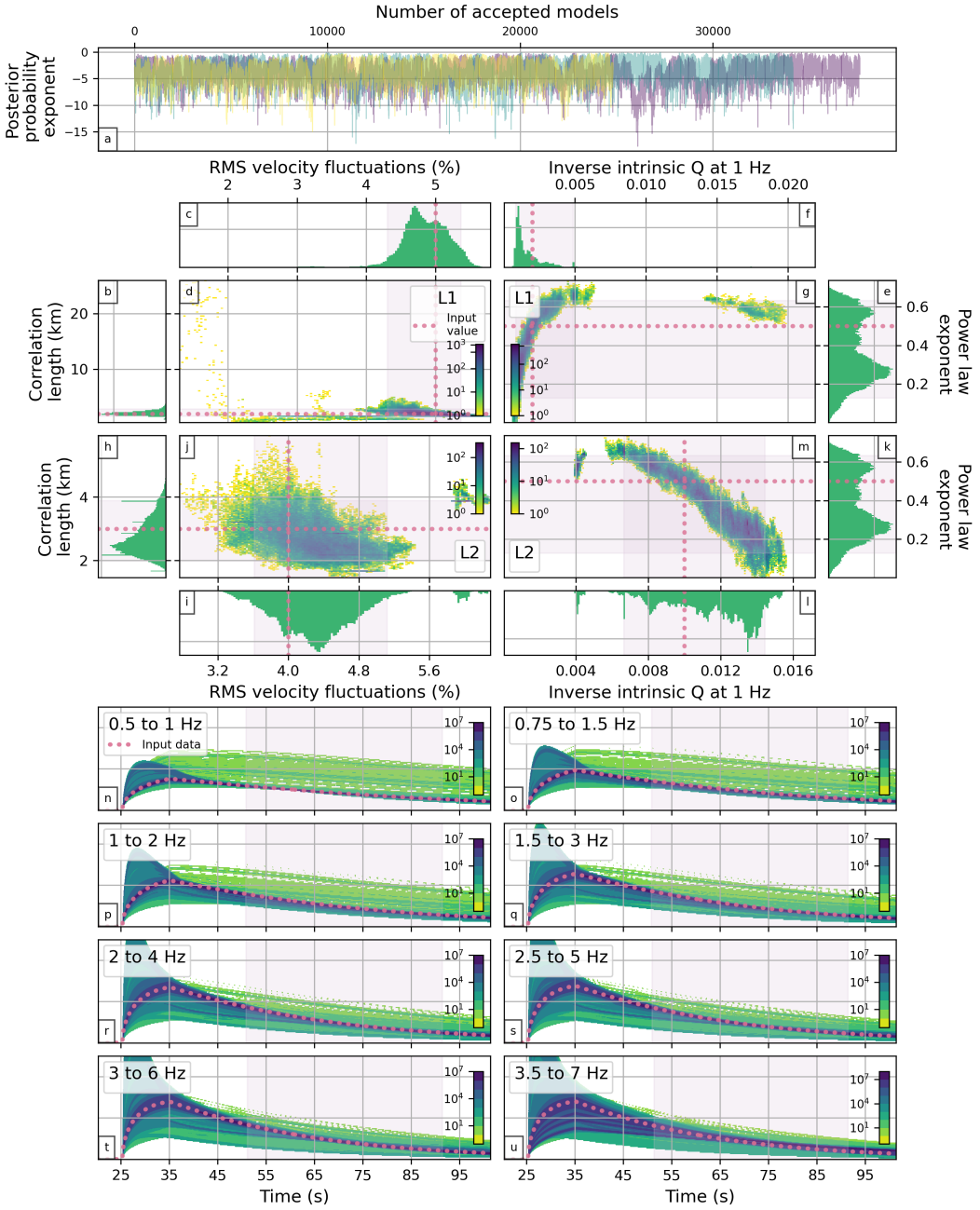

Figure A37: As Fig. A25, but for synthetic test 18 from Table 4.1.

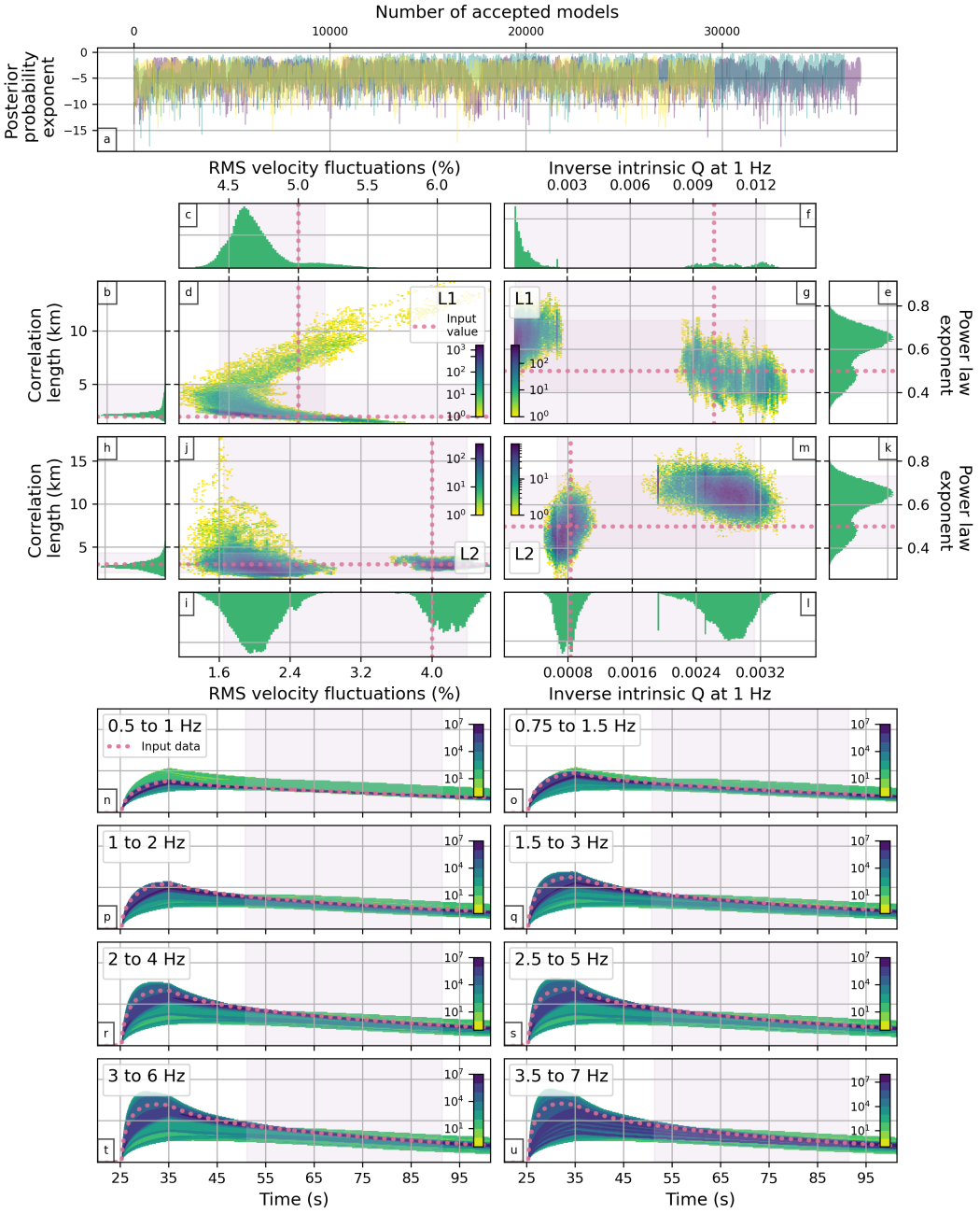

Figure A38: As Fig. A25, but for synthetic test 19 from Table 4.1.

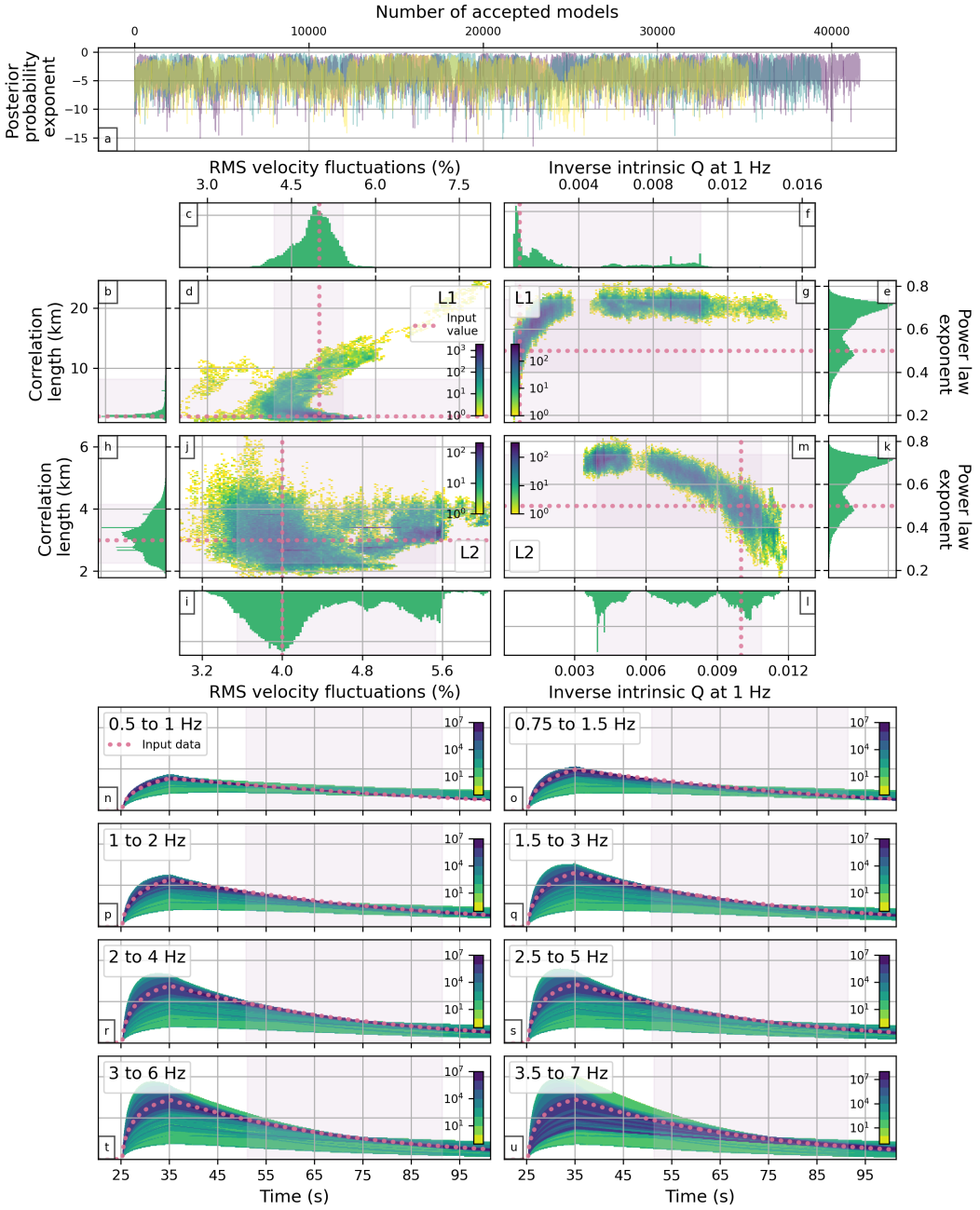

Figure A39: As Fig. A25, but for synthetic test 20 from Table 4.1.

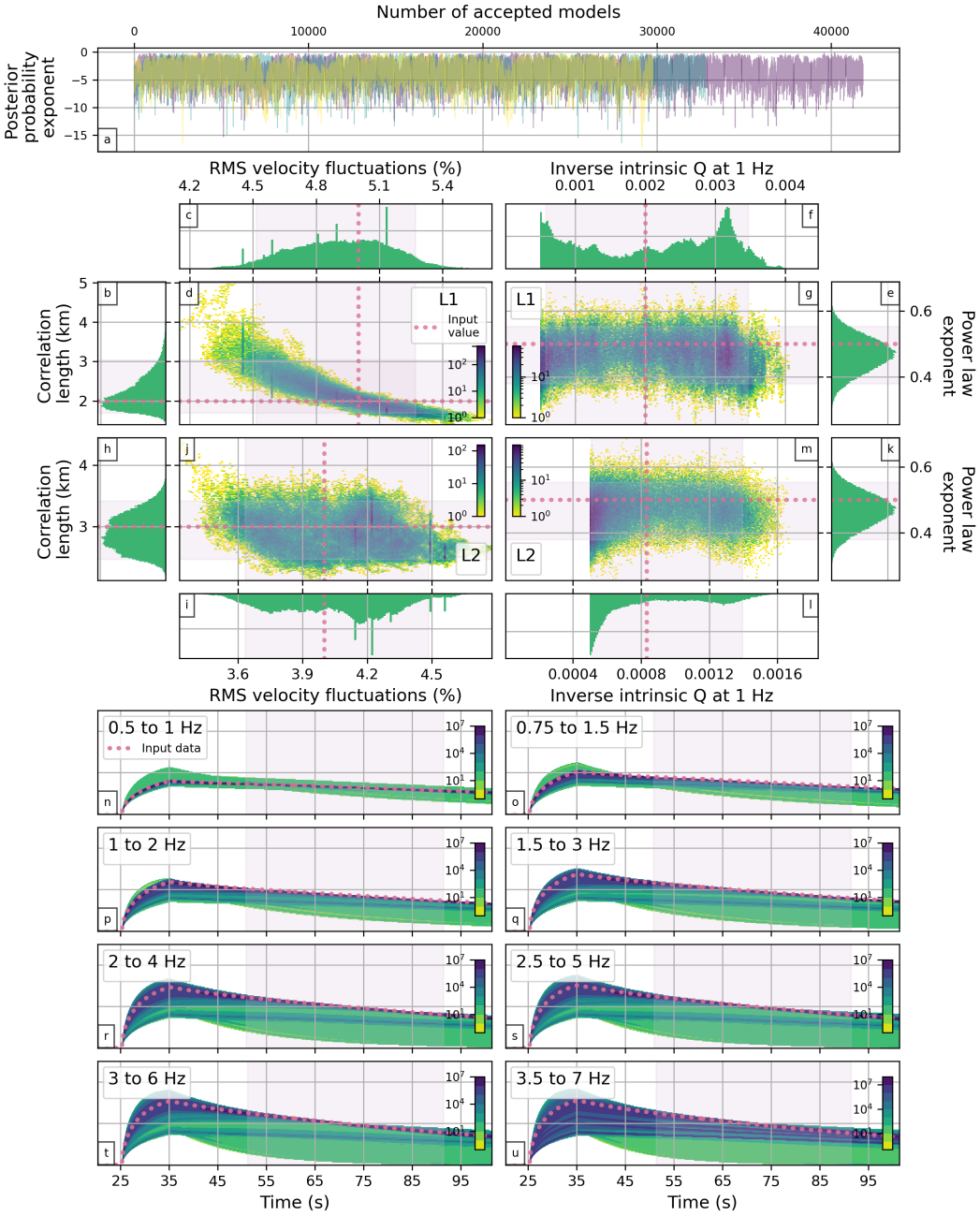

Figure A40: As Fig. A25, but for synthetic test 21 from Table 4.1.

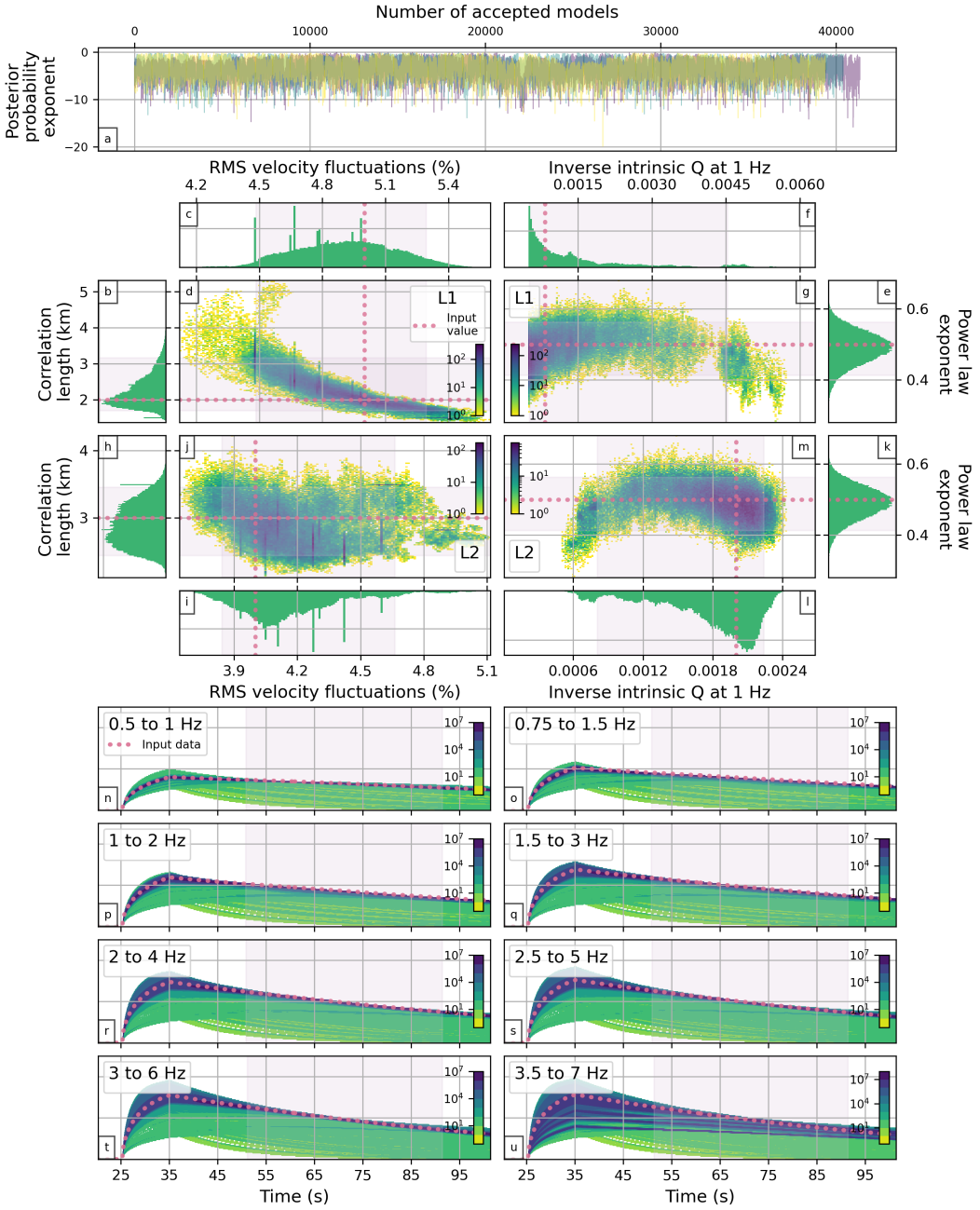

Figure A41: As Fig. A25, but for synthetic test 22 from Table 4.1.

A.3.2 Synthetic tests PDF marginals

Figures 4.12 and 4.13, in Section 4.1.2, contain the joint PDFs for all parameters and layers in the model for synthetic tests 9 and 7, respectively. This section gathers analogous figures for the remaining synthetic tests for 2-layer models from Table 4.1.

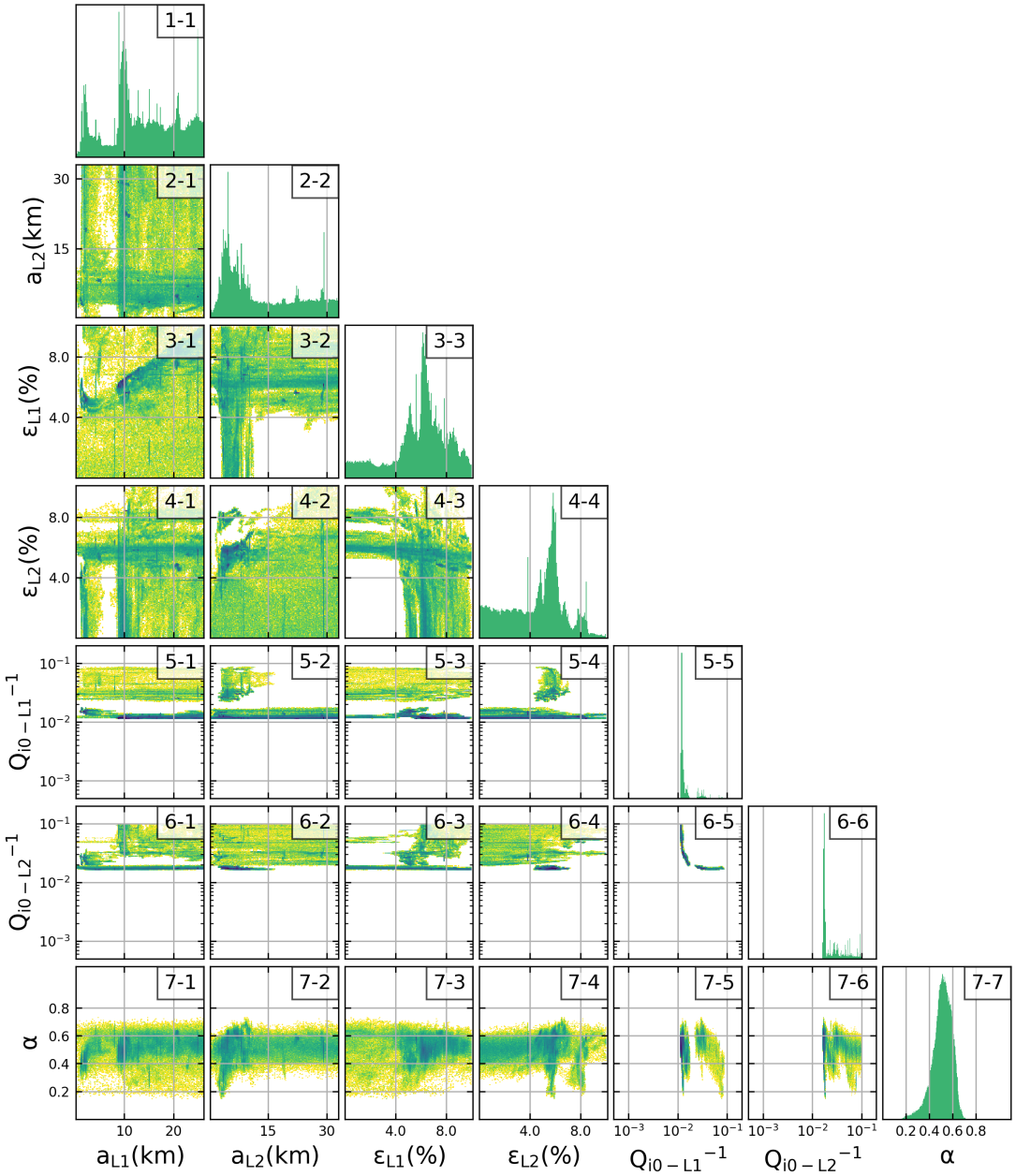

Figure A42: Obtained joint PDFs for all parameters and layers in synthetic model 5 from Table 4.1. Plots in the diagonal of the figure contain the individual PDF for the individual scattering and intrinsic attenuation parameters parameters.

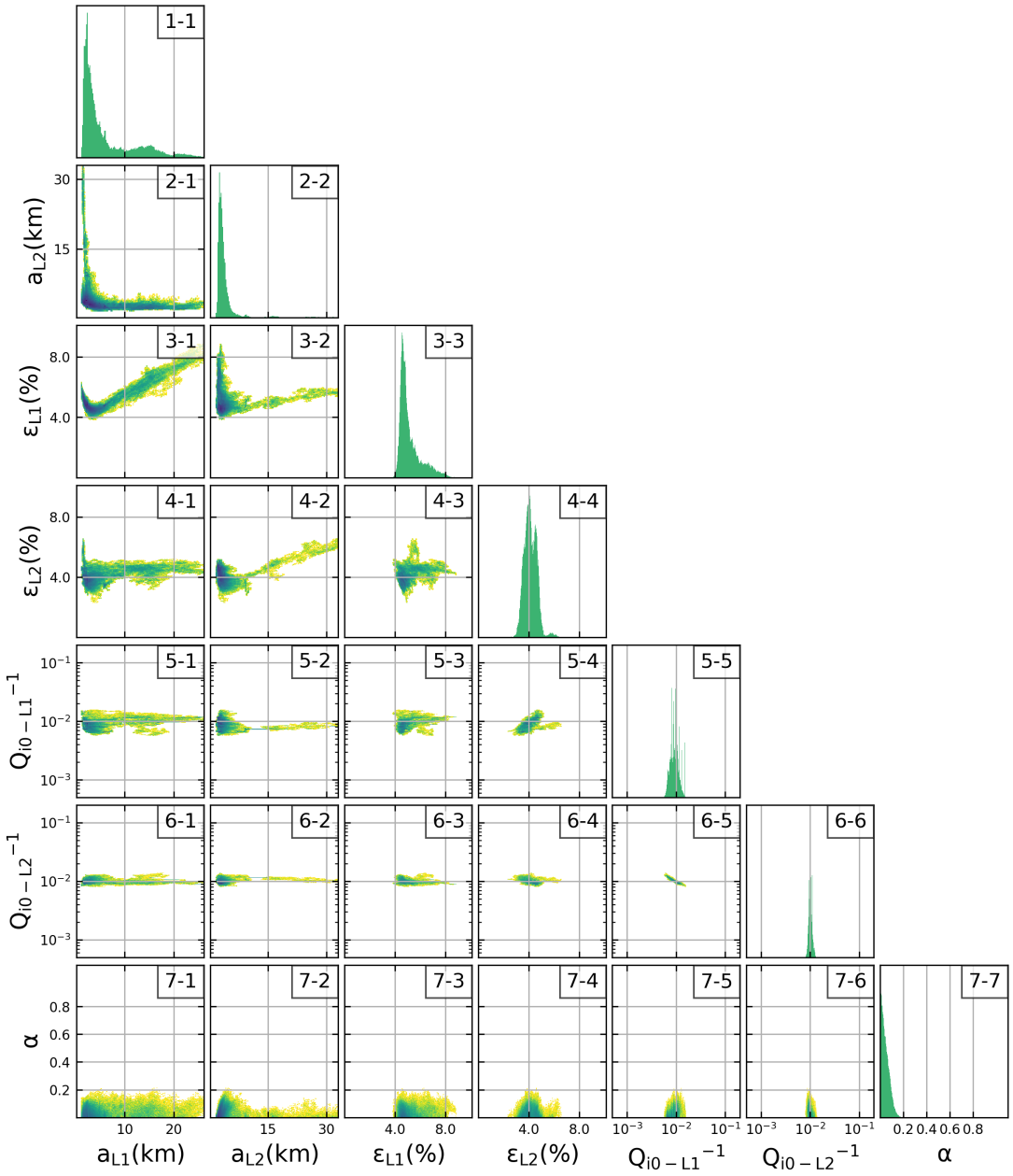

Figure A43: As Fig. A42, but for synthetic test 6 from Table 4.1.

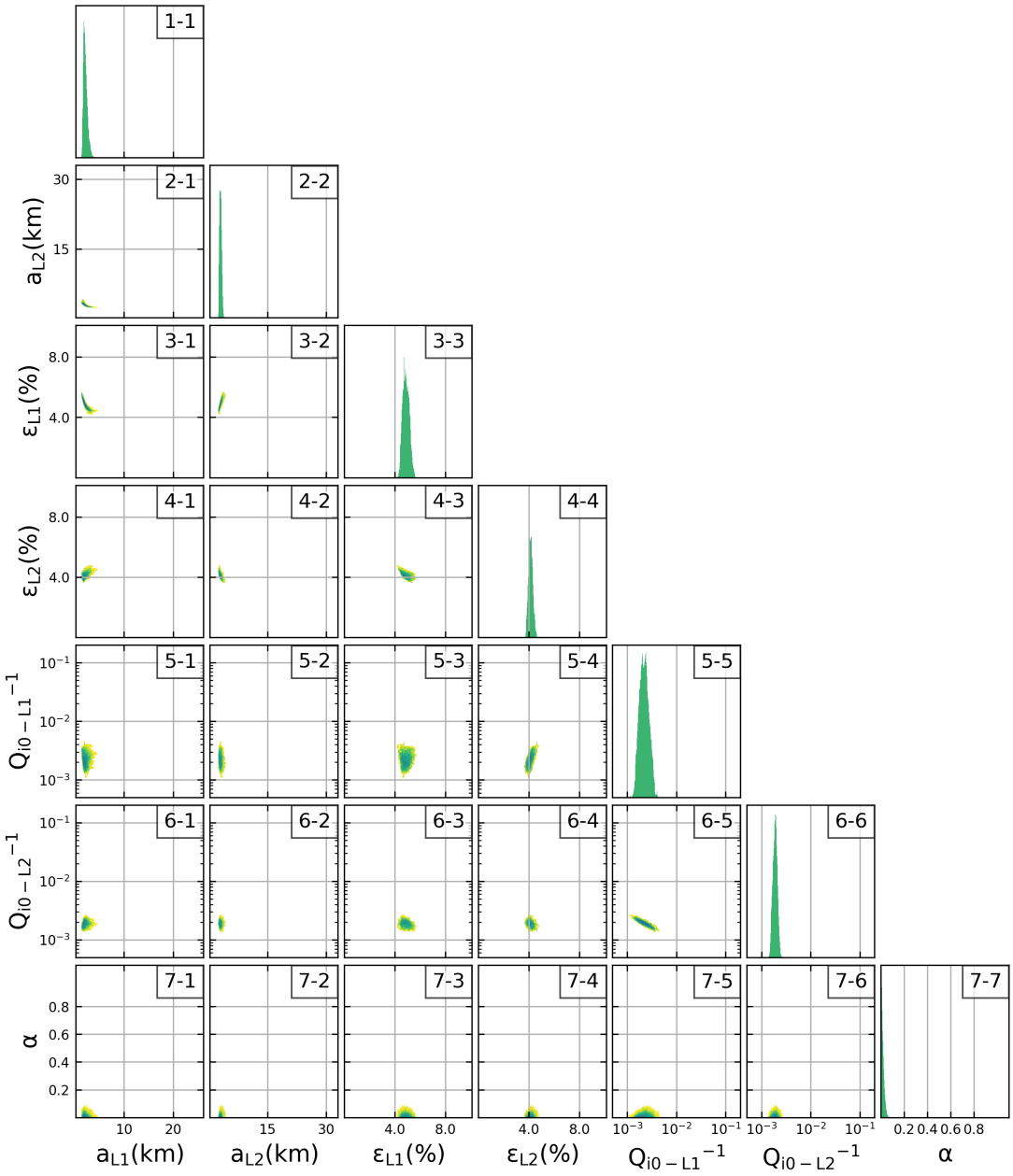

Figure A44: As Fig. A42, but for synthetic test 8 from Table 4.1.

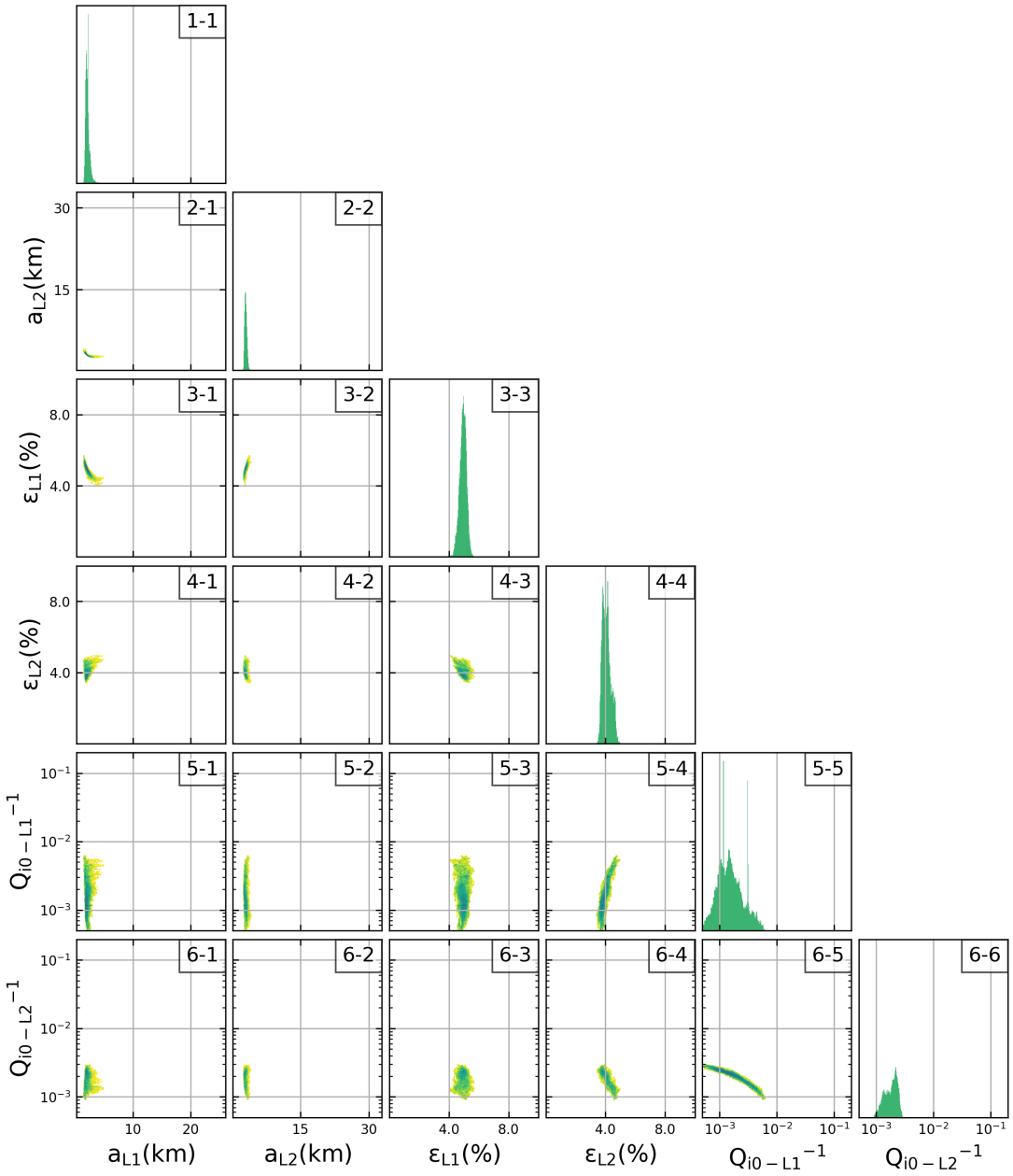

Figure A45: As Fig. A42, but for synthetic test 9* from Table 4.1.

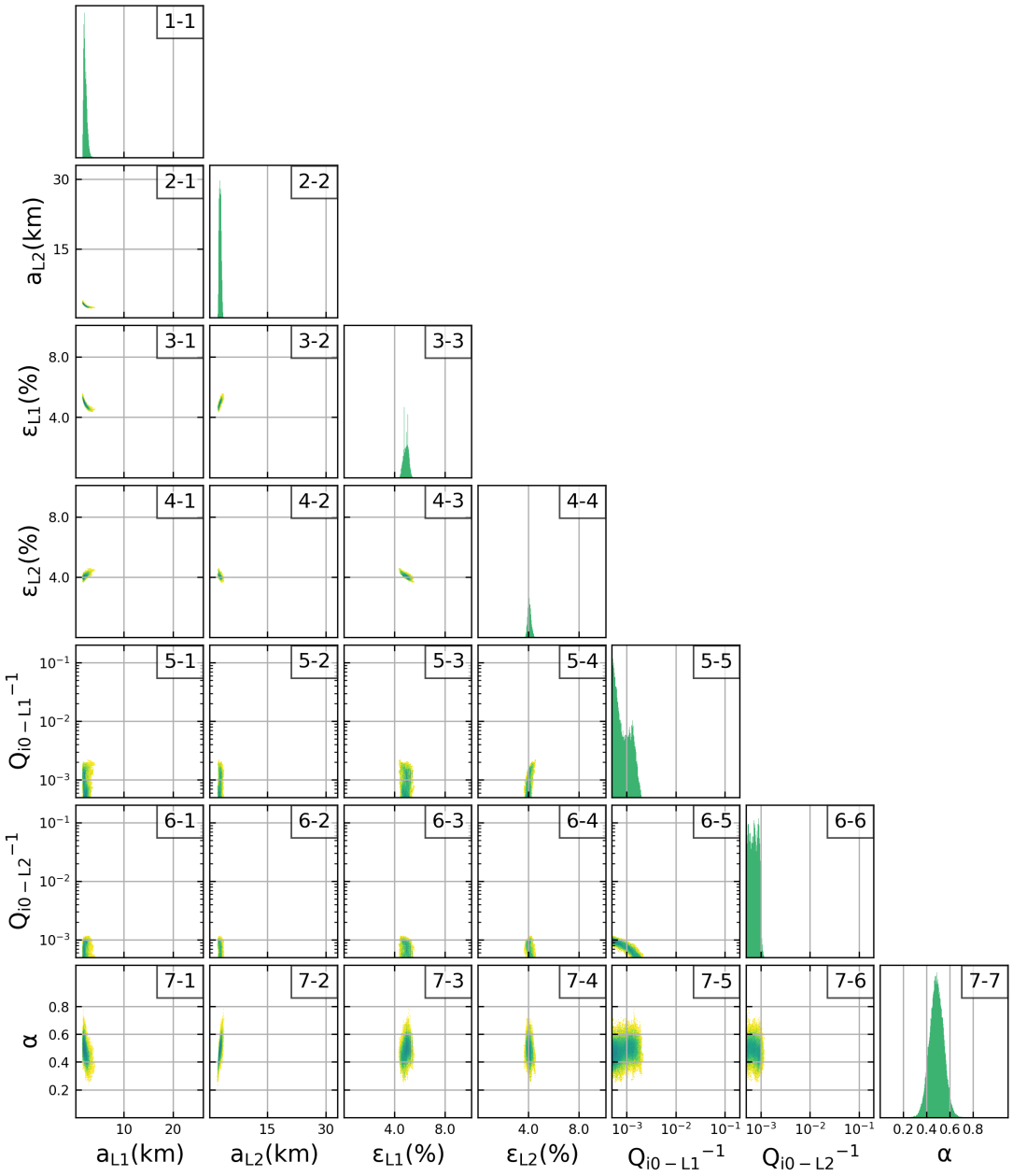

Figure A46: As Fig. A42, but for synthetic test 10 from Table 4.1.

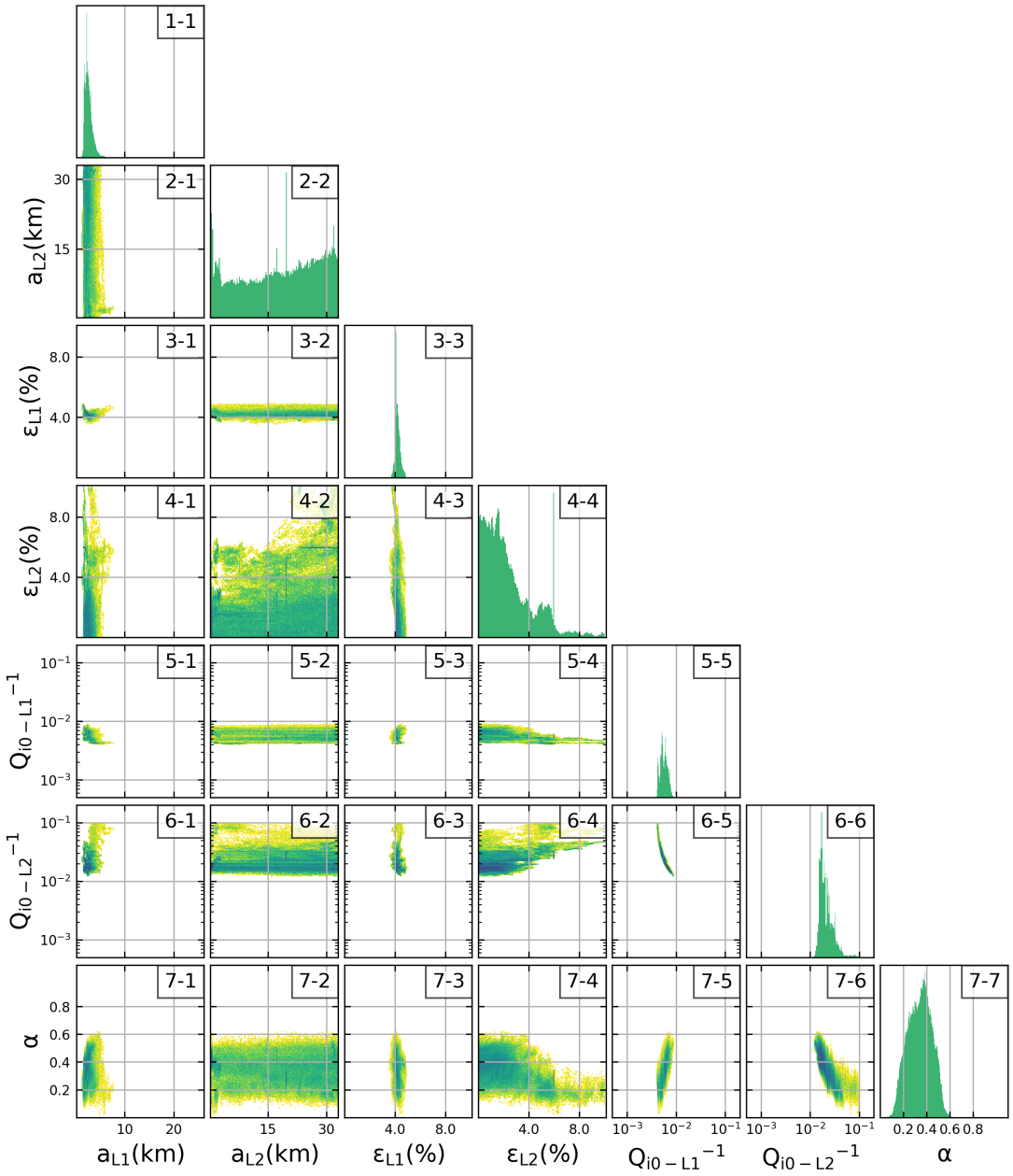

Figure A47: As Fig. A42, but for synthetic test 11 from Table 4.1.

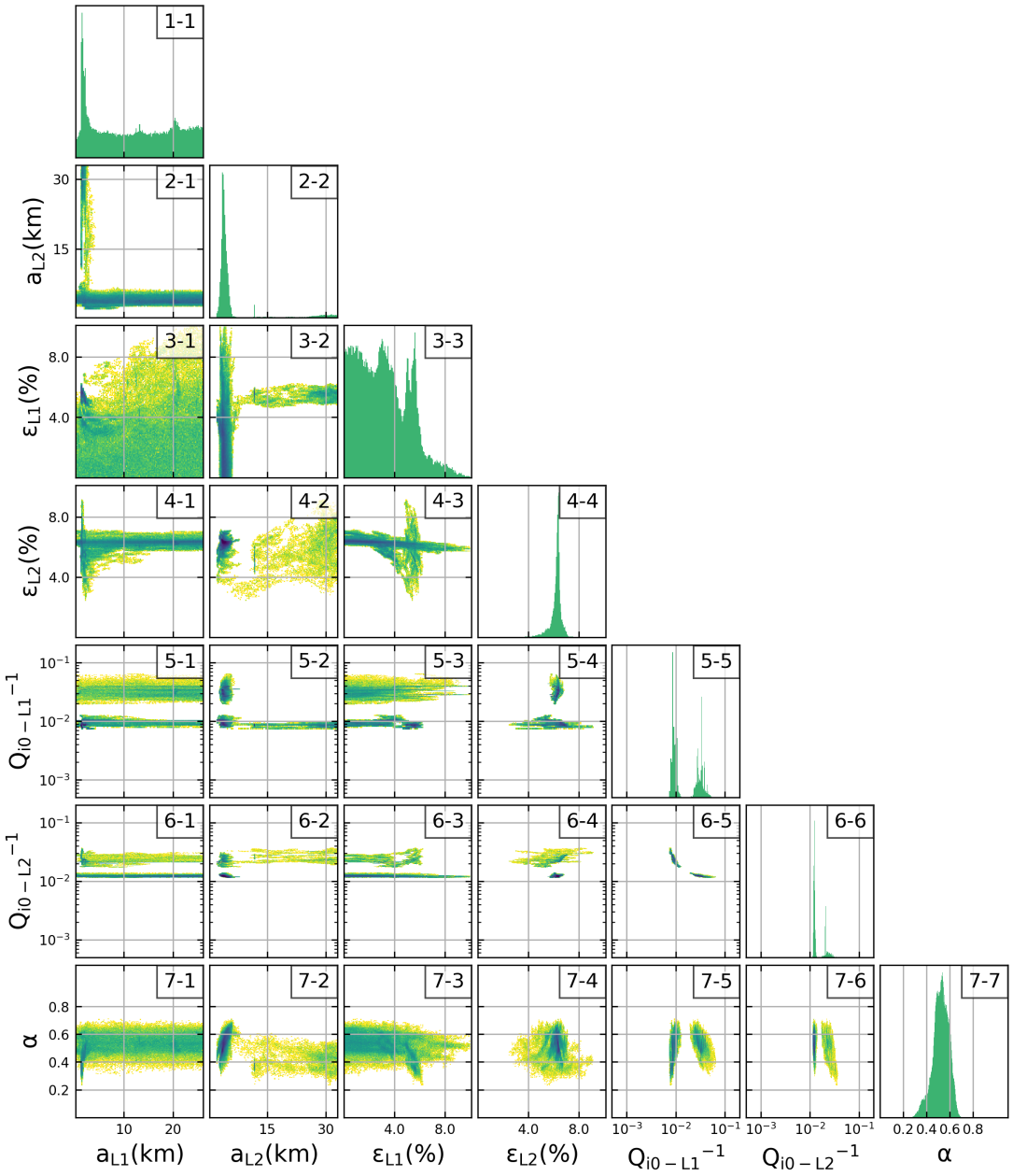

Figure A48: As Fig. A42, but for synthetic test 12 from Table 4.1.

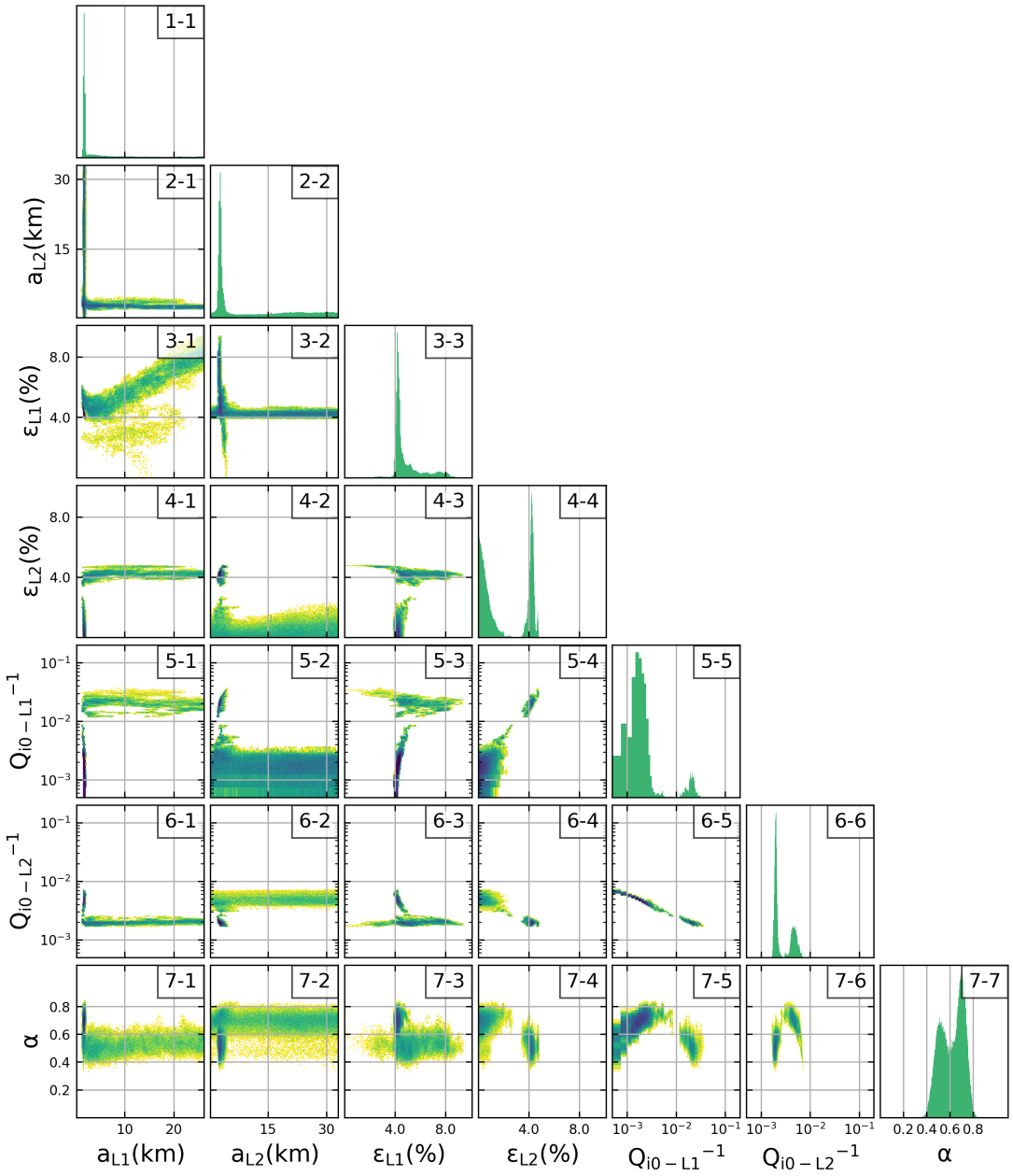

Figure A49: As Fig. A42, but for synthetic test 13 from Table 4.1.

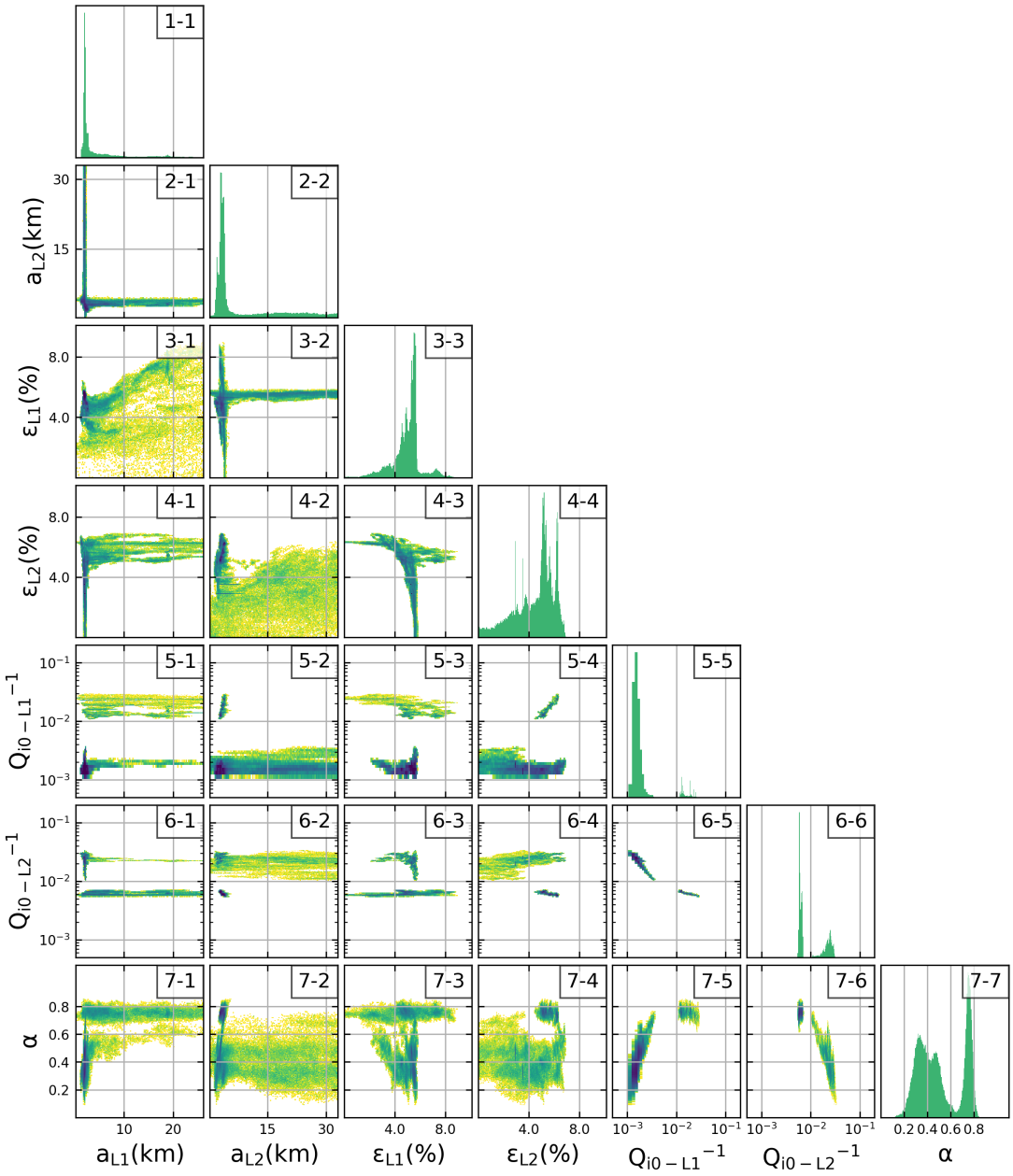

Figure A50: As Fig. A42, but for synthetic test 14 from Table 4.1.

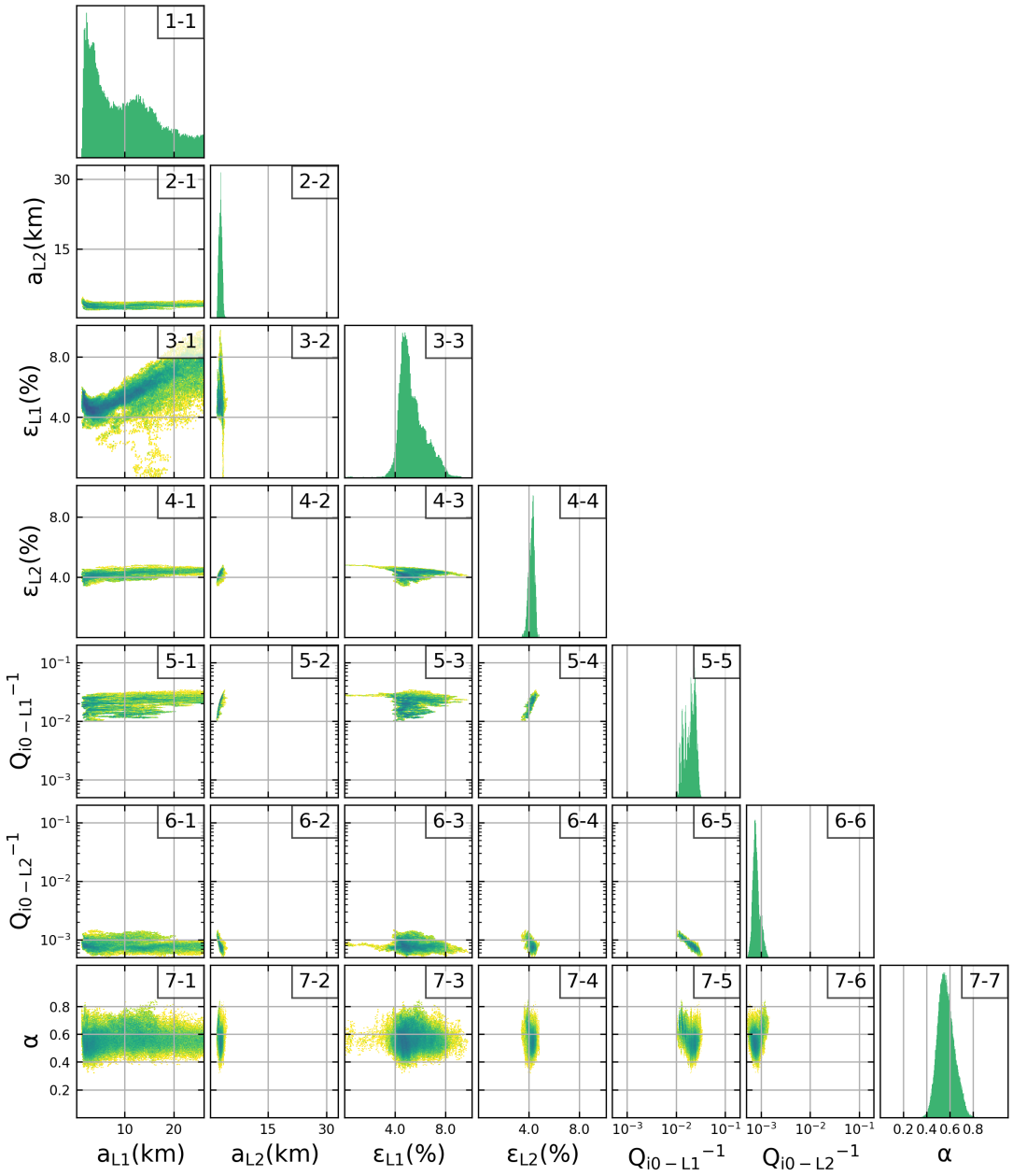

Figure A51: As Fig. A42, but for synthetic test 15 from Table 4.1.

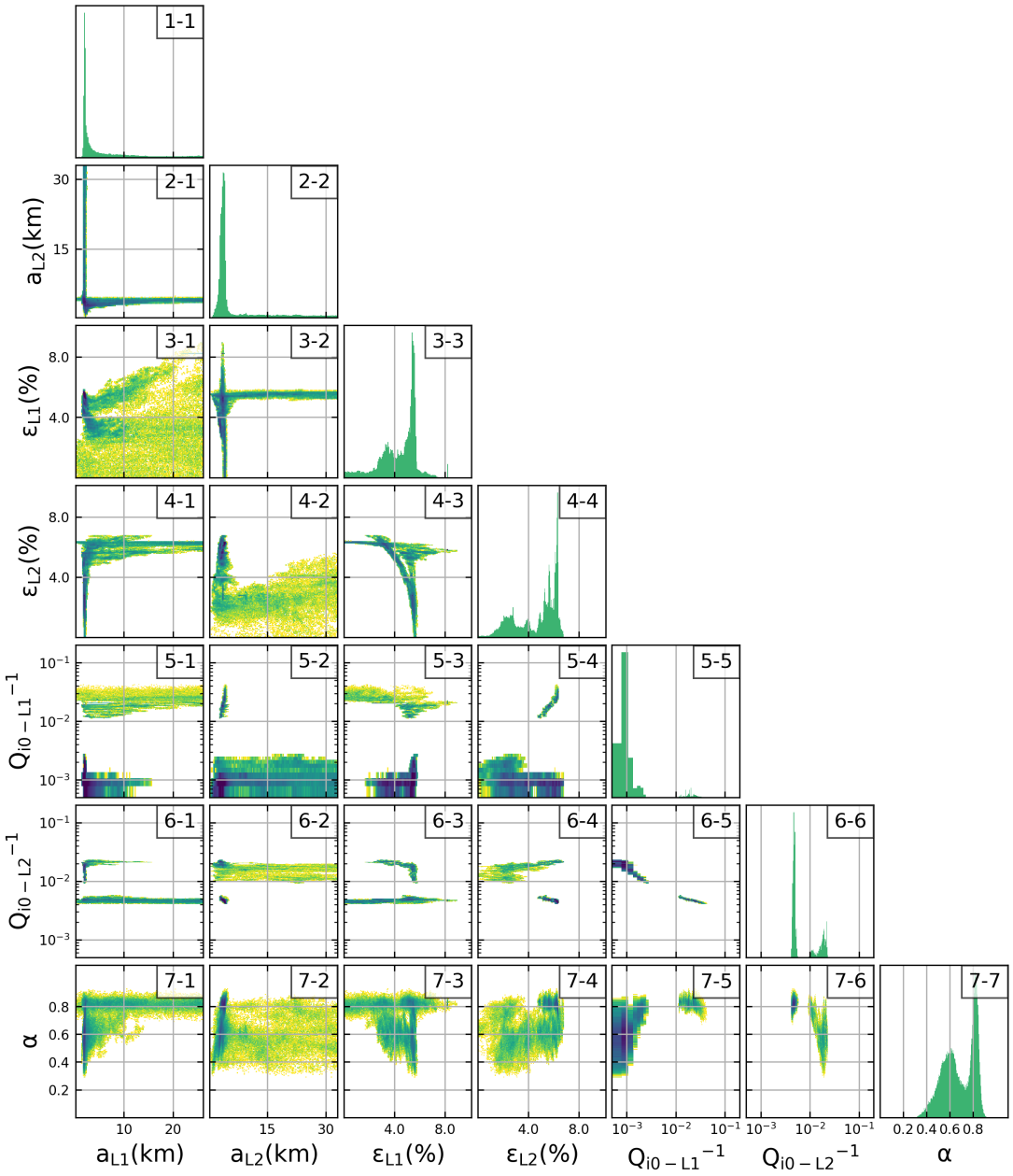

Figure A52: As Fig. A42, but for synthetic test 16 from Table 4.1.

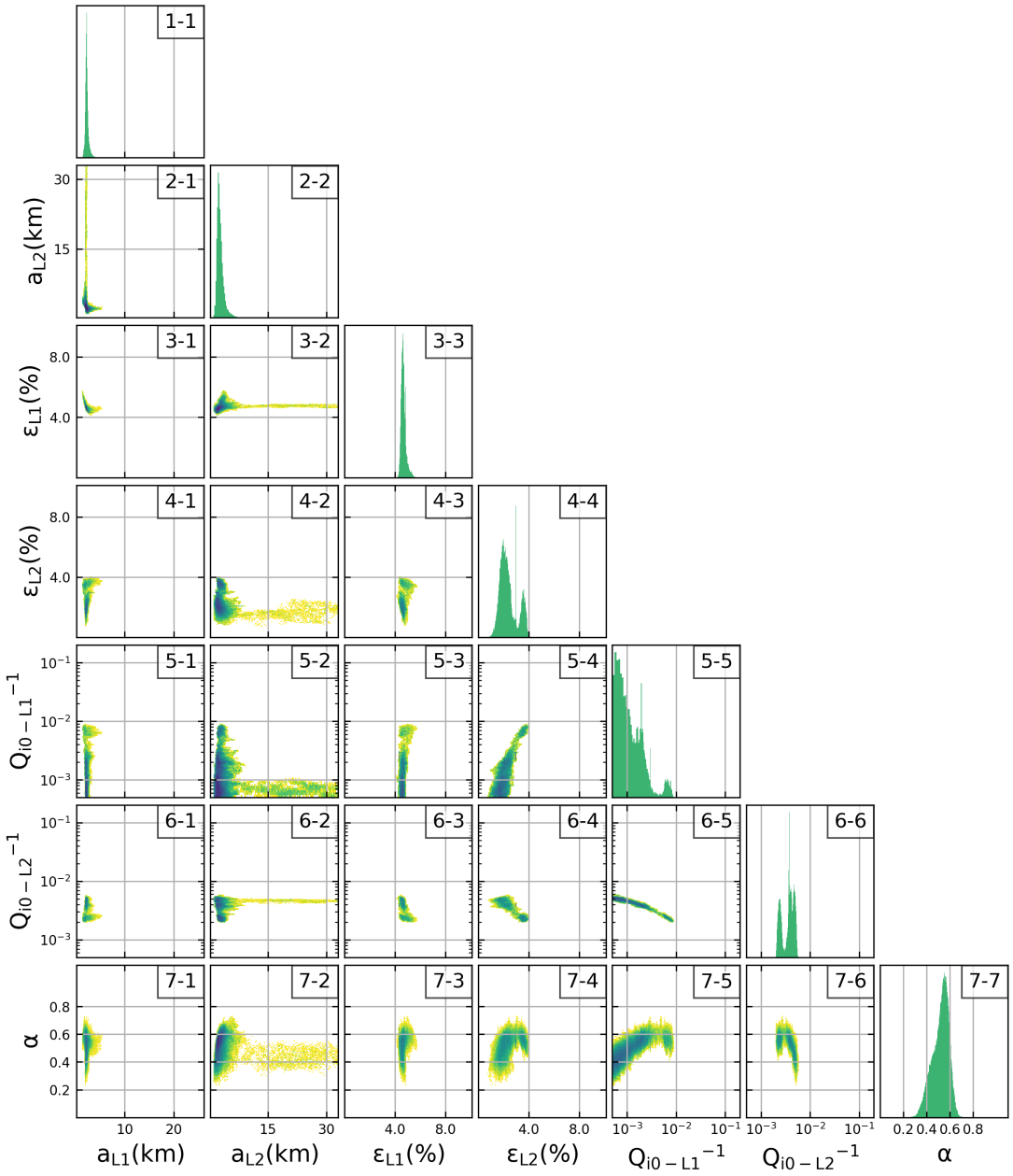

Figure A53: As Fig. A42, but for synthetic test 17 from Table 4.1.

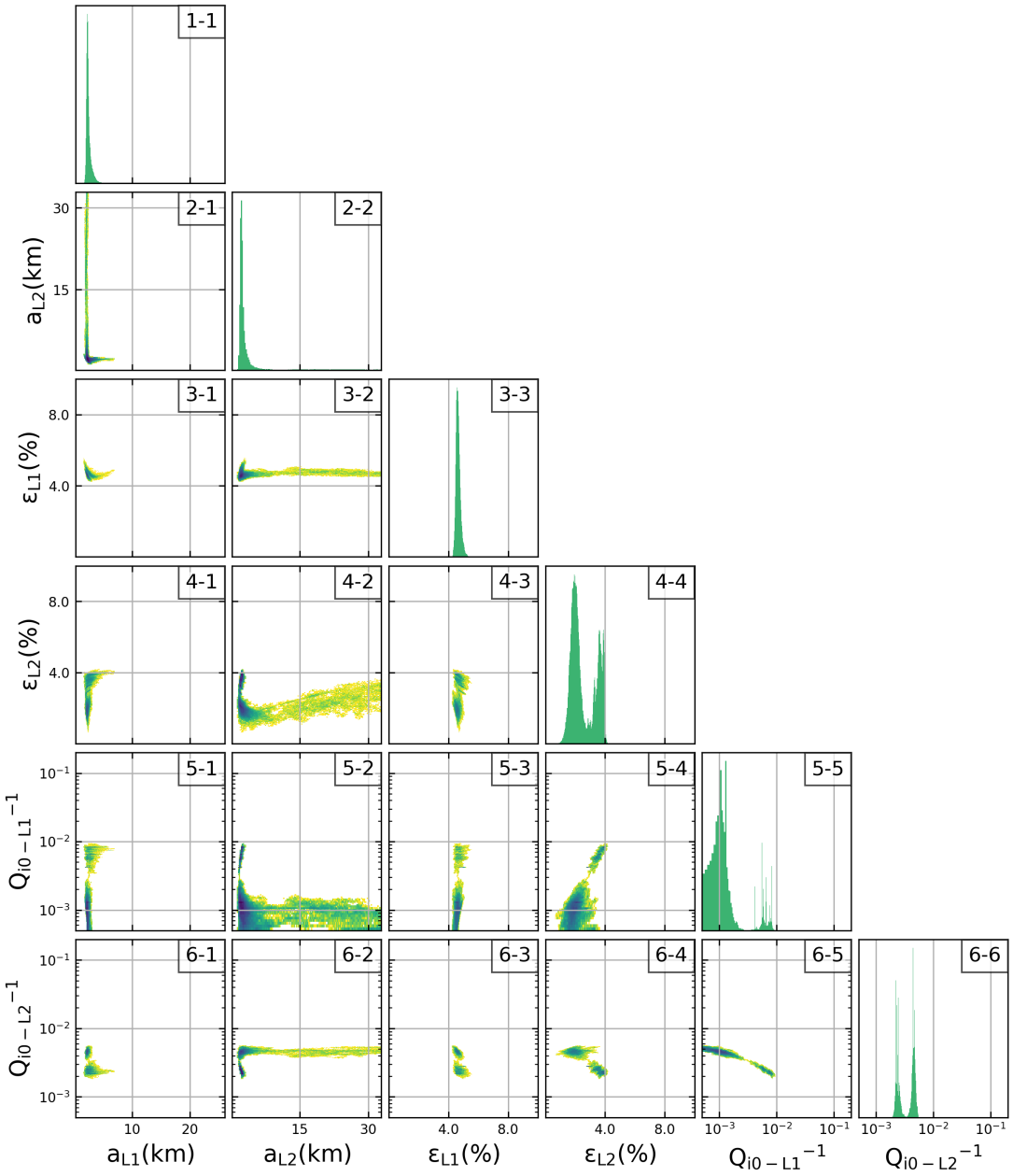

Figure A54: As Fig. A42, but for synthetic test 17* from Table 4.1.

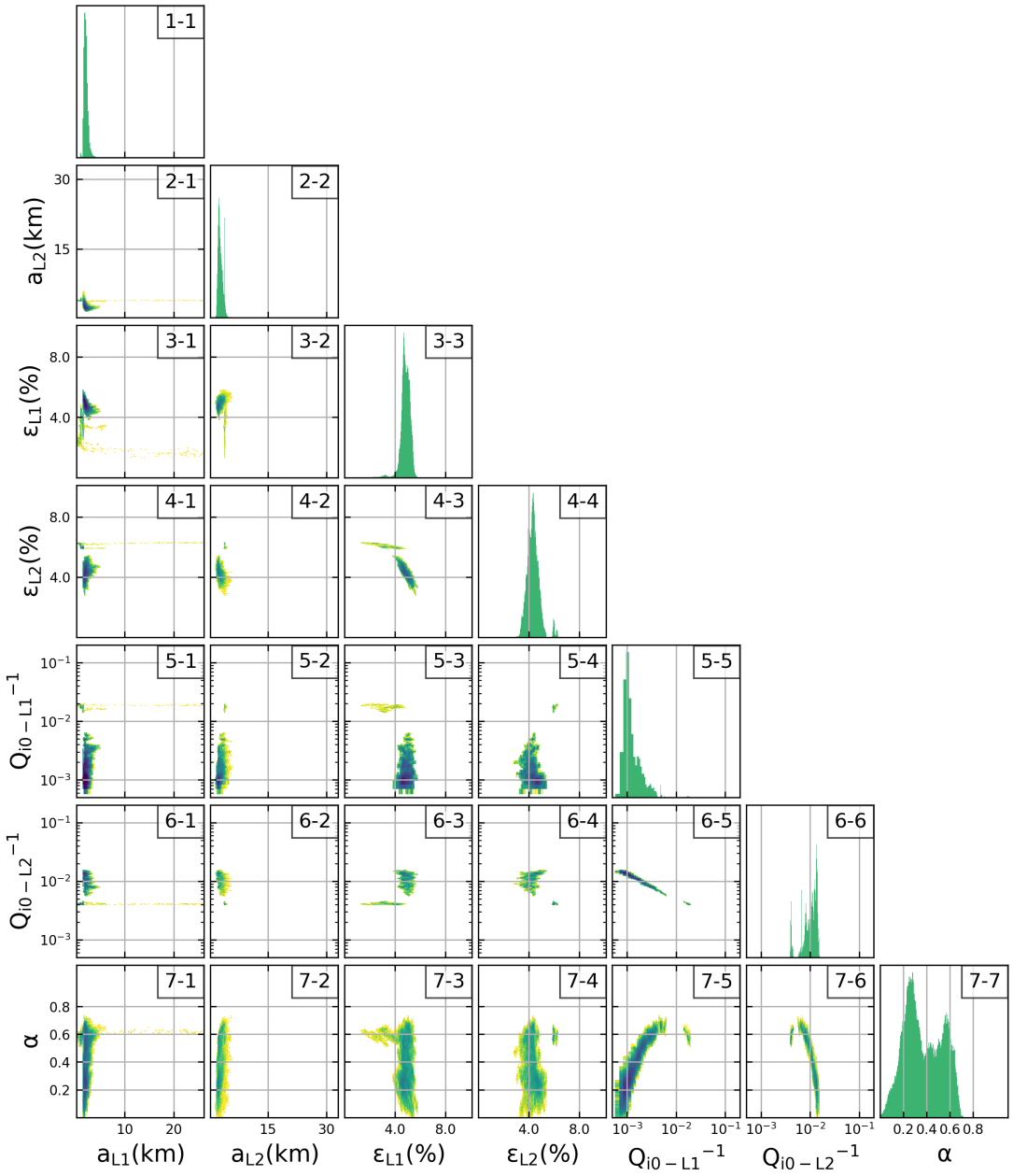

Figure A55: As Fig. A42, but for synthetic test 18 from Table 4.1.

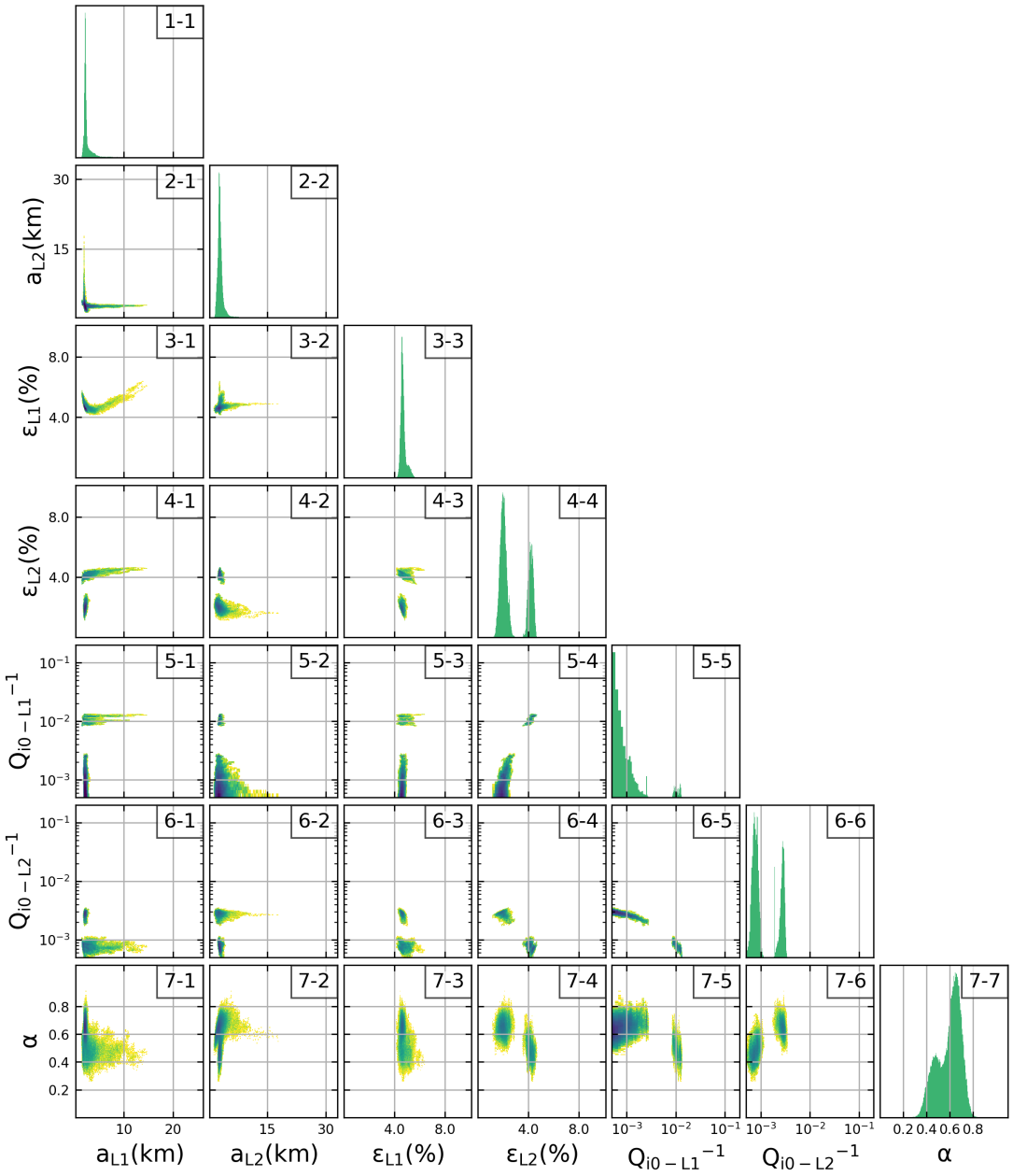

Figure A56: As Fig. A42, but for synthetic test 19 from Table 4.1.

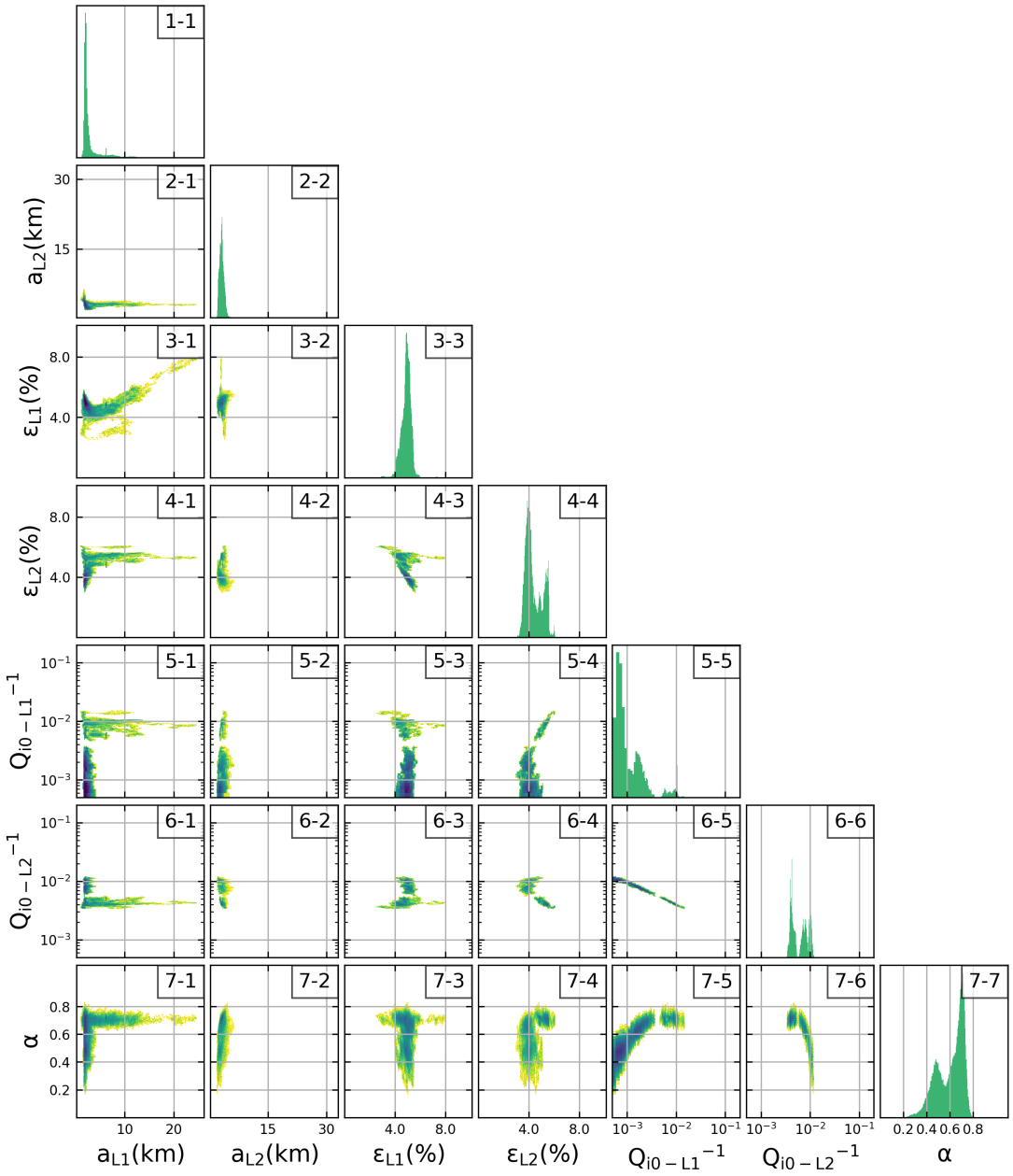

Figure A57: As Fig. A42, but for synthetic test 20 from Table 4.1.

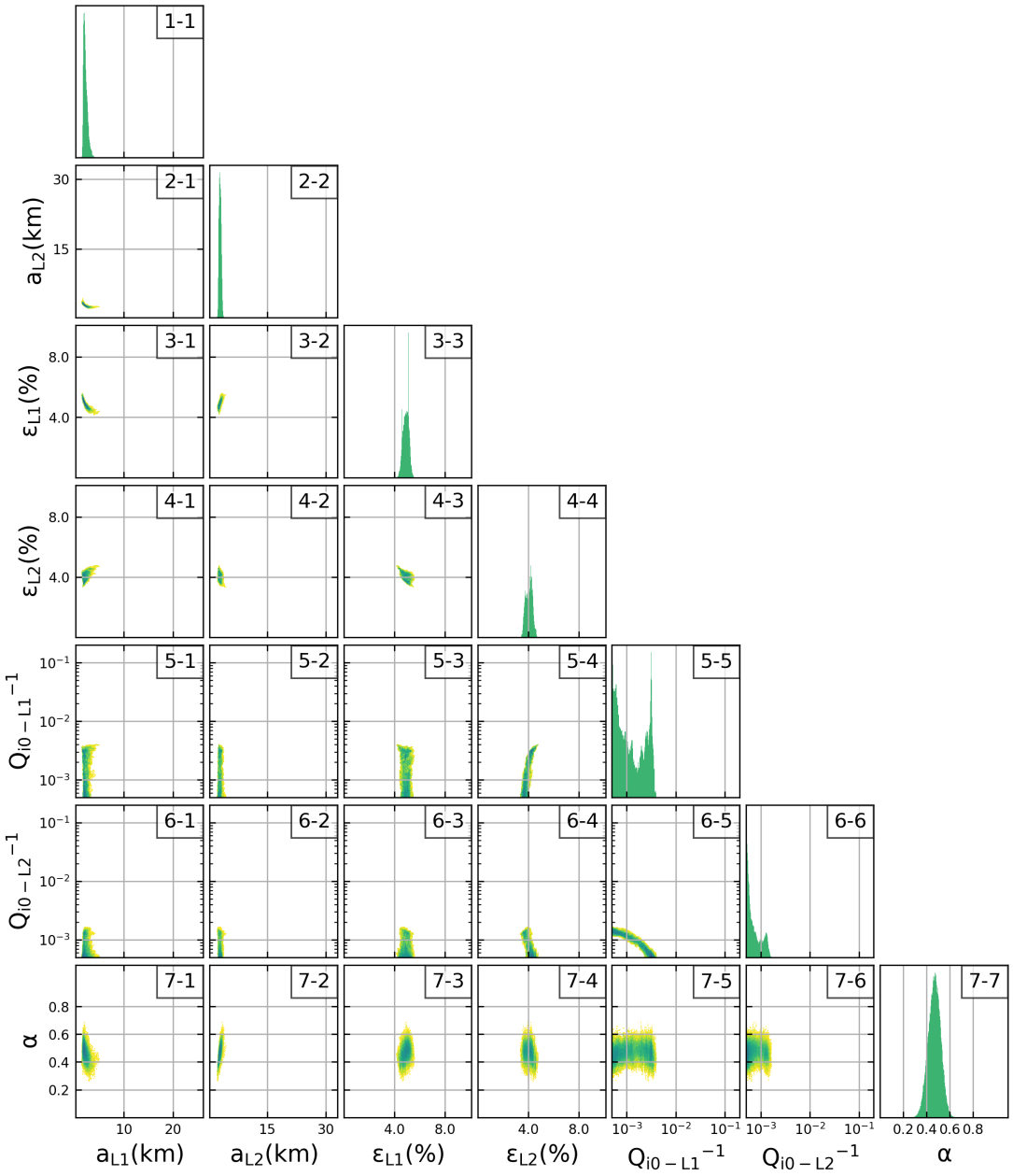

Figure A58: As Fig. A42, but for synthetic test 21 from Table 4.1.

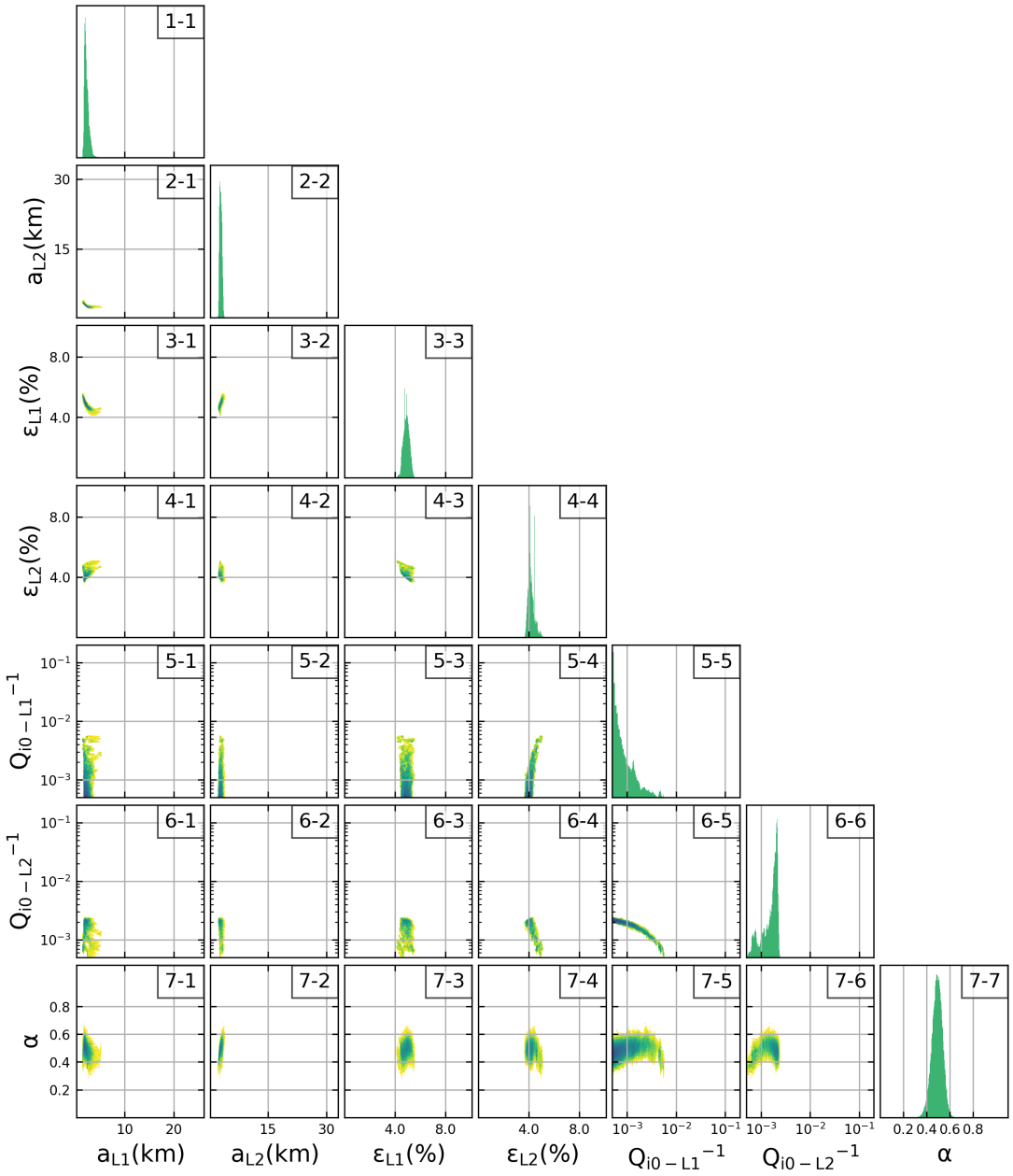

Figure A59: As Fig. A42, but for synthetic test 22 from Table 4.1.

A.3.3 E-EFMD Bayesian inversion results samples

In Section 4.1.2, I sampled the ensembles obtained for synthetic tests 5 and 11 (Table 4.1) by taking the models with the highest loglikelihoods (L) and plotting their scattering and attenuation parameters for each layer. Figures in this section contain similar samples for the rest of the synthetic tests in Table 4.1.

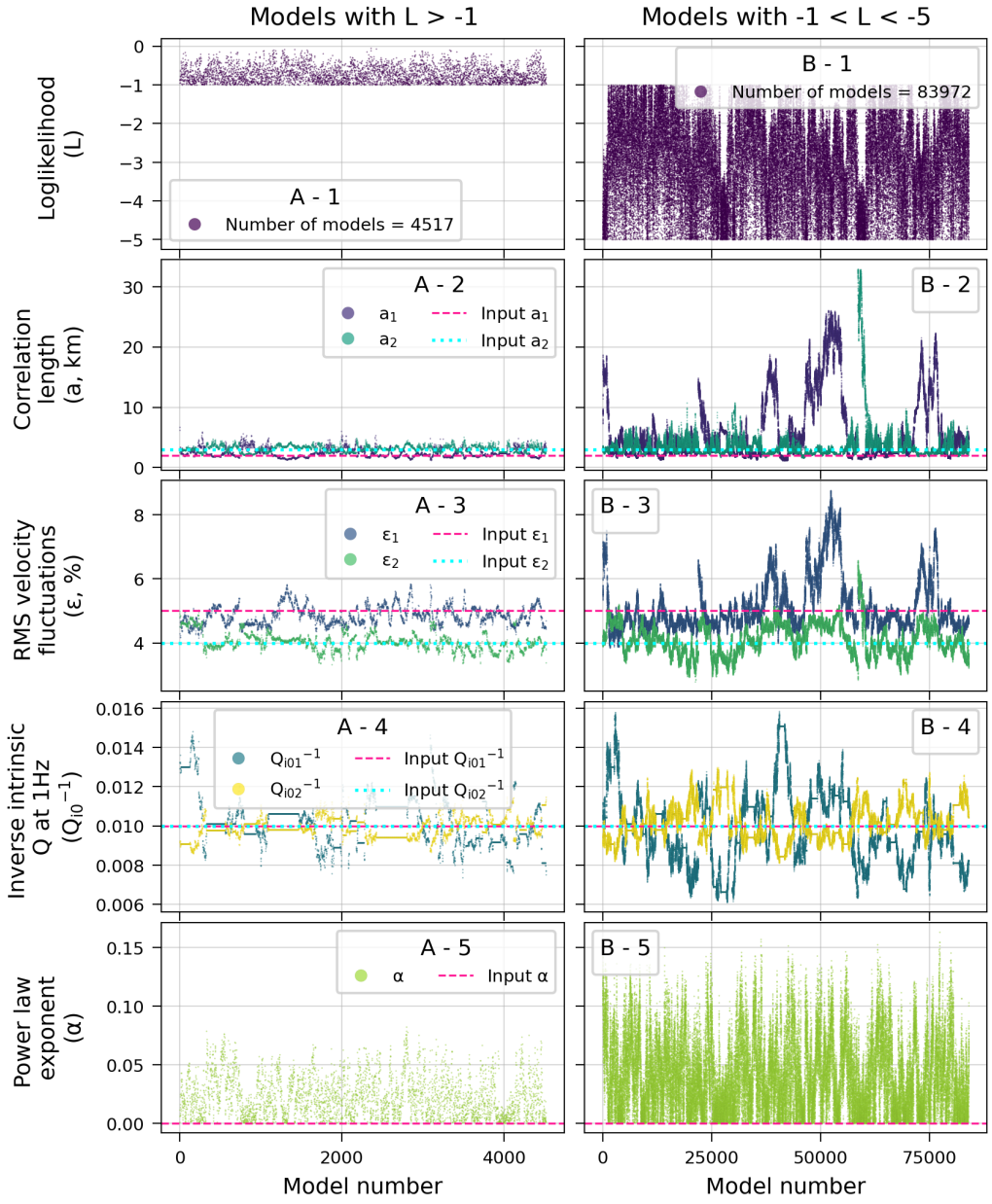

Figure A60: Samples of the E-EFMD results for synthetic test 6 from Table 4.1. Panels A1–A5 contain the loglikelihood (L), correlation length (a), RMS velocity fluctuation (ε), inverse intrinsic quality factor at 1 Hz (Q_{i0}^{-1}) and power law exponent (α) for all models with $L > -1$, as well as the input parameter values in each case. Panels B1–B5 have the same content, but for models with $-1 > L > -5$.

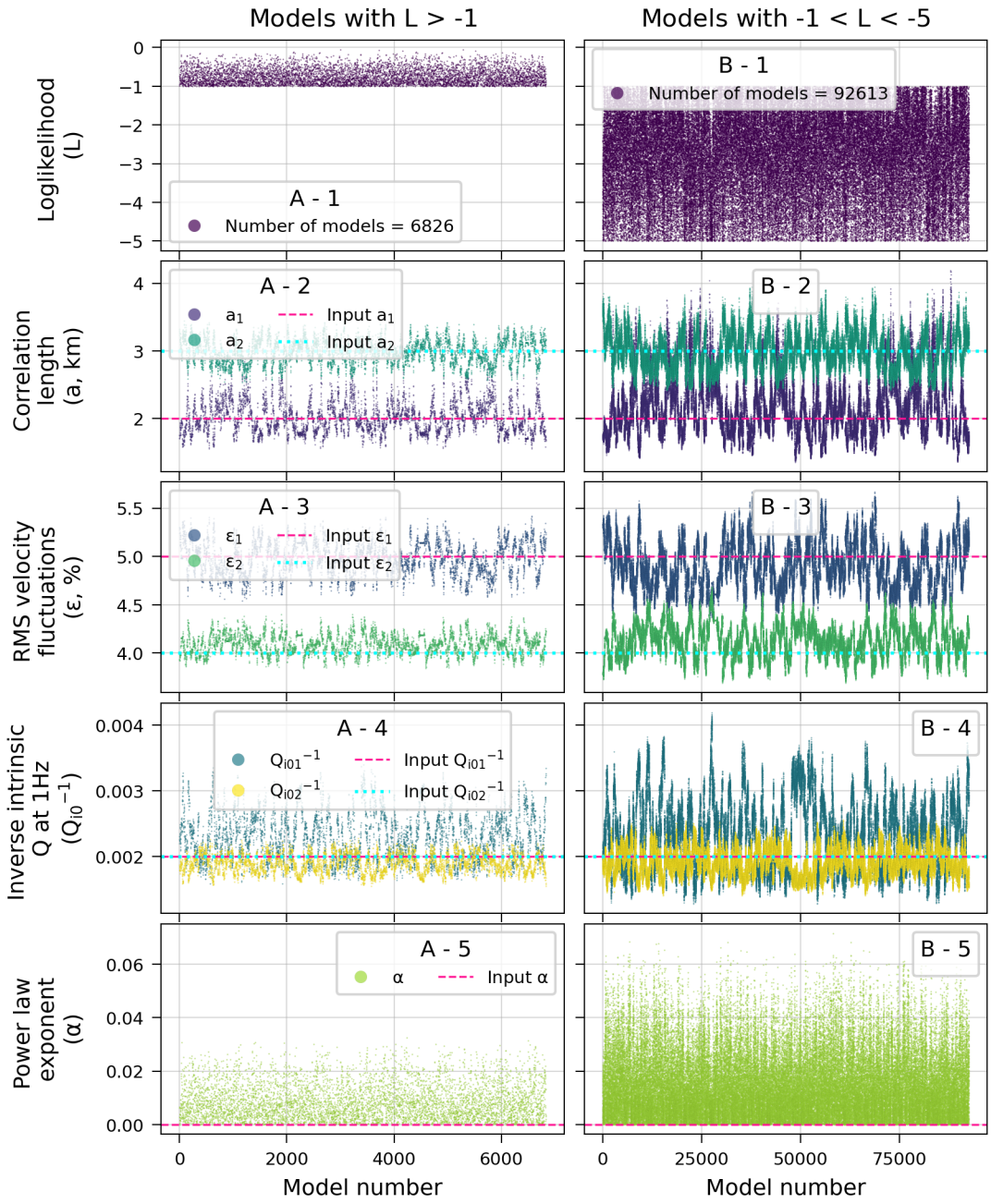

Figure A61: Same as Fig. A60 but for synthetic model 8 from Table 4.1.

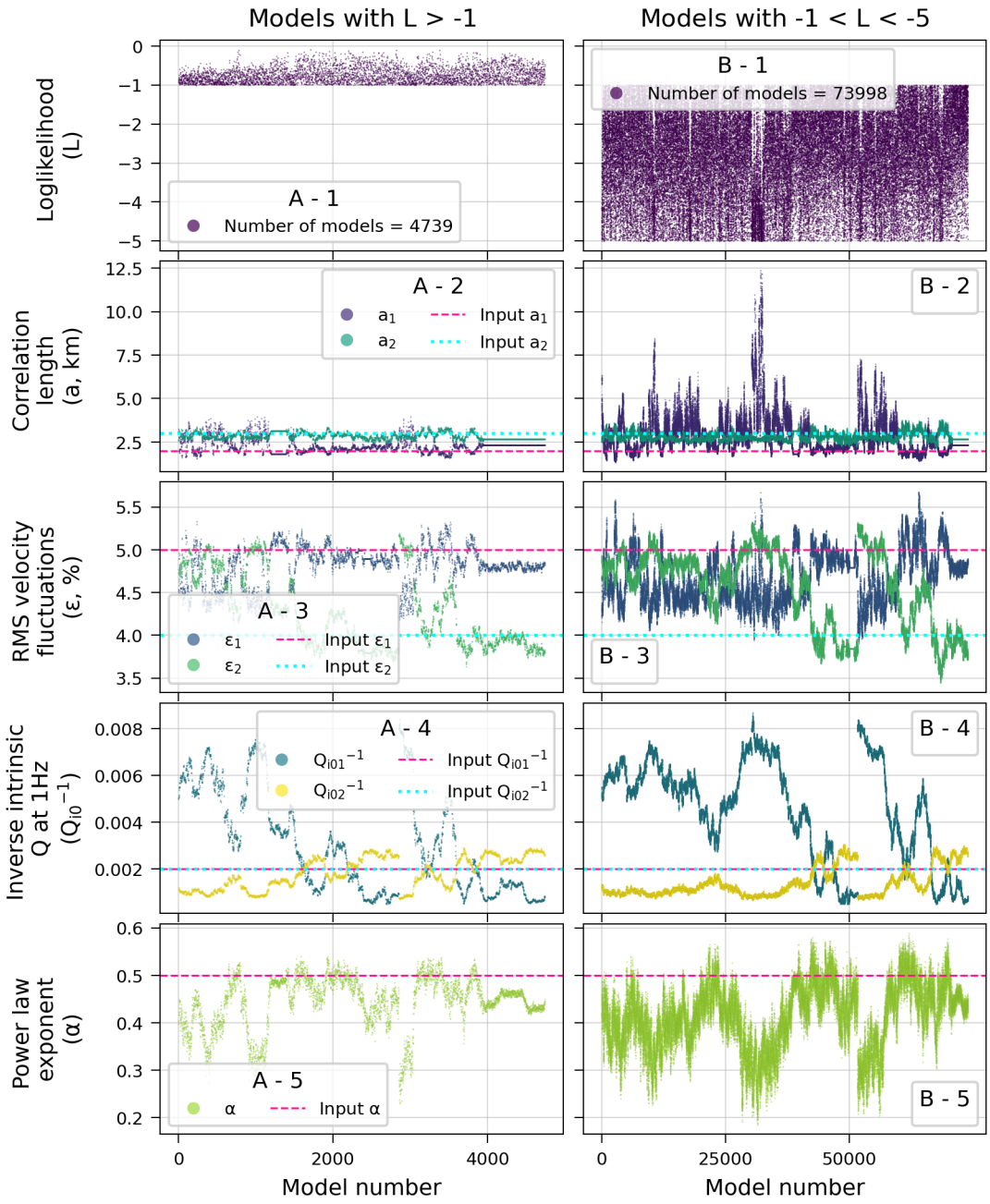

Figure A62: Same as Fig. A60 but for synthetic model 9 from Table 4.1.

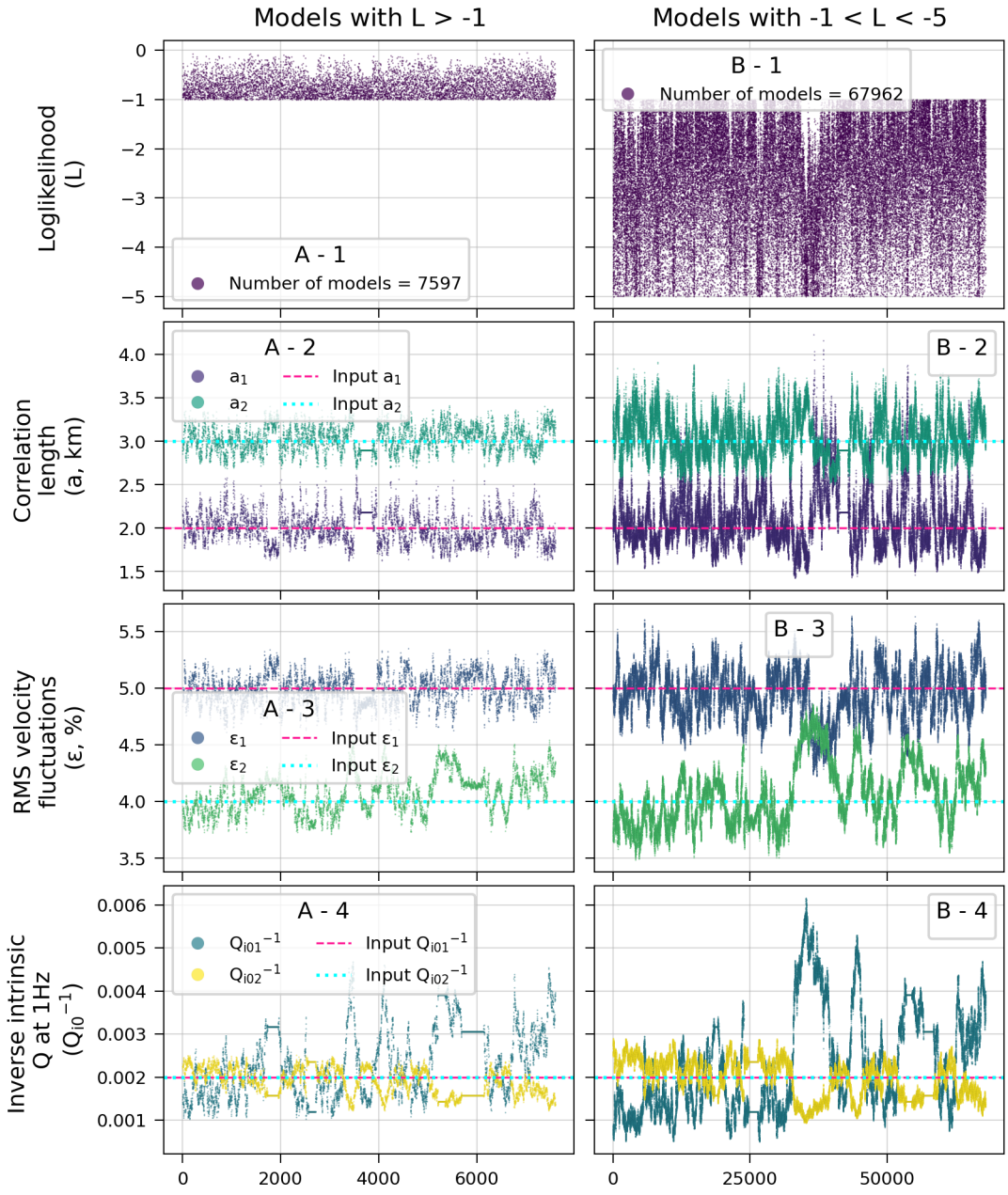

Figure A63: Same as Fig. A60 but for synthetic model 9* from Table 4.1.

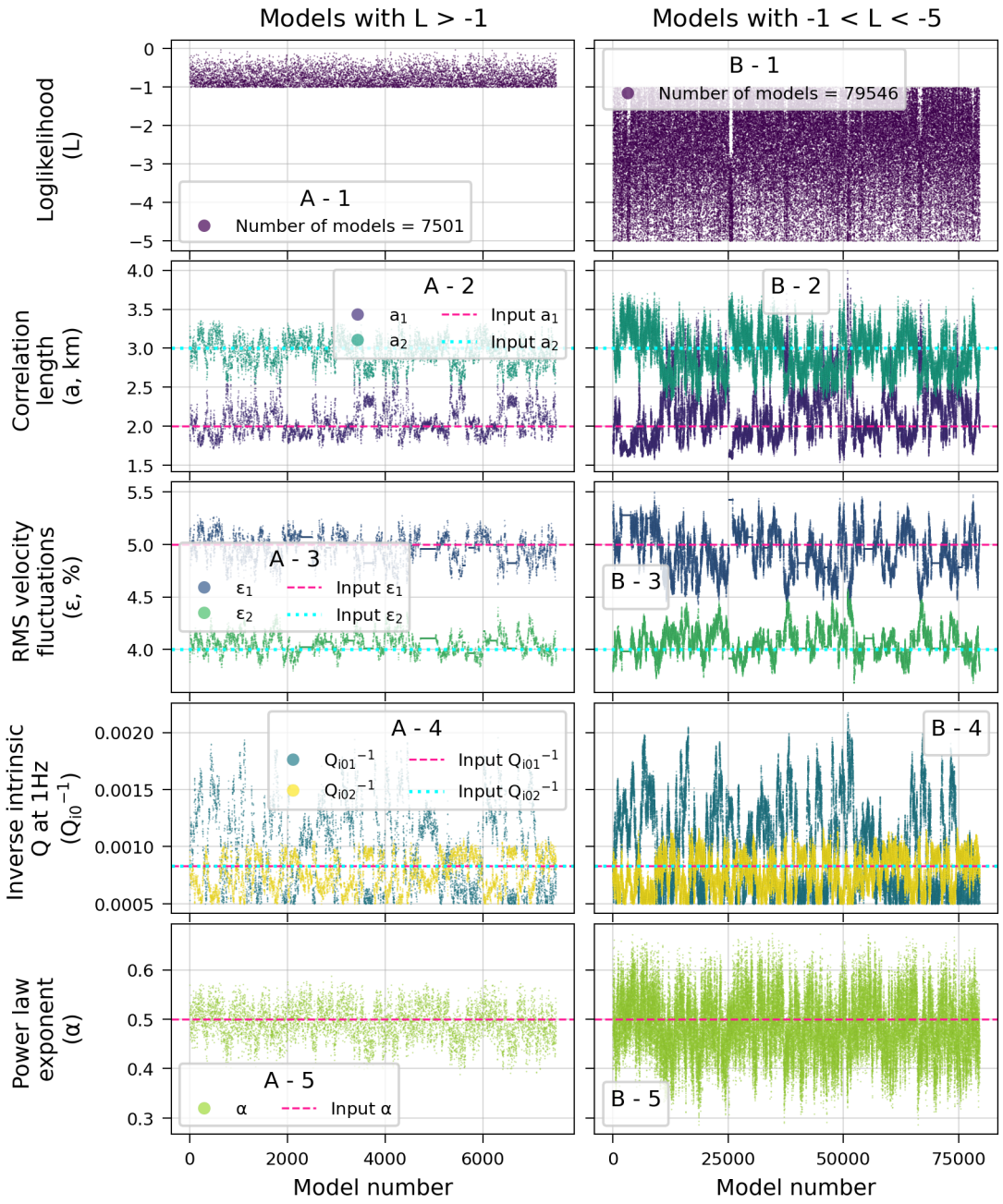

Figure A64: Same as Fig. A60 but for synthetic model 10 from Table 4.1.

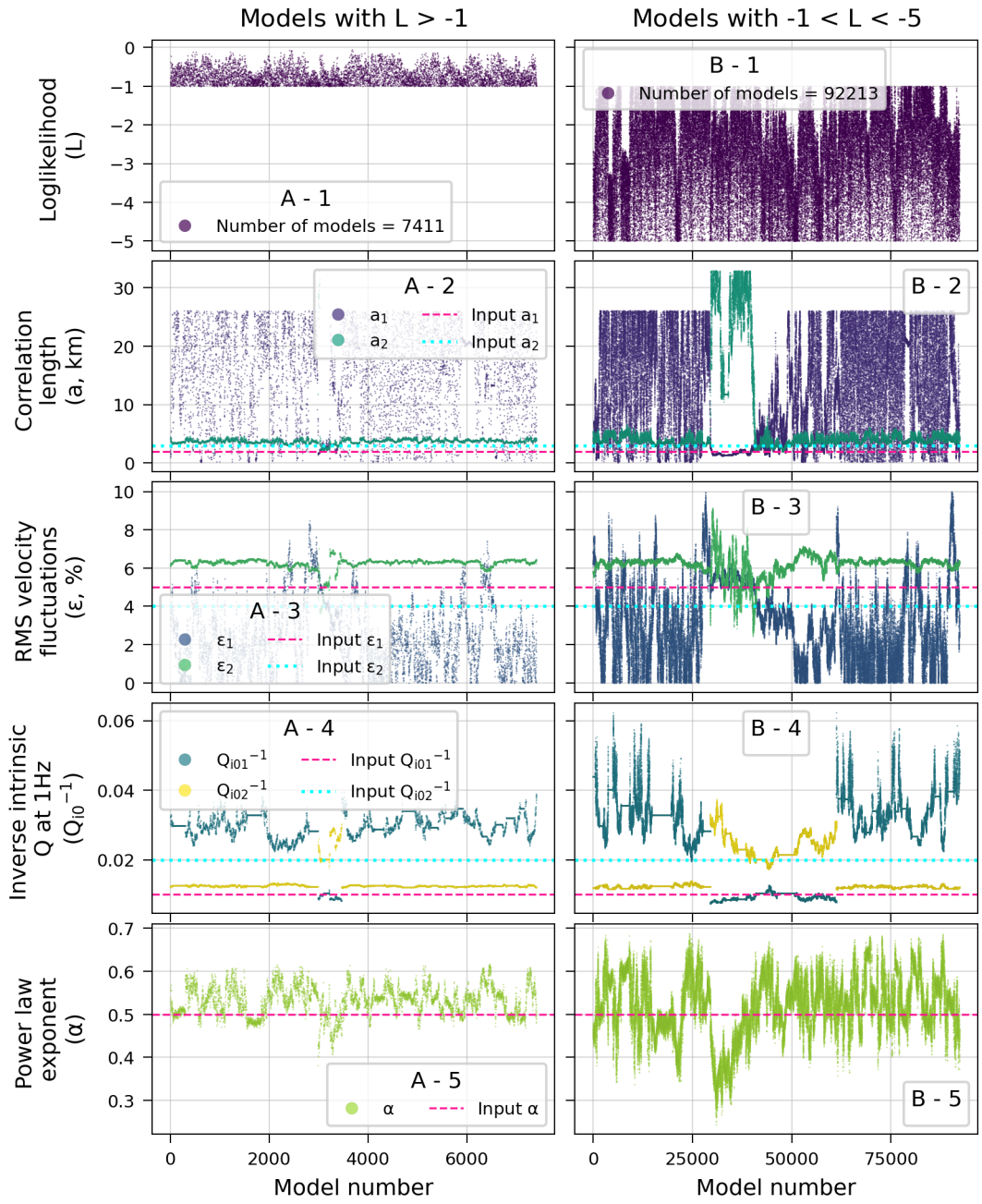

Figure A65: Same as Fig. A60 but for synthetic model 12 from Table 4.1.

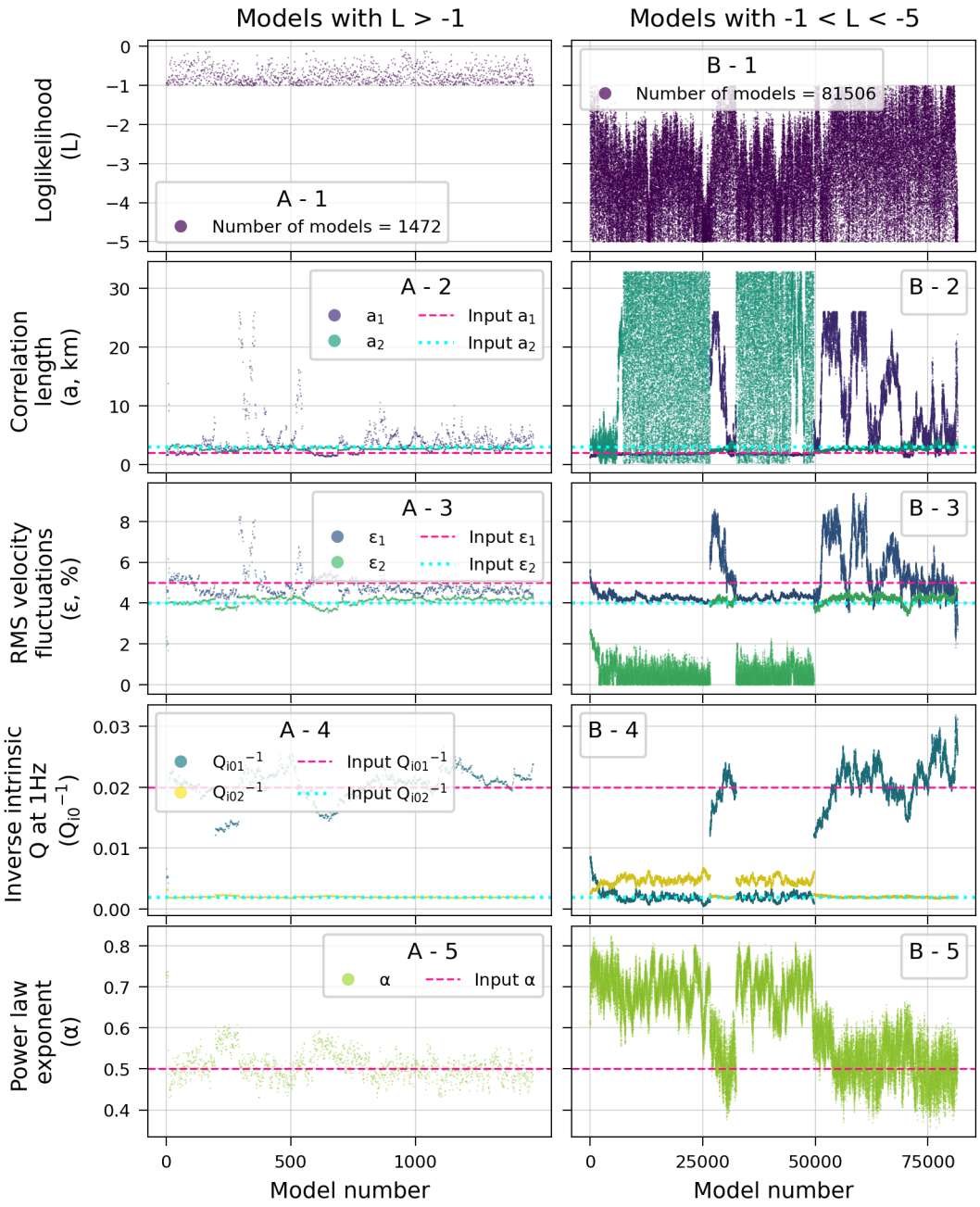

Figure A66: Same as Fig. A60 but for synthetic model 13 from Table 4.1.

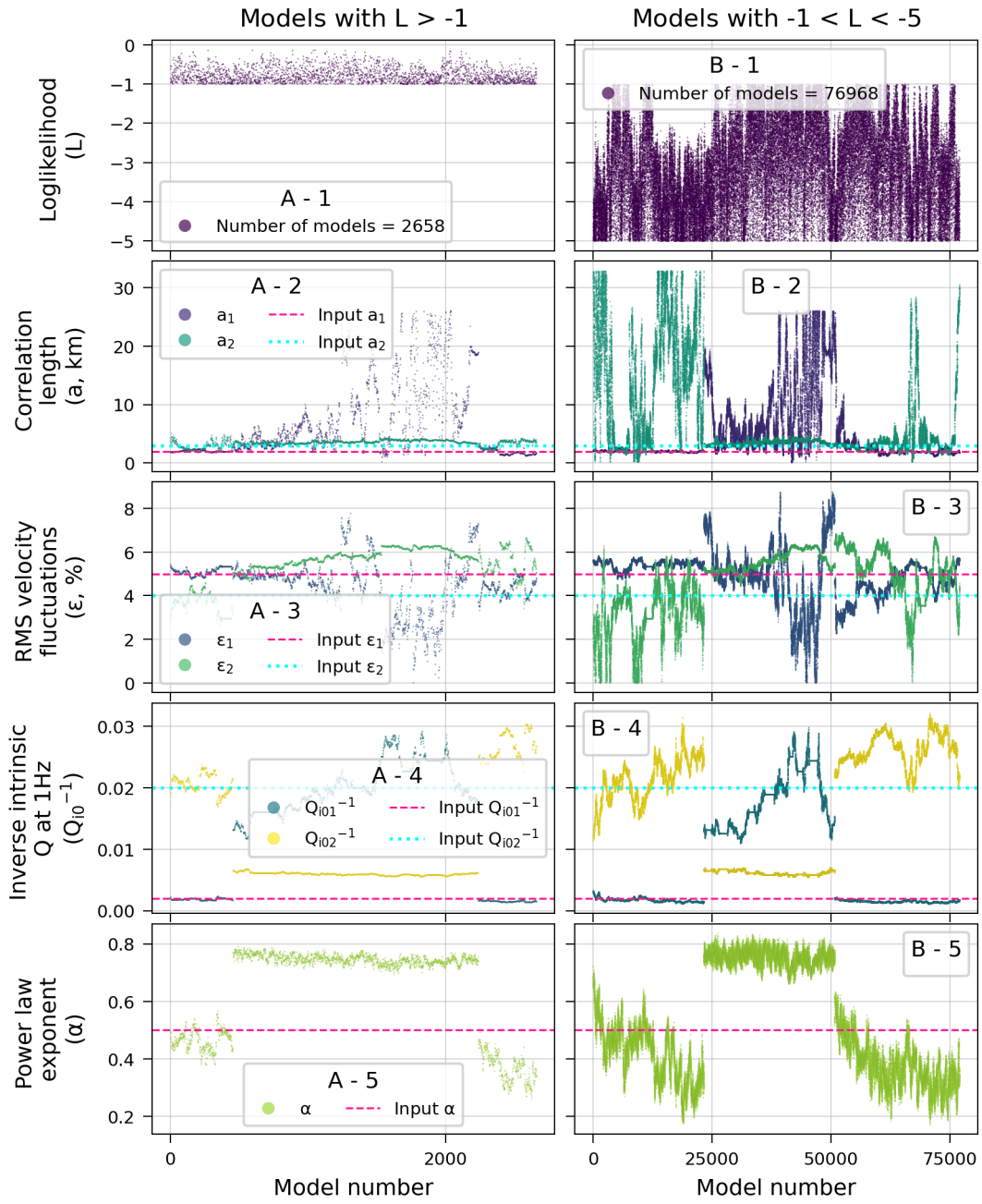

Figure A67: Same as Fig. A60 but for synthetic model 14 from Table 4.1.

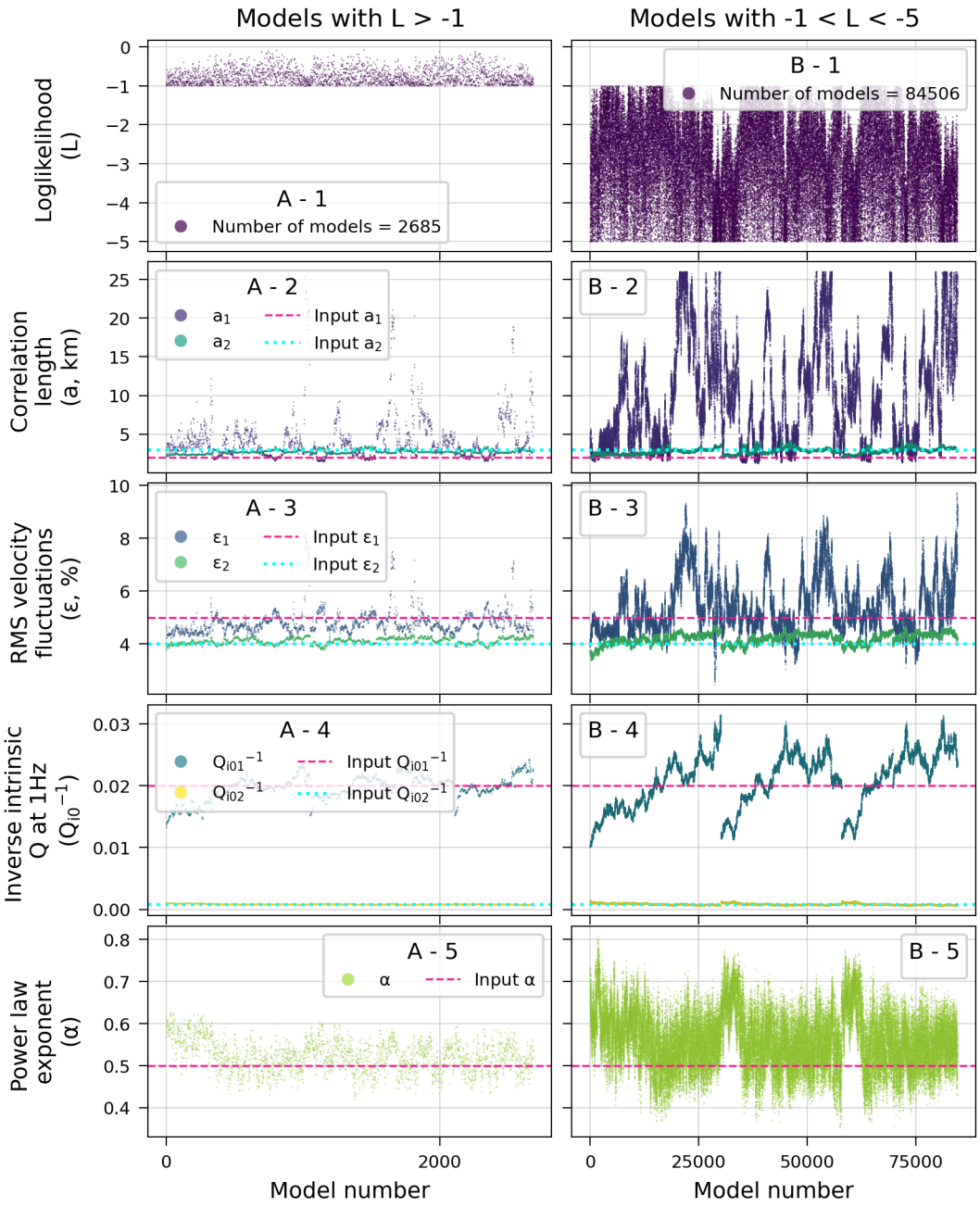

Figure A68: Same as Fig. A60 but for synthetic model 15 from Table 4.1.

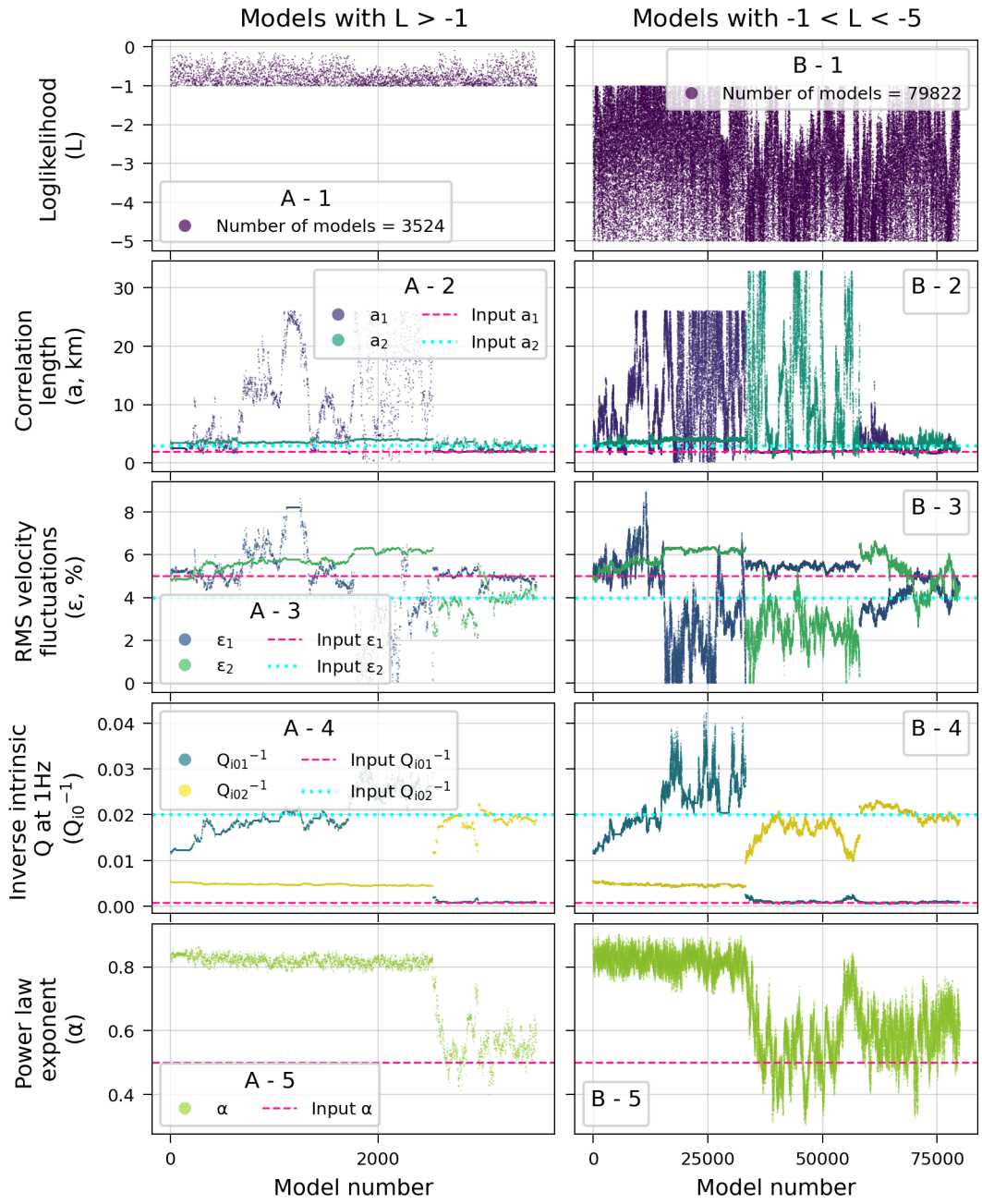

Figure A69: Same as Fig. A60 but for synthetic model 16 from Table 4.1.

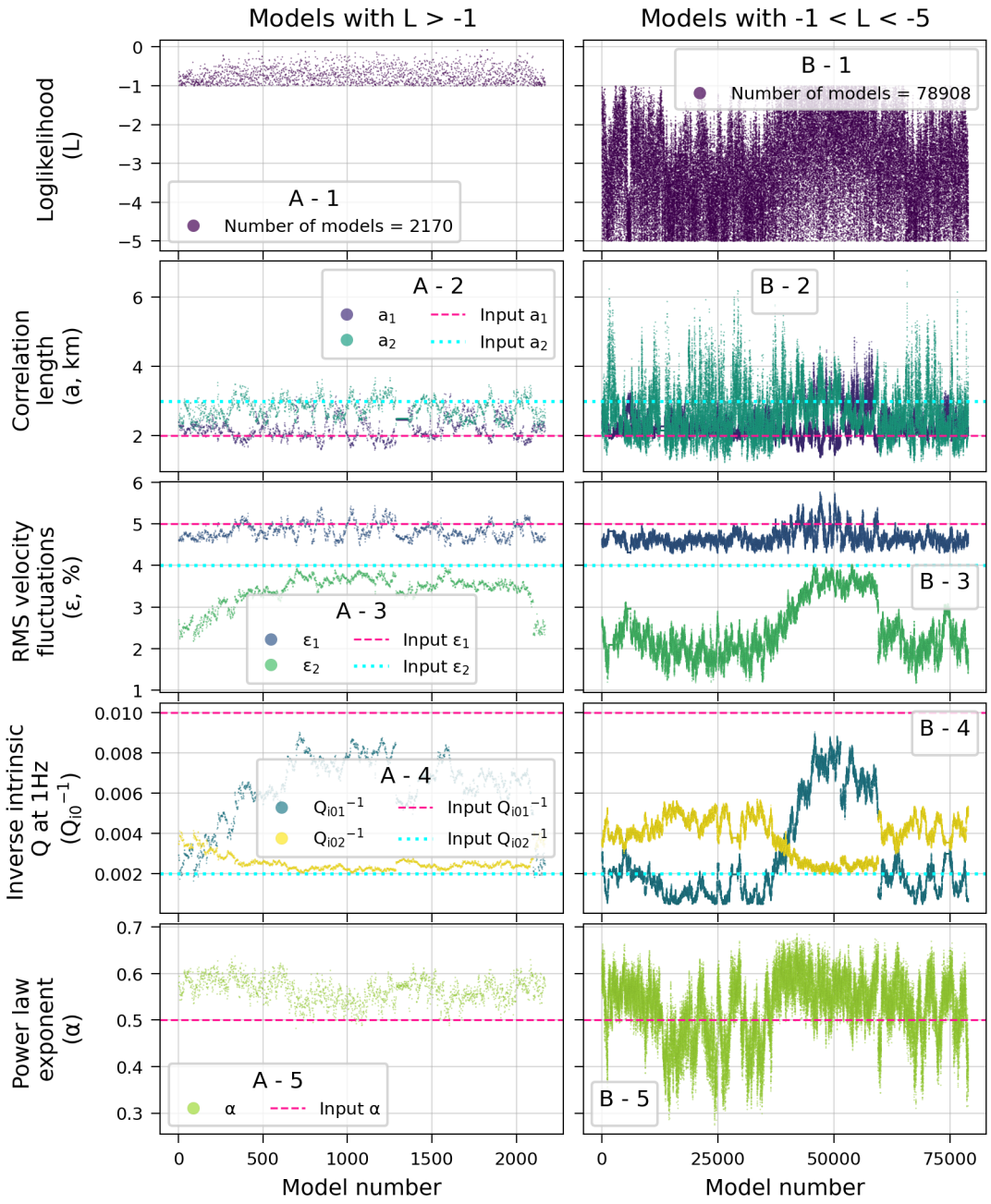

Figure A70: Same as Fig. A60 but for synthetic model 17 from Table 4.1.

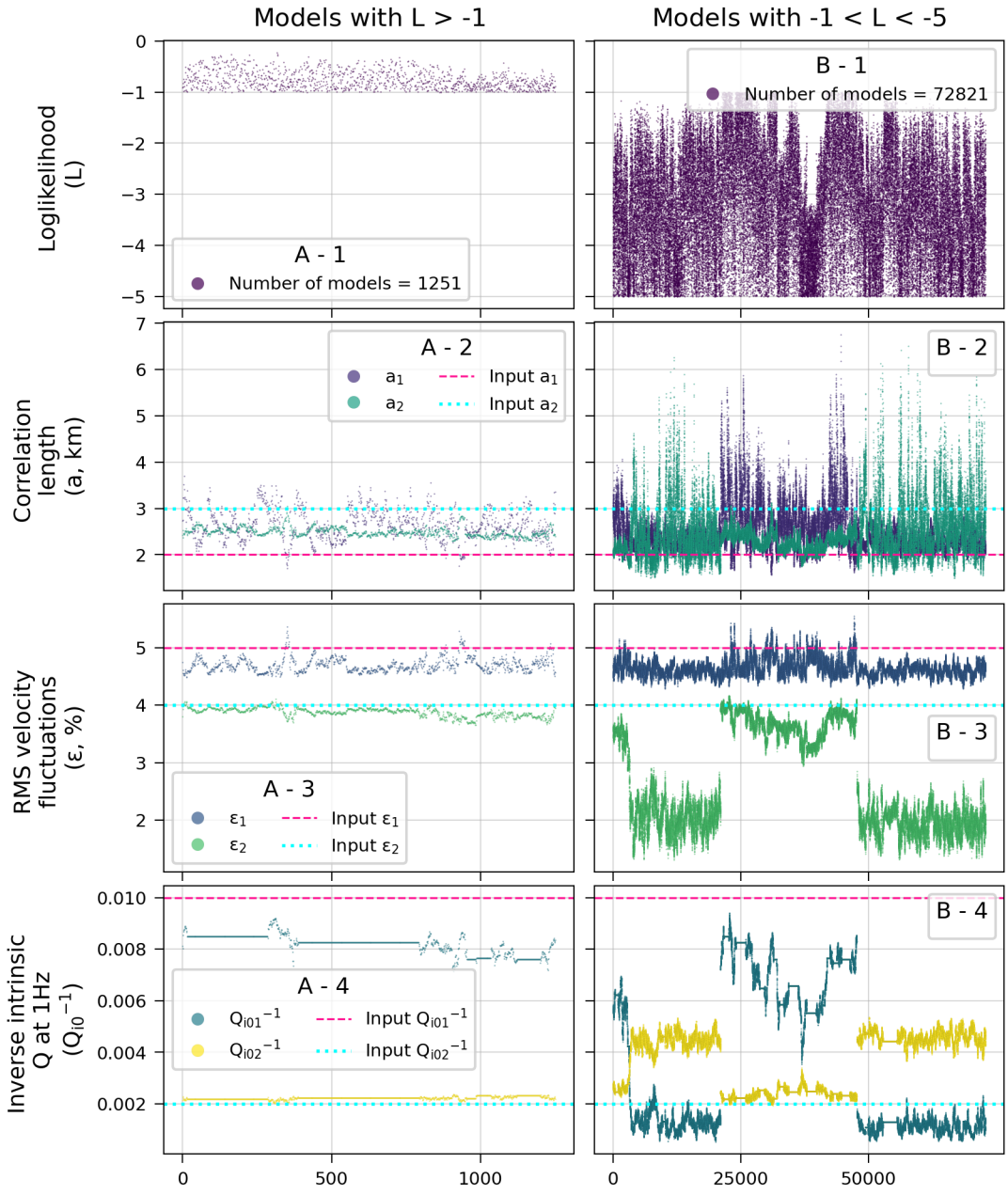

Figure A71: Same as Fig. A60 but for synthetic model 17* from Table 4.1.

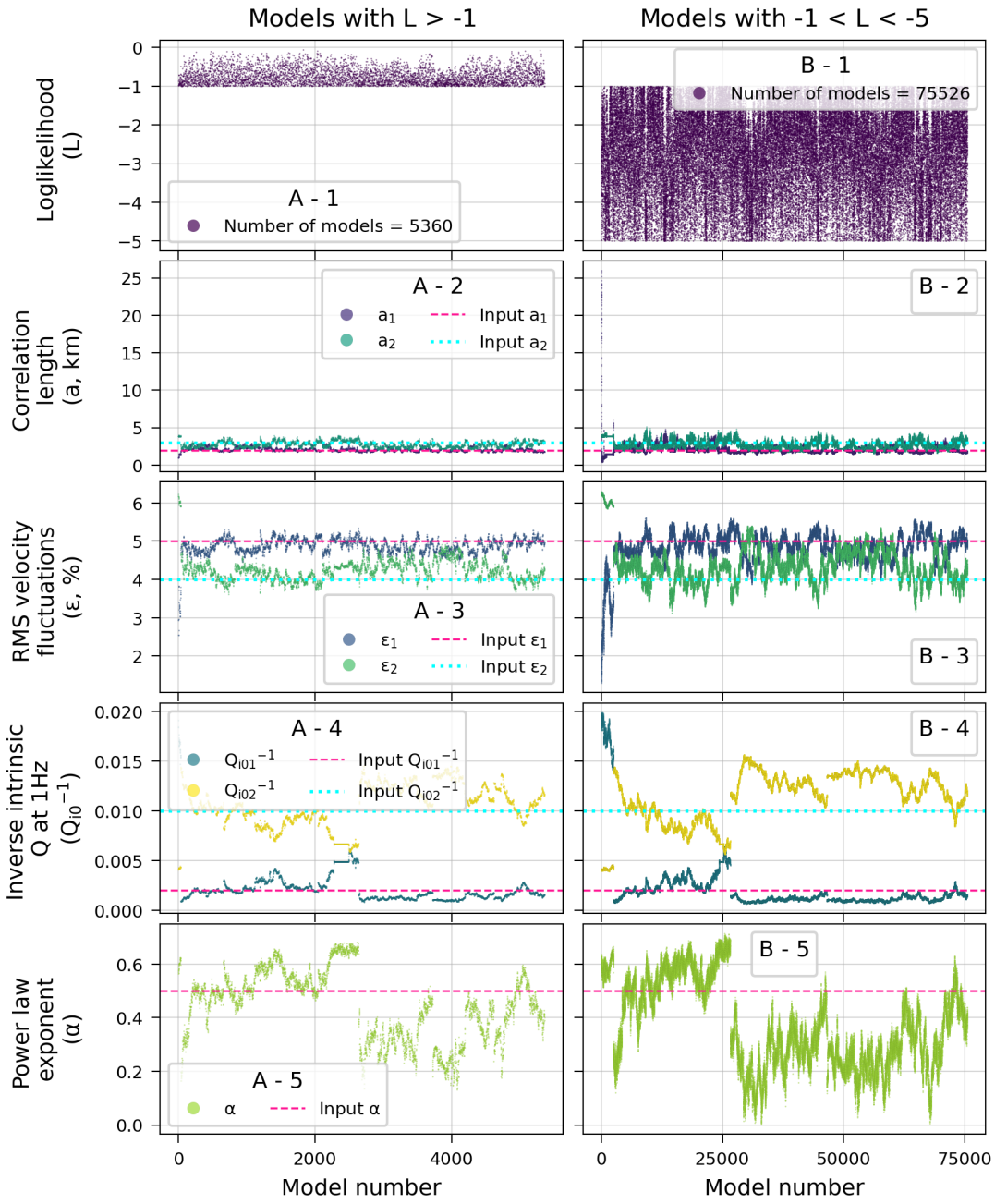

Figure A72: Same as Fig. A60 but for synthetic model 18 from Table 4.1.

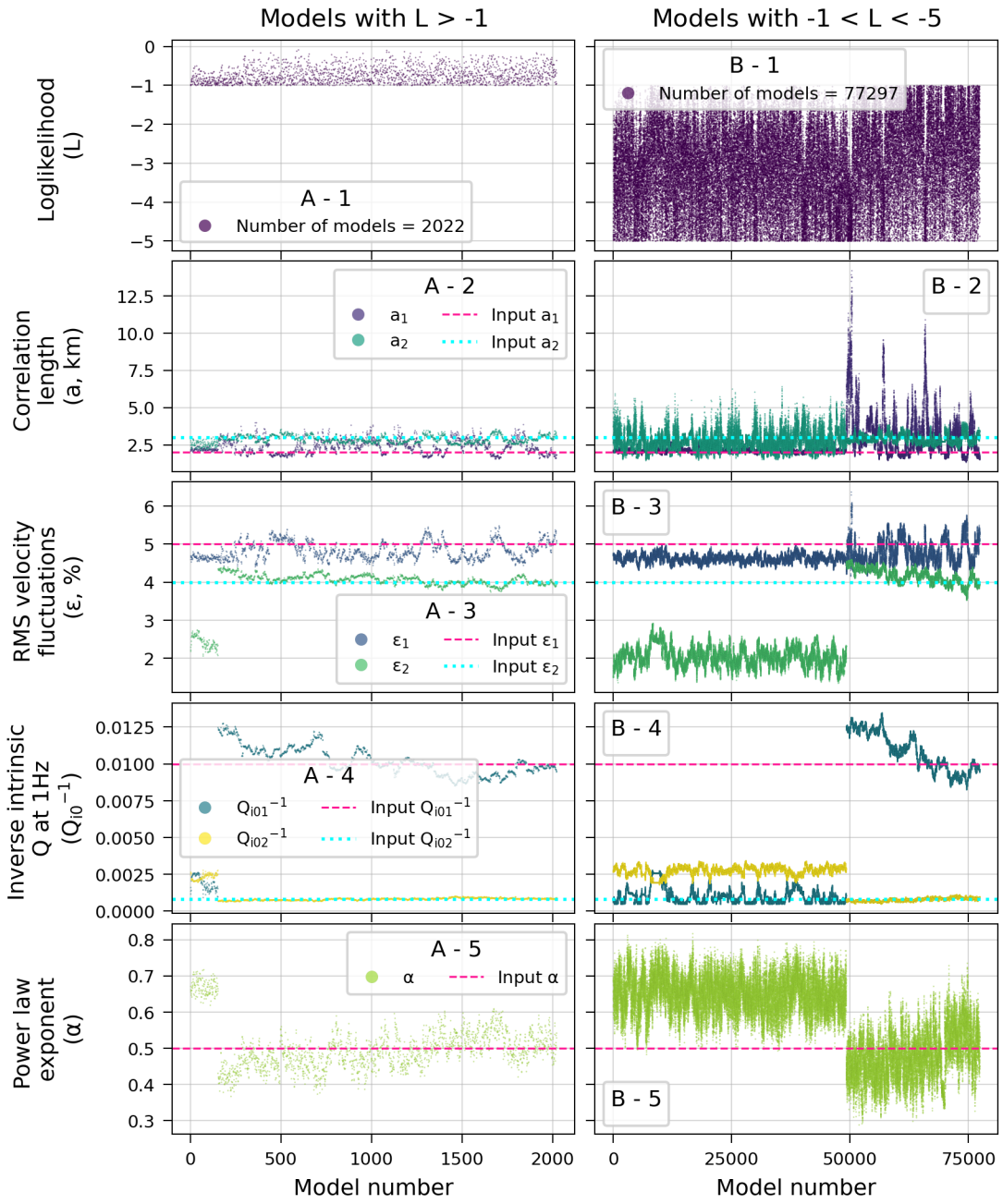

Figure A73: Same as Fig. A60 but for synthetic model 19 from Table 4.1.

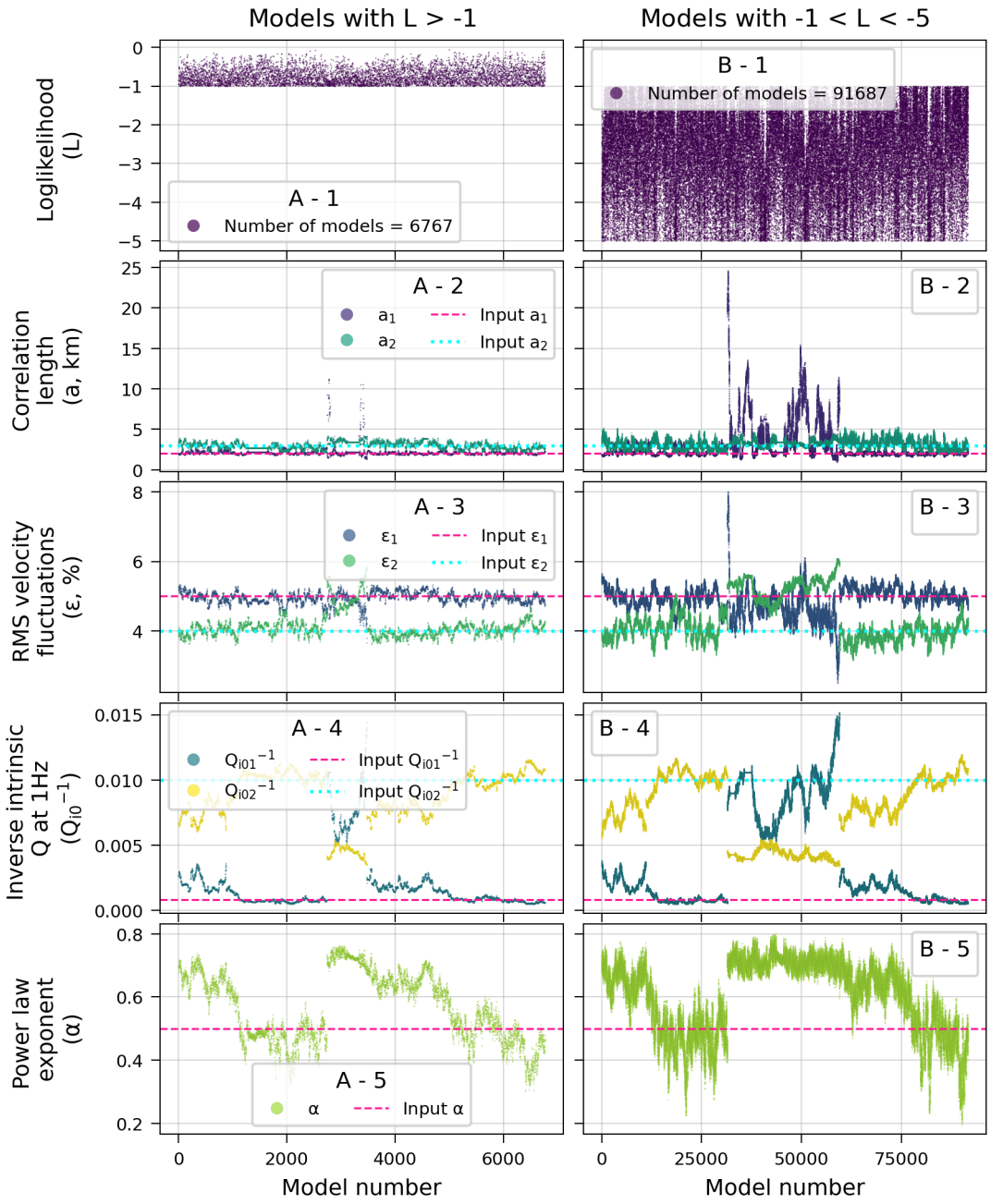

Figure A74: Same as Fig. A60 but for synthetic model 20 from Table 4.1.

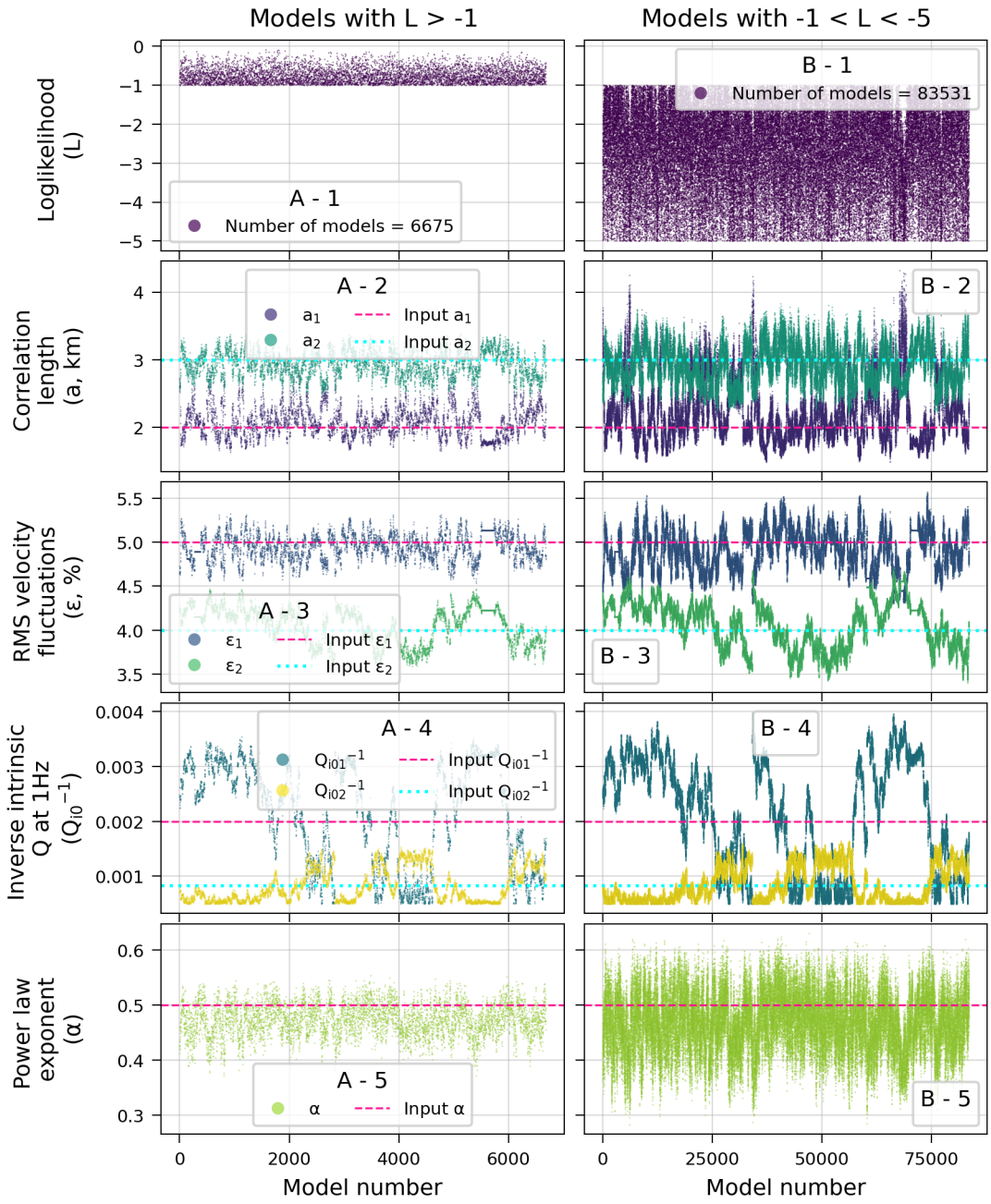

Figure A75: Same as Fig. A60 but for synthetic model 21 from Table 4.1.

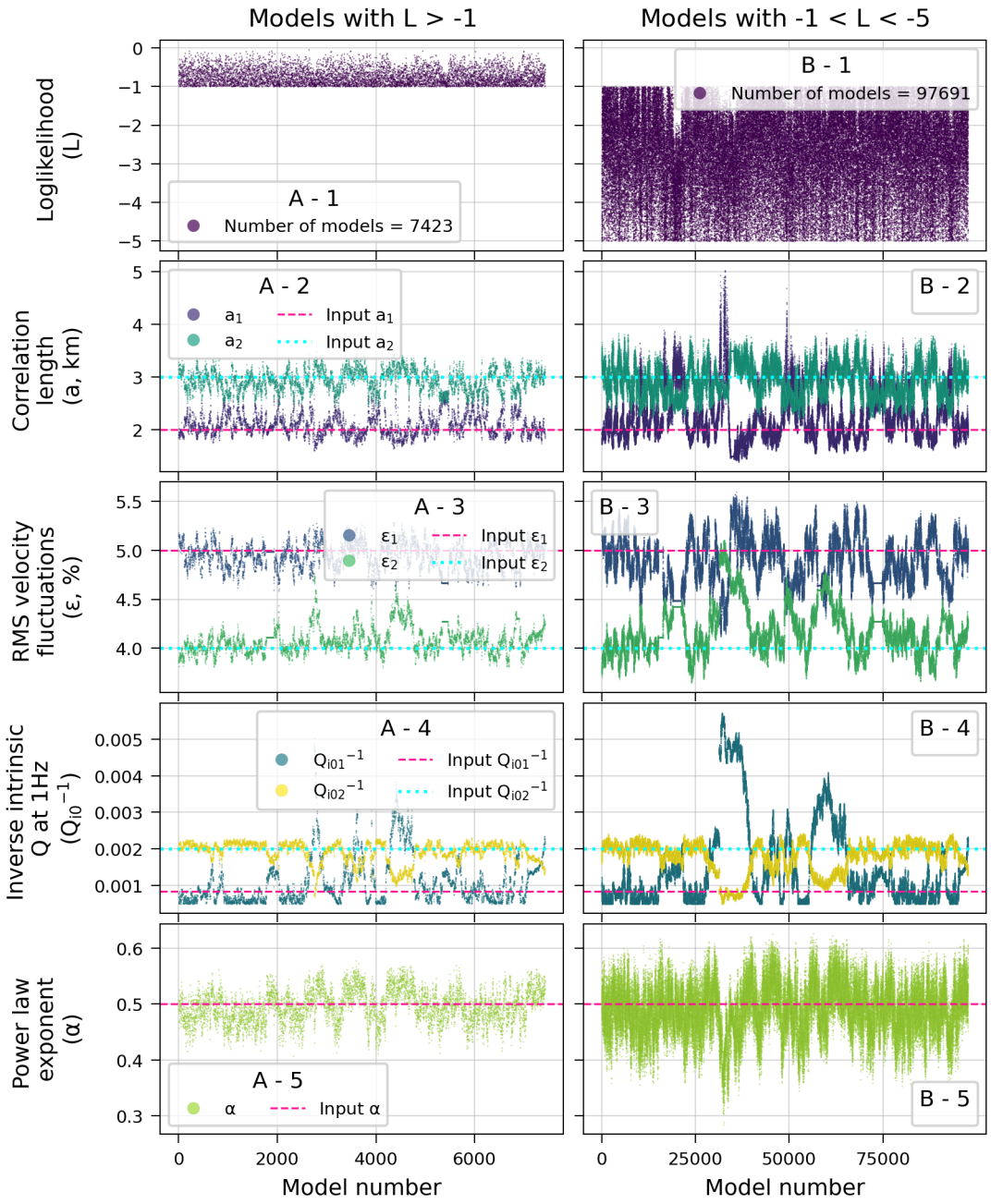

Figure A76: Same as Fig. A60 but for synthetic model 22 from Table 4.1.

A.3.4 E-EFMD solutions non-uniqueness

The results of my synthetic tests (Section 4.1.2) illustrate the extreme non-uniqueness of the Bayesian E-EFMD inversion solutions. To further demonstrate this point, I computed the synthetic envelopes for an extra set of models which represent a variety of scattering and attenuation scenarios but produce essentially identical coda envelopes throughout the entire frequency range of interest. Fig. 4.14, on Section 4.1.2, contains the envelpes for these datasets for frequency band D (Table 2.3). This section displays them for the rest of the frequency bands of interest.

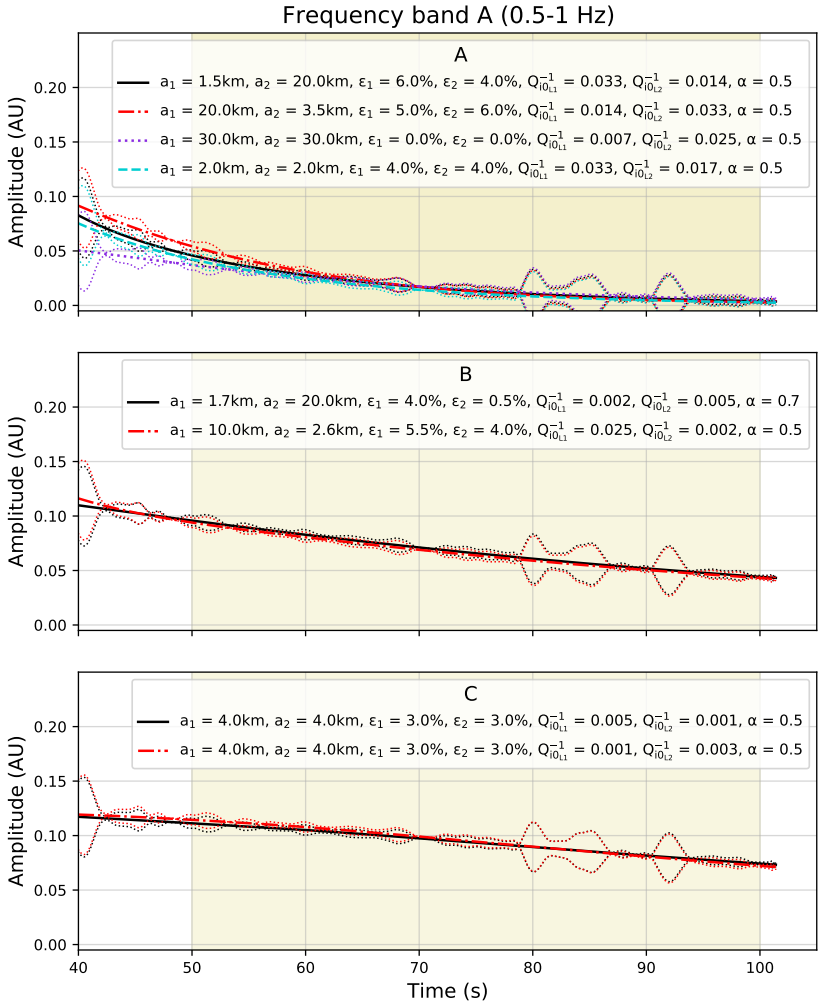

Figure A77: Synthetic envelopes for frequency band A (Table 2.3) and eight synthetic datasets that represent a variety of scattering and intrinsic attenuation scenarios. Models in panel A all have strong to extremely strong intrinsic attenuation ($0.00\overline{6} \leq Q_{i0}^{-1} \leq 0.02$) in the crust and/or lithospheric mantle and varying scattering strengths within each layer. Datasets in panel B represent models with strong contrasts in scattering between the two layers and weaker variations in anelasticity. Envelopes in panel C result from models with the same heterogeneity structure and sharp contrasts in intrinsic attenuation between the model layers. Shaded areas in all plots represent the time window used for the fit in the E-EFMD, and dotted lines the uncertainty associated to each synthetic envelope used in the inversion algoritm.

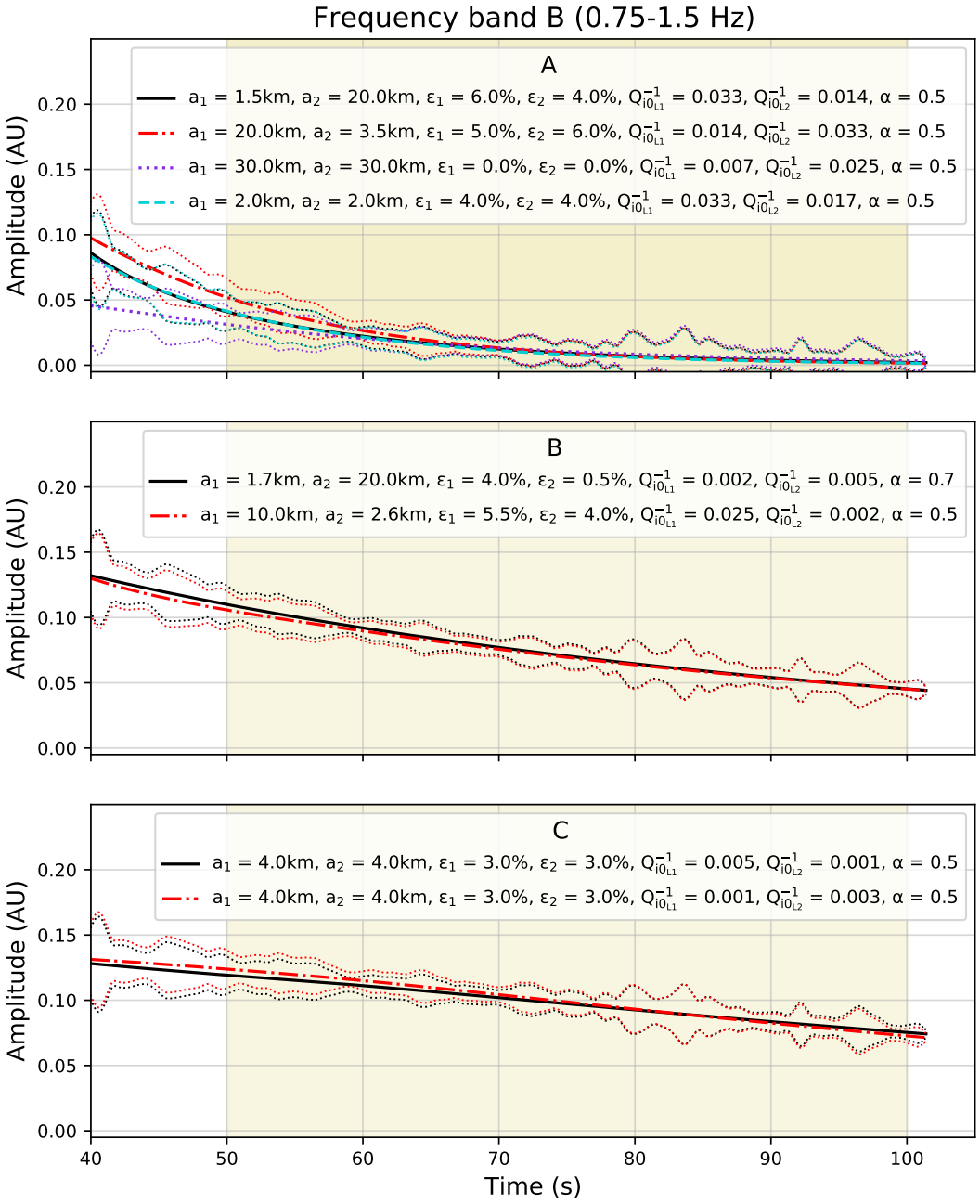

Figure A78: Same as Fig. A77 but for frequency band B from Table 2.3.

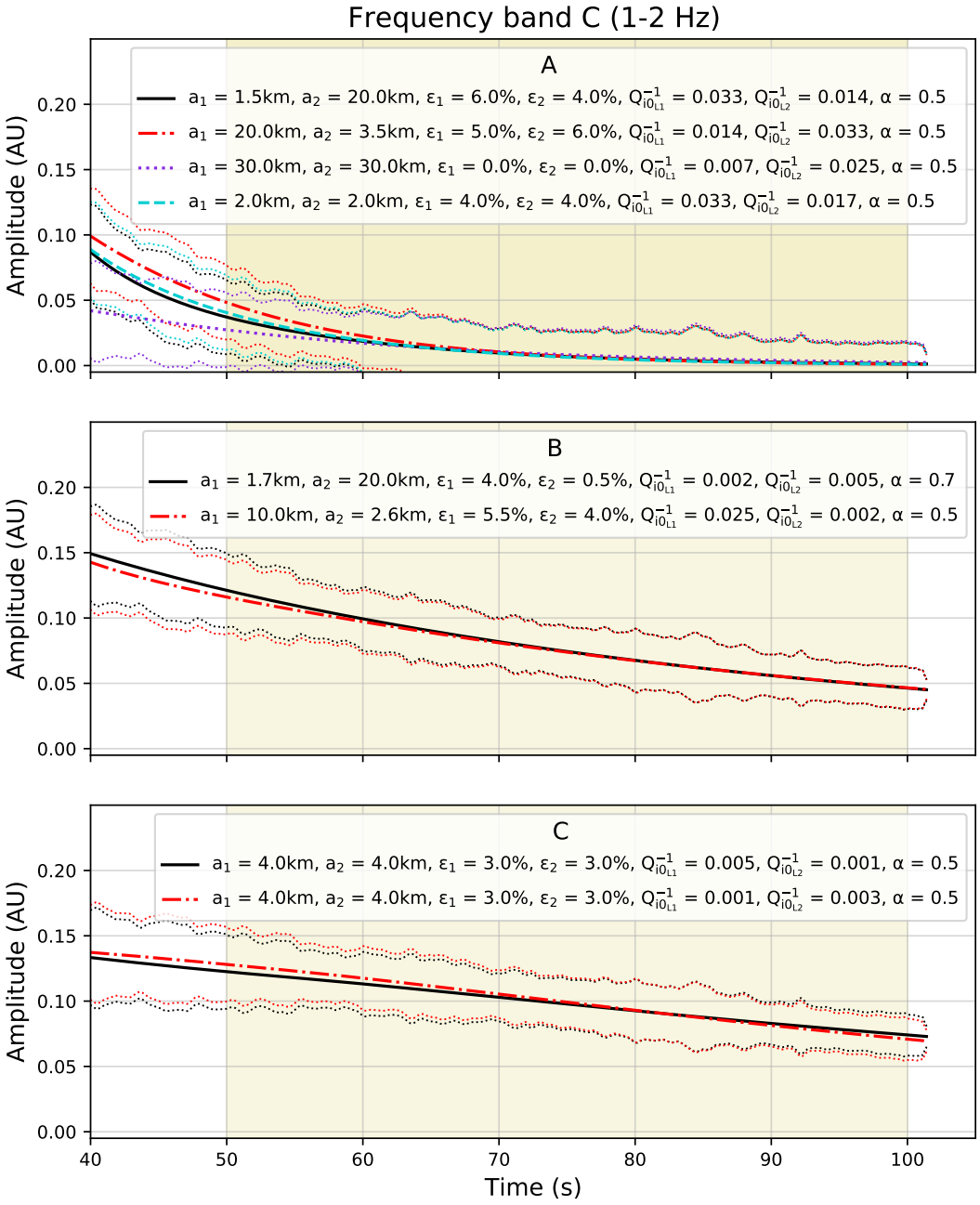

Figure A79: Same as Fig. A77 but for frequency band C from Table 2.3.

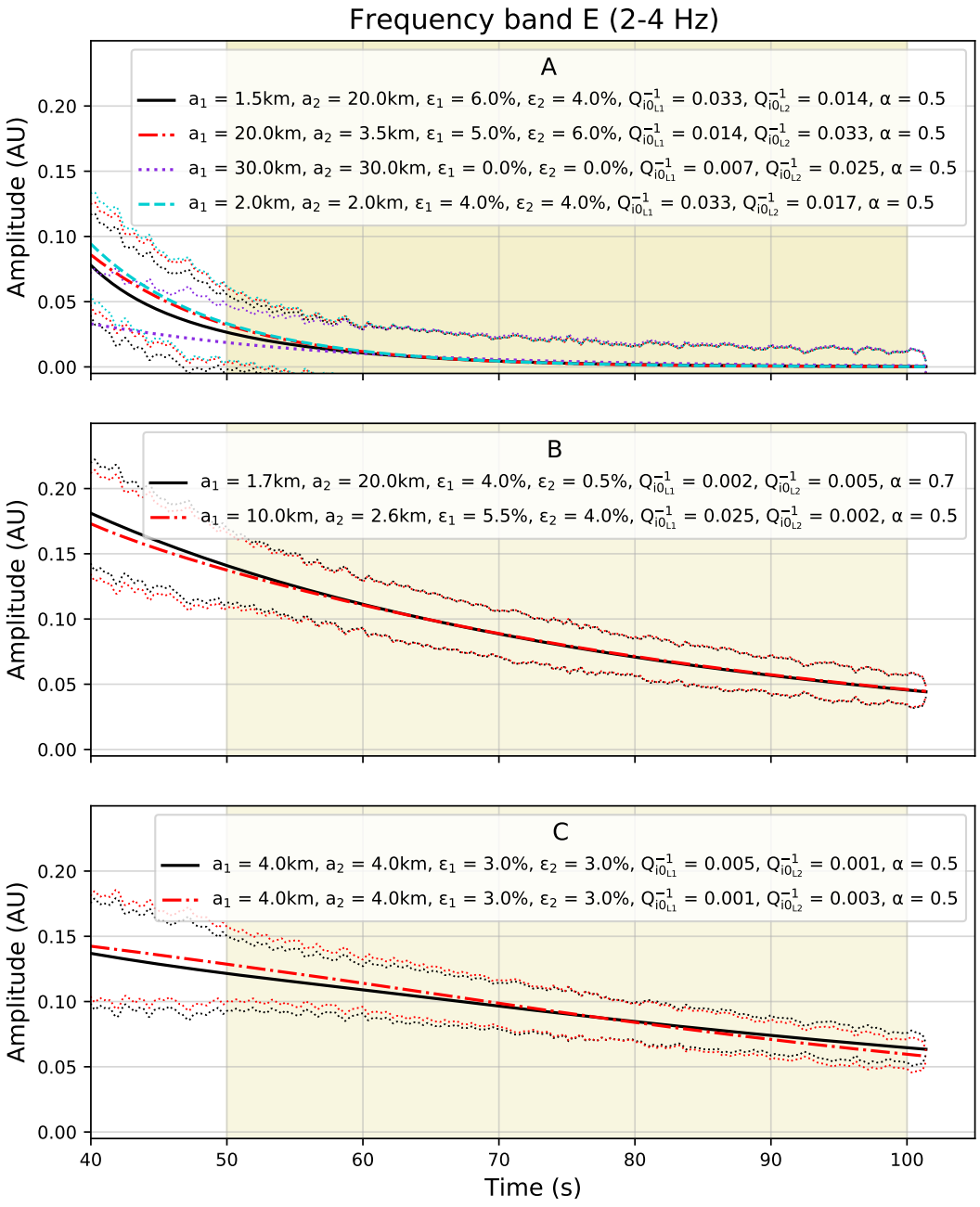

Figure A80: Same as Fig. A77 but for frequency band E from Table 2.3.

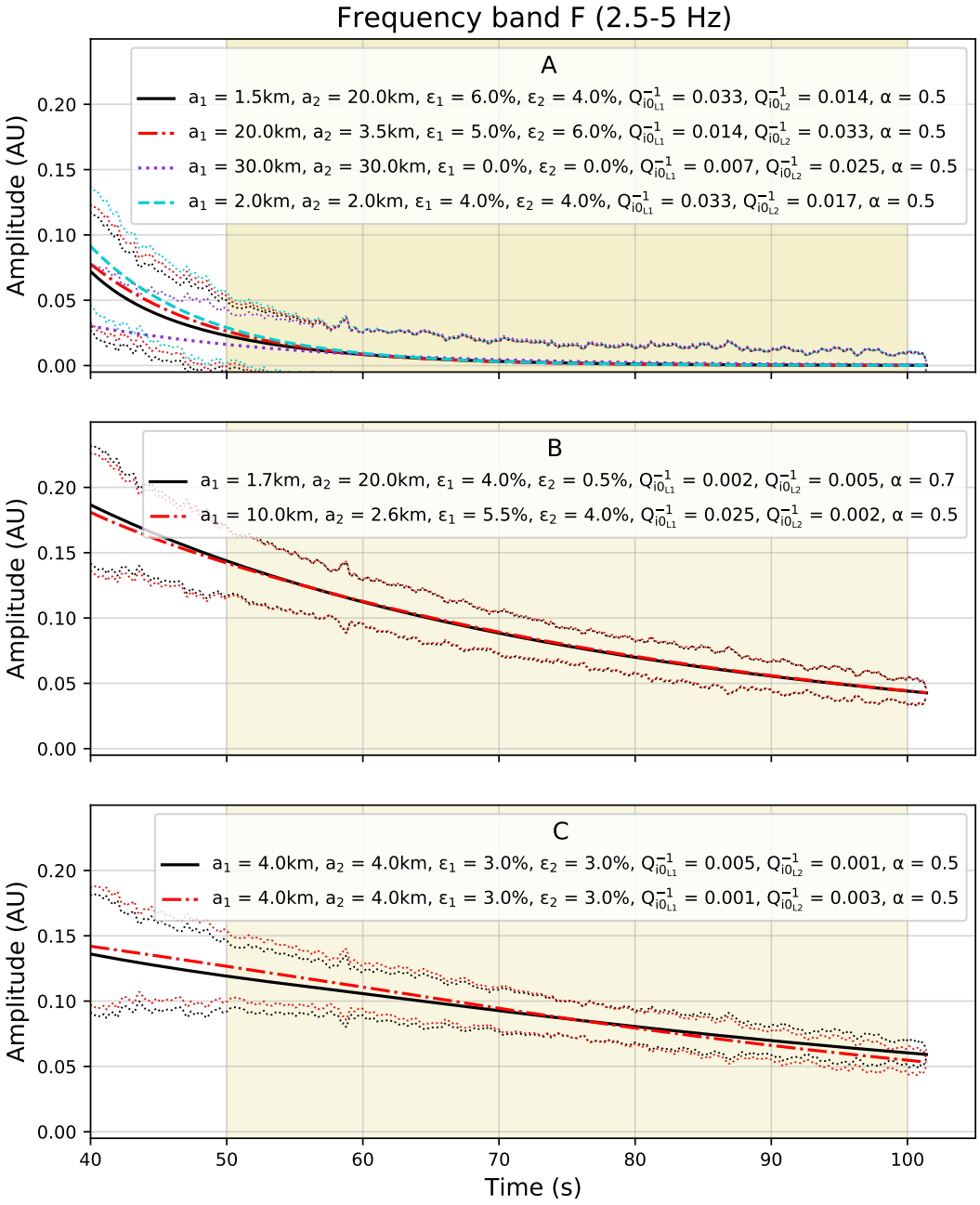

Figure A81: Same as Fig. A77 but for frequency band F from Table 2.3.

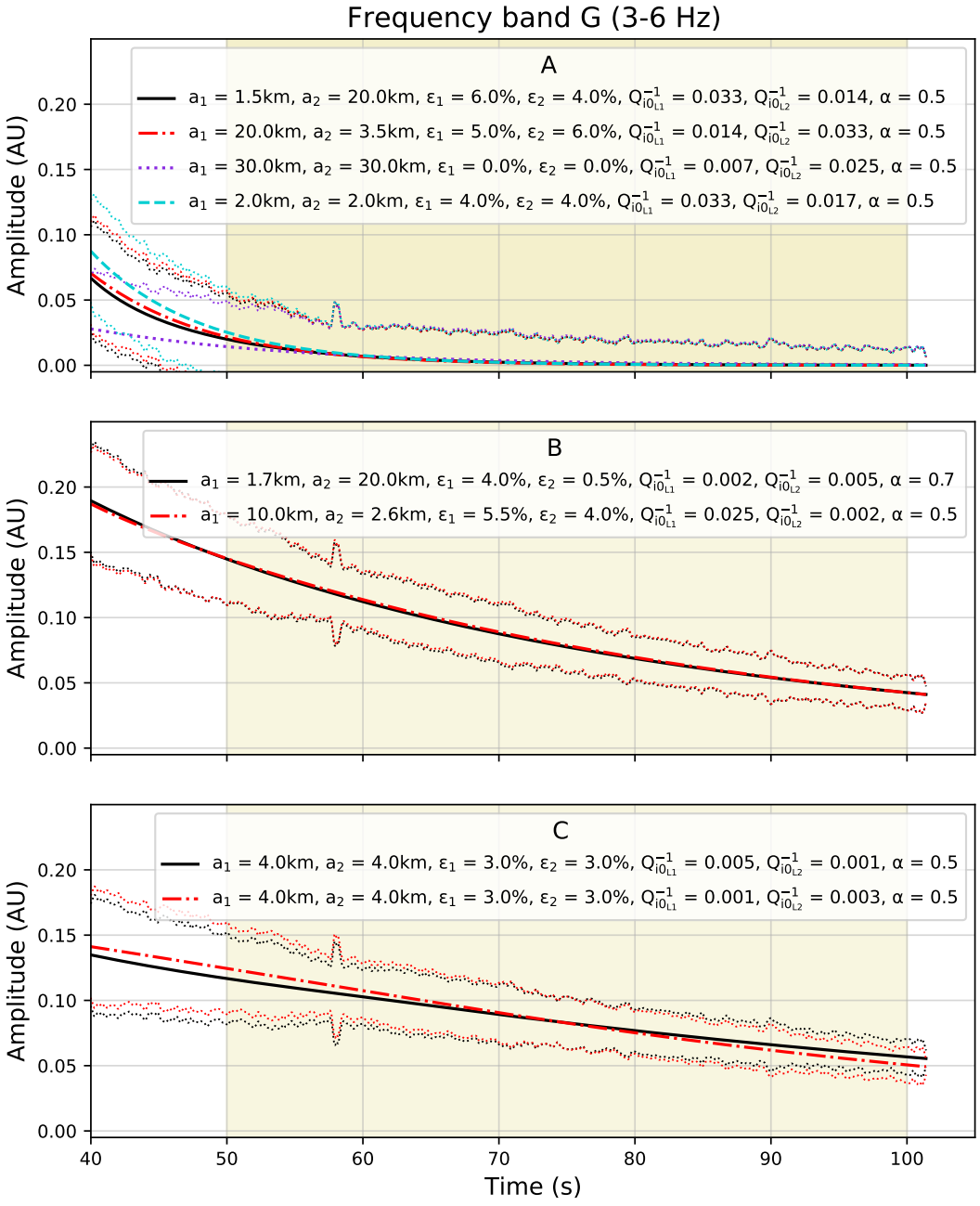

Figure A82: Same as Fig. A77 but for frequency band G from Table 2.3.

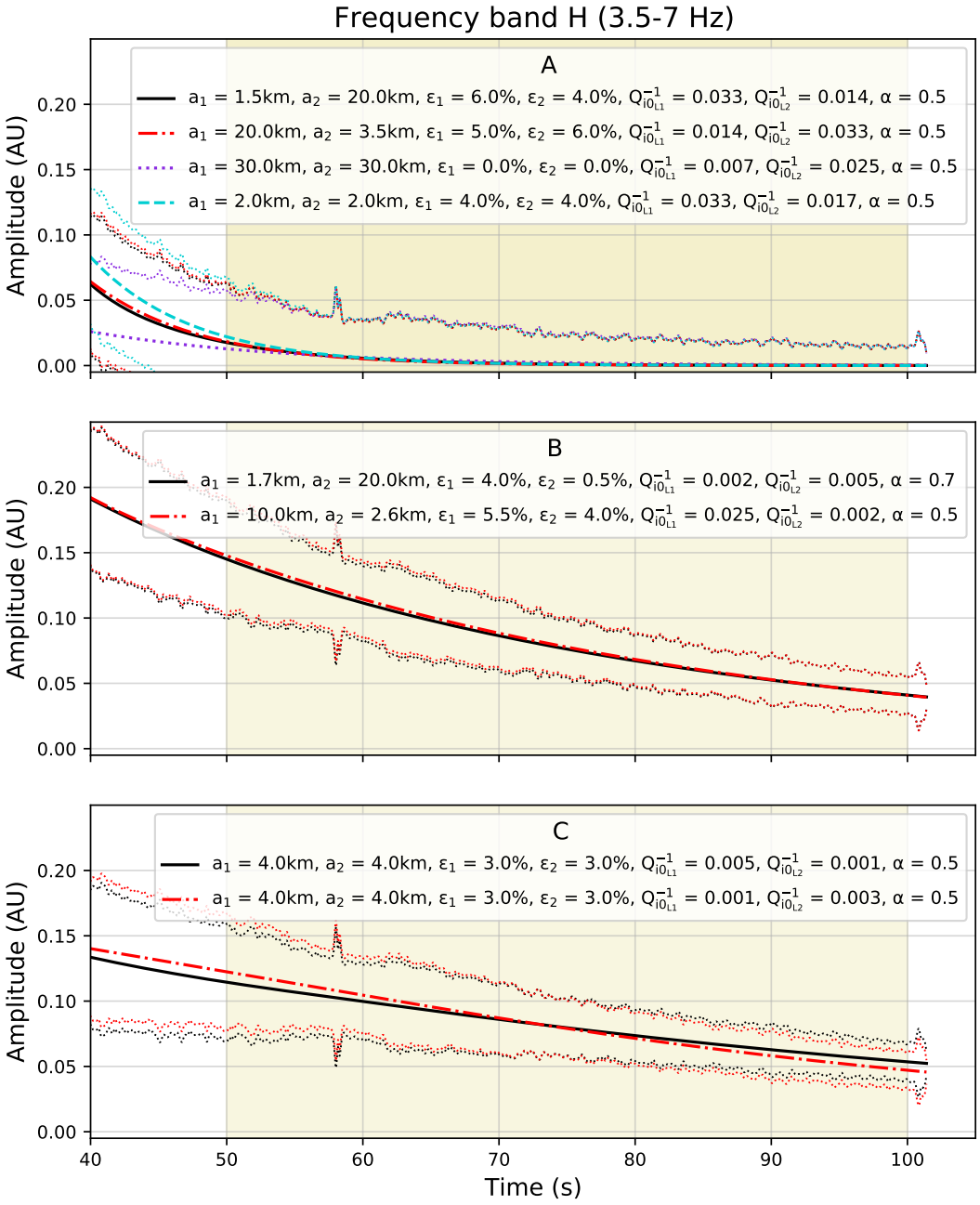

Figure A83: Same as Fig. A77 but for frequency band H from Table 2.3.

A.4 E-EFMD AU inversions complementary results

Table 4.3 summarises the layering and results of the inversions for the three Australian arrays analysed here (PSA, ASAR and WRA). Figures in this section help support the discussion in Section 4.2.

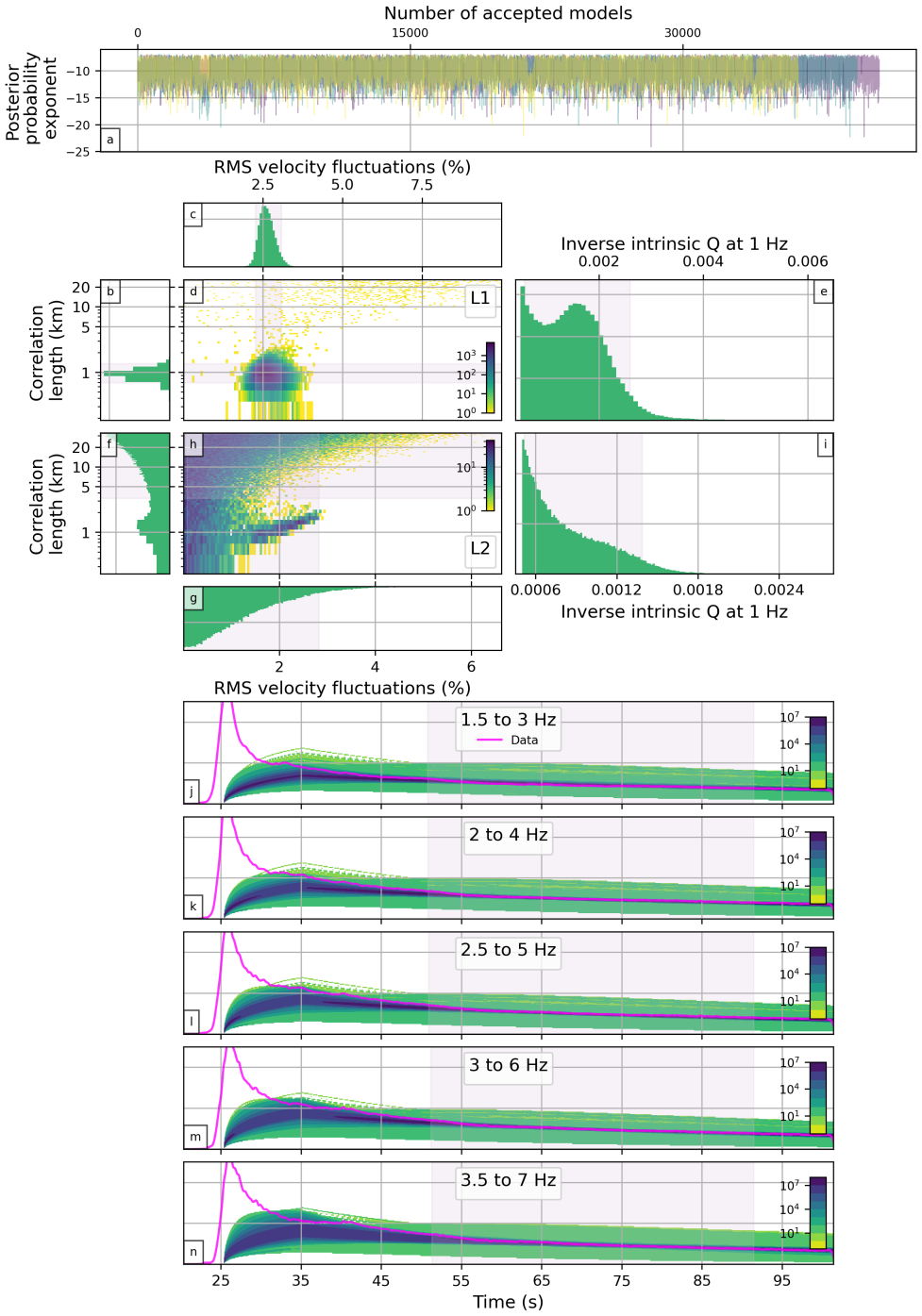

Figure A84: Summary of the results obtained from the alternative E-EFMD algorithm with fixed α for PSA. Panels content is as in Fig. A24.

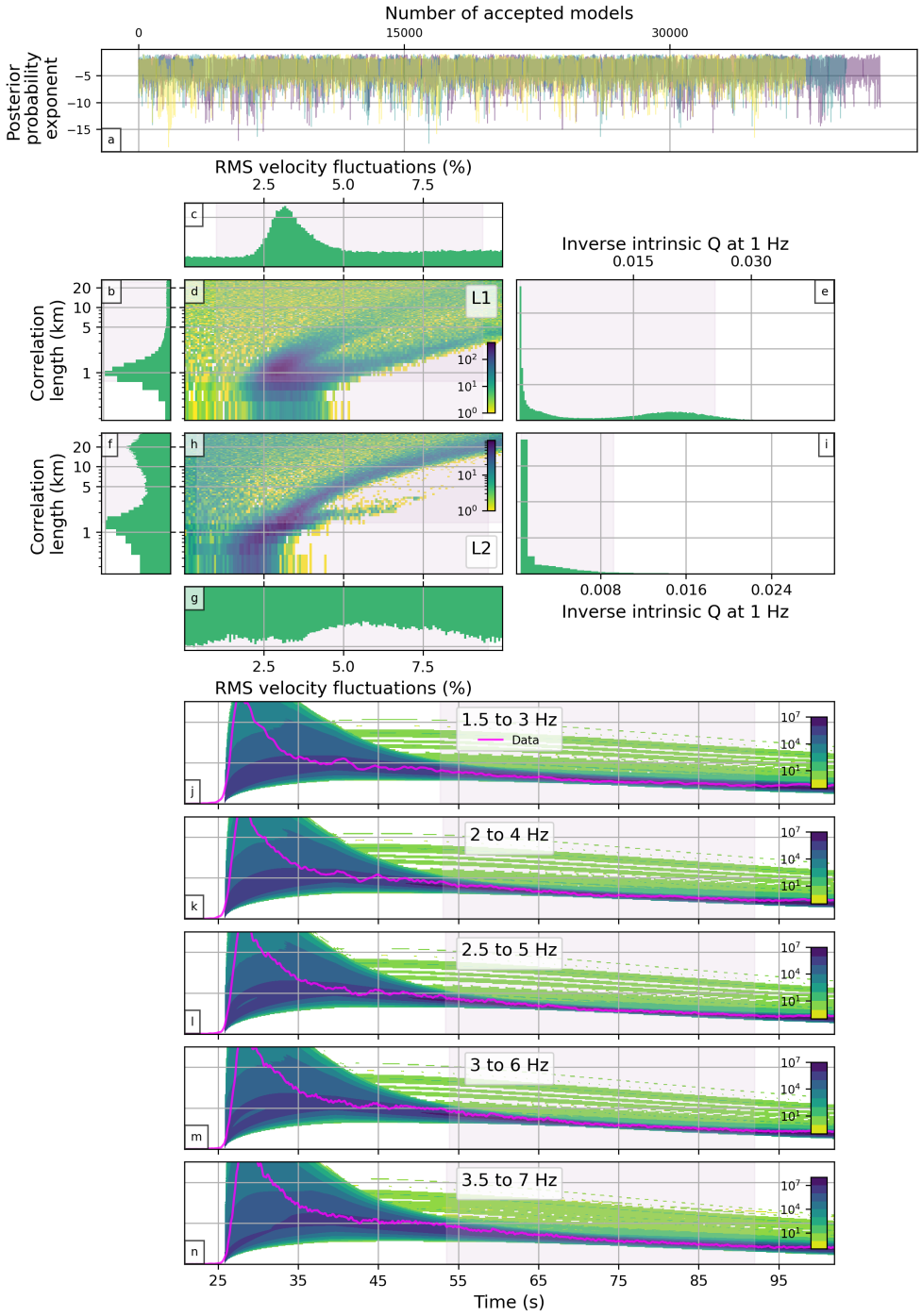

Figure A85: As Fig. A84 but for ASAR.

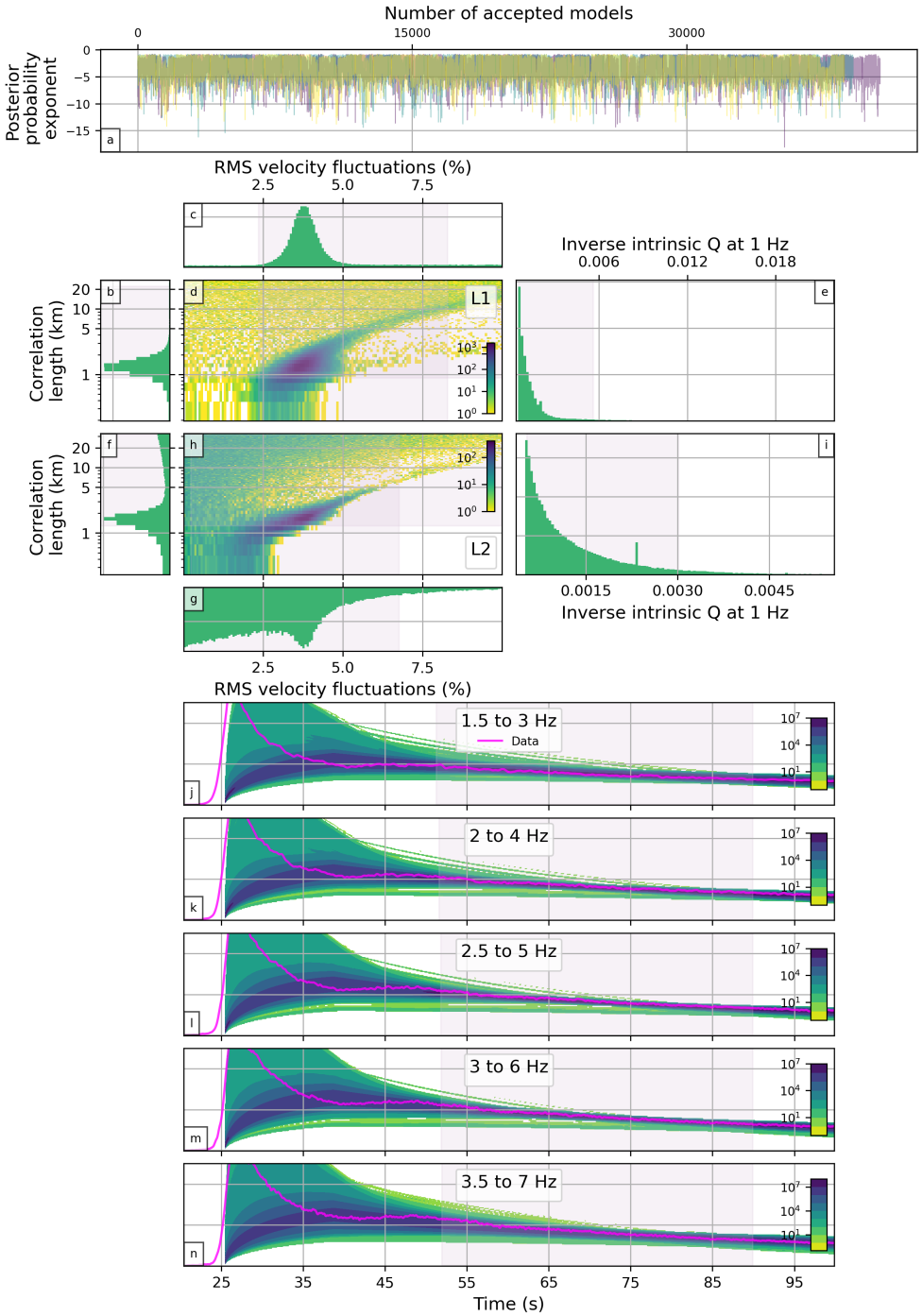

Figure A86: As Fig. A84 but for WRA.

A.5 E-EFMD IMS inversions complementary results

Results in this section from E-EFMD inversions of the data for the IMS stations (ILAR, PDAR, TXAR, YKA and BOSA) are complementary to those shown in Chapter 5.

E-EFMD results summaries for IMS stations

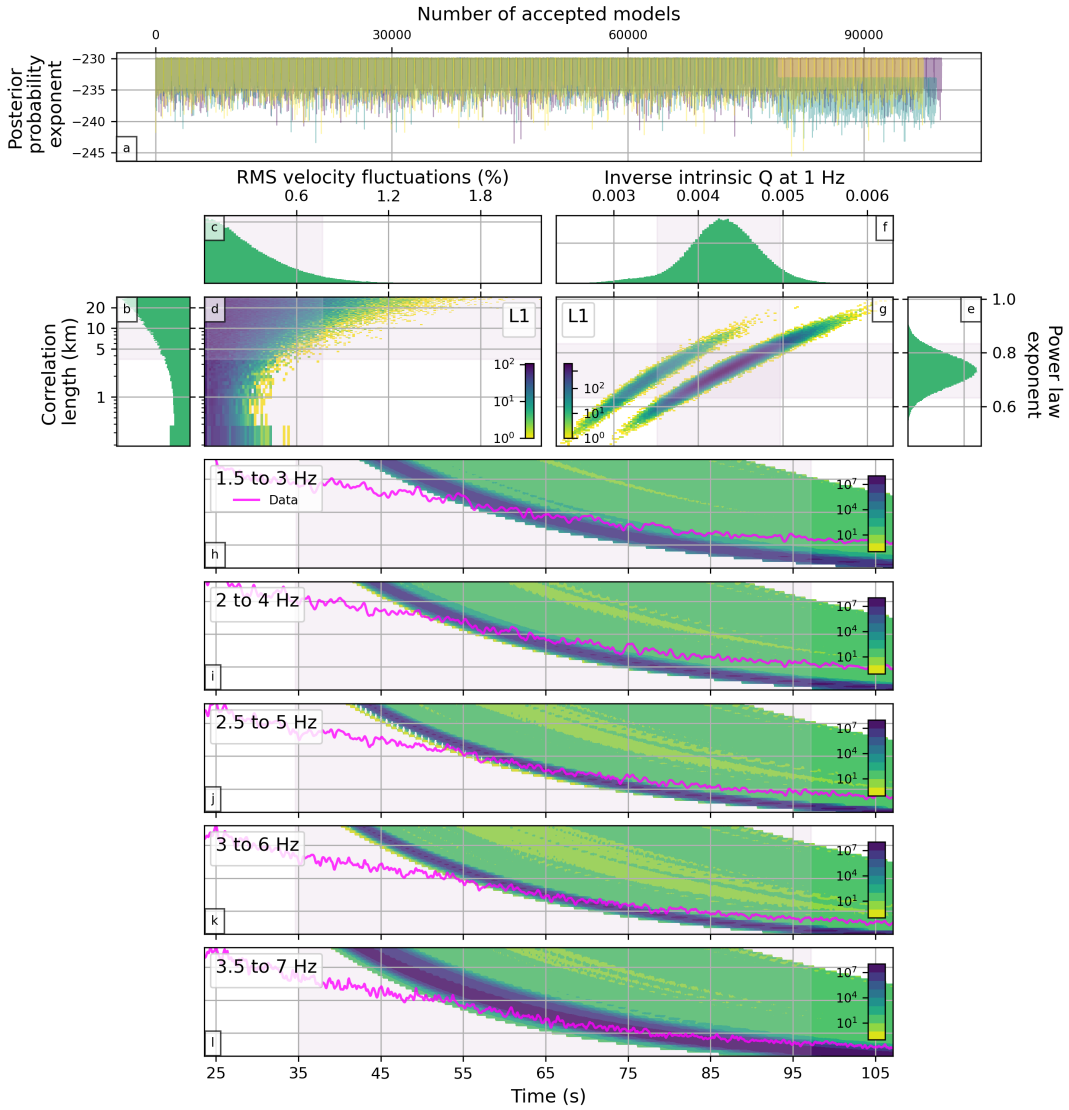

Figure A87: Summary of the results obtained from the E-EFMD algorithm for ILAR and a 1-layer model that encompasses the entire lithosphere. Panels content is as in Fig. A22.

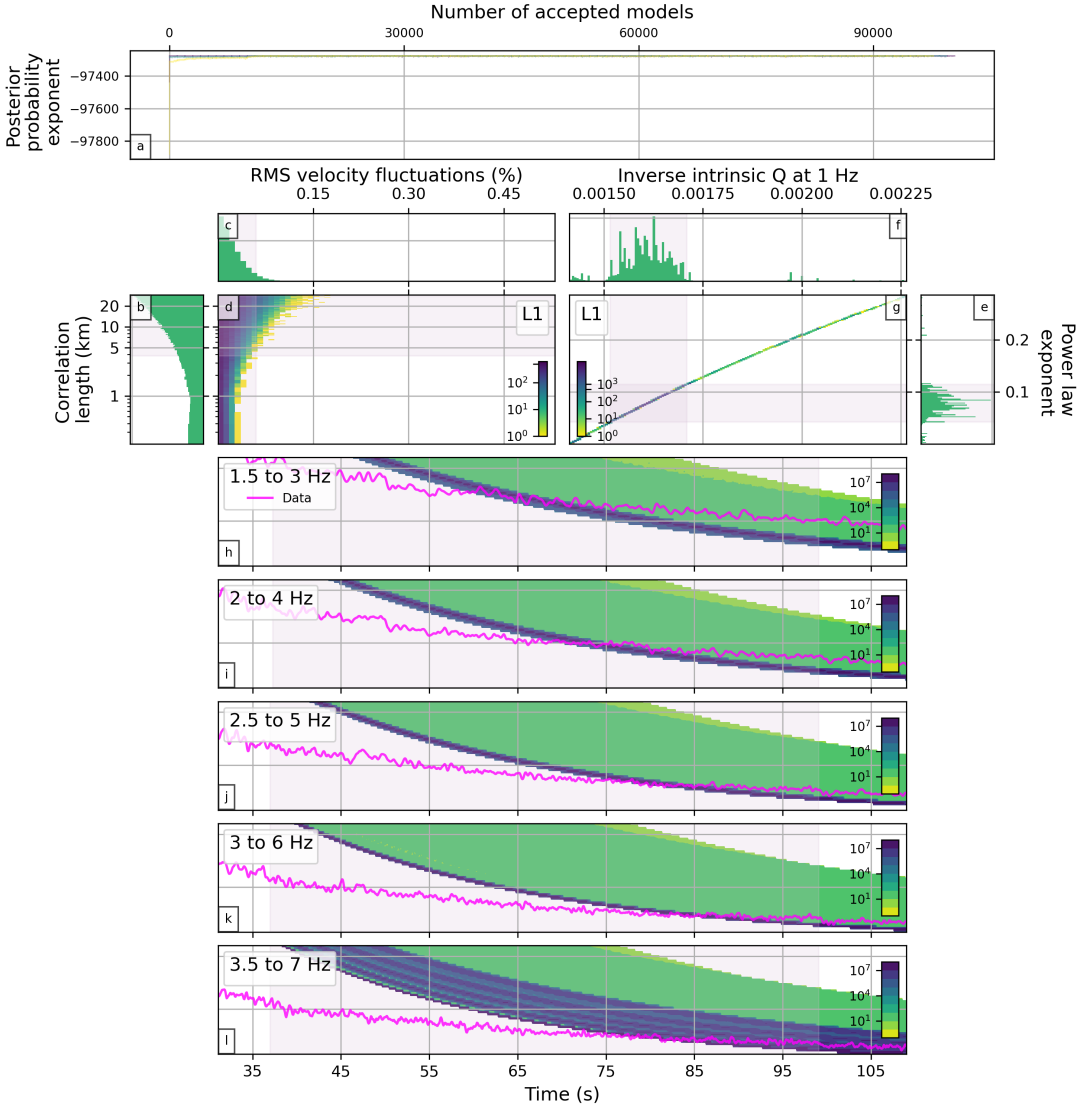

Figure A88: As Fig. A87, but for TXAR.

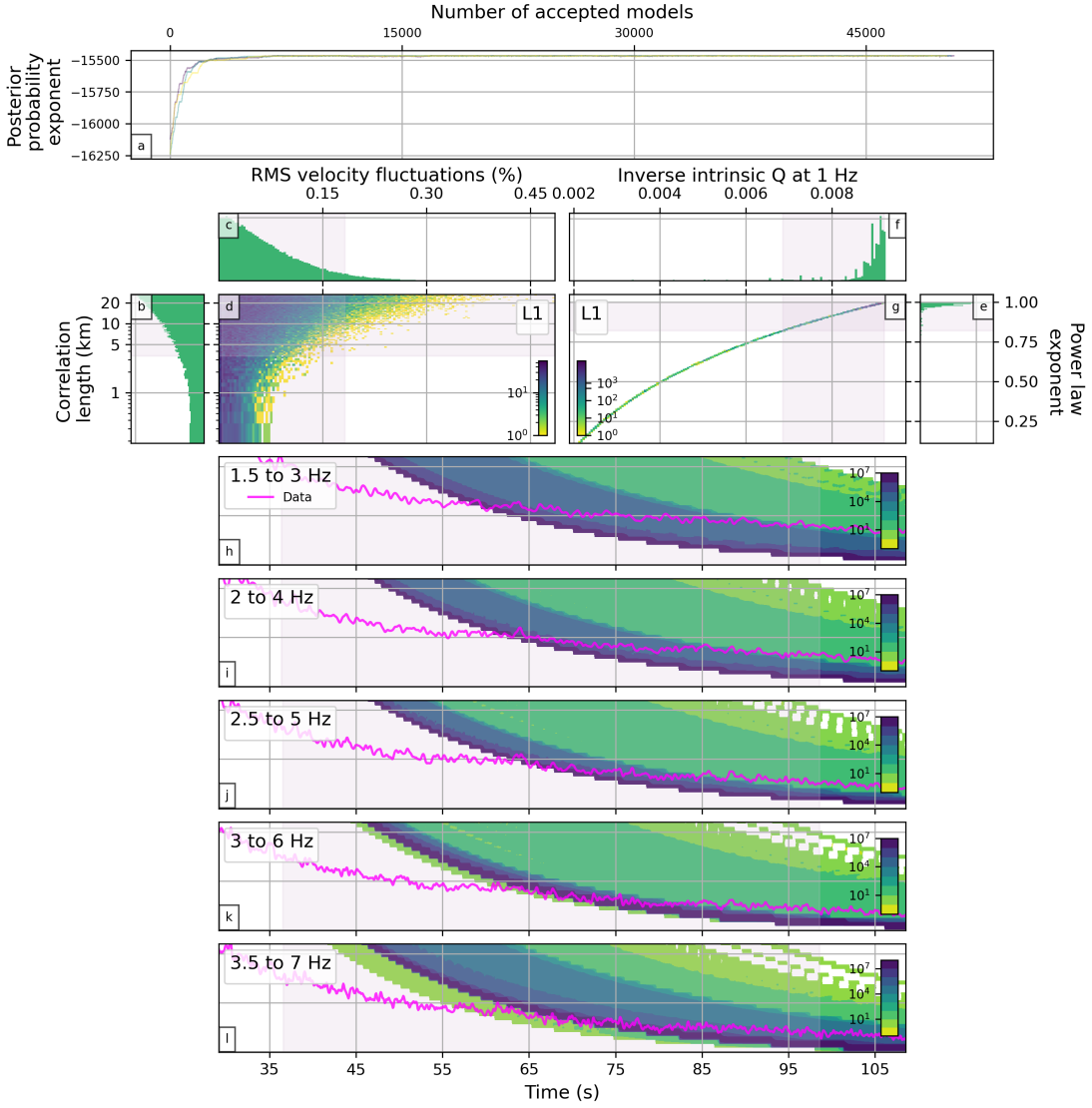

Figure A89: As Fig. 5.4, but for TXAR and a 1-layer model that only includes the crust.

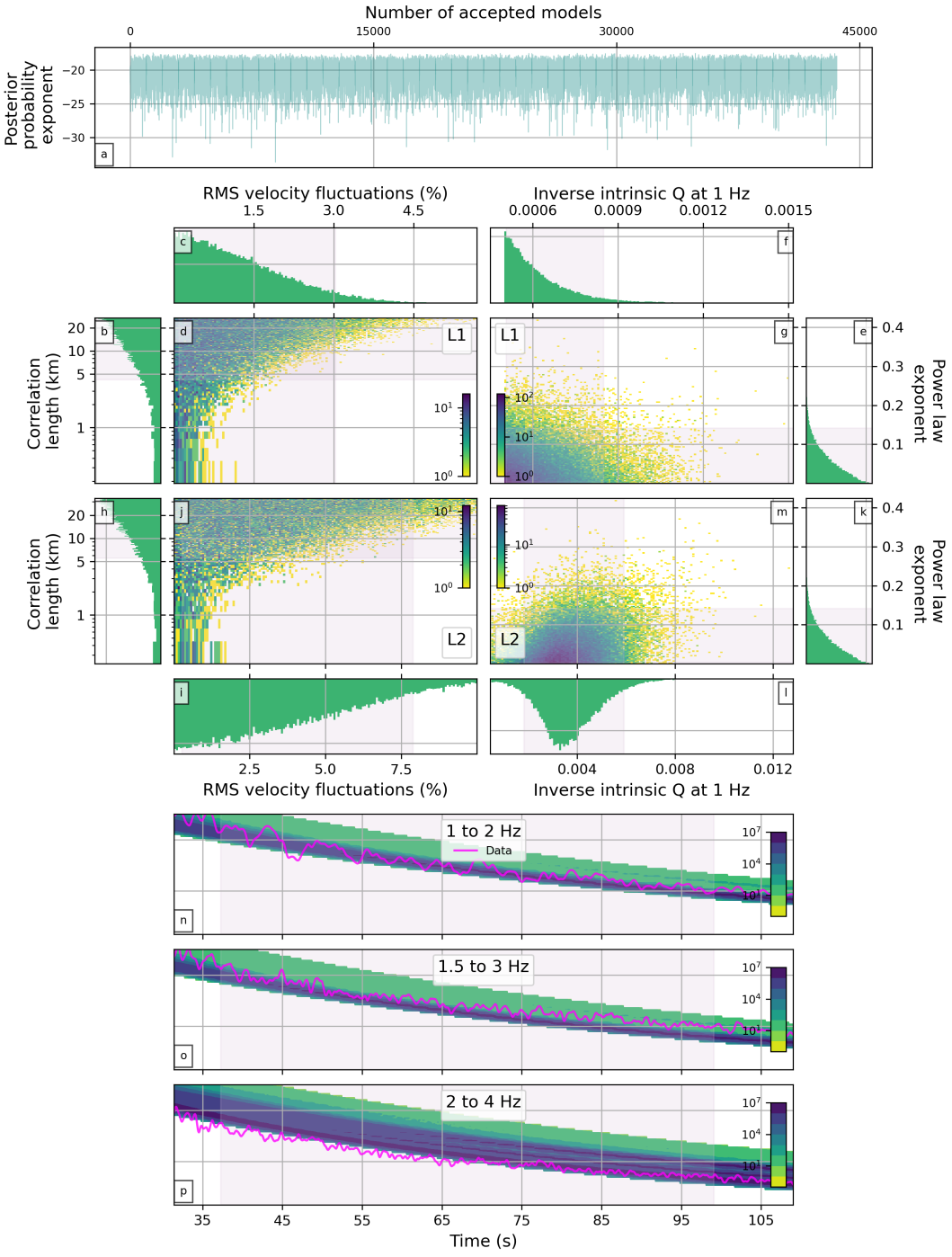

Figure A90: Summary of the results of the inversion of TXAR data using the E-EFMD approach with a 2-layer model and frequency bands C–E from Table 2.3. Panel content is as in Fig. A24.

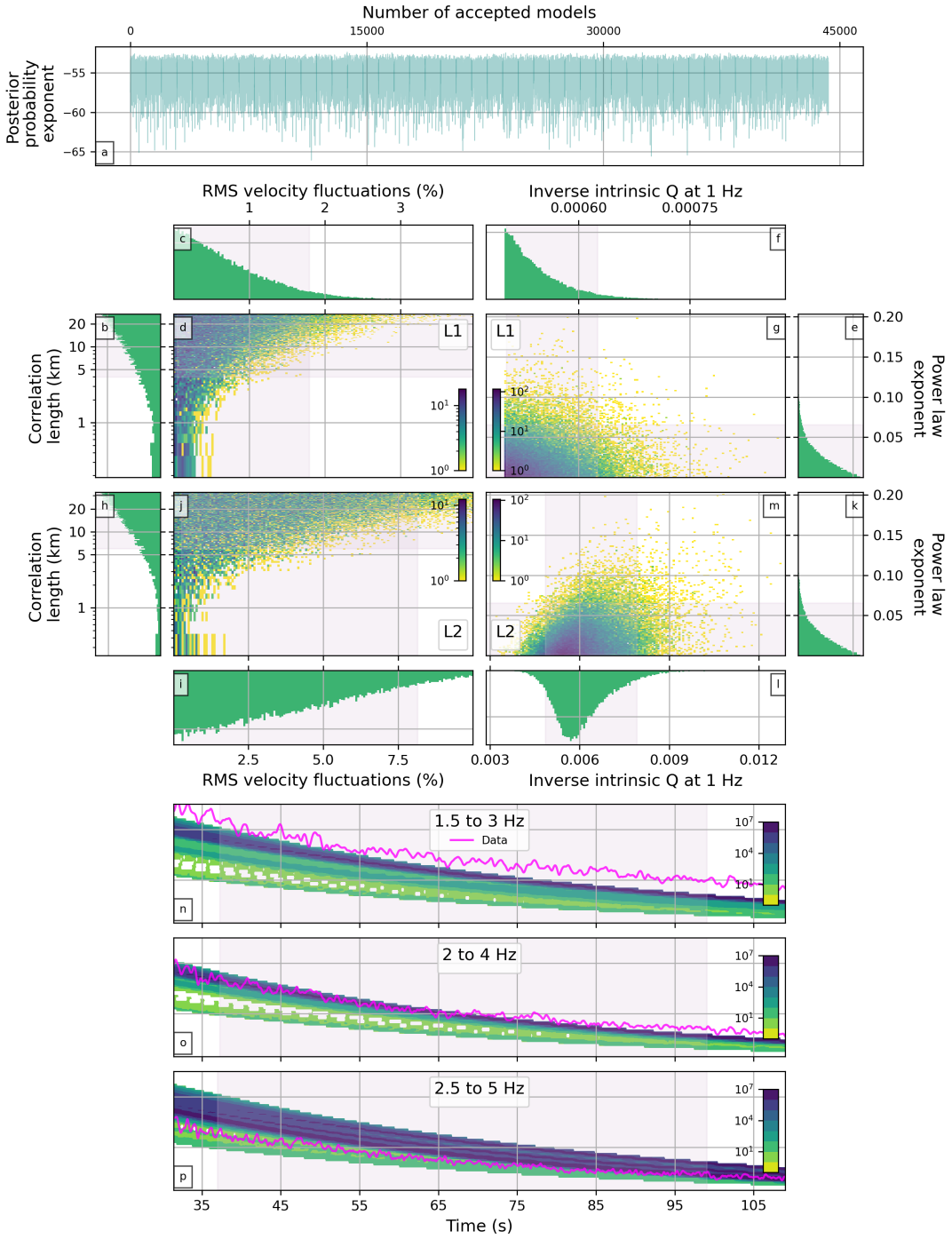

Figure A91: As Fig. A90 but for frequency bands D–F from Table 2.3.

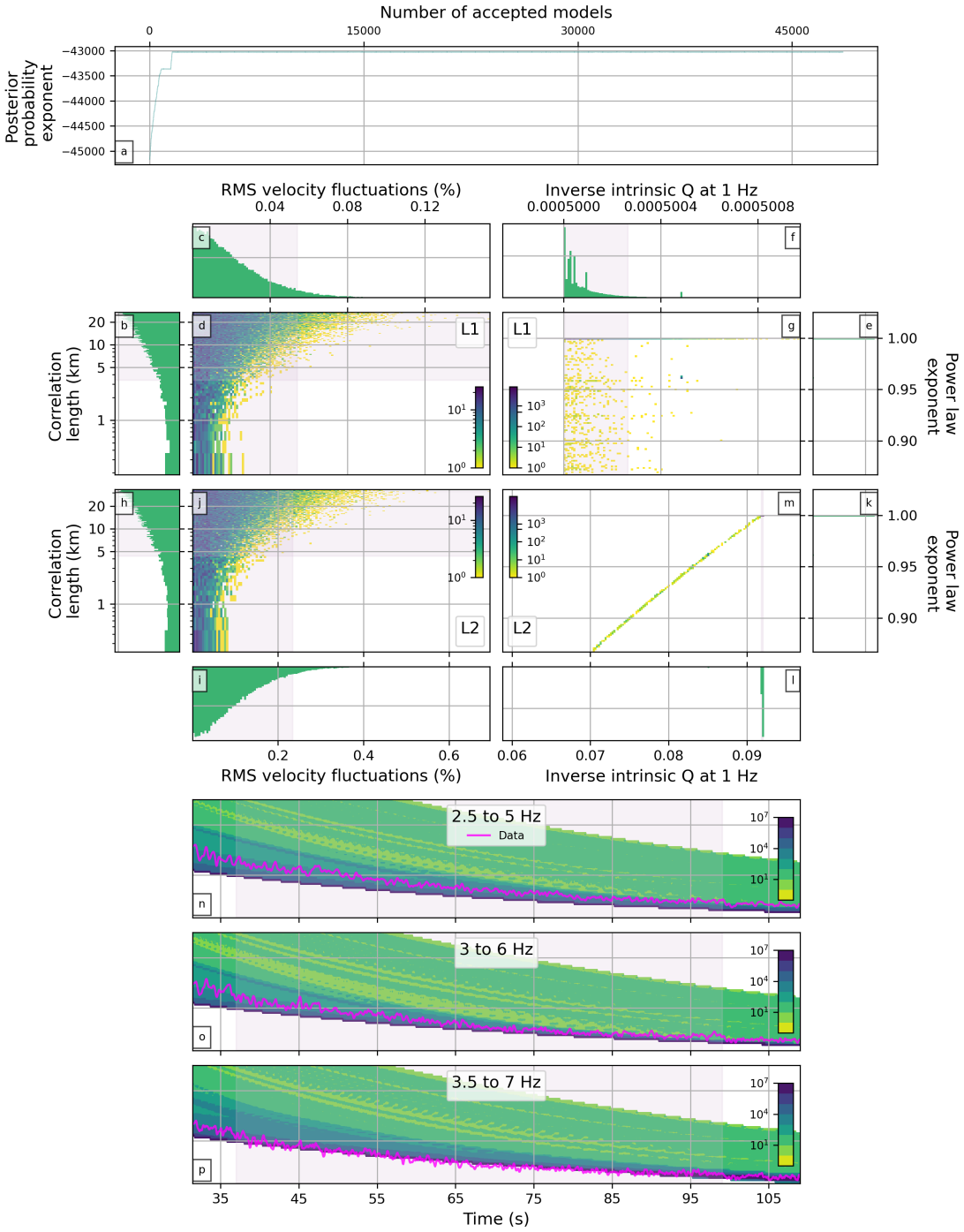

Figure A92: As Fig. A90 but for frequency bands F–H from Table 2.3.

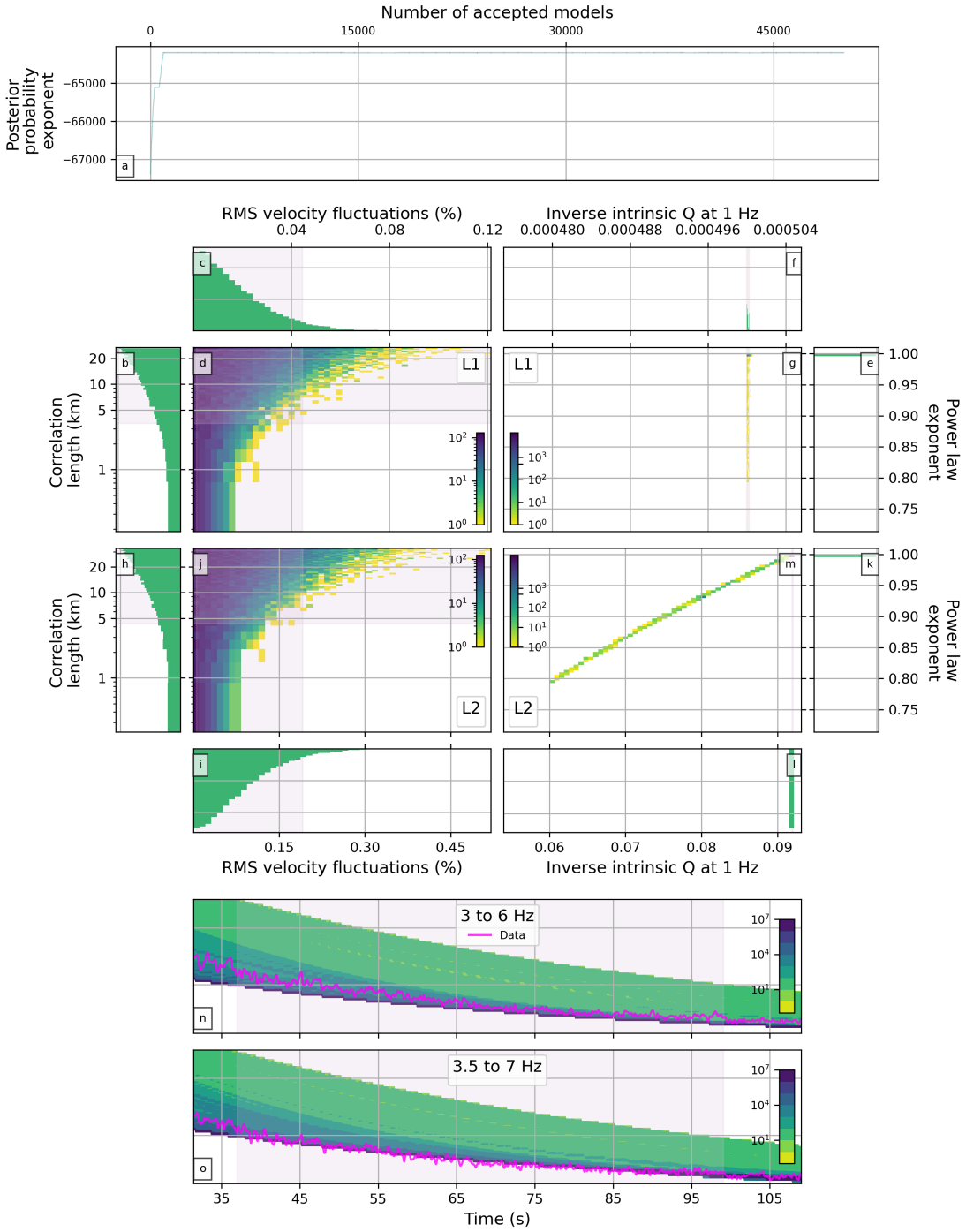

Figure A93: As Fig. A90 but for frequency bands G–H from Table 2.3.

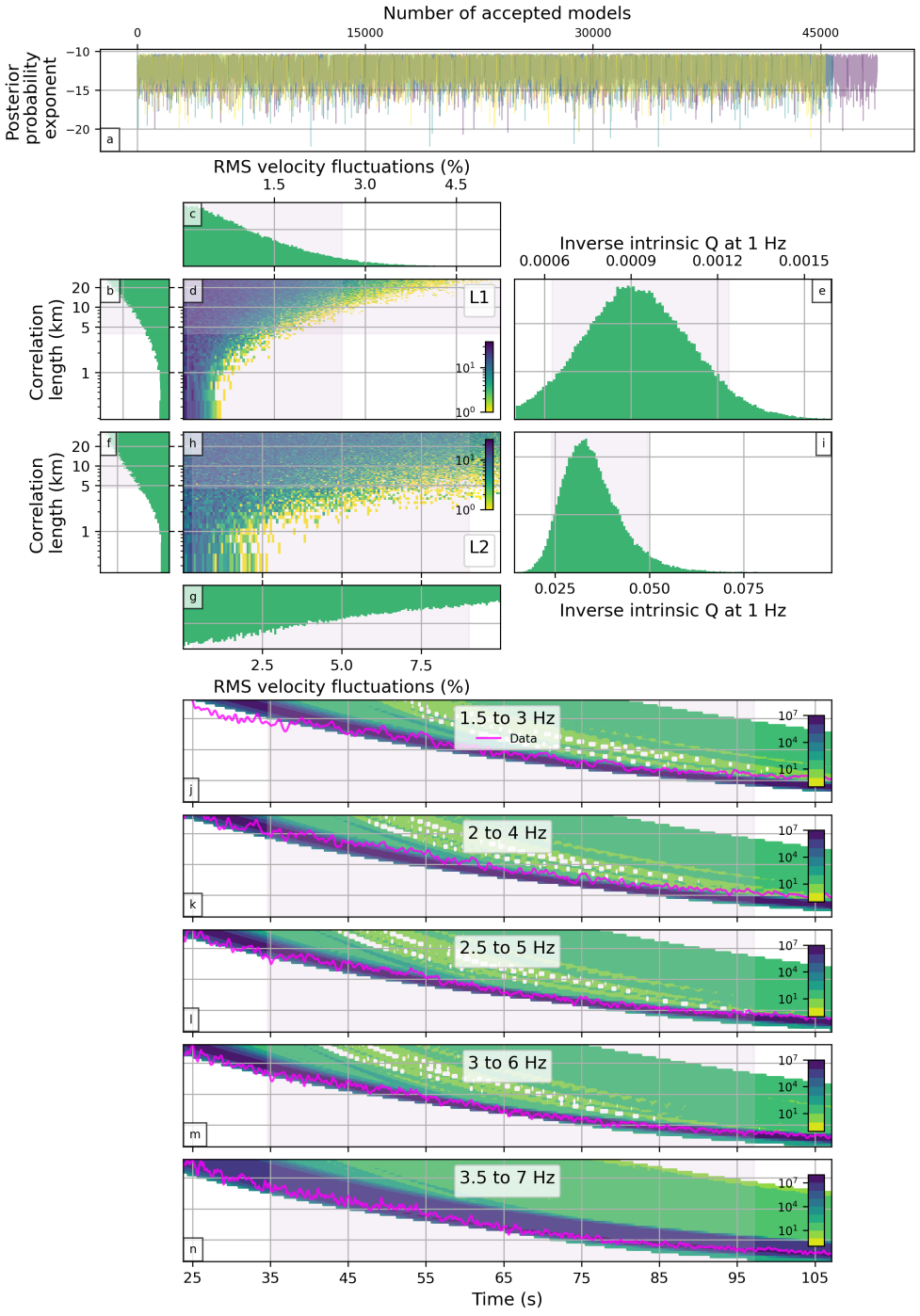

Figure A94: Summary of the results obtained from the E-EFMD algorithm in its alternative implementation for fixed α for ILAR and a 2-layer model. Panels content is as in A24.

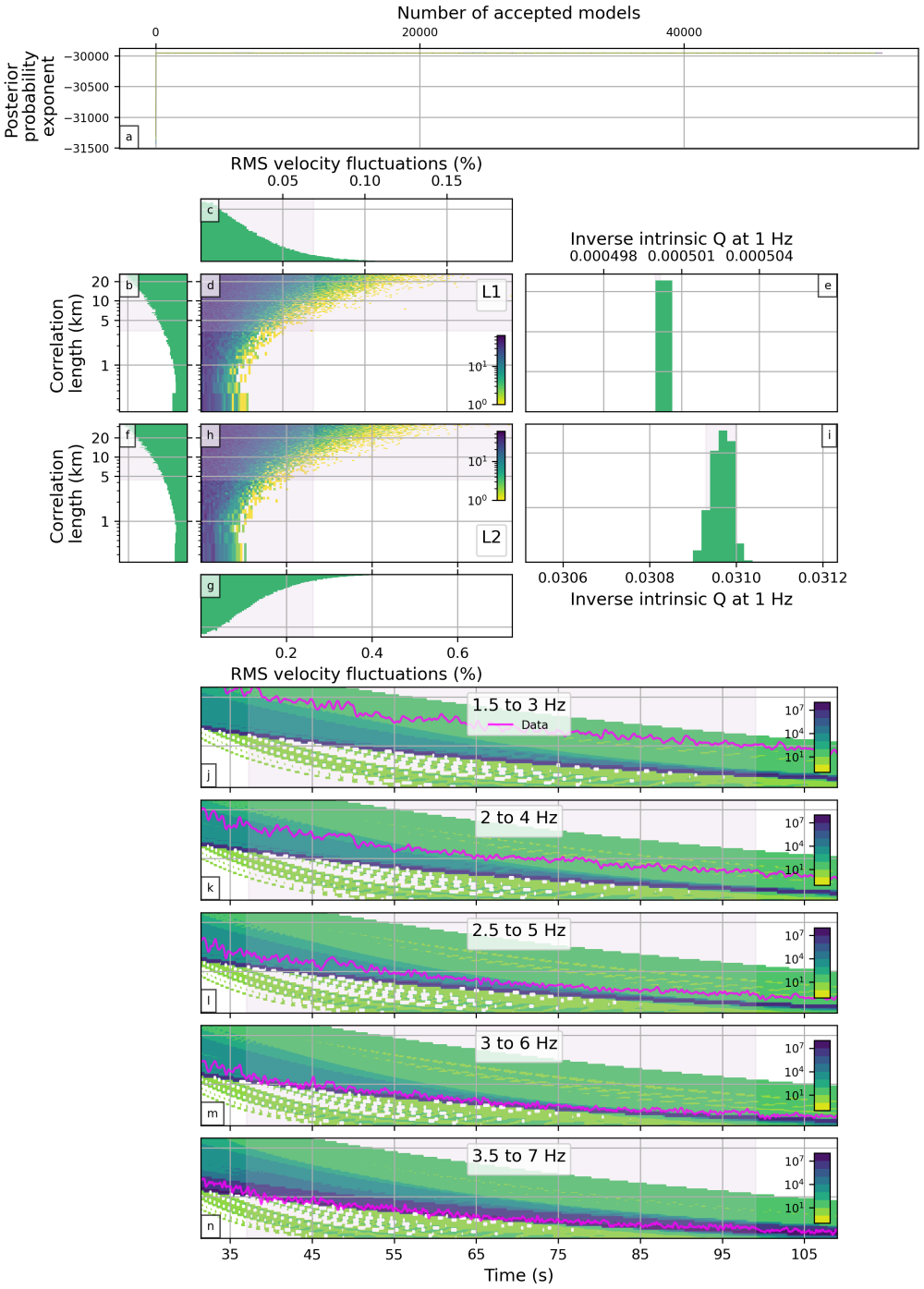

Figure A95: As Figl. A94 but for TXAR.

E-EFMD Bayesian inversion results samples for IMS stations

Samples of the E-EFMD results help analyse the behaviour of the algorithm and study the trade-offs between the parameters. Figures in this section complement those in Section 5.2.

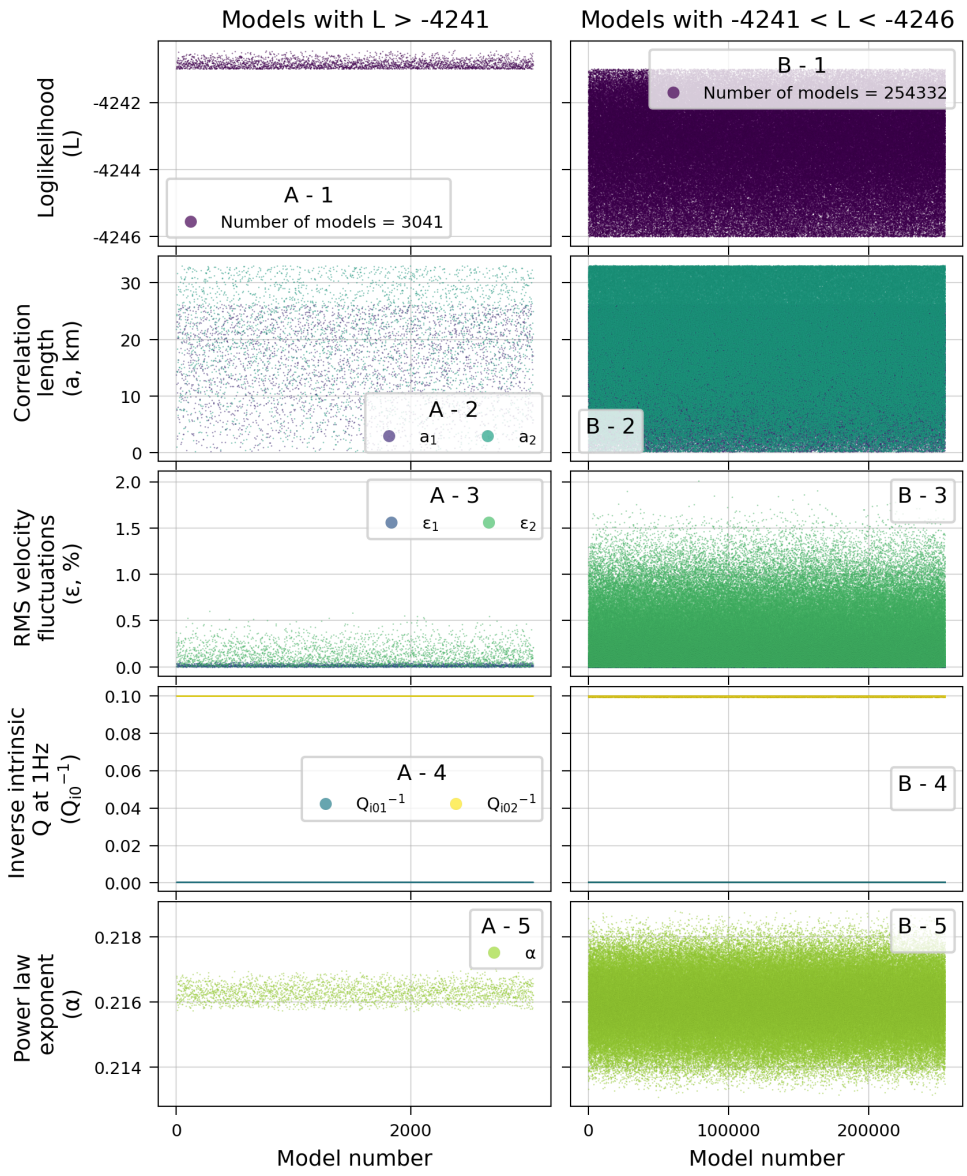

Figure A96: Samples of the E-EFMD results for PDAR and the 2-layer model. Panels A1–A5 contain the loglikelihood (L), correlation length (a), RMS velocity fluctuation (ε), inverse intrinsic quality factor at 1 Hz (Q_{i0}^{-1}) and power law exponent (α) for the models with the highest loglikelihood found during the inversions ($L > -4241$ in this case), as well as the input parameter values in each case. Panels B1–B5 have the same content, but for models with $-4241 > L > -4246$.

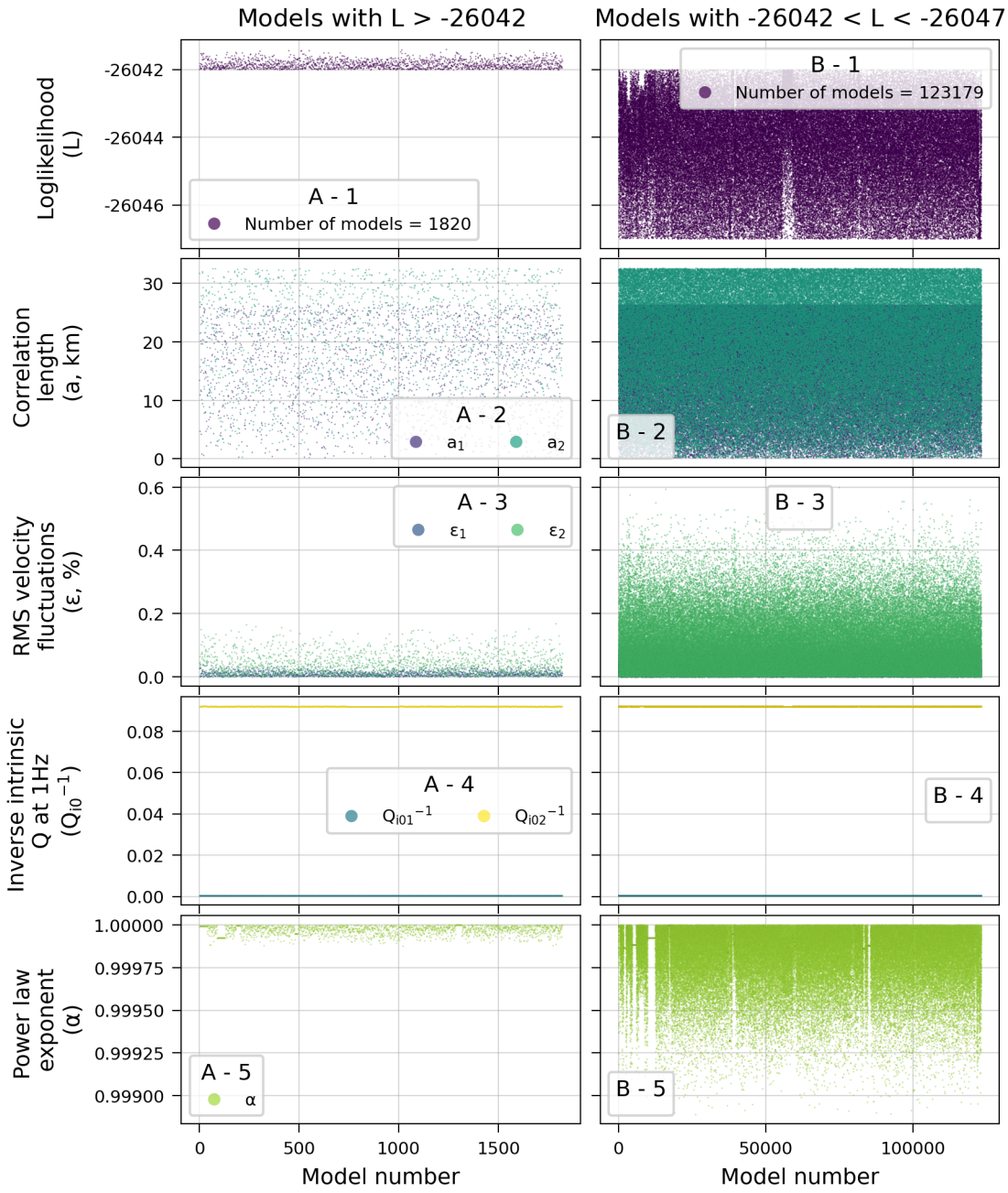

Figure A97: As Fig. A96 but for TXAR.

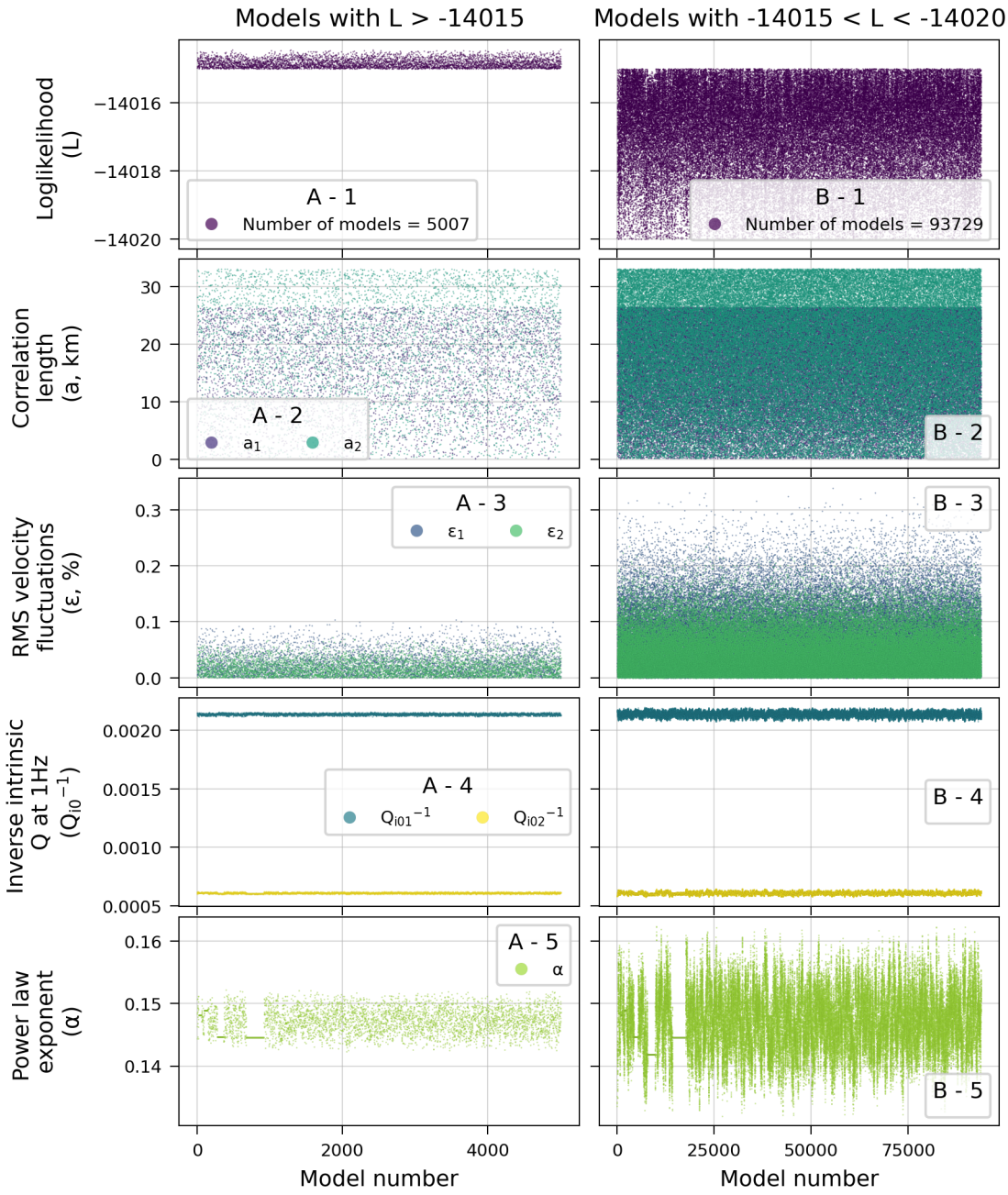

Figure A98: As Fig. A96 but for YKA.

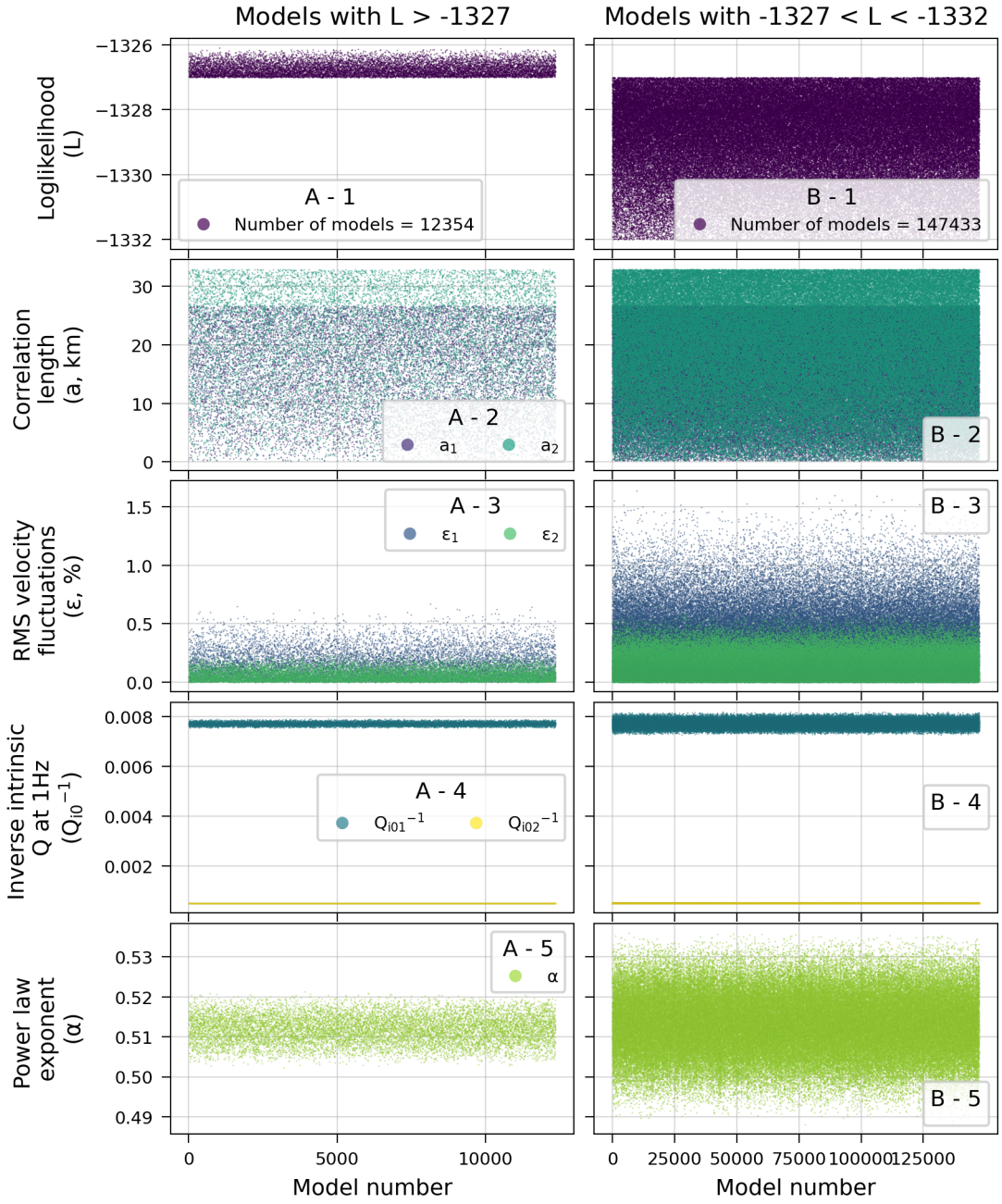

Figure A99: As Fig. A96 but for BOSA.

A.6 E-EFMD single frequency inversion results

In Chapter 5, I discuss an alternative implementation to the E-EFMD in which inversions are carried out for each individual frequency band without assuming any specific frequency dependence of the intrinsic quality factor. The figures in this section help complement that discussion.

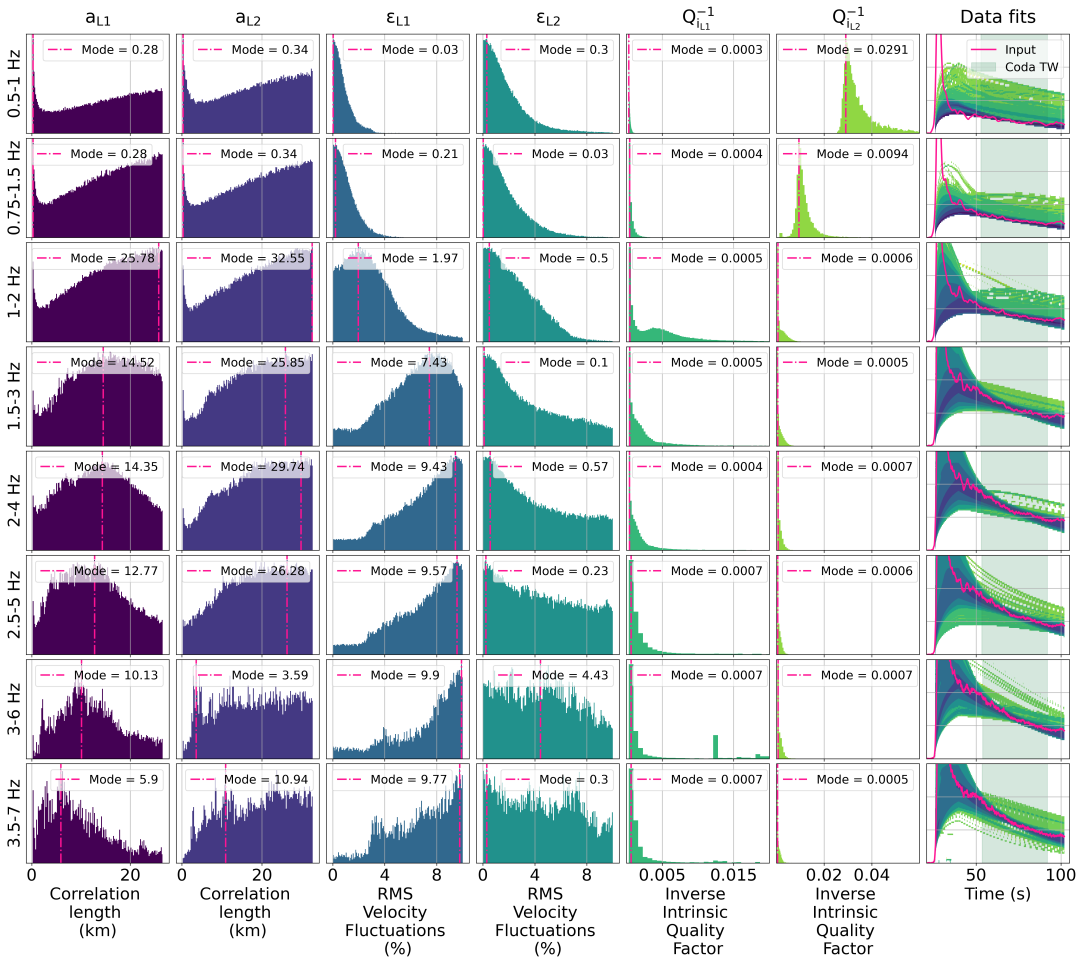

Figure A100: Results from the E-EFMD single frequency inversions for ASAR. Panels in each row contain the posterior PDFs for each parameter in the 2-layer model, as well as the fits to the data envelope for each of the frequency bands in Table 2.3. Modes for each parameter have been included in the legends for further reference.

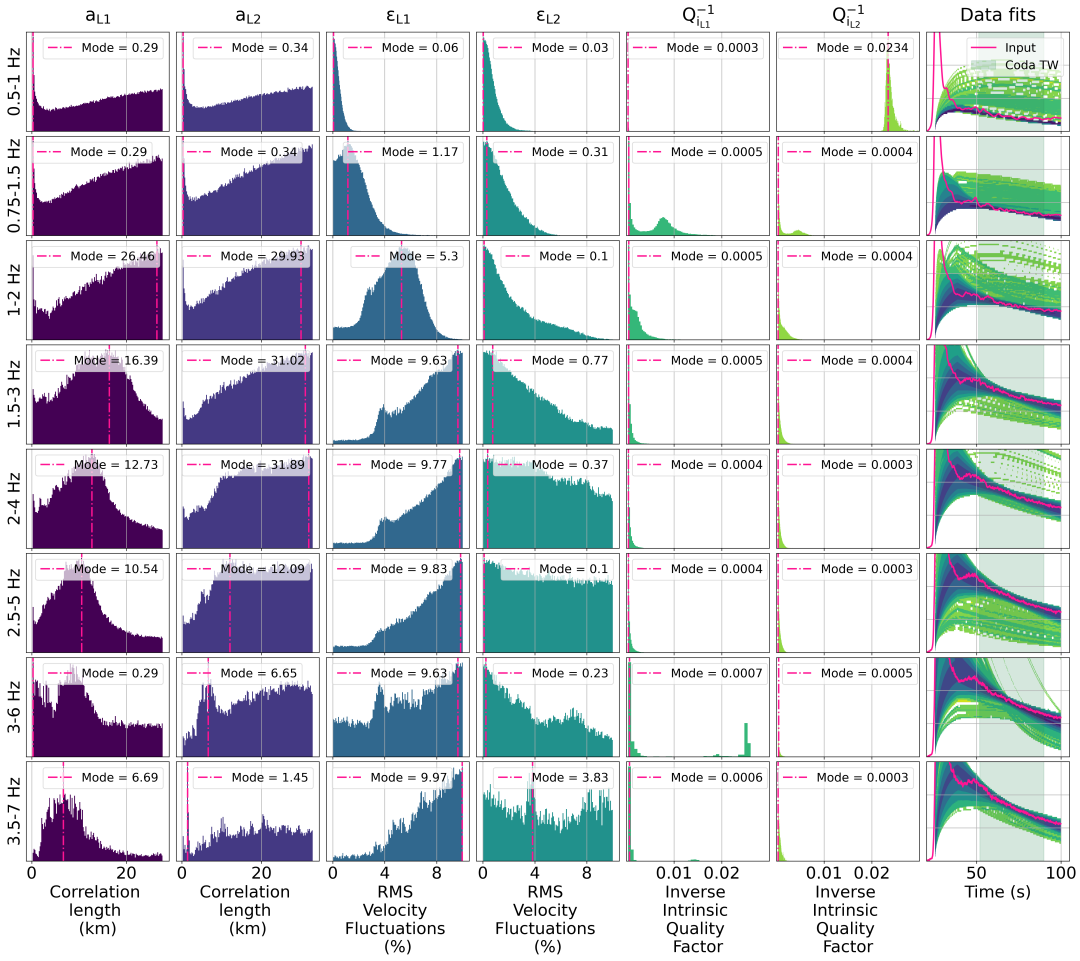

Figure A101: As Fig. A100 but for WRA.

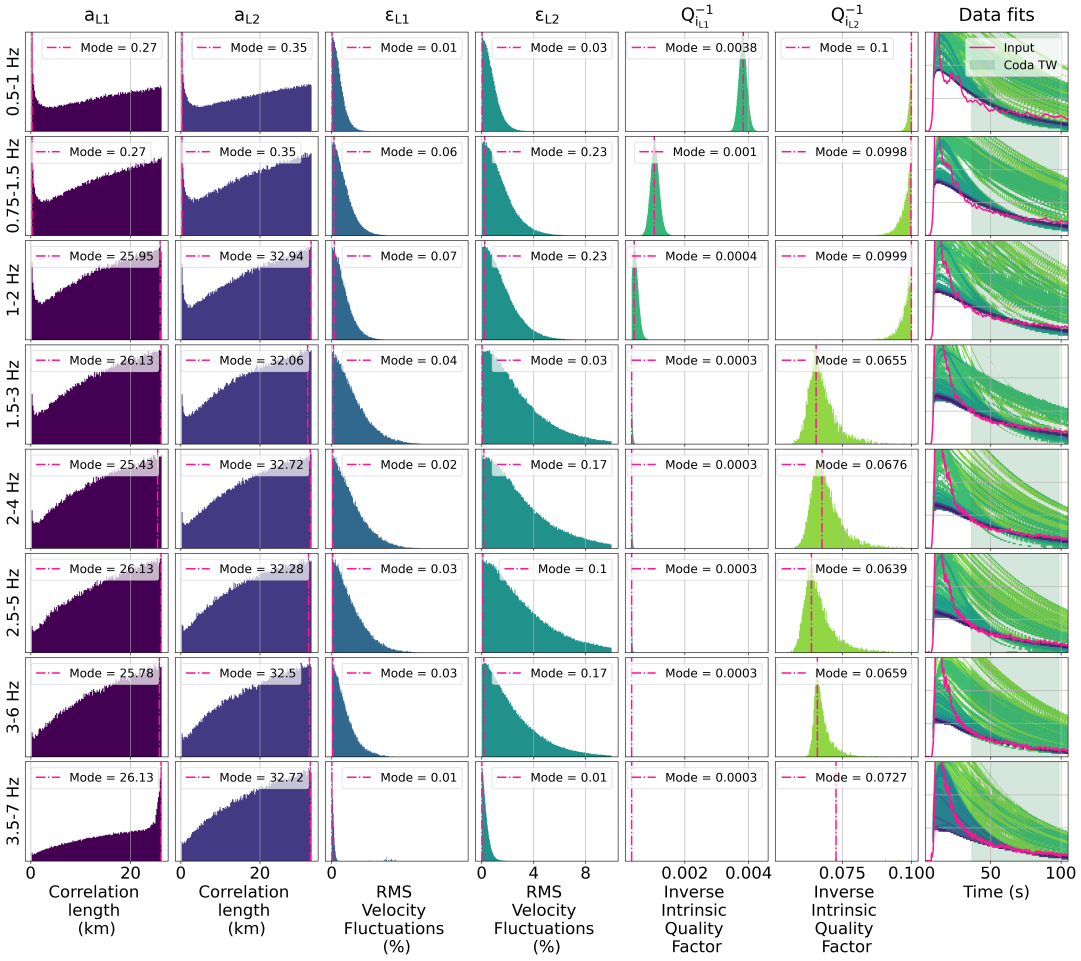

Figure A102: As Fig. A100 but for PDAR.

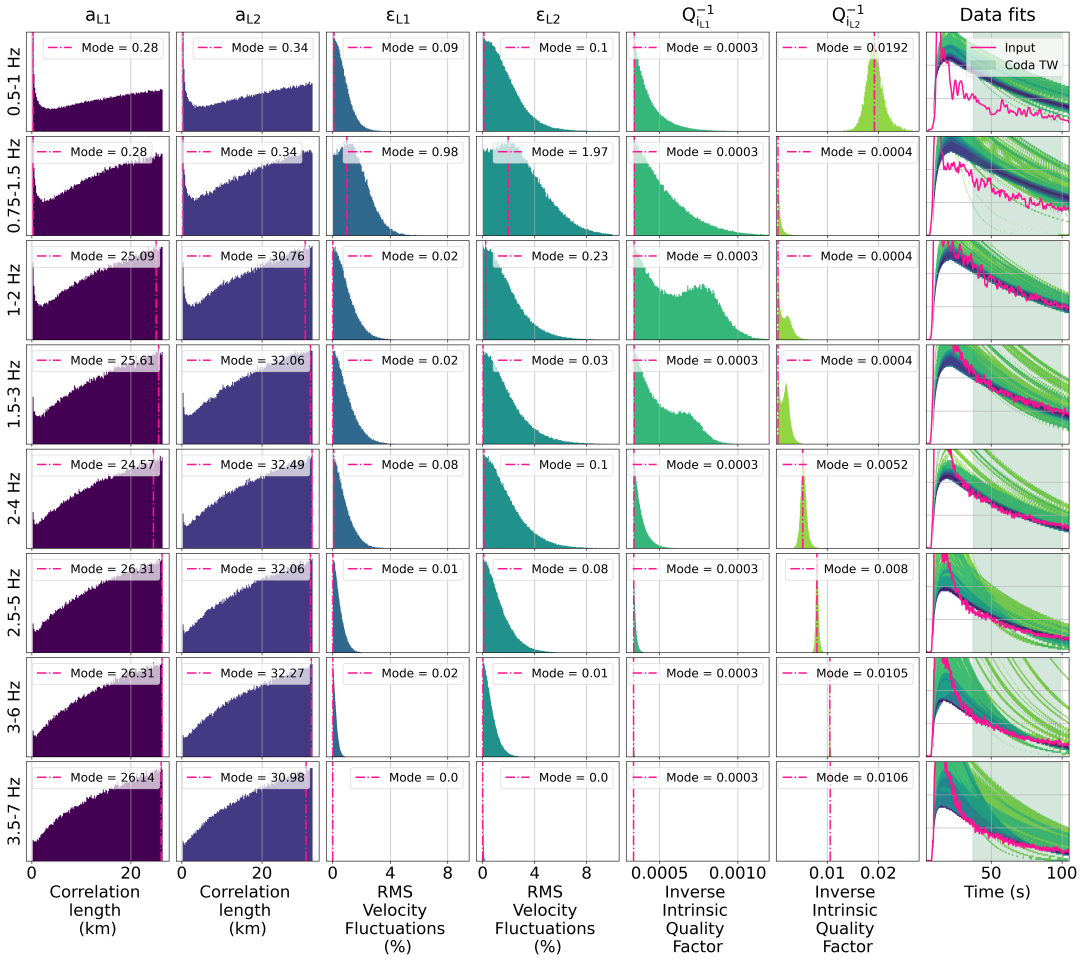

Figure A103: As Fig. A100 but for TXAR.

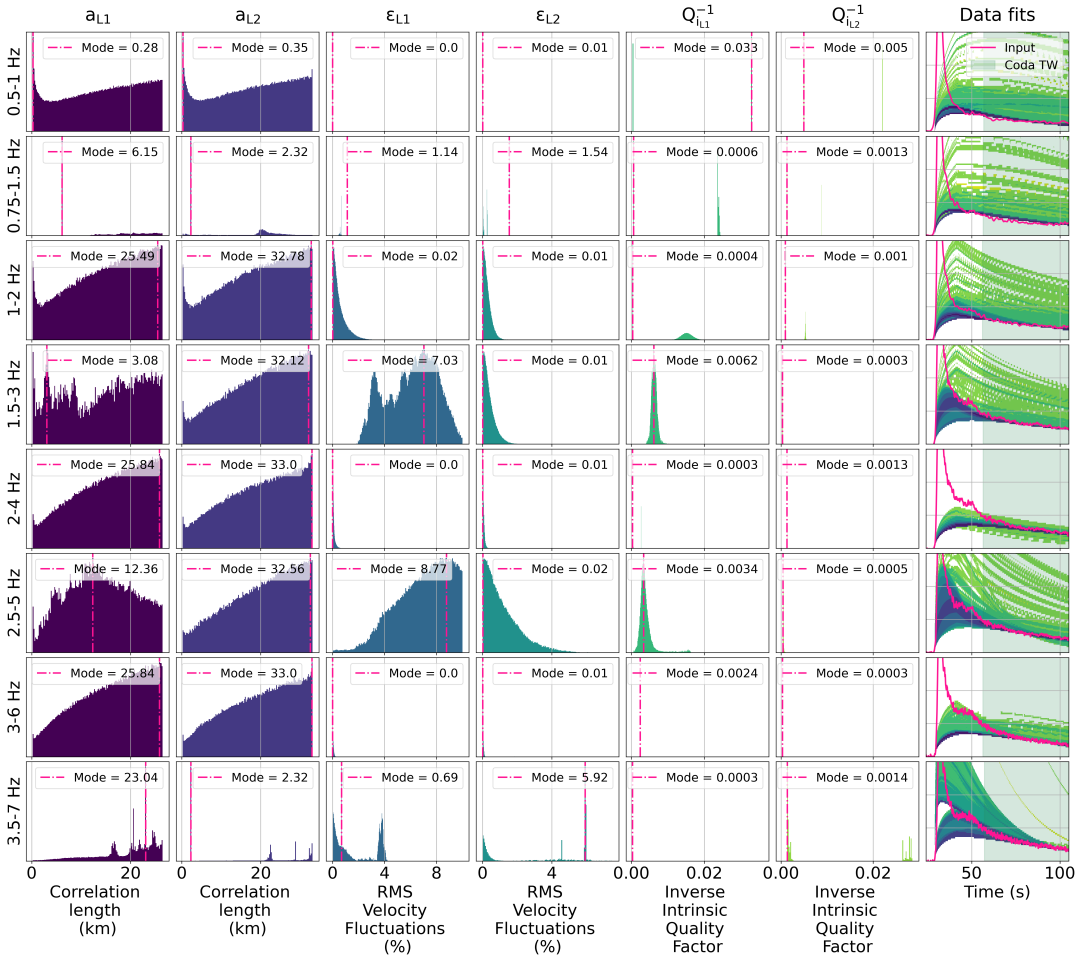

Figure A104: As Fig. A100 but for YKA.

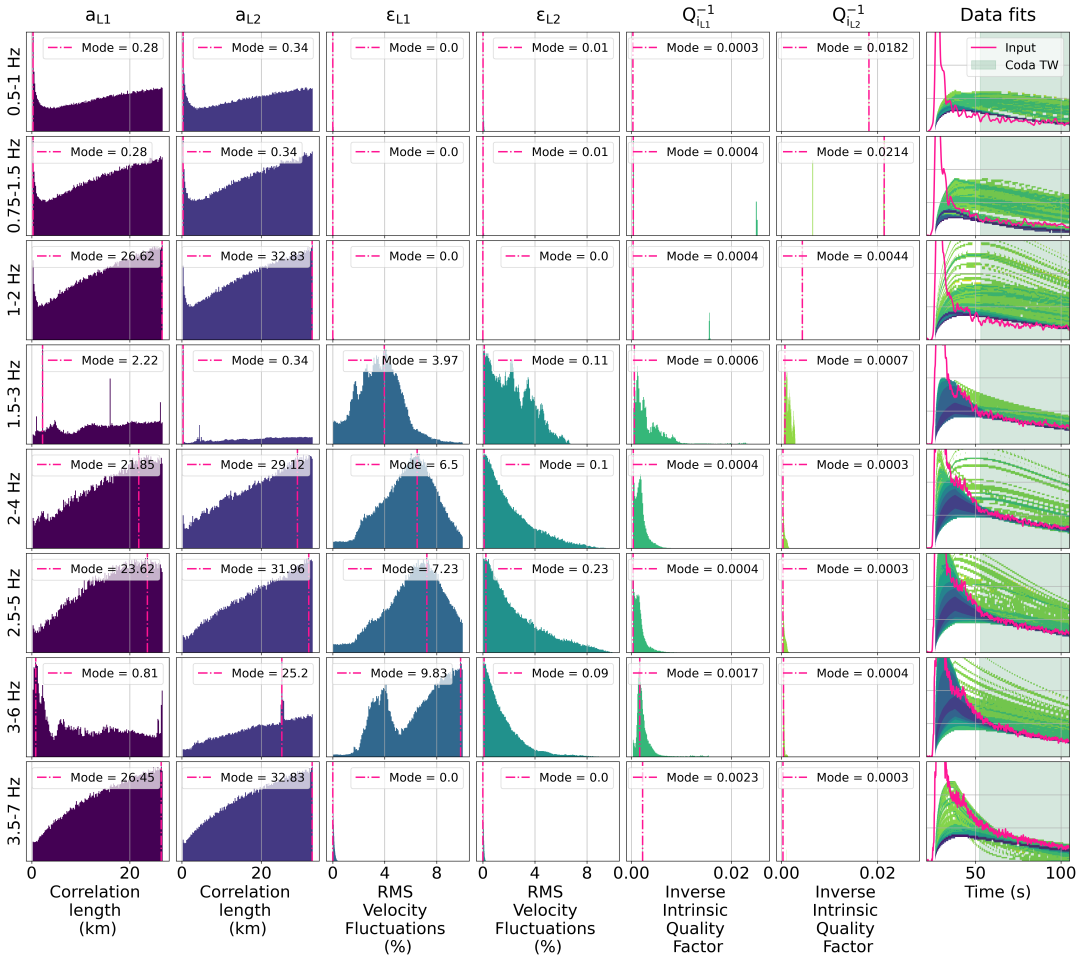

Figure A105: As Fig. A100 but for BOSA.

A.7 EFMD IMS inversions complementary results

A.7.1 EFM complementary results

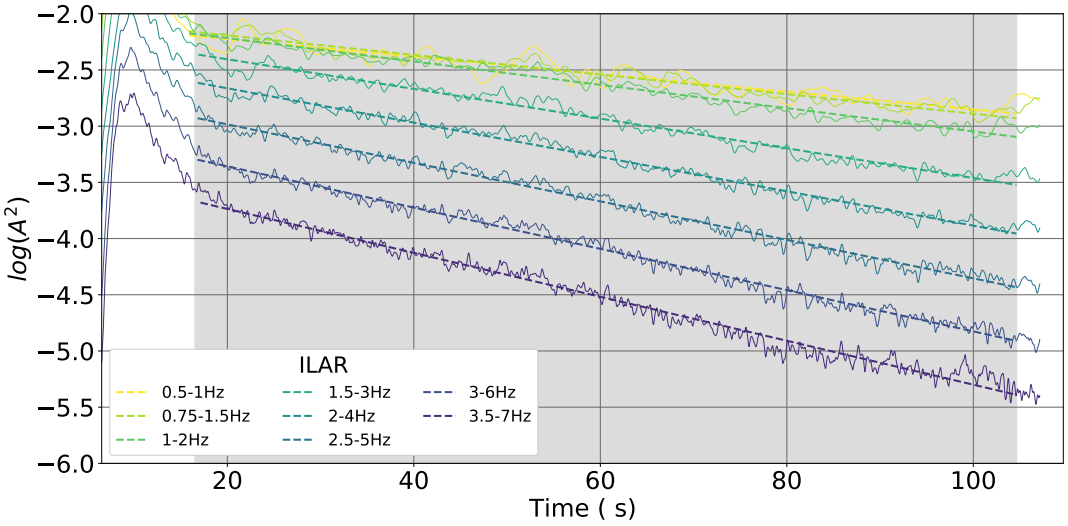

Figure A106: Linear fit of the logarithm of the squared normalised coda envelopes for all frequency bands and array ILAR, as described in Section 2.1.1. The shaded area represents the maximum time window used for the fits. Solid lines show my data envelopes, and dashed lines the results of the least-squares linear fitting.

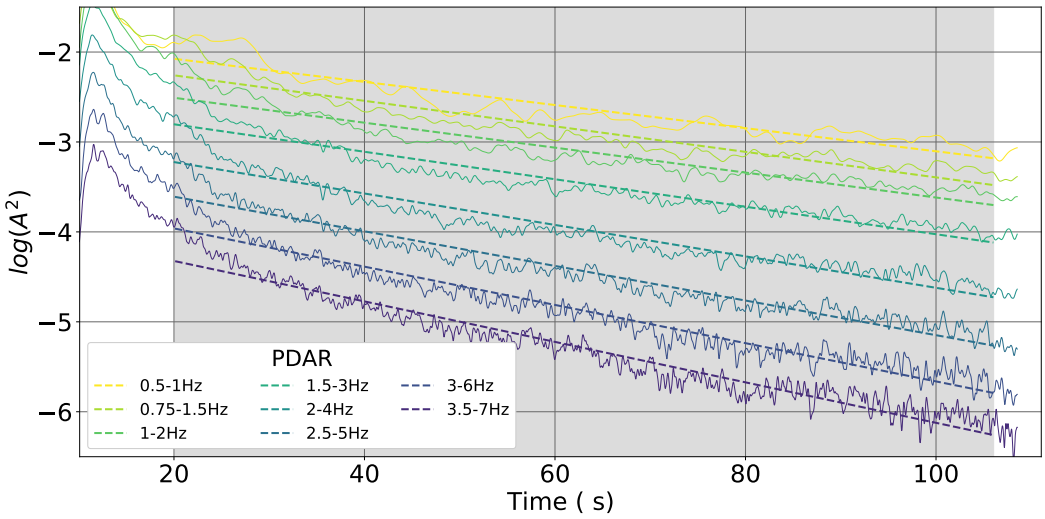

Figure A107: As Fig. A106, but for PDAR.

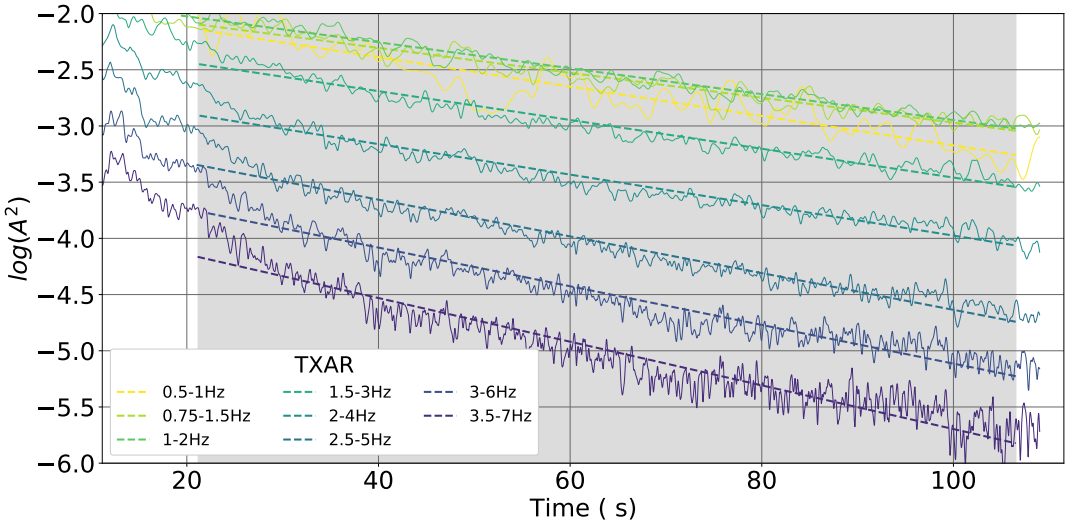

Figure A108: As Fig. A106, but for TXAR.

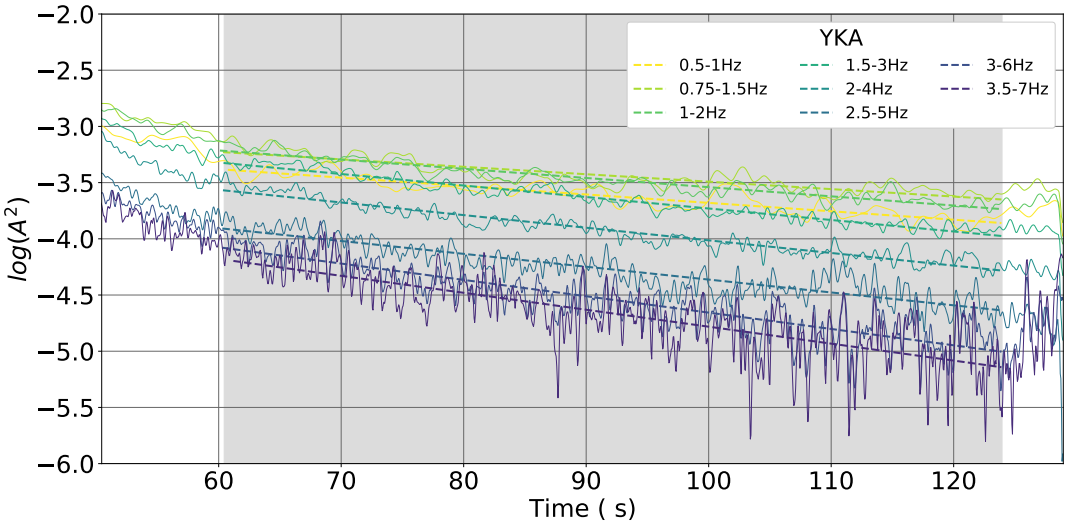

Figure A109: As Fig. A106, but for YKA.

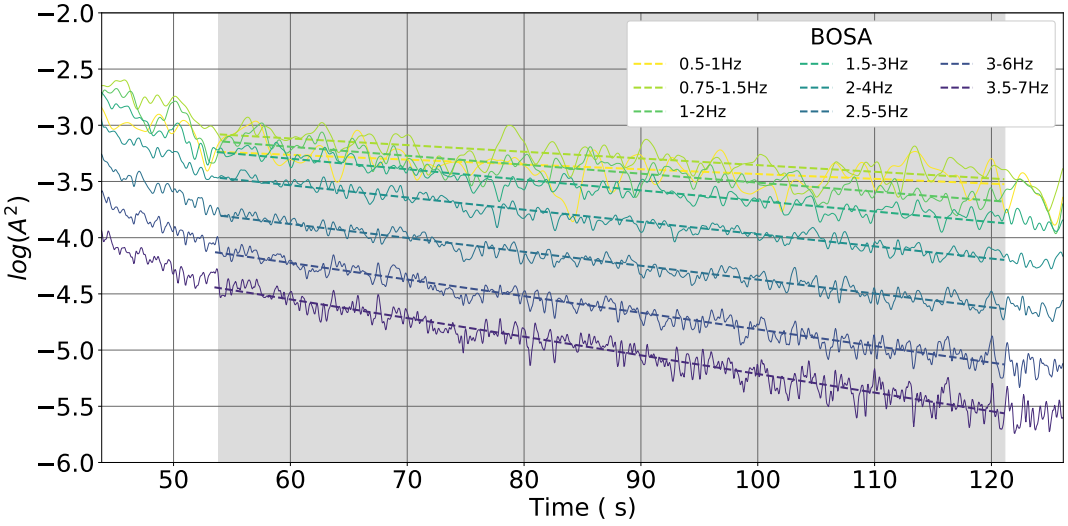

Figure A110: As Fig. A110, but for BOSA.

A.7.2 EFMD complementary results

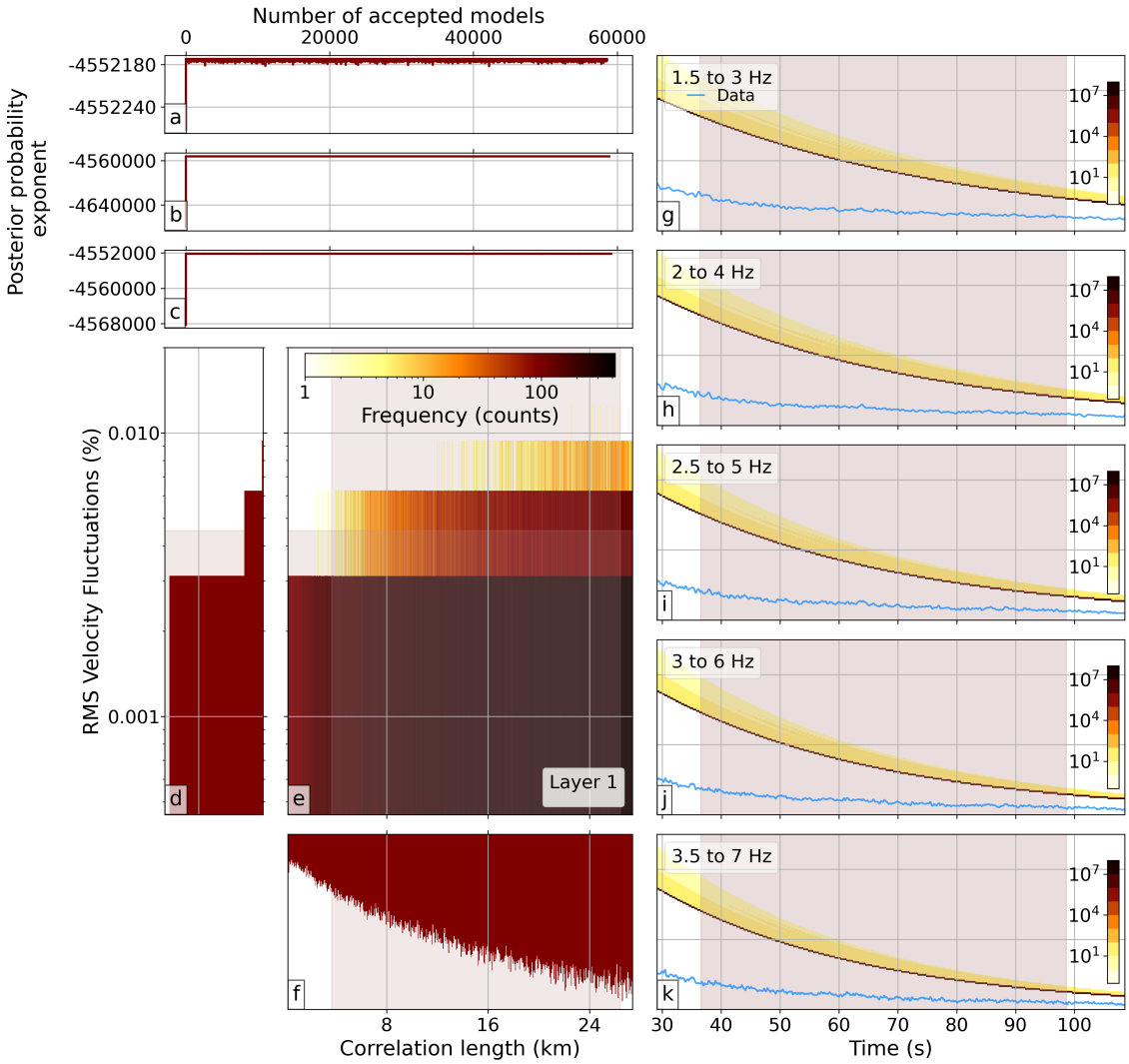

Figure A111: EFMD results summary for PDAR, the 1-layer model and frequency bands D–H from Table 2.3. Panel content is as in Fig. 3.12.

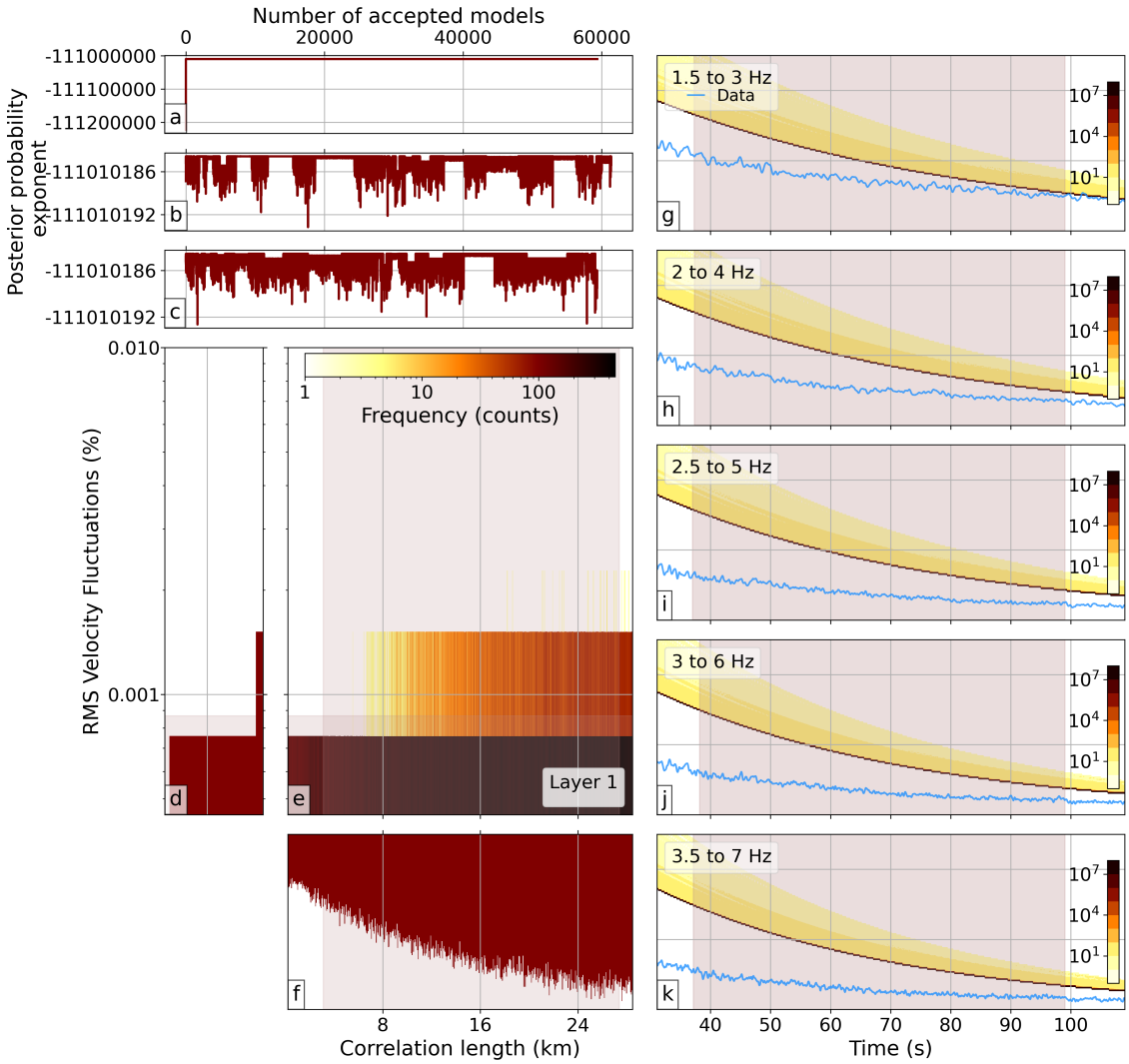

Figure A112: Same as Fig. 5.16 but for TXAR.

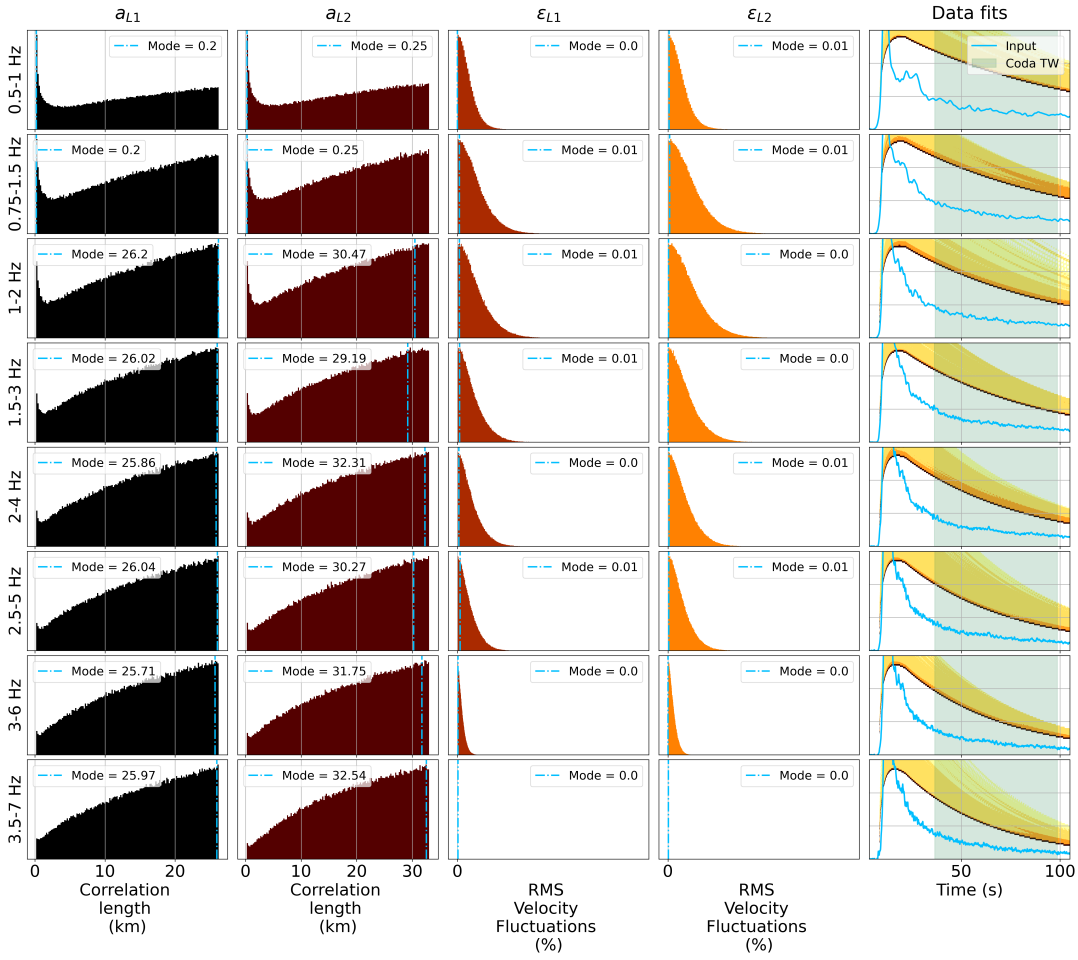

Figure A113: Results from the EFMD single frequency inversions for PDAR. Panels in each row contain the posterior PDFs for each parameter in the 2-layer model, as well as the fits to the data envelope for each of the frequency bands in Table 2.3. Modes for each parameter have been included in the legends for further reference.

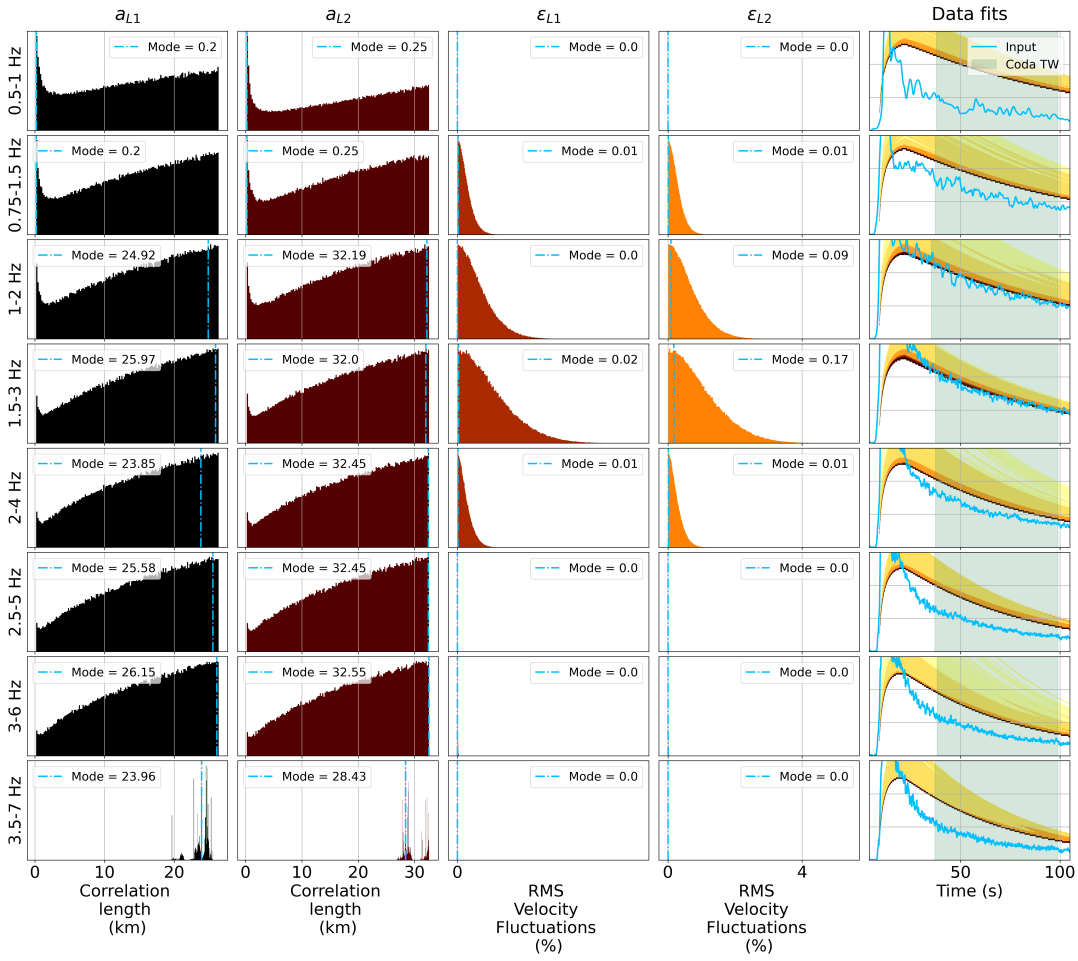

Figure A114: As Fig. 5.12 but for TXAR.

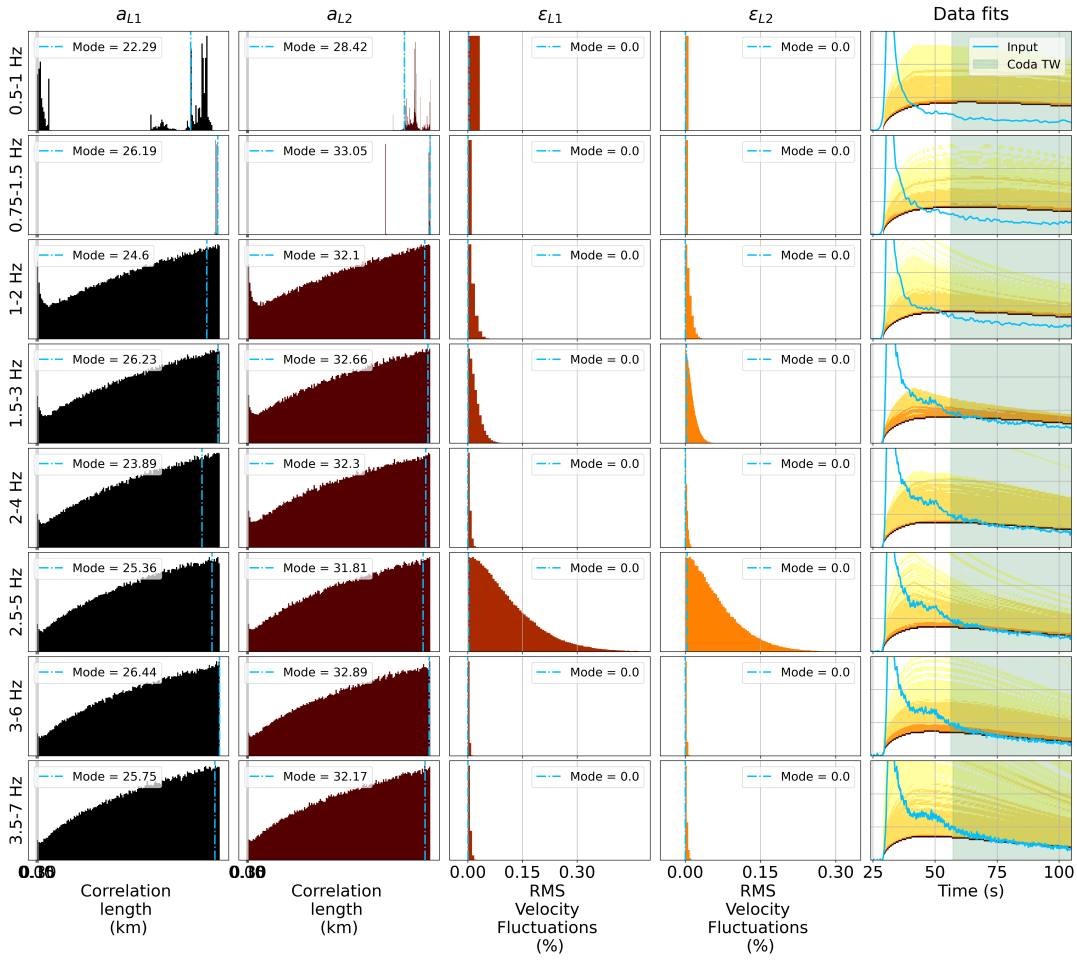

Figure A115: As Fig. 5.12 but for YKA.